This electronic thesis or dissertation has been downloaded from Explore Bristol Research, http://research-information.bristol.ac.uk

Author:
Harding, Lottie M

Title:
Evaluating the corrosion behaviour of uranium silicide phases

an advanced technology fuel study

General rights
Access to the thesis is subject to the Creative Commons Attribution - NonCommercial-No Derivatives 4.0 International Public License. A copy of this may be found at https://creativecommons.org/licenses/by-nc-nd/4.0/legalcode This license sets out your rights and the restrictions that apply to your access to the thesis so it is important you read this before proceeding.

Take down policy
Some pages of this thesis may have been removed for copyright restrictions prior to having it been deposited in Explore Bristol Research. However, if you have discovered material within the thesis that you consider to be unlawful e.g. breaches of copyright (either yours or that of a third party) or any other law, including but not limited to those relating to patent, trademark, confidentiality, data protection, obscenity, defamation, libel, then please contact collections-metadata@bristol.ac.uk and include the following information in your message:

- Your contact details
- Bibliographic details for the item, including a URL
- An outline nature of the complaint

Your claim will be investigated and, where appropriate, the item in question will be removed from public view as soon as possible.

Evaluating the Corrosion Behaviour of Uranium Silicide Phases

An Advanced Technology Fuel Study

By

LOTTIE M HARDING

School of Physics
UNIVERSITY OF BRISTOL

A dissertation submitted to the University of Bristol in accordance with the requirements of the degree of DOCTOR OF PHILOSOPHY in the School of Physics.

DECEMBER 2021

Word count: ~ 65000

Abstract

Advanced technology fuels (ATFs) are key in the drive to improve the overall performance and safety in the nuclear industry. The intermetallic uranium silicide phases are of significant interest to the nuclear fuel cycle, with three of the stoichiometric phases, U_3Si, U_3Si_2, and U_3Si_5 being highlighted as ATFs. These phases have the potential to offer higher thermal conductivities and uranium densities when compared to the widely used UO_2. For these phases to be implemented into the nuclear fuel cycle, the understanding of these materials must be extended across the entire uranium-silicon phase diagram. This will highlight how inclusions of secondary phases that may form as a result of the bulk fabrication process could alter the behaviour of the main fuel compound. Thin films provide idealised samples that are well suited for single parameter investigations. Epitaxial U_3Si, U_3Si_5, $\alpha-USi_2$, and USi_3, alongside poly-crystalline U_3Si_2 have been engineered for the first time using DC magnetron sputtering, allowing for novel measurements to be conducted on these materials. Characterisation of these phases using x-ray diffraction and x-ray photoelectron spectroscopy have provided information about the structural and chemical nature of each compound. X-ray photoelectron spectroscopy provided a unique insight into the chemical bonding and stoichiometry of each uranium silicide phase, presenting the metallic nature of these compounds, alongside their unique U:Si ratios using the U-4f and Si-2s core levels. Thin films also provide excellent samples upon which surface sensitive investigations can be conducted. Here, the ambient surface oxidation in air of each compound is presented, from which the results indicated the preferential oxidation of uranium sites, allowing for the formation of silicon-rich phases within the native oxide. The aqueous corrosion of uranium silicides within H_2O and H_2O_2 is also considered. These experiments provided further understanding of the preferential oxidation model, with indication that this mechanism applies to uranium silicides within aqueous environments. Finally, the implications of the results collected from each uranium silicide phase regarding its application as a nuclear fuel candidate are considered.

The FCC won't let me be...- *M. Mathers et al.,* 2002 [1].

Dedication and Acknowledgements

I would like to firstly thank the many people who have provided me with, guidance, support, and laughter over the course of my PhD. I have spent the past four years being surrounded by some of the most knowledgeable, talented, and inspiring individuals, and it has truly been an honour. You have all taught me an incredible amount, and you have all done this in your own unique ways. To everyone, past and present that reside within my research group, the **Interface Analysis Centre**, I would like to thank you all for providing me with a support, help, and *sometimes* chaos over the past four years. I would like to thank the **Engineering and Physical Sciences Research Council**, along with the **National Nuclear Laboratory** for funding and supporting this PhD project.

I would like to thank my supervisor **Ross Springell**. Spending the past five years working with you has been brilliant! You've filled the time with excellent guidance, relentless bad jokes, and lots of coffee breaks. So, thank you for being my supervisor, but mostly, thank you for being my friend. To **Gerry Lander**, thank you for your invaluable guidance. A special thanks to my industrial supervisor **Dave Goddard** for your insight and understanding. I would like to thank and acknowledge the team at the nanoESCA Facility, **Mattia Cattelan**, **Gary Wan**, and **Jude Laverock**, for helping with XPS data collection over the many COVID lockdowns. Finally, a huge thanks to **The Thin Filmers**, Sophie, Ellie, Dan, Joe, Jacek, Angus, Beckie, Jarrod, Florence, and Phil. Finally, a thanks to whoever is reading this. I've become attached to these uranium silicide phases, so I hope you enjoy them as much as I do.

This PhD journey has allowed for many friendships to blossom, this is something I will forever be grateful for. To **Ellie**, **Sophie**, and **Kate**, my lovely galentines, I was so lucky to have the three of you by my side, thanks for always being caring and silly. To **Dan**, thanks for travelling to Idaho Falls with me for possibly the weirdest 8 weeks of our lives, you've been a great friend from the start! To **Beckie**, thanks for discussing both *Skyrim* and *Eastenders* lore, this really has kept me sane during the write-up. To **Estelle**, thanks for all the chats, dinners, and high fashion wolf fleeces. To **dEAN**, for coffees, walks, and lots of laughs. To **Robbie**, for being the true M'Lord Dungeon Master. And finally, to **DK** and **Angus** (AKA Deekz and Angoose), *man oh man* what would I do without you two!

This thesis is dedicated to the **Harding/Morris** clan. To **Mum**, **Dad**, **Be**, and **Nan** for your unconditional love and support.

Now, if you'd like to understand how I got through writing this document, please follow the link to my **Spotify Wrapped** - it will not disappoint:
https://open.spotify.com/playlist/37i9dQZF1EUMDoJuT8yJsl?si=a6367217beb34e79.

Author's declaration

I declare that the work in this dissertation was carried out in accordance with the requirements of the University's Regulations and Code of Practice for Research Degree Programmes and that it has not been submitted for any other academic award. Except where indicated by specific reference in the text, the work is the candidate's own work. Work done in collaboration with, or with the assistance of, others, is indicated as such. Any views expressed in the dissertation are those of the author.

SIGNED: .... DATE: ....

Table of Contents

Page

List of Tables **xiii**

List of Figures **xvii**

1 Introduction **1**

1.1 The Significance of Nuclear Power 2

1.1.1 A Brief History of Nuclear Power 2

1.1.2 Reactor Design and Development 3

1.1.3 Nuclear Accidents and their Consequences 8

1.2 Advanced Technology Fuels 11

2 Uranium Silicide as a Nuclear Fuel **15**

2.1 The Uranium-Silicon System 15

2.1.1 The Chosen Fuels 17

2.2 Oxidation of Uranium Silicide Fuels 22

2.2.1 Oxidation Testing 22

2.3 Interaction with aqueous environments 28

2.4 Thesis Outline 33

3 Analytical Techniques **35**

3.1 X-rays 35

3.2 Interactions between X-rays and Matter 36

3.2.1 Sources 37

3.3 X-ray Diffraction 39

3.3.1 XRD Theory 39

3.3.2 XRD Measurement Types 44

3.3.3 XRD Data Analysis 50

3.4 X-ray Reflectivity 51

3.4.1 Theory 51

3.4.2 XRR Measurement and Analysis 60

3.5 X-ray Photoelectron Spectroscopy . . . 61
3.5.1 Theory . . . 61
3.5.2 Measurement . . . 62
3.5.3 Spectral Features . . . 65
3.5.4 Analysis . . . 67

4 Sample Growth **69**
4.1 Thin Films . . . 69
4.1.1 The Significance of Surface Research for Nuclear Materials . . . 70
4.1.2 Phase Stabilisation and the Uranium Silicide Phase Diagram . . . 71
4.2 Thin Film Fabrication . . . 72
4.2.1 Deposition Techniques . . . 73
4.2.2 DC Magnetron Sputtering . . . 74
4.2.3 Sputtering Modes . . . 75
4.2.4 Deposition Procedure . . . 78
4.2.5 List of samples used in this thesis . . . 86

5 Characterisation of Uranium Silicide Phases **89**
5.1 Understanding the U-Si phase diagram through epitaxial matching . . . 89
5.2 The structural characterisation of single phase uranium silicide surfaces . . . 90
5.2.1 Epitaxial $\mathbf{U_3Si}$ Thin Films . . . 90
5.2.2 Polycrystalline $\mathbf{U_3Si_2}$ Thin Film . . . 93
5.2.3 Epitaxial $\mathbf{U_3Si_5}$ Thin Film . . . 96
5.2.4 Epitaxial α-$\mathbf{USi_2}$ Thin Films . . . 98
5.2.5 Epitaxial $\mathbf{USi_3}$ Thin Films . . . 106
5.2.6 Discussion of Structural Characterisation . . . 110
5.2.7 Conclusions . . . 114
5.3 The Stoichiometry and Chemical Bonding of U-Si Phases . . . 116
5.4 Chemical Characterisation Results . . . 116
5.4.1 Discussion of XPS Results . . . 130
5.4.2 Conclusions . . . 137

6 The Surface Oxidation of Uranium Silicide Compounds **139**
6.1 Experimental Set-Up . . . 139
6.2 X-ray Diffraction Results . . . 141
6.2.1 U_3Si . . . 141
6.2.2 U_3Si_2 . . . 143
6.2.3 U_3Si_5 . . . 145
6.2.4 α-USi_2 . . . 146

6.2.5 USi_3 150
6.3 X-ray Photoelectron Spectroscopy Results 152
6.3.1 U_3Si 152
6.3.2 U_3Si_2 163
6.3.3 U_3Si_5 172
6.3.4 α-USi_2 181
6.3.5 USi_3 190
6.4 X-ray Reflectivity Results 200
6.4.1 U_3Si 201
6.4.2 U_3Si_2 203
6.4.3 U_3Si_5 204
6.4.4 α-USi_2 205
6.4.5 USi_3 209
6.5 Discussion of the Oxidation of U-Si phases 212
6.5.1 U_3Si 212
6.5.2 U_3Si_2 215
6.5.3 U_3Si_5 218
6.5.4 α-USi_2 220
6.5.5 USi_3 223
6.6 Conclusions 225

7 The Corrosion of Uranium Silicide Compounds 229
7.1 The Corrosion of U-Si Phases in Water 229
7.1.1 Experimental Set up 229
7.1.2 Results 230
7.2 Corrosion of U-Si phases in Hydrogen Peroxide 248
7.2.1 Experimental Set up 248
7.2.2 Results 248
7.3 Discussion of Corrosion Studies of U-Si Phases 269
7.4 Conclusions 273

8 Conclusions and Future Work 275

A Appendix A 281

Bibliography 283

List of Tables

Table **Page**

2.1 Fundamental structural properties of U-Si phases. *Formed after 120 K. 17

2.2 Fundamental properties of conventional and proposed advanced ATF fuels. * Measurement made at 1200 K. 18

3.1 Degeneracy of electron sub-shells 63

4.1 Table of samples used throughout this thesis. Samples are compared within their relative chapters. 87

5.1 Table showing crystallite size for each phase within SN1639. 95

5.2 Table of the FWHM values measured for each single crystal uranium silicide phase, alongside the FWHM of the corresponding substrate. 113

5.3 Table of the lattice parameters and unit cells for each uranium silicide, with reference to literature values. 114

5.4 Table of parameters used to fit the U-4f spectra for uranium silicide phases. T represents the asymmetric tail function applied to the metallic components of each U-4f spectra. 119

5.5 Table of parameters used to fit the Si-2s spectra for uranium silicide phases. 120

5.6 Table of parameters used to fit the O-1s and C-1s spectra for uranium silicide phases. 126

5.7 Table of calculated stoichiometries for each uranium silicide phase. 129

5.8 The binding energy position of U-4f$_{7/2}$ oxide components and relative satellite separation energy range associated to uranium valence states. Data summarised from [83] 130

6.1 Table showing crystallite size for each phase within SN1707. 145

6.2 O:U ratios calculated from the total areas extracted from the O-1s U-O, and the U-4f U(IV) areas in U_3Si, SN1711. Areas have been normalised to the total area of U-4f U(IV) at t = 0. 159

6.3 O:U ratios calculated from the total areas extracted from the O-1s Si-O, and the Si-2s oxide areas in U_3Si, SN1711. Areas have been normalised to the total area of Si-2s oxide area 2 at t = 0. 160

6.4 O:U ratios calculated from the total areas extracted from the O-1s U-O, and the U-4f U(IV) areas in U_3Si_2, SN1707. Areas have been normalised to the total area of U-4f U(IV) at t = 0. 169
6.5 O:Si ratios calculated from the total areas extracted from the O-1s Si-O, and the Si-2s oxide areas in U_3Si_2, SN1707. Areas have been normalised to the total area of Si-2s oxide at t = 0. 171
6.6 O:U ratios calculated from the total areas extracted from the O-1s U-O, and the U-4f U(IV) areas in U_3Si_5, SN1644. Areas have been normalised to the total area of U-4f U(IV) at t = 0. 178
6.7 O:Si ratios calculated from the total areas extracted from the O-1s Si-O, and the Si-2s oxide areas in U_3Si_5, SN1644. Areas have been normalised to the total area of Si-2s oxide at t = 0. 180
6.8 O:U ratios calculated from the total areas extracted from the O-1s U-O, and the U-4f U(IV) areas in α-USi_2, SN1645. Areas have been normalised to the total area of U-4f U(IV) at t = 0. 187
6.9 O:Si ratios calculated from the total areas extracted from the O-1s Si-O, and the Si-2s oxide areas in αUSi_2, SN1644. Areas have been normalised to the total area of Si-2s oxide 2 at t = 0. 189
6.10 O:U ratios calculated from the total areas extracted from the O-1s U-O, and the U-4f U(IV) areas in USi_3, SN1700. Areas have been normalised to the total area of U-4f U(IV) at t = 0. 196
6.11 O:Si ratios calculated from the total areas extracted from the O-1s Si-O, and the Si-2s oxide areas in USi_3, SN1700. Areas have been normalised to the total area of Si-2s oxide 2 at t = 0. 199
6.12 Layer thicknesses extracted from the modelled U_3Si_5 XRR spectra, SN1644. 205
6.13 Table showing crystallite size for each phase within SN1639 and SN1707. 216
6.14 Table of structural constants collected from pristine and oxidised epitaxial (100) U_3Si_5 thin films. Parameters extracted from SN1512 and SN1644. 218
6.15 Table of structural constants collected from pristine and oxidised epitaxial (004) α-USi_2 thin films. Parameters extracted from SN1645 and SN1702. Bulk values shown for structural comparison. 221
6.16 Table of structural constants collected from pristine and oxidised epitaxial (001) USi_3 thin films. Parameters extracted from SN1700 and SN1699. Bulk values shown for structural comparison. 224
6.17 The oxide thicknesses and oxidation products forming on the surface of each uranium silicide phase under ambient conditions. 227

7.1 The modelled net thickness changes for each uranium silicide phase when exposed to H_2O for 24 hours, and H_2O_2 for 8100 s, with comparison to UO_2 and silicon. 270

7.2 The calculated dissolution rates for each uranium silicide phase when exposed to H_2O and H_2O_2 with comparison to UO_2 and silicon. Negative rates indicate a thickness gain. 272

List of Figures

Figure **Page**

1.1 Neutron energy spectra. 4
1.2 Molten-Salt Fast Reactor Schematic. 5
1.3 Nuclear fission schematic. 5
1.4 Nuclear reactor roadmap. 6
1.5 Schematic of Pressurised Water Reactor. 7
1.6 Aerial photograph of the Fukushima Daiichi nuclear reactor site. 10
1.7 Comparison of standard and ATF cladding under accident scenarios. 12
1.8 Proposed ATF fuel candidates. 14

2.1 Uranium-Silicon Binary Phase Diagram. 16
2.2 Thermal conductivities of ATF candidates compared against UO_2. 19
2.3 Oxidation concentration as a function of oxygen exposure for U-Si compounds 23
2.4 XPS spectra of Coffinite ($USiO_4$) collected by *Pointeau et al.,*. 24
2.5 Isothermal testing of U-Si phases obtained from TGA analysis conducted by *Sooby Wood et al.,*. 26
2.6 Reactions occurring as a result of water radiolysis. 30
2.7 XRD spectra collected from U_3Si_2 prior and post steam exposure. 31
2.8 U_3Si_2-steam interaction mechanism. 32

3.1 Schematic of how x-rays interact with matter. 37
3.2 The range of energies generated using a laboratory x-ray tube source. 38
3.3 Schematic of Bragg's law in the case of a 2-dimensional lattice 39
3.4 Schematic of wavevector momentum transfer 41
3.5 Geometric two-dimensional Ewald sphere. 44
3.6 Schematic of the PANalytical X'Pert diffractometer 45
3.7 Schematic of the specular, 2θ-ω scattering from a sample surface. 46
3.8 Example 2θ-ω spectra measured from an (001) oriented USi_3 thin film, SN1699. . . . 48
3.9 Schematic diagram for the off-specular scanning geometry. 49
3.10 Schematic diagram for the omega scan geometry. 50
3.11 X-ray reflectivity spectra for an infinite surface. 54

3.12 X-ray reflectivity schematic for a finite film. 55
3.13 X-ray reflectivity spectra for a single finite layer. 56
3.14 X-ray reflectivity spectra for a multilayer. 58
3.15 X-ray reflectivity spectra indicating increased roughness. 60
3.16 Electron configuration diagram. 63
3.17 Schematic of Concentric Hemispherical Analyser. 64
3.18 XPS spectra from U-4f of U_3Si using different pass energyies 66

4.1 Figure of epitaxial growth modes. 73
4.2 DC Magnetron Schematic. 75
4.3 Labelled figure of deposition chamber magnetron guns and heating element. 76
4.4 X-ray reflectivity spectra from Si and U-metal thin films. 77
4.5 Uranium-Oxygen binary phase diagram. 78
4.6 Image of deposition chamber used to synthesise thin films. 80
4.7 Uranium contamination monitoring using high-angle XRD. 81
4.8 The deposition chamber in bake-out mode. 82
4.9 RHEED diffraction patterns obtained from CaF_2 and USi_3 (001) surfaces. 83
4.10 X-ray reflectivity data and model of (001) oriented single crystal CaF_2 substrate. 85
4.11 UO_2 epitaxial match to YSZ. 86

5.1 U_3Si high angle x-ray diffraction. 91
5.2 U_3Si omega data. 92
5.3 U_3Si off-specular data. 93
5.4 U_3Si uranium sites, atomic positions, and unit cells of U_3Si and CaF_2. 94
5.5 High angle diffraction spectra from polycrystalline U_3Si_2. 95
5.6 U_3Si_5 high angle x-ray diffraction. 96
5.7 U_3Si_5 omega data. 98
5.8 U_3Si_5 off-specular data. 99
5.9 Schematic of the two domain U_3Si_5 single crystal. 99
5.10 High angle data of $\alpha-USi_2$ deposited on (002) oriented MgO. 100
5.11 $\alpha-USi_2$ omega data. 101
5.12 $\alpha-USi_2$ off-specular data. 102
5.13 SN1645 high angle diffraction data. 103
5.14 SN1645 omega data. 104
5.15 SN1645 off-specular phi data. 105
5.16 Epitaxial match between $\alpha-USi_2$ and CaF_2. 106
5.17 High angle diffraction data from single crystal USi_3, SN1699 107
5.18 Rocking curve data and models of USi_3 and CaF_2 from SN1699. 108
5.19 Off-specular data from SN1699. 109

5.20 Epitaxial match between USi_3 and CaF_2. 109
5.21 Comparison of high angle data and uranium-silicon phase diagram. 112
5.22 Survey data from uranium silicide phases with U-4f inset. 118
5.23 Modelled U-4f spectra obtained from uranium silicide phases. 121
5.24 Modelled valence band spectra obtained from uranium silicide phases. 122
5.25 Modelled Si-2s spectra obtained from uranium silicide phases. 124
5.26 Modelled O-1s spectra obtained from uranium silicide phases. 127
5.27 Modelled C-1s spectra obtained from uranium silicide phases. 128

6.1 XRD characterisation of U_3Si, SN1711 142
6.2 XRD of oxidised (001) U_3Si single crystal. 143
6.3 XRD of oxidised poly-crystalline U_3Si_2, SN1707. 144
6.4 XRD characterisation of oxidised single crystal U_3Si_5, SN1644. 146
6.5 XRD of oxidised single crystal α-USi_2, SN1645. 148
6.6 XRD of oxidised single crystal α-USi_2, SN1702. 149
6.7 XRD characterisation of oxidised single crystal α-USi_2, SN1702. 150
6.8 XRD of oxidised single crystal USi_3, SN1700. 151
6.9 XRD characterisation of oxidised single crystal USi_3, SN1700. 152
6.10 XPS spectra collected from the U-4f and Si-2s of U_3Si 153
6.11 XPS depth profile of oxidised U_3Si, SN1711 156
6.12 Normalised areas of spectra collected from U_3Si as a function of sputtering time. . . . 158
6.13 Normalised U-4f and Si-2s areas collected from U_3Si, SN1711. 161
6.14 The Si:U ratio as a function of sputtering time, data collected from SN1711. 163
6.15 XPS spectra collected from the U-4f and Si-2s of U_3Si_2 164
6.16 XPS depth profile of oxidised U_3Si_2, SN1707 166
6.17 Normalised areas of spectra collected from U_3Si_2 as a function of sputtering time. . . 168
6.18 Normalised U-4f and Si-2s areas collected from U_3Si_2, SN1707. 170
6.19 The Si:U ratio as a function of sputtering time, data collected from SN1707. 172
6.20 XPS spectra collected from the U-4f and Si-2s of U_3Si_5 174
6.21 XPS depth profile of oxidised U_3Si_5, SN1644 176
6.22 Normalised areas of spectra collected from U_3Si_5 as a function of sputtering time. . . 177
6.23 Normalised U-4f and Si-2s areas collected from U_3Si_5, SN1644. 179
6.24 The Si:U ratio as a function of sputtering time, data collected from SN1644. 181
6.25 XPS spectra collected from the U-4f and Si-2s of α-USi_2 182
6.26 XPS depth profile of oxidised α-USi_2, SN1645 184
6.27 Normalised areas of spectra collected from α-USi_2 as a function of sputtering time. . 185
6.28 Normalised U-4f and Si-2s areas collected from αUSi_2, SN1645. 188
6.29 The Si:U ratio as a function of sputtering time, data collected from SN1645. 190
6.30 XPS spectra collected from the U-4f and Si-2s of USi_3 191

6.31 XPS depth profile of oxidised USi_3, SN1700 . . . 194
6.32 Normalised areas of spectra collected from USi_3 as a function of sputtering time. . . . 196
6.33 Normalised U-4f and Si-2s areas collected from USi_3, SN1700. . . . 198
6.34 The Si:U ratio as a function of sputtering time, data collected from SN1700. . . . 200
6.35 XRR oxidation data from the surface of U_3Si, SN1711. . . . 201
6.36 Layer thicknesses and oxide growth from the surface of U_3Si as a function of exposure time, SN1711. . . . 202
6.37 XRR oxidation data from the surface of U_3Si_2, SN1707. . . . 203
6.38 XRR oxidation data from the surface of U_3Si_5, SN1644. . . . 204
6.39 XRR oxidation data from the surface of α-USi_2, SN1702. . . . 206
6.40 Total layer thickness of α-USi_2 measured using XRR (SN1702). . . . 207
6.41 XRR oxidation data from the surface of α-USi_2, SN1645. . . . 208
6.42 Total layer thickness of α-USi_2 measured using XRR (SN1645). . . . 209
6.43 XRR oxidation data from the surface of USi_3, SN1700. . . . 210
6.44 Total layer thickness of USi_3 measured using XRR (SN1700). . . . 211
6.45 Comparison of high-angle XRD data extracted from pristine and oxidised uranium silicide thin films. . . . 213
6.46 Schematic of the oxidised structure of U_3Si, SN1711. . . . 215
6.47 Schematic of the oxidised structure of U_3Si_2, SN1707. . . . 217
6.48 Schematic of the oxidised structure of U_3Si_5, SN1644. . . . 219
6.49 Modified binary phase diagram of uranium and silicon. . . . 220
6.50 Schematic of the oxidised structure of α-USi_2, SN1645. . . . 222
6.51 Schematic of the oxidised structure of USi_3, SN1700. . . . 225
6.52 Schematic of the ambient oxidation model for U-Si phases. . . . 228

7.1 High angle XRD data of U_3Si water dissolution. . . . 231
7.2 Isolated high-angle XRD data of U_3Si water dissolution, SN1711. . . . 232
7.3 X-ray reflectivity data of U_3Si water dissolution. . . . 233
7.4 Thickness of U_3Si water dissolution layers. . . . 234
7.5 High angle XRD data of U_3Si_2 water dissolution. . . . 235
7.6 X-ray reflectivity data of U_3Si_2 water dissolution, SN1707. . . . 236
7.7 Thickness of U_3Si_2 layers after water dissolution. . . . 237
7.8 Photo of U_3Si_2 sample after water dissolution. . . . 238
7.9 High angle XRD data of α-USi_2 water dissolution. . . . 239
7.10 X-ray reflectivity data from α-USi_2 water dissolution. . . . 240
7.11 Layer thicknesses extracted from α-USi_2 during water dissolution. . . . 241
7.12 Modelled high-angle XRD spectra of USi_3 as a function of H_2O exposure, SN1700. . . . 242
7.13 Modelled XRR data of (001) USi_3 water dissolution and change in thickness from dissolution, SN1700. . . . 244

7.14 Modelled XRR data of UO_2 water dissolution, SN1829. 246
7.15 Modelled XRR data of Si and Si-O water dissolution, SN1519. 247
7.16 Modelled high-angle XRD data of U_3Si dissolution using H_2O_2, SN1711. 250
7.17 Modelled XRR data of U_3Si dissolution using H_2O_2, SN1711. 251
7.18 U_3Si film thickness as a function of exposure to H_2O_2, SN1711. 252
7.19 Modelled high-angle XRD data of U_3Si_2 dissolution using H_2O_2, SN1707. 253
7.20 XRR spectra collected from U_3Si_2 after hydrogen peroxide dissolution. 255
7.21 Thickness of sample layers modelled from U_3Si_2 XRR spectra after hydrogen peroxide dissolution. 256
7.22 Photo of U_3Si_2 sample after hydrogen peroxide dissolution. 257
7.23 XRR and XRD changes extracted from α-USi_2 following H_2O_2 exposure, SN1702. . . 258
7.24 Sample thickness change as a result of exposing α-USi_2 (SN1702) to H_2O_2 exposure. 260
7.25 XRR and thickness changes extracted from USi_3 following H_2O_2 exposure, SN1700. . 262
7.26 Modelled high-angle XRD spectra of USi_3 as a function of H_2O_2 exposure, SN1700. . 263
7.27 Modelled high-angle XRD data collected from UO_2 during the H_2O_2 exposure experiments, SN1507. 264
7.28 Modelled omega data collected from UO_2 during the H_2O_2 exposure experiments, SN1507. 265
7.29 XRR and thickness changes extracted from (001) UO_2 following H_2O_2 exposure, SN1507.266
7.30 Modelled XRR spectra from silicon after H_2O_2 exposure, SN1519. 267
7.31 Thickness of silicon thin film after exposure to H_2O_2, SN1519. 268
7.32 Schematic of uniform and island dissolution mechanisms. 273

A.1 Artistic depiction of nuclear fuel research circa October 2018. 282

Chapter 1

Introduction

The ability to harness the power of the atom has advanced the human race through multiple avenues. Arguably, producing vast amounts of energy via the splitting of the atom has been one of the greatest achievements in modern history. With the ever increasing demand for energy and the effects of climate change being present, nuclear power has become a global requirement. Nuclear power presents itself as a reliable, low-carbon alternative to fossil fuel technologies, making it a key element in the global efforts to decarbonise emissions whilst meeting electricity demands. As of October 2021, there are 442 nuclear power reactors in operation across 31 countries, with 51 reactors under construction [2, 3] . Of these, the United Kingdom has 13 operational reactors, providing around 17% of the electricity [2]. However, the nuclear sector within the UK may be at risk from the imminent shutdown and decommissioning of the Advanced Gas Reactor (AGR) fleet due to aging. Despite the large contribution nuclear power has on a global and national scale, the use of atomic energy is still a widely debated topic, it is because of this that the enhancement, safety, and reproducibility of nuclear power is at the forefront of research.

Where nuclear power has been available for civil use for over 60 years, there is still a continuous effort to improve each reactor in order to provide a more efficient and reliable system that has a significantly reduced carbon footprint and overall environmental risk. To fully realise these goals, it is vital to understand the fundamental behaviour of the element that is at the core of reactor technology - the nuclear fuel. The limitations of the current nuclear fuel, UO_2 were highlighted during the 2011 Fukushima Daiichi Nuclear Power Plant accident. Since then, efforts have been made to research and develop new fuels and claddings with advanced behaviours and improved accident tolerances. Originally coined Accident Tolerant Fuels, these

advanced fuels, or rather Advanced Technology Fuels (ATFs), have been selected such that they have advanced thermal properties that supersede the current ceramic uranium-oxide compound. Uranium Silicide, in particular, U_3Si_2, has been at the forefront of this research. This compound, due to its excellent thermal properties, has been highlighted as an advanced technology fuel. Uranium and silicon forms around six stoichiometric phases, of which three have been selected as advanced technology fuels: U_3Si, U_3Si_2, and U_3Si_5. Due to the range of potential phases that could form from uranium and silicon, the uranium silicide phases are relatively under-studied. Consequently, the main aim of this thesis is to dissect the fundamental properties of the uranium silicide phases that extend across the binary phase diagram, including the three ATF candidates, U_3Si, U_3Si_2, and U_3Si_5. Probing the structural and chemical behaviour of these phases will alow for an evaluation of how each compound may alter the behaviour of the ATF fuels.

1.1 The Significance of Nuclear Power

1.1.1 A Brief History of Nuclear Power

Elemental uranium was discovered in 1789 by Martin Heinrich Klaproth [4]. However, it wasn't until 1930's that the ability to split the atom was realised. Here, Otto Hahn found that the bombardment of elemental uranium with neutrons produced barium, with Lise Meitner interpreting this as the splitting of the uranium nucleus [5, 6]. This process was coined 'nuclear fission'. The discovery of nuclear fission aligned with the beginning of World War II, which prompted funding in nuclear technologies. It was in 1939 that Herbert L. Anderson, Leo Szilard, and Enrico Fermi conducted an experiment investigating the multiplication of neutrons from uranium, thus confirming that a chain reaction could occur from the nuclear fission of uranium [7]. Following this, a letter to President Roosevelt, signed by Szilard, Wigner, Teller, and Einstein warned of the potential of nuclear weapons [8]. This led to the authorisation of a uranium study from Roosevelt, whereby Enrico Fermi led the successful demonstration of a nuclear chain reaction of uranium metal and uranium oxide in 1942 [9]. The neutrons released from the fission process were moderated using graphite blocks, thus slowing the kinetic energies of the neutrons. As a result, this induced further fission events of the uranium. This event initiated The Manhattan Project, from which nuclear reactors were constructed, producing highly enriched nuclear fuel which permitted the weaponisation of nuclear material [7].

Following the devastating consequences of the deployment of these nuclear weapons, a route to utilise such a powerful energy source through the use of peaceful applications was sought. The ability to harness the large amount of thermal energy released from nuclear fission and in turn produce electricity was first demonstrated by EBR-1 in Idaho, USA in 1951. The electricity produced from this reactor was used to first power Arco, Idaho in 1955. The first demonstration

of the ability to produce electricity on a commercial level was through the use of the Calder Hall reactor (Cumbria, UK) in 1956 [10]. Where the Calder Hall reactor fleet was used to produce power, the reactor was also intended to produce weapons grade material for nuclear warheads. Despite the successful demonstration of nuclear power, showcasing its potential as a peaceful tool, there has also been significant fallout via human and environmental disasters. Nuclear accidents such as Chernobyl (1986), Three Mile Island (1999), and Fukushima (2011), damaged public perception and questioned the overall safety of nuclear power. However, commercial nuclear power is the only viable source of large scale electricity production that does not produce greenhouse gases upon the generation of the power [11]. Thus, in the light of the global demand for low-carbon, and clean energy resources, nuclear power becomes a viable option once again [3].

As the goal of nuclear power shifted from the production of weapons to the production of energy, the design of reactors also changed to accommodate this. Commercial reactors drifted away from the use of metallic fuels, adopting uranium oxide fuels into the nuclear fuel cycle as replacement, thus initiating the dawn of the Generation II nuclear reactor designs [12]. This saw the influx of water-cooled and water-moderated reactors, with the use of gas-cooled reactors such as Calder Hall becoming less common. Despite this, the UK is still heavily dominated by its unique ageing fleet of Advanced Gas-Cooled Reactors (AGRs). The following will explore the various reactor designs since the 1950s.

1.1.2 Reactor Design and Development

Neutrons can exist across a range of energies, this is depicted in Figure 1.1. The neutrons produced from the fission chain reaction exhibit kinetic energies in the MeV range, $\chi(E)$. These are referred to as *fast neutrons*. Through moderation, and thus over a number of scattering events, this kinetic energy is reduced, resulting in the neutrons slowing down. These are referred to as *thermal neutrons*, which exist in the lower kinetic energy range, M(E), of the spectra presented in Figure 1.1. Thermal neutrons are responsible for the initiation of the chain reaction, and therefore are vital in the ability to sustain nuclear fission [13].

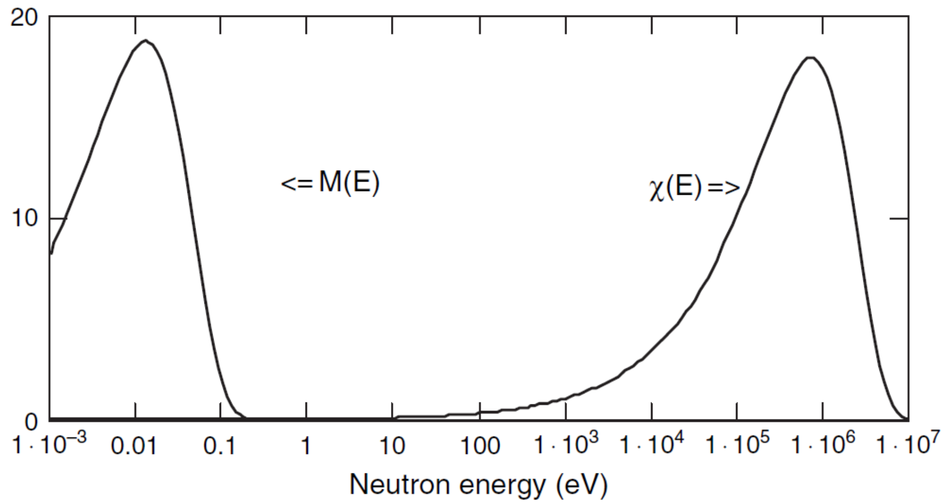

FIGURE 1.1. Figure depicting the fission and thermal energy spectra of neutrons. Figure taken from [13].

The experimental breeder reactor, EBR-1, operating out of Idaho,was purposely constructed to produce more fuel than required to operate the reactor, hence *breeder reactor*. Additionally, the EBR-1 was designed to demonstrate the feasibility of power generation. The reactor was cooled with liquid metal, and generated fast neutrons. The fast breeder reactors, produce energy alongside creating nuclear fuel through the use of fast neutrons [14]. The concept behind this reactor design is to remove materials from the reactor core that moderate the fast neutrons (slow down their kinetic energies), and increase the amount of fissile and fertile material within the reactor core as much as possible, to sustain a efficient utilisation of fast neutrons.

As mentioned, the EBR-1 reactor utilised liquid metal to cool the reactor. This choice of coolant, limits the moderation of neutrons within the core, and sustains the created material:destroyed material breeding ratio [13, 14]. Other examples of the fast breeder reactor concept aside from EBR-1 are: Dounreay Fast Reactor, UK (1962-1977), and EBR-2, Idaho USA (1964-1994). A schematic of the Molten-Salt Fast Reactor is depicted in Figure 1.2. This schematic depicts two molten-salt coolant loops, a primary loop surrounding the core of the reactor, and a secondary loop external to the main reactor vessel.

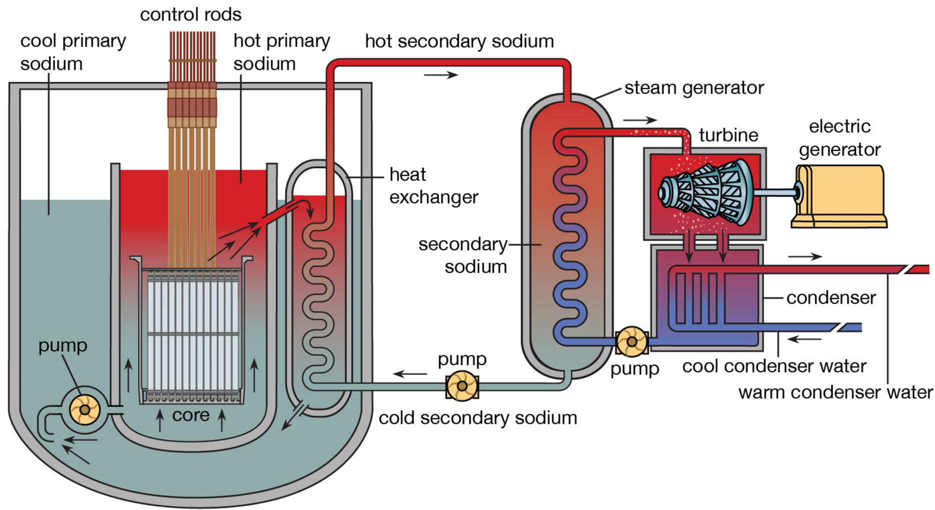

FIGURE 1.2. Schematic diagram depicting the Molten-Salt Fast Reactor design with a primary and secondary molten-salt loops. Figure taken from [15].

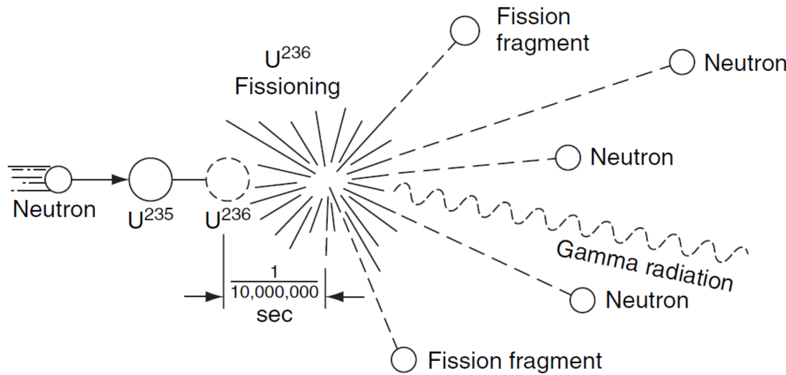

FIGURE 1.3. Schematic diagram depicting the nuclear fission of uranium. Figure taken from [13].

As the requirement for weapons grade material was limited, and global energy demand soared, the design of nuclear reactors shifted in order to produce vast amounts of commercial power. Natural uranium is comprised of two dominating main isotopes: U-235 and U-238. These isotopes proportionally exist as 0.711% and 98.28%, respectively by weight [16]. As U-235 is the fissionable isotope, uranium-based nuclear fuel must be enriched to increase the amount of fissile material. This also indicates that for the nuclear fission chain reaction to sustain for uranium, U-235 must be present. Figure 1.3 presents a schematic of the fission process for U-235. This figure shows how U-235 absorbs a neutron, transmuting to U-236, resulting in the atom splitting,

and the creation of free neutrons. As previously mentioned, the neutrons produced from fission event are categorised as fast, and therefore require moderation in order to continue the fission chain-reaction.

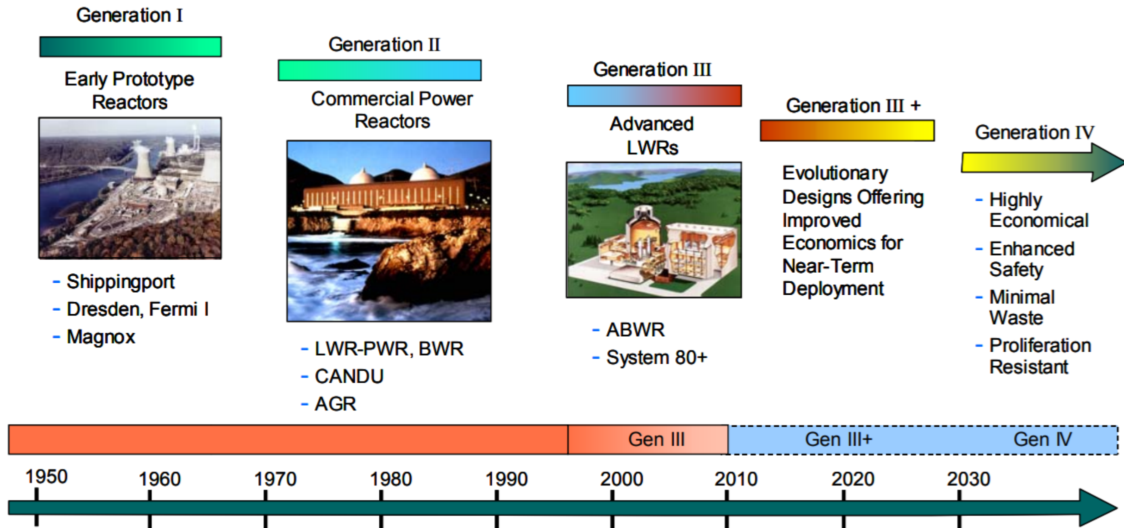

FIGURE 1.4. Schematic diagram of the historic and future nuclear reactor roadmap. Figure taken from [12].

Some commercial nuclear reactors, like Magnox and CANDU utilise the reduced amount of U-235 in natural uranium to produce electricity. However, the vast majority of Generation-II commercial reactors require the U-235 concentration to be increased to around 3 – 5% [13, 16]. Figure 1.4 presents a historical and future roadmap of the nuclear reactors. Here, it is shown that the Generation-II reactors consist of mainly light-water reactor types (LWRs). These are the Pressurised Water Reactor (PWR) and the Boiling Water Reactor (BWR). Both of these reactor types utilise the thermal neutron regime to induce further nuclear fission events and in turn, thermally produce a power output. In order to achieve this, these reactors utilise a moderator that causes the kinetic energies of neutrons to be in the thermal regime, M(E) (Figure 1.1). In total, the water cooled reactors are responsible for around 96% of the global nuclear electricity production, with the LWRs making up contributing to around 85% of this with a total of 377 operational reactors [17]. The LWRs predominantly use uranium dioxide, UO_2 fuel encased in zirconium alloy cladding. Both PWR and BWR reactor types use 'light-water' H_2O as both the reactor coolant and fuel moderator [13]. Note that Pressurised Heavy-Water Reactors, much like the CANDU reactors, utilise heavy-water, D_2O as the coolant and moderator. The low absorption cross-section of deuterated water allows for the CANDU reactor type to operate using natural

uranium. Figure 1.5 depicts a schematic of a PWR. Here, the reactor core can be seen, consisting of the fuel assembly, primary coolant system, and control rods within the pressure vessel. A secondary coolant circuit is used which extends outside of the main containment structure. This secondary circuit produces the steam that eventually produces electricity via the turbines, and acts as an additional safety barrier, preventing the release of radionuclides that may escape the fuel assembly from entering the water basin. For PWRs, the water is kept at a pressure of 155 bar, keeping the water liquid as the coolant is subjected to an inlet temperature of around 290 °C and an output temperature of 325 °C within the pressure vessel [16].

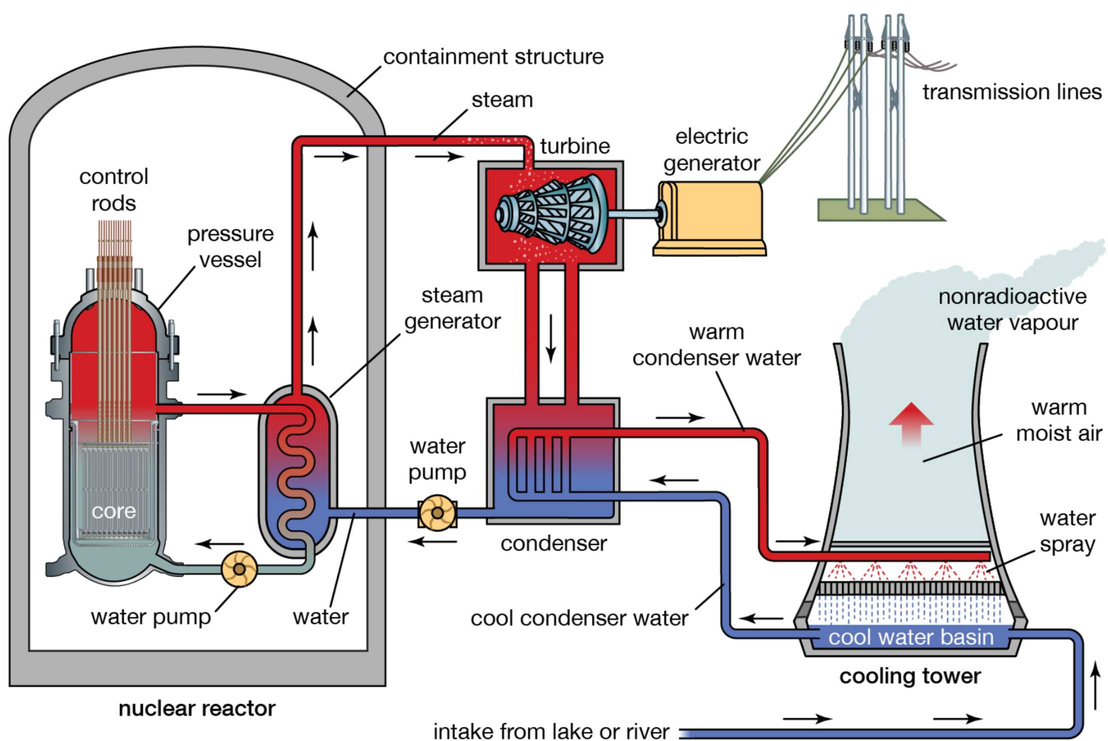

FIGURE 1.5. Schematic diagram of a Pressurised Water Reactor (PWR). Figure taken from [18].

The most significant difference between the two LWRs, is that the BWR allows for the water coolant to boil under a pressure of 72 bar [16]. This steam then directly drives the generation of electricity via the reactor turbines. This infers that the BWR has one coolant loop, connecting the main reactor vessel to the turbines and coolant condenser which both sit external to the main containment structure. Furthermore, the control rods of a BWR sit below the reactor core, minimising the potential for steam corrosion, whereas the control rods within a PWR sit above the fuel assembly, as depicted in Figure 1.5. The control rod configuration in BWRs could potentially cause

problems with reactor shut down, particularly in the case of a beyond-design basis (BDB) accident, as the control rods cannot rely on gravity for full insertion into the fuel assembly to stop reactivity.

The majority of the reactors currently under construction are categorised as Generation-III or Generation-III +. The requirement for these reactors are that there is a significant improvement with regards to reactor economics and overall reactor safety mechanisms. The Advanced Boiling-Water Reactor (ABWR), was manufactured with additional passive safety features including the Emergency Core Cooling System (ECCS) [14]. Despite the improvements made to LWRs, it was the eventual failure of the fuel/cladding system, that has resulted in the demand for Generation-IV reactor development.

1.1.3 Nuclear Accidents and their Consequences

The legacy reactors designed and constructed in the earlier decades of commercial nuclear power era were not equipped to predict, prevent, or mitigate beyond design basis (BDB) reactor accidents. [19]. Despite best efforts to equip the Generation-III reactors with additional safety features, the systems in place were not enough to stop partial, or full reactor core meltdowns.

Arguably the largest commercial nuclear power plant disaster occurred in 1986, at the Chernobyl Nuclear Power Plant, Ukraine. A total of four RMBK-1000 reactors operated at this site. The RBMK-1000 utilises water as its coolant, and is moderated using graphite. Similar to the LWRs, the RBMK uses the UO_2-Zr alloy fuel/clad system [13]. The cause of the reactor meltdown was attributed to unique design flaws in the RMBK reactor alongside human operational error [20]. The differences between this reactor type and accident circumstances are very different from the operating LWRs of interest, and therefore is not an accident of particular interest in for this body of work.

A significant accident occurred at the PWR at Three Mile Island (USA) nuclear power plant in 1979. The partial melting of the reactor core resulted in the release of radioisotopes into the coolant water [21]. The ability to remove heat from the primary system within the Three Mile Island PWR was prevented because of a testing error occurring in the emergency feedwater system [22]. As a result, a valve in the pressuriser system was left open, prompting a loss of coolant in the primary loop of the reactor, exposing the reactor fuel elements as the remaining coolant water began to boil. With the core temperature increasing, the oxidation of the zirconium cladding was initiated as it reacted with residue steam left in the PWR pressure vessel, producing hydrogen gas as a by-product of the formation of ZrO_2. This loss of coolant was a key component in the partial melting of the reactor core and subsequent fission product release. Multiple design flaws were responsible for this system failure, including operational procedures, and mechanical

features. The major outcomes of this accident were the developments made to further understand accident behaviour in LWRs, and to further the regulations of nuclear reactors and their operation [22].

The event that significantly shaped the future of nuclear power was the 2011 Fukushima Daiichi Nuclear Power Plant accident. This event was classified as a level 7 major accident, as defined by the International Nuclear and Radiological Event Scale (INES). The initiation of this nuclear accident stemmed from a 9.0 magnitude earthquake, which had an epicentre off the east-coast of Japan in the Pacific Ocean. The triple plate tectonic configuration, which includes a subduction zone, and subsequent seismic activity resulted in the formation of a tsunami. The BWRs located at the Fukishima Daiichi site (Figure 1.6) are equipped with seismic activity monitors, which allow for the rectors to enter an automatic shutdown if required [23]. This is due to the frequent tectonics that occur across Japan [24]. Each BWR was equipped with safety infrastructure such that in a loss of coolant accident (LOCA), the fuel would be cooled back to a safe temperature. Note that the operating temperature of a BWR is around 270 °C for the coolant inlet, and 285 °C for the output temperature [16]. The reactor pressure vessel would be cooled using the Residual Heat Removal (RHR) and the Emergency Core Coolant System (ECCS) [23]. For the Fukushima Daiichi units, these safety systems required a small amount of external power to operate, allowing for the circulation of cooling water, extracted from coastal seawater pumps. In such event, the use of backup generators located in the basement of each turbine hall would provide this power to the safety systems.

The Great Eastern Japan Earthquake occurred at 14 : 46 (UTC +09 : 0) on the 11^{th} March 2011, and resulted in two tsunami waves up to 33 m high, which swamped an area of eastern coastline totalling over 560 km^2, including the area in which the Fukishima Daiichi nuclear power plant units were located. The reactor units were subjected to an immediate shutdown after the initial seismic activity, allowing for a complete insertion of the control rods into the fuel assemblies. The earthquake also caused a loss of power to the reactor fleet, resulting in the use of the backup generators. This also triggered the ECCS, allowing for the fuel elements to be safely cooled. Despite a 5.7 m concrete seawall protecting the site from an influx of water, the tsunami waves arriving at the Fukishima Daiichi site were 4 and 15 m [23], and therefore were able to scale this wall. This subsequently flooded the basements in which the backup generators were located, resulting in a complete power blackout.

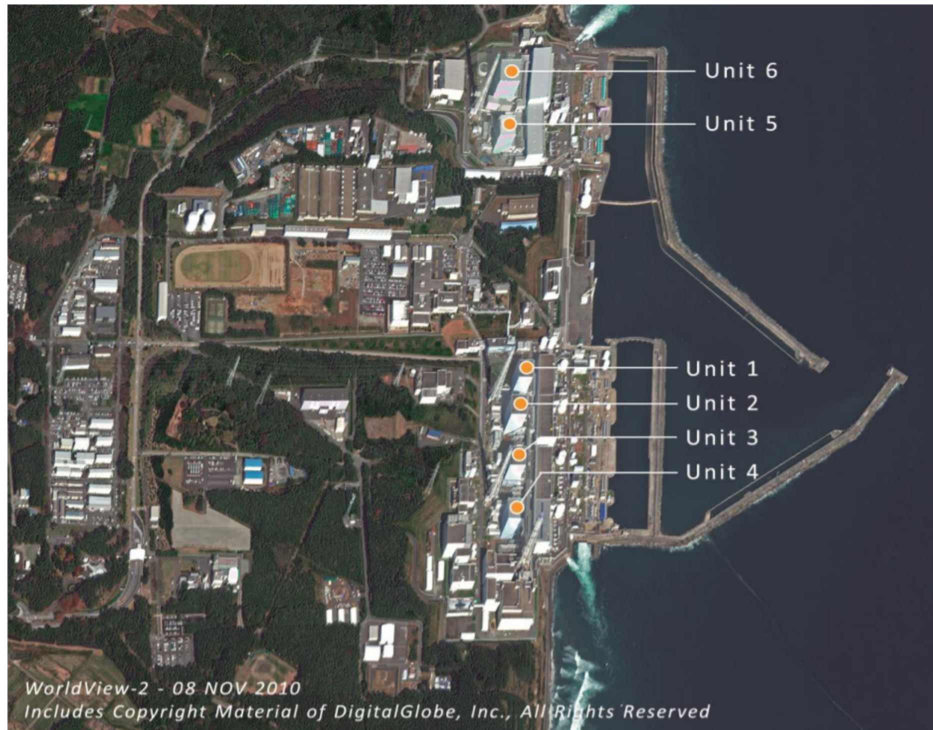

FIGURE 1.6. Aerial photograph of the Fukushima Daiichi nuclear reactor site. Annotations indicate the various reactor units located at the site. Figure taken from [25].

Without the fuel assembly within the reactor pressure vessel being subjected to sufficient cooling, the thermally hot fuel elements continued to heat the residue coolant and thus produced steam. This resulted in the water-level within Unit 1, as shown in Figure 1.6, dropping below the top of the fuel element. Much like the incident reported at Three Mile Island [22], this resulted in the oxidation of the zirconium cladding, producing hydrogen gas. Without additional coolant entering the reactor, the residue liquid continued to boil, reducing the water level significantly, reaching the base of the fuel assembly in around 5 hours [23]. Alongside the production of hydrogen gas, another significant threat stemmed from the ever increasing temperature of the ceramic nuclear fuel element: UO_2. The surface temperature of the reactor vessel was estimated to be around 2800 °C, resulting in a core meltdown. Following these initial events, there were subsequent explosions resulting in the release of radionuclides into the atmosphere [25]. Despite no direct casualties stemming from this particular incident, the events that occurred at the Fukushima Daiichi site have resulted in countless economic and social impacts. This event also revealed the true limitations of the UO_2-Zr alloy fuel/cladding system.

Even with nuclear power proving to be an environmentally positive and reliable source of power, the design-basis (DB) and beyond-design-basis (BDB) events presented here have indicated

that the continuation of reactor design improvements, economic benefits, and safety enhancement are still required.

1.2 Advanced Technology Fuels

The fuel/cladding system that has dominated the nuclear industry for decades revealed its significant thermal and mechanical limitations during the 2011 Fukushima Daiichi accident. The poor thermal conductivity of UO_2 has been shown to decrease as a function of temperature, thus during a LOCA, the temperature of the fuel soon matches the melting temperature. Multiple studies have investigated the thermal properties of UO_2, showcasing the phonon-dominated thermal conductivity of this material [26, 27] and how radiation damage, alongside fuel burnup, further limits the thermal capabilities. The thermal conductivity degradation as a function of temperature and irradiation can result in the formation of a porous structure at the rim of the fuel pellet [28, 29]. It is thought that this structure may affect the performance of the UO_2, in particular, decrease the rate of heat transfer to the surrounding coolant. It is this property that hinders UO_2 under accident scenarios. Additional factors can further effect the safety of the reactor, such as: cladding corrosion, pellet-cladding interaction, and structural degradation to both fuel and cladding [19]. As a result, significant efforts have been made to design, model, and engineer claddings and fuels with advanced thermal properties that exceed the performance of the UO_2-Zirconium alloy under normal operation and during accident conditions. These materials have been coined *Advanced Technology Fuels* (ATFs).

Under accident scenarios, ATFs are expected to outperform standard materials, permitting for an extended 'grace period' between the initial reactor incident, and the safe shut-down and stabilisation of the reactor core, thus avoiding partial or full core degradation. Figure 1.7, provided by *Zinkle et al.,* [19], presents an overview of how a standardised zirconium cladding would perform against an ATF material under accident conditions where there is a loss of coolant. This figure shows that both cladding materials increase in temperature after the initial coolant is lost. As the temperature of the fuel increases to around 800 °C, referring to the *Mid-Phase* region of the figure, there is an onset of material degradation within the core. The *balloon and burst* notation on the figure indicates an event where the fuel rod breaks open releasing fuel materials and fission products into the reactor vessel. For the LWR UO_2-Zirconium alloy system, this is expected to happen around 700 – 1200 °C [19]. From the figure, it is noted that the *balloon and burst* event is expected to be delayed within an ATF cladding material. This delay in the onset of physical and chemical degradation of the fuel and cladding, alongside the potential of release of radionuclides, and in extreme cases the production of vast quantities of hydrogen gas, emphasise the requirement of ATFs with imminent implementation into Generation-III and

future Generation-IV nuclear reactors.

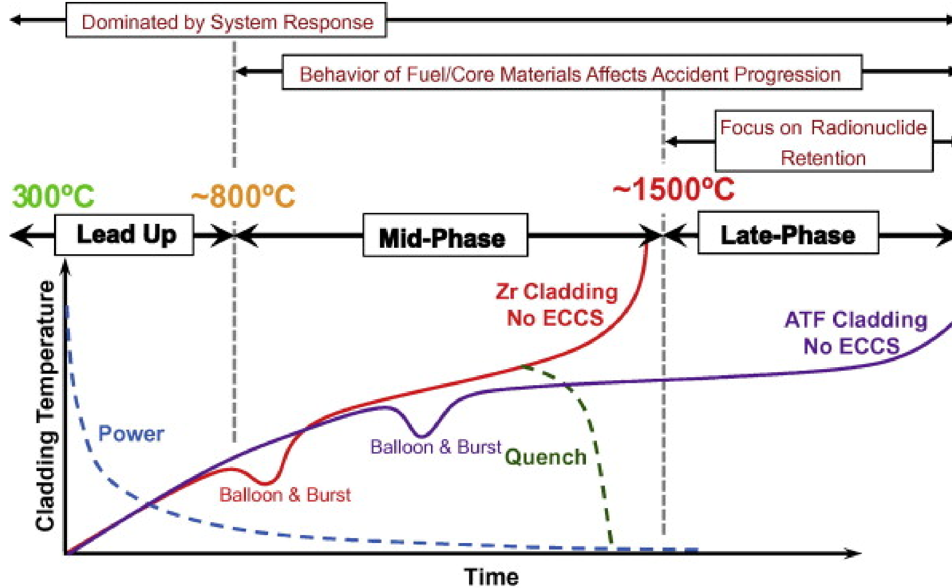

FIGURE 1.7. Comparison of standard and advanced cladding materials during an accident scenario as a function of increasing time and temperature. Figure taken from [19].

1.2.0.1 Cladding

Arguably, the most significant flaw of the current LWR cladding, zirconium-alloy, is its exothermic corrosion behaviour upon interacting with high-temperature aqueous environments [19, 22, 30, 31]. Therefore, efforts are being made to improve the corrosion resistance of the zirconium-alloy cladding used in LWRs, or to replace the material entirely with an ATF candidate. The cladding material acts as an initial barrier, protecting the reactor from radionuclide release should the structural integrity of the fuel element fail. Therefore, a suitable cladding material should be able to withstand elevated temperatures, and the potential swelling of the internal fuel element. The cladding material should also be able to withstand radiation damage, whilst sustaining and not hindering the overall neutronics of the reactor. One proposed ATF cladding concept, is zirconium-alloy with improved oxidation resistance [19, 32, 33]. A concept for an improved zirconium cladding is coating the clad material in chromium, allowing for a protective Cr_2O_3 layer to be formed, improving the behaviour of the zirconium cladding in high-temperature steam environments [31, 34].

Another ATF cladding concept is to remove the zirconium-alloy cladding from the LWR reactor vessel, and instead encase the fuel in replacement materials. One ATF clad concept is

silicon-carbide, SiC. This material is already used within the steam generators of LWRs, so the steam corrosion properties are well understood [35]. The SiC cladding concept also has favourable neutronics, a higher melting point, and an improved radiation resistance when compared to the zirconium-alloy concepts [36, 37]. Regardless, there are significant issues with the practical manufacturing routes [35], suggesting that significant work is required in order to use SiC claddings in LWRs commercially. An iron-based material, FeCrAl, has also been investigated as part of ATF cladding research. This material has proved to be highly oxidation resistant when compared to the zirconium-alloy [35]. However, the increased neutron cross-section of FeCrAl would have to be offset by either increasing the overall U-235 enrichment of the fuel, or matching the FeCrAl cladding with a fuel with an increased uranium density [35, 38].

1.2.0.2 Fuels

Improving the thermal characteristics of the nuclear fuel material would benefit the normal operation, economics, and the overall safety of the nuclear reactor [19]. The most significant flaw of UO_2 is its ability to efficiently evacuate thermal heat [26]. Additional studies have also investigated the potential anisotropic thermal conductivity and corrosion characteristic of UO_2 [26, 27, 39, 40]. These properties contribute to the increasing thermal gradient across the fuel pellet during an accident scenario, which causes degradation of the fuel elements. Therefore, improving the thermal properties of the fuel the centerline temperatures of the fuel element will be lowered during normal operation, and this will increase fission gas retention within the structure of the fuel pellet. Replacing the fuel element within LWRs is costly, so this must be offset with an economic benefit. This could be achieved by selecting a fuel with an increased uranium density, which could benefit the reactor economic via two avenues. Firstly, by extending the fuel life time with a higher burn-up thus reducing the refuelling events required for the reactor fuel assemblies, or secondly through the ability to reduce the overall U-235 enrichment.

Multiple ATF fuel concepts have been researched and developed since the 2011 Fukushima Daiichi accident - these include doped-UO_2, uranium carbide (UC), and uranium diboride (UB_2). The melting temperature and uranium density of multiple ATF fuel candidates is presented in Figure 1.8. This figure makes comparisons against the current LWR fuel UO_2. The ATF fuel candidates to gain the most traction are the metallic uranium silicides, carbides, and nitrides, namely U_3Si_2, UC, and UN. From Figure 1.8, the increased melting point and increased uranium density of UN makes this candidate extremely appealing as a replacement for UO_2. The uranium silicide candidate, U_3Si_2 has a significantly lower melting temperature, however its uranium density still exceeds that of UO_2. The metallic nature of both of these candidates also suggest good thermal properties. The historic use of the U_3Si_2 phase within the RERTR Program [41], alongside the ideal thermal properties, made this candidate the initial ATF front runner, however,

there are potential set-backs with regards to how these uranium silicide fuels behave in air and within aqueous environments. A more in-depth investigation of the properties of uranium silicide phases will be presented in the following chapter.

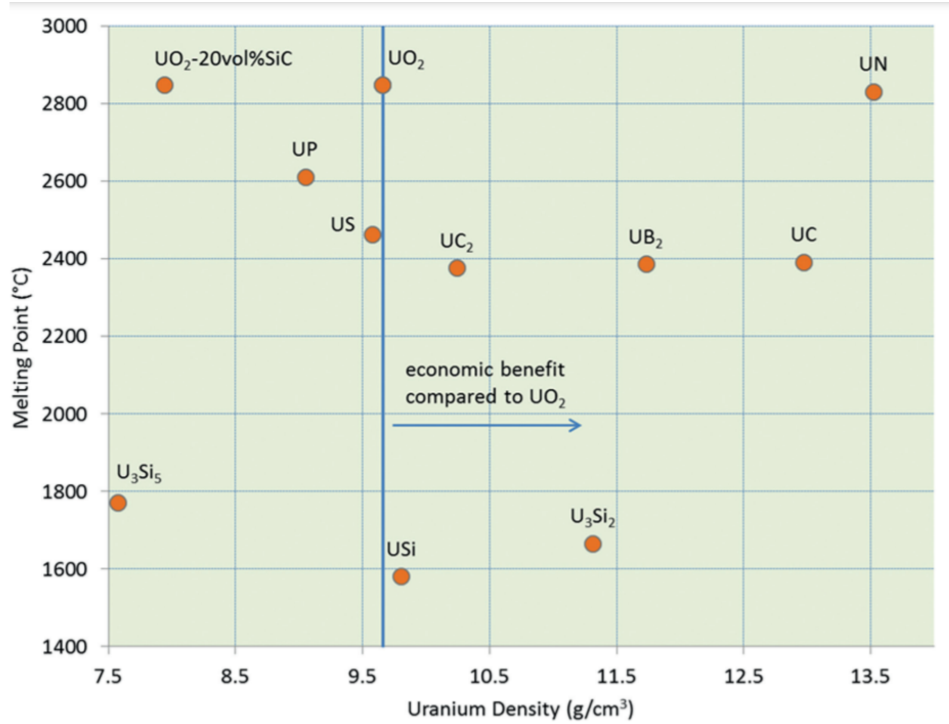

FIGURE 1.8. Comparison of the melting temperature and uranium density of proposed ATF fuel candidates. Figure taken from [33].

CHAPTER 2

Uranium Silicide as a Nuclear Fuel

For decades, the uranium-oxygen fuel system has dominated the nuclear fuel cycle. However, in the wake of the 2011 Fukushima Diiachi Nuclear Power Plant accident, a new approach was required with regards to the safety of nuclear energy. The limitations of the current UO_2-Zircalloy system revealed significant safety issues with thermal conductivity, hydrogen production, and structural integrity of the overall fuel-cladding system. Since this accident, efforts have been made to investigate and test fuel types with advance thermal properties and increased uranium densities that would supersede the performance of UO_2 *in-operando*, under accident scenarios, and within disposal environments. Multiple candidates, including uranium mononitride (UN), uranium carbide (UC), and uranium diboride (UB_2), have all been highlighted as fuel replacements, however, the uranium silicide fuel type sparked significant interest within the nuclear sector due to its advanced properties. This chapter aims to provide an overview of the fundamental properties of the U-Si system, highlighting the benefits and potential consequences of using one of the phases as a commercial nucleal fuel, based on current literature.

2.1 The Uranium-Silicon System

The uranium-silicon system is comprised of seven intermetallic stoichiometric phases, and around six mixed-phase compounds. These phases are mapped in Figure 2.1 as a function of silicon content within the binary phase diagram provided by *Middleburgh et al.,* [42]. In the phase diagram, it can be seen that each stoichiometric phase is a line compound, which indicates a fixed ratio between uranium and silicon is required to form each compound. Observing the phases, the uranium silicide with the lowest silicon content is U_3Si, with roughly 25 $at.\%$ of silicon. The phase with the highest silicon content is uranium trisilicide (USi_3), with around 75% at.% of silicon. The

remaining stoichiometric and mixed compounds are situated in-between these two phases, with the exception of $\alpha + U_3Si$ which is situated before the U_3Si line compound. Alongside the silicon content (at.%) required for each phase, the melting temperatures (T_m) are also indicated. Here, it can be seen that uranium disilicide (USi_2) has the lowest melting temperature, around 723 K. Table 2.1 presents the crystal structure, space group, and lattice constants for each of the main uranium silicide line compounds. From this, it can be seen that three uranium silicide phases exhibit a tetragonal crystal structure, with U_3Si and $\alpha - USi_2$ being classified as body-centered tetragonal, and U_3Si_2 being primitive tetragonal. Multiple studies [43–45] have shown that U_3Si forms three different crystal structures: an orthorhombic *Fmmm* α-phase below 120 K, a body-centered tetragonal $I4/mmm$ β-phase at 120 K, and a cubic $Pm3m$ γ-phase above 1050 K. The lattice constants for the tetragonal β-phase are presented in Table 2.1. In addition to this, the uranium disilicide phase, USi_2, forms two phases: the α-phase which exhibits a body-centered tetragonal $I4/amd$ structure, and the β-phase which has a hexagonal $P6/mmm$.

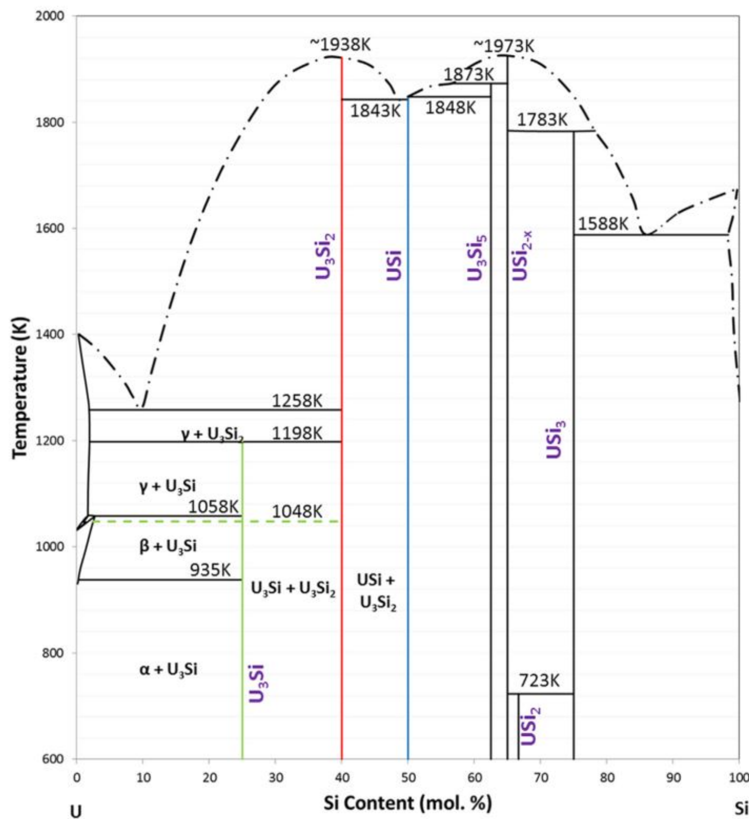

FIGURE 2.1. The binary phase diagram of uranium-silicon compounds. Figure taken from [44].

Structurally, the uranium silicide stoichiometric line compounds are well characterised.

Table 2.1: Fundamental structural properties of U-Si phases. *Formed after 120 K.

Phase	Crystal Structure	Space Group	a (Å)	b (Å)	c (Å)	Unit Cell (Å^3)
U_3Si [46]	Tetragonal*	I4/mcm	6.033	6.033	8.69(0)	316.29
U_3Si_2 [47]	Tetragonal	P4/mbm	7.331 ± 0.009	7.331 ± 0.009	3.900 ± 0.008	209.628
USi [48]	Orthorhombic	Pnma	7.67 ± 0.01	3.91 ± 0.01	5.66 ± 0.01	169.74
U_3Si_5 [49]	Hexagonal	P6/mmm	3.843 ± 0.001	3.843 ± 0.001	4.069 ± 0.001	60.093(6)
α-USi_2 [50]	Tetragonal	I 41/amd	3.922 ± 0.001	3.922 ± 0.001	14.154 ± 0.002	217.718
USi_3 [51]	Cubic	Pm-3m	4.060 ± 0.005	4.060 ± 0.005	4.060 ± 0.005	66.92(3)

However, the literature on the chemical characterisation is limited. Multiple studies have been conducted to investigate the electronic and mechanical properties of each compound. The total and partial density of states (DOS) have been calculated for U_3Si_2 [52], U_3Si_5 [53], USi [54], USi_2 [55], and USi_3 [56]. All of these studies have indicated that the phases are metallic due to the electronic density at the Fermi level.

Studies have also indicated the metallic nature of uranium silicide phases through the use of x-ray photoelectron spectroscopy. Here, the chemical characterisation is limited, as not all uranium silicide line compounds have been characterised in this way. However, a study which investigated the oxidation of uranium silicide phases, conducted by *Krummacher et al.,* [57], presented the pristine XPS data collected from the U-4f, Si-2s core levels of each phase. It was indicated that the phases exhibited strong photoemission peaks within the core levels corresponding to a uranium valency of U(0) at a binding energy of 377 eV, and metallic silicon with a binding energy of 150 eV. The uranium silicide phases investigated in this study were: U_3Si, USi, USi_2, and USi_3. Further XPS studies were conducted by *Yan et al.,* [58], investigated the ambient oxidation of sintered U_3Si_2 pellets. The metallic nature of U_3Si_2 was indicated with the U-4f and Si-2s core level spectra indicated metallic component binding energies around 377 eV, and 150 eV, respectively.

The metallic nature of the uranium silicide phases make them appealing as nuclear fuel types, as this suggests good thermal behaviours which are the result of electronic contributions across the metallic bonds. To fully realise the potential of using uranium silicide phases as nuclear fuels, the uranium density, and irradiation performance must be probed alongside the thermal behaviours.

2.1.1 The Chosen Fuels

The uranium-silicon system has been of significant interest as a nuclear fuel since 1988, where U_3Si and U_3Si_2 were initially utilised as a dispersion nuclear fuels by the Reduced Enrichment

Table 2.2: Fundamental properties of conventional and proposed advanced ATF fuels. * Measurement made at 1200 K.

Fuel	ρ $(g(U)cm^{-3})$	T_m (K)	κ ($Wm^{-1}K^{-1}$), 300 K	κ ($Wm^{-1}K^{-1}$), 583 K	κ ($Wm^{-1}K^{-1}$), 1500 K
UO_2	9.7 [42]	3138 [60]	8.4 [27]	4.8 [61]	3.6* [27]
UN	14.3 [62]	3120 [63]	13.2 [64]	17.0 [64]	24.8 [64]
U_3Si_2	11.3 [65]	1938 [42]	10.5 [65]	14.7 [65]	28.7 [65]
U_3Si	14.7 [62]	1258 [42]	13.5 [62]	19.9 [62]	-
U_3Si_5	7.5 [66]	2043 [42]	5.02 [66]	5.9 [66]	17.7 [66]

for Research and Test Reactors (RERTR) Program [41, 59]. This program was established in 1978 by the Department of Energy (DOE), with the primary objective to develop the technology to use Low-Enrichment Uranium (LEU) fuels rather than High-Enrichment Uranium (HEU) within research and test reactors. The requirement of the fuel was to maintain performance in the test reactors without occurring significant penalties in the experimental performance, reactor economics, or reactor safety. Here, both uranium silicide phases were used as dispersion fuels within an aluminium matrix. As dispersion fuels, U_3Si-Al has a uranium density of $6.1\,gUcm^{-3}$, however, the phase exhibited significant amorphisation under irradiating conditions. As a result, the fuel-type could not be used safely. The U_3Si_2-Al dispersion fuel has uranium densities of $4.8\,gUcm^{-3}$, and performed well under irradiation. As a result, the U_3Si_2-Al dispersion fuel was used in test and research reactors.

The heavy metal densities, and thermal properties of the U-Si compounds, make them appealing as nuclear fuels. However, when considering U-Si phases as commercial nuclear fuels, it is vital to consider how these compounds compare to the conventional UO_2 system. This comparison should take into consideration the thermal, irradiation resistance, and corrosion behaviours. In order for U-Si to replace the current ceramic uranium-oxide system, the phase that is chosen must supersede the current economic and safety standards that UO_2 upholds.

Three uranium silicide line compounds have been highlighted as potential replacement fuels for UO_2 in commercial light-water reactors. The phases considered are U_3Si, U_3Si_2, and U_3Si_5. Their desirable properties are presented in Table 2.2, alongside uranium mononitride (UN), and the current commercial nuclear fuel, UO_2. The data presented in Table 2.2, firstly indicates the uranium densities of each phases. Of the uranium silicide phases, U_3Si_2 exhibits the highest uranium density. The benefit of an increased uranium density, stems from having a higher fissile material content. This could reduce U-235 enrichment required to utilise the fuel, or it could extend the lifetime of the fuel elements. Three thermal conductivity values are presented in Table 2.2 for each phase, for 300, 589, and 1500 $Wm^{-1}K^{-1}$. This shows the thermal conductivities under ambient conditions, at the operating temperature for the primary coolant water in an

PWR [13], and finally the temperature at which a reactor core can reach during an accident scenario [67, 68]. From this, it can be seen that the thermal conductivity of uranium nitride, UN, is higher than the thermal conductivity of each uranium silicide phase at 300 K. The thermal conductivities of each phase presented in Table 2.2, are also presented in Figure 2.2 between a range of 237 and 1600 K. The thermal conductivity data of UO_2, collected from *White et al.,* [69], shows the decreasing thermal conductivity as a function of temperature. This behaviour contrasts the thermal conductivity behaviour of the metallic phases: U_3Si, U_3Si_2, U_3Si_5, and UN.

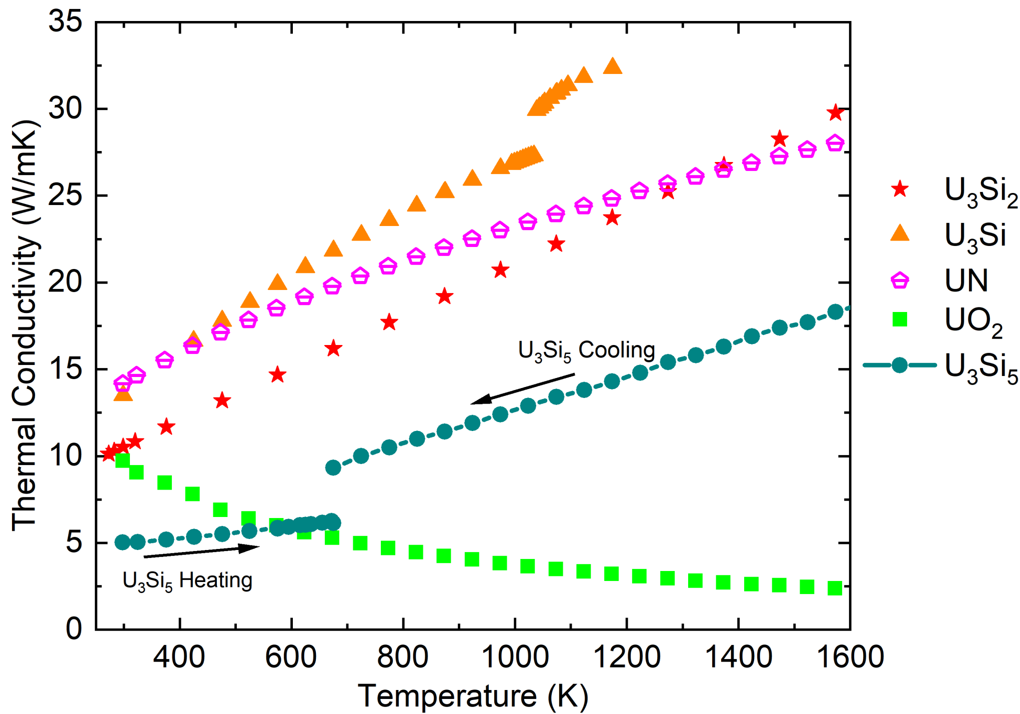

FIGURE 2.2. The thermal conductivities of ATF candidate fuels as a function of temperature. U_3Si, U_3Si_2, and U_3Si_5 data extracted from [62, 65, 66], UN data extracted from [64], and UO_2 data from [69].

Further observations indicate that the thermal conductivity behaviour of U_3Si exceeds the remaining compounds around 600 K. Despite the favourable thermal conductivity and high uranium density of U_3Si, the fuel-type has been shown to be susceptible to amorphisation and structural swelling once irradiated [70]. This renders the phase unusable as a commercial nuclear fuel, as the loss of structural integrity and loss of ordered crystalline structure restricts the thermal conductivity of the fuel. This behaviour has the potential to increase the centerline

temperature of the fuel, which could result in the fuel melting due to the low melting temperature of U_3Si.

The thermal behavior of U_3Si_5, was investigated by *White et al.,* [66]. Here, the thermal diffusivity, heat capacity, and thermal conductivity were investigated from ambient temperatures to 1773 K. The study probed sintered pellets of U_3Si_5, and through XRD analysis the samples were found to have inclusions of UO_2. The thermal conductivity data collected from this study is shown in Figure 2.2, as teal circles. For U_3Si_5, two data sets are presented indicated a cooling and heating regime. The reasons for the two regimes is the endothermic phase transformation that occurs to U_3Si_5 at 723 K. This phase transformation was shown to be reversible upon cooling of the U_3Si_5 sample. The authors [66] attributed the separate thermal conductivity regimes to this phase change. In addition to the phase change at 723 K, the authors further questioned the phase stability of U-Si compounds near the U_3Si_2 region of the phase diagram. The study concluded that there could be severe economic and safety consequences if U_3Si_5 were to be used as a fully realised commercial LWR fuel. Furthermore, the significantly lower heavy metal density that U_3Si_5 poses (Table 2.2), hinders the changes of the fuel being used as a replacement for UO_2 on a commercial scale.

Significant effort has been made to understand the thermal behaviour of U_3Si_2. A study conducted by *Wang et al.,* [52], investigated the electronic structures of U_3Si_2 through the use of density functional theory (DFT) calculations. Through investigating the crystal structure of U_3Si_2 it was determined that this phase exhibits a metallic nature, with U-Si, U-U, and Si-Si interactions being dominated by ionic, metallic, and covalent bonding types. Furthermore, through investigating the Density of States, it was indicated that the energy band of U_3Si_2 crossed the Fermi level, with contributions from the U-5f electrons. Here it was proposed that this could be the main source of the electron conduction in U_3Si_2. Further thermal investigations were conducted on bulk samples by *White et al.,* [65]. This study measured the heat capacity, thermal diffusivity, and thermal conductivity of sintered pellets of U_3Si_2, which were between 96% and 98% of the theoretical density of the phase which was taken to be $12.2gcm^{-3}$. The thermal conductivity was calculated as a function of temperature, between 273 to 1773 K, and was found to be proportional to the increasing temperature. Some values have been extracted from this study and are presented in Table 2.2. When compared to the remaining uranium silicide fuel candidates, it can be seen that the thermal conductivity of U_3Si_2 exceeds the other phases. The combined results from these two studies infer that the thermal properties of U_3Si_2 have electronic contributions that stem from the metallic bonding within the structure. This allows U_3Si_2 to have advanced thermal behaviours when compared to UO_2.

Irradiation testing is vital when assessing the behaviour of replacement nuclear fuels. Existing

studies that investigate the irradiation behaviour of UO_2 indicate that the thermal conductivity significantly deteriorates as a function of irradiation. Within a reactor, this causes an increase in the centerline temperature of the fuel pellet, leading to cracking and deformation of the structure [26, 71]. The relationship between the thermal conductivity of UO_2 and radiation damage reduces reactor efficiency and limits the lifetime of the fuel. For a fuel to replace UO_2, it must be able to retain its structure, and maintain its thermal transport abilities.

Initial studies conducted on the uranium silicide dispersion fuels, utilised in the RERTR program [41, 59], have been more recently investigated as part of interdiffusion studies. Here, the interaction between the uranium silicide 'fuel meat' and the aluminium matrix probed as a direct result of irradiation. The U_3Si-Al dispersion fuel has been shown to not perform well under irradiation, and exhibited unstable growth of fission-gas bubbles, causing the crystalline structure of U_3Si to become disordered and amorphous [72]. Further studies conducted on U_3Si by *Birtcher et al.,* [73] investigated the fuel-type as a stand alone fuel, not as a dispersion fuel. This study looked at the amorphisation of U_3Si when irradiated with 1.5 MeV Kr ions and through neutron irradiation. Through the means of neutron irradiation, amorphous zones were noted within the crystalline structure of U_3Si, which induced a crystallographic transformation from tetragonal to cubic. Complete amorphisation of the fuel was found to occur between 0.29 – 0.38 dpa. In addition, it was found that the temperature limit for total amorphisation of U_3Si during ion irradiation was $290°C$. This temperature is similar to the conditions of the primary coolant within an PWR ($316°C$) [13].

As a dispersion fuel, the U_3Si_2 fuel type has been investigated to probe its irradiation behaviour. Multiple studies , [72, 74, 75] have reported the accumulation of large fission gas bubbles as a result of the U_3Si_2 structure being irradiated. This caused swelling of the fuel, which can result in fuel failure if the structure becomes too strained. The authors [75], stressed that the presence of secondary uranium silicide phases, U_3Si and USi, being present in the fuel may be detrimental to the structural integrity of U_3Si_2, as these secondary phases have different swelling kinetics. Additional studies have been performed on U_3Si_2 fuel pellets to understand how this phase may behave as a commercial fuel. Bulk studies conducted by *Miao et al.,* [76] investigated the microstructure of U_3Si_2 as a result of 84 MeV Xe ion implantation at 600 °C. From high-temperature irradiation studies, U_3Si_2 has been found to retain its crystalline structure when exposed to temperatures above $250°C$ [77, 78]. At elevated temperatures, *Miao et al.,* [76] concluded that the Xe fission bubbles forming within the lattice of U_3Si_2 induced 1.54% swelling strain to the structure. Additional density functional theory (DFT) studies conducted by [79] suggest that Xe diffusion in U_3Si_2 are faster when compared to the uranium in UO_2.

Further studies conducted by *Yao et al.,* [80], compared the irradiation behaviour between

U_3Si_2 and U_3Si_5. Here, *in-situ* transmission electron microscopy (TEM), was utilised to probe the microstructural evolution as a result of ion beam irradiation. Both 1 MeV Ar^{2+} and 1 MeV Kr^{2+} ions were used to damage U_3Si_2, and the irradiation behaviour of U_3Si_5 was studied at room temperature and at 632 K using 1 MeV Kr^{2+} and 150 keV Kr^+ ions. The structure of U_3Si_5 was found to remain crystalline up to 8.8 dpa using 1 MeV Kr^{2+} ions under ambient conditions, whereas U_3Si_2 amorphised at 0.3 dpa. The authors [80] suggested the irradiation resistance of U_3Si_5 may be linked to its crystal structure ($p6/mmm$). The behaviour is similar to the irradiation resistance of UO_2, which exhibits a cubic crystal structure. UO_2 displays defect recovery in the disordered regions of the lattice when subjected to ion irradiation, whereas an anisotropic crystal structure, like orthorhombic U_3O_8, cannot recrystallise as easily [80–82].

From the studies conducted on the thermal behaviours of the three uranium silicide phases, it can be concluded that this behaviour type is well understood. The electron contribution to the thermal conductivity in all three phases makes the uranium silicide fuel type favourable. This advanced thermal behaviour supersedes the behaviour of UO_2, which solely relies on phonon contributions, thus weakening its ability to conduct heat at elevated temperatures. The irradiation behaviour of each ATF uranium silicide compound has also been investigated. The radiation tolerance appears to improve with increasing silicon content, indicating that U_3Si is the most susceptible to ion irradiation. The thermal and irradiation studies have allowed for the structural properties of each of these uranium silicide phases to be understood. For uranium silicide phases to be considered as replacements fuels which utilise water as its primary coolant, the corrosion behaviour of each uranium silicide phase must also be understood.

2.2 Oxidation of Uranium Silicide Fuels

2.2.1 Oxidation Testing

Understanding the oxidation behaviour nuclear fuel is a vital. The oxidation behaviour of a fuel type can dictate the implementation of the fuel into the nuclear fuel cycle. Often, the fuel type can be deemed unsuitable if the oxidation mechanism are detrimental to the overall structural integrity of the material. If uranium silicides are to be introduced into the commercial nuclear fuel cycle, the oxidation behaviour must be understood under multiple scenarios. This testing can include the formation of oxide as a function of temperature, to the change in oxidative behaviour as a result of irradiation. As the most promising ATF candidate, the majority of the studies investigating the oxidation of uranium silicides concentrates on U_3Si_2. Investigating the ambient and high-temperature oxidation of U-Si phases should be understood prior to investigating the dissolution. Here, the current literature detailing the oxidation of uranium silicide phases will be presented.

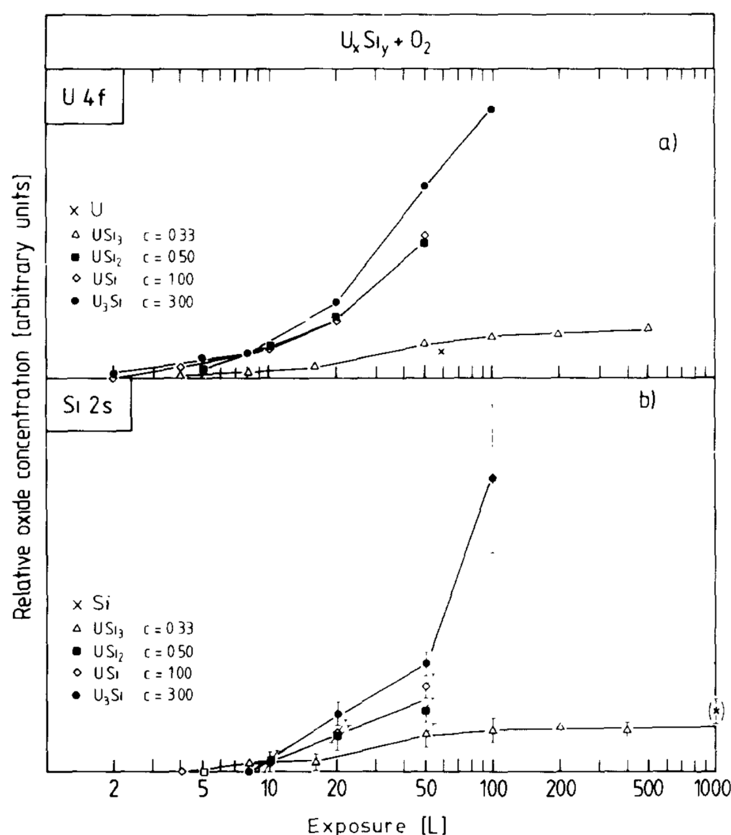

FIGURE 2.3. The relative oxide concentration observed in the U-4f and Si-2s core levels for U-metal, U_3Si, USi, USi_2, USi_3, and Si-metal as a function of ambient oxygen exposure . Figure taken from [57].

Initial oxidation studies conducted by *Krummacher et al.,* [57] in 1986, investigated the ambient oxidation of U_3Si, USi, USi_2, and USi_3 as a function of oxygen content. To investigate this oxidation, x-ray photoelectron spectroscopy was utilised to probe the environmental bonding of uranium and silicon. Through observing the U-4f and Si-2s core levels, this study showed that uranium silicides with a higher uranium concentration exhibited a stronger oxidation tendency. This is indicated from the data collected from the U-4f and Si-2s in Figure 2.3. A comparison is made between the U-Si compounds and elemental uranium and silicon, both indicated with black crosses. The c value indicated in the figure represents the U:Si concentrations for each compound. The authors concluded that the oxidation of uranium must break some of the U-Si bonds, allowing for increased activity of silicon in the U-Si bond. In addition, it was noted that the shift of the U-4f satellites, around 6.4 eV, with respect to the spectra collected from bulk UO_2, around 6.8 eV, infers that the oxidation of U in U-Si compounds does not result in the formation of UO_2.

Further oxidation studies using XPS were conducted by *Yan et al* [58], investigated the oxidation of the ATF candidate U_3Si_2 under ambient conditions. Spectra collected from the U-4f, Si-2s, O-1s, and valence band were collected from the surface of arc-melted pellets as a function of increasing oxygen concentrations. Two peaks associated with UO_2 were found in the U-4f spectra with binding energies of 380.7 and 391.6 eV. Both UO_2 photoemission peaks had associated satellites at 6.9 eV above the main U-4f peaks. These positions align with the uranium valency work reported by *Ilton et al.,* [83], suggesting a uranium valency of U(IV). The Si-2s spectra evolved from a metallic state, with a photoemission peak at 149.8 eV, to an oxidised state at a binding energy of 153.4 eV. The authors attributed this to the formation of a uranium silicate compound, $USiO_4$. Coffinite, $USiO_4$, is a naturally existing U^{4+} mineral [84], that was first discovered in the La Sal uranium mine in Colorado in 1955 [85]. This compound has been known to form as a result of UO_2 altering in spent nuclear fuel (SNF) geological repositories. Despite it's abundance in nature, the synthesis of $USiO_4$ is difficult, preventing a true understanding of how this compounds forms. The studies on coffinite, conducted by *Mesbah et al.,* [84], indicated that the stabilisation is determined by pH, temperature, Si:U ratio, and annealing time. Further characterisation on coffinite was conducted by *Pointeau et al.,* [86]. Coffinite was chemically characterised using XPS, probing the bonding environments present within the U-4f and Si-2s core levels. This data is presented in Figure 2.4, which draws binding energy comparisons between UO_2 and $UO_2(OH)_2$ in the U-4f core level, and SiO_2 and $ZrSiO_4$ for the Si-2s spectra.

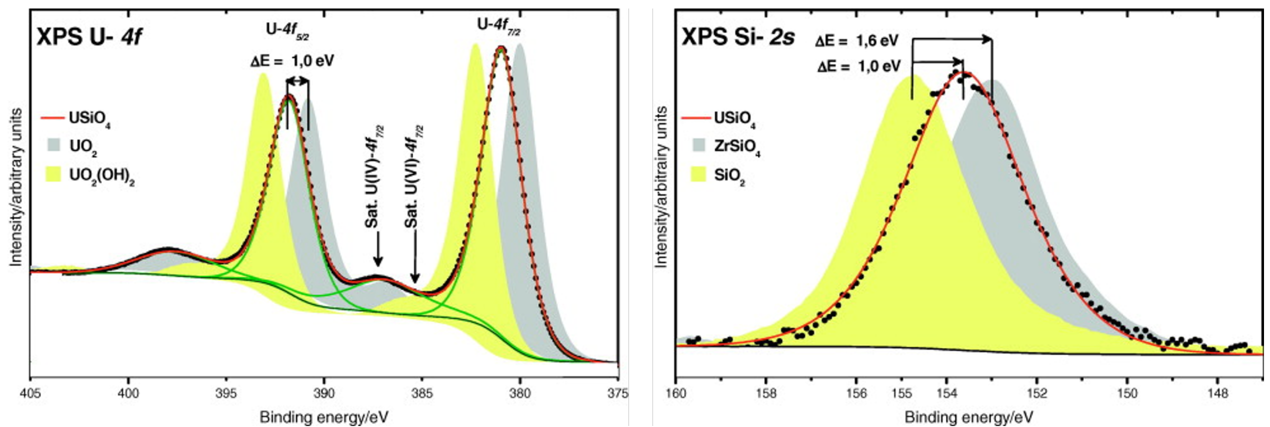

FIGURE 2.4. The XPS spectra collected from the U-4f and Si-2s of $USiO_4$. Figure taken from *Pointeau et al.,* [86].

The oxidation behaviour of U_3Si_2 was investigated experimentally and theoretically by *Jossou et al.,* [87]. The ambient oxidation of bulk U_3Si_2 samples were investigated experimentally through the use of Raman spectroscopy, x-ray diffraction (XRD), and scanning electron microscopy

(SEM). The experimental results indicated that the U_3Si_2 samples included a secondary phase of USi. This formation was attributed to the synthesis of the bulk sample. XRD spectra showed that only U_3Si_2 was present. The chemical data collected using Raman showed low intensity peaks that were attributed to uranium-oxide bonding. The theoretical calculation investigated the adsorption and surface reaction of oxygen on the three principal crystallographic surfaces, {001}, {110}, and {111}, with the intention to understand the initial mechanism that governs the oxidation of U_3Si_2. For all three cases, it was found that uranium sites are more active towards O_2 adsorption when compared to silicon, suggesting the preferential oxidation of U_3Si_2 at the uranium sites.

These studies all investigate the ambient oxidation of uranium silicide phases, with a large concentration on the oxidation of U_3Si_2. It is suggested that the uranium silicides oxidise less as the silicon content within the phase increases. There are discrepancies with regards to the oxide compound that forms initially as a result of U_3Si_2 oxidising. It is clear that the literature detailing the ambient oxidation of all uranium silicide compounds is very limited.

The high-temperature oxidation of uranium silicide phases, particularly U_3Si_2, is well documented [88–96]. Studies conducted by *Sooby Wood et al.,* [88], exposed U_3Si_2, USi, and U_3Si_5 arc-melted samples to a synthetic air environment, composed of 80% Ar and 20% O_2. The temperature of this environment was increased up to 1000 °C. The onset of breakaway oxidation was probed using thermogravimetric analysis (TGA), with phase changes being probed using high-angle x-ray diffraction (XRD). The high-temperature testing of these uranium silicide phases resulted in the complete pulverisation of each sample. The thermal analysis indicated that U_3Si_5 had a lower onset temperature that triggered the breakaway oxidation. This behaviour was linked to the phase change noted by *White et al.,* [66] at 723 K. It is believed that structural stresses caused by this phase change induced a quicker oxidation mechanism. Work conducted by *Snyder et al.,* [92], on refractory uranium compounds, observed the oxidation rates of U_3Si_2, USi, USi_2, and USi_3. *Snyder et al.,* claimed that the reaction rates with oxygen of the uranium silicide compounds increase with uranium content, which aligns with the ambient oxidation work conducted by *Krummacher et al.,* [57]. This work stated that the reaction of oxygen with uranium compounds can be expressed as:

$$w = kt^n \tag{2.1}$$

where w is the weight gain, measured in μg/cm^2, k is the rate constant, and t is time (s). The exponent term, n, is a constant which is determined by the rate law of the reaction that has occurred, thus, n = 1 (linear), n = 0.5 (parabolic), and n = 0.33 (cubic). The oxidation work conducted by *Sooby Wood et al.,* [88] at 50°C below the breakaway onset for each phase investigated did not align with either linear or parabolic reaction rates. Further isothermal oxidation tests were

conducted in this study [88], where the U-Si phases were held at temperatures that corresponded to 25°C above their respective oxidation breakaway temperatures. Figure 2.5 indicates the data collected from U_3Si_5 (red), USi (green), U_3Si_2 (blue), and U-metal (black). The three U-Si phases exhibit a more rapid linear oxidation when compared to U-metal. Additionally, there is significant mass gain (%) for both USi and U_3Si_2. The XRD analysis conducted on each U-Si phase indicated that U_3O_8 was the primary compound forming as a result of high-temperature oxidation. Each U-Si phase tested also had USi_3 and UO_2 forming as part of the oxidation process above the onset oxidation temperature. The study concluded that UO_2 is the first oxide to form on the surface during uranium silicide oxidation.

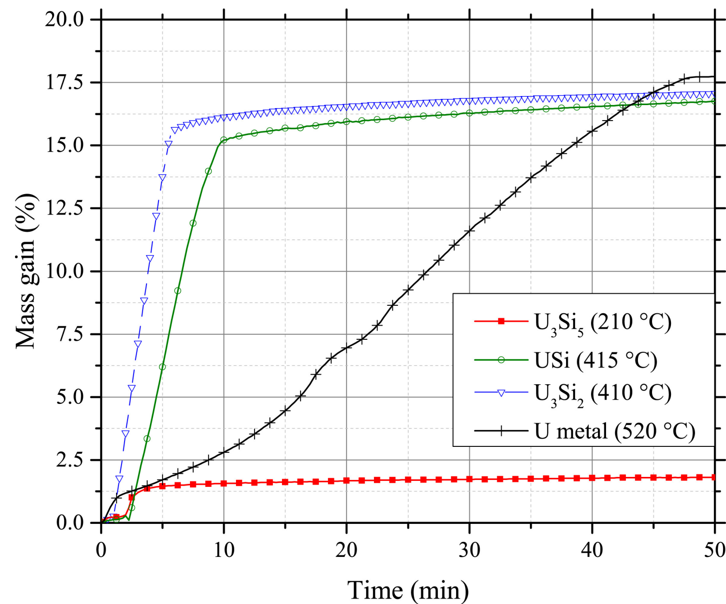

FIGURE 2.5. Isothermal oxidation testing of U-Si phases, 25°C conducted above their respective breakaway oxidation temperatures. Figure from [88].

Additional oxidation testing on ATF candidates were conducted by *Johnson et al.,* [91] on U_3Si_2, U_3Si_5. Their performances were compared to UN, a $UN-U_3Si_2$ composite fuel, and UO_2. TGA data extracted from each uranium silicide phase indicated a similar behaviour with regards to mass gain as a result of high-temperature oxidation when compared to by the *Sooby Wood et al.,* studies [88]. However, *Johnson et al.,* [91], suggested the formation of SiO alongside U_3O_8. A study on the oxidation of U_3Si_2, conducted by *Harrison et al.,* [90], showed that the oxidation also produced U_3O_8, but with no evidence of a SiO phase forming. This study argued that, theoretically, SiO_2 would form under high temperature oxidising environments. Regions of crystalline silicon were observed in the U_3Si_2 sample using scanning transmission electron microscopy (STEM). Further work conducted on a surrogate compound, Ce_3Si_2 by *Harrison et al.,* [97], investigated the oxidation of Ce_3Si_2 as a function of temperature. Through the use of XRD studies, it was

found that there was preferential oxidation of the Ce sites, when compared to the silicon. After heating the Ce_3Si_2 compound to $550\,°C$, Bragg reflections stemming from CeO_2 were identified. Prior to the formation of CeO_2, Bragg reflections from Ce_5Si_4 were also identified in the pristine XRD spectra, suggesting that both Ce-Si phases have oxidised at high-temperature to form CeO_2. In addition to this, *Yang et al* [94] showed the preferential oxidation of U_3Si_2 when exposing pellets to steam at temperatures between $400 - 900°$. It was shown that the uranium within U_3Si_2 oxidises to UO_2, whilst the silicon tend to form Si-rich uranium silicide phase: U_3Si_5, USi_2, and USi_3. The authors showed that the oxidation reaction of U_3Si_2 terminates with the formation of UO_2, SiO_2, and elemental silicon.

Investigations into the hydrogenation of U_3Si_2 have also been conducted [98–100]. Initial experimental studies conducted by *Maskova et al.,* [99], investigated the uptake of hydrogen into the tetragonal structure of U_3Si_2. It was found that the hydrogenation of this uranium silicide phase led to the formation of a ternary hydride: $U_3Si_2H_{1.8}$. This hydride was found to form at low hydrogen pressures, around 12 MPa, and induce a 10% volume expansion in U_3Si_2. This work was confirmed theoretically using DFT calculations. Here it was found that $U_3Si_2H_2$ also exhibited a similar volume expansion to $U_3Si_2H_{1.8}$. Recent work conducted by *Shivprasad et al.,* [100] indicated that U_3Si_2 was found to hydride at lower pressures when compared to uranium metal. The significant volume change for tetragonal U_3Si_2 when forming a hydride compound resonates with the high-temperature steam exposure studies conducted by *Sooby Wood et al.,* [101, 102], which found bulk U_3Si_2 fuel pellets to pulverise. This may suggest the uranium silicide hydride is forming under high-temperature aqueous conditions.

Efforts have also been made to improve the overall oxidation resistance of U_3Si_2. One study, conducted by *Sooby Wood et al.,* [103] investigated the effect of aluminium dopants within U_3Si_2. Both $U_3Al_2Si_3$ and U_3Si_2 + at%Al were investigated via TGA analysis and high-angle XRD. It was found that by increasing amounts of Al within U_3Si_2, the onset of breakaway oxidation in air (around $385\,°C$) is delayed. It was also found that a non-passivating layer of Al_2O_3 forms at 500 °C. Deeper investigations into the effect aluminium has on the oxidation resistance of U_3Si_2 were conducted by *Mohamad et al.,* [104]. This study inferred that only an addition of 1.8 at%Al was sufficient to increase the breakaway oxidation temperature to 550 °C, and additional thermal annealing allowed the Al_2O_3 oxide layer found in the work conducted by *Sooby Wood et al.,*, to become passivating. Further work conducted by *Mohamad et al.,* [105] doped sintered pellets of U_3Si_2 with $3\,mol\%$ yttria-stabilised zirconia (YSZ). It was found that this dopant increased the onset breakaway oxidation temperature of U_3Si_2 to 560 °C, which is a 176 °C increase when compared to un-doped U_3Si_2. Doping U_3Si_2 with chromium was investigated by *Gong et al.,* [106]. Various doping amounts ($3\,wt\%$, $5\,wt\%$, and $10\,wt\%$) were introduced into the sintered U_3Si_2 samples to understand the potential oxidation resistance induced by the presence of Cr-additives.

The addition of chromium increased the breakaway oxidation temperature of U_3Si_2 to 550°C.

A study conducted by *Kang et al.,* [107], investigated the oxidation behaviour of U_3Si in air between 250 – 400°C. Using high-angle XRD, it was found that this phase converted to UO_2, U_2O_5, and Si after being exposed to temperatures up to 275°C for 200 hours. At 300°, U_3Si had converted to UO_2, U_3O_7, SiO, and SiO_2, with U_3O_8 forming after 325°C. This indicates multiple oxidation regimes for the conversion of uranium silicides to U_3O_8. Much like U_3Si_2, the U_3Si sample also pulverised due to oxidation.

The high-temperature oxidation of U_3Si_2 is well-documented, however, there are still discrepancies within the literature about the onset of breakaway oxidation, the total mass gain as a result of oxidation, and the initial compounds that form at high-temperatures. In addition to this, oxidation investigations probing the behaviour of the remaining ATF fuels, U_3Si and U_3Si_5, are limited, with the remaining silicide line compounds having virtually no studies conducted on them at high-temperatures. Some work has been conducted on doping U_3Si_2, however, the feasibility of this work must be demonstrated fully. In addition, the basic oxidation properties of uranium silicide compounds must be understood prior to the dopant work. Furthermore, the link between ambient and high-temperature studies is lacking. The ambient studies presented here suggest the preferential oxidation of uranium, and the potential formation of uranium silicates. This work is not fully reflected in the high-temperature studies conducted on uranium silicide bulk material. There is a significant requirement for all uranium silicide phases to be investigated on an equal level if the preferential oxidation model is correct. Furthermore, surface sensitive chemical investigations are required to accurately identify oxidation compounds that are not being detected using high-angle XRD or TGA studies. There are gaps within the literature that link the ambient oxidation to high-temperature studies for all uranium silicide phases. By investigating the ambient oxidation for all uranium silicide compounds, it would provide a predictive model for the high-temperature oxidation.

2.3 Interaction with aqueous environments

Understanding the aqueous corrosion mechanisms of U-Si fuel candidates (U_3Si, U_3Si_2, U_3Si_5), and the secondary U-Si phases ($\alpha - USi_2$, USi_3) is imperative to the implementation of the fuel into the nuclear fuel cycle. Unpredictable corrosion behaviours can jeopardise the safety and the overall economics of the nuclear industry. This makes understanding the corrosion behaviours of potential replacement fuels a high priority.

Water-fuel interface interactions can occur throughout the nuclear fuel cycle, however, the most concerning interactions are expected during a reactor accident scenario, or during long

term storage as spent nuclear fuel (SNF). In-reactor accidents, for example, a cladding breach, would result in the fuel being subjected to elevated thermochemical environments [102]. Such conditions could result in the reduction of pellet structural integrity, or the complete pulverisation of the fuel, allowing highly soluble uranium species, formed via oxidation, into the LWR coolant circuit. Exposure to an aqueous environment during long-term storage could also result in the production of U^{VI} phases. This scenario has the potential to transport soluble radionuclides into groundwater systems [108, 109]. Both of these scenarios could significantly compromise the safety of the nuclear fuel cycle.

The particular temperatures, pressures, and water chemistry conditions will vary for each water/fuel interaction. However, scenarios that occur in-reactor or as SNF in storage will be in the presence of strong radiation fields. Therefore, there is a requirement to consider the effect radiation has on the aqueous corrosion of nuclear fuel. Radiolysis is the ionisation and excitation of water molecules from radiation. This process produces a series of oxidising compounds and short-lived reducing species, including: H_2O_2, $OH^{\bullet}$, $O_2^{\bullet-}$, $HO_2^{\bullet}$, and O_2 [40, 108, 110]. The species and reactions occurring as a result of water radiolysis are presented in Figure 2.6. Here three reaction stages are presented: physical, physio-chemical, and chemical stage. At each point, the species formed as a result of either the ionisation or excitation of H_2O are presented as a function of time.

Extensive studies have been conduced on the ionisation of water molecules and how the oxidising species formed effect the corrosion of UO_2 [40, 108, 111–114]. These bodies of work have shown that in the presence of oxidising species, dissolution of the UO_2 matrix occurs due to the conversion of U(IV) to U(VI), causing the formation of soluble UO_2^{2+} ions. What must be stressed, is that the dissolution and corrosion of UO_2 does not occur easily, and actually requires the highly corrosive products formed as a result of water radiolysis, as shown in Figure 2.6, or requires low pH solutions to take place under ambient conditions [109].

Research into the aqueous corrosion of U-Si phases has been previously conducted [101, 102, 106, 115], however there are still significant gaps and disparities within the literature, making our overall understanding of how these U-Si phases behave uncertain. Furthermore, the majority of the research focusses on high temperature water, and steam corrosion of the favoured fuel candidate, U_3Si_2. Therefore, this does not provide an insight into how silicon rich U-Si phases (U_3Si_5, USi_2, USi_3) behave in aqueous environments if formed as an inclusion in the original fuel melt, or as a oxidation product.

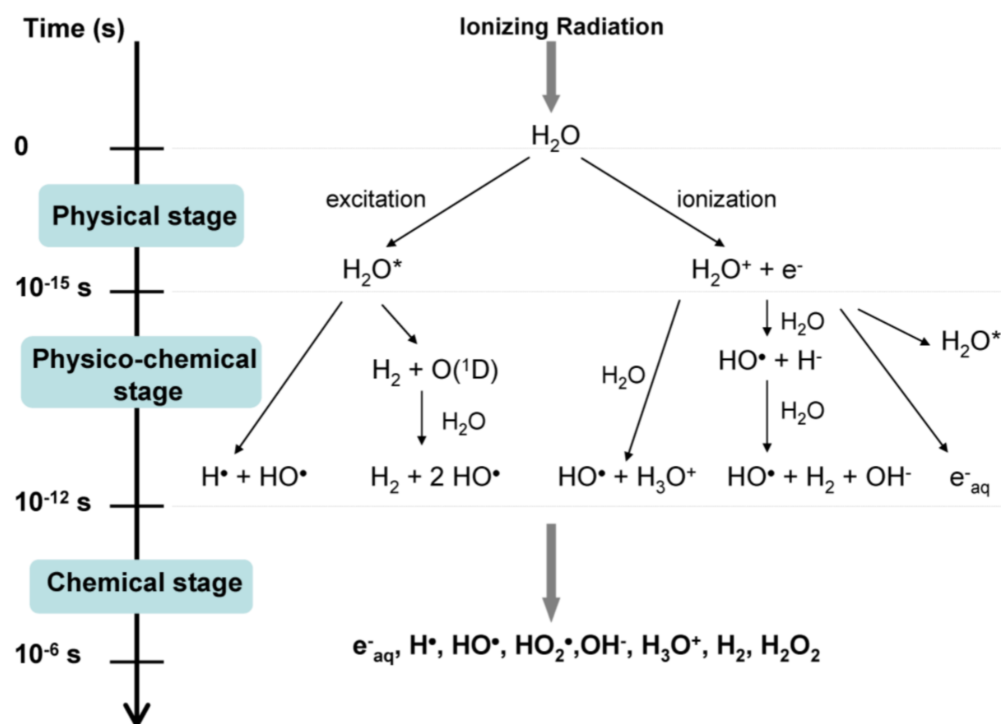

FIGURE 2.6. Schematic diagram depicting the main reactions and products formed as a result of water radiolysis. Figure from [116].

A proportion of the aqueous interaction investigations conducted on uranium silicide phases, mainly U_3Si_2, focusses on the behaviour of the fuel when in contact with steam. This reasoning stems from the likelihood of a cladding breach when the reactor is under normal operation. In the event of a cladding breach, there is an inrush of coolant into the fuel pin, which upon contact with the fuel, turns to steam. Understanding the impact on ATF fuels is vital for the implementation into the nuclear fuel cycle. In addition, as the ambient and high-temperature oxidation of uranium silicide fuels suggests the preferential oxidation of uranium within U-Si fuels, it is also ideal to understand the fuel/water interactions for all phases.

Substantial corrosion work was conducted by *Sooby Wood et al.,* [101], on how U_3Si_2 behaves in the presence of water and steam. The corrosion properties of U_3Si_2 sintered pellets was observed by flowing steam over the sample. Thermal ramp studies conducted on U_3Si_2 resulted in the expulsion of the sample from a crucible due to the energetic response from the sample as a result of fuel/steam interaction. This reaction occurred between $460-480°C$. Isothermal testing of U_3Si_2 within steam were conducted at 350 °C, 375 °C, and 400 °C. The isothermal testing at 350 °C resulted in the structural degradation of the U_3Si_2 sample. And the testings conducted at 375 °C and 400 °C resulted in the sample self-ejecting from the crucible after 4 and 1.5 hours, respectively. Figure 2.7 indicates the high-angle XRD spectra collected from U_3Si_2 once exposed

to air and steam environments. Pristine U_3Si_2 spectra is presented in black. The work conducted by *Sooby Wood et al.,* indicates that the products forming as a result of exposure to steam are: USi_3 and UO_2.

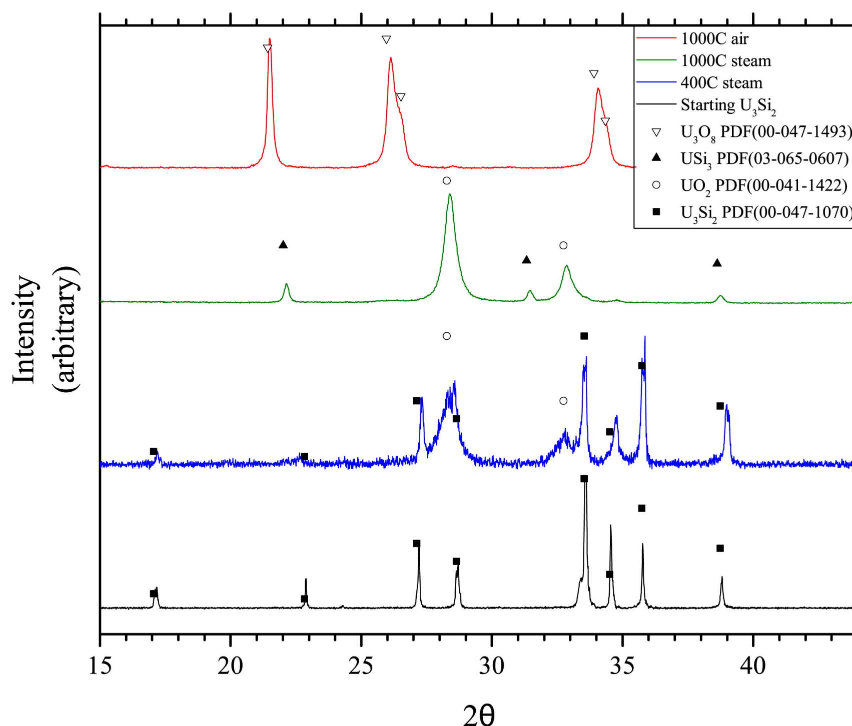

FIGURE 2.7. High-angle XRD spectra collected from U_3Si_2 after exposure to air at $1000°C$ (red), steam at $400°C$ (blue), and steam at $1000°C$ (green). Figure from [101].

These steam experiments on U_3Si_2 were furthered by *Nelson et al.,* [102] through investigating the corrosion behaviour within pressurised H_2O at temperatures between 300 – 350°C. This study also investigated U_3Si_5, UN, and UO_2 to allow for a comparison between ATF fuel candidates. This study probed the static and dynamical autoclave testing of each compound to investigate the evolution of oxidation as a result of water interaction. The dynamical testing of U_3Si_2 involved introducing redox buffer substances into the autoclave system. For this study case both Ni/NiO and Co/CoO were used, allowing for a deeper understanding of how U_3Si_2 behaves within oxidising and reducing environments. The oxygen, or hydrogen, content of the closed autoclave system is therefore dictated by the thermodynamic equilibrium of the buffer powders as a function of temperature. This therefore allowed for the chemistry of the autoclave system to be controlled. The dynamic autoclave testing on U_3Si_2 induced structural degradation to the pellets at 350°C, 85 bar, with 5 ppm of H_2. Pellets tested at 300°C had some retention in their structures. Dynamic autoclave testing of U_3Si_5 was not performed, as this phase was

found to pulverise during the static autoclave testings which were undertaken at 250°C and 300°C. XRD spectra collected from U_3Si_5 fragments indicated the formation of only UO_2 and USi_3. Here, the pulverisation mechanisms as a result of the autoclave testing, proposed by *Nelson et al.,* [102], is that a hydride forms within the internal structure of the fuel pellet, inducing the pulverisation of U_3Si_2. The source of the hydrogen could stem from oxidation of U_3Si_2 with molecular H_2O, forming hydrogen as a product and diffusing into the bulk structure. This type of hydride formation has been noted in zirconium cladding of PWRs [30, 117].

Oxidation testing of U_3Si_2 within steam, conducted by *Yang et al.,* [94], led to another oxidation mechanism description. Figure 2.8 presents the proposed oxidation mechanism for U_3Si_2 as a function of temperature. Here, four categories are indicated, 1-4, and are described as:

- (1) Si-depleted UO_2
- (2) U-Si compounds, i.e un-reacted U_3Si_2 and Si-rich U-Si compounds
- (3) Pure Si
- (4) UO_2 and SiO_2 mixtures

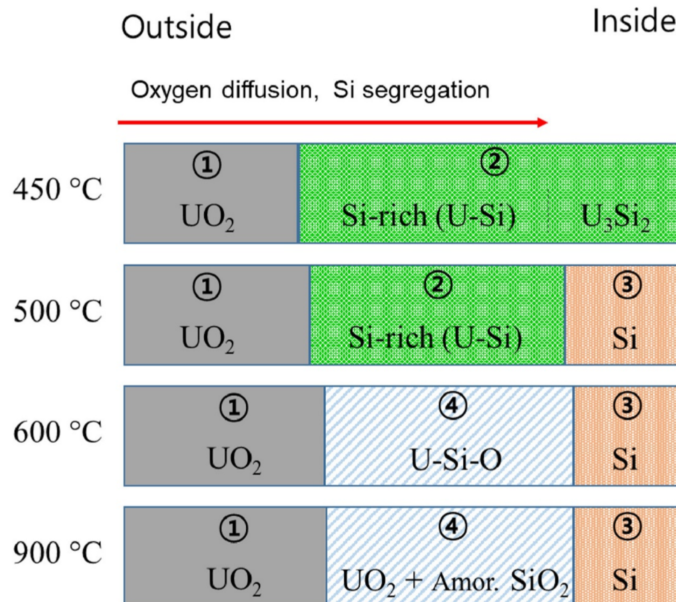

FIGURE 2.8. Schematic diagram of the U_3Si_2-steam interaction mechanism as a function of temperature proposed by *Yang et al.,*. Figure from [94].

With reference to Figure 2.8, outside and inside are indicating regions of a U_3Si_2 sample, therefore indicating that the outside region is the very surface of the oxide formation. As previously stated for the oxidation of uranium silicide phases, particularly U_3Si_2, in air, there is also a preferential oxidation of the uranium sites which permit for the formation of silicon-rich compounds up to USi_3, when eventually silicon dissociates and forms elemental silicon. This is noted for the steam experiments conducted at 450 °C and 500 °C by *Yang et al.,* [94]. Compounds formed after 600 °C indicate that the uranium within the U-Si phase is completely converted to UO_2, with some of the silicon converted to SiO_2. Alongside the oxidation compounds, the volume expansion of U_3Si_2 was theoretically calculated to be 79.4 % when exposed to H_2O under these conditions.

Additional work conducted by *Maier et al.,* [118], investigated the radiation induced dissolution of U_3Si_2. Here, the dissolution of U_3Si_2 ingots were exposed to both H_2O_2 solution and water in the presence of a 137 Cs γ-source, thus inducing the formation of H_2O_2. This study concluded that U_3Si_2 is more reactive to H_2O_2 when compared to UO_2. In addition, U_3Si_2 was found to not form any additional phases as a result of the dissolution process.

The literature discussing aqueous corrosion of uranium silicide phases is limited. The majority of the work naturally focusses on the prime ATF candidate, U_3Si_2. However, for the dissolution and corrosion mechanisms of the uranium silicide phases to be understood, investigations must be conducted on all of the phases. The high-temperature steam corrosion testing conducted by *Yang et al.,* [94], aligns well with the preferential oxidation mechanism proposed by *Jossou et al.,* [87]. However, significant studies must be undertaken on all uranium silicide compounds to allow for a substantial model to be formed for the ambient oxidation and aqueous corrosion of these materials.

2.4 Thesis Outline

The literature discussed above has provided an overview of the work conducted on uranium silicide compounds. This brief discussion is by no means a complete summary of the available literature on the uranium silicides, it does however, provide an indication into the mechanisms and characteristics that are understood about these nuclear compounds, alongside the clear gaps and discrepancies within the field. This summary has highlighted some of the advantages and disadvantages of using uranium silicide compounds as a nuclear fuel, when compared to UO_2. The overall increased uranium density of both U_3Si and U_3Si_2, alongside their improved thermal conductivities suggest promising nuclear fuels. The thermal performance of the chosen candidate uranium silicide fuels, U_3Si, U_3Si_2, and U_3Si_5, must however outweigh the concerns over oxidation breakaway and pulverisation within high-temperature aqueous environments.

The significant gaps within the literature, concerning the corrosion of uranium silicide phases, have been highlighted, and as a result these form the main focus of this thesis.

The primary aim of this thesis is to improve the understanding of uranium silicide phases by conducting fundamental experiments, thus gaining knowledge that is relevant to the implementation of uranium silicide as a nuclear fuel. Where large scale experiments on bulk nuclear material may be more realistic, they reduce the ability to replicate such experiments, and induce complexity into understanding the effects of isolated parameters. The aim here is therefore to reduce this complexity, allowing for single parameter studies to be conducted on uranium silicide compounds. This will be achieved through synthesising novel thin film samples of uranium silicides. The engineering of such idealised surfaces will be discussed alongside the advantages gained through studying nuclear fuel in this way in Chapter 4. Here, the methods used to form thin film samples will be described. A vital aspect of conducting and understanding the corrosion of the material is the characterisation of that material prior to experiment. Therefore, the structural and chemical characterisation of each uranium silicide phase produced will be presented in Chapter 5. The investigations presented here should provide additional insight into the intrinsic properties of uranium silicide compounds.

The synthesis and characterisation of such novel samples provides the basis for conducting experiments that probe the corrosion behaviour of uranium silicides. As previously discussed, the ambient oxidation of uranium silicide compounds is relatively understudied, therefore, the thin film samples will be used to examine the chemical and structural changes induced in the uranium silicides. This work will be presented in Chapter 6, where a multi-technique approach is used to uncover the ambient oxidation of these materials. These experiments probe the structural, chemical, and overall oxide thickness changes as a function of ambient air exposure for various uranium silicide compounds. Chapter 7 explores the corrosion properties of these phases as a result of being exposed to two aqueous environments: H_2O and H_2O_2. Therefore, the work presented here is an extension to the ambient air corrosion properties discussed in Chapter 6. Here, the dissolution is measured within two aqueous mediums using high-angle x-ray diffraction and x-ray reflectivity as a means to understand the phase and morphology changes occurring at the surface of each compound.
Finally a summary of the findings is presented in Chapter 8, along with the potential implications, improvements, and further questions raised.

CHAPTER 3

ANALYTICAL TECHNIQUES

This chapter details the techniques used throughout this thesis to accurately characterise and analyse uranium thin films. The combination of the x-ray based techniques: x-ray diffraction, x-ray reflectivity, and x-ray photoelectron spectroscopy, has proved invaluable to this thesis. Here, the origins of x-rays as crystal lattice probes will be shown, with the theory behind these analytical techniques being explained with relevance to this thesis.

3.1 X-rays

X-rays were discovered in 1895 by Wilhelm Roentgen, where he found that fluorescent sheets coated in barium platinocyanide discoloured when exposed to cathode rays [119]. Since their discovery, x-rays have been utilised to understand countless phenomena across all scientific disciplines. X-rays are high energy electromagnetic waves which extend across the electromagnetic spectrum with wavelengths in the range of 0.1Å and 100Å. This feature is on the scale of inter-atomic distances, making x-rays useful for investigating structural properties of materials. Additionally, x-rays have energies between 200 eV and 1 MeV, which are in the range of x-ray - electron interactions [120]. Therefore, x-rays can be tuned to probe the electron binding energies in materials for elemental and chemical characterisation, often performed through the use of techniques like x-ray photoelectron spectroscopy (XPS). This is further explained in section 3.5. This adaptability makes using x-ray to probe crystalline materials invaluable to this project, and it is for this reason that x-ray techniques have been used characterise and investigate uranium silicide thin films.

3.2 Interactions between X-rays and Matter

Before delving into the theory of x-ray diffraction and x-ray photoelectron spectroscopy, it is important to understand the different ways x-rays can interact with matter. It is the understanding of these interactions that allows for a plethora of information to be extracted from a material using x-rays. These interactions can be categorised into two regimes: scattering and absorption [120–123]. These are defined by the following:

Scattering: **Thomson Scattering** An incident photon with energy $h\nu$ elastically interacts with an electron with no loss of energy or change of phase.

Compton Scattering An incident photon, with energy $h\nu$, is inelastically scattered by an electron, resulting in a less energetic photon and a corresponding electron carrying the energy lost by the incident photon.

Absorption: **Photoelectron emission** An incident photon, with energy $h\nu$, is adsorbed by an electron, which is then excited. If the electron is excited with an energy greater than its binding energy, the electron will escape from the atom. The ejected electron is known as a photoelectron.

Fluorescence An incident photon, with energy $h\nu$ excites an electron to a higher energy level, i.e from the K-edge to the M-edge. This creates a vacant hole in the K-edge, which will eventually be filled by an electron from a higher energy level. Upon the vacant hole being filled, a photon with energy equal to the difference in energy levels will be emitted.

Auger electron emission An incident photon, with energy $h\nu$ removes an electron leaving a vacant hole in one of the energy levels, for example, the K-edge. When this vacant hole is filled from an electron situated in a higher energy level, i.e. M-edge, a photon, with energy equal to the energy difference, is emitted. This emitted electron may then excite and remove a secondary electron from the atom.

Figure 3.1 shows the schematics of each interaction described above. The utilisation of these interaction processes has led to the development of x-ray probing techniques that allow for the structural and chemical properties of materials to be analysed. Material characterisation is crucial over a wide range of disciplines, and x-ray probing techniques make it possible to conduct analysis on uranium silicide thin films for the purpose of this thesis. This chapter will cover the basic principals and analysis techniques of x-ray diffraction (XRD), x-ray reflectivity (XRR), and x-ray photoelectron spectroscopy (XPS).

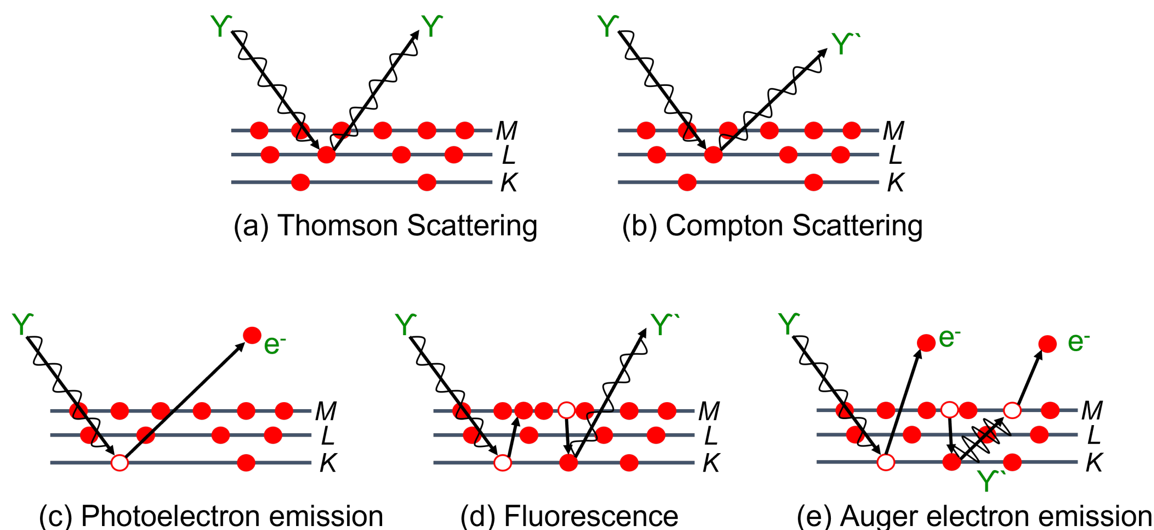

FIGURE 3.1. Schematic showing the various scattering and absorption interactions that x-rays have with matter. Scattering interactions are: (a) Thomson Scattering, (b) Compton Scattering. Absorption interactions are: (c) Photoelectron emission, (d) Fluorescence, (e) Auger electron emission.

3.2.1 Sources

X-rays can be generated through various means. The most commonly used method for generating x-rays is through the use of a standard x-ray tube. Tube source x-rays have fixed energies and wavelengths, which can limit their use. X-rays can also be generated via synchrotron radiation. The requirement of synchrotron sources stems from the limiting factors in laboratory sources. This provided a varied wavelength and radiation energy, enhancing many experimental studies. Only laboratory sources have been used to examine uranium silicide and oxide phases in this thesis, therefore the workings of synchrotrons will not be discusses here.

The original laboratory x-ray source was developed by William Coolidge in 1912 [124]. This device accelerated electrons, which were produced by a glowing filament, towards an anode. Upon collision, this electrons lost energy which manifested as radiation in the form of x-rays [125]. Only around 1% of the colliding electrons are converted into x-rays, the remaining are dissipated as thermal energy into the anode [125]. Despite the anode being water-cooled, the ability for the anode to remove the thermal energy is the limiting factor in the tube source intensity. Overall, the generation of an x-ray is governed by the change in velocity of electrons. Through the acceleration, deceleration, or direction change of electrons, x-rays can be produced. It is through these particular motions that electromagnetic energy is generated by an electron. This radiation is known as *Bremsstrahlung*, or breaking radiation. The range of x-ray energies

produced from *Bremsstrahlung* radiation is presented in Figure 3.2. Here, it can be seen that the overall spectrum is continuous. This continuous energy range is undesirable when utilising x-rays for characterisation purposes, therefore this is often filtered out. Alongside the *Bremsstrahlung* spectrum, there are protruding spectral features which exist at discrete photon energies. These are referred to as characteristic x-rays, and are produced as a result of fluorescence, which is when a incident electron causing an atomic electron to be removed from an inner electron shell, resulting in a vacant hole [124]. As an outer-shell electron relaxes into this vacancy, a photon is released which has a characteristic energy, equal to the energy difference between the two shells. This process is depicted in Figure 3.1 (d). These characteristic radiation features stem from the anode, and therefore are dependent on the energy levels of this material. This fixes the energy of the x-rays produced from the tube source anode, which are commonly made copper or molybdenum.

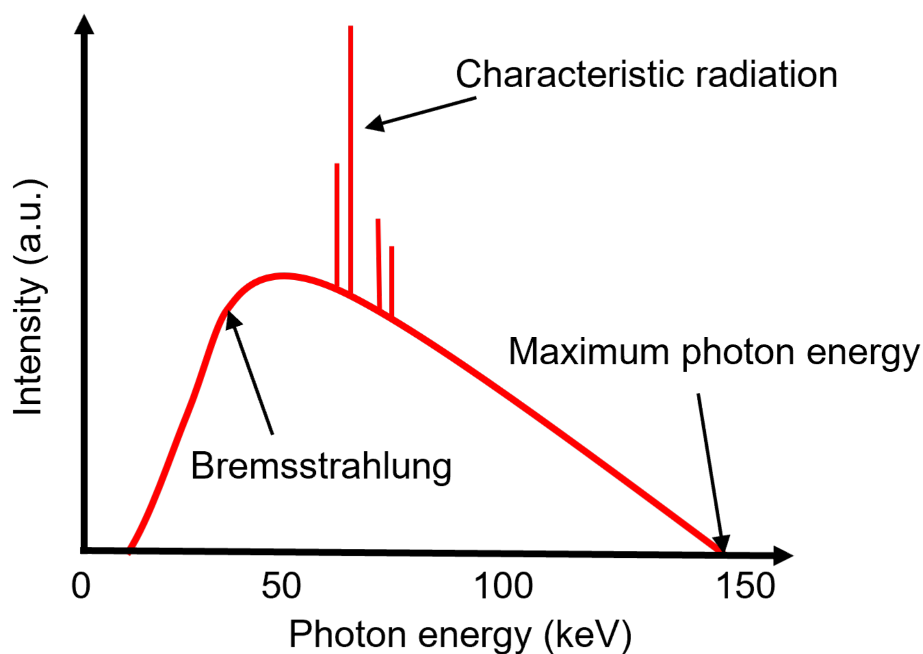

FIGURE 3.2. Schematic showing the range of energies produced using a laboratory x-ray tube source. The broad continuous spectrum is a result of the *Bremsstrahlung* radiation. Characteristic radiation lines are produced from fluorescence. Figure reproduced from [126].

3.3 X-ray Diffraction

The scattering processes described in Section 3.2 are for x-ray interactions with an individual atom. To fully understand the usefulness of x-ray interactions with matter, the model must be built from electron scattering, to whole atom scattering, and then eventually scattering from a crystal. This section provides and overview of the classical XRD theory, with the majority of the information presented here being obtained from *Elements of Modern X-ray Physics by J.Als-Nielsen and D. McMorrow* [124], *X-ray Diffraction: A Practical Approach by C. Suryanarayana and M. Grant Norton* [125], and *Introduction to Solid State Physics by C. Kittel* [127].

3.3.1 XRD Theory

The periodic arrangement of atoms is a distinguishing feature of any crystalline material, particularly when compared with amorphous substances [128]. It is this long-range order of the atoms in three spatial dimensions that is intrinsic to the Bragg theory of diffraction. Bragg's Law states that x-ray reflected from atomic planes within a crystalline material, with a lattice spacing d, give rise to constructive interference [124, 127]:

$$n\lambda = 2d\sin\theta \tag{3.1}$$

with nλ representing an integer number of wavelengths, d is the spatial distance between successive lattice planes, and θ is the angle of incidence. Figure 3.3 presents the Bragg construction, representing this interaction. Bragg's law is a good approximation for the constructive interference of waves within an ordered structure, however it is limited in that fact that it does not calculate the scattering intensity for which this constructive interference occurs [127, 128]. To build upon this theory, understanding the origin of x-ray scatting is required.

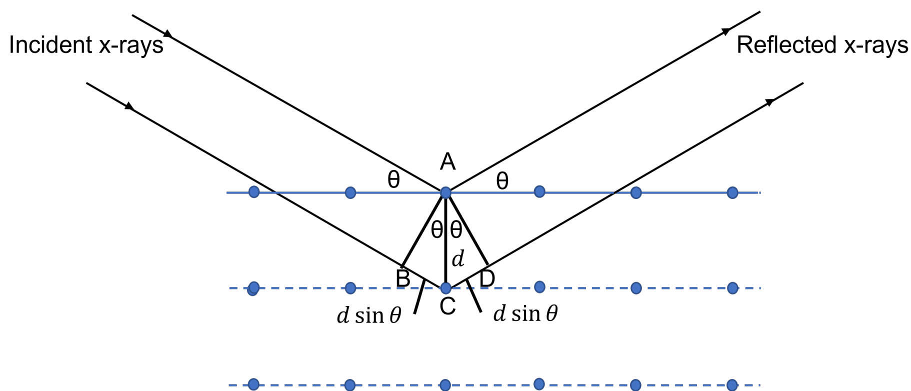

FIGURE 3.3. Schematic showing Bragg's law in the case of a 2-dimensional lattice.

3.3.1.1 Scatting from an Electron

Let's begin by first considering the classical scattering of electromagnetic waves, in this case x-rays, by a free electron. An linearly polarised incident x-ray beam will exhibit an electric field, E at time t, which is given by:

$$E = E_0 e^{i(\omega t - \phi)} \tag{3.2}$$

As this wave becomes incident on an electron, it will experience a coulombic interaction, where the force is equal to the product of the electron charge, q_e, and the electric field, E [129]. Therefore, the resulting acceleration, a, of the electron will become:

$$a = \frac{q_e}{m_e} E_0 e^{i(\omega t - \phi)} \tag{3.3}$$

Note that m_e is the mass of the electron. This interaction results in the creation of a field, $E(\mathbf{r})$, as the accelerated electron becomes a radiation source, essentially scatting the incident x-ray beam in all directions. At a position $\mathbf{r}$ in space, the field is given by Eqn 3.4:

$$E(\mathbf{r}) = \frac{q_e \mathbf{a} \sin\theta}{c^2 \mathbf{r}} = -E_0 \frac{q^{2_e}}{m_e c^2} \frac{1}{\mathbf{r}} \sin\theta \, e^{i(\omega t - \phi)} \tag{3.4}$$

where, θ is the angle between the position of the vector $\mathbf{r}$, and the direction of the acceleration, $\mathbf{a}$. Here, the direction of $E(\mathbf{r})$ is perpendicular to the acceleration, $\mathbf{a}$, with the magnitude of $E(\mathbf{r})$ being proportional to the acceleration. From the negative sign indicated on the right-hand side of Eqn 3.4, it can be deduced that the scattered radiation within the field is 180° out of phase with the incident electromagnetic wave, E. The Thomson scattering length, r_0, equivalent to the electron radius [124], is presented in Eqn 3.5. This equation represents the classical treatment of the scattered-to-incident amplitude ratio between two electromagnetic waves.

$$\frac{E(\mathbf{r})}{E_0} = -\frac{q^{2_e}}{m_e c^2} \frac{1}{\mathbf{r}} = -\frac{r_0}{\mathbf{r}} \tag{3.5}$$

3.3.1.2 Scattering from an Atom

This model will now be developed to understand the interaction between x-rays incident on a single atom, and thus the scattering of x-rays incident upon Z number of electrons. This scattering process will produce a scattered radiation field which is a superposition of the scattering contributions from these electrons [124]. To simplify the sum of all the electron contributions, the

electron distribution is referred to as a number density, $\rho(\mathbf{r})$. To evaluate this scattered radiation field, the phase, ϕ of the incident wave as it interacts with volume element initially, and at a position $\mathbf{r}$. The phase difference between the scattered wave from both volume elements is [124]:

$$\Delta\phi(\mathbf{r}) = (\mathbf{k} - \mathbf{k'}) \cdot \mathbf{r} = \mathbf{Q} \cdot \mathbf{r} \tag{3.6}$$

with **k** and **k'** are the wavevector at the origin and at position **r**, respectively, and **Q** is the *wavevector transfer*. From the schematic shown in Figure 3.4, it is shown that for a elastic scattering interaction, where $|\mathbf{k}| = |\mathbf{k'}|$, and under the condition this is a longitudinal scattering event where $\theta_i = \theta_f$ it can be shown that:

$$|\mathbf{Q}| = 2|\mathbf{k}|\sin\theta = \frac{4\pi}{\lambda}\sin\theta \tag{3.7}$$

with,

$$k = \frac{2\pi}{\lambda} \tag{3.8}$$

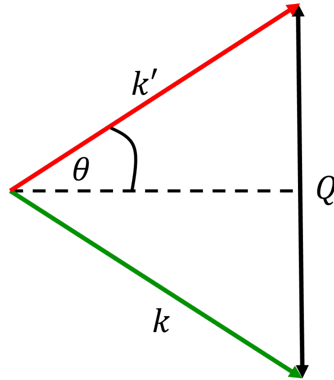

FIGURE 3.4. Schematic showing the geometry for the wavevector transfer.

here, λ is the wavelength of the incident radiation. A volume element, $d\mathbf{r}$ at position $\mathbf{r}$ will contribute an amount $-r_0\rho(\mathbf{r})d\mathbf{r}$ to the scattered field, with a phase factor of $e^{i\mathbf{Q}\cdot\mathbf{r}}$. From this, the total scatting atomic form factor, $f^0(\mathbf{Q})$ can be obtained through integrating over $\mathbf{r}$ [124], and thus:

$$-r_0 f^0(\mathbf{Q}) = -r_0 \int \rho(\mathbf{r}) e^{i\mathbf{Q}\cdot\mathbf{r}} d\mathbf{r} \tag{3.9}$$

Note that in the limit that Q tends to 0, all of the various volume elements scatter in phase so that $f^0(\mathbf{Q} = 0)$ equates to Z, i.e. the number of electrons within the atom. As the wavevector, Q increases, the volume elements begin to scatter out of phase, and thus as the atomic form factor,

$f^0(\mathbf{Q} \to \infty)$, it equates to 0 [124].

In reality, atomic electrons exist in discrete energy levels, with the most tightly bound electrons existing in the K-shell [130]. These electrons have energies comparable to a x-ray photon. For incident photons that exhibit energies that are lower than that binding energy of the K-shell, the overall electron response to the driving field is reduced [124]. If electrons are bound in higher electron shells (L, M,), they will respond to the driving field more closely, however, the scatting length of the atom will be reduced by an amount. This is denoted by f'. In the case that the incident energies are much greater than the binding energy, the electron will be treated as free and thus, $f' = 0$. If the *real* component of the scattering length if altered, then it is expected that the electron will experience a phase lag with respect to the driving field. Thus, the *imaginary* component, if'', is included. Therefore, the atomic form factor becomes:

$$f(\mathbf{Q}, \hbar\omega) = f^0(\mathbf{Q}) + f'(\hbar\omega) + if''(\hbar\omega) \tag{3.10}$$

with f' and f" known as the dispersion corrections to f^0 [124].

3.3.1.3 Scattering from a Crystal

Furthering the model for the x-ray scatting from an individual can be done so by considering the scattering of x-rays from an array of atoms, i.e. an entire crystal. The defining property of a crystal is its periodic nature, with the atoms arranged in a lattice formation. Therefore, the lattice vectors which ultimately describe the crystal are defined as [124, 127, 131]:

$$\mathbf{R}_n = n_1\mathbf{a}_1 + n_2\mathbf{a}_2 + n_3\mathbf{a}_3 \tag{3.11}$$

with $(\mathbf{a}_1, \mathbf{a}_2, \mathbf{a}_3)$ representing the basis vectors of the lattice, and (n_1, n_2, n_3) being integers. Using this periodic vector notation, and defining the position of the atoms with respect to any one lattice site to be $\mathbf{r}_j$. The position of any atom within the crystal is defined by the sum of $\mathbf{R}_n + \mathbf{r}_j$. Therefore, the scatting amplitude for an entire crystal is defined as [124]:

$$F_{crystal}(\mathbf{Q}) = \sum_{\mathbf{r}_j} f_j(\mathbf{Q}) e^{i\mathbf{Q}\cdot\mathbf{r}_j} \sum_{\mathbf{R}_n} e^{i\mathbf{Q}\cdot\mathbf{R}_n}. \tag{3.12}$$

The first summation term represents the unit cell structure factor, with the second term being the summation over the lattice sites. Considering the lattice site summation term. This is referred to as the *phase factor* [124]. For random values of $\mathbf{Q} \cdot \mathbf{R}_n$, this term will sum to 0, however if the condition,

$$\mathbf{Q} \cdot \mathbf{R}_n = 2\pi \times integer \tag{3.13}$$

is satisfied, then the phase factor will be non-zero. Solutions to Eqn 3.13, can be found by introducing the reciprocal lattice, which has a set of vectors defined as:

$$\mathbf{G} = h\mathbf{b}_1 + k\mathbf{b}_2 + l\mathbf{b}_3 \tag{3.14}$$

with, h, k, and l being integers and the reciprocal lattice vectors $\mathbf{b}_1$, $\mathbf{b}_2$, and $\mathbf{b}_3$ defined as:

$$\mathbf{b}_1 = 2\pi\frac{\mathbf{a}_2 \times \mathbf{a}_3}{\mathbf{a}_1 \cdot (\mathbf{a}_2 \times \mathbf{a}_3)}, \mathbf{b}_2 = 2\pi\frac{\mathbf{a}_3 \times \mathbf{a}_1}{\mathbf{a}_2 \cdot (\mathbf{a}_3 \times \mathbf{a}_1)}, \mathbf{b}_3 = 2\pi\frac{\mathbf{a}_1 \times \mathbf{a}_2}{\mathbf{a}_3 \cdot (\mathbf{a}_1 \times \mathbf{a}_2)}, \tag{3.15}$$

Each vector presented in Eqn. 3.15 is orthogonal to two axis vector of the crystal lattice [127]. The vector $\mathbf{G}$, depicted in Eqn 3.14 is thus the reciprocal lattice, and the accompanying values, h, k, and l, describe the plane that is perpendicular to $\mathbf{G}_{hkl}$. This reciprocal lattice vector provides a solution to Eqn. 3.13, when,

$$\mathbf{Q} = \mathbf{k}' - \mathbf{k} = \mathbf{G}_{hkl}, \tag{3.16}$$

giving rise to non-zero values of $F_{crystal}(\mathbf{Q})$. This solution is known as the Laue condition. This describes the conditions for the observation of constructive interference [131]. Recognising that $\mathbf{G}_{hkl} = \frac{2\pi}{d_{hkl}}$ and remembering that $\mathbf{Q} = \frac{4\pi \sin\theta}{\lambda}$, it can be stated that:

$$\lambda = 2d_{hkl}\sin\theta \tag{3.17}$$

showing that the Laue and Bragg formulations are equivalent. The Laue condition can be visualised in two-dimensions using an *Ewald sphere construction*.This determines the directions of **k'** for which constructive interference between the x-ray and lattice is satisfied. Figure 3.5 presents this geometrical construction. The reflections produced depend on the spacings between subsequent atomic planes.

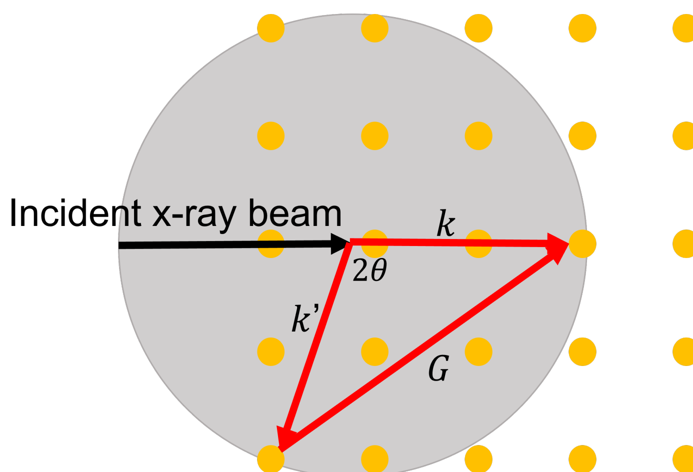

FIGURE 3.5. Schematic of the geometric Ewald sphere construction, indicating the satisfied Laue condition.

3.3.2 XRD Measurement Types

X-ray diffraction (XRD) has been utilised to probe the structure and to analyse the corrosion behaviours of U-Si phases. Through the use of laboratory source XRD measurements, longitudinal specular scans, off-specular scans, and rocking curve scans have been deployed to understand these behaviours.

3.3.2.1 X-ray Diffraction Instrumentation

The XRD measurements presented throughout this thesis have all been conducted through the use of a laboratory source, located at the University of Bristol. The instrument used to conduct the structural characterisation is a PANalytical X'Pert Pro diffractometer, which utilises a copper anode source, giving rise to characteristic spectral lines: $CuK_{\alpha 1}$ and $CuK_{\alpha 2}$. These spectral lines have characteristic wavelengths of $1.54060 Å$, and $1.54443 Å$, respectively. To optimise the beam for analytical sample characterisation a nickel foil is used to reduce any radiation that may stem from the CuK_{β} wavelength. Figure 3.6 depicts this particular geometry, with instrumental components labelled. The x-ray beam is controlled and refined using a series of divergence and soller slits. These are labelled on the schematic in Figure 3.6. On the incident side, soller slits are used to refine the vertical divergence of the x-ray beam and improves the peak shape and overall resolution in scan types that use the 2θ axis, especially at low scattering angles. The divergence slit is fitted in the incident beam path, and controls the horizontal divergence of the incident x-ray beam. The combination of this incident slit configuration controls the area of the sample stage that is irradiated by the incident x-ray beam. On the detector side, an anti-scatter slit is utilised to reduce diffuse scattering inflicted on the x-rays as a result of diffraction. A second set of soller slits are used to further improve resolution prior to the x-rays reaching the detector. This

slit configuration in vital in optimising the resolution of the detector, however, by controlling the beam in this way, there will be a reduction in the photon count rate at the detector. Therefore, an optimisation between resolution and data intensity is key for each x-ray diffraction experiment.

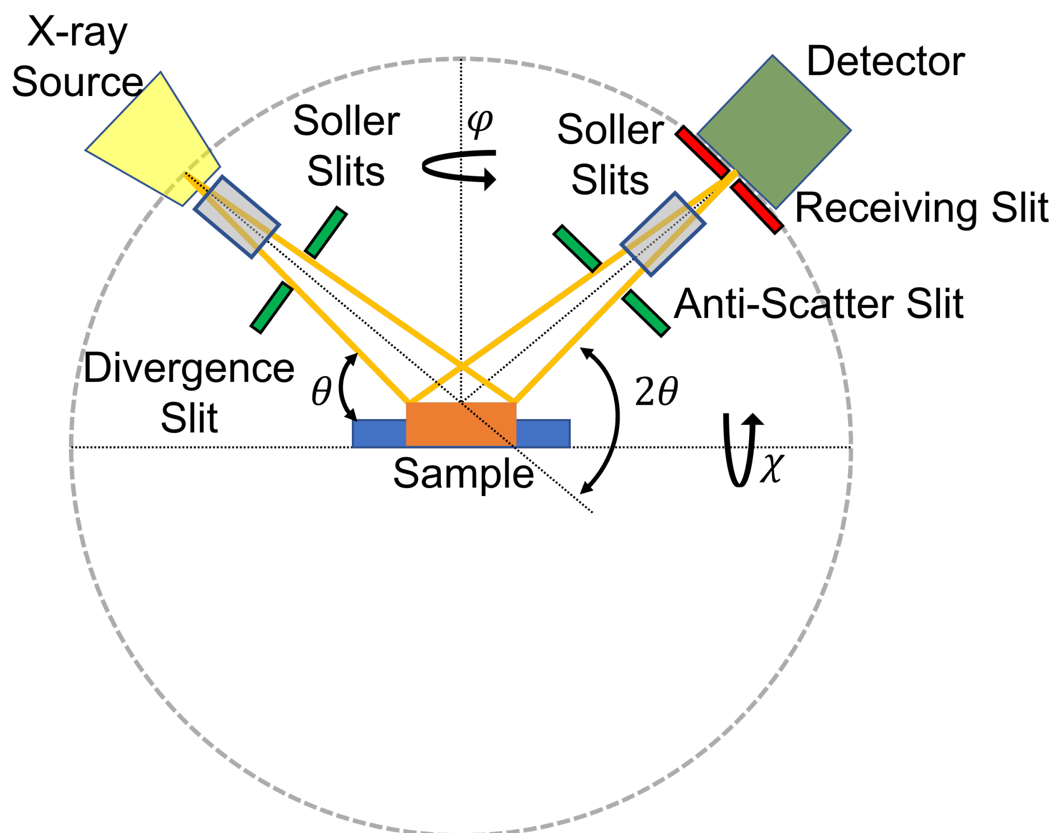

FIGURE 3.6. Schematic diagram of the Panalytical X'Pert diffractometer.

The θ-θ PANalytical X'Pert instrument, at the University of Bristol, uses a four circle Bragg-Brentano geometry. For this geometry, the diffraction vector is always normal to the sample surface. This is shown in the schematic in Figure 3.6. The instrument has an exchangeable sample stage in the centre of the diffractometer, this allows for multiple stages to be mounted onto the instrument for various experiments to be conducted. For example, *in-situ* high-temperature oxidation experiments can be conducted using the Anton Paar HTK 1200 high temperature oven. However, all diffraction studies presented in this thesis were conducted using the Open Eulerian Cradle.

Using the Eulerian Cradle, the sample remains stationary, with the x-ray source and detector able to move around the center of rotation. This allows for the control and alignment in four axis: 2θ, θ, χ, and ϕ, which are labelled on the schematic in Figure 3.6. θ, represents the angle between

the x-ray source and the sample surface, with 2θ equating to the angle between the source and the detector. χ is perpendicular to the vertical scattering plane, with ϕ being a rotation about the Z direction, where Z is perpendicular to the surface normal. The Eulerian Cradle is also equipped with a manually operated, adjustable height stage. This allows for the sample surface to be aligned in the centre of the θ-2θ circle. It is through the use of these four axis, that allows for the characterisation of thin film samples.

3.3.2.2 Longitudinal Specular Scans

For longitudinal, or 2θ-ω scans, the sample is probed in the specular direction, perpendicular to the surface normal. Figure 3.7 shows a schematic of the scanning geometry, with the scattering vector, Q perpendicular to the sample surface. In principle, the source and detector are moved around the centre of rotation of the Bragg-Brentano geometry, increasing the angular value of 2θ and θ. In practise, the sample at the centre of the Eulerian Cradle will not be perfectly aligned with the incident x-ray beam, and therefore, angular offsets are applied. To maintain alignment with the incident beam, an angular offset is applied to θ, referred to as ω, defined as ω=θ + offset. 2θ, is the angle between the incident beam and the detector. For the 2θ-ω scan, the direction of the Q vector remains fixed, however, the length of the Q vector increases, which probes larger lattice spacings that are perpendicular to the surface normal. As the sample is kept stationary, this further ensures that the direction of Q is not changed.

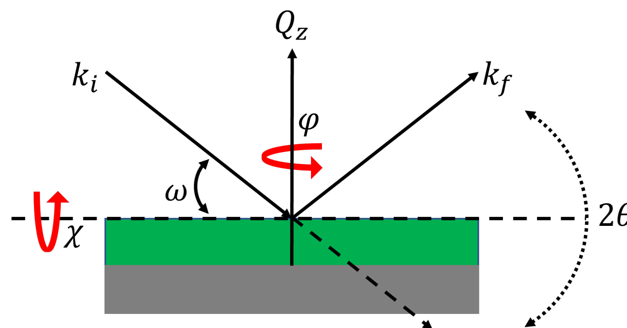

FIGURE 3.7. Schematic diagram of the specular scattering geometry. k_i and k_f are the incident and exit wavevectors, ω is the angle between the incident wavevector and the sample surface, 2θ is the angle between the incident wavevector and the detector. ϕ is the rotation about the Z-direction, perpendicular to the surface normal, and χ is a tilt perpendicular to the vertical scattering plane.

Specular scans vary depending on the type of crystal being probed. For true poly-crystalline samples, the orientation of crystallites have a perfect distribution. Therefore, for each set of crystallographic planes {hkl}, a portion of the crystallites will be oriented perpendicular to the

sample surface, and therefore to the direction of the scatting vector, Q. As a result, the specular diffraction profile obtained from a poly-crystalline sample will exhibit Bragg peaks for all allowed reflections. Further analysis of the specular reflections obtained from the poly-crystalline sample can provide information regarding the average crystallite size and strain profiles. Note that strain profiles have not been investigated for the work conducted in this thesis, however, for the poly-crystalline samples presented in Chapters 5 and 6, crystallite size analysis has been performed. The size of a crystallite (τ) can be calculated using the Scherrer equation:

$$\tau = \frac{\kappa\lambda}{\omega\cos(\theta)} \tag{3.18}$$

This equation utilises the wavelength of the incident x-rays, λ, 2θ position of the measured Bragg reflection, and the FWHM, ω of the same peak. The Scherrer equation also considers the crystallite shape, κ, which if spherical crystallites are assumed, equates to 0.94.

For single crystal analysis, all crystallites are aligned with one another. Through conducting specular 2θ-ω scans, only diffraction peaks from a singular reflection will be probed. Using an example of a face centered cubic (FCC) single crystal, if the crystal is oriented such that the [001] direction is aligned perpendicular to the sample surface, then the observed diffraction peaks from that sample will come from the <001> family of directions. Thus, for the case of an FCC crystal like UO_2, the accessible specular reflections would be: (002), (004), (006) etc,. However, conducting specular scans on a single crystal does not truly confirm the single crystal nature of the sample, this scan type only allows for the specular direction of the crystal to be probed.

Spectral features stemming from the use of specular scans can also be used to extract information about a sample. In the case of epitaxial thin films, which are often uniform in thickness and have smooth interfaces, well defined fringes that extend from the main specular peak can be noted within the data. Figure 3.8 presents an example of this feature. The broader peaks seen either side of the (001) specular peak of USi_3 are known as Laue fringes, and arise as a result of interference between layers. Laue oscillations are sensitive to crystalline disorder, indicating that the presence of these features are a good indication of a well ordered crystal. These features arise as a result of an interference effect. Within layered structures, such as thin films, x-rays are reflected from interfaces. Once reflected, x-rays undergo a phase shift, implying that these reflected x-rays can constructively or destructively interfere, giving rise to Laue oscillations within the spectra. The angular variation in the Laue oscillations, coincided with the specular Bragg lattice spacing can be analysed to determine the layer thickness.

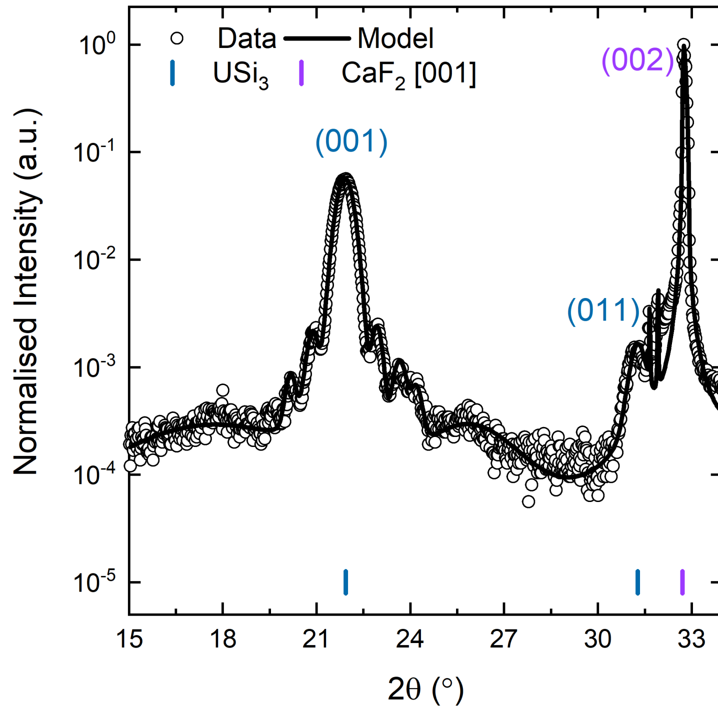

FIGURE 3.8. Example of a 2θ-ω spectra measured from an (001) oriented USi_3 thin films, stabilised upon (001) oriented CaF_2 substrate. Data taken from SN1699.

3.3.2.3 Off-Specular Scans

As previously stated, the utilisation of specular 2θ-ω scans does not confirm that a sample with reflections belonging to one set of diffraction peaks, <hkl>, is a single crystal. It is because of this, that the in-plane crystallography must also be investigated. Figure 3.9 indicates how in-plane crystallographic planes are probed. Here, the direction of the scattering vector, Q, is changed such that it is swept into the plane of the film, aligning perpendicularly to the crystallographic plane of interest. Practically, this is achieved by aligning to a 2θ Bragg peak, and applying an angular offset to ω. For the in-plane crystallographic plane to be observed, the total ω offset, ω_o applied to 2θ, must satisfy: $\omega_o \leq \frac{2\theta}{2}$. Once aligned, the sample can be rotated in ϕ, to observe a series of unique reflections stemming from the in-plane direction. This allows for the symmetry of the crystal to be probed. By observing multiple off-specular positions, it is possible to calculate the in-plane lattice parameters of the crystal. The nature of epitaxial lattice matching could infer that strain is induced into the crystal system. This strain could be a result of a lattice expansion or contraction. The investigation of the in-plane lattice parameters, alongside the specular parameters, allows for the nature of strain to be investigated.

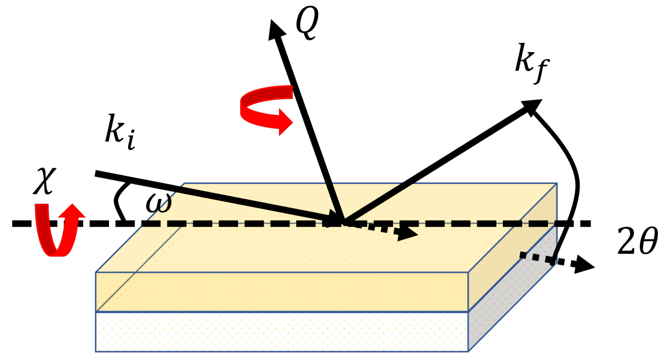

FIGURE 3.9. Schematic representing the off-specular scattering geometry. k_i and k_f are the incident and exit wavevectors, 2θ is the angle between the incident wavevector and the detector. ϕ represents the rotation in the plane of the sample. The sample is aligned such that the scattering vector Q has a component in the plane of the sample.

3.3.2.4 Rocking Curve Scan

Rocking curves, or ω scans are used to determine the crystalline quality of a sample. They are performed by fixing 2θ and scanning in either ω or χ. Due to the restrictive nature and poor horizontal resolution on the PANalytical detector, only ω scans were performed throughout this thesis. Figure 3.10 indicates a schematic diagram of an ω scan, here 2θ is at the position of a known Bragg reflection, with ω changing over a fixed range. By doing so, the sample is effectively tilted, and thus the scatting vector is moved into the plane of the film, such that Q_x is being scanned. In the case of a perfect single crystal, the alignment in the crystallites in the specular direction give rise to a sharp peak. Often, the misalignment of crystallites generate additional intensity, and thus broaden the peak. The alignment of these crystallites is termed the *mosaic spread* or *mosaicity* of the thin film, and is quantified by the FWHM of the omega peak.

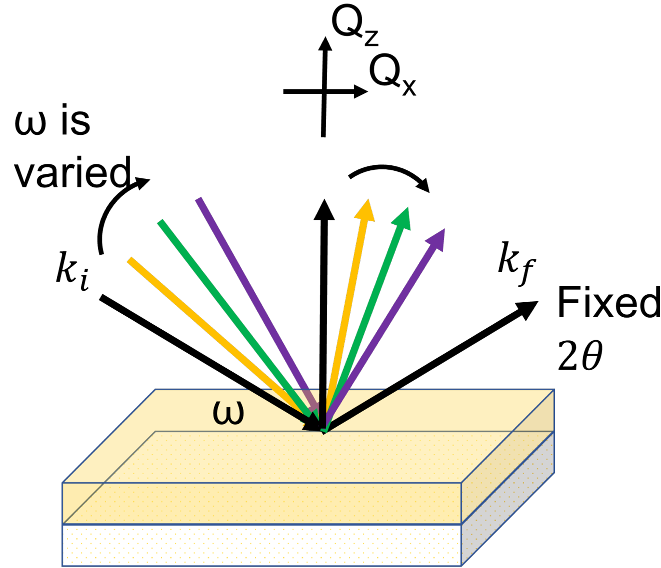

FIGURE 3.10. Schematic representing the omega scan geometry. k_i and k_f are the incident and exit wavevectors, ω is the angle between incident wavevector and the sample, and 2θ is the angle between the incident wavevector and the detector. The scattering vector Q is moved into the plane of the sample, scanning the crystallite arrangement in the Q_x direction.

3.3.3 XRD Data Analysis

To extract structural information from XRD measurements, analysis was conducted by fitting various functions to the data collected. This allowed for peak positions, amplitudes, and FWHM to be determined. The functions used to model the diffraction data included in this thesis are Gaussian, Lorentzian, Lorentzian^2, and PseudoVoigt. These functions are defined as:

Gaussian:

$$\begin{aligned} f_G(x,A,c,w) &= Aexp(-0.5\frac{(x-c)^2}{2w^2}), \\ FWHM_G &= 2\sqrt{2ln2}w \end{aligned} \tag{3.19}$$

Where A, c, and w are the peak amplitude, centre, and FWHM, respectively.

Lorentzian:

$$\begin{aligned} f_L(x,A,c,w) &= \frac{A}{\pi}\frac{w}{(x-c)^2+w^2}, \\ FWHM_L &= w \end{aligned} \tag{3.20}$$

Lorentzian^2:

$$\begin{aligned} f_{L^2}(x,A,c,w) &= (\frac{A}{\pi}\frac{w}{(x-c)^2+w^2})^2, \\ FWHM_{Lorentz^2} &= 2\sqrt{\sqrt{2}-1}w \end{aligned} \tag{3.21}$$

PseudoVoigt:

$$f_{PV} = \nu f_{Gauss} + (1-\nu) f_{Lorentz}, \tag{3.22}$$

The PseudoVoigt is a linear combination of a Gaussian and a Lorentzian with ν being a weighting between the two functions.

The specular and off-specular XRD spectra presented in this thesis were all modelled in GenX [132] using these functions. GenX software makes use of a differential evolution algorithm that allows for a user-defined fitting range for parameters. This allows for local minima to be avoided [40, 132].

3.4 X-ray Reflectivity

X-ray reflectivity (XRR) is a non-destructive probing technique that makes use of the low angle reflection and refraction of x-rays incident at interfaces to examine the structure of surfaces and thin films. The deployment of XRR allows for the layer thickness and interface roughness of thin films, and as a result, has been used throughout this thesis to study the corrosion behaviour of uranium silicide phases. A brief explanation of x-ray reflectivity theory is presented here, however, a more detailed guide can be found in *Elements of Modern X-ray Physics, by J, Als-Nielsen and D. McMorrow* [124].

3.4.1 Theory

Where x-rays are electromagnetic radiation, their behaviours are analogous to that of light when considering the interaction of a photon at the interface between two materials of different densities. The behaviour of the interaction is dependent on the refractive index n, and therefore, as an x-ray passes through an interface, the wavevector $\mathbf{k}$, of the incident x-ray changes to $n\mathbf{k}$ in a process called refraction. The refractive index depends on the energy of the incident photon, and thus the refractive index of x-rays displays resonant behaviour with electronic transitions in atoms and molecules [124]. As x-rays exhibit energies that are greater than most transition frequencies, the refractive index for x-rays tends to be $n = 1$. As a consequence of this, at low grazing angles, x-rays exhibit total external reflection from a flat interface of a material provided the incident angle θ_i, is smaller than the critical angle for total reflection, θ_c [133]. Calculating the reflection and refraction properties of x-rays that are incident upon a flat interface, both scattering and absorption processes must be considered. Absorption process occurring suggest that the x-ray beam is attenuated within the target material. Thus, after travelling for a distance z into the material, the intensity of the incident x-ray is attenuated by a factor $e^{-\mu z}$, with the

amplitude attenuated by a factor of $e^{-(\mu z)/2}$. This leads to the refractive index being expressed as [124]:

$$n = 1 - \delta + i\beta, \qquad with \quad \delta = \frac{2\pi \rho_a f^0(0) r_0}{k^2}, \qquad and \quad \beta = \frac{\mu}{2k}, \tag{3.23}$$

where, ρ_a and $f^0(0)$ are the atomic number density, and the atomic scattering length, respectively. This can also be described as the electron density ρ_e, and thus taking the product of both the electron density and the Thomson scattering length, i.e. $\rho_e r_0$, the scattering length density is obtained.

3.4.1.1 Reflectivity from an Ideal Surface

This section looks at the mechanism of x-ray reflectivity from an ideal surface. Firstly, considering an incident x-ray upon an interface of refractive index n, where the incident, reflected, and transmitted wavevectors, k_I, k_R, k_T, have corresponding amplitudes of a_I, a_R, and a_T, respectively. The wave incident at the interface must be continuous, and so must the derivative, therefore boundary conditions are applied such that:

$$\begin{aligned} a_I + a_R &= a_T, \\ a_I \mathbf{k}_I + a_R \mathbf{k}_R &= a_T \mathbf{k}_T \end{aligned} \tag{3.24}$$

The wavevector in vacuum is represented by k, which is equivalent to the absolute values of the incident or reflected wavevectors, and within the material the wavevector is nk, which represents the modulus of the transmission wavevector. In addition to this, the incident angle, θ_i is equal to the reflected angle θ_r, so can both be denoted as θ. The transmitted angle at which the x-ray passes through the interface is denoted as θ'. The components of the wavevector $\mathbf{k}$ parallel and perpendicular to the surface, it is shown that when the wavevector is parallel:

$$a_I k \cos\theta + a_R k \cos\theta = a_T (nk) \cos\theta', \tag{3.25}$$

with the wavevector perpendicular to the surface yielding:

$$-(a_I - a_R) k \sin\theta = -a_T (nk) \sin\theta' \tag{3.26}$$

Using equations 3.24 and 3.25, Snell's law is derived, such that:

$$\cos\theta = n \cos\theta' \tag{3.27}$$

Snell's law can be used to calculate the critical angle θ_c of transmission by setting $\theta' = 0$, such that $\theta_c = \sqrt{2\delta}$ [124]. The condition for the perpendicular wavevector (Eqn 3.26), in combination with Eqn 3.24 shows that:

$$\frac{a_I - a_R}{a_I + a_R} = n\frac{\sin\theta'}{\sin\theta} \cong \frac{\theta'}{\theta}. \tag{3.28}$$

From this, this Fresnel equations are derived for the amplitude reflectivity, r, and the transmissivity, t, which are defined as [124]:

$$\begin{aligned} r &\equiv \frac{a_R}{a_I} = \frac{\theta - \theta'}{\theta + \theta'} \\ t &\equiv \frac{a_T}{a_I} = \frac{2\theta}{\theta + \theta'} \end{aligned} \tag{3.29}$$

Note that the intensity reflectivity and intensity transmissivity are defined as the square of both a_R and a_T.

Given that the wavevector transfer, Q is:

$$Q = 2k\sin\theta \cong 2k\theta, \tag{3.30}$$

the dimensionless quantities, q and q', can be defined in a similar manor to θ and θ', such that,

$$q \equiv \frac{Q}{Q_c} \cong \left(\frac{2k}{Q_c}\right)\theta, \qquad and \quad q' \cong \frac{Q'}{Q_c} \cong \left(\frac{2k}{Q_c}\right)\theta', \tag{3.31}$$

inferring that, the Fresnel equations (Eqn 3.29) become:

$$r(q) = \frac{q - q'}{q + q'}; \qquad t(q) = \frac{2q}{q + q'} \tag{3.32}$$

If both θ and θ' are small, Snell's law (Eqn 3.27) can be expanded rewritten to include the dimensionless quantities, q and q', hence:

$$q^2 = q'^2 + 1 - 2ib_\mu, \qquad where \quad b_\mu = \beta\left(\frac{2k}{Q_c}\right)^2 = \frac{2k}{Q^{2c}}\mu. \tag{3.33}$$

.

Additionally, the penetration depth of the transmitted wavevector is found to be [124]:

$$\Lambda(q) = \frac{1}{Q_c Im(q')}. \tag{3.34}$$

Now equations 3.32, 3.33, and 3.34 can be evaluated for the solutions of $q \gg 1$, $q \ll 1$, and $q = 1$, recalling that $b_\mu \ll 1$ for all cases:

- $q \gg 1$: The solution to Eqn 3.33 yields both real and imaginary parts such that $Re(q) \cong q$ and $Im(q') \cong \frac{b_\mu}{q}$. This shows there is almost complete transmission of the wave, with the incident and reflected waves shown to be in phase. The intensity reflectivity, R, falls as $R(q) \cong (2q)^{-4}$, which is depicted in Figure 3.11.

- $q \ll 1$: For this case, q' is almost completely imaginary, hence $Im(q') \cong 1$, and $r(q) \cong -1$. This suggests that the reflected wave is out of phase with the incident wave, therefore the transmitted wave becomes weakened. The wave propagates parallel to the surface with minimal penetration depth of $1/Q_c$. This wave is independent of θ, provided $\theta \ll \theta_c$, and is termed an *evanescent wave*.

- $q = 1$: Eqn 3.33 becomes $q' = \sqrt{b_\mu}(1+i)$. As $b_\mu \ll 1$, the amplitude reflectivity is close to $+1$, thus the reflected wave is in phase with the incident wave. The evanescent amplitude is larger than the incident wave.

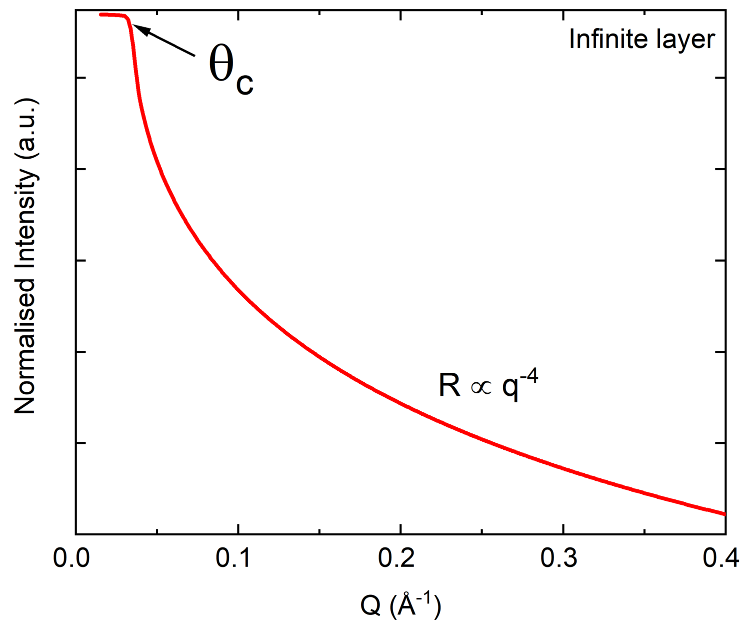

FIGURE 3.11. Schematic of the x-ray reflectivity spectra from an infinite surface. Reflectivity intensity decay is proportional to q^{-4}.

3.4.1.2 Reflectivity from an Ideal Film

This section presents the reflectivity theory from a film with finite thickness. This will consider the effects of two materials, with the film material, 1 having a refractive index n, and thickness d. The film will be situated upon a substrate material, 2, and the system will be in vacuum, denoted with 0. For this system, depicted in Figure 3.12 reflections can occur at the interface from vacuum to film (0 to 1) with an amplitude of r_{01}. Transmission can occur at the interface between the vacuum and film, 0 to 1 (t_{01}), with subsequent reflection at the film/substrate interface 1 to 2 (r_{12}), which is followed by wave transmission at the film/vacuum interface 1 to 0 (t_{10}). Additionally, transmission occurring at the vacuum/film interface (t_{01}) can result in a wave reflection at the film/substrate interface (r_{12}) with a continuous reflection at the film/vacuum interface (r_{10}) before transmitting into the vacuum from the film (t_{10}). This process can repeat infinitely.

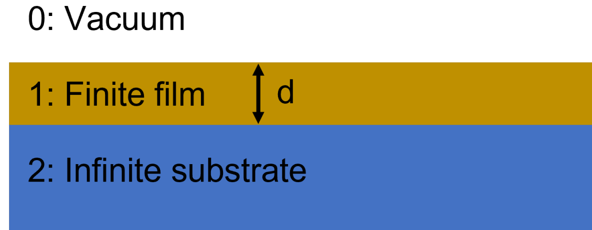

FIGURE 3.12. Schematic of the x-ray reflectivity medium system for a finite film. Vacuum denoted 0, finite film with 1, and infinite substrate material 2. Figure reproduced from [124]

The total amplitude reflectivity is calculated via the summation of all of these factors, whilst including the phase factor $p^2 = e^{iQ\Delta}$, therefore giving:

$$\begin{aligned} r &= r_{01} + t_{01}t_{10}r_{12}p^2 + t_{01}t_{10}r_{10}r_{12}^2p^4 + t_{01}t_{10}r_{10}^2r_{12}^3p^6 \ldots \\ &= r_{01} + t_{01}t_{10}r_{12}p^2 \sum_{N=0}^{\infty}(r_{10}r_{12}p^2)^N, \end{aligned} \tag{3.35}$$

Which can be evaluated to give,

$$r = r_{01} + t_{01}t_{10}r_{12}p^2 \frac{1}{1 - r_{10}r_{12}p^2} \tag{3.36}$$

Making use of the Fresnel equation (Eqn 3.32), stating that $q = Q_0$ and $q' = Q_1$, thus $r_{01} = -r_{10}$ resulting in,

$$r^{01^2} + t_{01}t_{10} = \frac{(Q_0 - Q_1)^2}{(Q_0 + Q_1)^2} + \frac{2Q_0 2Q_1}{(Q_0 + Q_1)^2} = \frac{(Q_0 + Q_1)^2}{(Q_0 + Q_1)^2} = 1. \tag{3.37}$$

Utilising the Fresnel equations stated previously, substitutions can be made such that $r_{01} = -r_{10}$ and $r^{01^2} + t_{01}t_{10} = 1$, leaving,

$$r = \frac{r_{01} + r_{12}p^2}{1 + r_{10}r_{12}p^2} \tag{3.38}$$

Through plotting the square of Eqn 3.38, as a function of Q, a reflectivity curve is obtained. This is presented in Figure 3.13. The periodic oscillations in the intensity are a result of interference between vacuum/film and film/substrate interfaces. The peaks and troughs presented throughout the spectra correspond to scattering that is in and out of phase, respectively. The oscillations are referred to as Kiessig fringes, and have a spacing of $\Delta Q = 2\pi/d$, with d representing the thickness of the finite film, measured in Å. The distance of two Kiessig fringes and two Laue fringes are both a measure of sample thickness. However, the difference between these two features, is that Laue oscillations are a result of crystalline structure, while Keissig fringes originate from two interfaces which are independent of the crystallinity of the sample.

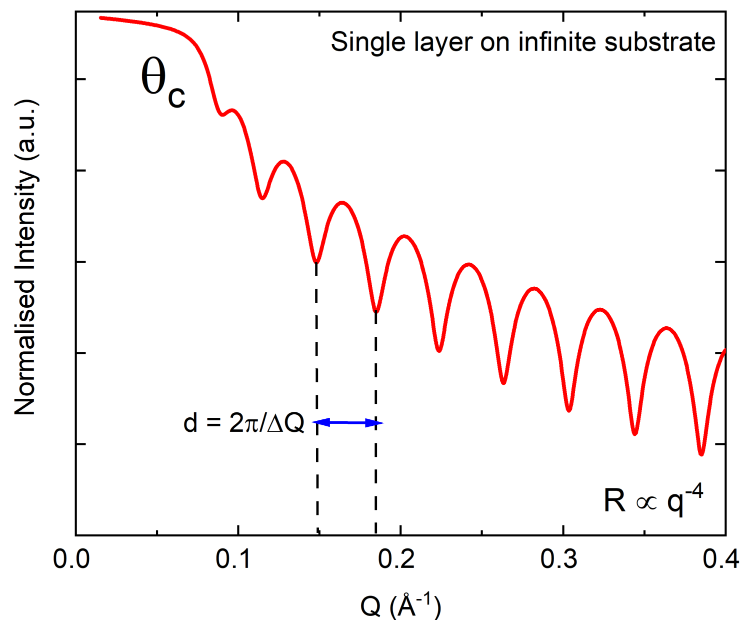

FIGURE 3.13. Schematic of the x-ray reflectivity spectra from an single finite surface upon an infinite substrate.

3.4.1.3 Specular reflectivity from Multiple Layers

So far, the reflectivity from an ideal single finite and infinite layer has been shown, however, it is also important to calculate the specular reflected intensity for a film that consists of multiple layers. X-rays are excellent probing tools when investigating multilayered structures, as the contrast in the scattering density between the materials gives rise to scattering. However, the calculation of the reflected intensity for a film with multiple layers is challenging, and approximations must be made. General approaches extend the model used for reflectivity from a single layer to include multiple reflections, and the refraction effects. However, assumptions can be made such that these effects are small at angles sufficiently larger than the critical angle, i.e. $Q \gg Q_c$. This is referred to as the kinematical regime, and yields results that are similar to those used to describe the scattering of light through a diffraction grating [124].

L.G. Parratt in 1954 [134] developed an exact recursive method, which described and accounted for refraction and scattering for a system composed of N layers upon an infinitely thick substrate. Here, the system was labelled such that the first layer is at the very surface, with the N^{th} layer sitting at the infinitively thick substrate. Each layer situated in the stack has a thickness of d_j and a refractive index of $n_j = 1-\delta_j + i\beta_j$. This refractive index will determine the wavevector in each j^{th} layer, such that $k_j = n_j k$. The component of the wavevector that propagates parallel to the surface direction (the x direction) is conserved in each layer, giving $k_{x,j} = k_x$ for all values of j. However, this is not true for the component normal to the surface, i.e. the z-direction, with this value being:

$$k^{z,j2} = (n_j k)^2 - k^{x2} = (1-\delta_j + i\beta_j)^2 k^2 - k^{x2} \cong k^{z2} - 2\delta_j k^2 + 2i\beta_j k^2. \tag{3.39}$$

As the wavevector transfer becomes $Q_j = 2k_j \sin\theta_j = 2k_{z,j}$, the wavevector transfer for each layer is therefore,

$$Q_j = \sqrt{Q^2 - 8k^2\delta + i8k^2\beta_j} \tag{3.40}$$

The reflectivity from each interface between the j^{th} and $j+1^{th}$, which neglects multiple reflections, can be derived from the previously stated Fresnel equations (Eqn 3.32), giving,

$$r'_{j,j+1} = \frac{Q_j - Q_{j+1}}{Q_j + Q_{j+1}}. \tag{3.41}$$

Using this result, alongside the reflectivity for a single layer, presented in Eqn 3.38, the reflectivity from the interface between the bottom of the N^{th} layer and the infinite substrate can be calculated. As the substrate is defined as being infinitely thick, no multiple reflections are to be considered. Eqn 3.41 can be applied to the interface between the substrate and the

bottom of layer N, denoted by $r'_{N,\infty}$. The prime symbol indicates that the reflectivity does not include multiple reflections, as previously stated. This can therefore can be applied to subsequent interfaces above the substrate, and is summarised for a single layer, with $p^{j2} = e^{id_jQ_j}$, hence,

$$r_{N-2,N-1} = \frac{r'_{N-2,N-1} + r_{N-1,N}p^2{}_{N-1}}{1 + r'_{N-2,N-1}r_{N-1,N}p^2{}_{N-1}} \tag{3.42}$$

An example of the reflectivity gathered from a multilayer system is presented in Figure 3.14. Here, the interference stemming from the thick layer is represented by the narrow Keissig fringes, with the broader periodic fringes representing the thinner layer.

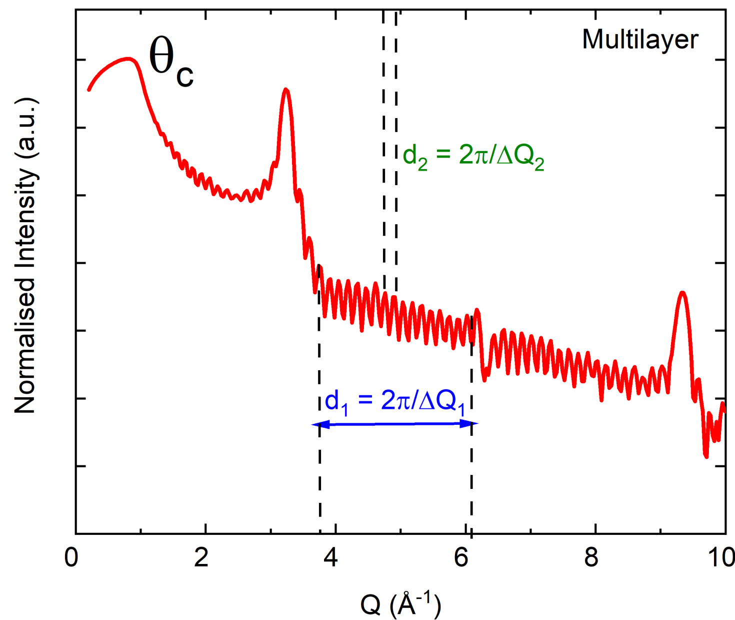

FIGURE 3.14. Schematic of the x-ray reflectivity spectra from a multilayer. Data taken from GenX software [132]

3.4.1.4 Reflectivity from Non-Ideal Surfaces

The reflectivity models presented so far have assumed that each layer probed has a perfectly flat, sharp interface. For real engineered systems, it is important to include the effect of graded interfaces, referring to a non-ideal system in z, and also the effect interface roughness, hence being non-ideal in x, may alter the reflectivity collected from the sample.

In order to account for graded interfaces within a system, the product of the intensity from an

ideal multilayer, $R_I(Q)$ and a factor describing the graduated change in the electron density across the interface is calculated. Describing the electron density as a function of z, hence, $f(z)$, the changes within each layer of the graded interface can be accounted for by integrating the density gradient over z, thus:

$$R(Q) = R_I(Q) \left| \int_0^{\inf} \left(\frac{df(z)}{d(z)} e^{iQ_z} dz \right) \right|, \tag{3.43}$$

where the ratio between the real and idealised reflectivity spectra is the absolute square term of the Fourier transform of the electron density gradient across the interface [124]. This formula allows for an error function to be incorporated, describing the electron density at an interface within the system. The derivative of the error function is a Gaussian, and the Fourier transform of a Gaussian is another Gaussian [124], leaving the *master formula*,

$$R(Q) = R_F(Q) e^{-Q^2\sigma^2}, \tag{3.44}$$

where, σ is a measure of the width of the graded region.

As previously stated, an non-ideal surface can change in two main ways: perpendicular to the surface, z, and parallel to the surface, x. An interface is considered *rough*, when there are changes in layer thickness as a function of x. This change can be averaged across the interface to give a thickness distribution in z [124]. Assuming the height variation at different positions are uncorrelated, the roughness of the interface can be understood by varying the refractive index. Using a method initially proposed by *Nevot and Croce* [135], which as been further adapted and combined with the *Parratt* method [134, 136, 137], this uncorrelated roughness was implemented into the model such that,

$$n_j(z) = n_j + (n_{j+1} - n_j) F(z, \sigma_j), \qquad where \quad F(z) = \frac{1}{\sigma_j \sqrt{2\pi}} \int_{-\infty}^{z} e^{\left(-z^2/2\sigma_j^2\right)} dz. \tag{3.45}$$

By taking the product of $R_I(Q)$ with a factor that describes the uncorrelated roughness, the reflectivity intensity of an interface exhibiting roughness is given by:

$$R(Q) = R_I(Q) e^{-Q^2 {\sigma_j}^2} \tag{3.46}$$

This equation is identical to Eqn 3.44, however the term σ_j represents the root mean square (rms) of the vertical interface roughness [137]. The similarity in these two equations (Eqn 3.44 and 3.46) highlights the difficulty in the ability to distinguish between interface gradients and interface roughness effects when observing specular reflectivity. Figure 3.15 presents three x-ray

reflectivity spectra with increasing interface roughnesses. Here, as the roughness increases, the definition in the Keissig fringes reduces.

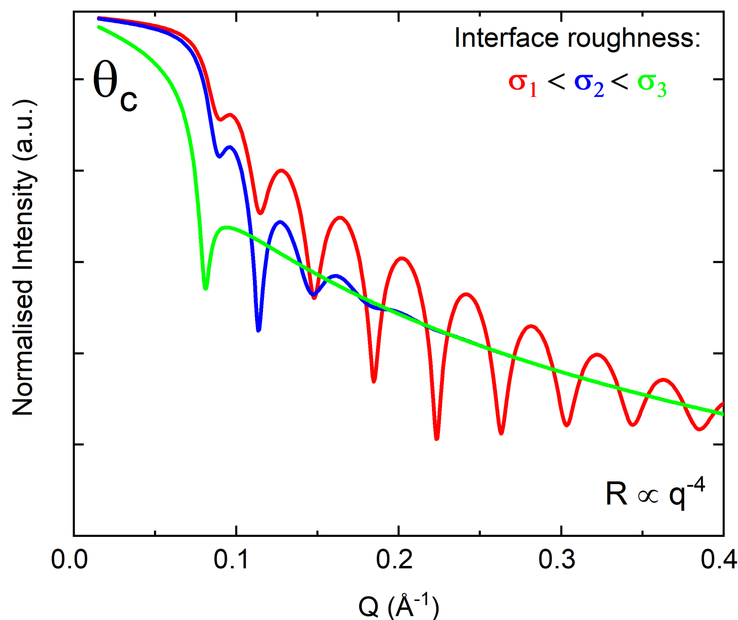

FIGURE 3.15. Schematic of the x-ray reflectivity spectra from three finite layers with increased roughnesses.

3.4.2 XRR Measurement and Analysis

The x-ray reflectivity (XRR) measurements presented throughout this thesis were taken using the same apparatus and experimental set-up as the specular x-ray diffraction (XRD) measurements discussed previously in this chapter. Here, all x-ray reflectivity measurements were conducted using a PANalytical X'Pert Pro diffractometer. The measurements conducted on each sample were performed at low incident angles. As a result, this makes XRR sensitive to the alignment of the sample. Before data collection, the sample surface was aligned in both ω and χ allowing for the surface normal to be the specular direction.

X-ray reflectivity analysis was performed using GenX software [132]. GenX contains a built-in model that is used to simulate specular x-ray reflectivity data, which makes use of the *Parratt* algorithm [134]. The roughness is assumed to have a Gaussian distribution as per the *Nevot-Croce model* [135]. The software also allows for full control over the instrumental parameters including

resolution and beam footprint.

To simulate the XRR spectra, a sample is defined as a series of layers, and in-turn these are described by a series of parameters, including: composition, density ($atoms/\AA^3$), thickness ($\AA$), and interface roughness ($\AA$). This allows the user to construct a layered model which is placed upon an infinitely substrate material. The optimisation of the calculated model, instrument and sample parameters are optimised over a user-defined range using a differential evolution algorithm, which aims to minimise the difference between the simulated model and the raw data. The difference between the model and the data is calculated using a *Figure of Merit* (FOM), which compares how well the simulation matches to the data. GenX software provides a range FOM functions which can be chosen accordingly. For the optimisation of the XRR simulations presented in this thesis, a $LogR_1$ FOM was used. This function is ideal for fitting data that spans over several orders of magnitude along the y-axis, which XRR spectra does. This FOM gives all data points equal weighting, which is achieved when using logarithmic scaling.

3.5 X-ray Photoelectron Spectroscopy

X-ray photoelectron spectroscopy (XPS) has been utilised throughout this thesis to chemically characterise thin film surfaces, allowing for elemental composition and overall sample stoichiometry to be analysed. Combined with the use of diffraction techniques, XPS has furthered the understanding of the electronic bonding in uranium silicide phases (Chapter 5), and how these phases change when exposed to oxidising environments (Chapter 6).

3.5.1 Theory

The principal that underpins x-ray photoelectron spectroscopy is the photoelectron effect, where the energy of emitted electrons, or photoelectrons, from a surface is analysed. The escape depth of a photoelectron is of the order of nanometers (nm), making XPS a surface sensitive technique. This allows for information about the chemical state and electronic bonding environment to be extracted from different materials. Experimentally, samples are irradiated with a monochromatic x-ray source, which causes photoelectrons to be emitted from the sample surface and detected with an analyser. Theoretically, the photoelectron emission process involves an incident photon, with energy $h\nu$, that is absorbed by a surface atom [121]. The result of this absorption process is the ejection of a photoelectron with a kinetic energy E_k that is equal to:

$$E_K = h\nu - E_B - \Phi \tag{3.47}$$

Where E_B corresponds to the binding energy of the electron, and Φ is the work function of the spectrometer. The photoelectron will only be ejected if $h\nu$ is greater than the binding energy

of the electron. The work function, Φ, of the analyser, and the energy $h\nu$ of the x-ray source are both known and fixed. Therefore, the equation above (3.47) can be arranged so that the binding energy, E_B of the ejected photoelectron can be measured. Hence,

$$E_B = h\nu - E_K - \Phi \tag{3.48}$$

Thus, making it possible to examine the binding energies in materials, which builds a profile of the electronic states. The binding energies are unique to each individual element, as each element has its own unique electron configuration. Additionally, these binding energies are effected by that particular elements bonding environment. This makes XPS extremely useful for compound materials.

3.5.1.1 Electron Configuration

The peaks observed through XPS are defined by a discrete set of quantum numbers, $n\ell_j$. The *principal quantum number*, n, defines the magnitude of the orbital and atomic energies through a set of positive integers, where $n \geq 1$ [138]. The second value is the *orbital angular momentum*, ℓ, which defines the spectroscopic subshell orbital shape through a set of positive integers where: $\ell \geq 0$. The electron subshells are labelled with s, p, d, and f for $\ell = 0,1,2,3$, respectively. The final value used is the *total angular momentum* $\jmath$, where $\jmath = \ell + s$, and s is the intrinsic spin of the particle involved. The spin for leptons, including electrons, is $\pm\frac{1}{2}$ [122, 130]. From this definition of the *total angular momentum*, $\jmath$ must equate to values which are dependent on the spectroscopic subshell being observed, i.e. $\jmath = \ell + \frac{1}{2}$ and $\jmath = \ell - \frac{1}{2}$. Therefore, for $4f$ subshell, observed when measuring uranium, $n = 4$, $\ell = 3$, and $\jmath = \frac{7}{2}, \frac{5}{2}$. This splitting of the orbital, often referred to as fine structure, is a result of spin-orbit splitting and occurs for every orbital with the exception of the s-level ($\ell = 0$). A full depiction of electron configuration is shown in Figure 3.16. The area ratio between the two states can be calculated by observing the total amount of states, or degeneracy, of the doublet peak. Again, using the $4f$ as an example, the available states for the $4f_{\frac{7}{2}}$ are: $-\frac{7}{2}$, $-\frac{5}{2}$, $-\frac{3}{2}$, $-\frac{1}{2}$, $\frac{1}{2}$, $\frac{3}{2}$, $\frac{5}{2}$, $\frac{7}{2}$. Therefore, there are 8 available states for the $4f_{\frac{7}{2}}$. Similarly, for the $4f_{\frac{5}{2}}$, there are 6 available states. Consequently, the area ratio for the $4f$ doublet peak is equal to $4:3$. The same principal has been applied to the remaining ℓ values in Table 3.1.

3.5.2 Measurement

The XPS measurements presented in this thesis were all taken using the University of Bristol NanoESCA facility, which utilises a monochromatic Al x-ray source. Typically Al or Mg sources are used for lab based XPS instruments, with energies of 1486.6 eV and 1253.6 eV respectively. Due to the characteristic x-ray emission from both Al and Mg sources, the elements are essentially

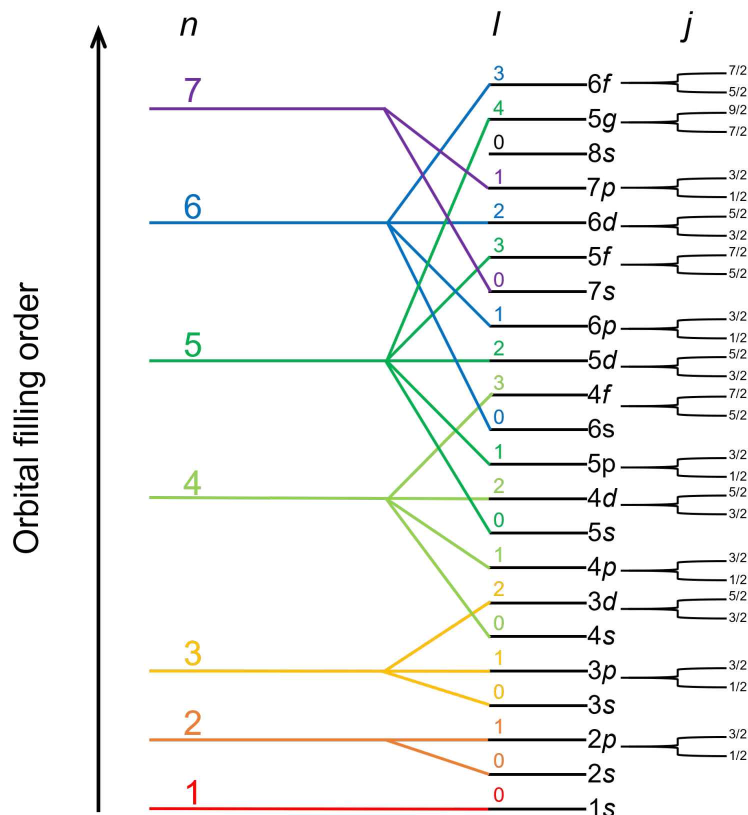

FIGURE 3.16. Depiction of the electron configuration filling order for sub-shells. Principal quantum number, orbital angular momentum, and total angular momentum values are labelled as n, ℓ, and $\jmath$ respectively.

TABLE 3.1. Table showing the $\jmath$ values related to each subshell, alongside the area ratio between the splitting of each doublet peak.

Shell	ℓ value	$\jmath$ value	Ratio
s	0	1/2,	N/A
p	1	1/2, 3/2	1 : 2
d	2	3/2, 5/2	2 : 3
f	3	5/2, 7/2	3 : 4
g	4	7/2, 9/2	4 : 5

monoenergetic. This removes the need for a monochromator within the instrument.

The NanoESCA collects high resolution XPS data from the kinetic energies of emitted photoelectrons through the use of a Scientaomicron XPS ARGUS analyser. This analyser has an energy resolution of less than 300 meV. Prior to the photoelectrons reaching the analyser, there are a series of processes that it must go through. Firstly, the ejected photoelectron must be

travelling under UHV conditions to reduce the probability of collisions with molecules within the XPS chamber. If significant scattering events occur, the photoelectron will no longer contain the information that is representative of its original state. Additionally, the mean free path of the emitted photoelectrons is short, therefore XPS can only probe the electron orbitals from molecules present in the 1 – 10 nm into the surface of the sample. This makes XPS is a highly surface sensitive analytical technique.

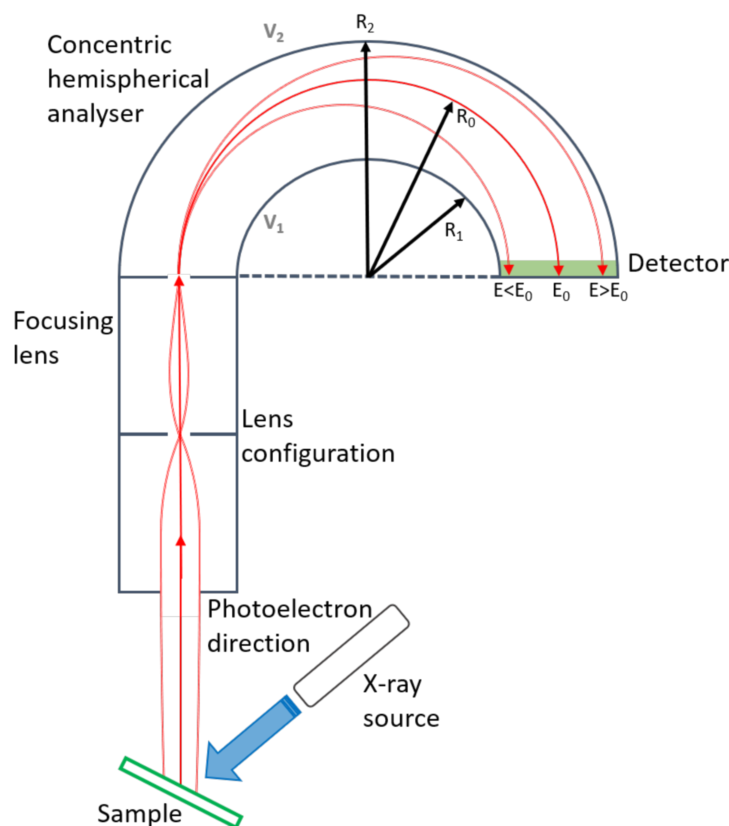

FIGURE 3.17. Schematic of an XPS system indicating the photoelectron path within the concentric hemispherical analyser (CHA).

$$E_0 = e\Delta V \frac{R_1 R_2}{R_2^2 - R_1^2} \tag{3.49}$$

Following their ejection from the sample surface , the electrons are then passed through a set of extraction lenses. These lenses work to slow and then minimise the angular dispersion of the photoelectrons into the Concentric Hemispherical Analyser (CHA). The hemispherical analyser utilises an electrostatic field to spatially separate the photoelectrons that pass through the system via their kinetic energies. Two potentials, V_1 and V_2, are applied to the inner and outer concentric hemisphere electrodes with different radius' of R_1 and R_2. As a result, the electrostatic

field between the two hemispheres has a $1/R^2$ dependance. The electrostatic fields within the hemispherical analyser are set to only allow electrons with a certain energy, E_0, to be imaged at the center of the detector, R_0. This is known as the pass energy (PE). These photoelectron trajectories are depicted in Figure 3.17. Thus, the combination of the lens configuration works to both focus and slow the photoelectrons passing through so that their kinetic energy after passing through the lenses matched the pass energy of the hemispherical analyser. Therefore, by altering the field strength across the hemisphere configuration, the pass energy can be changed, as shown in Equation 3.49.

The pass energy is integral to the measurement being taken as it dictates the spread of energies that reach the detector. A lower pass energy will improve the resolution of the data acquired, however the photoelectron transmission will decrease, therefore decreasing the counts at the detector. The resolution of the data will often influence the fitting parameters used to model the data, as the higher counts from an increased pass energy can result in the broadening of peaks. Figure 3.18 presents the U-4f spectra from U_3Si using two different pass energies. From this, it is clear that the higher pass energy of 20 eV, shown in black, has a much larger intensity when compared to the data collected with a pass energy of 6 eV. However, the U-4f spectra collected with a pass energy of 6 eV has a much finer resolution, allowing for peak positions to be extracted with a higher precision.

Utilising the UHV of the NanoESCA facility, the measurements performed for this thesis were conducted at pressures below 10^{-9} mbar. Minimising contamination is vital for investigating uranium silicide surfaces. This is due to their susceptibility to surface oxidation. To further protect the uranium silicide surfaces from contamination when transferred to the NanoESCA preparation chamber, the thin film samples were capped. This protective capping layer was removed prior to data acquisition using Ar sputtering. This process involves Ar^+ ions bombarding the sample surface, which removes the capping layer and exposes the bulk of the film.

3.5.3 Spectral Features

The data acquisition process can result in the observation of many spectral features from the sample being measured. These spectral features may be the result of the technique, the chemical or physical state of the sample being observed, or instrumental effects.

3.5.3.1 Photoelectron Spectra

The photoelectron lines are the most intense features observed in the spectra, and are inherent to the technique. These spectral features are often symmetric and are typically narrow. Photoelectron lines from metallic samples can exhibit asymmetric features, which stems from the coupling

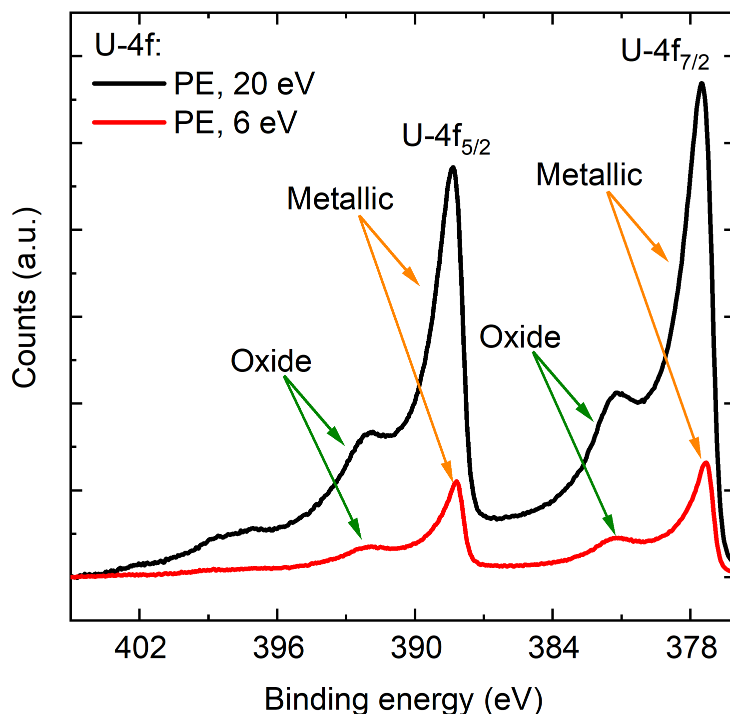

FIGURE 3.18. Example of how the intensity and resolution changes as a function of pass energy. Spectra collected from U-4f of U_3Si. PE = 6 eV shown in red, PE = 20 eV shown in black. Metallic and oxide regions labelled, alongside the U-4$f_{7/2}$ and U-4$f_{5/2}$. Data collected from SN1513.

with conduction electrons [139]. Localised changes in the chemical bonding of the material can result in the alteration of photoelectric lines. This can include changes in the spectral position, peak width, peak shape, and the valence band. Binding energy shifts due to the chemical bonding can be attributed to the differences in the electronegativity between the elements involved. This difference results in the shift in the core level orbitals shifting to a higher binding energy [121]. Using the example of metal oxides, when a metallic atom bonds to an element with a higher electronegativity, for example oxygen, the electrocharge of the metal becomes positive, and thus increases the binding energy. Metallic and oxide bonding features are presented in Figure 3.18. Here the asymmetric metallic states from the U-4f spectra are located at a lower binding energy, this is around 377 eV for U-4$f_{7/2}$). The oxide bonding sites are located at higher binding energies around 380 and 390 eV.

3.5.3.2 Auger Electrons

A photon incident on an atom can remove an electron from a core level sub-orbital provided the incident energy of that photon is greater than the binding energy of the electron [140]. Upon this removal, the electron leaves a vacancy, or positive 'hole', which can be filled by an electron from a higher sub-orbital [141]. The filling of the vacancy results in the emission of a photon with energy, $h\nu$. This photon can then induce the ionisation of a second electron from the atom, which typically comes from the valence band, and is referred to as an *Auger electron* [121].

3.5.3.3 Satellite Peaks

Satellite peaks within the spectra can be formed through a number of processes. Peaks can appear as a result of the use of a non-chromatic x-ray source, however, these satellites can be easily removed from the spectra as the characteristic lines of Al and Mg sources are well known.

The photoelectrons that are emitted from the atom may interact inelastically with electrons in the valence band. This interaction can excite the valence electron to an unoccupied higher energy state. As a result, the initial core photoelectron will lose energy. This interaction will manifest itself in distinctive ways for different materials. The valence band for insulating materials is away from the Fermi edge, therefore these scattered photoelectrons will appear as separate peak in the spectra. These are referred to as 'shake up' satellites. These satellites that appear in the acquired spectra always appear at the higher binding energy side of the main photoelectron peak. Metallic materials, however, have their valence band on the Fermi edge, therefore the satellite produced from this interaction appears as an asymmetric tail on the main photoelectron peak [142, 143].

Interactions between the ejected photoelectrons and surface electrons can result in the formation of energy loss, or plasmon, lines within the spectra. Plasmons appear at higher binding energies when compared to the main photoelectron line [144]. This is due to their lower arrival kinetic energies at the detector site within the XPS analyser. The appearance of plasmons within the spectra vary with material type. For insulators, the peak is often muted, however, plasmons that arise as a result of conduction electron interactions can be well defined and prominent within the spectra.

3.5.4 Analysis

The XPS data presented in this work has been analysed using CasaXPS software [141]. CasaXPS software allows users to model the background type and peak shape for both XPS and AES data.

Additionally, CasaXPS allows for the doublet peak ratio, peak separation, and line width to be specified. The metallic uranium silicide compounds studied in this work observed the U-4f, Si-2s, O-1s, Si-2p / U-5d, and the Valence Band to understand the valency transformations when these materials are oxidised. Prior to fitting the spectra, the data sets were calibrated. Traditionally, compounds are calibrated to the C-1s spectra, however, due the metallic nature of uranium silicides, the Fermi edge was used.

The analysis conducted in Chapters 5 and 6 utilised Gaussian-Lorentzian product line shape applied to Linear and Shirley background types. The Linear background type is used on spectra that do not have a large step in the intensity over the energy range covered by that peak, whereas, the Shirley algorithm utilises the area information about the peaks within a set energy range to construct the background. Peaks were fitted using the Gaussian-Lorentzian product, $GL(x)$, line shape which allows for a weighting value, $\%GL$, to be assigned, with $\%GL = 0$ for pure Gaussian contribution, and $\%GL = 100$ for a pure Lorentzian contribution. Metallic actinide peaks were assigned an asymmetric profile, $T(x)$, to their components. For peaks centered on x_c, this spreads the component for $x \leq x_c$ as defined by:

$$Y(x) = GL(x) + (1 - GL(x)) \cdot T(x), \quad T(x, \tau, w, x_c) = \begin{cases} e^{\frac{\tau(x-x_c)}{w}} & \text{for}\, x \geq x_c \\ 0 & \text{otherwise.} \end{cases} \tag{3.50}$$

From Equation 3.50, the value τ defines the amount of peak asymmetry that is applied to the component. This value ranges from $0-1$. For the analysis, components with the $GL(x)$ line shape were created for each spectra, with initial guesses made for component area, position, intensity, and width prior to fitting . Coupled components were used to model spectra in sub-orbitals where $\ell \geq 1$, keeping the peak width, or FWHM, equal and utilising the ratio that stems from the spin-orbit degeneracy to model the coupled areas (Table 3.1). The stoichiometry of each sample was investigated by calculating the ratio between spectra. This was performed by normalising the total area of the spectra to their respective orbital cross-sections, as shown by *Yeh et al.,* [145].

Chapter 4

Sample Growth

For the purpose of this work, uranium silicide and oxide thin films have been engineered at the University of Bristol. The thin films have been produced via the physical vapour deposition (PVD) technique DC magnetron sputtering. This chapter details the advantages of using thin films for nuclear fuel research, and the procedure required to synthesise such actinide surfaces within ultra-high vacuum (UHV) systems.

4.1 Thin Films

Thin films are fabricated by depositing materials on a bulk substrate, with the aim of the 'thin film' being that an appropriate number of atoms are deposited on a substrate to form a particular surface or compound [146]. Thin films are often defined as low-dimensional materials and can be engineered from bulk materials, in the case of physical deposition or, they can be formed from solutions and vapour so that a particular compound is formed at the surface of the chosen substrate via chemical deposition [147]. Thin films can posses a range of thicknesses and uses - from micron thick ceramic coatings used for industrial purposes, to nanometer (nm) or Ångstrom (Å) atomic layers used for quantum devices. The use of thin films for more fundamental research has also proved invaluable for electronic, structural, chemical, and magnetic investigations. For the purpose of this thesis, thin films have been utilised to observe surface reactions of nuclear fuels.

4.1.1 The Significance of Surface Research for Nuclear Materials

Investigating surface behaviours are of significant interest across a range of research fields. Probing corrosion behaviors, for example, has allowed for a deeper understanding of the materials used around us. Thin films have proven to be an effective way of investigating these behaviours experimentally, especially when compared to bulk materials. The ability to reduce the amount of material contained within a thin film allows for surface studies to be performed on potentially toxic or hazardous materials. For example, thin films can be used to study the growth kinetics of oxidation processes at ambient and elevated temperatures, which can help evaluate how these features evolve and aid in optimising procedures to alter and potentially prevent such behaviours. The use of thin films allows the researcher to be sensitive to any changes to the surface, particularly when using techniques such as, x-ray reflectivity (XRR) and x-ray photoelectron spectroscopy (XPS). Slight changes at the atmosphere-film interface will be indicated within the spectra collected. This information is particularly useful for probing complex uranium based compounds used for commercial nuclear research.

For the current fuel UO_2, once spent nuclear fuel (SNF), $> 90\%$ of radionuclides produced from fission reactions are retained within the bulk fuel matrix. At temperatures below $100\,^{\circ}C$, the diffusion of these radionuclides out of the fuel matrix is slow. This makes SNF corrosion or dissolution the primary process for releasing these fission products. The solubility of the uranium ions, and therefore their valency of the ions within the fuel provide the biggest indicator to how the fuel may behave once exposed to corrosive environments. If uranium silicides are to replace UO_2 as the primary fuel, it will be necessary to investigate the oxidation mechanisms, and the subsequent dissolution kinetics. This will allow for the corrosion behaviour of the phases to be understood prior to becoming SNF, providing a simplistic model that could form the basis for predicting the radionuclide fission product release from uranium silicides.

Surface work has been previously conducted on a range of uranium based compounds [26, 40, 111, 112, 148–150]. Investigations on uranium dioxide (UO_2) and uranium mononitride (UN) have also been conducted in order to probe both the oxidation and dissolution behaviours. These studies were undertaken from a nuclear fuel perspective, resulting in an indication of how the corrosion performance of proposed replacement fuel, UN, compared to UO_2. *Rennie et al.,* [40] initially performed dissolution studies on UO_2 single crystals, in order to understand how the crystallographic orientation altered the dissolution rate. The high-quality single crystal films allowed for changes in the layer thickness to be observed through x-ray reflectivity. These results provided a dissolution rate for each orientation, and concluded that the surfaces oriented in the (111) direction had the slowest dissolution rate. A later study, conducted by *Bright et al.,* [112] compared the dissolution rates of nanocrystalline UO_2 to that of proposed advanced technology fuel, UN, and it's intermediate oxidation layer, U_2N_3 when exposed to H_2O_2. This study indicated

that UN was more corrosion resistant when compared to UO_2. Both of these studies justified the use of thin films to study nuclear materials on both laboratory and synchrotron x-ray sources. Furthermore, both studies demonstrated the advantages to using thin film surfaces, where their use allows for a range of nuclear fuel compounds and various crystallographic orientations to be accessed. Example investigations like these further validate using thin films to explore the corrosion behaviour of uranium silicide phases.

Where nuclear material is inherently complex, the ability to reduce the radiation dose and overall activity being handled provides an additional benefit for using thin films. Furthermore, the nuclear fuel cycle is heavily dependent on simulation, models, and physical testing of fuel prior to implementation. This includes understanding how nuclear fuel behaves in accident or disposal scenarios which often include elevated temperatures and oxidising environments. The ability to reduce the amount of material being investigated mitigates against experimental scenarios which could be dangerous. Thin films are excellent candidates for understanding how fuel materials may behave in these scenarios because they allow idealistic single parameter studies to be compared to theoretical models, bridging the gap between theory and experiment.

The thin films used for this project are synthesised using depleted uranium which has an activity of 14656 Bq/g. Typically a U_3Si_5 thin film sample of 500 Å deposited on a $10 \times 10 \times 0.5$ mm CaF_2 substrate will have overall activity of 0.233 Bq. This activity is lower than typical background levels, and considerably reduced when compared to pure U_3Si_5 of the same volume which would have an activity of approximately 14 kBq. This reduced activity makes thin films safer to work with when compared to bulk material, and often makes them exempt from transport under IAEA guidelines [151].

4.1.2 Phase Stabilisation and the Uranium Silicide Phase Diagram

The advantage of using thin films to study the uranium silicide fuel type, stems from the ability to isolate single phases. The uranium-silicon binary phase diagram is comprised of line compounds, which indicates a fixed stoichiometry for each compound, and therefore a fixed ratio between uranium and silicon. The ability to adjust this ratio allows for the phase diagram to be travelled across as a function of either uranium or silicon provided the amount of one element is kept constant. This can be performed during thin film synthesis, but altering the power supplied to each elemental target. Furthermore, through careful epitaxial lattice matching (described in 4.2) , it is possible to form single crystals of uranium silicide phases. This process of epitaxial matching stabilises the compound in a particular crystallographic orientation, enhancing the ability to 'lock-in' a particular U-Si stoichiometry. Therefore, through varying growth parameter, it is possible to stabilise uranium silicide epitaxial thin films.

4.2 Thin Film Fabrication

The most significant advantage of using thin films is their controllability. The thickness, stoichiometry, phase, crystal structure, and crystallinity can all be controlled through varying deposition procedures and the chosen substrate material. The variation of these parameters can result in the engineering of different film structures, which are classified as follows [152]:

Perfect Epitaxial: A single crystal film grown in perfect registry with a single crystal substrate.

Nearly Perfect Epitaxial: A single crystal film grown with minor imperfections in the film/single crystal substrate registry.

Textured Epitaxial: The deposited layer has a close registry with the single crystal substrate, and is formed of mosaic blocks.

Textured Polycrystalline: Deposited crystallites are preferentially orientated in the specular direction, perpendicular to the substrate below. Their orientation is random in-plane, and they have a distribution in crystallite size.

Perfect Polycrystalline: Deposited crystallites have perfect random orientation, and have similar shapes and sizes.

Amorphous: Deposited material that has no long-range order.

From this categorisation, it is possible to identify the crystallinity of the deposited film through a series of experimental diffraction techniques.

The epitaxy of thin film layers can be heavily influenced by the growth modes that occur during deposition. These growth modes can be the result of mechanisms that occur in-situ by both physical and chemical factors, such as, lattice mismatch and deposition energy. Epitaxial growth can be the result of any of the following growth modes: Frank-van der Merwe, Volmer-Weber, and Stranski-Krastanov [153]. Figure 4.1 depicts these growth modes and how they evolve with atomistic deposition. Figure 4.1(a) shows the island growth of the Volmer-Weber mode. The island growth occurs when the bonding energy between the deposited atoms is significantly larger than the energy between the deposited film and the substrate. The mechanics of Frank-van der Merwe layer-by-layer growth is depicted in Figure 4.1(b). For layer-by-layer formation, atoms deposit as monolayer islands onto the substrate. The atoms continue to deposit to form a continuous monolayer before forming significant clusters of atoms above. This growth mode is influenced

by the total surface layer energy, where the energy of the deposited atoms are less than the bonding energy between deposited atoms and the substrate. The final mode, Stranski-Krastanov, as shown in Figure 4.1(c), is a combination of both Volmer-Weber (island) and Frank-van der Merwe (layer) growth mechanisms. The deposition is initiated with the growth of one or two monolayers, before changing to island growth. This transition is often associated with the lattice relaxation from induced strain caused by an imperfect registry or lattice mismatch between the deposited layer and substrate [153, 154]. Where these growth modes provide a good indication of how surfaces are deposited, in truth, the overall deposition process is heavily influenced by the kinetics of the system including deposition rate, system pressure, and substrate temperature. As a result, it is important to consider the method used to deposit material.

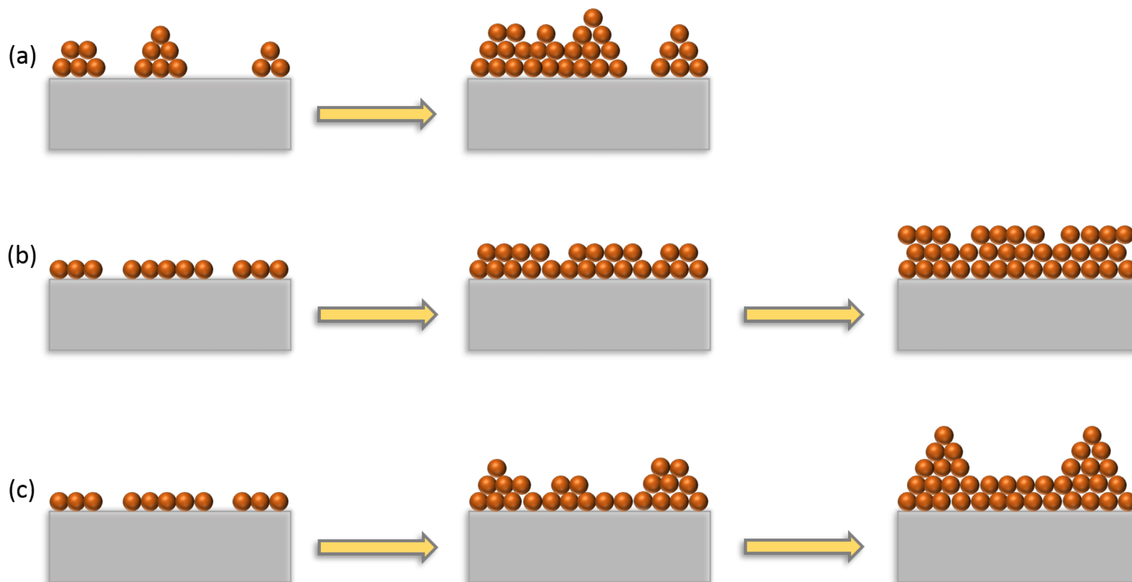

FIGURE 4.1. Figure depicting the three growth modes that can occur during epitaxial deposition. (a) Volmer-Weber growth mode, showing the island growth mechanism, (b) Frank-van der Merwe growth mode, indicating the layer-by-layer deposition of atoms, (c) Stranski-Krastanov growth mode, showing the combination of both island and layer deposition mechanisms.

4.2.1 Deposition Techniques

Thin film fabrication can stem from a range of techniques, which are often separated into two regimes: Chemical Vapour Deposition (CVD) and Physical Vapour Deposition (PVD). Within these two categories, surfaces can be engineered through vacuum, plasma, gaseous, and electrolytic environments; all of which can be adjusted to produced the desired surface.

Chemical Vapor Deposition (CVD) can be used to apply solid thin film coatings to surfaces, and for producing bulk materials and powder. The fundamental principal behind CVD is that, a gas or gases are passed into a chamber containing heated objects. Chemical reactions occur near to the surface of the heated objects, which result in the deposition of thin films [155]. This technique allows for a range of compounds to be formed with a high degree of repeatability as the formation of the thin film surface is reliant on the recipe of the chemical reaction.

Physical vapor deposition (PVD) processes are atomistic events where material is vaporised from a solid or liquid sources in the form of atoms or molecules. When removed, these atoms and molecules are transported through a vacuum or low pressure gaseous environment towards a substrate, where upon collision, they condense [156]. PVD techniques involve evaporation, sputter deposition, arc-vapor deposition, and ion plating. This thesis utilised the PVD method of DC magnetron sputtering to form all of the thin films for this thesis. This method is described below.

4.2.2 DC Magnetron Sputtering

DC magnetron sputtering, a PVD fabrication technique, utilises magnetic fields to confine plasmas close to the target material [157]. The use of a magnetic field enhances the efficiency of the plasma and therefore sputtered material [153]. The technique involves the acceleration of high energy positive gaseous ions towards a target material, held at a constant negative potential (4.2). The use of an applied external magnetic configuration acts to trap electrons. Therefore, upon collison with the target material, the ions cause an ejection of sputtered atoms from the target by a magnetically confined plasma [157]. These atoms then condense onto a chosen substrate, forming the desired thin films. In addition to the sputtered atoms, *secondary electrons* are also emitted and accelerated away from the target surface as a result of the ion bombardment. These *secondary electrons* contribute significantly to sustaining the plasma, by further ionising neutral gaseous atoms, and helping sustain the glow discharge [158].

The usefulness of DC magnetron sputtering to this body of work can be attributed to several factors; the ability to utilise thermally conducting metallic targets allows for the temperature of each elemental target to be controlled through water cooling, which allows for a larger range of applied power densities to be supplied to target materials. This factor is beneficial for reaching multiple stoichiometries when co-sputtering materials. DC magnetron sputtering also allows for a range of compositions to be unlocked over a short period of time due to high deposition rates, often measured in $\AA s^{-1}$, of metallic targets. The combination of these factors contributes to the usefulness of using surfaces for nuclear fuels research, allowing in a range of nuclear fuel

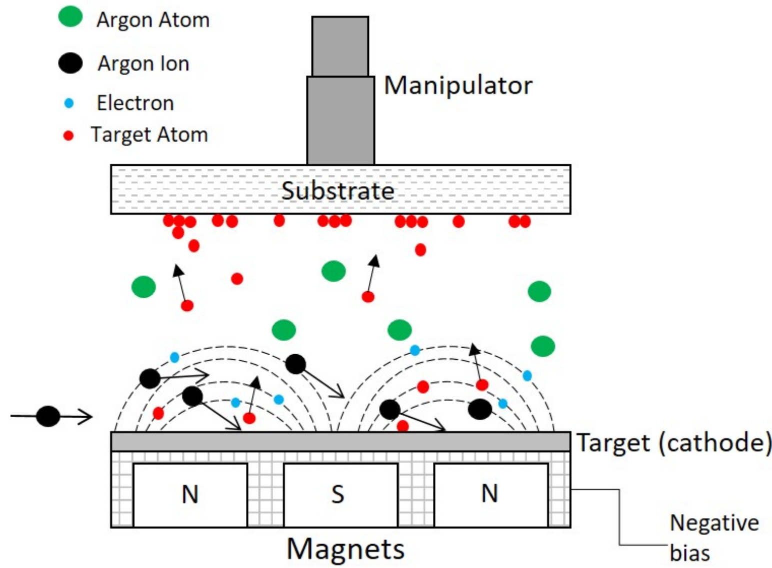

FIGURE 4.2. Schematic depicting the process of DC magnetron sputtering. This PVD technique was utilised to fabricate all thin film samples used in this thesis.

materials, in particular fuels and fuel candidates to be engineered using this technique.

4.2.3 Sputtering Modes

Engineering nuclear fuel materials using DC magnetron sputtering can be performed in a manner of ways. The procedure required to form such materials depends on the starting elements of each nuclear fuel compound. Understanding the fuel compounds on an elemental level aids in deciphering the correct sputtering mode required to form each phase.

4.2.3.1 Co-Sputtering

Co-sputtering DC magnetron sputtering involves the sputtering of multiple metallic targets, simultaneously within a pure inert gas environment (Figure 4.3) . This sputtering mode is primarily used to form compounds from solid target materials, including the formation of metals, intermetallic compounds, and alloys. It is possible to engineer compounds from a metallic sputtering target with a pre-determined stoichiometry, however, the nature of DC magnetron sputtering means that removal of atoms from the surface of that target may not be sputtered simultaneously. As such, the stoichiometry of the final film may not match the original target. Figure (4.4) shows the x-ray reflectivity (XRR) spectra from uranium metal and silicon thin films both sputtered at 50 W of power for 300 s. The spectra for uranium and silicon were modelled using GenX [132], and the deposition rates were found to be 0.81 and 0.53 Ås^{-1}, respectively. The difference in spectra indicates that the sputtering rate from different metallic targets can

change significantly between elements. Therefore, co-sputtering from separate targets allows for a better control over the stoichiometry of the compound being formed. Understanding the deposition rates of each target material helps fine tune the combined deposition rate (Ås^{-1}), to accurately match the required ratio for a particular phase or alloy. For example, U_3Si_2 requires a U:Si ratio of 3:2 between each element. Changing the current, and therefore power (W), supplied to a target material directly effects the amount of material deposited at any one point. This control allows for various phases to stabilised across a range of applied target powers (W). The thickness of the engineered surface will therefore be dependent on the overall growth time (s).

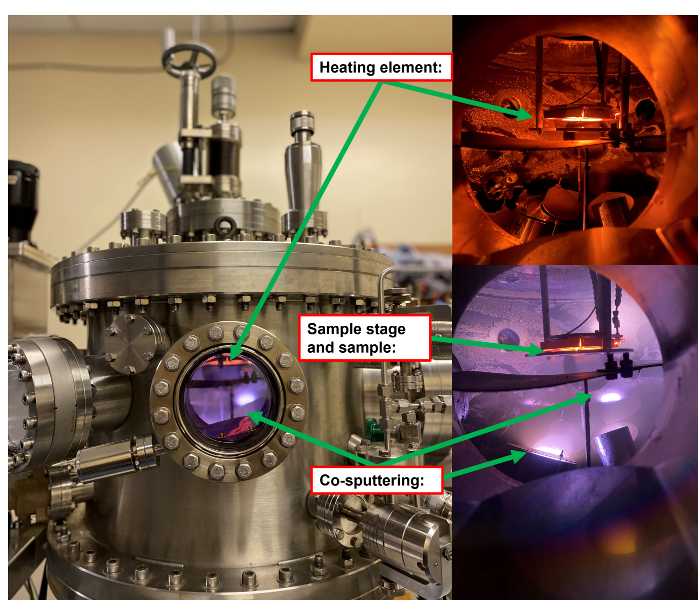

FIGURE 4.3. Labelled image of the actinide deposition chamber whilst sputtering. Heating element, sample holder, and magnetron guns are shown.

4.2.3.2 Reactive Sputtering

Reactive sputtering involves the formation of compounds from a single metallic target in the presence of a reactive gas alongside the chosen inert sputtering gas. This method of phase formation is often preferred when the secondary element is either not thermally or electrically conductive, making that element unsuitable for DC magnetron sputtering. One of the benefits of this sputtering mode is that it can allow for stoichiometries of a particular phase to be explored by only adjusting the partial pressure of the chosen reactive gas. For example, Figure (4.5) shows the binary phase diagram for uranium and oxygen. The range of compounds that form between U:O indicate that by changing the concentration of oxygen, the phase that is formed changes. This can be replicated in DC magnetron reactive sputtering by changing the partial pressure, or

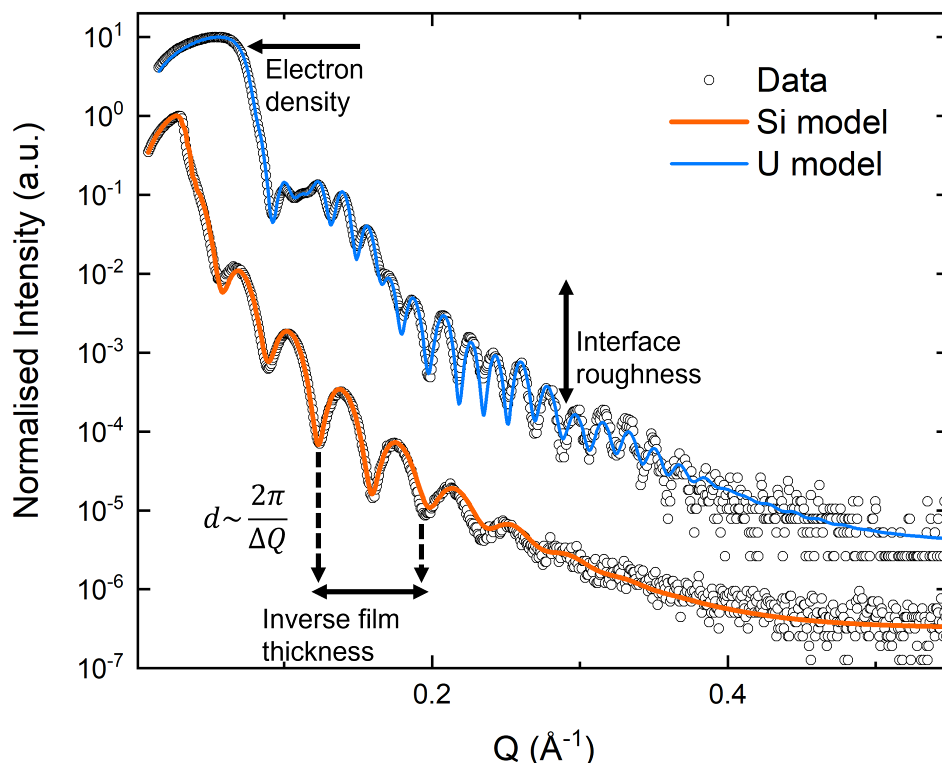

FIGURE 4.4. The spectra collected from Si and U-metal thin films. Both samples were grown for 300 s using the same deposition power rating of 50 W. The uranium sample is buffered and capped with niobium to prevent oxidation. Deposition rates for uranium and silicon are 0.81 and 0.53 $\mathring{A}s^{-1}$, respectively.

concentration, of oxygen that is fed into the deposition chamber.

4.2.3.3 Epitaxial Growth

A way of further controlling the formation of engineered surfaces is through lattice matching, or epitaxial growth. Epitaxy is a growth mechanism for forming single crystal thin films upon a single crystal substrate. The substrate acts as a crystallographic lattice template for the deposited phase to match on to for bond determined epitaxy (BDE). For ideal epitaxial growth, the two lattices will grow in perfect registry. Imperfections can still occur during the growth of the single crystal, which can be a result of substrate imperfections, or as a result of deviations in the deposition procedure. Furthermore, strain can be induced within the single crystal due to

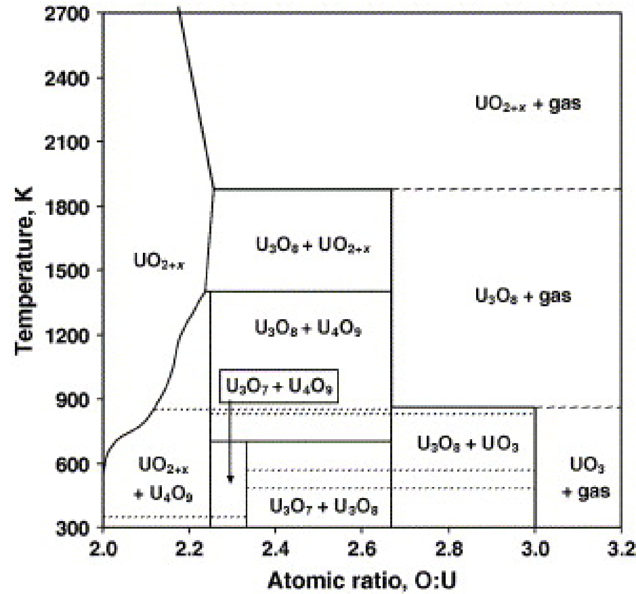

FIGURE 4.5. The binary phase diagram of uranium and oxygen. Figure indicates the phases formed as a function of oxygen concentration and of temperature (K). Figure from [159].

crystal lattice mismatches between the chosen substrate and the engineered surface. Both of these factors can significantly contribute to the distortion of the single crystal, with the structural impurities forming as an attempt to mediate the induced epitaxial strain, therefore determining the crystalline quality of the thin film.

4.2.4 Deposition Procedure

For the purpose of this thesis, uranium containing thin films, namely uranium silicides, and oxides, were produced using a dedicated ultra-high vacuum UHV actinide deposition chamber. This facility is housed in the School of Physics at the University of Bristol, and primarily utilises DC magnetron sputtering. This section details the methodology used to acquire high quality epitaxial thin films, produced via co- and reactive DC magnetron sputtering.

4.2.4.1 Aspects of UHV Chamber

The dedicated actinide deposition chamber is comprised of two chambers, a larger main growth chamber, and a loading chamber with a smaller volume, which is used for substrate preparation. This chamber is shown in Figure 4.6 Each chamber is evacuated by using a turbomolecular pump, which is backed by a scroll pump. The combination of these pumps allows each chamber to operate

within UHV conditions; 10^{-11} and 10^{-9} mbar for the main and loading chamber, respectively.

The main chamber houses four magnetron sputtering guns that create the discharge plasma over each metallic target. This deposition chamber does have evaporation and RF abilities, however, for the purpose of this thesis only DC magnetron sputtering was used. The main chamber is continuously under constant vacuum, and this is only interrupted for maintenance procedures, such as a target change. Due to the number of magnetron sputtering guns and the large volume of the chamber, the maintenance conducted on the main chamber is sparse, minimising the contamination of target materials, substrates, and thin films.

A gate valve separates the two chambers, this is to allow for the removal and replacement of samples within the loading chamber, whilst simultaneously keeping the main chamber under vacuum. Therefore, with contamination levels being kept to a minimum within the main chamber, a higher degree of quality can be sustained throughout all samples grown within this facility.

When preparing the loading chamber for the removal and replacement of substrates, the turbomolecular and scroll pumps are switched off, allowing for the chamber to vent to an atmospheric pressure. During this process, nitrogen gas is passed through the loading chamber at an approximate pressure of 0.2 bar. This is to inhibit the influx of the water and air molecules that can enter the system once the chamber is opened.

Prior to their introduction into the loading chamber, substrates are fixed onto circular molybdenum sample holders that are specifically designed for the transfer arm and samples stage within the deposition chamber. Each substrate sits within a 12×12 mm recess located at the center of the holder, and are held in place using molydenum clips. Once secured within the chamber, the chamber door is closed and each pump is turned back on, the nitrogen inlet gas is stopped, and the chamber is pumped back down to a UHV regime. Upon an appropriate vacuum regime being reached, the deposition facility is considered to be suitable to start engineering actinide surfaces.

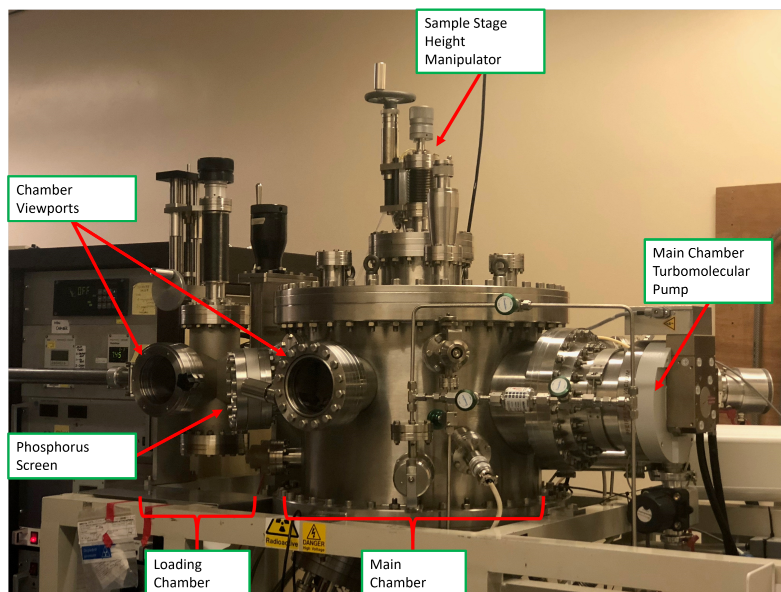

FIGURE 4.6. Labelled figure of the actinide deposition chamber used to synthesise thin film samples.

4.2.4.2 UHV System Preparation

In order to successfully produce high quality surfaces, the deposition chamber must undergo a series of processes to reach suitable growth conditions. These processes minimise the contaminating species within the chamber that may arise from a range of sources: contaminated target materials, heating components, or gas inlets. The range of components on the deposition chamber means that a series of steps are taken to minimise these factors:

Bake Out: In the event that the main deposition chamber of the system is vented to perform essential maintenance work or to conduct a target change, it is vital to remove any adsorbed gases from the chamber that were introduced as a result of the venting process. To achieve this, the chamber is ‘baked out’, which involves heating the chamber using internal and external high current filament lamps (Figure 4.8). These lamps are set to 120 V to induce radiative heating of the chamber up to 120°C, for a period of 24 - 72 hours. During this time period, the heating of the chamber removes adsorbed gases which are evacuated by the turbomolecular and scroll pump system. This initial process helps the main chamber to reach ultra-high vacuum status.

Target Cleaning and Calibration Growth: The silicon, copper, and niobium targets were purchased from Goodfellow Cambridge Ltd., all three targets were 99.999%, 99.99%,

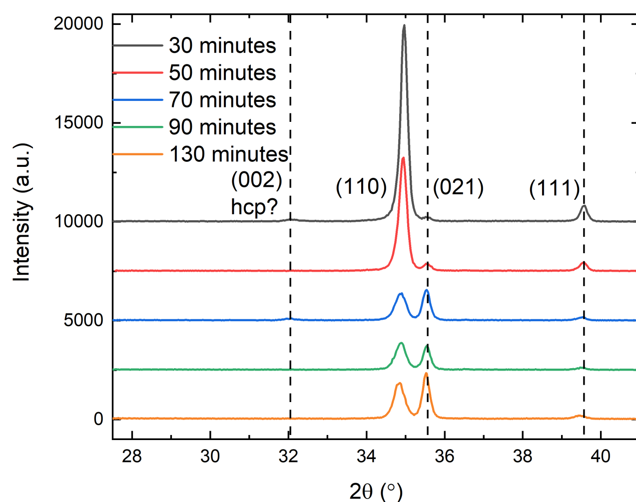

FIGURE 4.7. High-angle XRD spectra of cleaning iterations of the uranium target within the deposition chamber. Formation of α-U reflections are monitored as a function of cleaning time. Diffraction data indicates minimal oxygen contamination on target surface.

and 99.9% pure. In the case of uranium, high purity depleted uranium targets were acquired from the Atomic Weapons Establishment, AWE plc., Targets used were not kept under vacuum prior to installation into the deposition chamber. This can result in the formation of an oxide layer on the target surface. In addition, during any maintenance event performed on the main chamber, the target materials within the magnetron guns will be exposed to contaminants. Therefore, after the bake out procedure, each target within the chamber is cleaned. This involves removing the layers of oxidised atoms for set time periods until the target is confirmed to be clean. For materials that are susceptible to oxidation, like uranium, the oxide removal process is initiated by polishing the target to a mirror finish. Remaining surface oxidation is monitored once installed in the chamber by growing calibration samples on Corning glass substrates to observe the reduction in oxide growth via high-angle x-ray diffraction, XRD. Figure 4.7 indicates an example of this process. The data strongly indicates minimal oxygen contamination due to the presence of multiple uranium Bragg reflections. Once the targets have undergone a cleaning procedure, calibration samples are grown to obtain deposition rates for each material.

Gas Line Purge: The main chamber of the deposition system has multiple gas inlets for the purpose to both standard and reactive sputtering. Line purging was conducted for both the argon and oxygen gas lines to remove air contaminants when each gas cylinder was

installed onto the deposition chamber.

Substrate Preparation: The substrates used to form the thin films in this thesis are purchased commercially from MTI Corp. Each substrate is atomically polished prior to shipment, therefore no further surface preparation was required before loading into the deposition chamber. Prior to sample growth of uranium silicide phases, CaF_2 and MgO substrates were heated to 800 °C and 500 °C, respectively, to remove any contaminants that may have adsorbed onto the substrate during the loading procedure, preventing unwanted oxidation of the sample during growth.

With the completion of chamber preparation, a series of techniques are used to ensure the formation of high quality thin films.

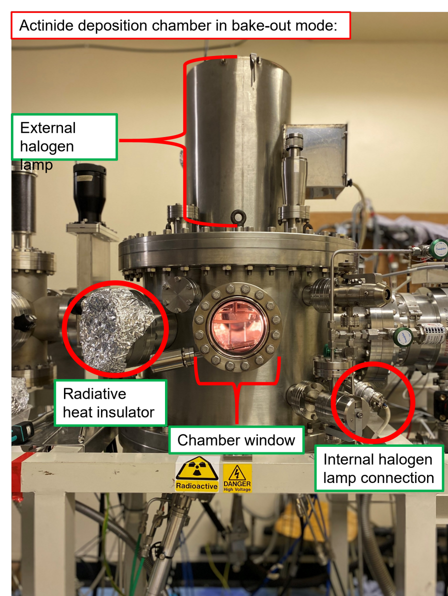

FIGURE 4.8. Figure depicting the deposition chamber used to synthesise actinide thin films in 'bake-out' mode. The components used to heat the system are labelled.

4.2.4.3 In-Situ Heating

In-situ heating is provided by a custom made resistive heater. The heater is comprised of 0.25 mm diameter niobium wire which is encased in alumina tubing. This device is situated directly above the sample stage within the deposition chamber, providing direct radiative heat to the back of the sample. The temperature of the heater is controlled using a manual variable current supply. This

is calibrated using a pyrometer which sits external to the main chamber, as seen in Figure 4.8.

4.2.4.4 In-Situ RHEED

When engineering thin films, it is useful to understand the crystallinity of the sample during growth. Reflective High Energy Electron Diffraction (RHEED) is deployed to monitor the crystallinity of thin films during the growth process. This in-situ technique allows single-crystals, poly-crystals, and textured layers to be identified prior to capping or exposure to atmospheric pressures. The diffraction patterns identified via diffraction vary with the structure of the sample, indicating epitaxial single crystals through to amorphous layers. If no pattern is present, it is likely that the layer has a near amorphous structure, whereas the presence of diffraction rings could indicate that a layer is polycrystalline. Diffraction spots and streaks could represent a layer that has preferred orientation, if these features become more defined, it could indicate epitaxial growth. Example RHEED patterns for two different single crystals are depicted in Figure 4.9, which indicate that the diffraction spots can also vary with epitaxial quality. The diffraction spots for CaF_2 substrates are more defined when compared to the diffraction pattern obtained from an epitaxial USi_3 layer.

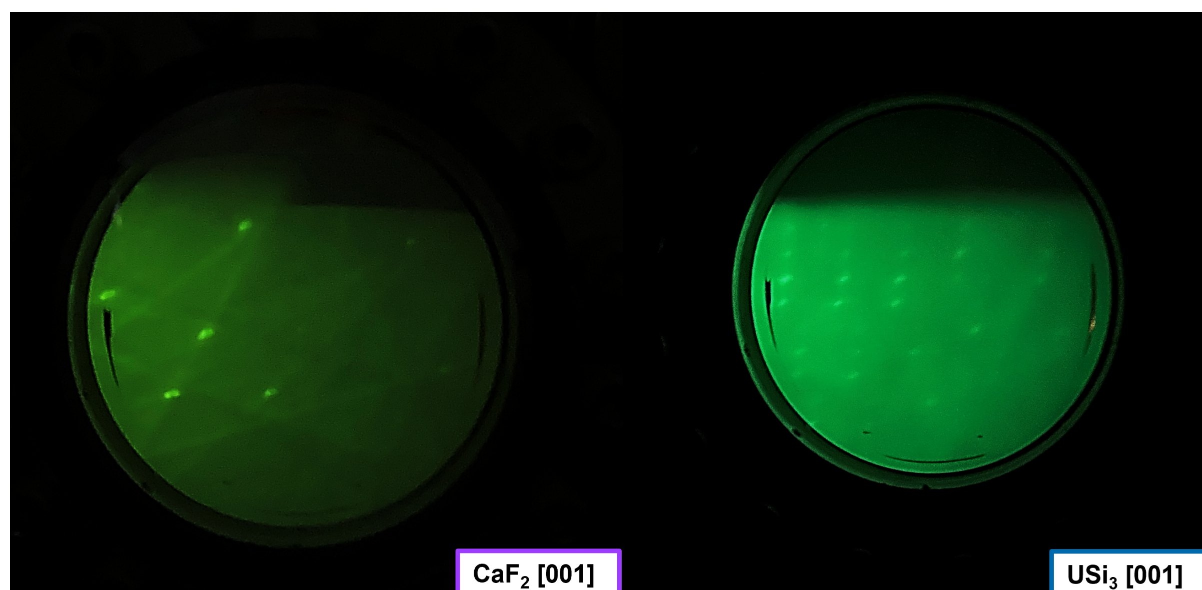

FIGURE 4.9. RHEED diffraction patterns obtained from the (001) surfaces of CaF_2 and USi_3 surfaces. The CaF_2 pattern was observed after the substrate was annealed at 800 °C, with the USi_3 RHEED pattern being observed after deposition.

4.2.4.5 Substrate Selection and Preparation

To ensure high-quality uranium silicide phases are formed, the substrate that the surfaces are grown upon must be chosen carefully. The most vital aspect of engineering these compounds is to ensure that minimal oxygen contamination occurs on the substrate prior to growth and within the chamber during growth. The oxygen contamination within the chamber is minimised using the procedures previously discussed, therefore, the substrate is the final component that could present severe oxygen contamination to the U-Si surfaces. When considering substrates for the formation of uranium silicides, three factors must be considered: substrate composition, substrate melting temperature, and substrate lattice parameters. Substrates that did not contain oxygen were used to minimise the oxygen contamination when growing uranium silicide phases. Namely, Calcium Fluoride, CaF_2 was the primary substrate used to grow all uranium silicide phases for this thesis, with the exception of SN1379 which was grown on Magnesium Oxide (MgO) substrates (Table 4.1). Using CaF_2 substrates resulted in adsorbed surface contamination being the last remaining source of potential disruption to forming high quality uranium silicide surfaces. This surface contamination is depicted in Figure 4.10, which indicates the x-ray reflectivity spectra obtained from a CaF_2 single crystal substrate. The data was modelled using Gen-X [132], and it was found to have a 12.68Å calcium oxide, CaO, layer that had formed upon the substrate. This potential contamination was overcome by annealing the substrate prior to U-Si deposition. The substrate was annealed at 800 °C under UHV conditions, allowing for the adsorbed contaminants to be removed. Additionally, this process further contributes to the deposition chamber reaching UHV conditions.

The use of MgO substrates required the use of a protective buffer layer to prevent unwanted oxidation to the uranium silicide film. Epitaxy between Cu (001) and MgO (001) is achieved through fitting 7 unit cells of Cu upon 6 unit cells of MgO. This allows for a cube-on-cube match between a MgO (001) substrate and a Cu layer deposited at 100 °C. The good registry, and 0.1% mismatch between the two phases prevents unwanted oxidation to the surfaces deposited upon the Cu buffer later. This growth procedure was followed from Purswani *et al.,* [160].

Some single crystal substrates were considered as direct epitaxial matches with U_3Si_2 due to their lattice parameters. These substrates include [001] oriented yttrium orthovanadate (YVO_4) and [001] oriented lithium fluoride (LiF). As the YVO_4 structure contains oxygen, the deposition of U-Si onto the surface resulted in the contamination of metallic uranium atoms, resulting in the formation of UO_2. Much like CaF_2, the LiF structure does not contain oxygen, suggesting minimal contamination. However, the melting temperature of LiF is around 850 °C [161], which resulted in U-Si phases being deposited onto this substrate at lower temperatures when compared to those deposited on CaF_2, and therefore crystallisation of U-Si phases was hindered.

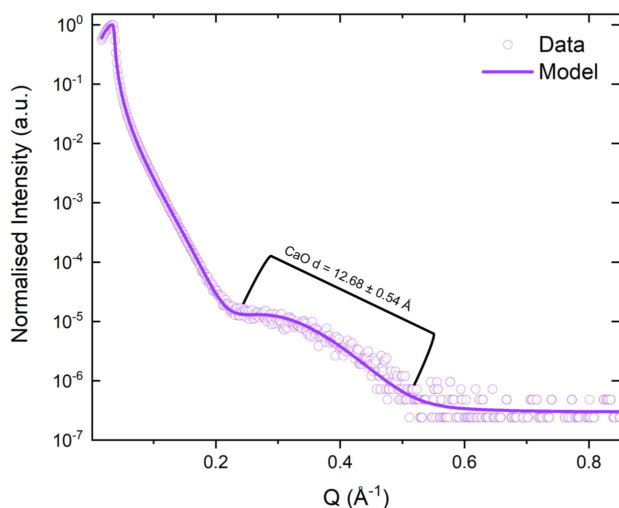

FIGURE 4.10. X-ray reflectivity data and model of a single crystal CaF_2 substrate oriented in the (001) direction. Model indicated an oxide layer which was modelled as CaO with a thickness of 12.68Å.

4.2.4.6 Uranium and Silicon Oxide Thin Films

For this thesis, a series of uranium dioxide thin films were grown in order to compare the dissolution behaviour to uranium silicide phases. These samples were grown directly upon yttria-stabilised zirconia, YSZ, substrates which were purchased commercially from MTI Corp. The substrates used were (001) oriented, which allowed for (001) oriented uranium dioxide, UO_2 surfaces to be grown. UO_2 forms an epitaxial match with YSZ in all three principal crystallographic directions (Figure 4.11), however for the purpose of this thesis, only the (001) direction was used as a comparison. In addition, metallic silicon was deposited onto Corning glass substrates. This sample, SN1519, detailed in Table 4.1, was used as a control sample to assess the corrosive effect of H_2O and H_2O_2 on silicon and silicon oxide thin films.

4.2.4.7 Capping

In order to characterise each uranium silicide phase, the films engineered were capped with a protective metal layer to prevent unwanted oxidation. This procedure minimises the probability that the experimental results will be influenced by structural changes from oxidation products within the sample. The samples presented in this thesis that were not used for corrosion experiments were capped with 100 – 120Å of niobium, with the exception of SN1379 which was capped with Cu. The thickness was chosen to ensure that XRR reflectivity measurements were still feasible.

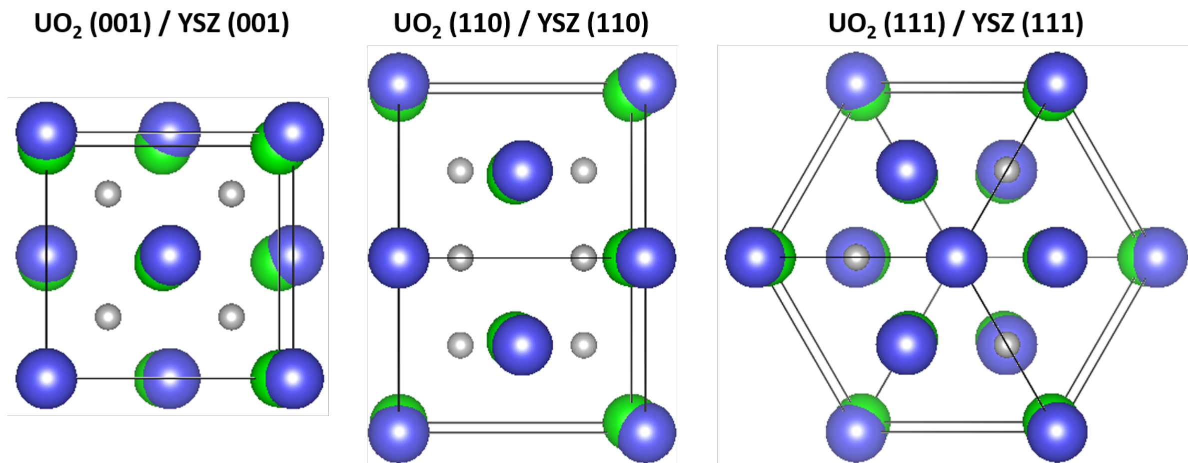

FIGURE 4.11. Schematic depicting the epitaxial matches of UO_2 onto YSZ in all three principal crystallographic orientations, (001), (110), and (111), shown left to right. Uranium atoms are shown in purple, and YSZ atoms shown with green, and oxygen atoms with grey. Figure produced using Vesta [162].

Niobium was used as it forms a passivating Nb_2O_5 oxide layer of around 20 – 40 Å within ambient air conditions [163]. This characteristic prevents the entire Nb layer from oxidising, and therefore protects the thin film. Depositing the capping material at ambient temperatures once the film has cooled further prevents interaction between film and capping layer. The formation of copper oxide under ambient temperatures indicates an initial layer of Cu_2O growing before an additional layer of CuO. Copper oxide layers have been measured within the literature [164], and have been quoted to be approximately between 20 – 50 Å and 10 – 13 Å, respectively. This therefore prevents the oxide layer of Cu from contaminating the layer below. All capping layers used in this thesis were deposited at room temperature to avoid layer interactions between compounds. The crystallinity of the deposited capping layers are classified as polycrystalline, as they do not form an epitaxial match with the adjacent film.

4.2.5 List of samples used in this thesis

Table 4.1: Table of samples used throughout this thesis. Samples are compared within their relative chapters.

Sample Number	Substrate	Film	Si Power (W)	U Power (W)	Heater Temperature °C	Chapter Ref.
SN1512	CaF_2 (001)	U_3Si_5 (100) / Nb	46	19	800/RT	5,6
SN1513	CaF_2 (001)	U_3Si (001) Nb	46	45	800/RT	5,6
SN1639	CaF_2 (001)	U_3Si_2 (poly) / Nb	46	30	800/RT	5,6
SN1379	MgO	Cu (001) / $\alpha-USi_2$ (001) / Cu	48	5.5	100/500/RT	5,6
SN1645	CaF_2 (001)	$\alpha-USi_2$ (001)	46	19	800	5, 6
SN1699	CaF_2 (001)	USi_3 / Nb	46	5	800/RT	5,6
SN1711	CaF_2 (001)	U_3Si (001)	46	36	800	6, 7
SN1707	CaF_2 (001)	U_3Si_2 (poly)	46	23	800	6, 7
SN1644	CaF_2 (001)	U_3Si_5	46	30	800	6
SN1702	CaF_2 (001)	U_3Si_5 (100) $\alpha-USi_2$ (001)	46	10	800	6, 7
SN1700	CaF_2 (001)	USi_3 (001)	46	5	800	6, 7
SN1507	YSZ (001)	UO_2 (001)	0	50	550	7
SN1829	YSZ (001)	UO_2 (001)	0	50	550	7
SN1519	Corning Glass	Si	50	0	RT	7

Chapter 5

Characterisation of Uranium Silicide Phases

This chapter details the structural and chemical characterisation of uranium silicide thin films. This chapter builds upon the characterisation techniques discussed in chapters 3 and 4 in order to understand and characterise uranium silicide thin films that have been grown using DC magnetron sputtering. Allowing for the phase diagram of U-Si to be delicately mapped for thin films as a function of uranium content.

5.1 Understanding the U-Si phase diagram through epitaxial matching

For the purpose of this work, a series of high-temperature U-Si surfaces were grown in order to further understand the U-Si binary phase diagram, and decipher whether this phase diagram is unique for thin films. By keeping the silicon content constant for each film, the uranium content was changed and thus, a range of thin films have been grown which expand across the uranium-silicon phase diagram. The purpose for this work was to characterise each U-Si phase individually by exploring the crystal structure, the crystallographic orientation, and the stoichiometry for each compound. The following examples highlight how the uranium silicide phases have been stabilised, and how the majority of the phases have been grown as single crystals through the use of epitaxial matching.

5.2 The structural characterisation of single phase uranium silicide surfaces

5.2.1 Epitaxial U_3Si Thin Films

Single crystal triuranium silicide, U_3Si was epitaxially stabilised onto single crystal calcium fluoride, CaF_2 substrates. U_3Si, is the U-Si compound with the lowest silicon content, with 25 mol.% of silicon [42]. Figure 5.1, depicts the specular high angle XRD data from sample SN1513. This sample is a single crystal of U_3Si, orientated in the (001) direction with a tetragonal crystal structure. The crystal was epitaxially matched to an (001) calcium fluoride, CaF_2, single crystal substrate, and was deposited at 800 °C, using DC magnetron sputtering. The (002) Bragg reflection of CaF_2 is indicated in Figure 5.1 with a purple drop line at $2\theta = 32.7°$. Two unidentified peaks are situated at 33.59° and 36.21°. The (110) Bragg reflection of Nb is also visible within the spectra. Nb was used as a physical and chemical capping layer to prevent unwanted oxidation or surface alterations of the U_3Si crystal.

Transverse scans were conducted on the specular Bragg reflections of SN1513. Figure 5.2 indicates the modelled data from both the CaF_2 and U_3Si single crystal ω scans. Data is shown as open circles, with the model for each data set shown with a solid line. The data sets for each rocking curve were modelled using a psuedo-Voigt function. This modelling allowed for the FWHM for each rocking curve to be extracted. This parameter provides an indication about the mosaic of the crystal, and about how the crystal planes are aligned in the specular direction. The mosaic for U_3Si was calculated to be $0.79 \pm 0.01°$, with the FWHM of the CaF_2 substrate being $0.065 \pm 0.001°$.

To further confirm the structural nature of SN1513, off-specular scans were conducted to investigate the crystallinity of the sample. Figure 5.3 indicates the peaks from the {206} reflection family from U_3Si, and the {224} reflection family from CaF_2 which have been modelled with Gaussian peaks. These scan types can help identify the epitaxial relationship between the thin film and substrate.

For a bulk single crystal of tetragonal ($a = b \neq c$) U_3Si, with one domain, one would expect to see a total of 4 peaks in a 360° rotation, with 2 peaks in 180° for the (206) reflection. These peaks would be symmetric and have a periodicity of $\Delta\Phi = 90°$ between each peak. From Figure 5.3, it can be seen that there are a total of 4 peaks within a 0° – 180° phi range. This indicates that this single crystal of U_3Si has two domains. These domains are further confirmed by the significant intensity contrast between the two sets of peaks which both have a periodicity of $\Delta\Phi = 90°$.

Furthermore, the data in Figure 5.3 shows the phi data from the (224) of CaF_2. For this cubic

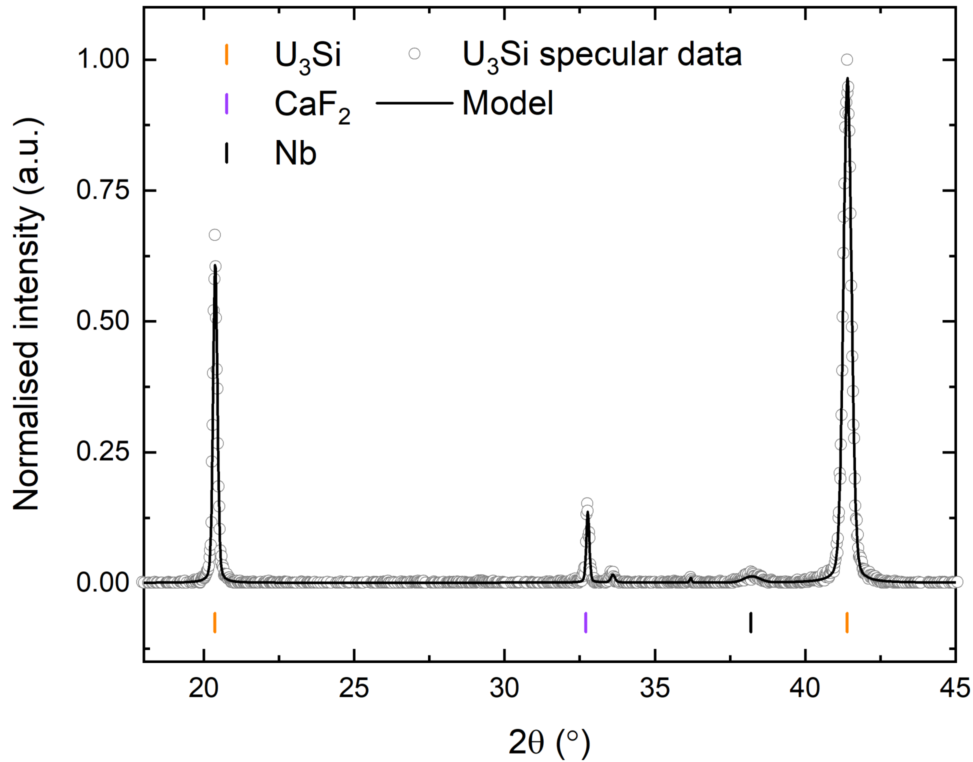

FIGURE 5.1. X-ray diffraction spectra from (001) oriented U_3Si single crystal thin film. Bragg reflections from the U_3Si film are depicted with orange drop lines, and the Bragg reflection from the CaF_2 substrate are in purple. Data from SN1513.

system (a = b = c), 4 peaks are expected in a 360° phi range, with two peaks between 0° – 180°. This matches the data presented in Figure 5.3, where the peaks have a periodicity of $\Delta\Phi = 90°$.

The phi data from the (206) of U_3Si and (224) of CaF_2 allows for the epitaxial relationship between the two crystals to be investigated. Geometrically, there should be a 45° separation between the two reflections. This separation is correctly represented by the lower intensity U_3Si (206) peaks. This infers that the higher intensity (206) peaks belong to a domain that is rotated 45°, aligning with the CaF_2 (224) reflections with a phi difference of 0°. This rotated domain is the strongest of the two.

To further understand the epitaxial relationship between U_3Si and CaF_2, Figure 5.4(a) indicates how the uranium and silicon atoms are positioned within one unit cell of U_3Si. This figure

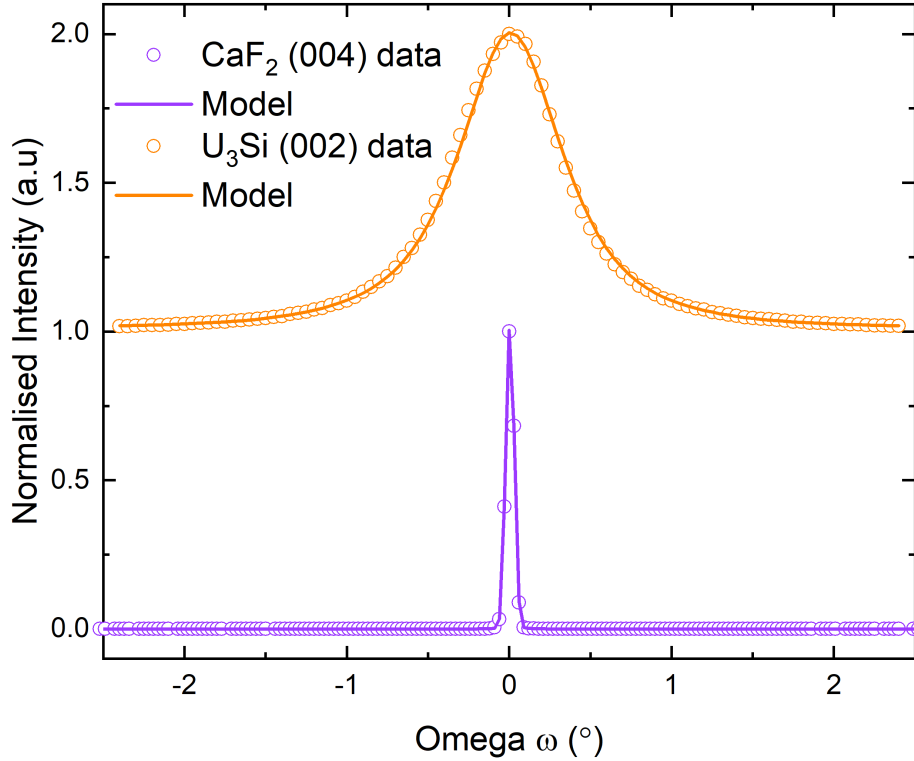

FIGURE 5.2. Omega scan from the (002) Bragg reflection of U_3Si and the (004) of CaF_2. Open circles indicate data points and solid line shows the fit in orange and purple for U_3Si and CaF_2 respectively. Data from SN1513.

shows how the uranium sites alternate throughout the unit cell, and Figure 5.4(c) indicates how these two uranium sites sit relative to one another. From Figure 5.4(d) the relative atomic positions of both uranium sites (U1, U2) are overlayed the CaF_2 unit cell (Figure 5.4(b)) in the [001] direction. The suggestion here is that the epitaxial match between the uranium sites in U_3Si and CaF_2 has two possible solutions.

Using the specular (002) Bragg reflection peak, where 2θ = 20.37° and the off-specular (206) reflection, where 2θ = 72.31°, the lattice parameters were calculated for tetragonal U_3Si. The parameters were calculated using:

$$\frac{1}{d^2} = \frac{h^2 + k^2}{a^2} + \frac{l^2}{c^2} \tag{5.1}$$

where, a and c are the tetragonal lattice parameters. The lattice spacing is represented by d,

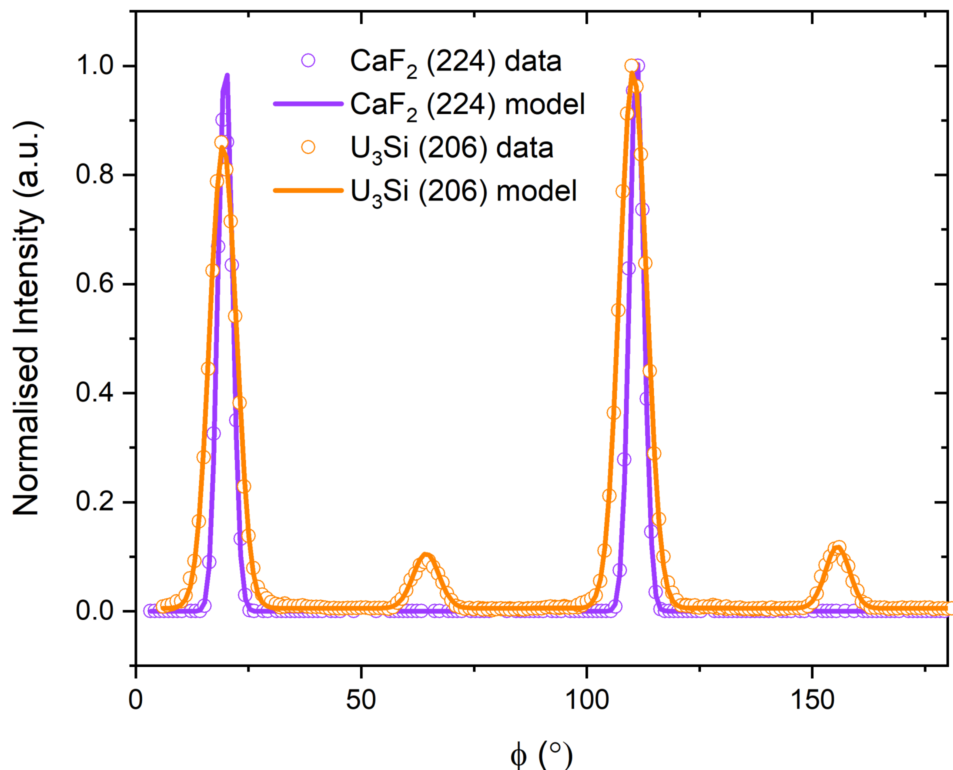

FIGURE 5.3. Off-specular phi data collected from the (206) of U_3Si and the (224) of CaF_2. Open circles indicate data points and solid line shows the fit. Higher intensity peaks belong to the first domain which is rotated 45°, with the lower intensity peaks belonging to the second domain. Data from SN1513.

and h, k, and l are the miller indices of the lattice plane. For SN1513, the lattice parameters of U_3Si were calculated to be: $a = 6.045 \pm 0.009$Å and $c = 8.71 \pm 0.02$Å, where $a/c = 0.694$. The unit cell of SN1513 was calculated to be 319.12 ± 1.27Å^3.

5.2.2 Polycrystalline U_3Si_2 Thin Film

Triuranium disilicide, U_3Si_2 was stabilised on [001] oriented CaF_2 single crystal substrates. This phase of uranium silicide is the most favourable for replacing UO_2 as the fuel within commercial nuclear reactors, with a uranium:silicon ratio of 3:2. The spectra presented in Figure 5.5 indicates the high angle diffraction data obtained from SN1639, a polycrystalline U_3Si_2 sample. Uranium and silicon were simultaneously deposited using DC magnetron sputtering (as discussed in

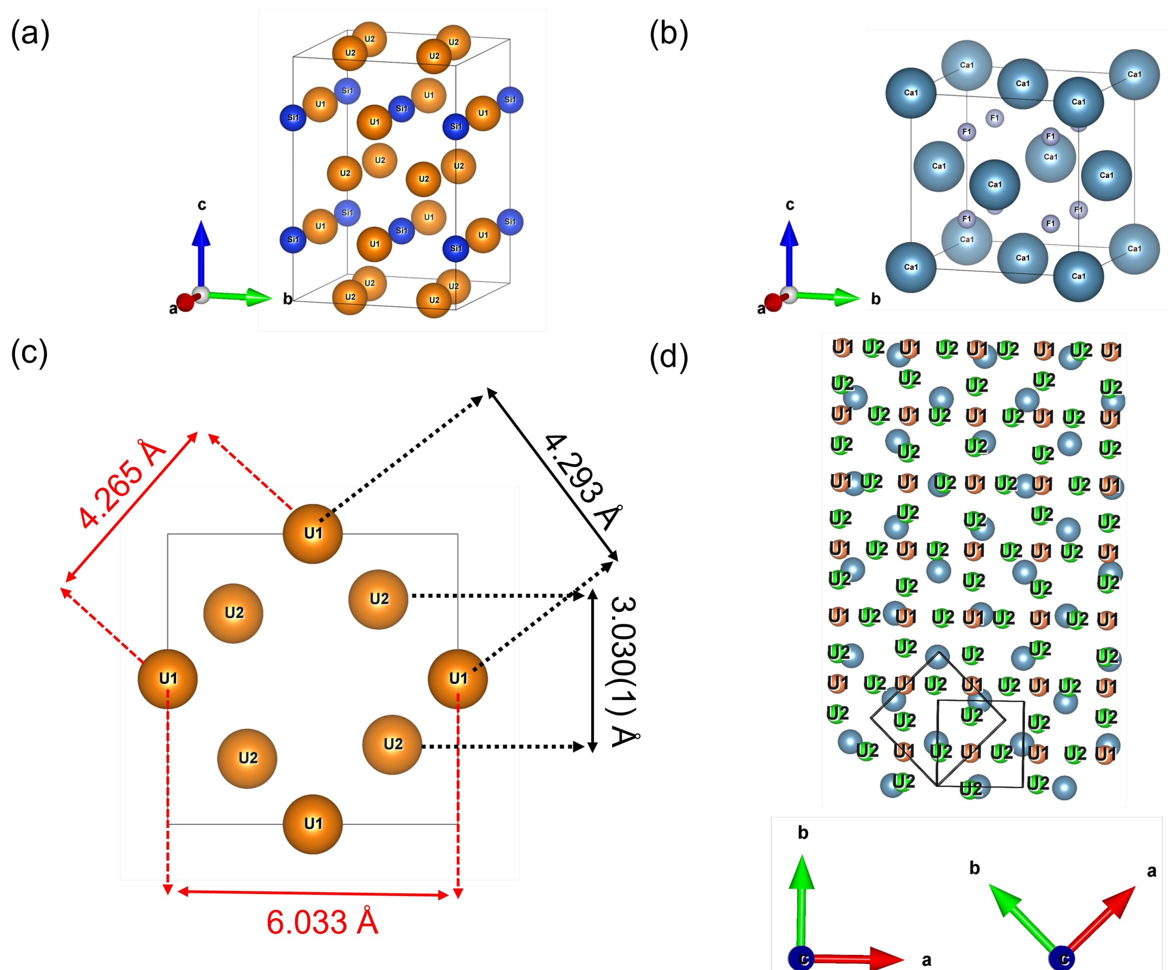

FIGURE 5.4. (a) The unit cell of U_3Si with both uranium sites labelled, and silicon positions labelled. (b) The unit cell of CaF_2 with calcium and fluorine labelled. (c) Image indicating the atomic distances between the uranium sites and their relative positions within the unit cell. Atomic distances taken from [46]. (d) The epitaxial match between U_3Si and CaF_2 unit cells, with the unit cell of U_3Si rotated 45°. Figure indicates two possible solutions for the atomic positioning of the epitaxial match, with the [001] direction perpendicular to the page.

Chapter 4), onto CaF_2 at 800 °C, and capped with niobium at room temperature.

The spectrum in Figure 5.5 indicates that U_3Si and U_3Si_5 phases have also crystallised as minor phase impurities, alongside U_3Si_2 which is the major phase. The minor U-Si phases have crystallised in a preferred orientation manner with only one crystallographic direction being present for both compounds. For U_3Si the (002) reflection has crystallised, and for U_3Si_5 the (100) reflection is present.

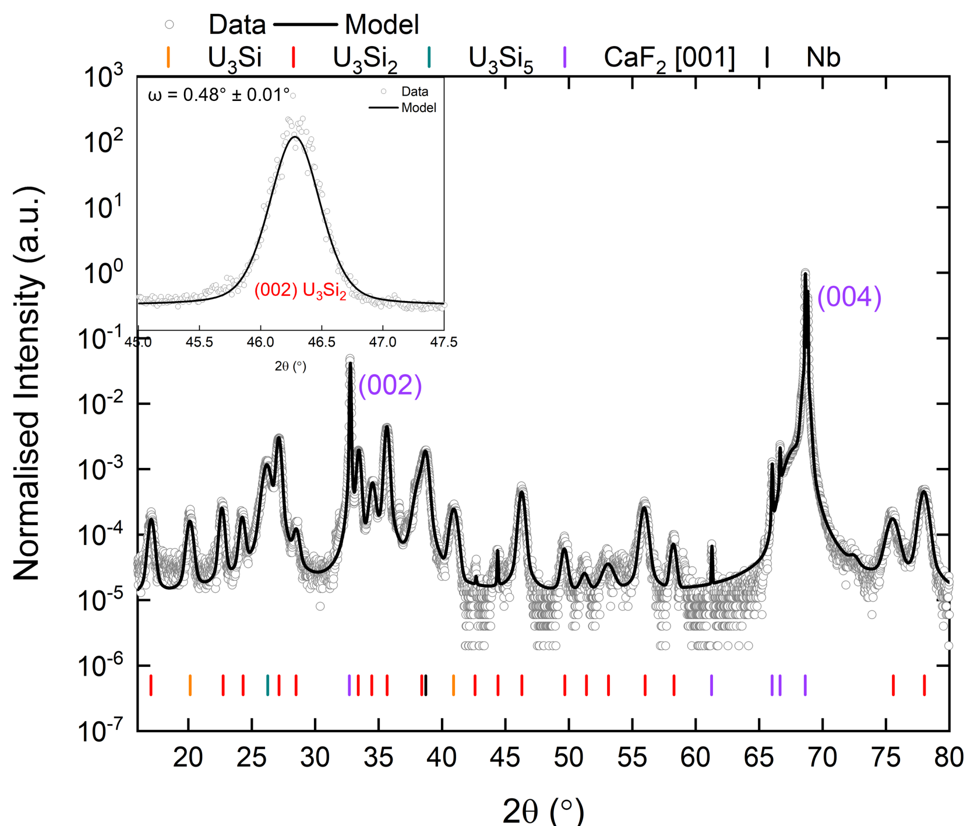

FIGURE 5.5. High angle x-ray diffraction data collected from a polycrystalline thin film of U_3Si_2 (SN1639). Sample includes impurities of U_3Si and U_3Si_5, represented with orange and teal drop lines respectively. U_3Si_2 and CaF_2 are indicated with red and purple drop lines. Inset of the (002) Bragg reflection of U_3Si_2 used to calculate crystallite size, FWHM = 0.48° ± 0.01°.

Table 5.1: Table showing crystallite size for each phase within SN1639.

Phase	2θ position °	FWHM °	Crystallite size (nm)
U_3Si_2 (002)	46.283 ± 0.002	0.48 ± 0.01	19 ± 2
U_3Si (002)	20.146 ± 0.003	0.35 ± 0.01	24 ± 1
U_3Si_5 (100)	26.203 ± 0.004	0.63 ± 0.01	14 ± 1

The crystallite size of the three phases within SN1639 were calculated using the Scherrer equation, as described in Chapter 3. This calculation provides an average crystallite size for the three phases. The crystallite sizes, alongside the 2θ positions, and FWHM for the chosen Bragg

reflection can be found in Table 5.1. From the calculations, the U_3Si crystallites are marginally larger when compared to the crystallite sizes of U_3Si_2 and U_3Si_5. However, all crystallites are of the order of nm in size.

5.2.3 Epitaxial U_3Si_5 Thin Film

Hexagonal triuranium pentasilicide, U_3Si_5, was stabilised in the [001] direction. This single crystal was deposited at 800 °C, and was capped with 100 Å of Nb to prevent unwanted oxidation to the film surface. The high angle x-ray diffraction data from SN1512 is presented in Figure 5.6, where open circles indicate the data, and the solid line shows the model. The (100) and (200) Bragg reflections of U_3Si_5 are indicated with teal drop lines.

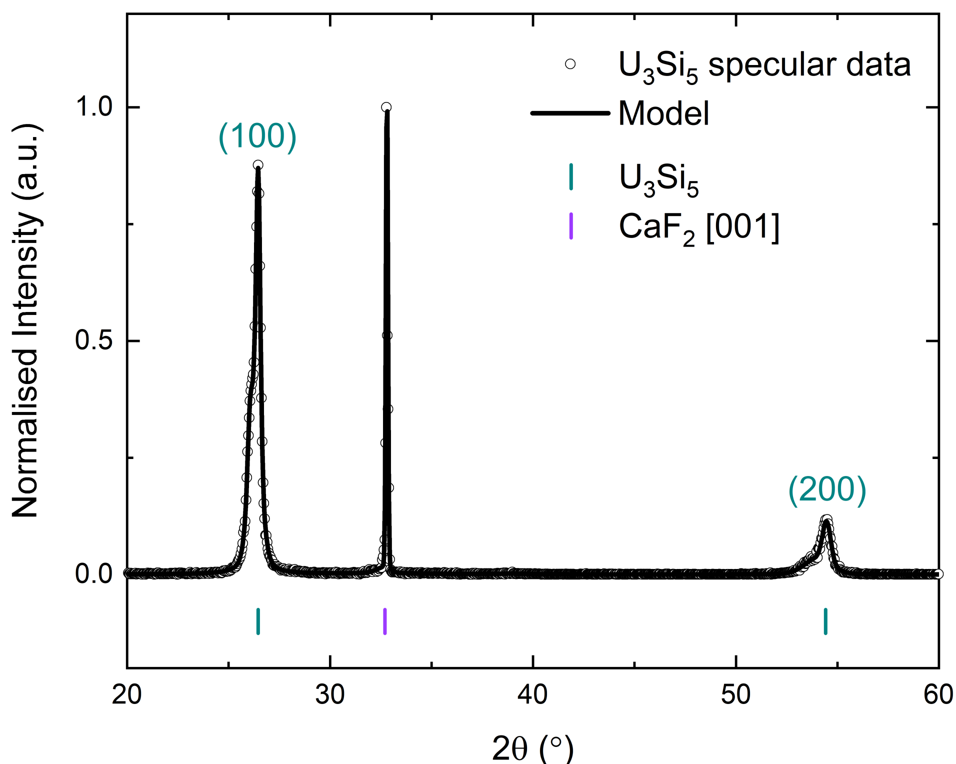

FIGURE 5.6. X-ray diffraction spectra from (100) oriented U_3Si_5 single crystal thin film. Bragg reflections from the U_3Si_5 film are depicted with teal drop lines, and the Bragg reflection from the CaF_2 substrate are in purple. Data from SN1512.

Shoulder-like features are present on the lower 2θ side of both specular (100) and (200) reflections from U_3Si_5 (Figure 5.6). These features were investigated through the use of transverse omega scans (Figure 5.7). It was found that the shoulder feature did not exhibit unique positions in omega. To further understand the crystallinity of the sample, transverse scans were conducted on the (100) of U_3Si_5 and the (002) of CaF_2. Figure 5.7 shows the modelled data from both CaF_2 and U_3Si_5. Data is shown as open circles and the model is presented as solid lines in teal and purple for U_3Si_5 and CaF_2, respectively. By modelling the data with a psuedo-voigt function, the FWHM of each rocking curve was extracted, indicating how well aligned the crystal planes are in the specular direction. The FWHM for U_3Si_5 was modelled to be $1.51 \pm 0.02°$, with the FWHM of the CaF_2 was modelled to be $0.052 \pm 0.002°$. The difference between these ω values indicates how much the quality of the single crystal varies. This difference could be attributed to the epitaxial match between the film and substrate.

Where there is a preferred orientation in the high angle diffraction data for SN1512, with the specular reflections for U_3Si_5 being (100) and (200), it is important to further understand the crystalline structure. This was conducted using off-specular scans, and rotating the sample in ϕ to investigate unique reflections, and to further understand the lattice parameters of the sample. The {201} reflection family of U_3Si_5 was used to investigate these parameters. Figure 5.8 depicts the ϕ data from this reflection, alongside the ϕ data from the (044) of CaF_2.

For a perfect single crystal of hexagonal U_3Si_5 with 'a' being the specular direction, one would expect there to be a total of 2 reflections to be present in a 360° ϕ rotation. This would indicate a single crystal with one domain. However, the data presented in Figure 5.8, there are 2 reflections in 180° indicating that the single crystal of U_3Si_5 has two domains. Physically, this suggests that the two crystal domains are situated perpendicular to one another with the 'a' direction of the hexagonal structure in the specular direction. This is indicated in Figure 5.9.

Using the off-specular data collected from the {201} reflection family of U_3Si_5, the lattice parameters were calculated. The U_3Si_5 crystal (SN1512) was treated as a hexagonal close packed (HCP) structure, with a = b ≠ c. Eqn. 5.2 was used to calculate the 'a' and 'c' lattice parameters, utilising the distance between the lattice planes, d, and the Miller indicies, (hkl) of the specular and off-specular Bragg reflection 2θ positions:

$$\frac{1}{d^2} = \frac{4(h^2 + hk + k^2)}{3a^2} + \frac{l^2}{c^2} \tag{5.2}$$

From this, the 'a' and 'c' lattice parameters were calculated to be 3.89 ± 0.01Å and 3.97 ± 0.05Å, respectively. The lattice parameter values provided a c/a ratio of 1.021. The unit cell for SN1512 was calculated to be 59.74 ± 0.79Å^3.

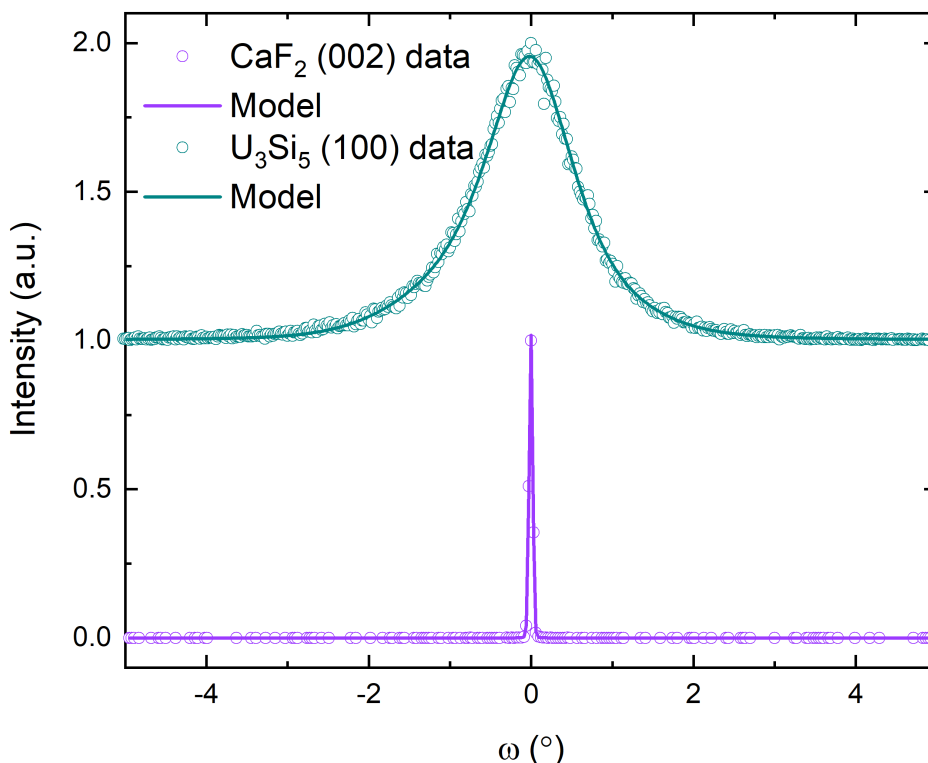

FIGURE 5.7. Omega scan from the (100) Bragg reflection of U_3Si_5, and the (002) Bragg reflection of CaF_2. Open circles indicate data points and solid line shows the fit in teal and purple for U_3Si_5, and CaF_2 respectively. Data from SN1512.

5.2.4 Epitaxial α-USi_2 Thin Films

5.2.4.1 MgO Stabilisation

Uranium disilicide can form two crystallographic phases: $\alpha-USi_2$ and $\beta-USi_2$. Here, the α-phase has been stabilised via epitaxial lattice matching onto single crystal [001] oriented MgO. To successfully stabilise the tetragonal $\alpha-USi_2$ phase onto MgO without oxidising the silicide film, a layer of copper was deposited in-between the substrate and U-Si film. Copper epitaxially matches to [001] oriented MgO, this is explained in Chapter 4. This epitaxial match between the buffer and substrate provides a single crystal substrate onto which the USi_2 layer can be stabilised. The U-Si film was then capped with a layer of Cu to prevent surface oxidation. Figure 5.10 indicates the high angle diffraction data obtained from SN1379, a single crystal of USi_2. The high angle data indicates the specular reflections from the (004) and (008) of $\alpha-USi_2$, the (002)

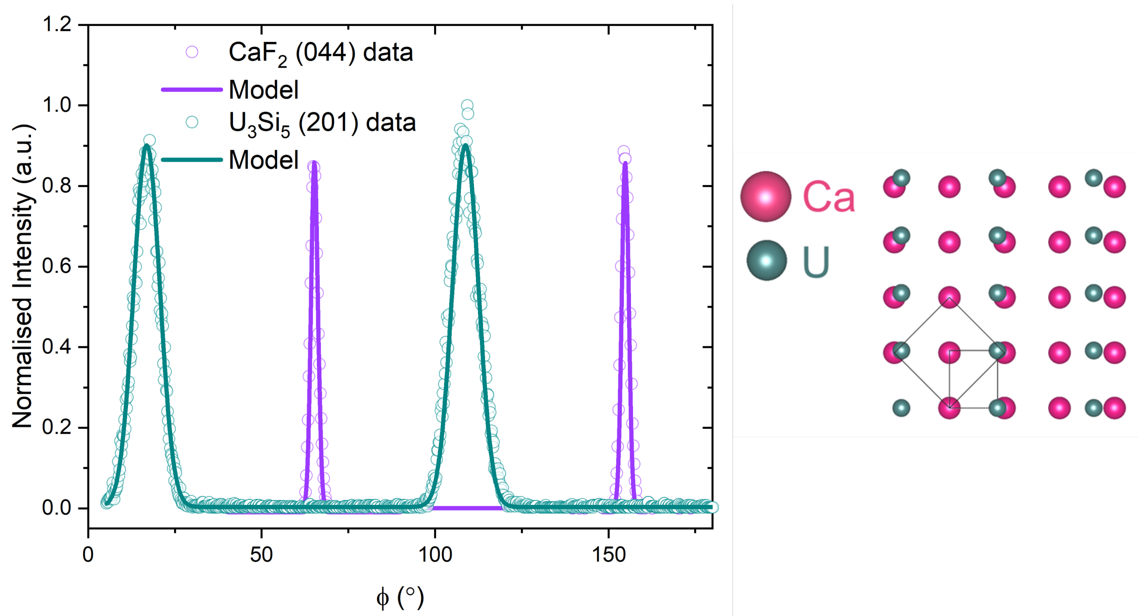

FIGURE 5.8. Off-specular phi data collected from the (201) of U_3Si_5 and the (044) of CaF_2. Open circles indicate data points and solid line shows the fit. Data from SN1512.

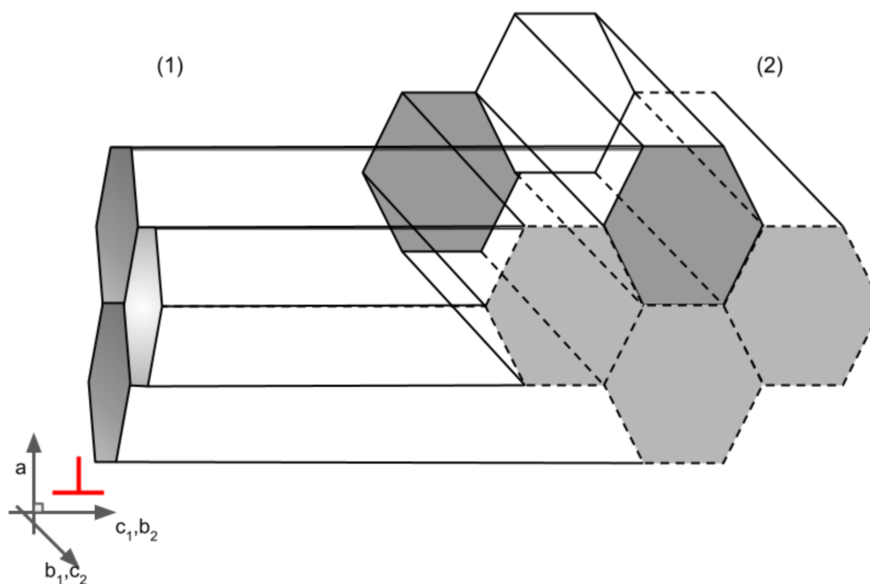

FIGURE 5.9. Schematic showing the orientation of the two domains that exist in the U_3Si_5 single crystal. Diagram indicates how the two domains sit perpendicular to one another, with the (h00) plane being the specular direction. Grey shading indicates the effective start and end of each domain between two hexagonal faces.

of Cu, and the (002) of MgO. These are denoted with green, blue, and red drop lines, respectively.

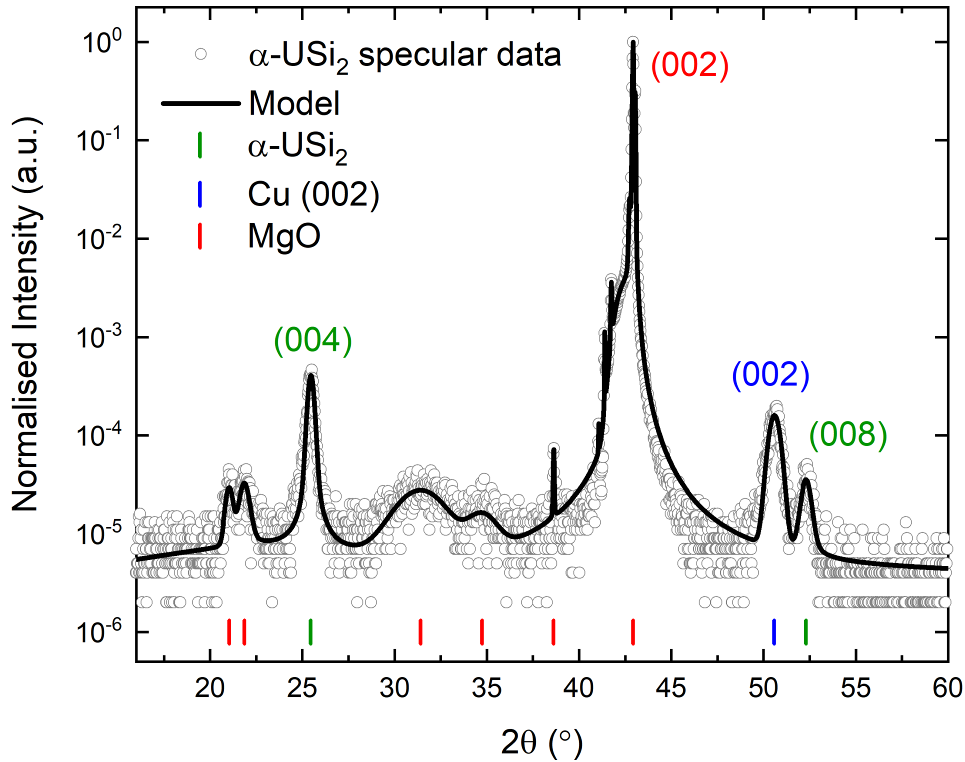

FIGURE 5.10. X-ray diffraction spectra from (001) oriented α-USi_2 single crystal thin film. Bragg reflections from the α-USi_2 film are depicted with green drop lines, (002) Cu drop lines in blue, and MgO drop lines in red. Data from SN1379.

To further understand the crystalline quality of the epitaxial matches, omega scans were conducted on the specular Bragg reflections for $\alpha - USi_2$ (004), Cu (002), and MgO (002). Figure 5.11 shows the data collected from these Bragg reflections, with the data for each phase shown with open diamonds, circles, and squares for $\alpha - USi_2$, Cu, and MgO, respectively. These data sets were all modelled using a psuedo-voigt, allowing for the FWHM to be extracted. The modelled curves are represented with solid lines. The mosaic for the (004) of $\alpha - USi_2$ was calculated to be $3.75 \pm 0.01°$, with the FWHM of Cu calculated to be $3.26 \pm 0.03°$, and MgO calculated as $0.099 \pm 0.001°$. From this, it is clear that the crystalline quality of the U-Si phase is limited by the mosaic of the intermediate Cu layer.

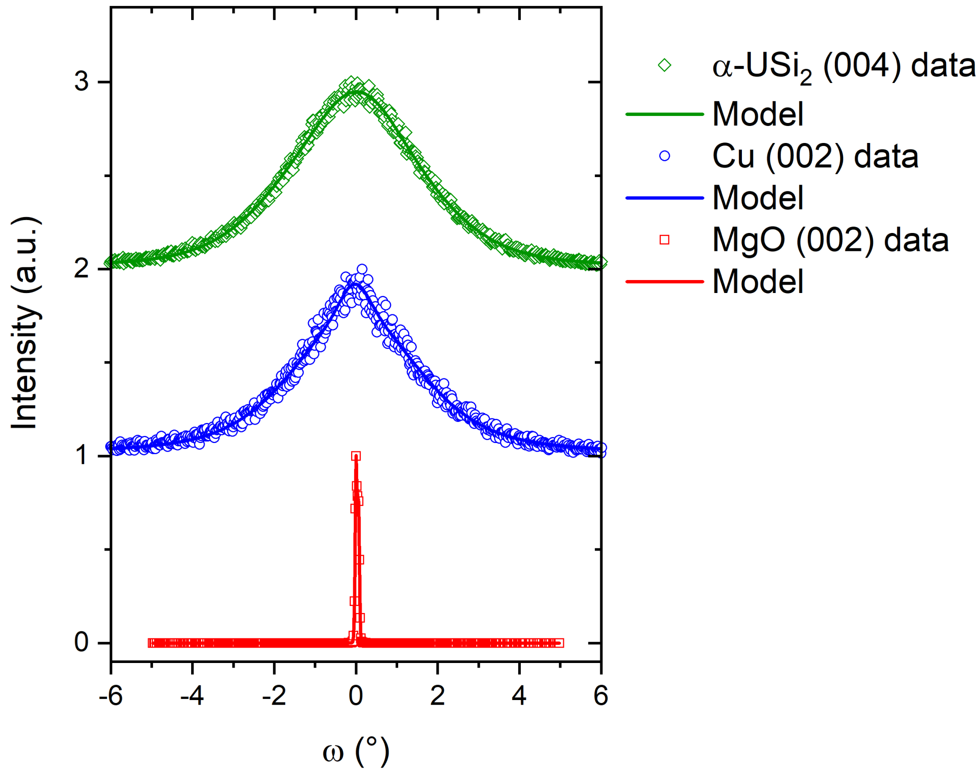

FIGURE 5.11. Omega scan from the (004) Bragg reflection of α-USi_2, the (002) of Cu, and the (002) of MgO. Open circles indicate data points and solid line shows the fit in green, blue, and red for α-USi_2, Cu and MgO respectively. Data from SN1379.

Azimuthal scans about the surface normal were conducted on SN1379 in order to confirm the crystal structure of $\alpha - USi_2$ and to further understand the epitaxial match between $\alpha - USi_2$ and Cu. The $\alpha - USi_2$ phase is tetragonal, so (hkl) Miller indices are used for reflection notation. Figure 5.12 indicates the off-specular phi scans from the (113) of the cubic MgO substrate, the (113) of the intermediate cubic Cu buffer layer, and the (3110) of the tetragonal $\alpha - USi_2$ film.

For bulk tetragonal $\alpha - USi_2$ single crystals, where a = b ≠ c, one would expect 8 reflections to be obtained from the (3110) reflection in a 360° rotation. Figure 5.12 indicates that there are a total of 4 reflections of the (3110) in 180°, indicating that the single crystal of $\alpha - USi_2$ is single domain. The epitaxial match between [001] oriented MgO and Cu is also shown in Figure 5.12, with the (113) reflections from both single crystals having a phi separation of $\Delta\phi = 0°$. This epitaxial match is a square on square match, as previously stated by *Purswani et al.,* [160]. The match between the intermediate Cu layer and the USi_2 film is slightly more complex due to the

presence of the two families of reflections in the (3110). This reflection has both {310} and {130} types. In Figure 5.12, we can see that there are two periodicities within the $0-180°$ ϕ range, which relate to the two families. The smaller periodicity is 36.8° apart which represents the {130} family. The larger periodicity represents the rotational difference between the {310} and {130} families. The difference, $\Delta\phi$, between the {310} peaks is roughly 143.2°.

The 2θ positions from specular and off-specular data sets were used to calculate the lattice parameters of the $\alpha-USi_2$ film. These calculations allowed for further confirmation that the disilicide phase stabilised was tetragonal $\alpha-USi_2$, where a = b ≠ c. Using the specular (004) and off-specular (3110) 2θ positions for $\alpha-USi_2$ the 'a' and 'c' lattice constants were calculated to be 3.96 ± 0.04Å and 13.977 ± 0.003Å, respectively. The unit cell for $\alpha-USi_2$ was calculated to be 219.02 ± 4.08Å^3. This was replicated for the intermediate Cu layer using the specular (002) and off-specular (113) reflections. Using the equation for cubic systems(Eqn. 5.3),

$$d^2 = \frac{a^2}{h^2+k^2+l^2} \tag{5.3}$$

the lattice parameter for Cu was calculated to be 3.6 ± 0.1Å. The unit cell for Cu was then calculated to be 46.82 ± 1.42Å^3.

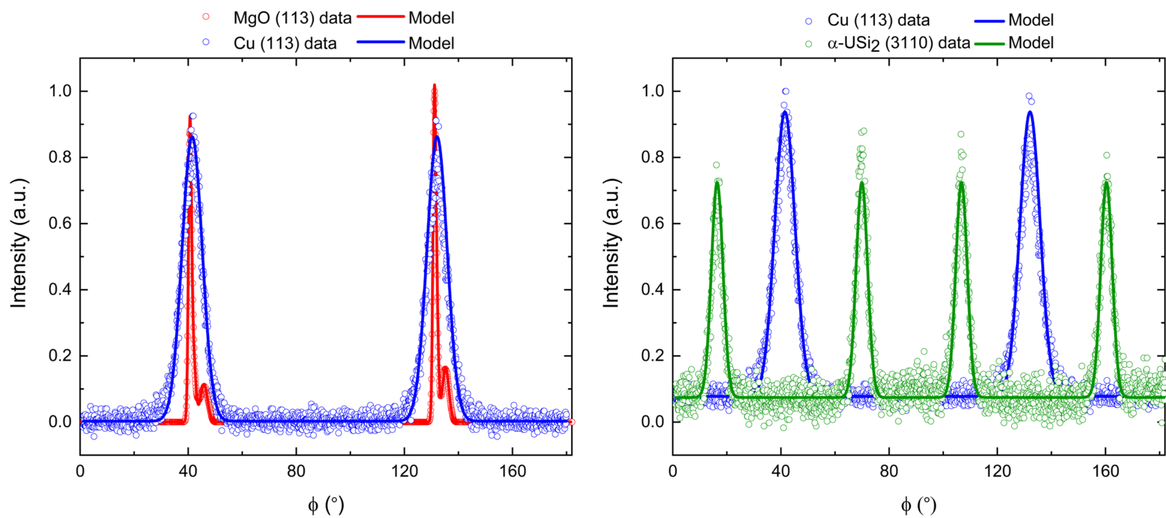

FIGURE 5.12. Off-specular phi data collected from the (3110) of $\alpha-USi_2$, and the (113) of both Cu and MgO. Open circles indicate data points and solid line shows the fit. Data from Cu and MgO shown on the left, Cu and $\alpha-USi_2$ overlayed on the right. Data from SN1379.

5.2.4.2 CaF_2Stabilisation

The $\alpha - USi_2$ phase was also stabilised directly onto [001] oriented CaF_2. This phase was deposited onto the substrate at 800°C. The particular sample presented here, SN1645, was not capped with a protective Nb layer as it was used as part of the oxidation and corrosion studies for this thesis (Chapters 6 and 7). Figure 5.13 indicates the high angle diffraction data collected from SN1645. The specular (004) Bragg reflection of $\alpha - USi_2$ is denoted with a green drop line, with the specular (002) CaF_2 Bragg reflection shown with a purple drop line. There are two unidentified reflections at 2θ positions of 36.66° and 37.89°. The (111) of aluminium is also present within the diffraction data. This is denoted with a black drop line. The presence of aluminium is attributed to the sample stage of the diffractometer, which has been detected due to the geometry of the sample.

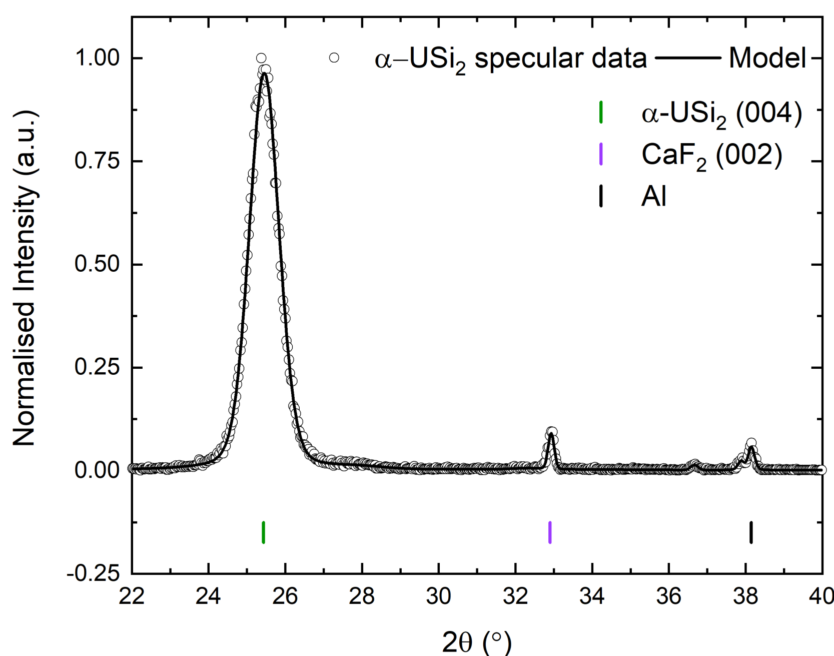

FIGURE 5.13. High angle diffraction data from a single crystal of $\alpha - USi_2$ deposited on [001] oriented CaF_2. Green, purple, and black drop lines represent $\alpha - USi_2$, CaF_2, and Al, respectively. Data from SN1645.

The mosaic of the film and substrate were investigated through conducting omega scans on the specular Bragg reflection of each phase. For SN1645, the (004) of $\alpha - USi_2$ and the (002) of CaF_2 were probed. Figure 5.14 indicates the two rocking curves for each phase and how they differ as a function of ω. The FWHM of each rocking curve provides an indication of the crystallinity of

the phase. Each rocking curve was modelled using a psuedo-voigt. These values were modelled to be 1.53 ± 0.01° for $\alpha - USi_2$, and 0.085 ± 0.001° for CaF_2.

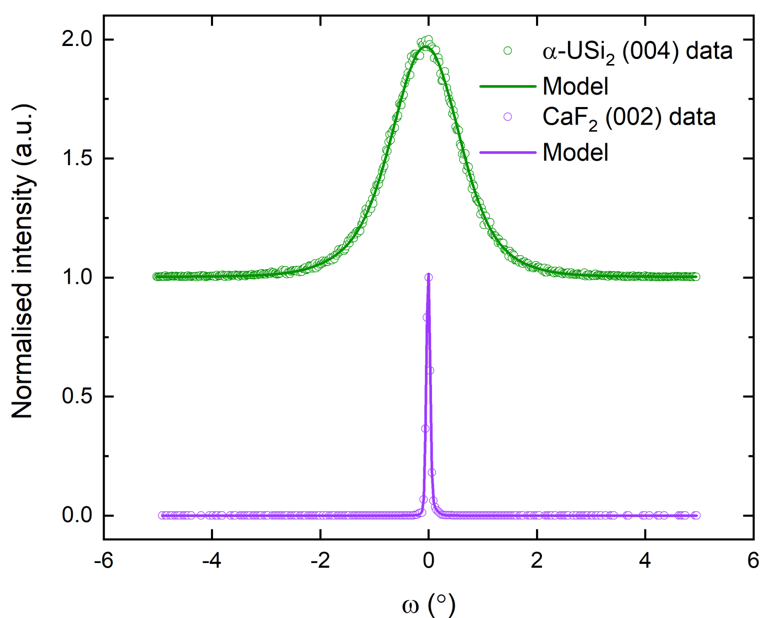

FIGURE 5.14. Omega data of the (004) of $\alpha - USi_2$ and the (002) of CaF_2. Data shown with open circles, with solid lines representing the model. Data from SN1645.

Much like the analysis conducted on SN1379 for MgO stabilisation, it was important to also confirm the phase of USi_2 and to understand the epitaxial match between $\alpha - USi_2$ and CaF_2 for SN1645. Off-specular scans were conducted on the (3110) of $\alpha - USi_2$ and the (135) of CaF_2. Figure 5.15 indicates the off-specular phi data from both of these reflections in a 0° − 180° phi range. From the phi data in Figure 5.15, there are a total of 4 reflections for the (3110) reflection, indicating that this crystal of $\alpha - USi_2$ is single domain, much like the crystal deposited on the Cu/MgO system.

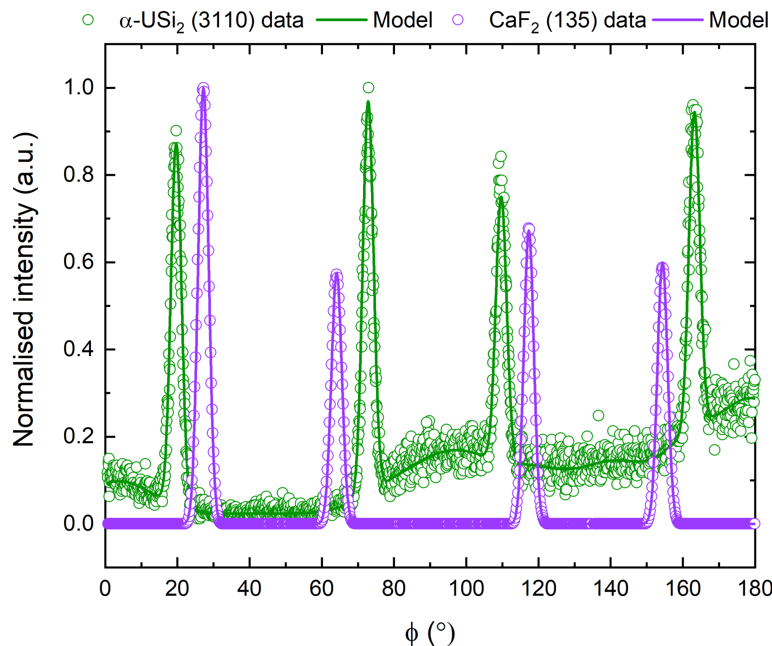

FIGURE 5.15. Off-specular phi data (open circles) collected from the (3110) of $\alpha-USi2$ and the (135) of CaF_2. Model shown with solid green and purple lines for $\alpha-USi_2$ and CaF_2, respectively. Data from SN1645.

To confirm the phase of USi_2, the off-specular 2θ positions were observed to calculated the lattice parameters. This sample of USi_2 was treated as tetragonal, much like SN1379. Therefore, the lattice parameters are so that a = b ≠ c. From the specular (004) reflection, the 'c' lattice parameter was calculated to be 13.98 ± 0.01Å. The (3110) reflection was used to find the 'a' lattice parameter, which was calculated as 3.930(2) ± 0.003Å. This resulted in a/c = 0.28. The unit cell of $\alpha-USi_2$ in SN1645 was calculated to be 215.98 ± 0.33Å^3. These calculations confirmed that the phase stabilised on CaF_2 was single crystal tetragonal $\alpha-USi_2$. The epitaxial match between tetragonal $\alpha-USi_2$ and cubic CaF_2 is shown in Figure 5.16. This figure indicates the two unit cells, with the CaF_2 unit cell rotated 45°. The [001] direction is facing perpendicular to the screen, indicating the specular direction of both crystals.

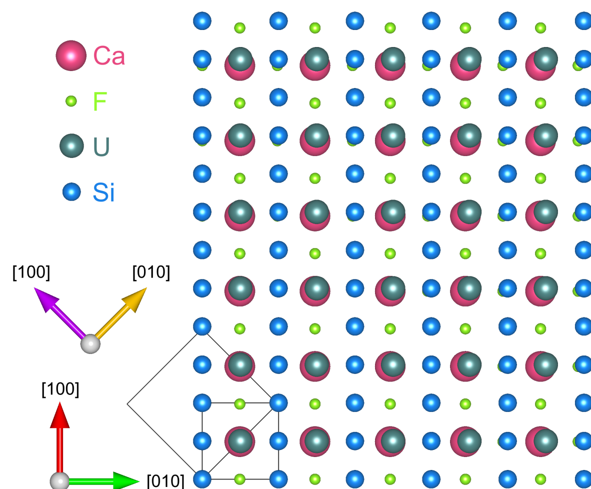

FIGURE 5.16. The epitaxial match between $\alpha - USi_2$ and CaF_2 unit cells, with the unit cell of CaF_2 rotated 45°. The (001) direction of both crystals is facing out of the page. Figure made using Vesta [162].

5.2.5 Epitaxial USi_3 Thin Films

Cubic uranium trisilicide was stabilised directly onto [001] oriented CaF_2 at 800 °C as a single crystal. The USi_3 phase was stabilised with the (001) in the specular direction. The film was capped with Nb, which was deposited at room temperature. This capping layer prevented surface contamination and the formation of surface oxides. Figure 5.17 shows the high angle x-ray diffraction data obtained from SN1699, a single crystal of USi_3. The specular (001) and (002) Bragg reflections of USi_2 are present within the sample, alongside the less intense (110) at $2\theta = 31.13°$. Blue, black, and purple drop lines indicate the reflections from USi_3, Nb, and CaF_2, respectively.

To further understand the crystallinity of the sample, omega scans were conducted on the (001) and (002) Bragg reflections of USi_3 and CaF_2, respectively. This data is presented in Figure 5.18. Here, breadth of the peak, or FWHM, provide information about the mosaic of each phase. These values were modelled in GenX, and were found to be: $1.23 \pm 0.01°$ for USi_3 and $0.054 \pm 0.001°$ for CaF_2.

Due to the presence of multiple USi_3 Bragg reflections within the high-angle diffraction data (Figure 5.17), the potential single crystal nature of SN1699 was probed further using off-specular phi scans. Figure 5.19 indicates the off-specular data acquired from the (113) and (115) reflections of USi_3 and CaF_2. Figure 5.19 indicates 4 total peaks for the cubic CaF_2 (115) reflection. If one was able to access all peaks for this reflection, there would be a total of 8 peaks in a $0-360°$ ϕ range, however, due to the restrictive geometry of the laboratory source, only 4 of these peaks are accessible, making the remaining degenerate. This is similar to the cubic USi_3 (113) reflection,

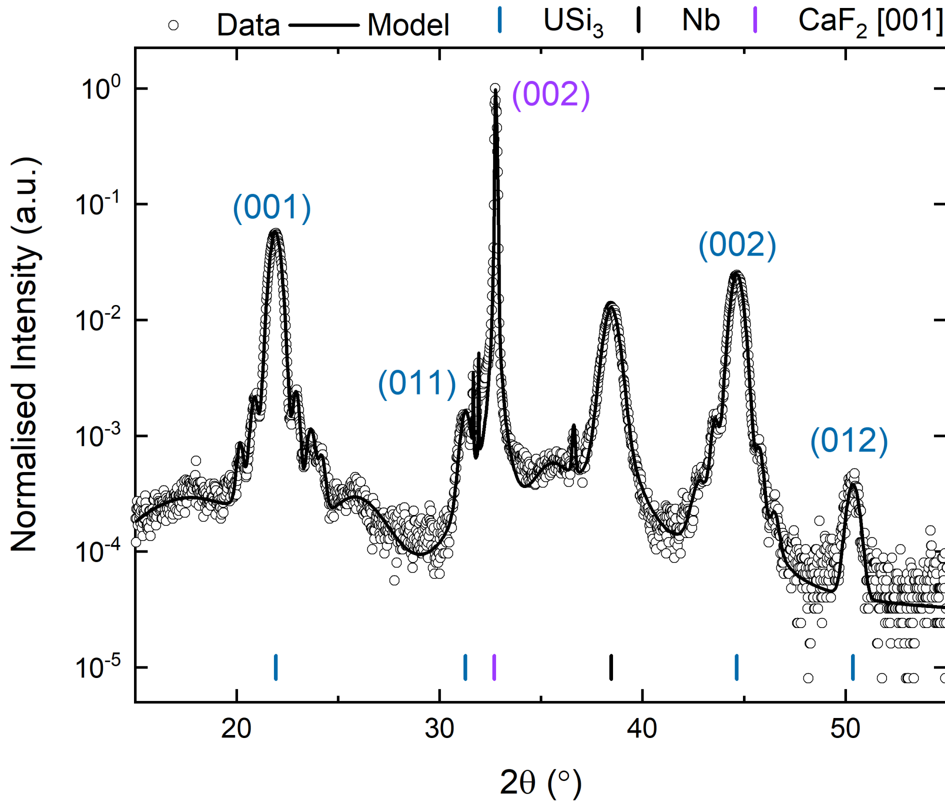

FIGURE 5.17. Figure of the high angle diffraction data obtained from single crystal USi_3 deposited on [001] oriented CaF_2. USi_3 film capped with Nb. Data indicated with open circles, with the model presented as a solid line. Bragg reflections are indicated with blue, black, and purple drop lines representing USi_3, Nb, and CaF_2, respectively. Data from SN1699.

where only 4 reflections are accessible, as shown in Figure 5.19. Accessing this reflection for the silicide phase indicates that SN1699 is a single crystal of USi_3 with one domain.

The off-specular phi data from each phase was also used to understand the epitaxial match between the substrate and the film. Figure 5.20 indicates the match between the two single crystals. We can see that there is a 45° rotation between the two cubic crystal faces. This coincides with the $\Delta\phi = 45°$ separation between the (113) and (115) reflections in Figure 5.19.

The lattice parameter of cubic USi_3 was calculated using the specular and off-specular Bragg reflections presented in Figures 5.17 and 5.19. As this phase was treated as cubic, Eqn 5.3 was

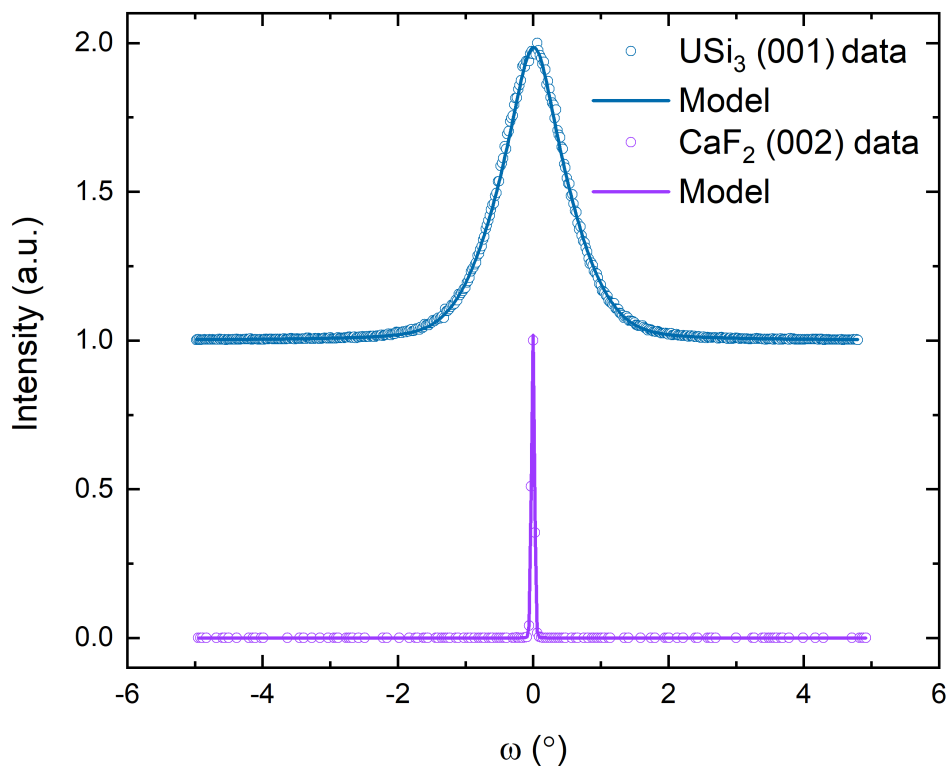

FIGURE 5.18. Omega scans of the (001) and the (002) of USi_3 (blue) and CaF_2 (purple). Data shown as open circles, with the solid line representing the model. Data from SN1699.

used. The lattice parameter, 'a', was calculated to be 4.05 ± 0.01Å. From this, the unit cell of USi_3 was calculated to be 66.54 ± 0.35Å^3.

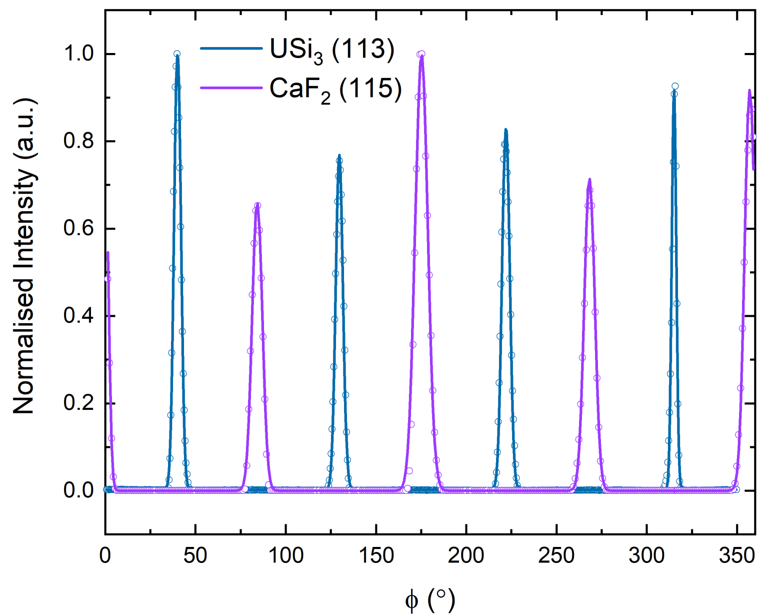

FIGURE 5.19. Off-specular phi data collected from the (113) of USi_3 and the (115) of CaF_2. Data from SN1699.

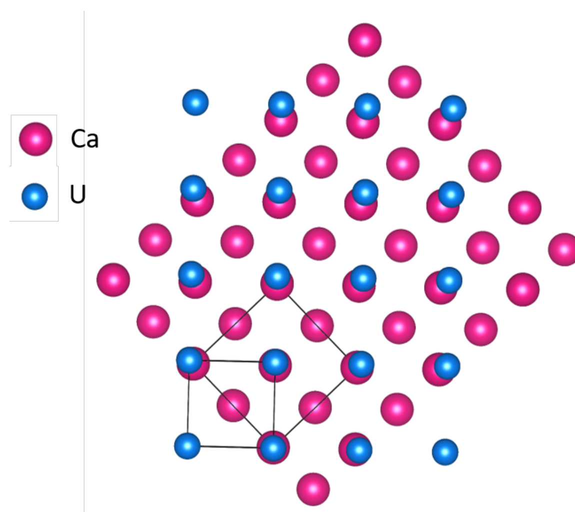

FIGURE 5.20. Diagram showing the epitaxial match between [001] oriented USi_3 and CaF_2 single crystals. Calcium and uranium atoms are depicted with pink and blue spheres. $(00l)$ plane facing out of page. Figure made using Vesta [162].

5.2.6 Discussion of Structural Characterisation

The structural characterisation of uranium silicide phases has shown that through the use of DC magnetron sputtering, a range of silicides that span across the binary phase diagram have been stabilised. The majority of these phases have been epitaxially matched to single crystal substrates, with the exception of U_3Si_2 which formed a polycrystalline sample (SN1639). The stabilisation of these phases has proven that fine tuning the power rating supplied to each target during DC magnetron sputtering has allowed for the phase diagram to be mapped out as a function of uranium content. Figure 5.21 shows the high angle diffraction from each sample presented in Chapter 5, alongside the uranium-silicon phase diagram, provided by *Middleburgh et al.,* [42]. The data and models shown in Figure 5.21 have been cropped to isolate the main region of interest for uranium silicide phases. For each phase presented, the main specular peaks in the data sets are situated within the 2θ range of $20-34°$. The phase diagram has been modified to indicate the relative powers supplied to the uranium target during sample growth. The silicon powers for each sample are detailed in Chapter 4.

The data presented in Figure 5.21, further indicates that the phases USi, and $\beta-USi_2$ have not been stabilised. The presence of these phases were not found in any of the high angle data sets collected for this thesis. There could be a possibility that stoichiometric uranium monosilicide phase, USi, may not exist. Multiple studies report two potential crystal structure for USi: $I4/mmm$ tetragonal, and FeB-type orthorhombic. The latter is thought occur in the presence of oxygen, which alters the atomic arrangement of the former tetragonal structure [165, 166]. The tetragonal USi phase was reported to be hyper-stoichiometric by *Le et al.,* [166]. Efforts made to travel across the phase diagram, within this work, as a function of uranium content, clearly show that neither USi phase was found as a crystalline compound within x-ray diffraction spectra. Furthermore, the phase diagram has been modified to indicate the temperatures in which the phases were stabilised. All phases grown on CaF_2 were stabilised at 800 °C. Sample SN1379 was stabilised at 500 °C and was epitaxially matched to MgO. This sample has been excluded from Figure 5.21 because the sample was grown using a different target configuration and gun system, this is indicated by the low relative uranium deposition power used. The specifications for SN1379 can be found in Chapter 4.

The data collected from SN1639, which is indicated with red lines in Figure 5.21, is referred to in this work as U_3Si_2. However, it is clear from the diffraction spectra, that the inclusion of the (002) Bragg reflection from U_3Si, suggests that this sample (SN1639), should technically be referred to as 'U_3Si + U_3Si_2', due to the presence of the uranium-rich U-Si phase. The annotation on the phase diagram in Figure 5.21, situates this sample, grown with a nominal uranium deposition of 30 W, at the mixed-phase position, and not at the stoichiometric U_3Si_2 position. Despite the mixing of the two phases within SN1639, the sample will continue to be referred to

as U_3Si_2 for the duration of this thesis, and therefore will maintain consistency for the reader.

From Figure 5.21, it can also be noted that both SN1512 and SN1645 were grown using the same uranium deposition power. This discrepancy between the two samples, ultimately forming two different phases, can be linked to the lack of Nb capping layer for SN1645, and will be explored further in Chapter 6, where the oxidation of uranium silicide phases will be discussed. The successful engineering of the phases presented here could indicate that the stabilisation of additional uranium silicide phases could be achieved through further fine tuning of the both the silicon and uranium deposition powers. The stabilisation of these compounds as single crystal thin films is significant. The ability to isolate phases of uranium silicide with reduced activity, has allowed for the structural characterisation of each phase to be conducted. Isolating phases has also provided a foundation on which single parameter studies can be conducted on individual uranium silicides. Furthermore, the unique crystallographic direction of each sample presented here provides a directional dependance for each investigation conducted. This provides a deeper understanding of each phase studied.

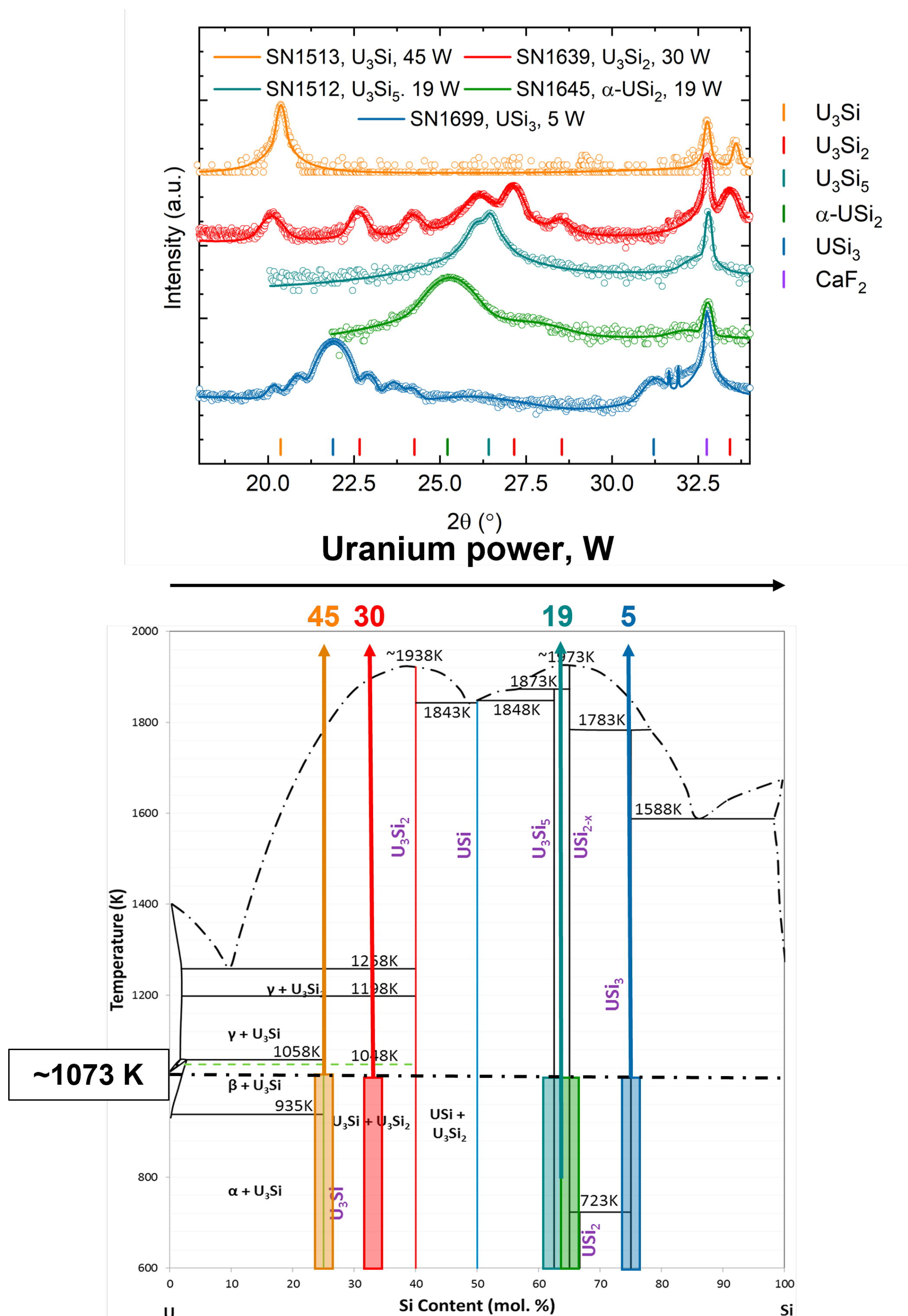

FIGURE 5.21. Diagram showing isolated high angle data from uranium silicide phases presented in Chapter 5, alongside the uranium-silicon binary phase diagram provided by [42]. Phase diagram has been labelled to indicate the relative uranium powers used to produce each sample. U_3Si is indicated with orange, U_3Si_2 with red, U_3Si_5 with teal, $\alpha-USi_2$ with green, and USi_3 with blue.

Structural x-ray diffraction investigations of U_3Si deposited on [001] CaF_2 has shown to be a single crystal with two domains, oriented in the (002) direction. The sample (SN1513) was shown to be tetragonal with lattice parameters of 6.045 ± 0.009Å for a, and 8.71 ± 0.02Å for c, with a/c = 0.694. The unit cell for tetragonal U_3Si was calculated to be 319.12 ± 1.27Å. These values are similar to those found in the literature of 6.033Å for a, and 8.69Å for c, giving a unit cell of 316.29$Å^3$ [46] . The slight differences in the a and c lattice parameters could be attributed to distortions caused by the two domain crystal. The crystal domains and epitaxial matches were investigated through the use of off-specular ϕ scans. Data collected from the (206) of U_3Si and the (224) of CaF_2 indicated that there is a 45° rotation in the [001] direction between the two crystals. Crystal quality was also investigated, with the FWHM of the (002) reflection measured to be 0.782 ± 0.001°.

Through conducting omega scans on the specular reflection of each phase, the single crystal of U_3Si was measured to have the best crystalline quality of all the phases stabilised in this study. The width of the U_3Si ω scan suggests a reasonable registry between the film and the CaF_2 substrate. The quality of each single crystal silicide presented here was also investigated. Where U_3Si was found to have the best registry with the CaF_2 substrate, $\alpha-USi_2$ stabilised on [001] MgO was found to be the broadest, with ω = 3.75 ± 0.01°. Table 5.2 indicates the FWHM of each uranium silicide phase, alongside the mosaic of the corresponding substrate.

Table 5.2: Table of the FWHM values measured for each single crystal uranium silicide phase, alongside the FWHM of the corresponding substrate.

Sample Number	Substrate	Substrate FWHM (°)	Phase	Phase FWHM (°)
SN1513	CaF_2 (002)	0.065 ± 0.001	U_3Si (002)	0.79 ± 0.01
SN1512	CaF_2 (002)	0.052 ± 0.002	U_3Si_5 (100)	1.51 ± 0.02
SN1379	MgO (002)	0.099 ± 0.001	$\alpha-USi_2$ (004)	3.75 ± 0.01
SN1645	CaF_2 (002)	0.085 ± 0.001	$\alpha-USi_2$ (004)	1.53 ± 0.01
SN1699	CaF_2 (002)	0.054 ± 0.001	USi_3 (001)	1.23 ± 0.01

The data in Table 5.2 indicates some variation in the FWHM of the CaF_2 single crystals used to stabilise the uranium silicide phases. However, this does not appear to strongly influence the registry between substrate and film as demonstrated by the FWHM values for each silicide phase. Furthermore, the FWHM measured and modelled for the uncapped $\alpha-USi_2$ deposited on CaF_2 has a significantly better registry with the substrate when compared to $\alpha-USi_2$ stabilised on the MgO/Cu system. This further indicates that the epitaxial match between Cu and MgO is limiting the quality of the deposited $\alpha-USi_2$ crystal.

The lattice parameters of each uranium silicide phase were investigated and compared to

Table 5.3: Table of the lattice parameters and unit cells for each uranium silicide, with reference to literature values.

Sample	Phase	a (Å)	c (Å)	Unit Cell (Å^3)	Ref.	Parameter % Change
SN1513	CaF_2 / U_3Si	6.054 ± 0.009	8.71 ± 0.02	319.12 ± 1.27	This study	a = 0.35 %
Bulk	U_3Si	6.033	8.69	316.29	[46]	c = 0.23 %
						Vol. = 0.90 %
SN1512	CaF_2 / U_3Si_5	3.89 ± 0.01	3.97 ± 0.05	59.74 ± 0.79	This study	a = 1.23 %
Bulk	U_3Si_5	3.843	4.069	60.094	[49]	c = 2.46 %
						Vol. = 0.59 %
SN1379	MgO / $\alpha-USi_2$	3.96 ± 0.04	13.977 ± 0.003	219.02 ± 4.08	This study	a = 0.96 %
						c = 1.26 %
						Vol. = 0.60 %
SN1645	CaF_2 / $\alpha-USi_2$	3.930 ± 0.003	13.98 ± 0.01	215.98 ± 0.33	This study	a = 0.20 %
						c = 1.24 %
Bulk	$\alpha-USi_2$	3.922	14.154	217.718	[50]	Vol. = 0.80 %
SN1699	CaF_2 / USi_3	4.05 ± 0.01	-	66.54 ± 0.35	This study	a = 0.25 %
Bulk	USi_3	4.06	-	66.92	[51]	Vol. = 0.55 %

literature values. The measured values from each film can be found in Table 5.3, with the a, c, and unit cell values calculated for each sample. The calculated values for this study are also compared to parameters found in the literature. The calculated 'a' lattice parameters align well with the literature values, with the calculated 'c' parameters having slightly more variation. The sample with the largest percentage difference is SN1512, where the 'a' and 'c' lattice parameters vary by 1.23 % and 2.46 %, respectively. This is reflected further in the calculated unit cells for each uranium silicide phase. However, the percentage difference between the calculated and literature lattice parameters are all ≤ 1%. The most significant is the difference between the U_3Si unit cells, with a unit cell increase of 0.89 %. The small variation between the thin film samples and bulk literature values suggest that minimal distortion has been inflicted on the sample presented here. Indicating that stabilising uranium silicide phases is an appropriate method for investigating nuclear fuels.

5.2.7 Conclusions

This section has provided structural analysis of uranium silicide thin film samples grown via DC magnetron sputtering. Through the use of x-ray diffraction, it has been shown that the fine tuning of relative deposition powers supplied to separate uranium and silicon targets allows for the binary phase diagram of uranium and silicon to be mapped as a function of uranium power. This in turn, has allowed for four major uranium silicide line compounds to be stabilised as single crystal thin films. These phases include: U_3Si, U_3Si_5, $\alpha-USi_2$, and USi_3. Triuranium disilicide, U_3Si_2 was stabilised as a polycrystalline sample (SN1639), that had inclusions of U_3Si and U_3Si_5. Crystallite size analysis was conducted on the high-angle diffraction data obtained from SN1639.

Using the Scherrer equation, it was found that the crystallites were of the order of 1 nm.

U_3Si films deposited on [001] oriented CaF_2 substrates were found to be single crystal, oriented in the [001] direction. When compared to the remaining phases, U_3Si was found to have the narrowest rocking curve, indicating a good registry with the substrate. Through off-specular phi scans, the crystal was found to have two domains, with the strongest domain rotated 45°. The lattice parameters of epitaxial U_3Si were calculated to be 6.054 ± 0.009 Å for a, and 8.71 ± 0.02 Å for c, resulting in a 0.35 % and 0.23 % difference when compared to the values provided by *Kimmel et al.,* [46].

The remaining phases were also stabilised on [001] oriented CaF_2 substrates at 800 °C. U_3Si_5 was stabilised in the [100] direction, and through off-specular phi scans, was found to exhibit two domains. The lattice parameters for U_3Si_5 had the largest deviation from literature values, with 'a' being 1.22 % larger, and 'c' being 2.46 % smaller than the values provided by *Brown et al.,* [49]. Uranium disilicide was stabilised in the α phase on both [001] MgO and [001] CaF_2. This phase was epitaxially stabilised on each substrate at 800 °C and 500 °C, respectively. In both cases, the $\alpha - USi_2$ crystal was found to be single domain. The stabilisation of $\alpha - USi_2$ on MgO was found to have a significantly broader rocking curve of 3.75 ± 0.01°, compared to the CaF_2 stabilised film which had a rocking curve of 1.53 ± 0.01°. This large variation was attributed to the epitaxial match between [001] MgO and the [001] Cu buffer layer, where it was concluded that the registry between MgO and Cu was limiting the quality of the $\alpha - USi_2$ crystal. The stabilisation of $\alpha - USi_2$ on CaF_2 only occurred without a capping layer. With the surface exposed to atmosphere, this indicates that the $\alpha - USi_2$ phase was partially oxidised. This will be investigated further in Chapter 6.

Finally, uranium trisilicide was stabilised in the [001] direction on CaF_2. This compound was stabilised in the cubic phase and was found to have one single crystain domain through off-specular phi investigations. USi_3 was to have a 0.25 % decrease in the lattice parameter, when compared to values obtained from *Brixner et al.,* [51], resulting in a slightly compressed unit cell of 66.541 ± 0.003 Å^3. The registry between the film and substrate was adequate, with a measured FWHM of 1.23 ± 0.01° for USi_3.

The results presented here show that single crystal epitaxial U_3Si, U_3Si_5, $\alpha - USi_2$, and USi_3 have been stabilised through the use of DC magnetron sputtering. The samples presented here are the first of their kind, and in some cases, are the first single crystals of uranium silicide phases. The use of these novel samples will allow for a range of experiments to be conducted on uranium silicide phases.

5.3 The Stoichiometry and Chemical Bonding of U-Si Phases

The uranium silicide phases presented in Section 5.2 have been characterised chemically using x-ray photoelectron spectroscopy (XPS) at the NanoESCA Facility based at the University of Bristol. This surface sensitive technique has allowed for the chemical bonding and stoichiometry of each uranium silicide phase to be probed as a function of uranium content. The experiments presented here allow for the structural characterisation presented in Section 5.2 to be confirmed, and for a deeper understanding of the bonding environment present in each uranium silicide phase.

This section will compare the bonding environments by investigating data collected from the U-4f, Si-2s, O-1s, C-1s, and the valence band. Data collected from an overall survey will also be presented. This will allow for the uranium silicide phases to be compared for each spectra observed. The samples investigated in this section are SN1513, SN1639, SN1512, SN1379, and SN1699. All of these samples were capped with either Nb or Cu protective layers, preventing unwanted changes to the surface. The preserved nature of these films allows each phase to be characterised without the influence of chemical bonding changes which could occur as a result of surface oxidation. For this reason, SN1645, uncapped $\alpha - USi_2$ stabilised on CaF_2, has been omitted from this section.

5.4 Chemical Characterisation Results

Data was acquired from the survey of each uranium silicide investigated, using a pass energy of 50 eV. These data sets were collected once Nb and Cu capping layers were removed from the sample surfaces. Figure 5.22 indicates the survey spectra obtained from each sample, all with an inset of the raw data obtained from the U-4f spectra. From the spectra in Figure 5.22, it can be seen that all samples exhibit signal from uranium, silicon, and their corresponding substrates. For phases deposited on CaF_2, the Ca LMM edge is present, alongside the F-1s. For SN1699 (Figure 5.22 **(e)**) the F KLL edge is also visible. This feature is due to the overall thickness of the sample, indicating that the sample thickness is less than the remaining uranium silicide samples. SN1379 (Figure 5.22 **(d)**) was deposited on (001) MgO, with a (001) Cu buffer and polycrystal Cu capping layer. This is represented in the figure, with signal stemming from the Mg-1s, Cu-2p, Cu-3p, and the Cu LMM edge.

Each survey presented in Figure 5.22 is accompanied by an inset figure of the U-4f spectra collected from the same sample. Each of these U-4f spectra exhibit asymmetry in the peak shape, indicating a metallic system, as described in Chapter 3. The metallic components collected from U_3Si and U_3Si_5 are more pronounced when compared to the remaining spectra in the figure.

The U-4f peaks are also accompanied by a more symmetric peak at a higher binding energy, indicating the presence of metal-oxide bonding in the uranium state. This oxide contribution is more apparent in Figure 5.22 **d**. Data collected from USi_3 (SN1699), indicated in Figure 5.22 **e**, has a lower binding energy shoulder that sits below the asymmetric U-4f state. This peak positioning, is influenced by the Nb cap deposited on SN1699, and will be discussed further when presenting the analysed data from the U-4f spectra.

Data collected from the U-4f spectra of each uranium silicide phase presented in this chapter is shown in Figure 5.23. These data sets were collected using a pass energy of PE = 6 eV, and were modelled using CasaXPS [167]. Here, the U-4f$_{7/2}$ is presented, and the U-4f$_{5/2}$ has been omitted from the figure. The differences in the U-4f$_{7/2}$ states of each uranium silicide phase can be noted in this figure. Here, the components used to model the data are indicated with open shapes, with the data points as open grey circles, and the Shirley background indicated with crosses. Total fits for each phase are shown in orange, red, teal, green, and blue for U_3Si, U_3Si_2, U_3Si_5, $\alpha - USi_2$, and USi_3, respectively.

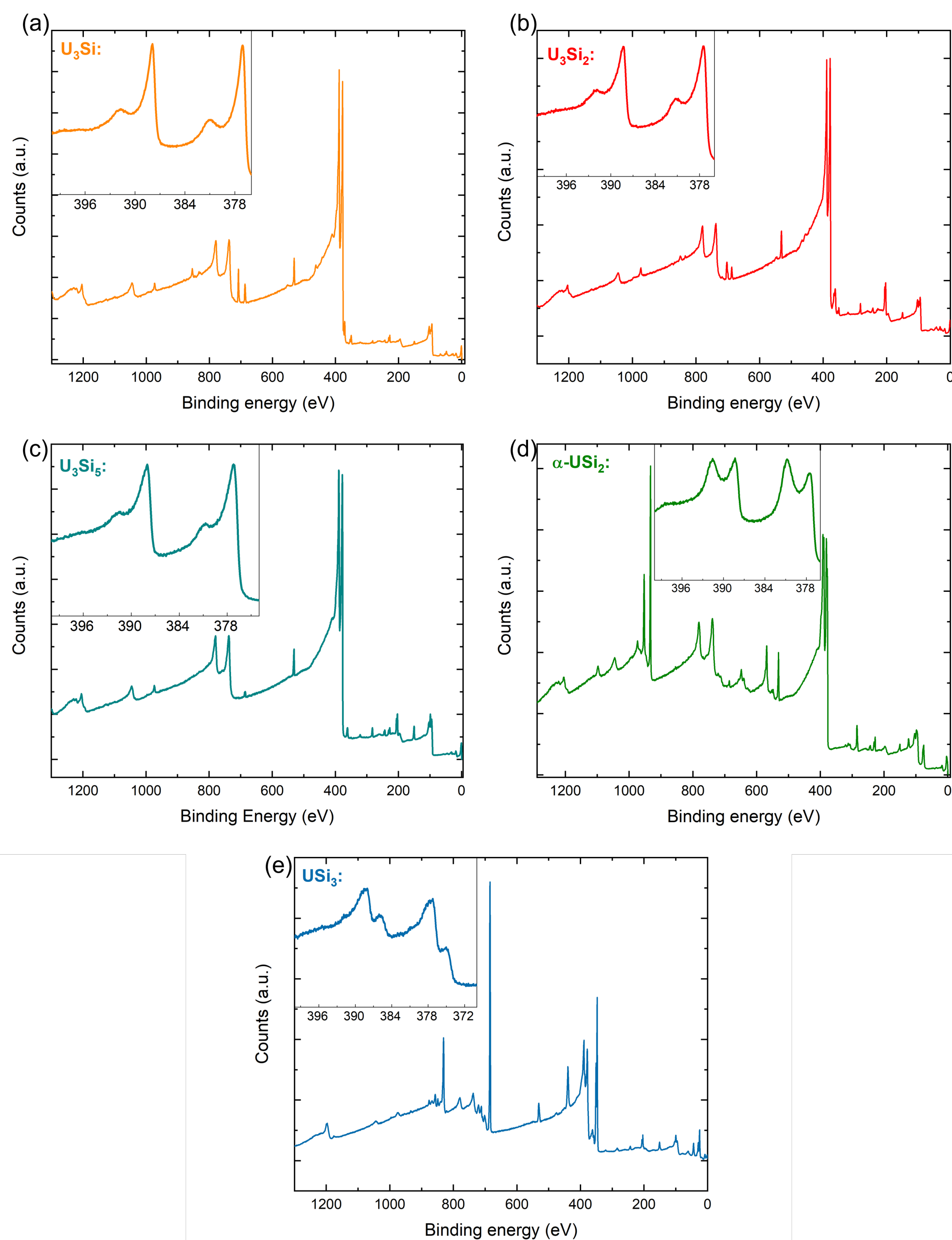

FIGURE 5.22. XPS survey scans of the **(a)** SN1513 - (001) U_3Si on CaF_2, **(b)** SN1639 - Poly-crystalline U_3Si_2 on CaF_2, **(c)** SN1512 - (100) U_3Si_5 on CaF_2, **(d)** SN1379 - (001) $\alpha-USi_2$ on MgO, **(e)** SN1699 - (001) USi_3 on CaF_2. All survey scans include an inset of the U-4f spectra obtained from that sample.

Table 5.4: Table of parameters used to fit the U-4f spectra for uranium silicide phases. T represents the asymmetric tail function applied to the metallic components of each U-4f spectra.

Sample	Peak	Position (eV)	Satellite separation (eV)	FWHM (eV)	%GL	T
U_3Si	U-4$f_{7/2}$ metal	377.31	-	0.77	15	0.5
	U-4$f_{7/2}$ oxide	381.23	2.73	2.5	30	-
	Oxide satellite	383.96	-	2.5	60	-
U_3Si_2	U-4$f_{7/2}$ metal	377.43	-	0.81	80	0.4
	U-4$f_{7/2}$ oxide 1	379.28	6.74	2.5	30	-
	U-4$f_{7/2}$ oxide 2	381.23	2.39	2.5	30	-
	Oxide satellite 1	383.62	-	2.5	20	-
	Oxide satellite 2	386.02	-	1.16	30	-
U_3Si_5	U-4$f_{7/2}$ metal	377.39	-	0.92	70	0.5
	U-4$f_{7/2}$ oxide	381.08	2.51	2.5	30	-
	Oxide satellite	383.59	-	1.84	60	-
$\alpha-USi_2$	U-4$f_{7/2}$ metal	377.30	-	0.70	80	0.15
	U-4$f_{7/2}$ oxide	380.87	5.48	1.66	80	-
	Oxide satellite	386.35	-	2.5	15	-
USi_3	U-4$f_{7/2}$ metal	377.38	-	1.61	15	0.3
	U-4$f_{7/2}$ oxide	381.01	2.3	2.5	60	-
	Oxide satellite	383.31	-	2.29	30	-

Table 5.4 presents the fitted peak positions, widths, and line-shapes for each component used to model the U-4$f_{7/2}$ spectra presented in Figure 5.23. From the data sets it can be seen that all peaks used to fit the asymmetric peaks, associated with metallic sites, have a binding energy in the range of 377.43 − 377.30 eV. Poly-crystal U_3Si_2 (SN1639) exhibits the highest binding energy for the metallic component, with a position of 377.43 eV. Furthermore, SN1639, poly-crystal U_3Si_2 is the only phase presented here that required two symmetric components, and two corresponding satellite components to model the oxide region of the U-4$f_{7/2}$ state. Additionally, the U-4$f_{7/2}$ of $\alpha-USi_2$ is the most asymmetric when compared to the remaining uranium silicide phases. The peak widths of each phase sit within a range of 0.91 eV, between 0.70 − 1.61 eV. $\alpha-USi_2$, when compared to the remaining phases, has the most narrow FWHM of 0.70 eV. Uranium trisilicide, USi_3, has the broadest metallic peak, with a FWHM of 1.61 eV. The broadening in this metallic peak could indicate changes in the bonding states, which may be influenced by the oxidised Nb-3p state situated to the right of the metallic U-4f. This feature is also noted in the survey spectra of SN1699, found in Figure 5.22 **(e)**.

The positioning of oxide and satellite components presented in each of the U-4f spectra have been monitored, with the intention to assign valence states to each oxide peak. The satellite energy separation from main oxide components are presented in Table 5.4. Following the uranium oxide quantification, provided by *Ilton et al.,* [83], valencies can been assigned to poly-crystal U_3Si_2 (SN1639). The satellite difference between the oxide component positioned at 381.23 eV, indicates a U(IV) valency for the oxide. The positioning of the oxide component and the corre-

sponding satellite peak for $\alpha-USi_2$ could indicate either a U(IV)/U(V) valency, however, this is not conclusive. Finally, the remaining phases have oxide and satellite components with peak positions that do not align with the work conducted by *Ilton et al.,* [83], however, this study does not provide the oxide energy position variation for uranium silicide phases. The quantification of the oxidation of uranium silicide will be presented in Chapter 6.

The influence of uranium-oxide bonding can also be seen in the data extracted from the valence band of each uranium silicide phase. Figure 5.24 indicates the valence band structure of the uranium silicide phases studied in this chapter. Each U-Si phase exhibits a strong, asymmetric, peak at the Fermi edge (E_F). The remaining features, situated at higher binding energies, provide an indication of the metal-oxide bonding effects. Shoulder features, to the left of the U-5f component, exist in the valence band structure of U_3Si, U_3Si_2, and U_3Si_5. These features are considerably weaker when compared to the more prominent features in the valence band spectra of $\alpha-USi_2$ and USi_3. The broad peak situated at 2.51 eV is associated with the electrons in the U-5f state being bound to oxygen. This particular bonding is also presented in work conducted by *Van den Berghe et al.,* [168]. If the oxygen content were to increase, the asymmetric peak present in all U-Si valence spectra belonging to the U-5f would disappear from the Fermi edge. Further sub-orbitals contributing to the valence band spectra of the uranium silicide phases also include, Si-3p, O-2p, and the Si-3s, which are situated at binding energies of: 3, 7, and 8 eV, respectively. Bonding between U-O further influences the valence band spectra. This is indicated as broad structures around a binding energy of 5.7 eV.

Table 5.5: Table of parameters used to fit the Si-2s spectra for uranium silicide phases.

Sample	Peak	Position (eV)	Valency	FWHM (eV)	%GL
U_3Si	Si-2s A	150.10	Si^0	1.50	30
	Si-2s B	+2.33	Si^{3+}	2.5	60
U_3Si_2	Si-2s A	150.18	Si^0	1.45	30
	Si-2s B	+1.58	Si^{2+}	2.5	60
	Si-2s C	+3.56	Si^{4+}	2.5	30
U_3Si_5	Si-2s A	150.29	Si^0	1.44	60
	Si-2s B	+1.82	Si^{2+}	2.5	60
	Si-2s C	+4.14	Si^{4+}	2.5	60
$\alpha-USi_2$	Si-2s A	150.24	Si^0	1.48	60
	Si-2s B	+1.72	Si^{2+}	2.5	30
	Si-2s C	+3.63	Si^{4+}	2.5	30
USi_3	Si-2s A	148.19	Si^0	2.03	30
	Si-2s B	+2.39	Si^0	1.68	30
	Si-2s C	+3.84	Si^{3+}	1.39	30
	Si-2s D	+5.18	Si^{4+}	2.5	30

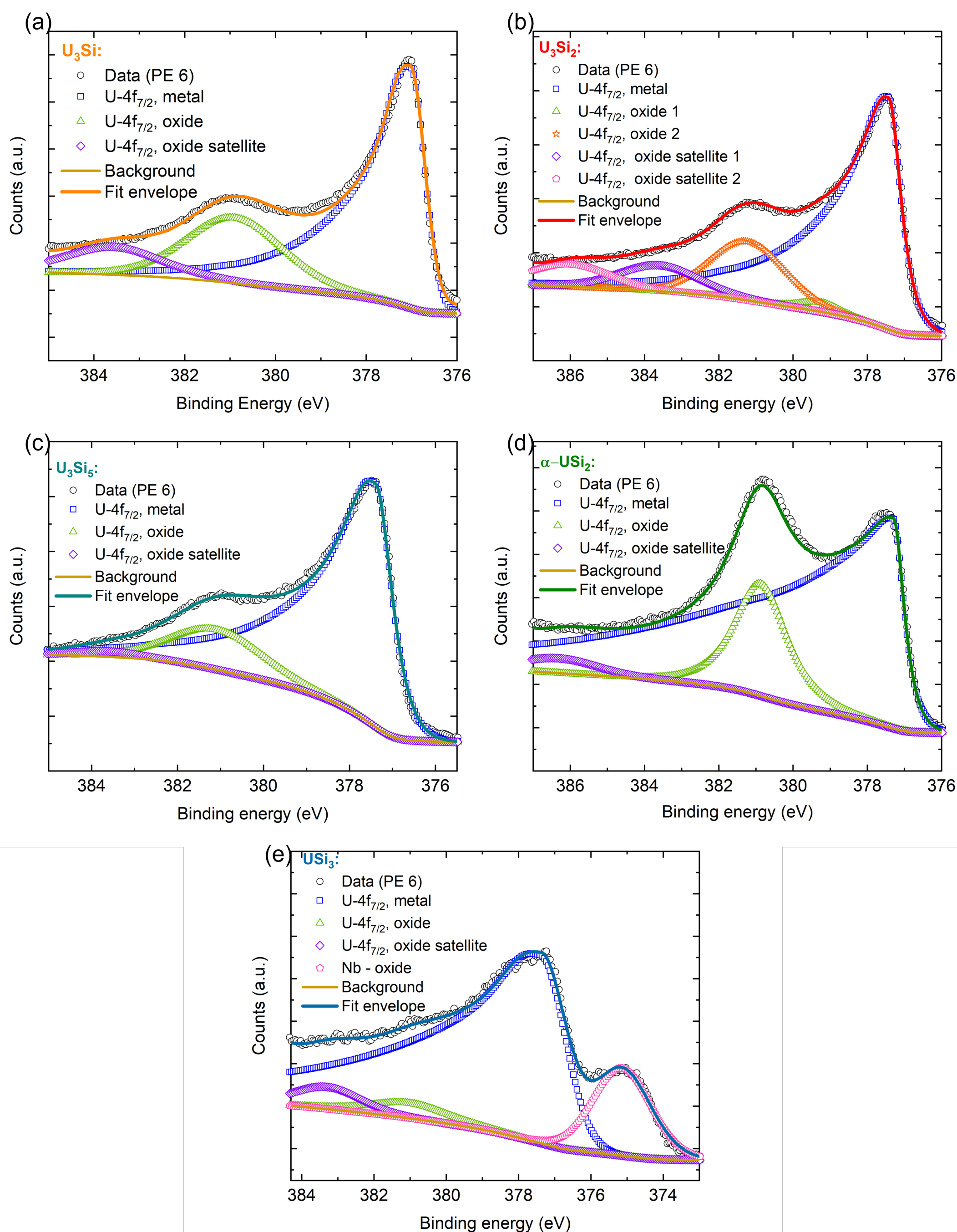

FIGURE 5.23. Modelled XPS U-4f data obtained from the **(a)** SN1513 - (001) U_3Si on CaF_2, **(b)** SN1639 - Poly-crystalline U_3Si_2 on CaF_2, **(c)** SN1512 - (100) U_3Si_5 on CaF_2, **(d)** SN1379 - (001) $\alpha-USi_2$ on MgO, **(e)** SN1699 - (001) USi_3 on CaF_2. Total fits are shown with solid lines, fit components are shown with symbols, and Shirley backgrounds are shown with crosses.

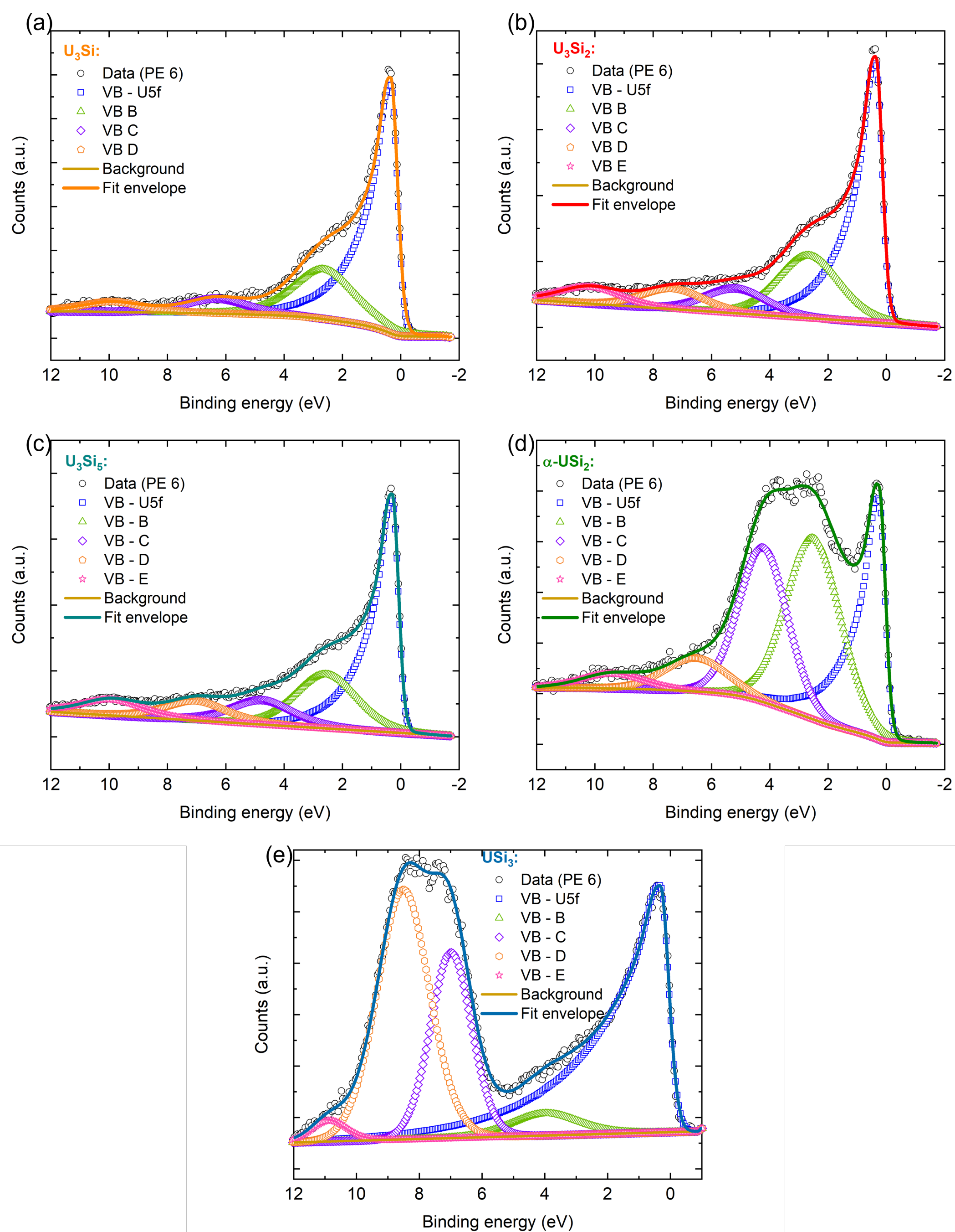

FIGURE 5.24. Modelled XPS valence band data obtained from the **(a)** SN1513 - (001) U_3Si on CaF_2, **(b)** SN1639 - Poly-crystalline U_3Si_2 on CaF_2, **(c)** SN1512 - (100) U_3Si_5 on CaF_2, **(d)** SN1379 - (001) $\alpha-USi_2$ on MgO, **(e)** SN1699 - (001) USi_3 on CaF_2. Total fits are shown with solid lines, fit components are shown with symbols, and backgrounds are shown with crosses.

The Si-2s spectra has been used, combined with the U-4f, to understand the stoichiometry of these uranium silicide phases. The Si-2p was not used to characterise these phases as the overlapping of the Si-2p and the U-5d core level makes extracting peak positions, widths, and areas complex, particularly with the influence of oxygen bonding as noted in the valence band data. Figure 5.25 indicates the spectra collected from each uranium silicide phase. Here, up to four components were used to model the data obtained using a pass energy of 6 eV. A linear function was used to model the background of each spectra, with some of the uranium silicide phases having a more prominent gradient of that background. This is due to the Si-2s occupying a binding energy range that is around 50 eV higher than the overlapping U-5d/Si-2p core levels.

The components used to model each Si-2s indicate the metallic silicon position and the silicon-oxide bonding positions. The latter are indicated by components situated at a higher binding energy. Table 5.5 shows the peak positions of each component used to model the Si-2s data sets. Using this information, much like the U-4f satellite separation, valency states can be assigned to components in order to provide an indication of the bonding and the oxide species that may have formed. From the value presented in Table 5.5, the main component or 'Si-2s A' for each uranium silicide indicates that metallic or crystalline-silicon bonds have formed. The standardised peak position for this type of bonding is situated around 150 eV. Here, we can see that USi_3 has the lowest binding energy of 148.19 eV. Using the comparisons drawn between the Si-2s and Si-2p spectra from *Hollinger et al.,* [169] and *Krummacher et al.,* [57], Si valencies have been assigned to the Si-O bonding peaks in Table 5.5. This provides an indication that a variation of Si-O bonds form within each uranium silicide phase. Furthermore, there is evidence to suggest that SiO_2 is forming as part of the Si^{4+} valence state. The significantly lower binding energy for 'Si-2s A' in the data collected from USi_3 may indicate the formation of an additional Si-metal bond with residue Nb left on the surface of the sample. This component, with peak position of 148.19 eV, is significantly lower when compared to the remaining uranium silicide Si-2s components.

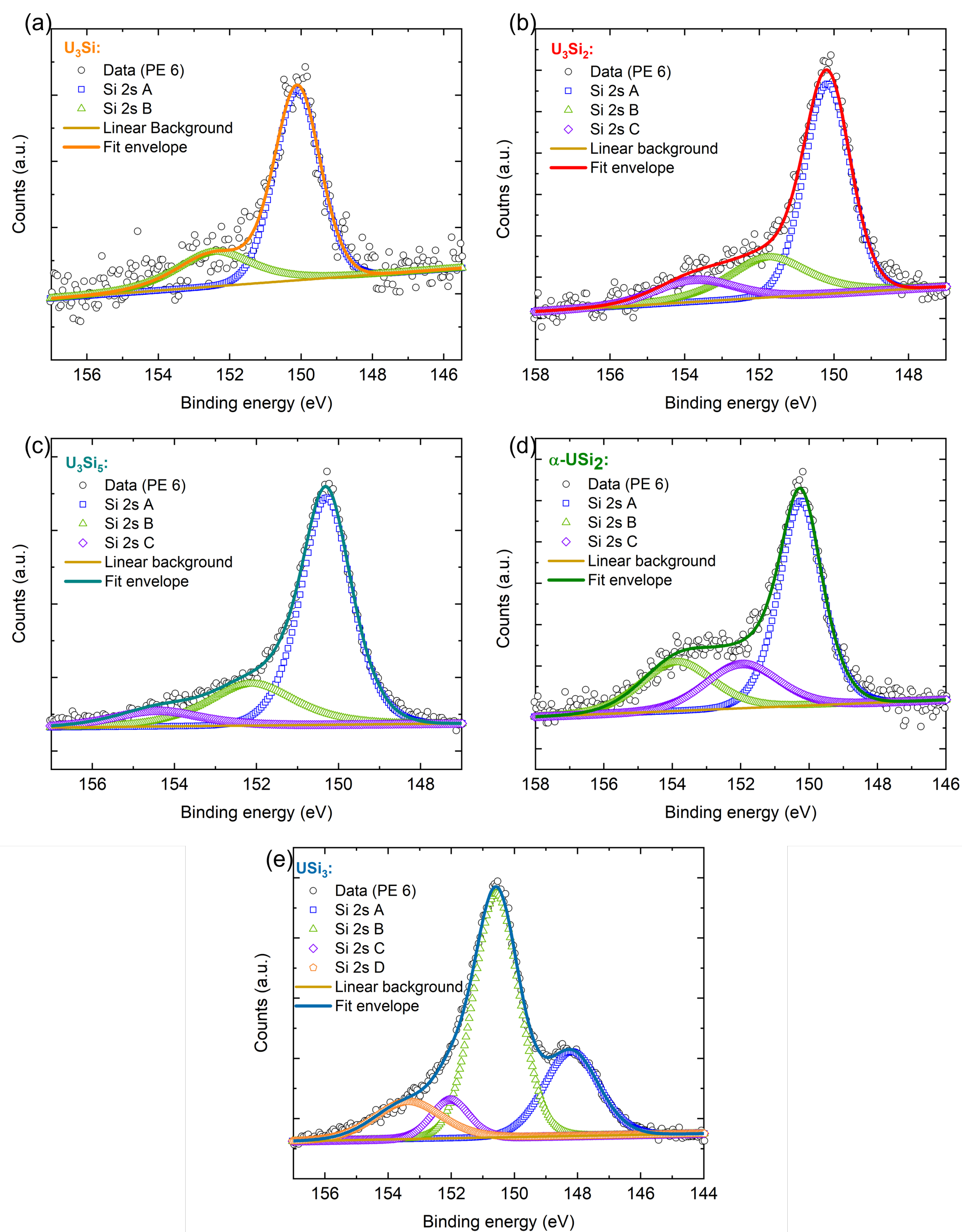

FIGURE 5.25. Modelled XPS Si-2s data obtained from the **(a)** SN1513 - (001) U_3Si on CaF_2, **(b)** SN1639 - Poly-crystalline U_3Si_2 on CaF_2, **(c)** SN1512 - (100) U_3Si_5 on CaF_2, **(d)** SN1379 - (001) $\alpha - USi_2$ on MgO, **(e)** SN1699 - (001) USi_3 on CaF_2. Total fits are shown with solid lines, fit components are shown with symbols, and backgrounds are shown with crosses.

Where the presence of oxygen bonds altered the spectra obtained from the U-4f, Si-2s, and the valence band structure, it was also accepted that the O-1s core level should be investigated. These data sets are presented in Figure 5.26. Each O-1s spectra was fitted with various components, indicated with open shapes, a linear back ground (crosses), with the total fit of the spectra modelled with a solid line. The data presented in Figure 5.26 was also collected using a pass energy of 6 eV.

The peak position of each component used to model the O-1s spectra provides an indication of the type of bonding that may have occurred. For metal-oxide bonds, the peak positions are situated approximately between 528 - 531.2 eV. The peak positions of each O-1s component are presented in Table 5.6. Each of the main components presented in the modelled data sit within this energy range, indicating that bonding has occurred with the metallic components of each sample. This includes the uranium, niobium, and copper layers. The oxidation of the uranium site was previously mirrored in the U-4f spectra for each uranium silicide layer. Components situated approximately between 532.5 - 533.5 eV indicate the presence of SiO_2. The contribution of Si-O bonds was also replicated in the data collected from the Si-2s spectra.

The C-1s spectra was probed to monitor carbon contamination within the samples. Figure 5.27 indicate the data collected from each of the uranium silicide samples. The results, collected using a pass energy of 6 eV, indicate some carbon contamination. All of the phases exhibit intensity in the region of 384 eV, suggesting carbon contamination to the surface or to the bulk of the sample. The component peak positions are presented in Table 5.6. Components with a energy position in the range of 280.5 - 283 eV, suggest the formation of a carbide. This would indicate that all uranium silicide phases presented in Figure 5.27 exhibit a form of carbide contamination. Components situated around 284 eV could indicate the formation of a Si-C bond, suggesting the formation of SiC. Components situated at a binding energy of approximately 287 eV would indicate the formation of C-O bonds. This is apparent in the spectra collected from U_3Si_2, $\alpha-USi_2$, and USi_3. The spectra collected from USi_3 shows the components situated at 280.14 eV and 288.52 eV have a larger influence on the total C-1s spectra, when compared to the remaining uranium silicides. This is contrasting to the C-1s spectra from U_3Si where the data collected is undefined and exhibits a much noisier appearance.

Table 5.6: Table of parameters used to fit the O-1s and C-1s spectra for uranium silicide phases.

Sample	Peak	Position (eV)	FWHM (eV)	%GL
U_3Si	O-1s A	531.06	0.98	80
	O-1s B	532.37	2.33	40
	C-1s A	281.97	1.19	30
	C-1s B	285.42	2.29	60
U_3Si_2	O-1s A	531.07	1.11	60
	O-1s B	532.20	2.46	40
	C-1s A	282.22	0.43	30
	C-1s B	282.70	1.40	30
	C-1s C	285.51	1.85	30
	C-1s D	288.13	2.5	30
U_3Si_5	O-1s A	530.91	1.08	30
	O-1s B	531.70	1.50	40
	O-1s C	532.86	2.5	30
	C-1s A	282.49	1.08	30
	C-1s B	284.86	2.5	70
$\alpha-USi_2$	O-1s A	530.88	1.16	30
	O-1s B	532.02	2.15	30
	O-1s C	534.62	2.5	30
	C-1s A	282.43	1.25	60
	C-1s B	284.73	1.69	30
	C-1s C	286.73	2.5	30
	C-1s D	289.74	2.5	60
USi_3	O-1s A	528.34	1.76	30
	O-1s B	530.69	2.33	30
	O-1s C	533.21	2.46	30
	C-1s A	280.14	1.49	30
	C-1s B	282.94	2.08	30
	C-1s C	285.02	2.5	30
	C-1s D	288.52	2.5	30

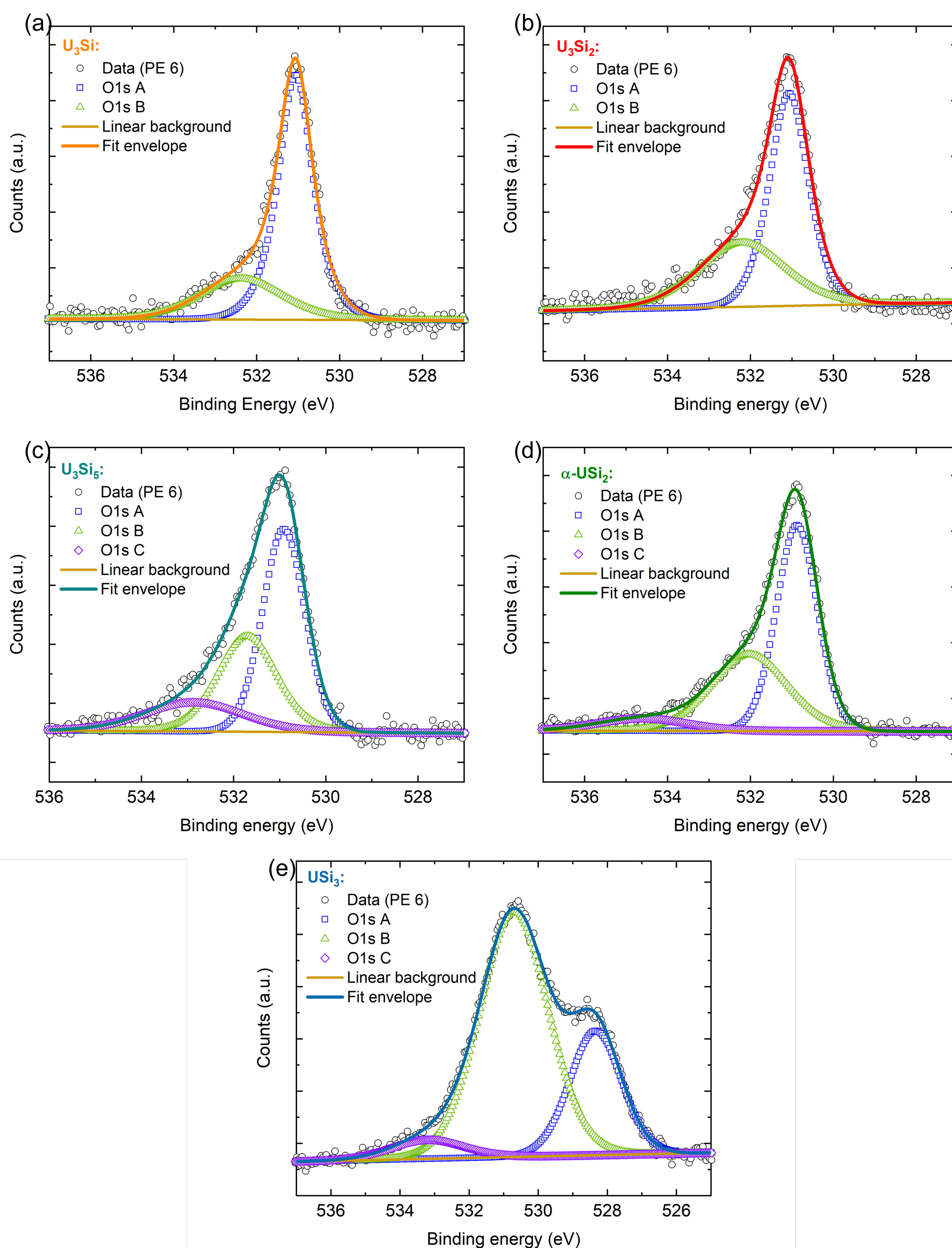

FIGURE 5.26. Modelled XPS O-1s data obtained from the **(a)** SN1513 - (001) U_3Si on CaF_2, **(b)** SN1639 - Poly-crystalline U_3Si_2 on CaF_2, **(c)** SN1512 - (100) U_3Si_5 on CaF_2, **(d)** SN1379 - (001) $\alpha-USi_2$ on MgO, **(e)** SN1699 - (001) USi_3 on CaF_2. Total fits are shown with solid lines, fit components are shown with symbols, and backgrounds are shown with crosses.

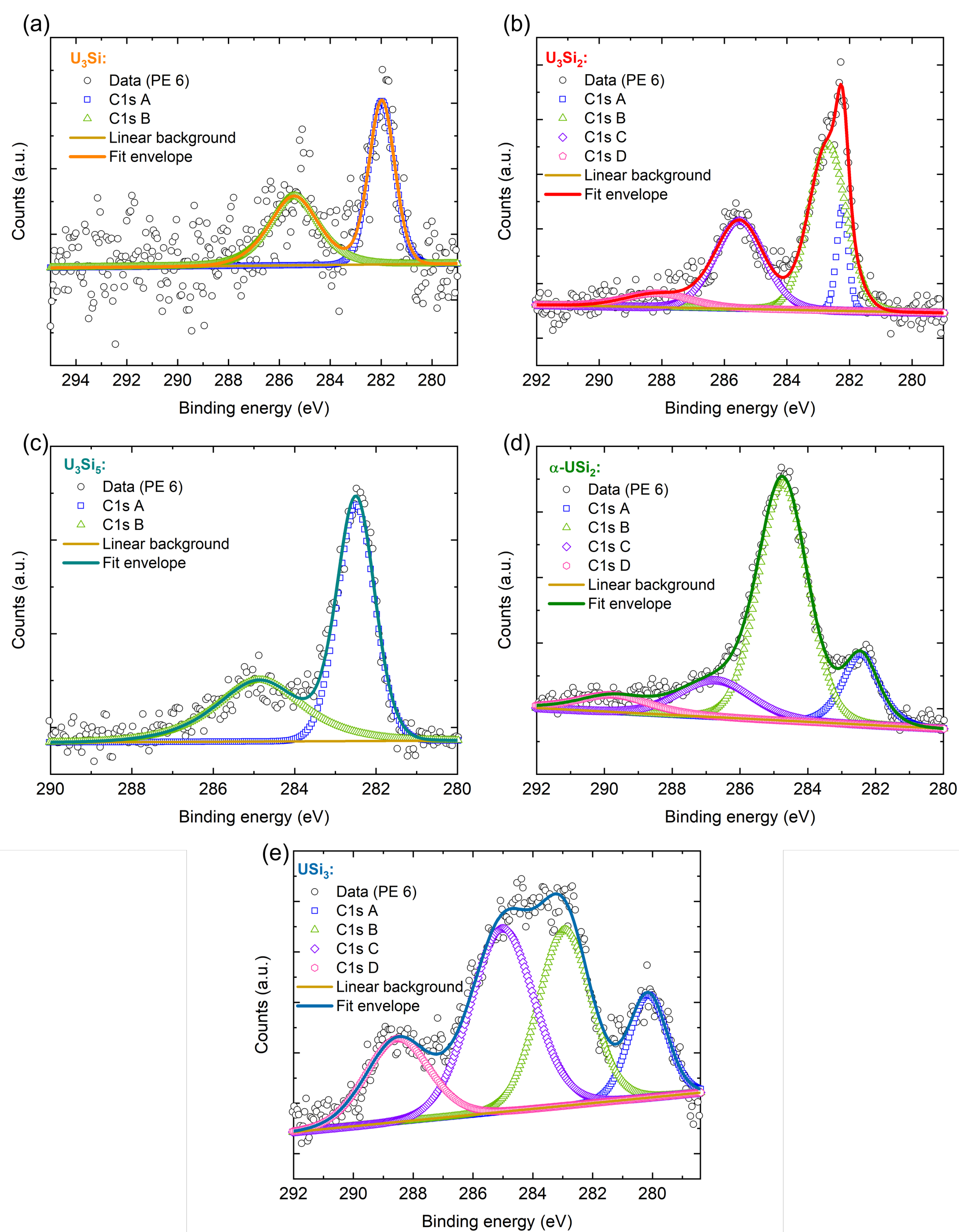

FIGURE 5.27. Modelled XPS C-1s data obtained from the **(a)** SN1513 - (001) U_3Si on CaF_2, **(b)** SN1639 - Poly-crystalline U_3Si_2 on CaF_2, **(c)** SN1512 - (100) U_3Si_5 on CaF_2, **(d)** SN1379 - (001) $\alpha - USi_2$ on MgO, **(e)** SN1699 - (001) USi_3 on CaF_2. Total fits are shown with solid lines, fit components are shown with symbols, and backgrounds are shown with crosses.

Finally using the information collected from the U-4f and Si-2s, relative ratios between metallic sites have been used to understand the stoichiometry of the uranium silicide phases. By normalising the area of each metallic component to the photoionisation cross section, provided by *Yeh et al.,* [145], the stoichiometries of each phase can be extracted. Table 5.7 presents the normalised areas and the final stoichiometries of each uranium silicide phase. The area values have been normalised to the photoionisation cross section values for the U-4f and Si-2s when using an Al source. The stoichiometries have been presented as the Si:U ratio for each phase.

Table 5.7: Table of calculated stoichiometries for each uranium silicide phase.

Sample	Component	Normalised Area	Si:U Ratio	Phase
U_3Si	U-4f	131083.497	0.32 ± 0.14	$U_{3.1}Si$
	Si-2s	42307.692		
U_3Si_2	U-4f	135011.768	0.69 ± 0.18	$U_{2.9}Si_2$
	Si-2s	93169.231		
U_3Si_5	U-4f	133240.754	1.67 ± 0.34	U_3Si_5
	Si-2s	220546.154		
$\alpha - USi_2$	U-4f	69901.933	0.90 ± 0.14	$U_{2.2}Si_2$
	Si-2s	63084.615		
USi_3	U-4f	81074.671	3.07 ± 0.33	$U_{0.975}Si_3$
	Si-2s	248753.846		

The Si:U ratio calculated for U_3Si is a slightly lower stoichiometry than expected for pure triuranium silicide. This slight reduction in the Si:U ratio could be attributed to the contribution of metal-oxygen and silicon-oxygen bonds presented in both Figure 5.23 and Figure 5.25. However, the ratio between uranium and silicon is still stoichiometric within the calculated error. Triuranium disilicide, U_3Si_2, has a slightly higher Si:U ratio of 0.69 ± 0.18, indicating a lower overall stoichiometry. This could be an effect of the inclusions of U_3Si and U_3Si_5, as noted in the structural characterisation of SN1639 (Figure 5.5). The Si:U ratio calculated for U_3Si_5 was found to be 1.67 ± 0.34 which suggests a stoichiometric uranium silicide phase. The results calculated from the normalised U-4f and Si-2s areas of $\alpha - USi_2$ show a significantly reduced Si:U ratio. The stoichiometry calculated indicate an almost 1:1 ratio between uranium and silicon suggesting uranium monosilicide. The bonding presented in the U-4f, Si-2s, and valence band structure of $\alpha - USi_2$ (SN1379) exhibit strong oxide bonding, particularly in the valence band structure. These bonds could have an influence over the relative ratio between silicon and uranium. The final stoichiometry calculated was for uranium trisilicide, USi_3. This was found to be 3.07 ± 0.33, indicating stoichiometric USi_3.

5.4.1 Discussion of XPS Results

Chemical characterisation via x-ray photoelectron spectroscopy (XPS), has proven invaluable to the understanding of uranium silicide compounds. Combined with structural characterisation, highlighted in Section 5.2, it has been shown that through the use of DC magnetron sputtering, it is possible to alter the uranium content in uranium silicide phases to produce single phase compounds with varied stoichiometries. Quantitative area analysis of each phase has shown that the Si:U ratios for structurally U_3Si, U_3Si_2, U_3Si_5, $\alpha-USi_2$, and USi_3 are 0.32 ± 0.14, 0.69 ± 0.18, 1.67 ± 0.34, 0.90 ± 0.14, and 3.07 ± 0.33, respectively. This indicates that each sample investigated is stoichiometric, within errors, with the exception of $\alpha-USi_2$ which exhibits a stoichiometry closer to a uranium monosilicide phase. For this discussion, the uranium silicide phases will be discussed individually, providing an insight into the bonding mechanisms in these compounds.

Table 5.8: The binding energy position of U-4$f_{7/2}$ oxide components and relative satellite separation energy range associated to uranium valence states. Data summarised from [83]

Valence State	U-4$f_{7/2}$ Binding Energy Range (eV)	Satellite Separation Energy Range (eV)
U(IV)	379.9 – 380.4	6.6 – 7.3
U(V)	380.1 – 381.0	7.9 – 8.3
U(VI)	380.5 – 382.3	3.6 – 4.6 , 9.5 – 10.5

5.4.1.1 U_3Si

The chemical environment of single crystal U_3Si, deposited on CaF_2 was investigated to help understanding how uranium silicide compounds vary chemically. The initial results obtained from quantitative analysis of the normalised areas of the U-4f and Si-2s spectra suggest that the sample of U_3Si (SN1513) is stoichiometric within error. The Si:U ratio calculated was 0.32 ± 0.14. The presence of oxygen components in both the U-4f and Si-2s spectra are assumed to contribute to the slight deviation from stoichiometric U_3Si.

Investigating the U-4f spectra highlighted both metallic and oxide components within the phase. The U-4$f_{7/2}$ metal peak position was found to be 377.31 eV, which aligns with peak position found for bulk U_3Si of 377.3 ± 0.1 eV, by *Krummacher et al.,* [57]. Once oxidised, bulk U_3Si exhibits a 3.3 eV peak separation between the metallic and oxide component. This does not align with the results obtained from SN1513, where the metal-oxide separation was found to be 3.92 eV. The higher binding energy of the oxide component in SN1513, measured at 381.23 eV, suggests the formation of a uranium-oxide bond with a different valence state to the oxide valency presented in the bulk study. Through investigating the satellite separation between the oxide component in SN1513 and the associated oxide satellite, the separation was found to be 2.73 eV. *Ilton et al.,* investigated how the valency of uranium oxides varies with oxide peak

position and primary satellite separation. Table 5.8 indicates these findings. From this data, it is apparent that the satellite separation found for the oxide component of U_3Si (SN1513), does not align with these findings. Clearly, there is a requirement for a deeper investigation into how the triuranium silicide oxidises. Comparisons were made between the data collected for U_3Si and the XPS literature values for coffinite, $USiO_4$. This compound is believe to form as a result of the surface oxidation of triuranium disilicide, U_3Si_2 [58, 170]. The U-4$f_{7/2}$ peak position for $USiO_4$, as reported by *Pointeau et al.,* [86], is located at 380.8 eV with a satellite separation of 6.0 eV. This position does not align with the data collected from U_3Si (SN1513).

Further investigations were conducted on the Si-2s spectra to further understand the chemical bonding in U_3Si. The components used to model the Si-2s spectra had binding energy positions of 150.10 and 152.43 eV. These particular positions indicate silicon valencies of Si^0, suggesting crystalline metallic bonding, and Si^{3+}, suggesting Si_2O_3. The assignment of this particular silicon valency was taken from the assumptions made by *Krummacher et al.,* [57], based on the SiO_2/Si work conducted by *Himpsel et al.,* [169], where the oxide valency of the Si-2p spectra was investigated. The formation of $USiO_4$ is not plausible for this uranium silicide phase, as the Si-2s peak position for coffinite has been reported to be 153.6 ± 0.3 eV [86].

Additional oxide contamination was present in the valence band structure of U_3Si. The component positioned at 2.63 eV indicate valence electrons from the U-5f sub-orbital forming bonds with oxygen. The asymmetric component, relating to the U-5f valence electrons, at the Fermi edge confirms the metallic nature of U_3Si. Observing the C-1s and O-1s core levels allowed for potential contaminants to be monitored. It was noted that the binding energy position of the C-1s peak at 281.97 eV indicated carbide bonding within the sample, with additional carbon contamination indicated with the component situated at 285.42 eV. The O-1s photoemission spectra confirmed metal-oxide bonding with modelled peaks positioned at 531.06 eV, and Si-O bonding with a peak situated at 532.37 eV. The results found here further confirmed the oxide influence on both the U-4f and Si-2s core levels.

Overall, the data collected from the U_3Si sample (SN1513), indicates a stoichiometric film with slight deviations due to oxide contamination. The Si:U ratio further confirms the structural data collected in Section 5.2, indicating a [001] oriented tetragonal single crystal of U_3Si.

5.4.1.2 U_3Si_2

The quantitative analysis conducted on the U-4f and Si-2s spectra of poly-crystalline U_3Si_2, deposited on [001] CaF_2 showed the Si:U ratio to be 0.69 ± 0.18. The Si:U ratio calculated for this sample indicates a slightly lower stoichiometry when compared to bulk U_3Si_2. This deviated

stoichiometry was expected from SN1639, as the high-angle x-ray diffraction presented in Section 5.2 showed (002) and (100) Bragg reflections from U_3Si and U_3Si_5, respectively. Investigations into the U-4f and Si-2s core level spectra displayed oxide features, similar to those found in U_3Si, further supporting the lowered stoichiometry.

Metallic and oxide component binding energy positions were extracted from the U-4f core level of U_3Si_2. The asymmetric metallic component was modelled to have a binding energy position of 377.43, this value aligns with the U-4$f_{7/2}$ position, 377.0 eV, provided by *Yan et al.,* [58]. This study investigated the oxidation of bulk U_3Si_2. Four components were used to model two oxide positions and their respective shake-up satellites. These positions were 379.28, 381.23, 383.62, 386.02 eV, respectively. The satellite separation energy range from the main photoemission peak are: 6.74 and 2.39 eV. The separation of 6.74 eV corresponds to the photoemission peak situated at 379.28 eV, which suggests a uranium valency of U(IV). The second photoemission peak at 381.23 eV, and shake-up satellite at 383.62 eV provided an energy separation of 2.39 eV. This energy separation does not align with the literature values provided in Table 5.8, suggesting that this energy range does not indicate a U(IV), U(V), or U(VI) valency.

In addition to the energy positions provided by *Ilton et al.,* (Table 5.8), the photoemission peaks were also compared to the binding energies of $USiO_4$. The XPS study on coffinite, conducted by *Pointeau et al.,* [86], showed that the U-4$f_{7/2}$ binding energy position is situated at 380.8 ± 0.3 eV, with a shake-up satellite separation of 6.0 eV, confirming a U(IV) valency for $USiO_4$. Comparing this to the results obtained from U_3Si_2, the photoemission peak positions do not align with those found for coffinite. Further to this, the energy positions of the components used to model the Si-2s spectra was investigated to understand the bonding environment of silicon within U_3Si_2. Here, peak positions were modelled at 150.18, 151.76, and 153.74 eV, indicating silicon valencies of Si^0, Si^{2+}, and Si^{4+}. These particular valencies would suggest the formation of crystalline silicon, SiO, and SiO_2. However, the component positioned at 153.74 eV does align with the Si-2s binding energies associated with $USiO_4$ (coffinite), proposed by *Pointeau et al.,* [86], where the Si-2s photoemission peak was located at 153.6 ± 0.3 eV. Furthermore, this binding energy position was noted by *Yan et al.,* [58], at a position of 153.4 eV, after exposing bulk U_3Si_2 to an oxygen environment. Due to the U-4$f_{7/2}$ not coinciding with the peak positions attributed with coffinite, it is unlikely that this compound has formed.

The C-1s and O-1s core levels, and valence band structure of U_3Si_2 were investigated to identify potential contaminants. The valence band exhibited features at 2.66 eV, showing the bonding between oxygen and U-5f valence electrons. The sharp asymmetric Fermi edge feature was still present, highlighting the metallic nature of U_3Si_2. The presence of oxygen bonding in the valence band was replicated within the O-1s spectra, with metal-oxide bonding modelled at

531.07 eV, and Si-O bonding modelled at 532.20 eV. This further confirms the influence oxygen contamination has had on the U-4f and Si-2s spectra. Similar to U_3Si, the C-1s spectra of U_3Si_2 suggested carbide bonding with a component positioned at 282.22 eV. Additional carbon contamination was apparent at 285.51 eV and 288.13 eV, which can be attributed to C-O bonding in the sample.

Overall, the XPS investigations conducted on poly-crystalline U_3Si_2 firstly concluded the Si:U ratio to be 0.69 ± 0.18. The oxide contamination in the U-4f and Si-2s spectra was assigned to Si-O and U-O bonding instead of the formation of coffinite, $USiO_4$. However, a deeper understanding of the oxide that forms is required.

5.4.1.3 U_3Si_5

The x-ray photoelectron studies conducted on U_3Si_5 were the first of their kind. The [100] oriented U_3Si_5 sample used to chemically characterise this uranium silicide phase was deposited on [001] oriented CaF_2 (SN1512). Through quantitative area analysis of the U-4f and Si-2s spectra of U_3Si_5, a Si:U ratio of 1.67 ± 0.34 was extracted. This suggests stoichiometric U_3Si_5 was synthesised via DC magnetron sputtering, matching the expected stoichiometry of bulk U_3Si_5.

From the U-4f spectra it is clear that, much like the other uranium silicide phases, U_3Si_5 exhibits a similar asymmetric component situated at the lower binding energy side. The peak position found for the U-4$f_{7/2}$ at 377.39 eV is 0.04 eV lower when compared to the metallic component of U_3Si_2. This photoemission peak position aligns with the position stated by *Krummacher et al.,* [57], 377.3 ± 0.1 eV, which was applied to various uranium silicide phases, but not U_3Si_5. The component attributed to the oxide site of the U-4f spectra was found at 381.08 eV, and has a shake-up satellite separation of 2.51 eV. This energy range does not coincide with any of the uranium valencies investigated by *Ilton et al.,* [83]. However, U_3Si and U_3Si_2 posses similar shake-up satellite energy separations. The U-4$f_{7/2}$ components were further compared to data extracted from $USiO_4$. The main photoemission peak of coffinite is found at 380.8 ± 0.3 eV, which does not match that of U_3Si_5. Similarly, the Si-2s spectra of U_3Si_5 was compared to the Si-2s spectra of $USiO_4$. For coffinite, the main photoemission peak of Si-2s is situated at 153.6 ± 0.3 eV. This does not align with any of the components used to model the Si-2s of U_3Si_5, which were situated at 150.29, 152.11, and 154.43 eV. These positions suggest silicon valencies of Si^0, Si^{2+}, and Si^{4+}, associated to the formation of crystalline silicon, SiO, and SiO_2.

The valence band structure exhibited an asymmetric peak at the Fermi edge, which is associated with the valence electrons situated in the U-5f sub-orbital. The shoulder feature situated at 2.56 eV indicates the partial metal-oxide bonding of U-5f electrons. This oxide bonding further

prompted the investigation of the O-1s and C-1s spectra to understand the potential bonds that could be forming within U_3Si_5. The modelled O-1s spectra had components situated at 530.91, 531.70, and 532.86 eV, suggesting the formation of metal-oxide and Si-O bonds. These bond types were replicated in the data collected from the U-4f and Si-2s of U_3Si_5. For the modelled C-1s spectra, components situated at 282.49 and 284.86 eV, were attributed to the formation of carbides, and carbon contamination within the sample.

The chemical characterisation SN1512, [001] oriented U_3Si_5 firstly aligns well with the structural characterisation conducted on this phase in Section 5.2. Furthermore, the Si:U ratio calculated from the normalised areas of the U-4f and Si-2s indicate a stoichiometric sample of U_3Si_5. The oxide contamination present in the sample, much like the previous uranium silicide phases, sparks significant interest with regards to the oxide positioning in the U-4f core level, implying that a deeper understanding of the oxidation of U_3Si_5 is required.

5.4.1.4 α-USi$_2$

The understanding of the chemical bonding within SN1379, [001] oriented $\alpha-USi_2$ deposited on [001] MgO was conducted via XPS. Through qualitative analysis of the normalised areas of both the U-4f and Si-2s core level sub-orbitals, the Si:U ratio was calculated to be 0.90 ± 0.14. This result contradicts the findings found in Section 5.2, which depicts the x-ray diffraction data collected from SN1379, confirming a tetragonal single crystal of $\alpha-USi_2$ oriented in the [001] direction. The stoichiometry calculated here for SN1379, would suggest the formation of uranium monosilicide, USi, rather than $\alpha-USi_2$, where one would expect a Si:U ratio of 2:1.

Spectra collected from the U-4f core level indicated two strong components within the U-4f$_{7/2}$, stemming from metallic and oxide regions. Comparing the spectra from SN1379 to the other phases investigated, the features of the U-4f are drastically different. The asymmetric component, associated with metallic bonding, was modelled at a binding energy of 377.30 eV. This peak position aligns with the study conducted by *Krummacher et al.,* on various uranium silicide phases including USi_2 which had a U-4f$_{7/2}$ binding energy of 377.3 ± 0.1 eV. The modelled oxide component of SN1379, was found to have a binding energy of 380.87 eV, with a shake-up satellite energy separation of 5.48 eV. These findings do not align to the uranium valency data compiled by *Ilton et al.,* [83]. However, this is not wildly different from a U(IV) valency, indicating the formation of UO_2. When compared to the $USiO_4$ data provided by *Pointeau et al.,* [86], the peak positioning of SN1379 could also suggest the formation of coffinite.

To further understand the oxide structure in SN1379, the Si-2s spectra was used. The modelling of this spectra utilised three components, with binding energies of 150.24, 151.96, and

153.87 eV. This suggests silicon valencies of Si^0, Si^{2+}, and Si^{4+}. The Si^0 valency confirms the formation of crystalline silicon, with the remaining valence states indicating the formation of SiO, and SiO_2, respectively. Alternatively, the component situated at 153.87 eV is similar to the peak position of coffinite in the Si-2s spectra as stated by both *Yan et al.,* [58] and *Pointeau et al.,* [86]. However, the formation of $USiO_4$ was not found in the work conducted by *Krummacher et al.,* [57] on bulk samples of USi_2.

The valence band structure of SN1379 varied significantly when compared to U_3Si, U_3Si_2, and U_3Si_5. Much like the previous uranium silicides, the large feature situated between 2.5 and 4.2 eV indicates the bonding between oxygen and valence electrons within the U-5f level. As pure metallic uranium starts to oxidise, the sharp asymmetric feature at the Fermi edge, associated with the valence electrons of the U-5f, starts to decrease and eventually disappears once oxidation is complete. The larger feature here does suggest that SN1379 has a higher oxide contribution when compared to the other uranium silicide phases. From these findings, the O-1s and C-1s levels were observed to identify any further contaminants. Three components were used to model the O-1s spectra, each with a binding energy of: 530.88, 532.02, and 534.62 eV. Once again, the positions found in the O-1s spectra of a uranium silicide indicate the formation of Si-O, and metal-oxide bonding. The C-1s spectra indicated the formation carbide contaminants, positioned at 282.43 eV, with further C-C and C-O bonds associated with the remaining positions.

The chemical characterisation of SN1379 is inconclusive. Structurally, the sample presented here is a tetragonal single crystal of $\alpha-USi_2$. However, the Si:U ratio would suggest a compound with a much higher uranium content. The major difference between this sample investigated here, and the remaining uranium silicide phases is the substrate used to epitaxially match the compound. SN1379 was grown upon a [001] oriented layer of Cu which was epitaxially matched to [001] MgO. The poor crystallinity of both the Cu buffer layer and the $\alpha-USi_2$ could have an influence on the oxygen contamination within the sample. The stoichiometry of USi_2 phases will be explored further in Chapter 6, where the oxidation of the uncapped $\alpha-USi_2$ sample (SN1645) presented alongside SN1379 in Section 5.2 will be investigated.

5.4.1.5 USi$_3$

The final uranium silicide phase that was chemically characterised was uranium trisilicide, USi_3. This sample, SN1699, was stabilised in the [001] direction on [001] oriented CaF_2. The sample was then capped with niobium, with the aim to prevent unwanted oxidation to the uranium silicide film. Through quantitative analysis of the U-4f and Si-2s spectra, the Si:U ratio was found to be 3.07 ± 0.33. This indicates a stoichiometric sample of USi_3, within error. The results obtained for the Si:U ratio support the structural characterisation conducted on SN1699, showing

the stabilisation of cubic USi_3.

The structure of the U-4f spectra of SN1699 exhibits features that differ from the previously characterised uranium silicide phases. Figure 5.23 indicates the spectra collected for USi_3, with the most significant difference being the lower binding energy shoulder, situated at 375.01 eV. This component is attributed to the Nb-$3p_{1/2}$. This artifact in the spectra appears due to remaining Nb on the sample surface. The main photoemission peak of the U-$4f_{7/2}$ has a binding energy position of 377.38 eV. This positioning aligns with the metallic positioning of the former uranium silicide phases presented, and also with the literature value for bulk USi_3, provided by *Krummacher et al.,* of 377.3 ± 0.1 eV. The component used to model the oxide component was found to have a binding energy of 381.01 eV, and a shake-up satellite separation of 2.30 eV. The energy separation between the photoemission peak and the satellite mimics the findings of the former uranium silicides. The spectra collected from USi_3 does not align with the data from coffinite, which has a position of 380.8 ± 0.3 eV and a satellite separation of 6.0 eV.

Through investigating the Si-2s spectra, it was found that the components used to model the spectra have binding energy positions of 148.19, 150.58, 152.03, and 153.37 eV. The two components with the lowest binding energy represent metallic bonding in Si, with a valency of Si^0. These are attributed to the bonding between Si-Nb and Si-U. The dominating component within the Si-2s spectra for USi_3 at 150.58 eV aligns with the Si^0 positions for the other uranium silicide phases, indicating the Si-U bonding. This suggests that the component situated at 148.19 eV is a result of Si-Nb metallic bonding. The components with larger binding energies are representative of silicon bonds with valencies of Si^{3+} and Si^{4+}, suggesting the formation of Si_2O_3 and SiO_2. The component at 153.37 eV also aligns well with the Si-2s position of coffinite, provided by *Pointeau et al.,*. However, because the U-4f positions do not correspond with the positioning of coffinite, it is unlikely that this compound has formed as part of an oxide.

The valence band spectra of USi_3 was further investigated to understand the influence of oxygen and residue niobium. The characteristic asymmetric metallic feature, attributed to the valence electrons in the U-5f orbital, was present at the Fermi edge. A small shoulder feature was noted between 3 – 4 eV. This is an indication of the Nb-4d spectra, which was not as apparent in the former uranium silicides due to the higher influence of metal-oxide bonding on the U-5f valence electrons. The stark contrast between the valence spectra of SN1699 and the other uranium silicides is the prominent feature situated between 6 – 10 eV. These features are attributed to the O-2p and the Si-3s. Further investigations were undertaken on the O-1s and C-1s core levels. Three components were used to model the O-1s spectra, suggesting the formation of metal-oxide and silicon-oxide bonds at 528.34, 530.69, and 533.21 eV. The Si-O bond formation agrees well with the Si^{4+} valency found in the Si-2s spectra. Carbide contamination was once again found

in SN1699, with components situated at 280.14 and 282.94 eV. C-C and C-O bonds were noted between 285 and 289 eV.

Overall, the data collected from SN1699 does suggest a stoichiometric sample of USi_3, with a Si:U ratio of 3.07 ± 0.33. This agrees well with the structural characterisation conducted on SN1699 in Section 5.2, where [001] oriented single crystal USi_3 was successfully grown via DC magnetron sputtering onto an [001] CaF_2 substrate. From the chemical characterisation of SN1699 it can be stated that $USiO_4$ has not been formed as a initial oxide, however, the oxide species formed on the surface of USi_3 was not identified. Different silicon valencies were identified within the Si-2s structure, suggesting the formation of Si_2O_3 and SiO_2 alongside metallic silicon bonds with uranium. The overall oxide contamination present within USi_3, does further confirm that a deeper understanding of how the oxide species of uranium silicide phases is required.

5.4.2 Conclusions

This section has provided a comprehensive chemical characterisation of various uranium silicide phases, including: U_3Si, U_3Si_2, U_3Si_5, $\alpha-USi_2$, and USi_3. Through the use of qualitative area analysis on the U-4f and Si-2s spectra of each phase, it has shown that the majority of these phases align with their expected stoichiometries. The characterisation of SN1379, which is structurally tetragonal [001] $\alpha-USi_2$, showed that chemically the Si:U ratio to be 0.90 ± 0.14 indicating a stoichiometry closer to a uranium monosilicide. However, the remaining phases presented have shown huge potential in utilising idealised thin film surfaces to stabilise uranium silicides with varied stoichiometries. Therefore mapping out the phase diagram as a function of uranium content.

Each of the samples presented exhibited a form of oxide contamination. This was noted in all of the spectra investigated. What must be stressed, is that even under UHV conditions, total prevention of the oxidation of uranium metal surfaces cannot be avoided. From this initial characterisation study, it cannot be confirmed if the source of the oxide contamination is a product of the growth conditions, or if the metal-oxide bonds are formed during XPS data acquisition. The carbon bonding has also been consistent throughout each of the uranium silicide phases.

Overall, through the use of DC magnetron sputtering, a range of uranium silicide thin films have been structurally and chemically characterised using x-ray diffraction and x-ray photoelectron spectroscopy. This has emphasised the usefulness of delicately altering the content of uranium within uranium silicides to map the U-Si binary phase diagram. The collection of high resolution data on these samples has provided a new insight into the chemistry of uranium silicide phases, providing chemical information for U_3Si_5 for the first time. This understanding

now allows for the corrosion behaviour of uranium silicide phases to be probed.

Chapter 6

The Surface Oxidation of Uranium Silicide Compounds

Oxidation of metallic fuels has been at the forefront of nuclear research for many years. The surface oxidation of metallic and intermetallic fuels plays a crucial role in the stability, performance, and overall structural integrity of the fuel compound. This can jeopardise the fuel before, during, and after reactor operation. For these reasons, it is crucial to understand the initial oxide layer that forms on uranium silicide compounds, and how the oxide varies as a function of uranium content. Understanding the native oxide under ambient conditions may help to predict how the oxide species evolves as a function of temperature, oxygen content, or even within aqueous environments. This chapter will build upon the ability to structurally and chemically characterise U-Si phases shown in Chapter 5, with the aim to answer three questions: (1) How much do the uranium silicide phases change as a function of uranium content once exposed to ambient conditions? (2) What compounds form within each uranium silicide oxide layer? (3) How thick is the oxide layer that grows on each uranium silicide under ambient conditions? Here, the uranium silicide phases will be investigated individually.

6.1 Experimental Set-Up

A combination of x-ray diffraction (XRD), x-ray reflectivity (XRR), and x-ray photoelectron spectroscopy (XPS) were used to chemically and structurally probe the oxidation of uranium silicide compounds. Initially, surfaces of uranium silicides were grown via DC magnetron sputtering, as discussed in Chapter 4. All phases were deposited onto 10 × 10 × 0.5 mm [001] oriented CaF_2 single crystal substrates, which were commercially purchased from MTI Corp. Unlike the samples presented in Chapter 5, these samples were deposited without a protective Nb or Cu capping layer, allowing for the surface to be exposed to atmospheric conditions. The samples used for

these oxidation experiments were: SN1644, SN1645, SN1700, SN1702, SN1707, and SN1711. The details of these samples can be found in Chapter 4. All samples were characterised via x-ray diffraction to confirm the single crystal nature of each phase, with the exception of SN1707, which is poly-crystalline U_3Si_2.

The first set of experiments involved observing the oxidation layer growth as a function of time. This was conducted with the combined use of XRD and XRR. Due to the uncapped nature of the samples investigated, the on-set of surface oxidation occurs with the first exposure to air, which therefore initiates as the sample is removed from the sputtering system loading chamber. Therefore, the first measurements were taken as soon after unloading the sample as possible. The oxide growth was observed for 96 hours initially, with intermittent data sets collected from each sample up to 55 days, allowing for the sufficient formation of an oxide surface layer on each U-Si phase. XRD and XRR data sets were acquired at batches, this allowed for continuous data collection over the initial 96 hour period. This also allowed for the sample to be probed without being adjusted, ensuring alignment throughout the initial data collection period. However, due to the timescale in which the oxide layer growth was measured, it was necessary to move the sample from the x-ray diffractometer. To minimise any changes caused by this, the sample position, orientation, and position on the sample stage were noted and marked. Following this, samples were cut up into 5 × 5 mm pieces, providing four identical samples for each phase and therefore allowing further experiments to be conducted. Fitting of XRR and XRD data was performed using GenX software [132], as described in Chapter 3.

The second set of experiments involved XPS depth profiling, where the valency of uranium and silicon were probed. These experiments were conducted at the NanoESCA Facility, based at the University of Bristol. Due to the COVID-19 pandemic and subsequent laboratory restrictions, XPS measurements were taken by Dr. Jude Laverock and Dr. Gary Wan. The process of depth profiling involved the acquisition of data with intermittent layer removal. Oxidised layers were removed using a magnetically confined Ar^+ ion sputtering source, which confines the direction of the Ar^+ ions onto the surface of the sample, removing atoms from the sample. The Ar^+ source is kept perpendicular to the sample surface, with a continuous $\rho_{Ar} = 5 \times 10^{-5}$ mbar, to ensure a uniform sputtering profile. After each sputtering cycle, data is acquired from the sample surface. To minimise additional oxidation to the surface, the XPS chamber operates at a pressure below 5×10^{-10} mbar. For this experiment, data acquisition was conducted after each 120 s sputter cycle, and this was repeated around 12 times for each uranium silicide phase. Some samples required additional sputter cycles due to the nature of the sample itself. This will be explicitly stated for each phase presented. For each uranium silicide, data was collected from the U-4f, Si-2s, O-1s, and valence band. Data collection from the Si-2p was avoided due to the overlap with the U-5d core level. All XPS spectra was modelled using CasaXPS software [167].

The combination of these experiments provide an insight into the formation of the oxidation layer for each uranium silicide, and the potential compounds that form as a result of surface oxidation.

6.2 X-ray Diffraction Results

High angle x-ray diffraction was deployed to probe structural changes to each of the uranium silicide phases. Each of the uncapped uranium silicide compounds were observed for up to 55 days in order to understand how atmospheric conditions alter their structures. Omega and phi scanning techniques were also used to understand the crystallinity of each uncapped phase investigated.

6.2.1 U_3Si

Triuranium silicide, U_3Si was epitaxially stabilised in the [001] direction onto [001] single crystal CaF_2. The phase was deposited at 800°C and left to cool to an ambient temperature before being exposed to an atmospheric environment. Figure 6.1 shows the fitted x-ray diffraction data extracted from the oxidised surface of SN1711. The data presented here indicates that the compound deposited onto CaF_2 is a single crystal of U_3Si. This is shown with the off-specular phi data collected from the (206) of U_3Si, confirming that there are unique reflections within a 180° phi rotation, which are shown to have a periodicity of $\Delta\phi$ = 45°. This matches the characterisation of U_3Si described in Chapter 5, with SN1513. Through conducting omega scans on the (002) Bragg reflection of U_3Si, the FWHM of the peak was found to be 1.08 ± 0.01°. This is a 31% increase when compared to the pristine U_3Si sample, SN1513. In Figure 6.1 (a), it was found that the sample had inclusions of U_3Si_2. These reflections are indicated with red drop lines, and their Bragg reflections are noted. The U_3Si_2 phase included in this sample is polycrystalline.

Figure 6.2 depicts the surface oxidation of SN1711 through the use of high angle x-ray diffraction. Here five data sets are presented, all of which have been modelled in GenX, using a series of psudo-voigts. SN1711, was monitored continuously for 4 days initially, with periodic data sets collected from the sample. Presented in Figure 6.2 are the data sets collected from hour: 1, 10, 24, 48, and 1322 (approximately 55 days). U_3Si, U_3Si_2, and CaF_2 Bragg reflections are denoted with orange, red, and purple drop lines. From the diffraction spectra presented, it is clear that there has not been a significant change to the sample. From the enlarged FWHM of U_3Si, collected from the (002) omega data, it can be stated that changes to the sample have occurred. Furthermore, there are inclusions of U_3Si_2, which may also have an effect on this crystallinity. Observing the U_3Si_2 reflections in Figure 6.2, it can be seen that these reflections do not change as a function

time.

Despite the high-angle diffraction data extracted from U_3Si showing no indication of structural change, this does not mean that there has been no alteration to the surface of this uranium silicide phase. In order to probe the changes to U_3Si, surface sensitive techniques are required to help understand these structural and chemical changes.

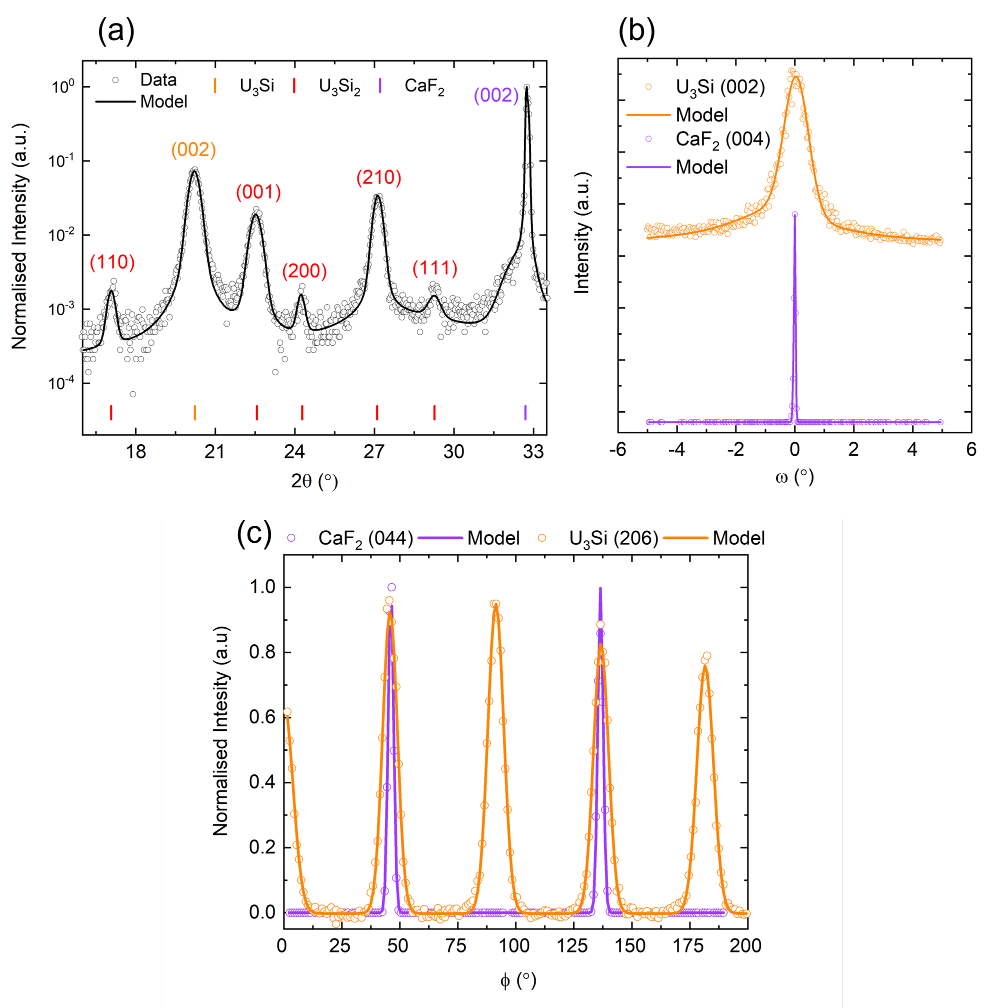

FIGURE 6.1. The fitted (a) specular x-ray diffraction, (b) omega, and (c) phi spectra from [001] oriented U_3Si single crystal deposited onto [001] oriented CaF_2. Data extracted from SN1711.

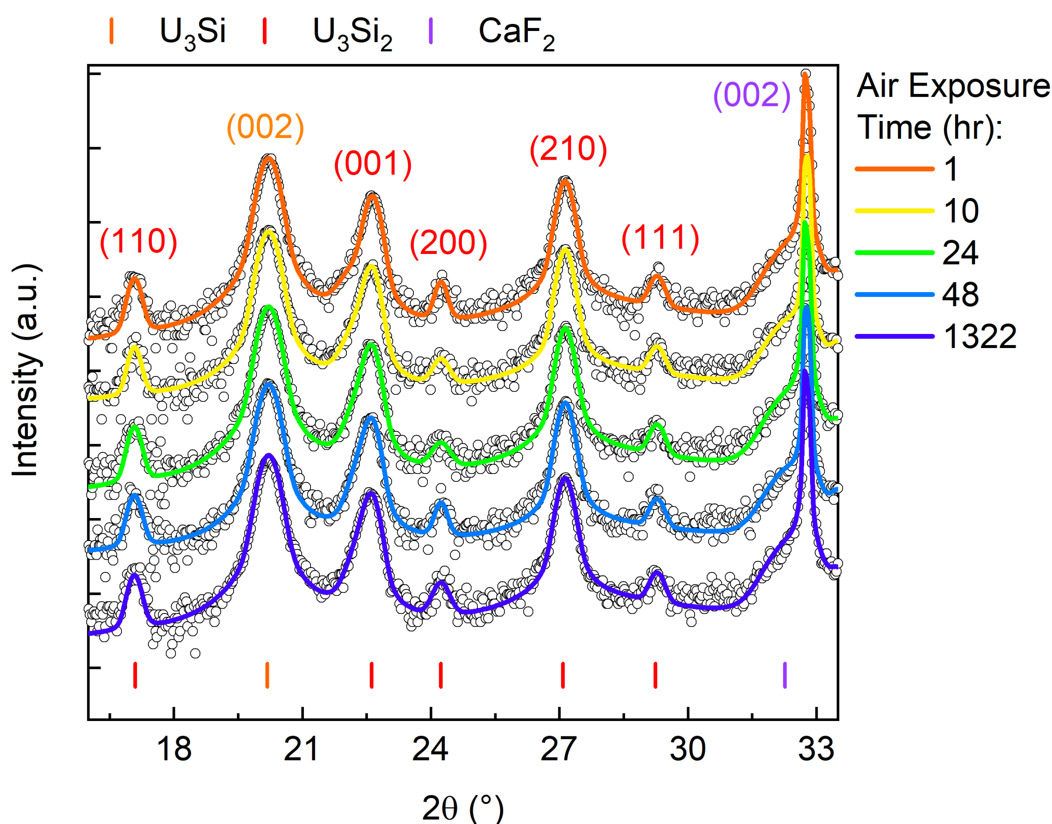

FIGURE 6.2. XRD of oxidised [001] U_3Si single crystal, indicating the progression of structural changes as a function of time. Time stamps of 1, 10, 24, 48, and approximately 1322 hours are shown. Data is presented with open circles, and models indicated with solid lines. Data collected from SN1711.

6.2.2 U_3Si_2

Triuranium disilicide, U_3Si_2, was stabilised as a polycrystalline phase onto [001] oriented CaF_2. The sample, SN1707, was deposited at 800°C onto the substrate, and was allowed to cool to an ambient temperature under UHV conditions before being exposed to atmospheric conditions. Upon exposure, the structural changes to the sample were monitored using high angle x-ray diffraction. Data extracted from the sample is presented in Figure 6.3. Here, 5 data sets are presented, which indicate the XRD patterns of SN1707 as a function of exposure time. This sample of U_3Si2 was monitored for 55 days to probe any structural changes that may take place on the surface as a result of atmospheric contamination. From these diffraction spectra, it is clear that the sample exhibits similar Bragg reflections to those collected from SN1711 (Figure 6.2). The data collected from SN1707 has additional U_3Si_2 reflections that the U_3Si sample lacked.

Furthermore, SN1707 did not have unique reflections when conducting off-specular phi scans on the (206) of U_3Si, confirming that SN1707 is not a single crystal of U_3Si with U_3Si_2 inclusions.

From Figure 6.3, there is no indication of structural changes as the exposure time increases. This can be seen through observing the various U_3Si_2 and U_3Si reflections. As the exposure time increases, there are no new reflections that appear as a result of surface oxidation, nor do the reflections present in the spectra alter in intensity or width. This does not infer that there are no changes to the U_3Si_2 phase. The lack of change could suggest that the surface oxidation thickness is so small, such that high-angle x-ray diffraction is not as sensitive to the surface to detect the oxide phases forming.

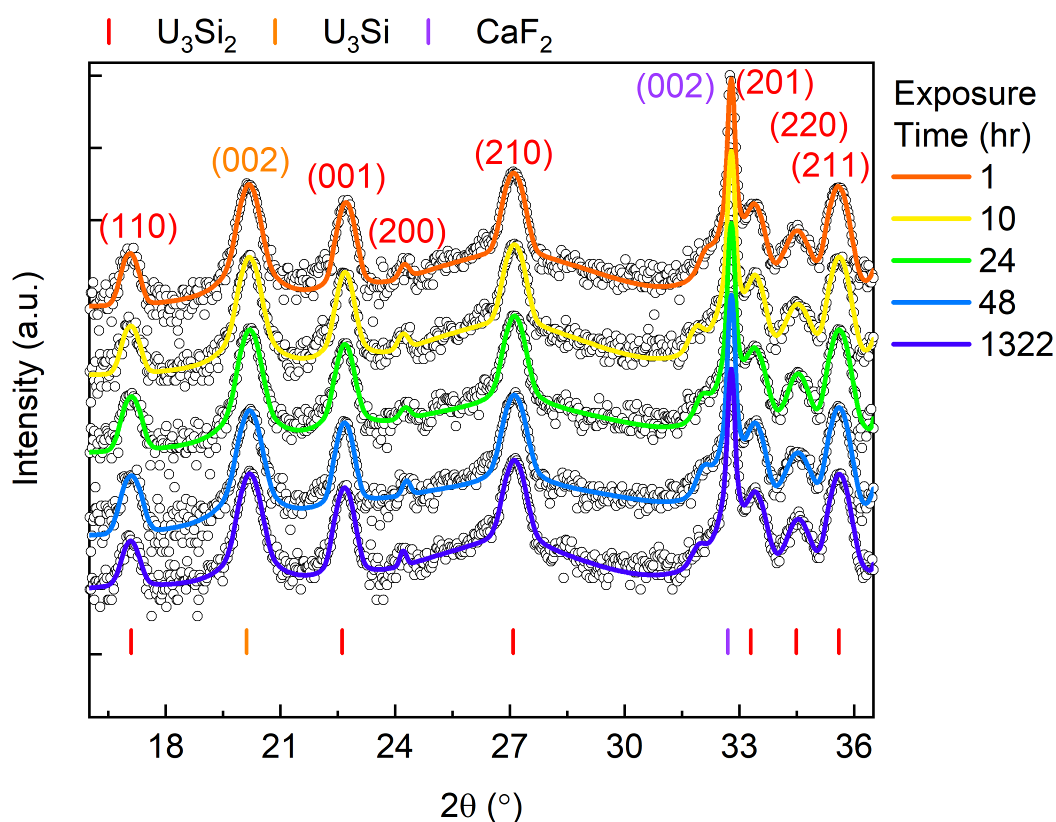

FIGURE 6.3. XRD of oxidised poly-crystalline U_3Si_2. Spectra is indicating the structural change of U_3Si_2 as a function of exposure time to air. Data is presented with open circles, and models indicated with solid lines. Spectra collected from 1, 10, 24, 48, and approximately 1322 hours are shown. Data collected from SN1707.

Crystallite sizes in SN1707 were calculated using the Scherrer equation, as described in Chapter 3. Table 6.1 presents an example of the crystallite sizes extracted from SN1707 with reference to the two uranium silicide phases present within the sample: U_3Si_2 and U_3Si. Here, two examples are shown from the U_3Si_2 phase, indicating that the crystallite size is around 20 nm.

Table 6.1: Table showing crystallite size for each phase within SN1707.

Sample	Phase	2θ position °	FWHM °	Crystallite size (nm)
SN1707	U_3Si_2 (001)	22.72 ± 0.01	0.39 ± 0.01	22 ± 2
	U_3Si_2 (210)	27.098 ± 0.002	0.469 ± 0.007	18 ± 3
	U_3Si (002)	20.176 ± 0.001	0.443 ± 0.004	19 ± 2

6.2.3 U_3Si_5

U_3Si_5 (SN1644) was stabilised onto [001] oriented CaF_2 at 800°C as an uncapped uranium silicide phase. This sample of U_3Si_5 was stabilised using an increased uranium deposition power of 30 W. This is substantially greater when compared to the deposition power used to stabilise SN1512, epitaxial (100) U_3Si_5 capped with Nb, which was 19 W. The phase originally stabilised using a deposition power of 30 W was U_3Si_2, as indicated with the characterisation of SN1639. Figure 6.4 (a) indicates the high-angle data collected from the oxidised surface of SN1644. From this, it can be seen that only one reflection sits between the $2\theta = 20-30°$ range. The peak located at $2\theta = 26.086 \pm 0.001°$ indicates the (100) Bragg reflection of U_3Si_5, matching the 2θ position of the specular peak measured for SN1512 in Chapter 5. The characterisation of SN1644 is indicated in Figure 6.4 (b) and (c). Despite the increased uranium content, the formation of a crystalline single crystal of U_3Si_5 was achieved. This is shown with the omega data collected from the (100) Bragg reflection of U_3Si_5, and through the use of off-specular phi scans conducted on the (201) reflection. Much like the capped sample of U_3Si_5, the sample presented here has also exhibits a two-domain single crystal system, this is noted with the additional phi reflection collected from the (201). The FWHM of U_3Si_5 was modelled to be 1.64 ± 0.02°, which is a 8.25% increase when compared to SN1512. Suggesting that the oxidation of this sample, SN1644, has an influence over the crystallinity of the compound.

The unexpected stabilisation of U_3Si_5 using a uranium power of 30 W, resulted in the missed opportunity to study the evolution of oxide growth on SN1644. Despite this, from observing the high-angle XRD data collected from SN1644, it is clear that only one Bragg reflection belonging to U_3Si_5 is present within the spectra.

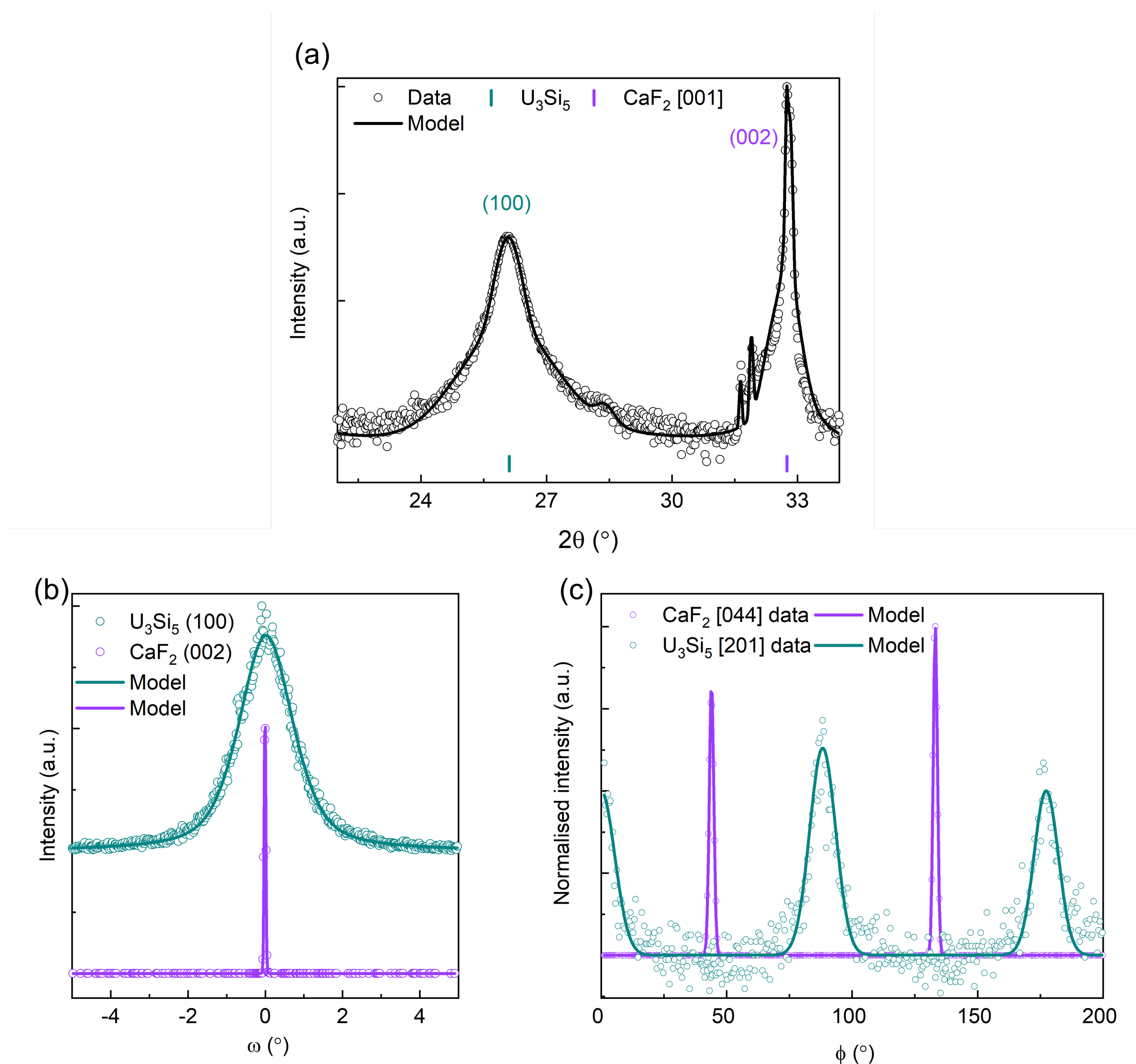

FIGURE 6.4. (a) High angle data collected from the oxidised surface of [100] oriented U_3Si_5. (100) and (002) Bragg reflections of U_3Si_5 and CaF_2 are indicated with teal and purple drop lines, respectively. (b) Omega data collected from the (100) and (002) Bragg reflections of U_3Si_5 and CaF_2, respectively. (c) Phi data collected from the (201) and (044) reflections of U_3Si_5 and CaF_2, respectively. All data is presented with open circles, and models indicated with solid lines. Data collected from SN1644.

6.2.4 α-USi_2

The surface oxidation of $\alpha-USi_2$ was investigated through the use of two epitaxial samples. SN1645, a sample previously characterised in Chapter 5 which utilised a uranium deposition

power of 19 W, and SN1702, which required a uranium deposition power of 10 W to stabilise the phase. As the characterisation of SN1645 has already been presented, the high-angle XRD structural data will not be presented again. However, from the sample characterisation presented in Chapter 5, it was found that uncapped $\alpha - USi_2$ has a vastly improved crystallinity when compared to the capped phase deposited on MgO. The crystallinity of $\alpha - USi_2$ is improved by around 84%, when stabilised upon CaF_2. However, what must be stressed, is that $\alpha - USi_2$ has not been stabilised on CaF_2 as a pristine 'capped' sample. From the work conducted on this phase, this sample is only stabilised onto (001) CaF_2 when exposed to atmospheric environments. In addition to this, the deposition power supplied to uranium (19 W) to form this sample (SN1645) was the same deposition power used to stabilise U_3Si_5 (SN1512). The second sample presented here, SN1702, was stabilised using a uranium deposition power of 10 W, which suggests the stabilisation range in which $\alpha - USi_2$ is larger than originally thought and could infer that this phase is not strictly a *line-compound* as suggested by the uranium-silicon binary phase diagram. Therefore inferring that a pre-determined ratio between uranium and silicon is not required to stabilise these compounds.

The uncapped sample of $\alpha - USi_2$ (SN1645), stabilised using a uranium deposition power of 19 W, was probed using high-angle x-ray diffraction to investigate the structural changes that may occur to the compound once exposed to atmospheric conditions. Figure 6.5 depicts the XRD data, indicating the oxidation progression as a function of time. The (004) of $\alpha - USi_2$ is indicated with a green drop lines, with the [001] oriented CaF_2 substrate indicated with purple. The progression of spectra indicates that minimal structural changes have occurred to SN1645.

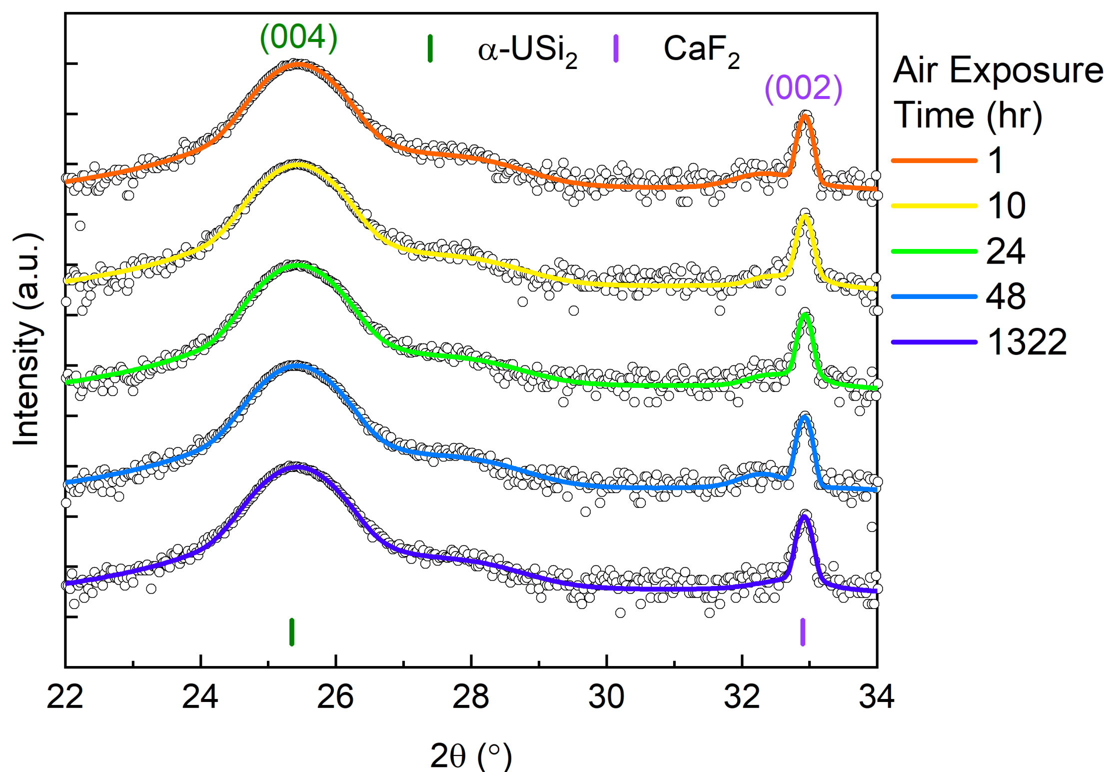

FIGURE 6.5. XRD of oxidised [001] oriented α-USi$_2$. Spectra is indicating the structural change of α-USi$_2$ as a function of exposure time to air. Data is presented with open circles, and models indicated with solid lines. Spectra collected from 1, 10, 24, 48, and approximately 1322 hours are shown. Data collected from SN1645.

Where there were no phase or significant 2θ position changes for SN1645, there were subtle changes in the data collected from SN1702. Figure 6.6 indicate the high angle x-ray diffraction spectra collected from an uncapped sample of $\alpha-\mathrm{USi}_2$. Where this is very similar to the previous sample (SN1645) of the sample compound, the engineering and stabilisation of this sample utilised a lower uranium power of 10 W. From the spectra, there is a shift in the position of the (004) reflection of $\alpha-\mathrm{USi}_2$ suggesting an alteration in the lattice parameter of the phase as a function of air exposure time. Through analysing the data, it was found that there has been a 0.924% increase in the ‘c‘ lattice parameter. The variation in the lattice parameter may be due to the increased silicon content present within SN1702.

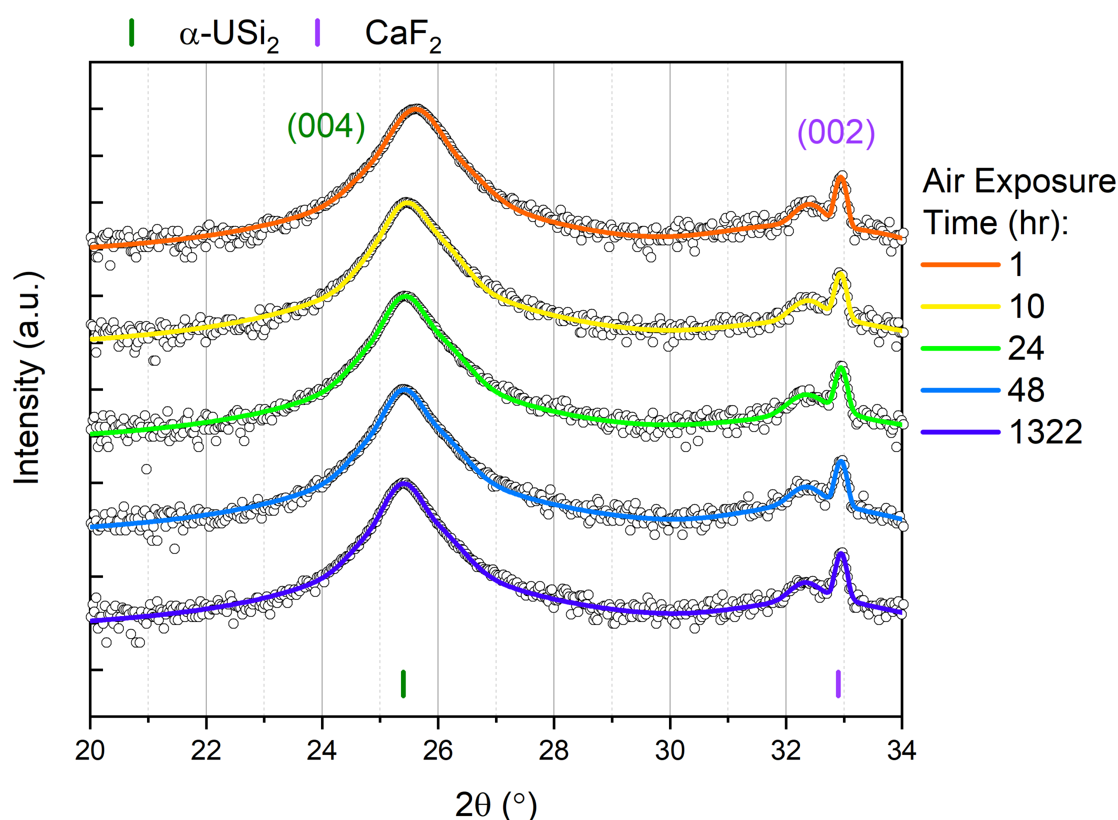

FIGURE 6.6. XRD of oxidised [001] oriented α-USi_2 . Spectra is indicating the structural change of α-USi_2 as a function of exposure time to air. Data is presented with open circles, and models indicated with solid lines. Spectra collected from 1, 10, 24, 48, and approximately 1322 hours are shown. Grid lines are used to help with the visual tracking of the specular data. Data collected from SN1702.

The structural characterisation of the 10 W $\alpha - USi_2$ is presented in Figure 6.7 (a). Here the omega data collected from the (004) Bragg reflections of $\alpha - USi_2$ and CaF_2. The FWHM of $\alpha - USi_2$ was modelled to be $1.66 \pm 0.01°$, which varies by 8.2% when compared to the FWHM of SN1645, which was modelled to be $1.53 \pm 0.01°$. The crystallographic nature of SN1702 was investigated by probing the off-specular reflections of $\alpha - USi_2$ and CaF_2. Figure 6.7 (b) indicates the off-specular spectra collected from the (3110) of tetragonal $\alpha - USi_2$ and the (115) of CaF_2. Note that the Miller indices notation used here are (hkl). Much like the data collected from (001) orientated $\alpha - USi_2$ stabilised upon [001] MgO (SN1379), the spectra indicates the same square on square match that is exhibited in the off-specular data collected from SN1379. This shows that the SN1702, is an epitaxial thin film of tetragonal $\alpha - USi_2$.

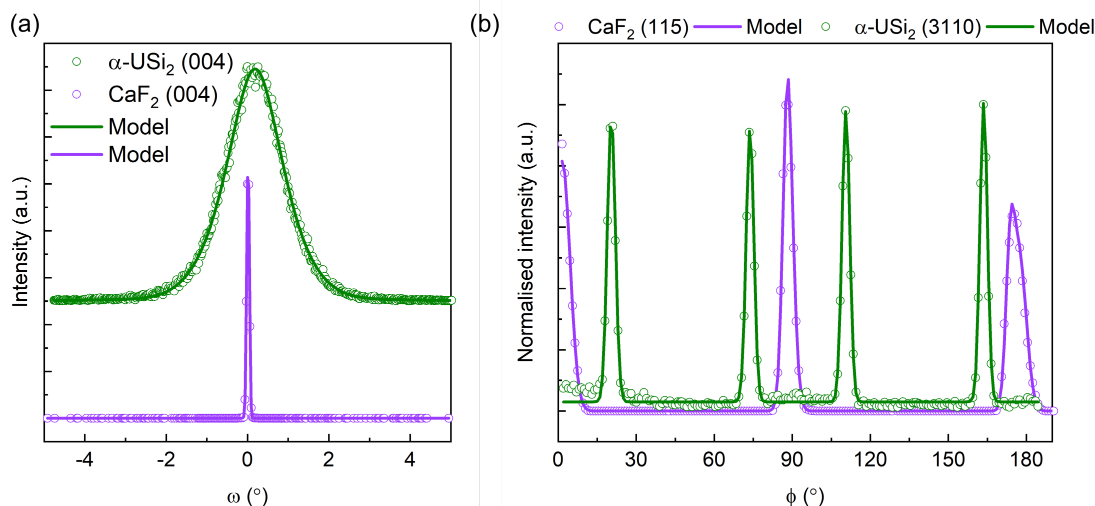

FIGURE 6.7. Data is presented with open circles, and models indicated with solid lines. (a) Indicates the omega data collected from the (004) Bragg reflections of α-USi_2 and CaF_2. (b) Phi data collected from the (3110) and (115) reflections of α-USi_2 and CaF_2, respectively. Data collected from SN1702.

6.2.5 USi_3

Uranium trisilicide, USi_3 was epitaxially stabilised onto [001] oriented CaF_2 at 800°C. This sample, SN1700, was not capped with a protective capping layer, so was allowed to cool to an ambient temperature under UHV conditions before being exposed to an atmospheric environment.

Figure 6.8 indicates the high angle x-ray diffraction data extracted from the surface of USi_3 once exposed to an atmospheric environment. The spectra shows how the structure changes as a function of air exposure, with the (001) and (002) of USi_3 and CaF_2 indicated with blue and purple drop lines. It is clear that there is minimal change to the structure of USi_3, with no additional phases growing as a result of surface oxidation. The (110) reflection of USi_3 is also present in this spectra. This reflection was also noted in the capped sample of USi_3, suggesting that this additional reflection is not a result of oxidation. Due to the multiple USi_3 reflections, the sample was further characterised to understand the crystallinity and epitaxy of the sample.

Figure 6.9 shows the omega data extracted from the Bragg reflections of USi_3 and CaF_2, alongside the off-specular phi data collected from the (113) and (115) reflections of USi_3 and CaF_2, respectively. Firstly, through modelling the (001) omega data of USi_3, it was found that the

FWHM was equal to: 0.879 ± 0.001°. This is a 33.3% improvement when compared to the FWHM collected from capped USi_3 (SN1700). Where there are no significant structural differences between the two samples, the difference in crystallinity will be due to the overall thickness of the deposited compound. Secondly, through conducting off-specular phi scans, the (113) reflection of USi_3 was probed. Much like SN1699, it was also confirmed that SN1700 is also a single crystal of USi_3, with a epitaxial match to [001] oriented CaF_2 that is rotated 45° with [001] being the specular direction.

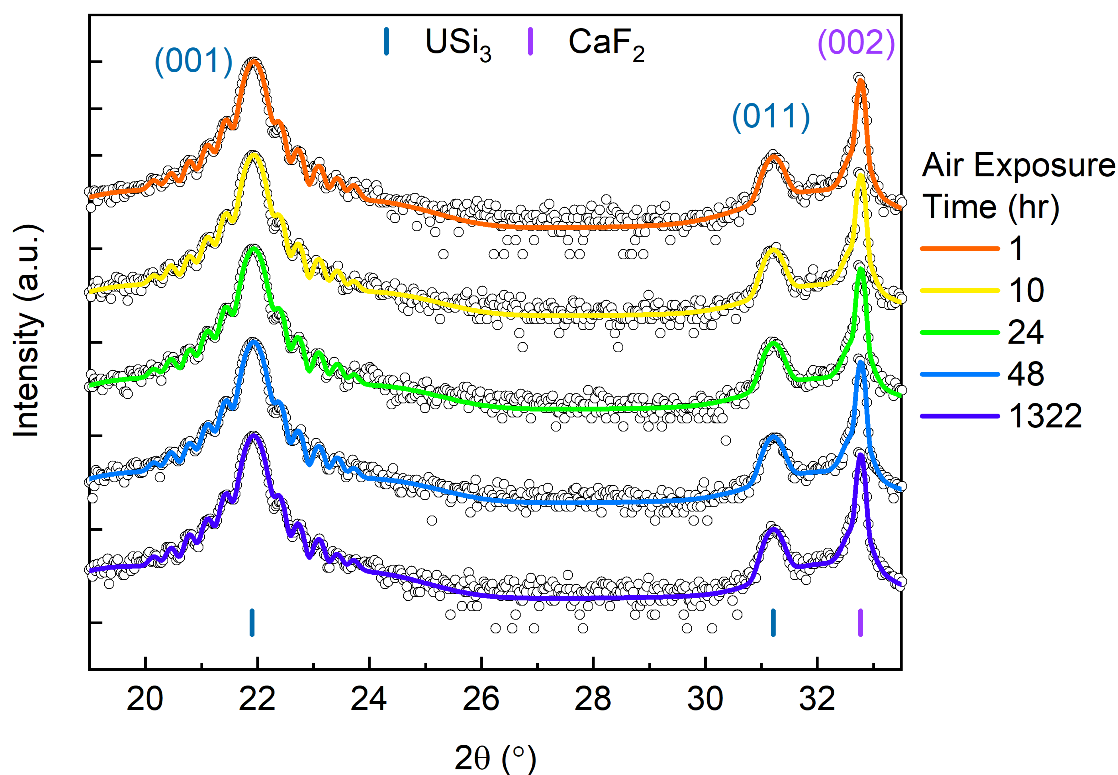

FIGURE 6.8. XRD of oxidised [001] oriented USi_3 . Spectra is indicating the structural change of USi_3 as a function of exposure time to air. Data is presented with open circles, and models indicated with solid lines. Spectra collected from 1, 10, 24, 48, and approximately 1322 hours are shown. Data collected from SN1700.

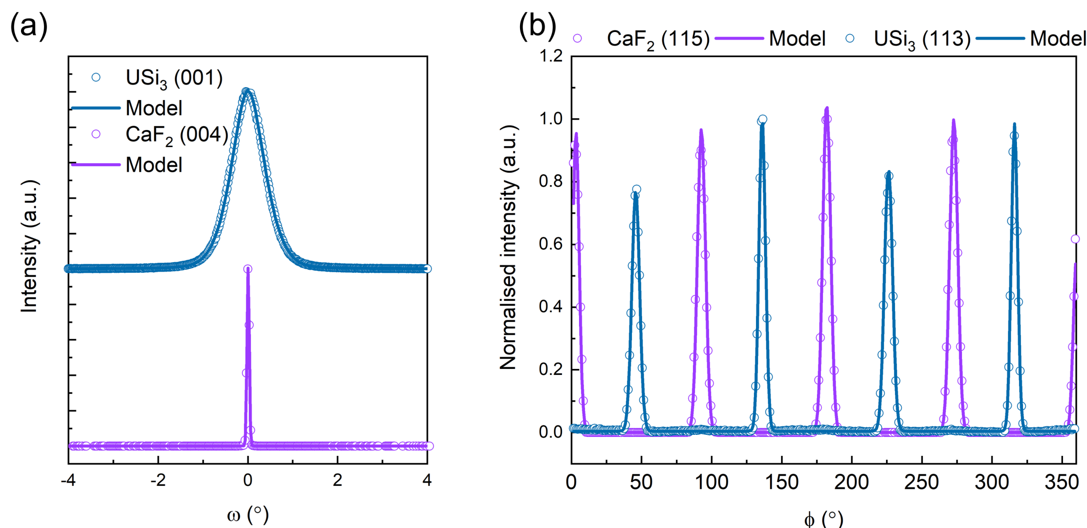

FIGURE 6.9. XRD scans of oxidised [001] oriented USi_3 . (a) The omega data collected from the (001) of USi_3 and (004) of CaF_2, (b) indicates the phi data collected from the (113) of USi_3 and (115) of USi_3. Data is presented with open circles, and models indicated with solid lines. Data collected from SN1700.

6.3 X-ray Photoelectron Spectroscopy Results

This section presents the x-ray photoelectron (XPS) results obtained from the oxidised uranium silicide phases presented in this chapter. Through the means of depth profiling, oxide layers were sputtered away to reveal the metallic uranium silicide compounds below. During this sputtering process, data was acquired from the surface to provide an insight into the potential oxide compounds that form and how the oxide layer may change as a function of uranium content for each phase. This section will present the findings from each uranium silicide individually.

6.3.1 U_3Si

Investigating the oxidation of U_3Si was performed on SN1711 using XPS. Data was acquired from the previously characterised sample, using a depth profiling technique. Utilising Ar^+ sputtering, layers from the oxidised surface of U_3Si were removed allowing for the bonding and valency of the uranium, silicon, and oxygen states to be probed as a function of depth. Figure 6.10, shows the calibrated spectra collected from the U-4f and Si-2s spectra of U_3Si. Here, the spectra collected after each sputtering cycle are plotted on top of each other to help understand the transition from oxide dominated spectra, to metallic states within the sample.

From Figure 6.10, it can be seen how the first acquired data sets from the U-4f and Si-2s, shown in pink, vary significantly when compared the remaining spectra presented. This is due to the influence of additional surface contaminants, such as carbon. The presence of adsorbed surface contaminants is also indicated in the significantly lower intensity collected from the U-4f spectra. Once removed, it can be seen that the spectra transitions from a more oxidised state back to an expected metallic state in an almost linear fashion, with the overall intensity stemming from the U-4f oxide component continuously reducing. Figure 6.10 (a), shows the U-4f spectra, with the U-4$f_{7/2}$ and U4$f_{5/2}$ highlighted. The second spectra collected after 2 minutes of sputtering, shown in red, exhibits a strong U-4$f_{7/2}$ peak around 381.0 eV, with a spin-orbit split between the U4$f_{5/2}$ state of 10.8 eV. Through modelling this spectra, two components were used to model the oxide peak, positioned at 380.1 and 381.0 eV, which is consistent with U(IV) and U(V) valencies. There is no indication of the presence of an asymmetric metallic peak. Satellite peaks can be clearly seen for the U-4$f_{5/2}$, with the U-4$f_{7/2}$ satellite intensity being dominated by the metallic U-4f state once the oxide is removed. The final metallic binding energy position was found to be around 377 eV after 28 minutes of surface sputtering.

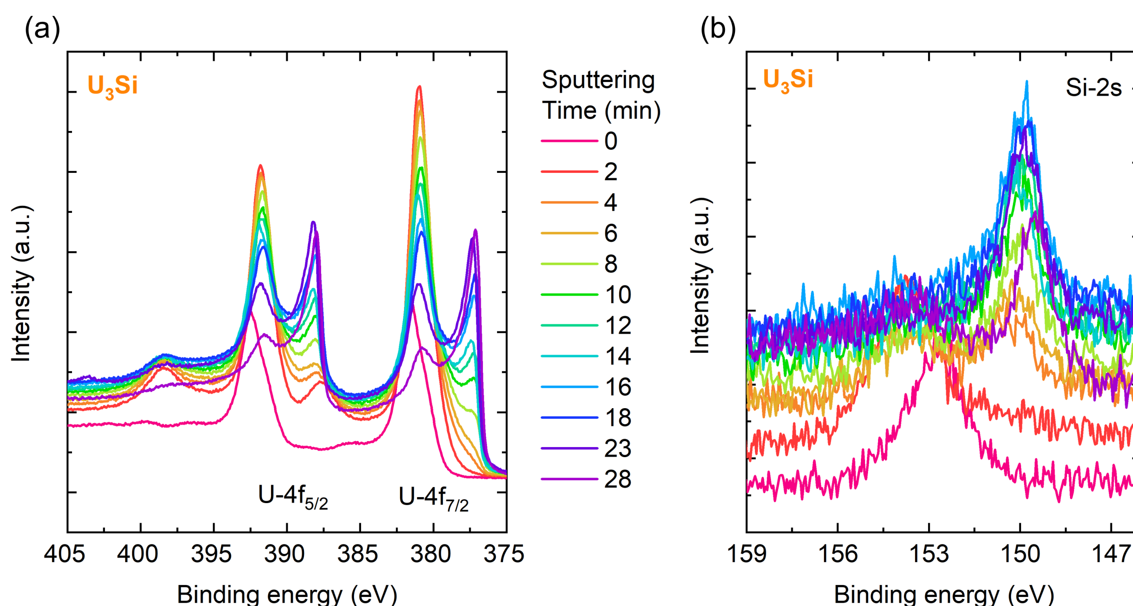

FIGURE 6.10. Graph showing the data extracted from the (a) U-4f and (b) Si-2s spectra of U_3Si as a function of sputter time. Data collected from SN1711.

The Si-2s spectra collected from U_3Si is indicated in Figure 6.10 (b). The most immediate difference between the Si-2s and U-4f is the resolution, intensity, and overall quality of the spectra

collected. The Si-2s spectra has a significantly lower photoelectron cross-section when compared to the Si-2p core level, as reported by *Yeh et al.,* [145]. The Si-2p spectra overlaps with the U-5d spectra, making characterisation and analysis on this spectra difficult to quantify, particularly when investigating oxidation. Furthermore, the spectra was collected using a pass energy of 6 eV, allowing for the resolution in peak position to be increased, this however, reduces the overall intensity of the spectra, which for the Si-2s, significantly reduces the quality. Despite this, the spectra collected from the Si-2s of U_3Si firstly exhibits a binding energy shift as a function of sputtering time. This binding energy change, moving the spectra to a lower binding energy of 150 eV, indicates the removal of Si-O bonds situated around 153 eV. Much like the initial spectra collected from the U-4f at 0 minutes, shown in pink, the Si-2s spectra also has surface contaminants that effect the overall peak position and intensity. The Si-2s peak position after 2 minutes of sputtering is located at 153.8 eV, suggesting a silicon valency of Si^{4+}. As the oxide layers are sputtered away, the presence of a metallic state (Si^0) become more dominant within the spectra. After 28 minutes of sputtering, the Si-2s spectra, shown in purple, has a dominating peak situated at 149.6 eV, suggesting metallic silicon. This peak is accompanied by an oxide peak situated around 153 eV. This feature is not as present in the spectra collected after 23 minutes of sputtering suggesting an external factor has reintroduced oxygen to the surface of SN1711.

The fitted depth profile spectra collected from U_3Si is shown in Figure 6.11. This indicates the spectra collected from the O-1s, U-4f, Si-2s, and the valence band of U_3Si (SN1711). The total fit envelope of each spectra is shown with a solid line, with the components used to model the spectra shown with dashed lines, and the background presented as a dotted line. Here, the evolution of each spectra is shown as a function of sputtering time. As the oxide layers are removed, the spectra collected from each core level has a shift to a lower binding energy. This indicates the removal of oxide bonds, in the case of the U-4f and Si-2s spectra, which evolve into metallic states. The spectra collected from the O-1s spectra shows how the total intensity of the spectra decreases as a function of sputtering time, indicating the removal of oxygen from the sample. The evolution of the valence band indicates the bonding between the valence electrons in the U-5f band with oxygen. This bonding is shown with the peak situated around 2.5 eV. As the oxide bonding is removed from the sample, the valence band begins to form a sharp, asymmetric peak situated at the Fermi edge, E_F, which represents the U-5f valence electrons. This peak becomes more prominent as the sputtering time increases.

With the exception of the final spectra, collected after 28 minutes of sputtering, it can be seen that the oxide component used to model the Si-O bonding in the Si-2s spectra is reduced after 8 minutes of sputtering. This is vastly different when compared to the dominating oxide component in the U-4f spectra which is significantly harder to remove. This could suggest that the uranium bonding sites are far more susceptible to oxygen bonding when compared to silicon.

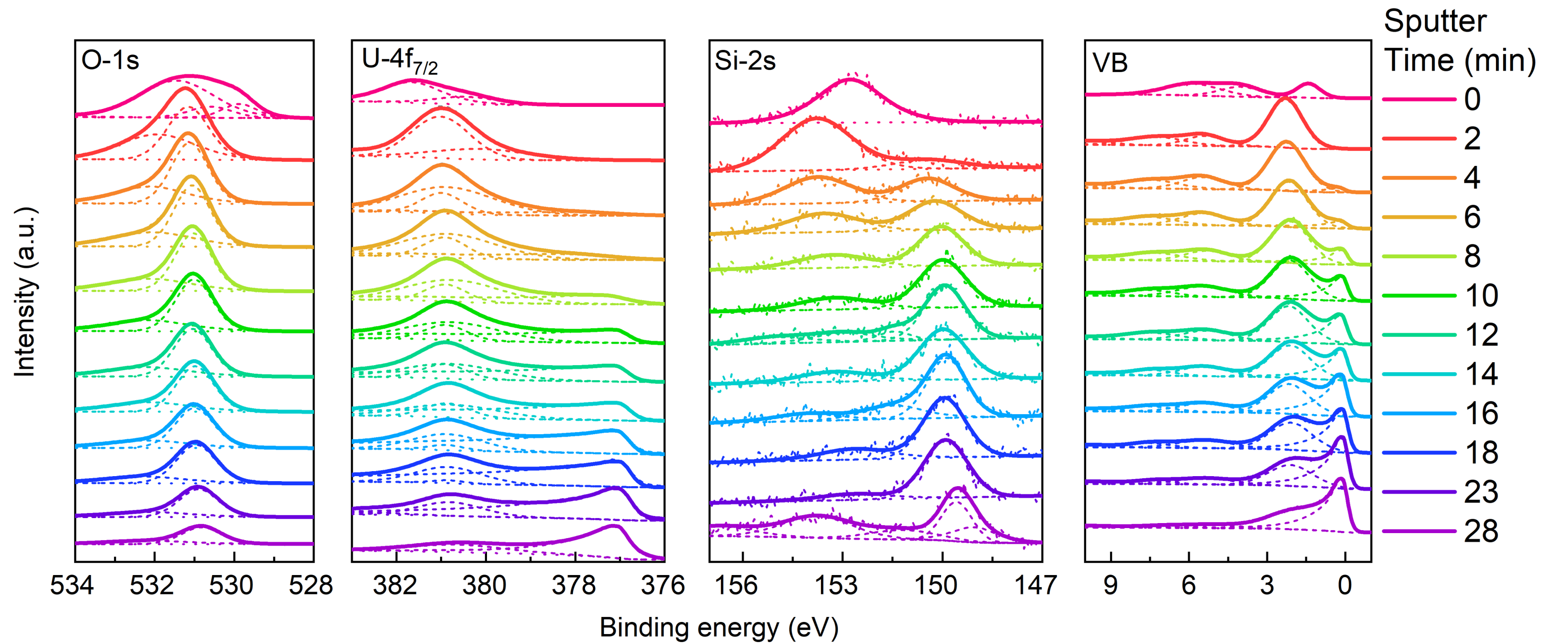

FIGURE 6.11. The fitted O-1s, U-4f, Si-2s, and valence band spectra from [001] oriented U_3Si single crystal. Data acquired as a function of depth from the oxidised surface of U_3Si. Components used to model each spectra are shown with dashes, background is modelled with dots, and total fit is shown as solid line. Data from SN1711.

The total fitted area of each spectra is presented in Figure 6.12. The areas for each spectra presented has been normalised against their respective photoionisation cross-sections, provided by *Yeh et al.,* [145]. The figure shows how the total area collected from each spectra evolves as a function of sputtering time. From this analysis, the overall stoichiometry of the sample can be probed through investigating the ratio between Si:U areas collected from the metallic sites of the Si-2s and U-4f. From the data collected from the O-1s spectra, shown with purple crosses, it is clear that as the sputtering time increases, the overall oxygen content within the sample decreases. The increase in the total oxygen content after 2 minutes of sputtering be attributed to the removal of adsorbed contaminants being removed, making the surface vulnerable to reactions. After this, the O-1s total area continues to decrease. The component responsible for the metallic bonding in the U-4f state, shown with dark grey squares, steadily increases until 18 minutes of surface sputtering. After this, the total U-4f metal area begins to decrease. This behaviour could be attributed to the removal of the bulk film during the sputtering process, suggesting that the oxide has been sputtered through.

On average, the components responsible for the U-4f oxide, shown with red circles, decrease as a function of sputtering time. The increase after 2 minutes of sputtering, can also be attributed to the removal of adsorbed contaminants making the sample susceptible to surface reactions. The second increase in the total U-4f oxide area occurs at 8 minutes of sputtering. This increase could be a result of the sample being left in the UHV XPS system before the next sputtering cycle begins. Despite the sample being kept in an atmosphere below $1x10^{-10}$ mbar, it is inevitable that metallic and inter-metallic systems will oxidise. After 8 minutes of sputtering, the total U-4f oxide area does decrease as a function of sputtering time. The Si-2s total metal and total oxide areas behave in a similar manner to the U-4f components. As the sputtering time increases, the total Si-2s metal component increases with the exception of the final data point after 28 minutes of sputtering. This change to the Si-2s spectra after 28 minutes, this is presented in Figure 6.11. There is a broad oxide photoemission peak situated around 153 that is much more prominent in this spectra when compared the former spectra collected after 23 minutes of sputtering. The final area modelled for the final Si-2s oxide does not exceed the area modelled after 2 minutes of sputtering. This increase in oxide could also be attributed to exposure to small amount of oxygen in the UHV XPS system.

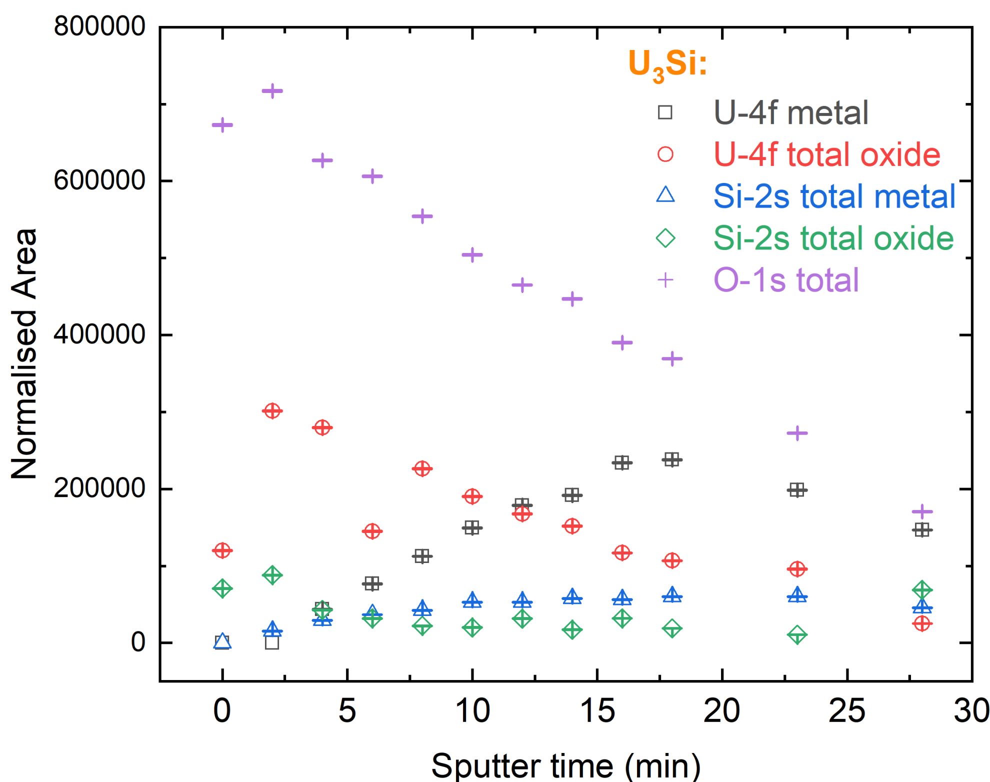

FIGURE 6.12. Graph showing the normalised area intensities from the U-4f, Si-2s, and O-1s states collected from U_3Si, after increasing the sputtering time. Data indicates the total fitted areas of each peak, showing the total metal and oxide areas within each spectra. Data collected from SN1711.

To gain a deeper understanding on how both uranium and silicon behave as oxides within uranium silicide phases, the components responsible for oxide bonds within the U-4f, Si-2s, and O-1s were separated. Figure 6.13 presents the separated components contributing to the U-4f, Si-2s, and O-1s. For the U-4f data, the two oxide components that sum to be the total area presented in Figure 6.12, have been separated, alongside the component responsible to U-O bonding in the O-1s. The U-4f metallic component is also presented in Figure 6.13. Here, all four components have been normalised to the total area of the U-4f U(IV) component at t = 0. This allows for the stoichiometries between oxide components to be tracked. Much like the areas presented in Figure 6.12, the components have the similar relationships with sputtering time. The O-1s U-O area presented in Figure 6.13 decreases as function of sputter time. This behaviour does not match the initial total area of the O-1s in Figure 6.12. The relative O:U ratios

are presented in Table 6.2. Here, the relative ratio between the O-1s U-O and the U-4f oxide responsible for U(IV) bonding were calculated to allow for any potentially stoichiometric uranium oxides to be identified. The values presented indicate a dominant O-1s U-O presence within the sample, with little indication of a stoichiometric UO_2 compound forming as part of a surface oxide in U_3Si.

Table 6.2: O:U ratios calculated from the total areas extracted from the O-1s U-O, and the U-4f U(IV) areas in U_3Si, SN1711. Areas have been normalised to the total area of U-4f U(IV) at t = 0.

Sputter time (min)	O-1s U-O area	U-4f U(IV) area	O:U ratio
0	7.55	1.00	7.6 ± 0.8
2	4.93	1.12	4.4 ± 0.4
4	4.50	0.86	5.2 ± 0.5
6	4.46	0.80	5.6 ± 0.6
8	4.23	0.68	6.2 ± 0.6
10	3.83	0.59	6.5 ± 0.7
12	3.57	1.00	3.6 ± 0.4
14	3.72	0.71	5.2 ± 0.5
16	3.08	0.24	13 ± 1
18	3.00	0.17	18 ± 2
23	2.19	0.31	7.1 ± 0.7
28	1.31	0	-

The data collected from the Si-2s and O-1s are presented on the right in Figure 6.13. Here, the components responsible for the metallic and oxide bonding in the Si-2s are presented alongside the component responsible for the Si-O bonding in the O-1s. All areas have been normalised to the Si-2s oxide 2 component, represented with blue triangles. This oxide has a binding energy position around 153 eV and is responsible for the Si^{4+} valency in the silicon oxide. Normalising all areas to this particular silicon oxide allows for the stoichiometry of this Si^{4+} oxide to be tracked against the O-1s Si-O area. There are two other silicon oxide components that are also tracked in this figure. Si-2s oxide 1, shown as red circles, has a binding energy around 151 eV and is responsible for the Si^{1+} valence state, whereas Si-2s oxide 3, shown as purple stars, has a binding energy of 156 eV. Through segregating the components responsible for the silicon and oxide contributions in U_3Si, it is possible to understand how these oxides behave as a function of oxide thickness. Firstly, the Si-O bonding component in the O-1s core level is initially absent from the sample after t = 0, and t = 2. This could suggest that the oxide forming on the very surface of U_3Si is comprised of U-O bonds. After 4 minutes of surface sputtering, the Si-O component from the O-1s has a O:Si ratio of roughly 8:1, with Si-2s oxide 2. The metallic Si-2s area, attributed to a silicon valency of Si^0, increases as a function of sputtering time until 23 minutes. At this point, the total metallic area begins to decrease. All silicon oxide components increase, with Si-2s oxide 2 having a more dominant area when compared to the remaining oxides. Table 6.3 showcases the relative ratios calculated between the O-1s Si-O and Si-2s oxide 2 normalised areas. The ratios

calculated indicate an excess of oxide contribution stemming from Si-O bonding in the O-1s. After 28 minutes of surface sputtering, the O:Si ratio indicates the formation of a hyper-stoichiometric SiO_2 compound forming.

Table 6.3: O:U ratios calculated from the total areas extracted from the O-1s Si-O, and the Si-2s oxide areas in U_3Si, SN1711. Areas have been normalised to the total area of Si-2s oxide area 2 at t = 0.

Sputter time (min)	O-1s U-O area	Si-2s oxide area	O:Si ratio
0	0	1.00	-
2	0	1.245	-
4	4.10	0.603	6.8 ± 0.7
6	3.23	0.449	7.2 ± 0.7
8	2.99	0.312	10 ± 1
10	2.54	0.245	10 ± 1
12	2.33	0.193	12 ± 1
14	2.10	0.104	20 ± 2
16	1.65	0.166	10 ± 1
18	1.66	0.159	10 ± 1
23	1.46	0.130	11 ± 1
28	1.11	0.518	2.1 ± 0.2

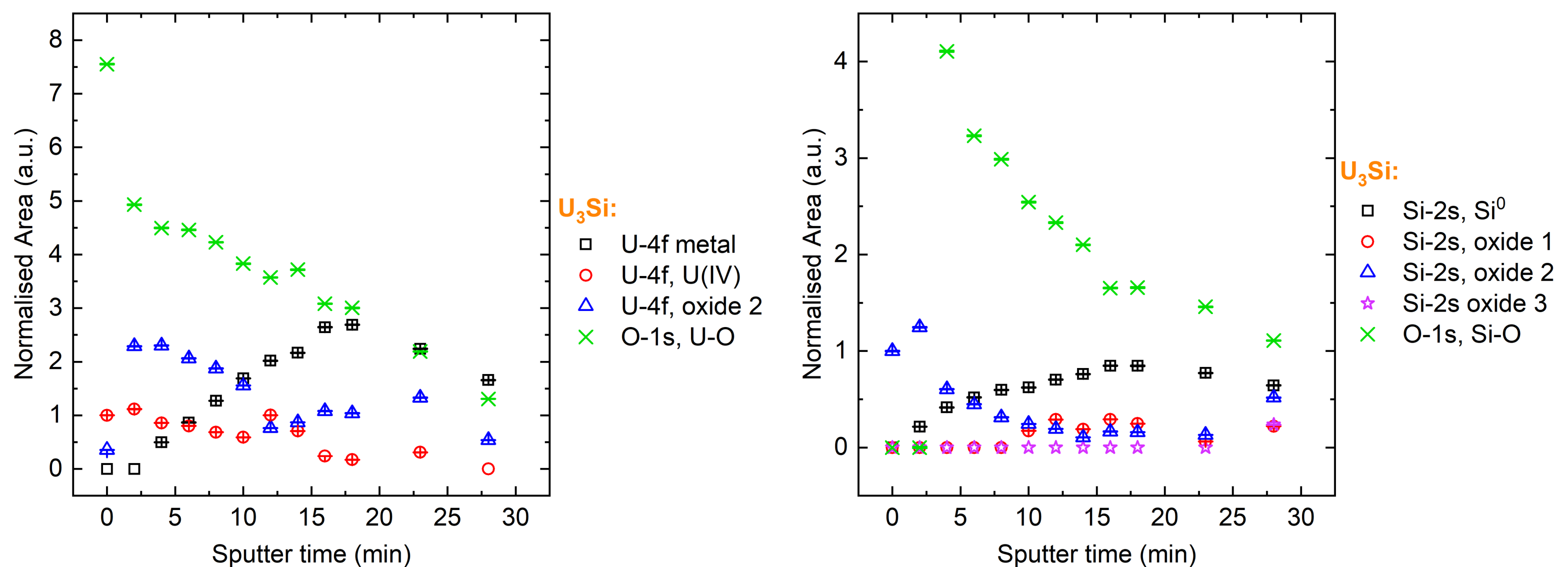

FIGURE 6.13. Graphs showing the normalised areas of U-4f and Si-2s are a function of sputtering time. *left*: Shows the components used to model the U-4f spectra as a function of time, alongside the component responsible for U-O bonding in the O-1s. Areas have been normalised to the total U-4f U(IV) area at t = 0. *right* Shows the components used to model the Si-2s spectra as a function of time, alongside the Si-O bonding component from the O-1s. Areas have been normalised to the total Si-2s oxide 2 area at t = 0. Data taken from SN1711.

Through modelling the spectra collected from U_3Si, it was possible to observe the evolution of the stoichiometry between silicon and uranium metallic components. Figure 6.14 presents the Si:U ratio, and therefore the stoichiometry of SN1711 as a function of sputtering time. Probing this stoichiometry as a function of sputter time allows for a deeper understanding into how the sample is behaving as the surface oxidises. From Figure 6.14, it can be seen that the Si:U ratio measured after 4 minutes of sputtering time is has a stoichiometry that would infer that a compound similar to U_3Si_2 compound has formed as part of the oxidation process. A Si:U ratio of 0.67 would suggest the formation of stoichiometric U_3Si_2. As this phase was present within the structural characterisation of SN1711, it makes sense for this particular Si:U ratio to be measured. This could suggest that U_3Si_2 may form as part of the oxidation process and not as a result of sample synthesis. After 18 minutes, the overall Si:U ratio has decreased past the limit for the first U-Si line compound, U_3Si. As this sputtering time increases to 28 minutes, a stoichiometry is calculated that would indicate the formation of U_3Si, with a Si:U ratio of 0.31. This matches the structural characterisation conducted on SN1711. Overall, the metallic Si:U ratio fluctuates around 0.3 after 8 minutes of surface sputtering, suggesting that oxide layer has been sputtered through to reveal the underlying epitaxial U_3Si film. This therefore indicates that the surface oxidation of U_3Si could potentially passivate, forming a stable oxide under ambient conditions, with a finite thickness.

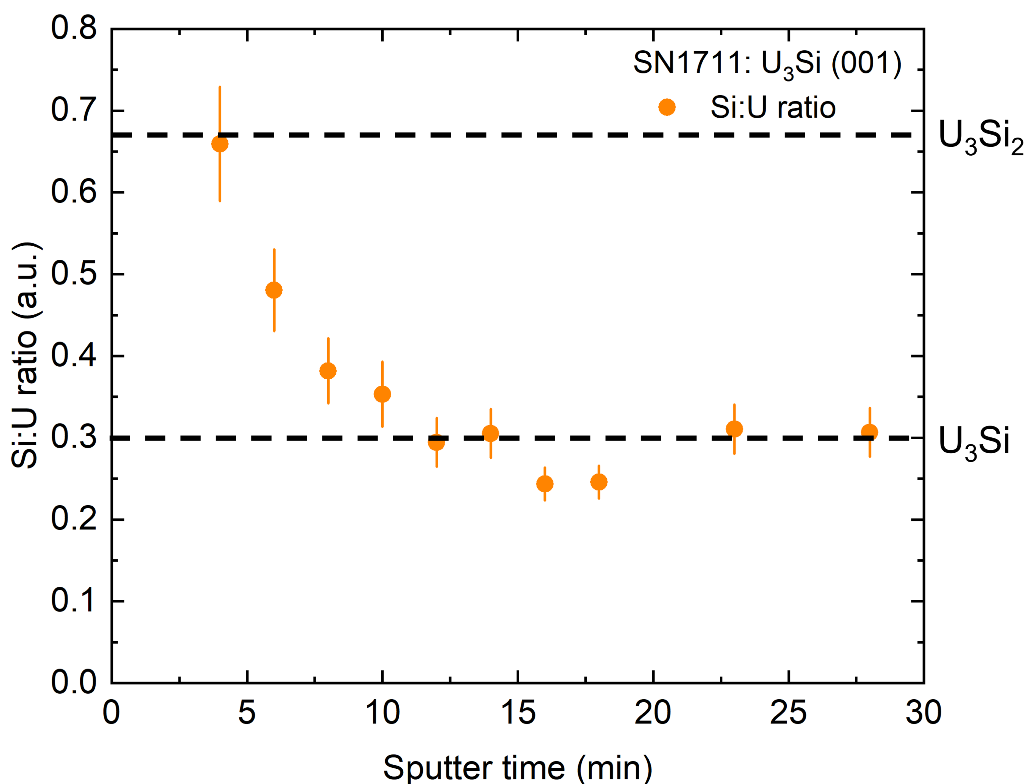

FIGURE 6.14. Graph showing the Si:U ratio as a function of sputtering time. Areas were collected from the metallic U-4f and Si-2s components in U_3Si. Data collected from SN1711.

6.3.2 U_3Si_2

The surface oxidation of poly-crystalline U_3Si_2 was investigated using XPS depth profiling. This method allowed for a deeper understanding into how this proposed ATF oxidises, and the for the potential oxidation compounds that form as a result of atmospheric exposure to be determined. Through the used of Ar^+ sputtering, layers were removed from the surface of the sample, SN1707, allowing for the localised elemental bonding environments to be probed as a function of depth. Figure 6.15 shows the calibrated spectra from the U-4f and Si-2s spectra of poly-crystalline U_3Si_2. The data presented here was collected using a pass energy of 6 eV. Spectra collected after each sputtering cycle has been plotted on top of each other to help understand the evolution from oxide to metallic states.

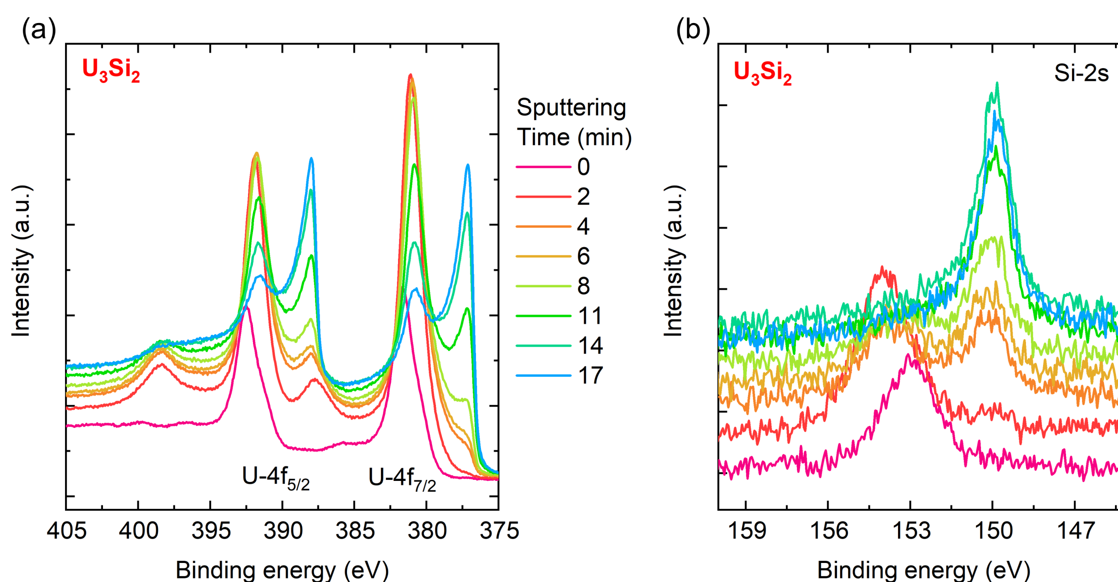

FIGURE 6.15. Graph showing the data extracted from the (a) U-4f and (b) Si-2s spectra of U_3Si_2 as a function of sputter time. Data collected from SN1707.

Figure 6.15 (a) shows the spectra collected from the U-4f core level. Here, the U-4$f_{7/2}$ and U-4$f_{5/2}$ are labelled. The first data set collected, shown in pink, is significantly lower in intensity when compared to the remaining spectra. This lowered intensity is due to the influence of surface contaminants from the atmosphere, which have deposited as a result of surface exposure. Once removed, the U-4$f_{7/2}$ spectra has an initial binding energy position of: 381.0 eV, with a satellite separation energy of 6.6 eV. Comparing this to work conducted by *Ilton et al.,* [83], this suggests uranium bonding with a valency of U(IV) or U(V). As the sputtering time increases, the oxide component of the spectra, situated around 380 eV, is slowly removed, with the asymmetric peak, corresponding to the metallic bonding in the U-4f, gradually increasing around a binding energy of 377 eV. However, after 17 minutes of surface sputtering, the oxide component is still prominent within the spectra.

The spectra collected from the Si-2s of U_3Si_2 is shown in Figure 6.15 (b). The removal of Si-O bonds is shown as a function of Ar sputtering time, alongside the increase in the silicon-metal bonding intensity. Much like the U-4f spectra, the initial data set, shown in pink, has a significantly reduced intensity when compared to the remaining spectra. This is due to surface contaminants, which is a result of atmospheric exposure. The quality of the spectra is also hindered due to the low photoionisation cross-section of the Si-2s spectra, and because a 6 eV pass energy was used to obtain data. Once the sputtering cycles begin, there is an immediate

change in the binding energy positions of the Si-2s spectra. After 2 minutes of surface sputtering, the binding energy position of the spectra is around 153.9 eV, suggesting a silicon valency of Si^{4+}. Observing the work conducted by *Hollinger et al.,* [171], this would indicate the formation of a Si-O compound, typically SiO_2, at the surface of U_3Si_2. After 17 minutes of Ar^+ sputtering, the Si-2s spectra has shifted to a lower binding energy position of 149.8 eV, indicating a silicon valency of Si^0. This energy position is inherent with metallic bonding in Si [171], therefore indicating the bonding with uranium atoms.

The fitted depth profile spectra collected from U_3Si_2 (SN1707), are shown in Figure 6.16. This figure indicates the spectra obtained from the O-1s, U-4f, Si-2s core levels, and the valence band spectra. Each spectra was observed after each sputtering cycle, with the time intervals indicated in the Figure. Spectra was initially collected from an unaltered surface. These data sets are shown in pink. The spectra collected at 0 minutes appears different when compared to the remaining data sets. This is due to the effect of surface contaminants, which adhere to the surface of the sample as a result of atmospheric exposure. The O-1s spectra showcases this well with a significant broadening in the peak shape. The evolution of the valence band collected from U_3Si_2 highlights the formation of metal-oxide bonds, and the gradual removal of oxygen from the sample. The valence band, after 2 minutes of sputtering has a dominant peak located around 2.5 eV. This forms as a result of the U-5f valence electrons bonding with oxygen. As the sputtering time increase, this peak at 2.5 eV slowly reduces, and the formation of an asymmetric peak at the Fermi edge starts. This peak gradually gets more intense and sharper, accompanied by a reduced metal-oxide positioning shoulder to the left of the Fermi edge.

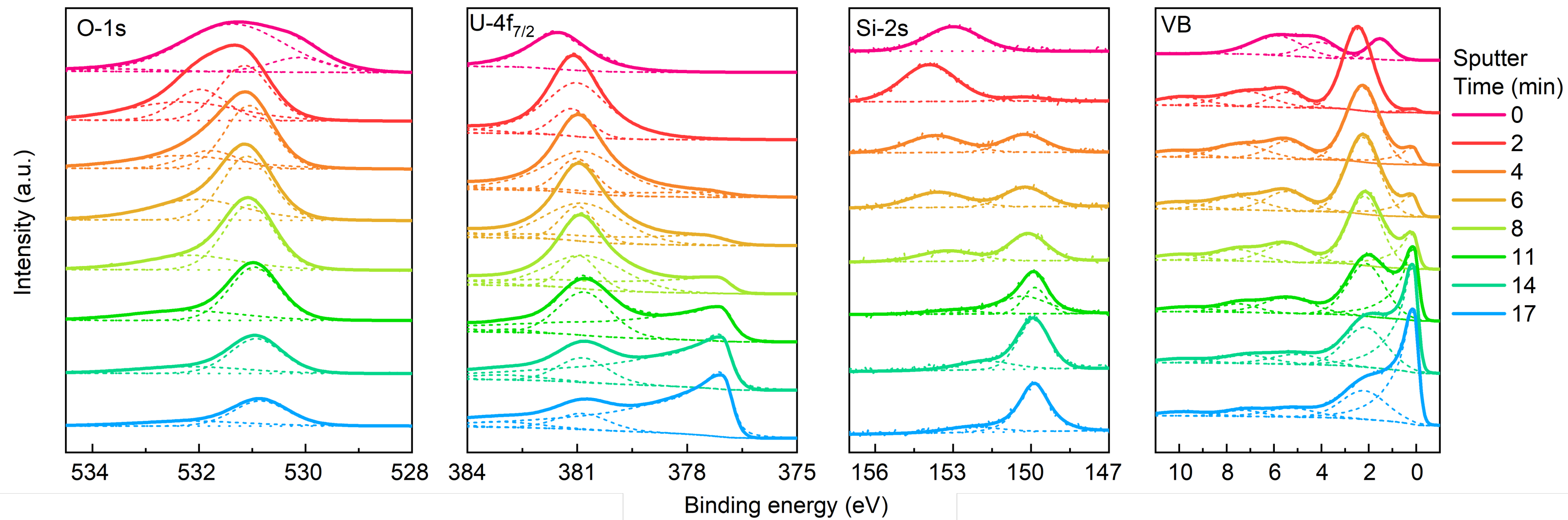

FIGURE 6.16. The fitted O-1s, U-4f, Si-2s, and valence band spectra from poly-crystalline U_3Si_2. Data acquired as a function of depth from the oxidised surface of U_3Si_2. Components used to model each spectra are shown with dashes, background is modelled with dots, and total fit is shown as solid line. Data from SN1707.

The spectra collected from the Si-2s rapidly changes as a function of sputtering time. The Si-O bonding position, situated around 154 eV is significantly reduced after 4 minutes of sputtering, with the photoemission peak shifting to a lower binding energy indicating the si-metal bonding within the sample. The removal of oxide bonds is not as prominent within the U-4$f_{7/2}$ spectra presented in Figure 6.16. Features situated around 381 eV signify the presence of uranium-oxide bonds, with the metallic bonding attributed to uranium-silicon bonds at lower binding energies around 377 eV. The presence of oxygen within the U-4f spectra could indicate that the uranium sites are more susceptible to oxygen bonding when compared to silicon. Furthermore, as the sample used to collect the data is poly-crystalline (SN1707), it could further suggest the formation of metal-oxide bonds in between grain boundaries.

The relative change in the overall component areas is shown in Figure 6.17. This shows how the normalised areas of each core level change as a function of sputtering time. Here, the fitted areas of the U-4f metal, U-4f total oxide, Si-2s metal, Si-2s total oxide, and O-1s total, are all shown. The areas have been normalised to their respective photoionisation cross sections, provided by *Yeh et al.,* [145]. This normalisation allows for the ratio between Si:U to be observed as a function of oxygen contamination, and to further understand how the oxide progresses as a function of depth. From Figure 6.17, it can both the Si-2s metal and U-4f metal areas increase as a function of sputtering time, with the oxide areas for both spectra decreasing after 4 minutes of sputtering. This delay in the oxide content decreasing could be attributed to the surface contamination noted in Figures 6.15 and 6.16. The Si-2s oxide content is less than the metal content after 8 minutes of sputtering, whereas the U-4f oxide continues to be higher than the metal up to 12 minutes of sputtering. This further suggests the increased susceptibility of uranium metal preferentially oxidising over metallic silicon.

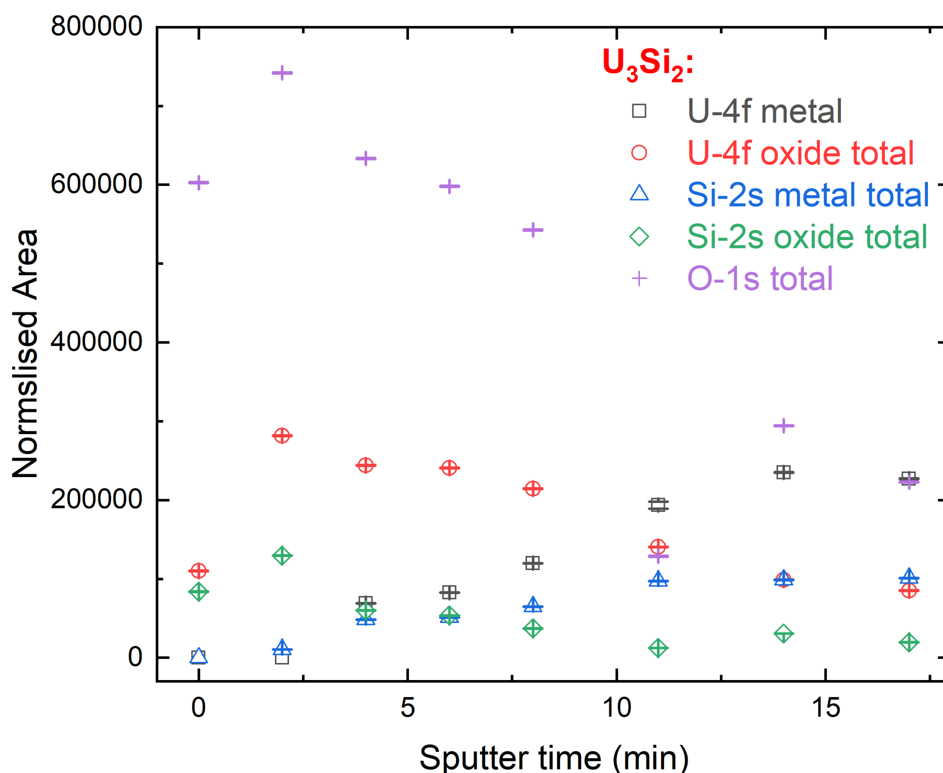

FIGURE 6.17. Graph showing the normalised area intensities from the U-4f, Si-2s, and O-1s states collected from U_3Si_2, after increasing the sputtering time. Data indicates the total fitted areas of each peak, showing the total metal and oxide areas within each spectra. Data collected from SN1707.

Figure 6.18 focusses on the normalised ares extracted from the U-4f, Si-2s, and O-1s core levels. Here, the components responsible for the oxide bonding in uranium and silicon have been separated to provide a deeper understanding into the compounds that may form as a function of surface oxidation. Figure 6.18, showcases the U-4f component areas alongside the O-1s component responsible for U-O bonds. Each area has been normalised to the U-4f U(IV) total area at t = 0. This helps with understanding the stoichiometry of this uranium oxide when compared to the O-1s. Observing the U-4f metal component, shown as black squares, the total area of this component increases with sputter time. This behaviour was also presented in Figure 6.17. The total area of the U-4f U(IV) component increases initially, then after 2 minutes of sputtering the total area decreases. The secondary U-4f oxide exhibits the same behaviour. After 4 minutes, the O:U ratio between the O-1s and U-4f U(IV) components indicate the presence

of a sub-stoichiometric uranium oxide, with a O:U ratio of 1.97 ± 0.71. As the surface layer are sputtered away, this O:U ratio increases to indicate the formation of a hyper-stoichiometric uranium oxide compound. Table 6.4 indicates the evolution of O:U ratios as a function of time. From this, there is no clear indication of stoichiometric UO_2 forming as an oxide compound.

Table 6.4: O:U ratios calculated from the total areas extracted from the O-1s U-O, and the U-4f U(IV) areas in U_3Si_2, SN1707. Areas have been normalised to the total area of U-4f U(IV) at t = 0.

Sputter time (min)	O-1s U-O area	U-4f U(IV) area	O:U ratio
0	4.95	1.00	0.7 ± 0.1
2	2.92	1.99	1.5 ± 0.1
4	3.57	1.81	1.9 ± 0.2
6	3.31	1.54	2.2 ± 0.2
8	3.40	1.36	2.5 ± 0.3
11	2.76	1.13	2.4 ± 0.2
14	1.87	0.67	2.8 ± 0.3
17	1.41	0.36	3.9 ± 0.4

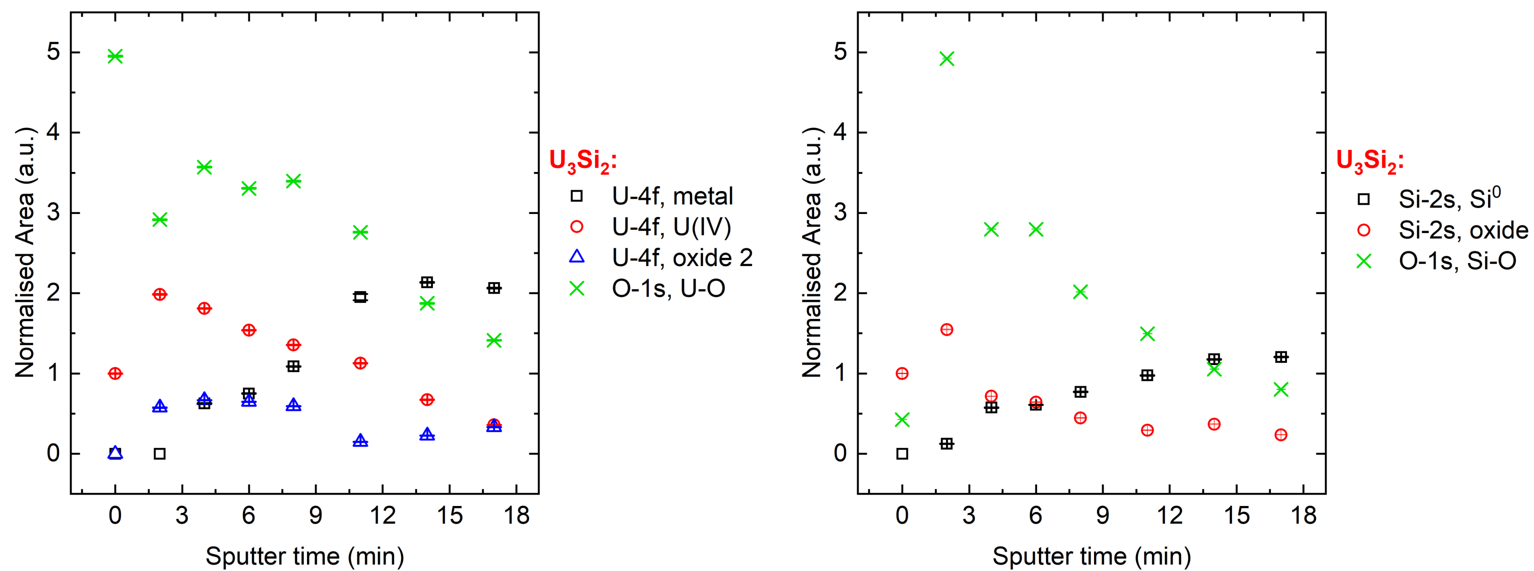

FIGURE 6.18. Graphs showing the normalised areas of U-4f and Si-2s are a function of sputtering time. *left*: Shows the components used to model the U-4f spectra as a function of time, alongside the component responsible for U-O bonding in the O-1s. Areas have been normalised to the total U-4f U(IV) area at t = 0. *right* Shows the components used to model the Si-2s spectra as a function of time, alongside the Si-O bonding component from the O-1s. Areas have been normalised to the total Si-2s oxide area at t = 0. Data taken from SN1707.

The components investigated to further the understanding of silicon oxides present in U_3Si_2 are shown in Figure 6.18. Here the Si-2s metal component, the Si-2s oxide, and the component responsible for Si-O bonding in the O-1s are presented. The area of each component has been normalised to the total area of the Si-2s oxide, shown with red circles, at t = 0. The positioning of this oxide was found to be around 153 eV, indicating a silicon valency of Si^{4+}. Observing the evolution of the O-1s Si-O areas, shown with green crosses, it can be seen that the ratio between this O-1s component and the Si-2s oxide would indicate a sub-stoichiometric oxide present on the undisturbed surface of U_3Si_2. As the sputter cycles commence, the total area of the O-1s Si-O component increases by approximately 11 times it's starting area. This area continues to decrease after 2 minutes of surface sputtering. This mirrors the behaviour of the Si-2s metal component, shown with black squares, which increases with time. Table 6.5 indicates the relative ratio between the O-1s Si-O areas and the Si-2s oxide areas as a function of sputter time. Here, we can see that there is not indication that the oxide components form a stoichiometric silicon oxide compound.

Table 6.5: O:Si ratios calculated from the total areas extracted from the O-1s Si-O, and the Si-2s oxide areas in U_3Si_2, SN1707. Areas have been normalised to the total area of Si-2s oxide at t = 0.

Sputter time (min)	O-1s Si-O area	Si-2s oxide area	O:Si ratio
0	0.436	1.000	0.44 ± 0.04
2	4.921	1.547	3.2 ± 0.3
4	2.79	0.715	3.9 ± 0.4
6	2.80	0.641	4.4 ± 0.4
8	2.016	0.445	4.5 ± 0.4
11	1.495	0.292	5.1 ± 0.5
14	1.052	0.367	2.9 ± 0.3
17	0.803	0.235	3.4 ± 0.3

Alongside tracking the oxide compounds that form, it was also possible to track the stoichiometry between the metal components of the U-4f and Si-2s collected from SN1707. This allows for the uranium silicide phase to be tracked as a function of oxide layer removal. Figure 6.19 showcases the Si:U ratios extracted from the areas of each component across the entire depth profile. From tracking the Si:U stoichiometry as a function of sputtering time, it was found that initially the Si:U ratio after 4 minutes of sputtering was indicating a U_3Si_2 compound with a slightly lower uranium content than expected for pure U_3Si_2. As the sputter time increases, the uranium content within the sample appears to increase. This is indicated by the decreasing Si:U ratio. The final Si:U metallic stoichiometry, measured after 17 minutes of surface sputtering, was calculated to be 0.44 ± 0.04. This is indicating a U-Si phase that is structurally U_3Si_2 with a reduced silicon content.

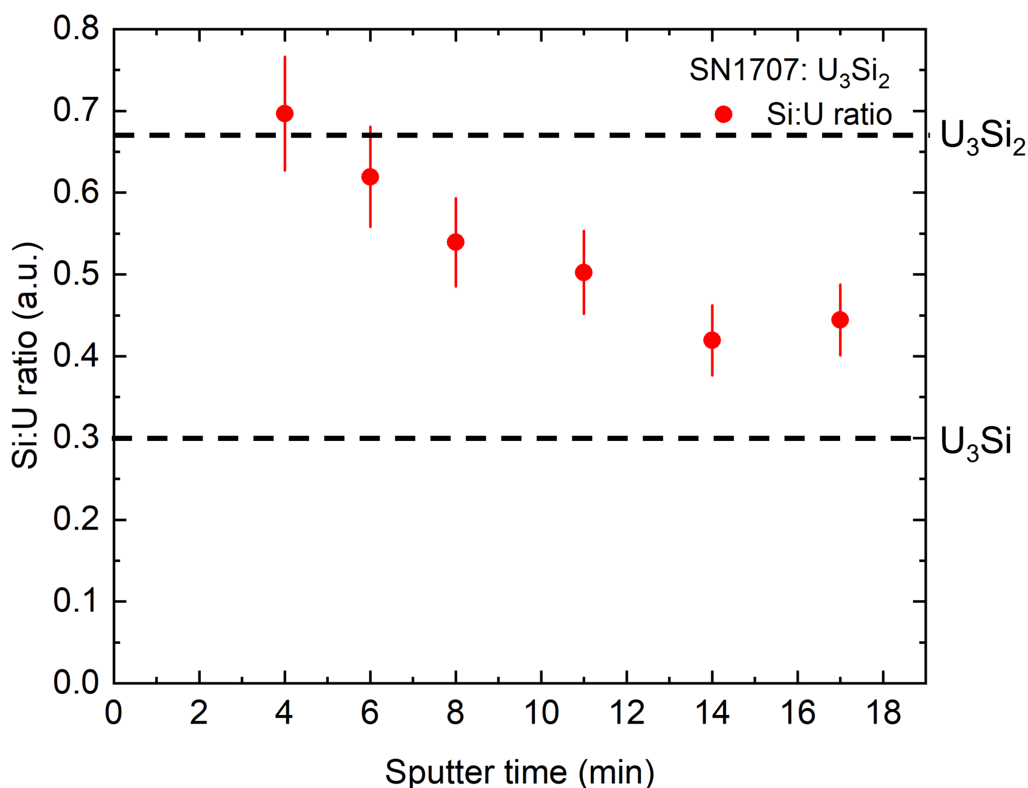

FIGURE 6.19. Graph showing the Si:U ratio as a function of sputtering time. Areas were collected from the metallic U-4f and Si-2s components in U_3Si_2. Data collected from SN1707.

6.3.3 U_3Si_5

The mysterious stabilisation of U_3Si_5 using a uranium deposition power of 30 W indicated that the chemical characterisation of SN1644 was required. The structural characterisation of this sample showed that through the use of specular and off-specular XRD scans, SN1644 is an epitaxial thin film of U_3Si_5 oriented in the [100] direction. Therefore, through the use of x-ray photoelectron spectroscopy, it is possible to further understand how this phase was stabilised, despite not being a replica of it's capped counterpart - SN1512, which was stabilised using a uranium deposition power of 19 W. XPS allows for the local electron bonding to be probed, making it invaluable for understanding the bonding mechanisms that made it possible for this phase to stabilise.

Figure 6.20 shows the data collected from the U-4f and Si-2s spectra of U_3Si_5 using a pass

energy of 6 eV. The data shown here indicates how these two core level orbitals change as a function of sputtering time. Spectra was collected from the surface of U_3Si_5 after each sputtering cycle. Figure 6.20 (a) showcases the data collected from the U-4f, with the U-4$f_{7/2}$ and U-4$f_{5/2}$ labelled. The first spectra collected at 0 minutes, shown in pink, provides significant information about the surface of the sample. Firstly, the intensity of this spectra is heavily reduced when compared to the later spectra collected. This indicates the presence of adsorbed contaminants onto the surface of the sample, which form as a result of exposure to the atmosphere. Secondly, there is a clear splitting that can be seen in the main photoemission peaks around 382 and 392 eV. For the U-4$f_{7/2}$, two components were used to model this spectral feature (Figure 6.21), which were situated at binding energies around 381 and 382 eV, suggesting that the initial surface uranium oxide has a valency of U(V)/U(VI).

As the sputtering cycles begin, substantial changes happen to the U-4f spectra. After 2 minutes of surface sputtering, shown in red, the shake-up satellites associated with the main photoemission peaks are visible around 387 and 398 eV. The presence of the shake-up satellites dwindle as the sputtering time increases, and the U-4f metallic state becomes more prominent. There is a significant increase in the intensity of the metallic bonding state between 14 and 16 minutes of sputtering. This could suggest a sharp interface between the oxide layer and the bulk film. After 18 minutes of surface sputtering, the final photoemission peaks corresponding to the metallic and oxide components are around 377.5 and 381.5 eV, respectively. Comparing to the positions stated by *Ilton et al.,* [83], this suggests uranium valencies of U(0) and U(VI). When compared to the spectra collected after 16 minutes, the oxide component has an increased intensity after 18 minutes. This could be the result of surface oxidation under UHV conditions, contributing to the overall oxygen content within the sample. This type of oxidation was previously seen on the capped samples presented in Chapter 5.

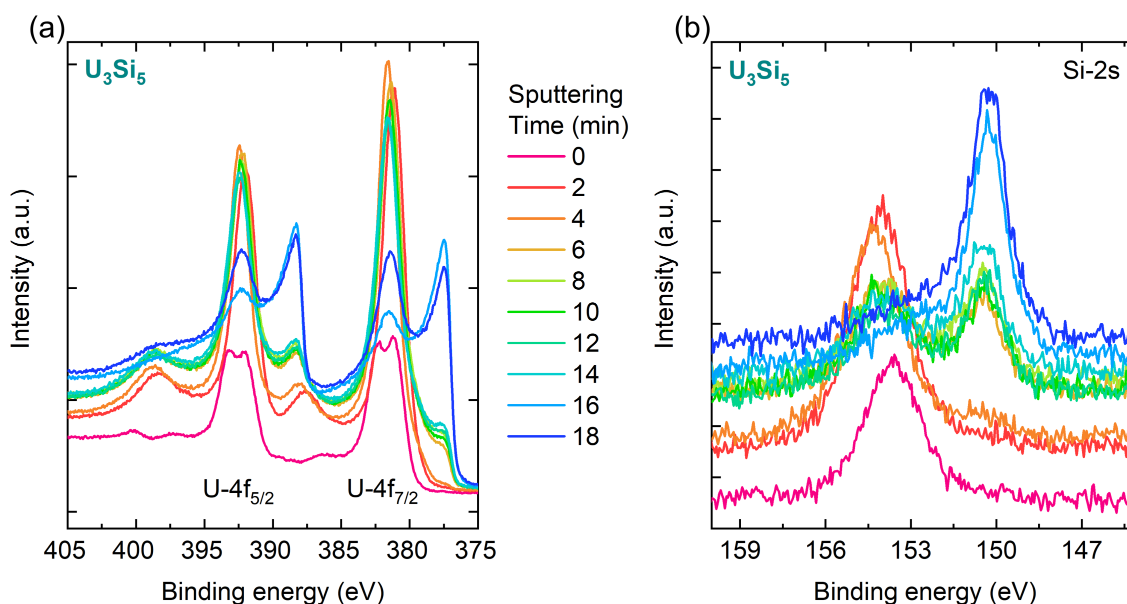

FIGURE 6.20. Graph showing the data extracted from the (a) U-4f and (b) Si-2s spectra of U_3Si_5 as a function of sputter time. Data collected from SN1644.

The spectra collected from the Si-2s spectra evolves in a similar manner to the U-4f of U_3Si_5. The initial data set collected at 0 minutes of sputtering, has a reduced intensity and a peak position shifted to a lower binding energy when compared to later spectra. This affect has been attributed to contaminants adsorbed to the surface of the sample, which is a result of atmospheric exposure. Once removed, the full extent of the Si-O bonds present within the sample are revealed. The binding energy position of the photoemission peak is situated around 153 eV, attributed to Si-O bonding. After 6 minutes of surface sputtering, the oxide and metallic peak intensities are almost equal. Past this point, the metallic site begins to dominate the spectra, continuously increasing as a function of sputtering time. The final binding energy position of the Si-2s photoemission peak is situated around 150 eV. This position is inherent with metallic bonding in silicon, with a valency of Si^0.

The modelled data collected from the O-1s, U-4$f_{7/2}$, Si-2s, and the valence band are shown in Figure 6.21. The use of surface sputtering allowed for the evolution of each spectra to be monitored as a function of sputtering time. Each spectra is colour coordinated with each other, and corresponds to a sputtering time, measured in minutes, which is shown in the legend. The total fit envelope of each spectra is shown with a solid line, the fitting components used to model the data are shown with dashed lines, and the background is shown with dotted lines.

The initial data set, collected at 0 minutes and shown in pink, presents each spectra in their undisturbed state. Each spectra collected from the various core levels and the valence band vary visually when compared to the remaining spectra. This variation in the data is a result of adsorbed compounds on the surface of U_3Si_5, which alters the overall surface bonding and is not representative of the metal-oxide bonding we wish to observe.

The evolution of the O-1s spectra can be observed in the spectra presented in Figure 6.21 on the far left. Through following this spectra as a function of sputtering time, it is shown that the oxygen contamination present within U_3Si_5 (SN1644) is hard to remove but does slowly decrease with the sputtering cycles. The relative intensity of the O-1s spectra does not begin to reduce until after 14 minutes of sputtering. This is reinforced when observing this normalised area data collected from the O-1s, which is presented in Figure 6.22.

When comparing the U-4$f_{7/2}$ and Si-2s spectra in Figure 6.21, it can be seen that there are metal-oxide components present in both spectra. This bonding is less prominent in the Si-2s spectra of U_3Si_5, with the metallic bonding dominating after 12 minutes of sputtering. The U-4$f_{7/2}$ spectra retains the metal-oxide bonding as the dominant component until 16 minutes of sputtering, indicating that the uranium bonding sites are susceptible to oxygen uptake when compared to silicon. The valence band of U_3Si_5 follows the same pattern as the U-4$f_{7/2}$ spectra. There is a dominating peak positioned around 2.5 eV, which corresponds to the U-5f valence electrons in uranium being bonded to oxygen. This peak is strong within the valence band spectra until 16 minutes of surface sputtering. Both the U-4$f_{7/2}$ and valence band spectra are subject to strong oxygen bonding up to this time stamp.

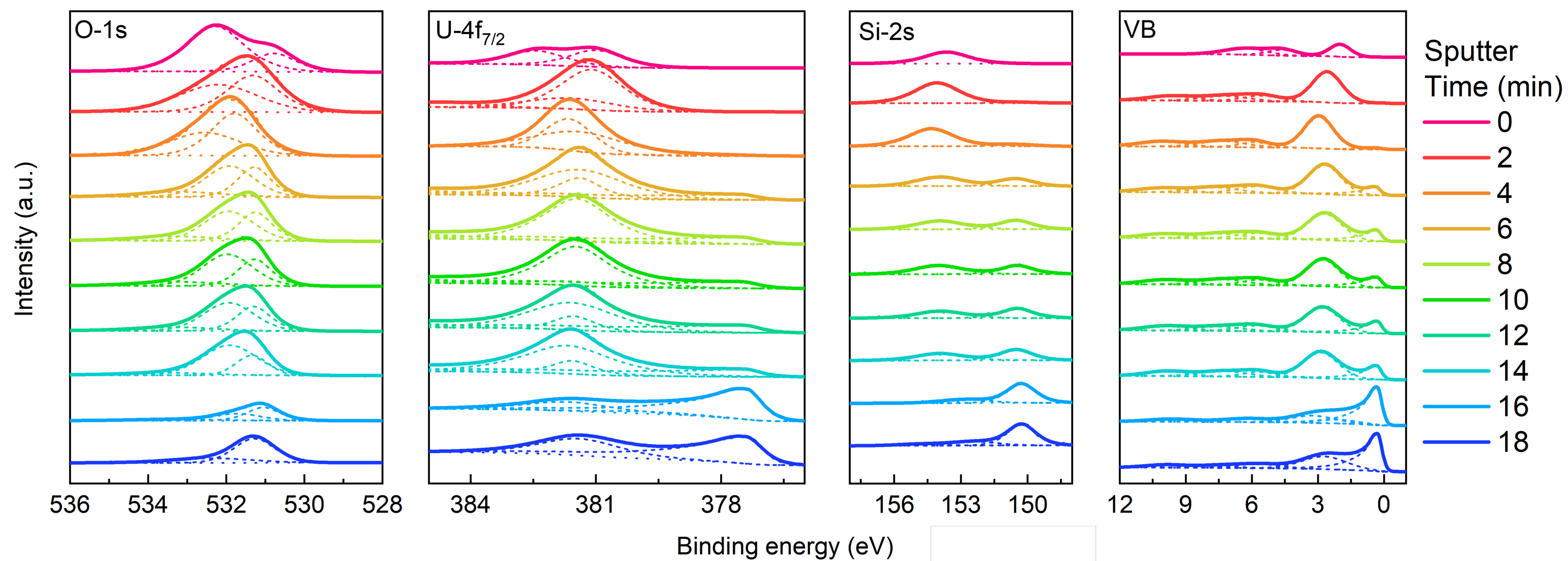

FIGURE 6.21. The fitted O-1s, U-4f, Si-2s, and valence band spectra from poly-crystalline U_3Si_5. Data acquired as a function of depth from the oxidised surface of U_3Si_5. Components used to model each spectra are shown with dashes, background is modelled with dots, and total fit is shown as solid line. Data from SN1644.

Through modelling the spectra collected from the U_3Si_5 depth profiling experiment, it was possible to extract the areas of each component used to model the data. Figure 6.22 shows how the normalised area of each spectra varies as a function of sputtering time. Each data point presented in Figure 6.22 is representative of the area extracted from its corresponding spectra from Figure 6.21. Here, it is clear that the oxygen content within the sample dominates until 16 minutes of sputtering. This behaviour was noted in Figure 6.21, with the O-1s, U-$4f_{7/2}$, and valence band. The U-4f metal, shown with dark grey squares, gradually increases as a function of sputtering time. This component does not exceed the total area extracted from the U-4f oxides, shown with red circles, until 16 minutes of surface sputtering. This behaviour is replicated between the areas extracted from the Si-2s metal (blue triangles) and Si-2s total oxide (green diamonds).

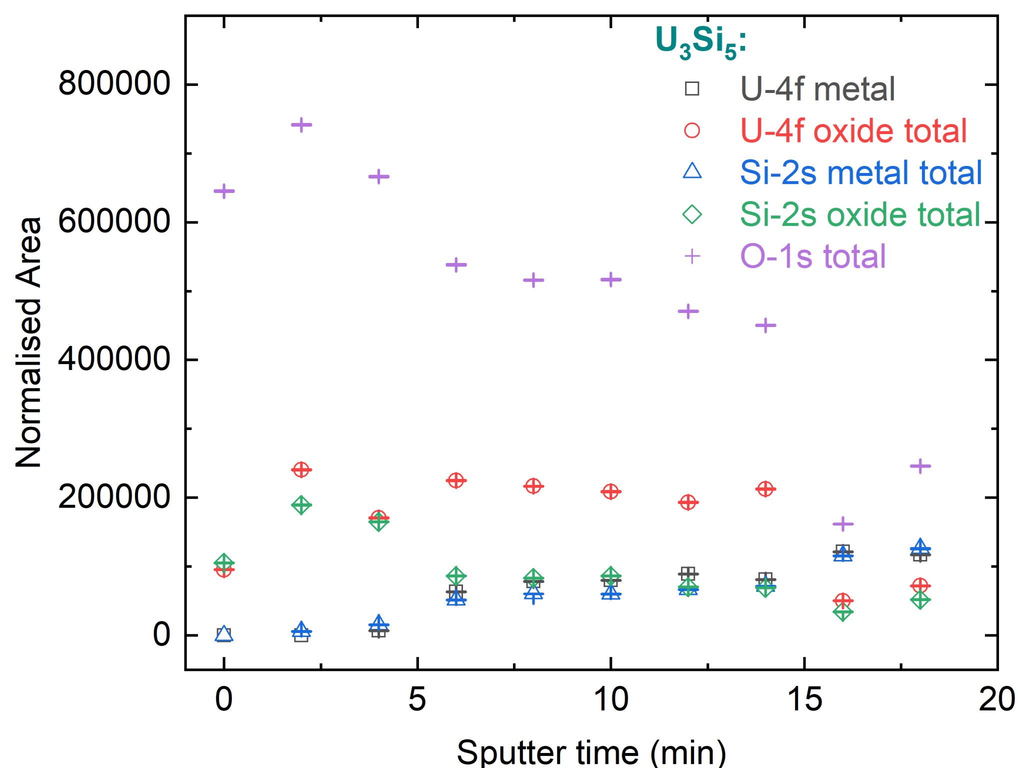

FIGURE 6.22. Graph showing the normalised area intensities from the U-4f, Si-2s, and O-1s states collected from U_3Si_5, after increasing the sputtering time. Data indicates the total fitted areas of each peak, showing the total metal and oxide areas within each spectra. Data collected from SN1644.

To further understand the bonding environments inflicted onto uranium and silicon as a result of oxygen exposure, the U-4f and Si-2s were investigated further. Figure 6.23 showcases the components responsible for oxide bonding in uranium and silicon. Here, the U-O and Si-O components used to model the O-1s have been separated to allow for the oxide compounds in both the U-4f and Si-2s to be probed. The separated U-4f and O-1s U-O components are presented in Figure 6.23. Here, all spectra have been normalised to the total area of the U-4f U(IV) component at t = 0. This allows for the normalised area of the U-4f U(IV) component, shown with red circles, to be equal to 1 when t = 0. Observing the evolution of this component, it can be seen that the total area increases with some fluctuations, before decreasing again after 8 minutes of surface sputtering. With the exception of the area modelled after 8 minutes of sputter time, the U-4f oxide 2 component, shown with blue triangles, exhibits a similar behaviour. Much like the two U-4f components, the component responsible for the U-O bonding in the O-1s, shown with green crosses, has fluctuations in the total area modelled. The area of this component does decrease with increasing sputter time. The total area collected from the U-4f metallic component, shown with black squares, increases with sputter time. This indicates the presence of the metallic film situated below the oxidised surface.

The normalisation with the U-4f U(IV) component allows for the stoichiometry between the O-1s U-O component to be monitored as a function of sputter time. Table 6.6 indicates the normalised areas as a function of time, with the O:U ratios calculated. From the ratios calculated it can be seen that the U-O oxide forming is a hyper-stoichiometric compound. There is little indication that the U-O oxide compound that forms is stoichiometric UO_2. Furthermore, the ratio between oxygen and uranium does not increase nor decrease in a linear fashion. The ratios calculated suggest the O:U contamination fluctuates throughout the surface oxide layer.

Table 6.6: O:U ratios calculated from the total areas extracted from the O-1s U-O, and the U-4f U(IV) areas in U_3Si_5, SN1644. Areas have been normalised to the total area of U-4f U(IV) at t = 0.

Sputter time (min)	O-1s U-O area	U-4f U(IV) area	O:U ratio
0	3.14	1.000	3.1 ± 0.3
2	7.30	3.20	2.3 ± 0.2
4	7.67	1.95	3.9 ± 0.4
6	5.09	3.59	1.4 ± 0.1
8	4.35	3.99	1.1 ± 0.1
10	3.59	3.31	1.1 ± 0.1
12	4.23	2.96	1.4 ± 0.1
14	3.84	3.51	1.1 ± 0.1
16	2.06	0.846	2.4 ± 0.2
18	3.74	1.36	2.8 ± 0.3

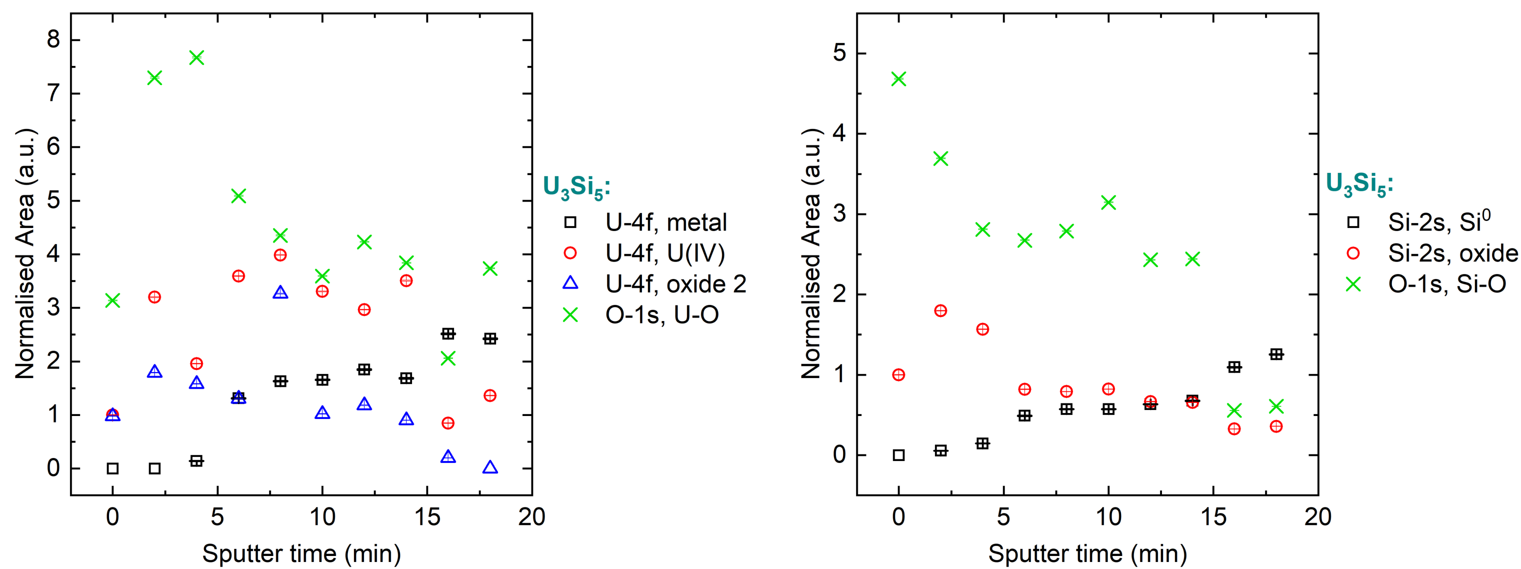

FIGURE 6.23. Graphs showing the normalised areas of U-4f and Si-2s are a function of sputtering time. *left*: Shows the components used to model the U-4f spectra as a function of time, alongside the component responsible for U-O bonding in the O-1s. Areas have been normalised to the total U-4f U(IV) area at t = 0. *right* Shows the components used to model the Si-2s spectra as a function of time, alongside the Si-O bonding component from the O-1s. Areas have been normalised to the total Si-2s oxide 2 area at t = 0. Data taken from SN1644.

The relative oxide areas that contribute to the formation of Si-O bonds were also probed. Figure 6.23 also presents the normalised areas extracted from the Si-2s and O-1s of U_3Si_5 (SN1644). Here, the areas have all been normalised to the total area of the Si-2s oxide, shown with red circles, when t = 0. This equates the first area of the Si-2s oxide to 1 initially. Much like the total areas presented in Figure 6.22, here the components responsible for the Si-O bonds in SN1644 have been highlighted alongside the metallic component in the Si-2s spectra. Observing the total area of the Si-2s metal, shown as black squares, it can be seen that the area of this component increases with sputtering time. The evolution of the Si-2s oxide area has some minor fluctuations after 2 minutes of sputtering time. However, the total area decreases with sputtering time, indicating the removal of these Si-O bonds in the Si-2s. The overall area of the O-1s Si-O component, shown with green crosses, also decreases as a function of time. There is a slight increase in the area after 10 minutes of sputtering, which does align with an increase in the Si-2s oxide area. As the sample was kept under UHV conditions, this increase in overall oxide area could be attributed to minor oxide impurities within the XPS chamber. Table 6.7 indicates the O:Si ratio calculated as a function of sputter time. From the values presented, there is an indication that a compound similar to SiO_2 may have formed at the very surface of SN1644. The remaining O:Si ratios indicate the formation of a Si-O compound with an increased oxygen content, compared to silicon.

Table 6.7: O:Si ratios calculated from the total areas extracted from the O-1s Si-O, and the Si-2s oxide areas in U_3Si_5, SN1644. Areas have been normalised to the total area of Si-2s oxide at t = 0.

Sputter time (min)	O-1s Si-O area	Si-2s oxide area	O:Si ratio
0	4.68	1.000	4.7 ± 0.5
2	3.69	1.797	2.1 ± 0.2
4	2.81	1.565	1.8 ± 0.2
6	2.67	0.819	3.3 ± 0.3
8	2.79	0.791	3.5 ± 0.4
10	3.15	0.820	3.8 ± 0.4
12	2.431	0.666	3.7 ± 0.4
14	2.442	0.656	3.7 ± 0.4
16	0.556	0.326	1.7 ± 0.2
18	0.607	0.358	1.7 ± 0.2

Alongside tracking the oxide content within U_3Si_5, it was also possible to calculate the stoichiometry between the metallic components of U-4f and Si-2s as a function of sputter time. Figure 6.24 showcases these stoichiometries extracted from the metallic component areas of U-4f and Si-2s. The Si:U ratio calculated after 4 minutes of surface sputtering indicates the formation of a hyper-stoichiometric USi_2 phase. As the sputtering time increases, the Si:U ratio decreases, indicating the formation of a hypo-stoichiometric USi phase, with a lower silicon content. The final Si:U ratio presented in Figure 6.24, indicates that a more stoichiometric phase of uranium

monosilicide (USi), may have formed as part of the oxide layer growing on SN1644. This Si:U ratio does not match the structural characterisation conducted on SN1644, which was found to be an [100] oriented epitaxial U_3Si_5 sample. However, the uranium deposition power used to stabilise SN1644 was 30 W, which has been previously used to stabilise U_3Si_2. Therefore, the stabilisation could stem from the oxidation of the excess uranium content within the sample, resulting in the formation of USi within the surface oxide layer.

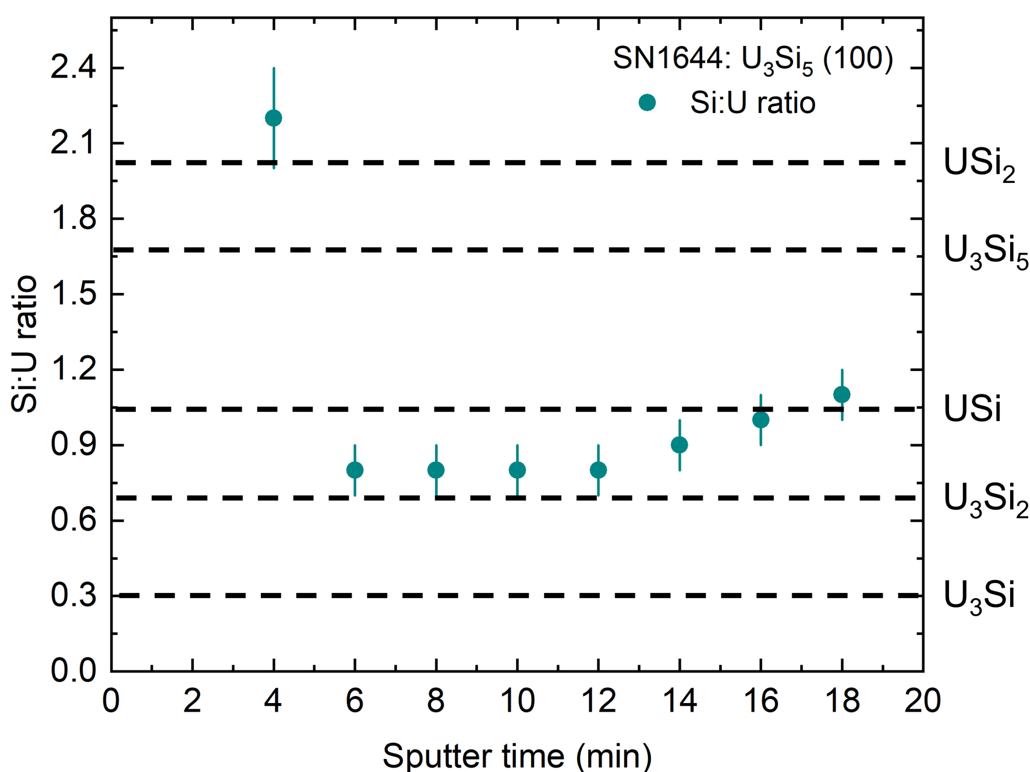

FIGURE 6.24. Graph showing the Si:U ratio as a function of sputtering time. Areas were collected from the metallic U-4f and Si-2s components in U_3Si_5. Data collected from SN1644.

6.3.4 α-USi$_2$

The oxidation of uncapped $\alpha - USi_2$ stabilised on [001] CaF_2 at 800°C was investigated using XPS. The sample used to investigate the ambient surface oxidation was SN1645. The structural characterisation of SN1645 showed that this sample was teteragonal $\alpha - USi_2$ stabilised in the

[001] direction. Previous chemical characterisation conducted on this uranium silicide phase indicate that the stoichiometry was closer to USi, indicating a lower silicon content than expected for $\alpha - USi_2$. The use of XPS depth profiling allows for the stoichiometry of this phase to be probed further.

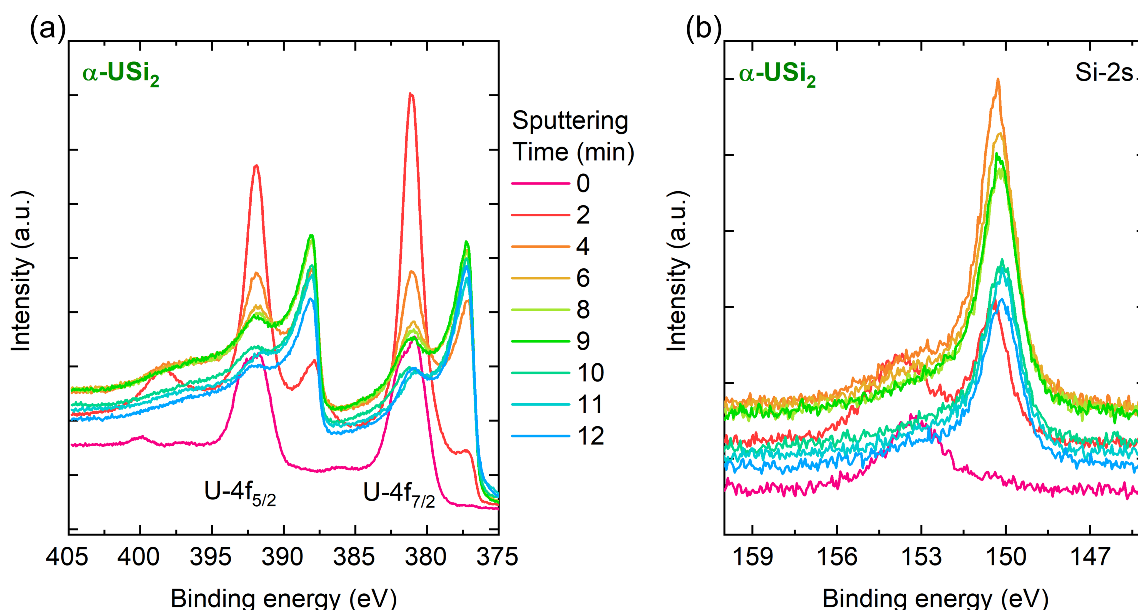

FIGURE 6.25. Graph showing the data extracted from the (a) U-4f and (b) Si-2s spectra of α-USi_2 as a function of sputter time. Data collected from SN1645.

Figure 6.25 shows the calibrated spectra obtained from the U-4f and Si-2s core levels using a pass energy of 6 eV. Each spectra presented shows the state of the core level as a function of sputtering time. Figure 6.25 (a) shows the U-4f spectra of $\alpha - USi_2$ with the U-4$f_{7/2}$ and U-4$f_{5/2}$ states labelled. The initial spectra, shown in pink, indicates the undisturbed spectra obtained from the surface of SN1645. The lower intensity is a result of the adsorbed compounds on the surface of the sample. These impurities are removed once the surface sputtering has started. The spectra after 2 minutes of sputtering has intense photoemission peaks situated around 381 and 392 eV. These binding energy positions are representative of uranium-oxide bonds. The work conducted on uranium oxide by *Ilton et al.,* [83] indicates that this positioning could be a uranium oxide with a valency of U(V). Alongside the oxide components, there are smaller asymmetric feature situated around 377 eV in the U-4$f_{7/2}$ and around 388 eV in the U-4$f_{5/2}$. This represents the metallic bonding in the sample. The appearance of this feature after 2 minutes of surface sputtering further suggests the thin oxide layer that grows on the surface of

[001] $\alpha - USi_2$. As the surface sputtering continues, the presence of the metallic photoemission peak gets more intense, resulting in the reduction of the oxide component. After 12 minutes of surface sputtering, the asymmetric component is completely dominating the U-4f spectra, with a binding energy situated around 377.1 eV. The oxide component in the U-4$f_{7/2}$ is around 381.0 eV.

The Si-2s spectra behaves in a very similar manner to the U-4f of $\alpha - USi_2$. The lower intensity spectra at 0 minutes of sputtering is representative of surface contaminates adsorbed to the undisturbed surface of SN1645. After 2 minutes of sputtering, the Si-2s spectra has a broader photoemission peak around 153 eV, and a sharper peak situated at a lower binding energy of 150 eV. The peak at 153 eV is characteristic of Si-O bonding. The work conducted on silicon oxides by *Himpsel et al.,* [169], would suggest a Si-O bond with a valency of Si^{4+}. The sharper peak at 150 eV is inherent in metallic silicon bonds, indicating the bonding between silicon and uranium within the sample. As the sputtering time increases, the oxide component within the Si-2s is significantly reduced, having almost no dominance in the spectra after 2 minutes of sputtering. The spectra background is increased from 4 to 9 minutes of surface sputtering, after this cycle, the background reduces. This increased background could be due to Si-O bonds having an influence over the spectra without possessing enough intensity to form a full photoemission peak. After 9 minutes of sputtering, only the metallic photoemission peak is present with the Si-2s spectra, with a binding energy position around 150 eV.

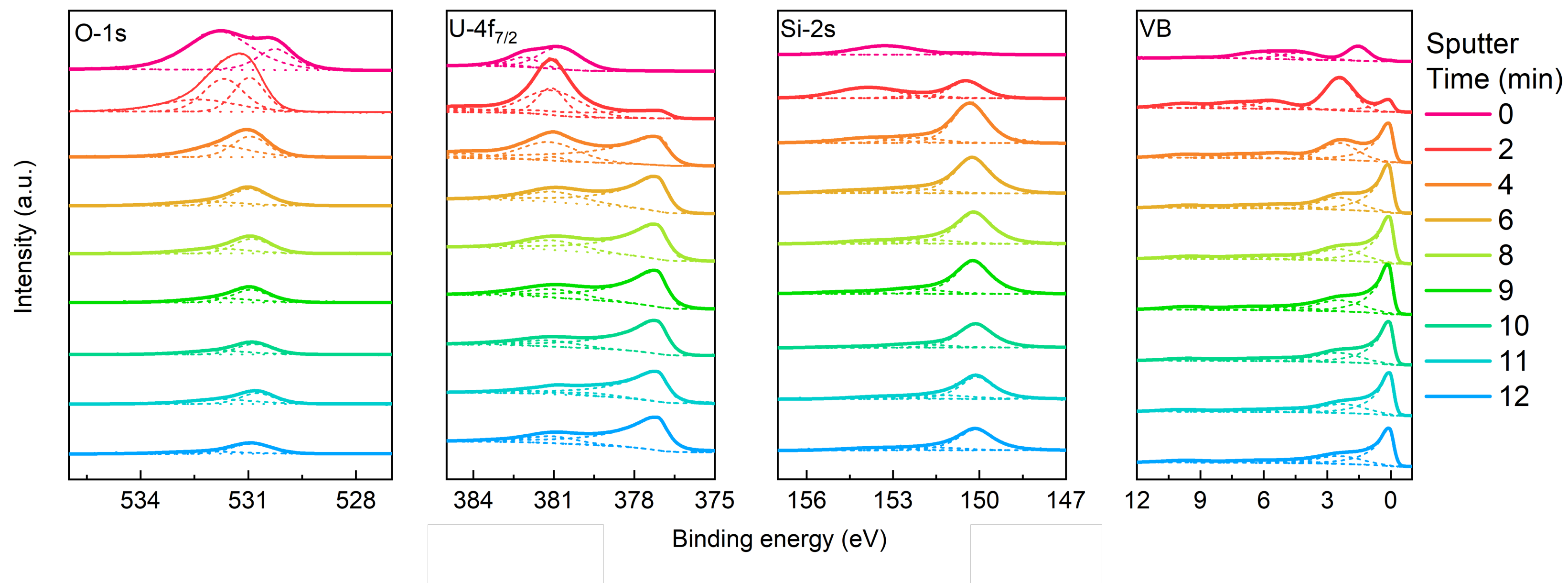

FIGURE 6.26. The fitted O-1s, U-4f, Si-2s, and valence band spectra from [001] α-USi_2 single crystal. Data acquired as a function of depth from the oxidised surface of α-USi_2. Components used to model each spectra are shown with dashes, background is modelled with dots, and total fit is shown as solid line. Data from SN1645.

The fitted spectra collected from the O-1s, U-4f$_{7/2}$, Si-2s, and valence band of $\alpha - USi_2$ are presented in Figure 6.26. The fit envelope of the each spectra is shown with a solid line, fitting components are shown with dashed lines, and the background with dotted lines. Each spectra is colour coordinated to indicate the same sputtering cycle. The legend for the figure shows the time for each sputtering cycle in minutes.

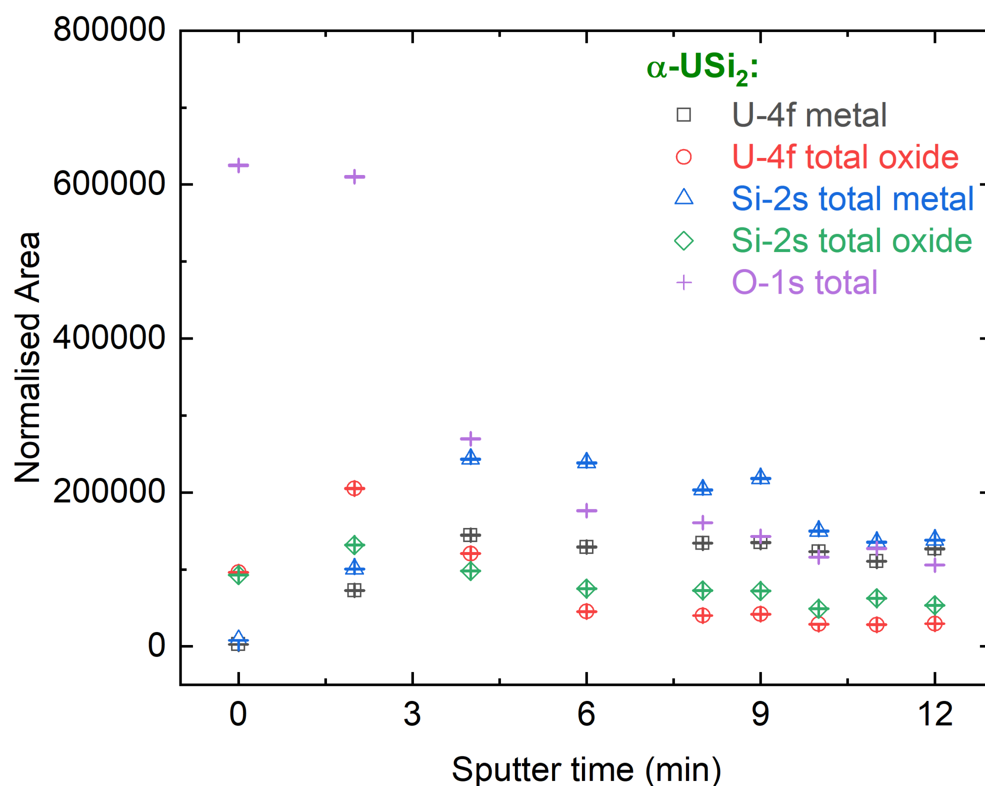

FIGURE 6.27. Graph showing the normalised area intensities from the U-4f, Si-2s, and O-1s states collected from α-USi_2, after increasing the sputtering time. Data indicates the total fitted areas of each peak, showing the total metal and oxide areas within each spectra. Data collected from SN1645.

Observing the evolution of the O-1s spectra collected from SN1645, it can be seen that after 4 minutes of sputtering, the overall intensity of the spectra is significantly reduced. The positioning of the O-1s photoemission peak is around 531 eV, indicating metal-oxide bonds. This binding energy is shifted in the first two spectra collected from the O-1s. The initial spectra, shown in pink, showcases the O-1s from an undisturbed state. The variation, and broadness in the spectra

is a result of adsorbed contaminants which have formed on the surface of SN1645 as a result of atmospheric exposure. The spectra collected after 2 minutes of surface sputtering required three components to model data. The positions of these components positioned around: 530, 531, and 532 eV. The component at 532 eV corresponds to the Si-O bonding in the sample, this bonding is also present in the Si-2s spectra. The remaining O-1s components correspond to metal-oxide bonding, which is attributed to the two component oxide peak present in the U-4$f_{7/2}$ spectra.

The removal of metal-oxide bonds can be seen with the evolution of the valence band of $\alpha - USi_2$. After 2 minutes of sputtering, the valence band spectra has features that stem from the U-5f valence electrons at the Fermi-edge (0 eV), and features that are a result of the U-5f valence electrons being bound to oxygen around 2.5 eV. Features between 3-9 eV represent further bonding between uranium and oxygen. This spectral feature is noted by work conducted by *Van den Berghe et al.,* [168] on uranium oxide layers. As the sputtering time increases, the intensity of the asymmetric metallic peak at the Fermi-edge increases, suggesting the breaking of oxygen bonds. This valence band feature is also shown in work conducted by *Fujimori et al.,* [172], when observing the valence band structure of the U/Si(111) interface. The evolution of both the fitted U-4$f_{7/2}$ and Si-2s spectra are also presented in Figure 6.26. After 6 minutes of sputtering, the metallic components modelling both spectra dominate the data sets. This aligns well with the evolution of the O-1s and valence band spectra, with the significant decrease in oxygen content.

Figure 6.26 shows the normalised area for the metal and oxide components extracted from the U-4f, Si-2s, alongside the total normalised area from the O-1s as a function of sputtering time. The areas have been normalised to their respected photoionisation cross sections, provided by *Yeh et al.,* [145]. Oberving the total areas from each core level provides an indication into how the sample is behaving as the surface oxide layer is being removed. Through following the total area of the O-1s, indicated with purple crosses, it is shown that the surface sputtering is reducing the total area as a function of time. The total O-1s area is a summation of the components used to model the U-O and Si-O bonds present within this core level. The area continues to decrease, with the exception of a slight fluctuation in the total area after 11 minutes of surface sputtering. This minor increase could be due to the surface being sensitive to residue oxygen molecules within the UHV XPS system. Areas extracted from the U-4f spectra have been segregated into two categories: U-4f metal, shown as dark grey squares, and U-4f total oxide, indicated with red circles. Following the total normalised areas of these components indicates how the U-4f is evolving as a function of surface oxide removal. From Figure 6.27, it is shown that after 4 minutes of surface sputtering, the U-4f metal component exceeds the total U-4f oxide area. This behaviour is replicated in the Si-2s, with the metallic component, shown with blue triangles, dominating after 4 minutes. The total areas collected from each spectra appear to plateau after 6 minutes of surface sputtering, with a slight decrease in the overall Si-2s metal area. This could suggest that

the bulk metallic film is being sputtered away, reducing the metallic content. Furthermore, the O-1s U-O and U-4f U(IV) areas increase after 12 minutes of sputtering, this behaviour is present in the spectra presented in Figure 6.26. Once again, as the sample was not exposed to additional oxygen during the depth profiling experiment, the source of the oxygen influence on the total oxide areas must be attributed to residue oxygen molecules in the UHV XPS system.

Table 6.8: O:U ratios calculated from the total areas extracted from the O-1s U-O, and the U-4f U(IV) areas in α-USi_2, SN1645. Areas have been normalised to the total area of U-4f U(IV) at t = 0.

Sputter time (min)	O-1s U-O area	U-4f U(IV) area	O:U ratio
0	2.11	1.000	2.1 ± 0.1
2	4.66	1.97	2.4 ± 0.2
4	1.98	0.387	5.1 ± 0.5
6	1.78	0.584	3.1 ± 0.3
8	1.44	0.579	2.5 ± 0.3
9	1.281	0.517	2.5 ± 0.2
10	0.989	0.365	2.7 ± 0.3
11	0.958	0.179	5.4 ± 0.5
12	1.059	0.429	2.5 ± 0.2

By separating the uranium and silicon components, it was possible to probe the potential oxide compounds that may form on the surface of $\alpha - USi_2$ further. Figure 6.28 indicates the normalised areas relating to the uranium states, on the left, and the silicon bonded states on the right. The areas collected from the O-1s core level have been separated into two components: Si-O bonds which have a binding energy of 532 eV, and U-O bonds which are positioned around 530 eV. The separation of these components helps understand the silicon and uranium oxides that may form. Observing the areas collected from the U-4f and O-1s levels, it is indicated that initially a hyper-stoichiometric UO_2 compound has formed. Here, each area has been normalised to the total U-4f U(IV) oxide area when t = 0. This indicates that a U-O oxide has formed on the very surface of $\alpha - USi_2$. Table 6.8 indicates the relative ratio between oxygen and uranium as a function of sputtering time. From the O:U ratios presented in Table 6.8, it is shown that the uranium oxides forming are potentially hyper-stoichiometric phases, with increased oxygen content. The oxygen content is significantly larger when compared to the contribution from the U-4f state after 11 minutes of sputtering. This ratio reduces after 12 minutes due to the increased U-4f U(IV) oxide area.

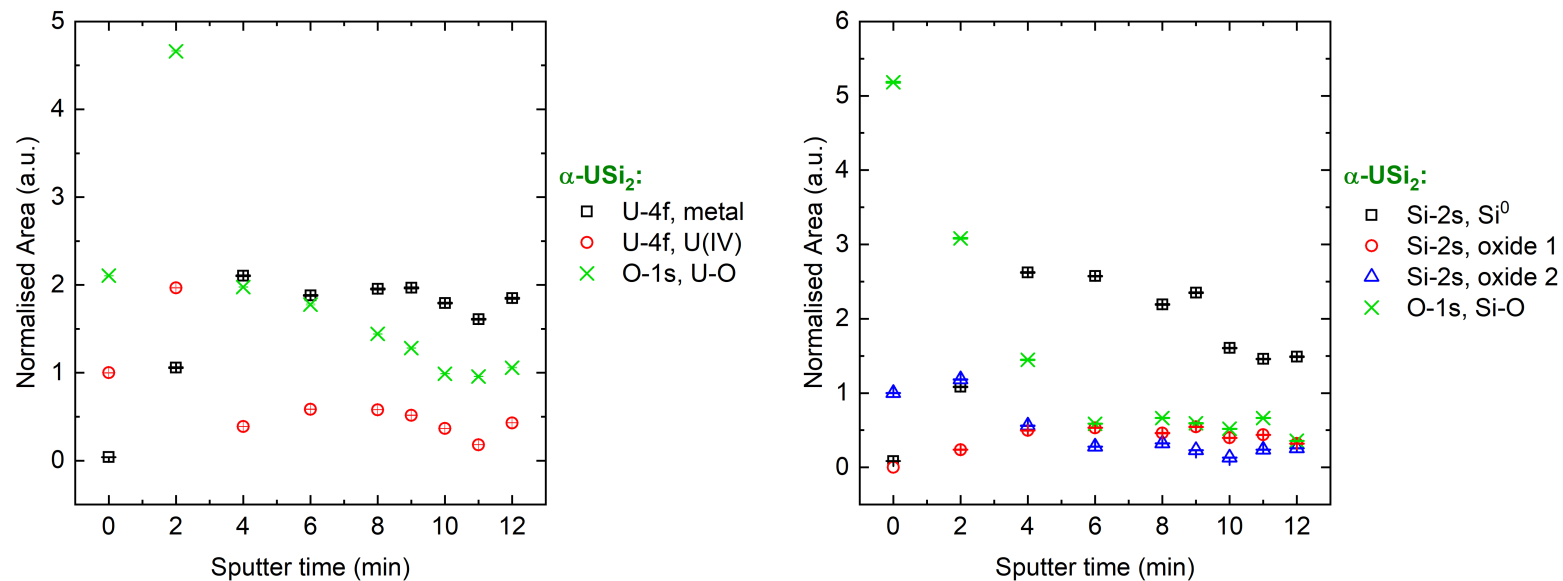

FIGURE 6.28. Graphs showing the normalised areas of U-4f and Si-2s are a function of sputtering time. *left*: Shows the components used to model the U-4f spectra as a function of time, alongside the component responsible for U-O bonding in the O-1s. Areas have been normalised to the total U-4f U(IV) area at t = 0. *right* Shows the components used to model the Si-2s spectra as a function of time, alongside the Si-O bonding component from the O-1s. Areas have been normalised to the total Si-2s oxide 1 area at t = 0. Data taken from SN1645.

The potential silicon oxides that may form as a result of $\alpha-USi_2$ surface oxidation were also probed. Figure 6.28 presents the normalised areas of components extracted from the Si-2s and the O-1s. Here, each component presented has been normalised to the total area of Si-2s oxide 2 when t = 0, equating the entire area to 1. This allows for the relative stoichiometries of the oxides forming to be tracked. Si-2s oxide 2, shown with blue triangles, has a binding energy around 153 eV. This particular binding energy position is attributed to silicon valencies of Si^{4+} [171]. The silicon oxide shown with red circles, Si-2s oxide 1s, has a binding energy around 151 eV, with the Si-2s metal component, shown with black squares, having a binding energy around 150 eV. Much like the uranium oxide bonds, it is possible to track the evolution of the Si-O related bonds as a function of sputter time. Similar to the total O-1s data presented in Figure 6.27, the component responsible for Si-O bonds in the O-1s core level decreases as a function of sputter time. After 4 minutes of sputtering time, the Si-2s metal component exceeds the area of the O-1s Si-O and both Si-2s oxide components. After 6 minutes of sputtering, the total Si-2s metal area begins to decrease. This behaviour may indicate that the metal film below the oxide surface is being sputtered away. Furthermore, after 6 minutes of sputtering, the Si-2s oxide 1 exceeds the normalised area of Si-2s oxide 2. Table 6.9 indicates the relative ratios calculated from the normalised areas of Si-2s oxide 2 and O-1s Si-O. The values presented here indicate a hyper-stoichiometric SiO_2 compound with an increased oxygen content.

Table 6.9: O:Si ratios calculated from the total areas extracted from the O-1s Si-O, and the Si-2s oxide areas in αUSi_2, SN1644. Areas have been normalised to the total area of Si-2s oxide 2 at t = 0.

Sputter time (min)	O-1s Si-O area	Si-2s oxide area	O:Si ratio
0	5.18	1.000	5.2 ± 0.5
2	3.08	1.183	2.6 ± 0.3
4	1.447	0.561	2.6 ± 0.3
6	0.587	0.278	2.1 ± 0.2
8	0.665	0.322	2.1 ± 0.2
9	0.593	0.232	2.6 ± 0.3
10	0.519	0.132	3.9 ± 0.4
11	0.665	0.237	2.8 ± 0.3
12	0.357	0.257	1.4 ± 0.1

In addition to probing the potential U-O and Si-O compound that may form on the surface of $\alpha-USi_2$, it was possible to track the metallic stoichiometry as a function of depth. Through comparing the total areas collected from the metallic components in the U-4f and Si-2s, the ratio between Si:U was found. Figure 6.29 presents the Si:U ratios calculated after each sputter cycle. From analysing the Si:U ratio, it was found that at the very surface of SN1645, a hypo-stoichiometric phase similar to USi_3 has formed. As the oxide layers are sputtered away, this Si:U ratio decreases. The Si:U ratio after 4 minutes of sputtering could indicate the formation of

a compound similar to U_3Si_5. After 12 minutes of surface sputtering, the Si:U ratio is 1.1 ± 0.1 indicating the formation of a compound similar to USi. This ratio aligns with the characterisation of $\alpha-USi_2$, presented in Chapter 5, which suggested that tetragonal $\alpha-USi_2$ had a stoichiometry closer to 1. Where the stoichiometry between the metallic components of U-4f and Si-2s do not indicate stoichiometric $\alpha-USi_2$, the formation of uranium silicide phases with increased silicon content does suggest that the uranium sites are far more susceptible to forming uranium-oxygen bonds when compared to the oxide bonds formed between silicon and oxygen.

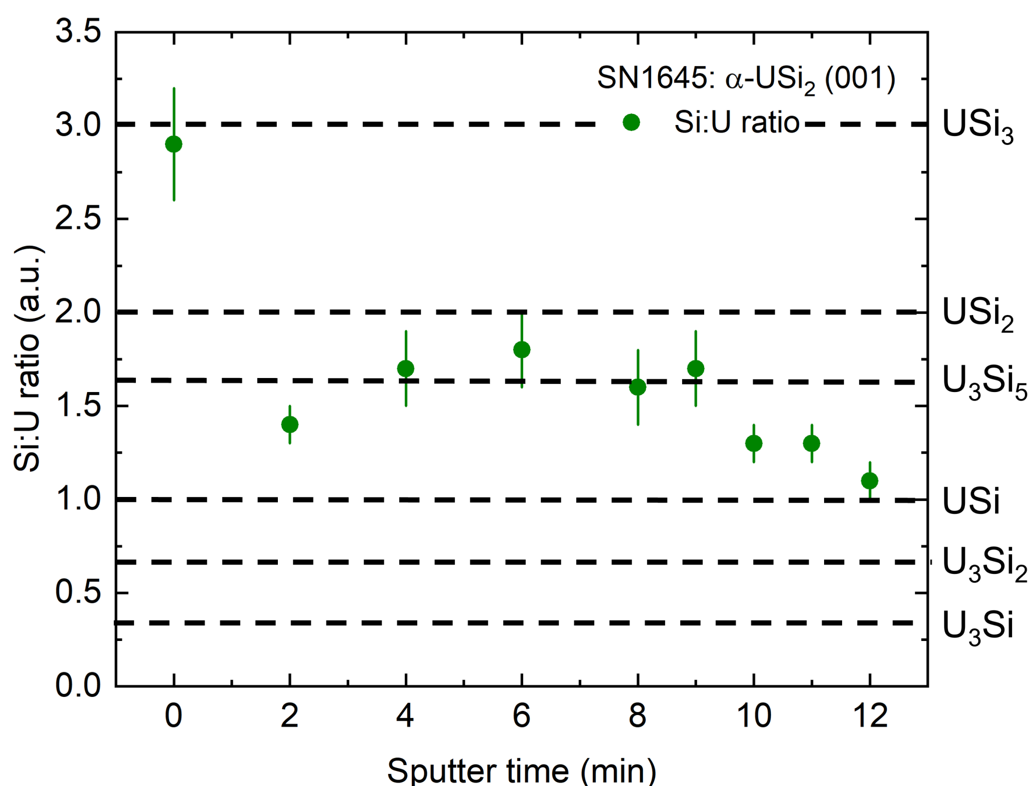

FIGURE 6.29. Graph showing the Si:U ratio as a function of sputtering time. Areas were collected from the metallic U-4f and Si-2s components in α-USi_2. Data collected from SN1645.

6.3.5 USi_3

The surface oxidation of uranium trisilicide, USi_3 was further investigated using XPS depth profiling techniques. As the uranium silicide phase with the highest silicon content, it is impor-

tant to understand the oxidation mechanisms of this compound, and how it compares with the remaining, lower silicon content uranium silicides. The high angle XRD data extracted from SN1700, indicates that the oxide layer that forms causes minimal changes to the structure of USi_3. Through the use of Ar sputtering, oxide layers were removed from the surface of SN1700 to further investigate the oxidation layer, providing an insight into the valency of both the uranium and silicon oxides that could form as a function of depth. Figure 6.30 shows the calibrated spectra collected from the U-4f and Si-2s of USi_3 using a pass energy of 6 eV. The spectra collected after each sputtering cycle has been plotted on top of each other to help understand how the data evolves as the oxide layers are sputtered away.

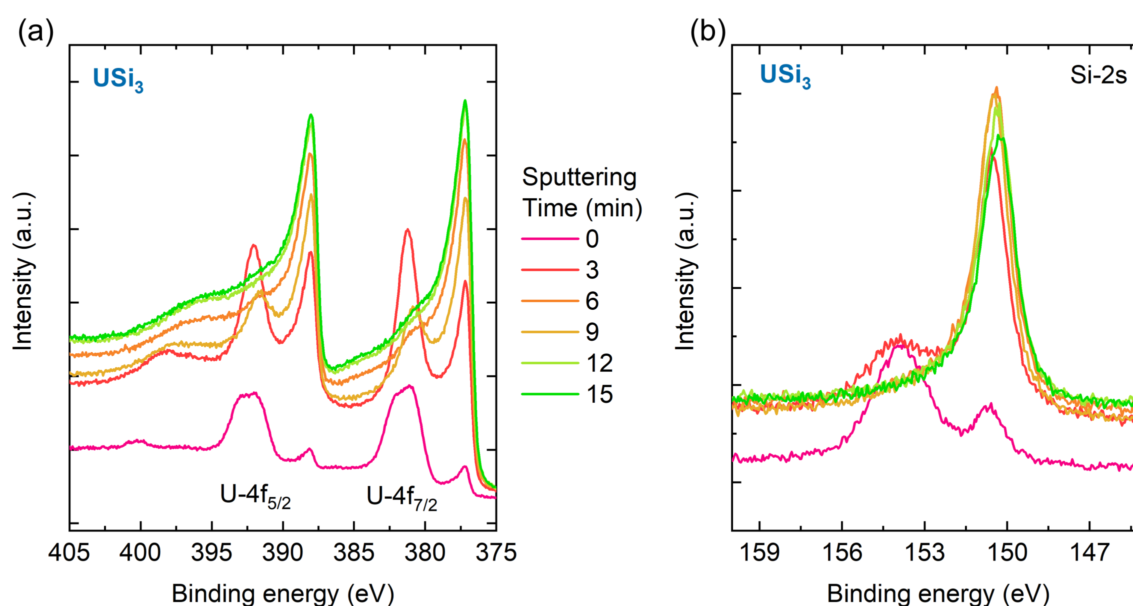

FIGURE 6.30. Graph showing the data extracted from the (a) U-4f and (b) Si-2s spectra of USi_3 as a function of sputter time. Data collected from SN1700.

Figure 6.30 (a) shows the U-4f spectra extracted from USi_3 with the U-4$f_{7/2}$ and U-4$f_{5/2}$ labelled. The first spectra collected at 0 minutes, shown in pink, has a significantly lower intensity when compared to the later data sets. Much like the uranium silicide phases presented before, this lowered intensity, and broadening in the U-4f spectra is due to adsorbed surface contaminants. These impurities are removed once the sputtering cycles begin, which is noted in the subsequent spectra collected from USi_3. A feature that is prominent in the U-4f spectra at 0 minutes, is the presence of metallic states which are situated at binding energies around 377 and 388 eV. After 3 minutes of surface sputtering, there are two prominent photoemission peaks in the

U-4$f_{7/2}$ at binding energies of 377 and 381 eV. Comparing these positions to the work conducted by *Ilton et al* [83] on uranium oxides, these positions are corresponding to U(0) and U(V) valencies. The evolution from oxide dominated, to metallic dominated spectra occurs after 6 minutes of surface sputtering, this is shown in orange. After 9 minutes of surface sputtering, the U-4f oxide component is not prominent enough in the spectra to form a strong photoemission peak. The metallic counterpart of the U-4f is situated around 377 eV for the U-4$f_{7/2}$ indicating a U(0) valency.

The evolution of the Si-2s spectra is presented in Figure 6.30 (b). Much like the first spectra of the U-4f, a lower intensity data set was extracted from the undisturbed surface of USi_3 from the Si-2s. Here, we can see two photoemission peaks situated around 154 and 151 eV, suggesting at least two bonding types are present within the Si-2s core level initially. As the sputtering cycles commence, the intensity of the Si-2s increases, and the spectra becomes dominated with metallic bonding sites. The most intense photoemission peak after 3 minutes of sputtering is located around 150 eV, indicating a silicon valency of Si^0. Comparing this peak position to work conducted by *Hollinger et al* [171], this would suggest the formation of metallic silicon bonds which is a result of the silicon uranium bonds present in USi_3. The photoemission peak situated around 154 eV suggests a silicon-oxide bond with a silicon valency of Si^{4+}. After 6 minutes of surface sputtering the signal stemming from the silicon-oxide bond has been removed, with the main photoemission peak of the Si-2s spectra at 150 eV. The removal of the silicon-oxide bonds happens faster, around 6 minutes, when compared to the removal of the oxide component in the U-4f spectra, around 12 minutes.

The fitted spectra collected from the O-1s, U-4$f_{7/2}$, Si-2s, and valence band spectra of USi_3 are presented in Figure 6.31. For each spectra, the fit envelope is shown with a solid line, the fitting components are shown with dashed lines, and the background with dotted. Shirley background types were used to model the U-4$f_{7/2}$ and valence band spectra, with linear backgrounds used to model the O-1s and Si-2s. The undisturbed surface of USi_3 is indicated with the spectra shown in pink. A range of spectral features are present, the O-1s, for example, required a series of components to fit the data collected from USi_3. These components, situated around 530, 532, and 534 eV, correspond to U-O, Si-O, and C-O bonds within the sample.

As the surface sputtering begins, the O-1s spectra evolves, such that the C-O bond is removed from the spectra, leaving behind the components associated with U-O and Si-O bonding. The second sputtering cycle, reduced the intensity of the O-1s spectra even further. This is indicated with the orange spectra, totalling 6 minutes of surface sputtering. At 9 minutes of sputtering, the intensity from the O-1s increases, this is due to local environmental contamination from oxygen molecules present in the UHV atmosphere. The NanoESCA chamber is kept at pressures below 10^{-10} mbar when acquiring data through XPS, however, even under these conditions it is

inevitable that the uranium silicide phases will oxidise. The O-1s spectra reduces again for the final two sputtering cycles. The fluctuation trends within the O-1s spectra can also be seen in the U-4$f_{7/2}$ of USi_3. The increase in oxygen content can be seen in the U-4$f_{7/2}$ spectra collected after 9 minutes of surface sputtering. Much like the O-1s, the component used to model the oxide states within the U-4$f_{7/2}$ has increased in intensity.

This behaviour does not appear to be replicated in the Si-2s spectra of USi_3, further indicating that the silicon bonding sites are not as susceptible to oxygen bonding when compared to uranium. The photoemission peak, responsible for the metallic bonding in the U-4f is present in the initial data set, shown in pink, and continues to increase in intensity as a function of sputtering time. After 6 minutes of sputtering time, the metallic site, situated around 377 eV, dominates the U-4$f_{7/2}$ spectra. The metallic bonding sites in the Si-2s dominate the spectra after 3 minutes of surface sputtering. The binding energy of this photoemission peak is around 150 eV, indicating metallic silicon with a valency of Si^0.

The valence band spectra of USi_3 exhibits a strong asymmetric peak at the Fermi edge after 3 minutes of surface sputtering. This represents the valence electrons in the U-5f orbital. The peak shifted to a higher binding energy, around 2.5 eV suggests the bonding of U-5f valence electrons to oxygen. As the sputtering time increases, the peak at 2.5 eV continues to decrease, suggesting the removal of oxygen from the sample and the breaking of U5f-O bonds. Features between 3-9 eV indicate additional U-O bond. These bonding features coincide with the uranium oxide components within the U-4$f_{7/2}$ spectra.

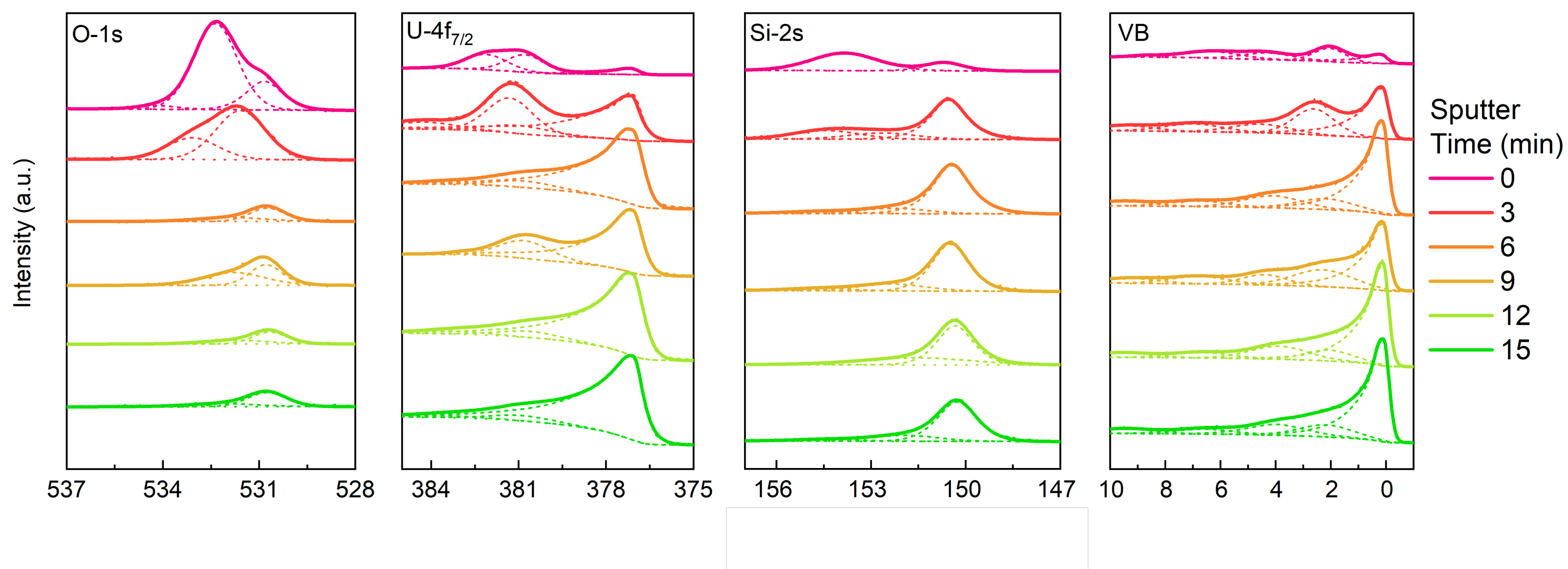

FIGURE 6.31. The fitted O-1s, U-4f, Si-2s, and valence band spectra from [001] USi_3 single crystal. Data acquired as a function of depth from the oxidised surface of USi_3. Components used to model each spectra are shown with dashes, background is modelled with dots, and total fit is shown as solid line. Data from SN1700.

The total fitted area from each core level are presented in Figure 6.32 as a function of sputtering time. Each area has been normalised to its corresponding photoionisation cross section, provided by *Yeh et al.,* [145]. The oxide components for the U-4f, Si-2s, and O-1s have been summed to indicate how the total oxide areas evolve as a function of depth. For the O-1s total area, the components corresponding to the U-O and Si-O bonding sites have been summed. Following the O-1s total, shown with purple crosses, it is indicated that the total area does decrease with increasing sputtering time. This shows that both the U-O and Si-O bonds are being removed via the Ar^+ sputtering. There is a slight increase in the total O-1s area after 9 minutes of surface sputtering, which is attributed to localised oxidation under UHV conditions. This behaviour has been noted in the previous uranium silicides. Tracking the behaviour of the silicon within USi_3, it can be seen that the Si-2s metal, shown with blue triangles, increases as a function of sputter time. The total area of the Si-2s metal exceeds the total Si-2s oxide area, shown with green diamonds, after 3 minutes of surface sputtering. The U-4f metal area, shown with black triangles, does not exceed the U-4f total oxide, shown with red circles, until 6 minutes of sputtering. After 15 minutes of surface sputtering, both metal areas extracted from the U-4f and Si-2s exceed their oxide counterparts and the total area from the O-1s core level.

To further probe the oxide compounds that may form as a result of USi_3 oxidising, the components responsible for the oxidation in uranium and silicon have been separated. Figure 6.33, shows the separated U-4f and Si-2s areas. Here, both core levels are accompanied by the O-1s component responsible for U-O or Si-O bonding. The O-1s U-O component has a binding energy around 530 eV, with the Si-O bonding component being situated around 532 eV. For the U-4f data, each component presented has been normalised to the total area of the U-4f U(IV), shown with red circles, when t = 0. This allows for the stoichiometry of this component to be tracked against the O-1s U-O area, shown with green crosses. Here, much like the data presented in Figure 6.32, the U-4f metal area, shown with black squares, increases with time. The area extracted from the U-4f metal exceeds the normalised area of the O-1s U-O, and U-4f U(IV) components after 3 minutes of sputtering. The U-4f U(IV) area fluctuates up to 9 minutes of sputtering, after which it begins to decrease. Table 6.10 presents the relative O:U ratios calculated from each normalised area. This allows for the potential U-O oxide compounds that may form to be tracked as a function of time. From the O:U ratios calculated, it is seen that there is an increased oxygen content potentially indicating the formation of hyper-stoichiometric U-O compounds. The ratios presented do not infer that stoichiometric UO_2 has formed as a result of uranium oxidation in USi_3.

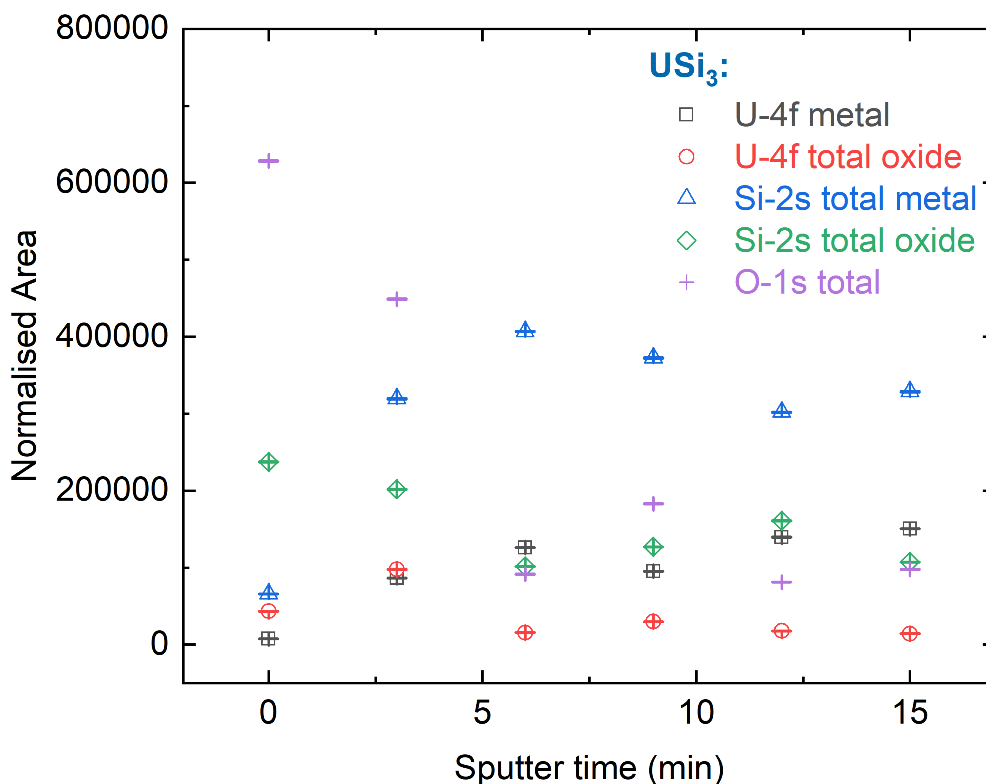

FIGURE 6.32. Graph showing the normalised area intensities from the U-4f, Si-2s, and O-1s states collected from USi_3, after increasing the sputtering time. Data indicates the total fitted areas of each peak, showing the total metal and oxide areas within each spectra. Data collected from SN1700.

Table 6.10: O:U ratios calculated from the total areas extracted from the O-1s U-O, and the U-4f U(IV) areas in USi_3, SN1700. Areas have been normalised to the total area of U-4f U(IV) at t = 0.

Sputter time (min)	O-1s U-O area	U-4f U(IV) area	O:U ratio
0	6.17	1.000	6.2 ± 0.6
3	3.76	1.35	2.8 ± 0.3
6	2.62	0.71	3.7 ± 0.4
9	3.80	1.35	2.8 ± 0.3
12	2.29	0.81	2.8 ± 0.3
15	3.11	0.65	4.8 ± 0.5

Alongside the uranium states being probed, the oxidation of silicon sites were also investigated. Figure 6.33, presented the normalised areas from extracted silicon components. These

components were taken from the Si-2s and the O-1s. Here, the Si-2s exhibited two oxide components, which were situated at 151 eV (Si-2s oxide 1), and 153 eV (Si-2s oxide 2). The silicon oxide responsible for Si^{4+} valencies is Si-2s oxide 2, shown with blue triangles. Each component presented here was normalised against the total area of Si-2s oxide 2 when t = 0. Tracking the evolution of Si-2s oxide 2, it is shown that after decreasing in total area, the area extracted from this silicon oxide plateaus after 6 minutes of surface sputtering. This behaviour is different from Si-2s oxide 1, which gives rise to a Si^{2+}/Si^{3+} valency [171]. The evolution of Si-2s oxide 1, shown with red circles, is initially not present within the surface oxide. The area of the silicon oxide reaches an area maximum after 12 minutes of surface sputtering before decreasing again. Much like the data presented in Figure 6.32, the Si-2s metal data, shown with black squares, continues to increase up to 6 minutes of sputtering. After this, the area decreases before rising again after 15 minutes of sputtering.

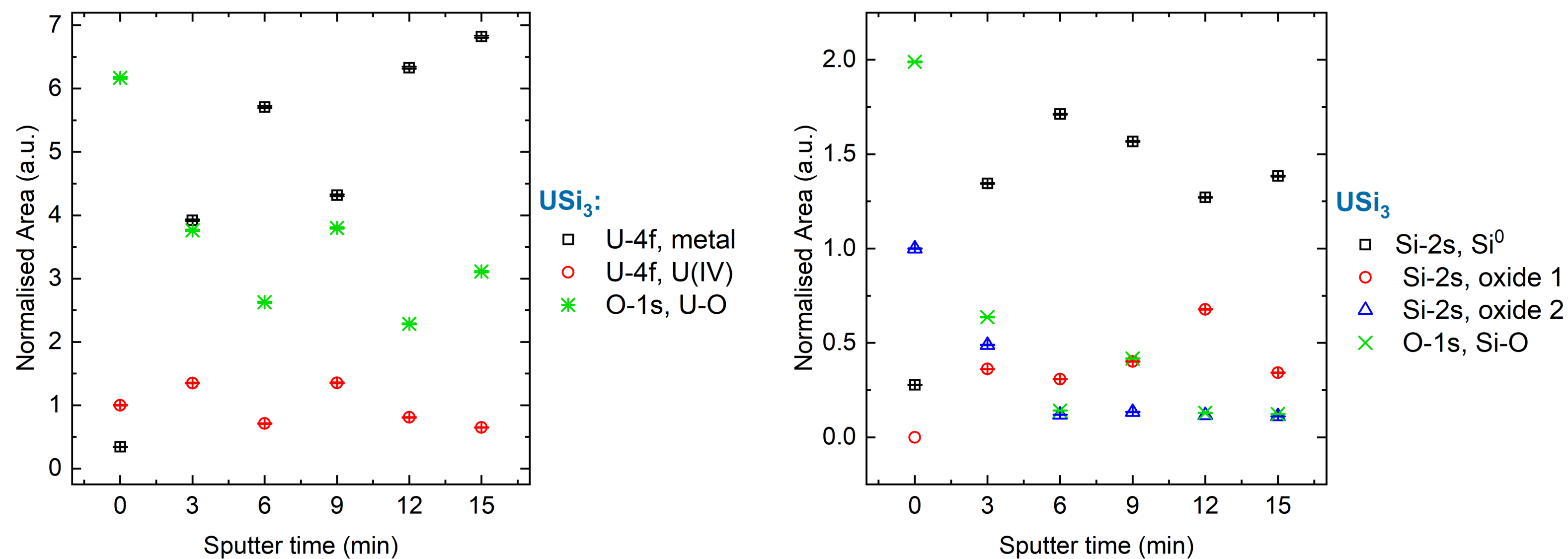

FIGURE 6.33. Graphs showing the normalised areas of U-4f and Si-2s are a function of sputtering time. *left*: Shows the components used to model the U-4f spectra as a function of time, alongside the component responsible for U-O bonding in the O-1s. Areas have been normalised to the total U-4f U(IV) area at t = 0. *right* Shows the components used to model the Si-2s spectra as a function of time, alongside the Si-O bonding component from the O-1s. Areas have been normalised to the total Si-2s oxide 2 area at t = 0. Data taken from SN1700.

The O-1s Si-O area, indicated with green crosses, decreases initially with a slight fluctuation after 9 minutes of surface sputtering. This component continues to decrease after 9 minutes, aligning with the behaviour exhibited by the Si-2s oxide 2 component. Table 6.11 indicates the relative O:Si ratios calculated from the normalised areas of O-1s Si-O and Si-2s oxide 2. From the ratios calculated here, it can be seen that the silicon oxide forming on the very surface of USi_3 is a stoichiometric SiO_2 compound, within error. As the sputter cycles commence, the O:Si ratio decreases with a slight increase in the ratio after 9 minutes of sputtering. This coincides with the data presented in Figure 6.33. The O:Si ratio after 12 and 15 minutes of sputtering would indicate the formation of a stoichiometric SiO compound, within error.

Table 6.11: O:Si ratios calculated from the total areas extracted from the O-1s Si-O, and the Si-2s oxide areas in USi_3, SN1700. Areas have been normalised to the total area of Si-2s oxide 2 at t = 0.

Sputter time (min)	O-1s Si-O area	Si-2s oxide area	O:Si ratio
0	1.989	1.000	2.0 ± 0.2
3	0.637	0.489	1.3 ± 0.1
6	0.142	0.119	1.2 ± 0.1
9	0.417	0.134	3.1 ± 0.3
12	0.129	0.116	1.1 ± 0.1
15	0.123	0.109	1.1 ± 0.1

Understanding the metallic compounds that form as a result of surface oxidation is vital for all uranium silicide compounds. This is conducted by calculating the ratios between the metallic components situated within the U-4f and Si-2s core levels. Figure 6.34 indicates the Si:U ratios extracted after each of the sputter cycles. The Si:U ratio collected from the very surface of SN1700 indicates a system with increased silicon content. A system with an increased metallic silicon content could infer that the uranium sites within USi_3 are more susceptible to oxidation. As the sputter cycles commence, there is a significant change in the Si:U ratios calculated for SN1700. After 6 minutes of surface sputtering, the Si:U ratio indicates the formation of a hyper-stoichiometric USi_3 compound with increased silicon content. The final Si:U ratio for SN1700 was found to be 2.2 ± 0.2, suggesting the formation of a stoichiometric USi_2 compound. Excluding the initial Si:U ratio extracted from the very surface of SN1700, the average of the remaining ratios would indicate the formation of uranium trisilicide. This coincides with the structural characterisation conducted on SN1700.

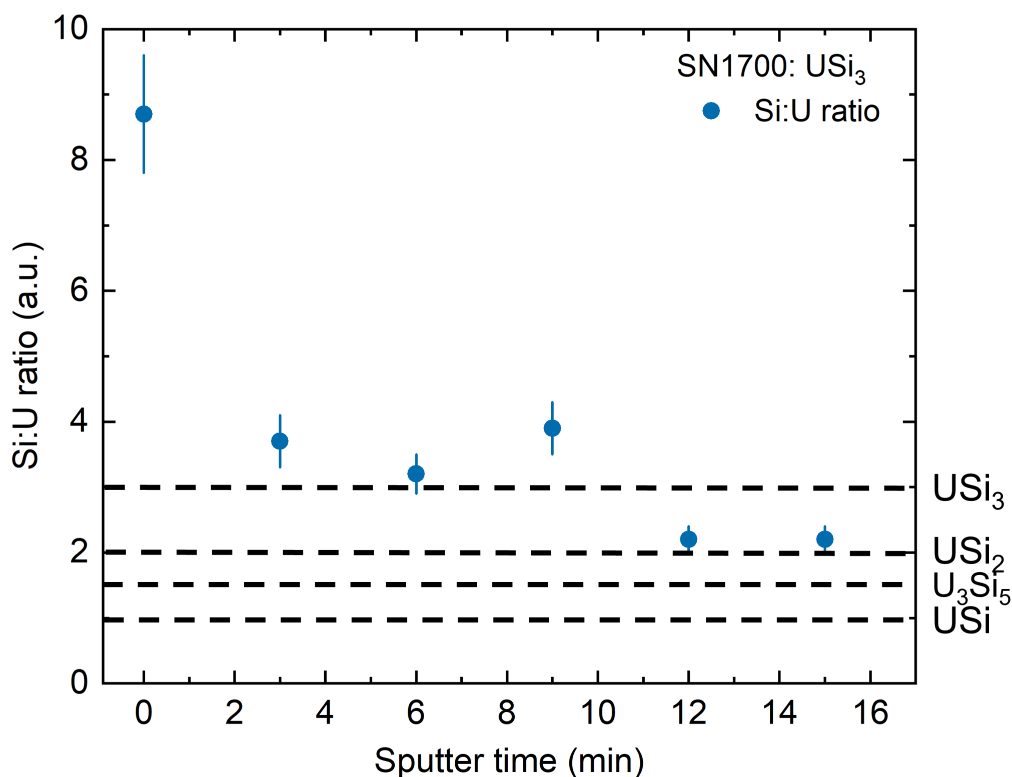

FIGURE 6.34. Graph showing the Si:U ratio as a function of sputtering time. Areas were collected from the metallic components modelled in U-4f and Si-2s spectra. Data collected from SN1700.

6.4 X-ray Reflectivity Results

X-ray reflectivity (XRR) allows for the interface thicknesses, roughnesses, and electron densities to be probed. Utilising this surface sensitive technique, each of the uranium silicide compounds were probed in order to measure the total oxide thickness. The structural and chemical characterisation previously conducted on these uranium silicide phases has answered questions addressing the changes each phase exhibit as a function of atmospheric exposure. Utilising the knowledge regarding potential oxidation compounds that form on the surface of uranium silicide phases has allowed for the total thickness of these oxides to be probed. Here, the XRR results collected as a function of exposure time will be presented for each uranium silicide phase.

6.4.1 U_3Si

The evolution of the surface oxide, present on U_3Si, was tracked through the use of x-ray reflectivity (XRR). The sample used to understand the oxide formation was SN1711, the sample previously used to characterise the structure and chemical bonding in U_3Si once exposed to atmospheric conditions. Figure 6.35 presents the x-ray reflectivity spectra as a function of exposure time. This spectra was collected *in-situ* allowing for the oxide thickness to be tracked dynamically as it forms up to 70 hours. The final spectra was collected after 55 days of exposure. The individual data sets are indicated with open black circles, with the corresponding model indicated with solid lines. Each data set has been offset to allow for an easier visual inspection of each spectra. Additionally, the spectra has been modified such that only a Q range of $0.01 - 0.45\,\text{Å}^{-1}$ can be viewed. To model the spectra, a layered sample was constructed using GenX software that included the information gathered from both the high-angle XRD and XPS spectra for SN1711. Therefore, the model used to simulate the XRR spectra was comprised of U_3Si, U_3Si_2, and a silicon oxide layer situated at the surface of the model.

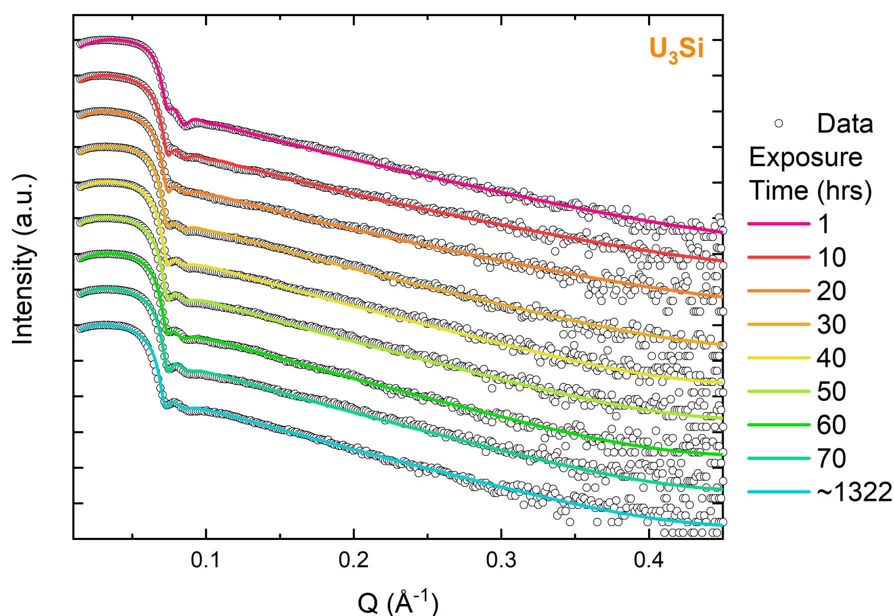

FIGURE 6.35. XRR data collected from oxidised [001] oriented U_3Si. Data is presented with open circles, and models indicated with a solid line. Data collected from SN1711.

The lack of Keissig fringes present with each spectra is a strong indication that the interface roughnesses are large. Furthermore, the lack of change within the spectra as a function of

exposure time indicates that the most significant change has occurred to the sample prior to the initial data set being collected. The most valuable parameter to be extract from SN1711 are the individual layer thicknesses as a function of time. These values are presented in Figure 6.36. From the plotted thicknesses, it can be seen that there is minimal change, within error, to the individual and total thicknesses as a function of time. The total film thicknesses modelled after around 55 days of exposure was found to be 245 ± 19 Å, with the film thickness being 200 ± 15 Å and the total oxide being 45 ± 12 Å.

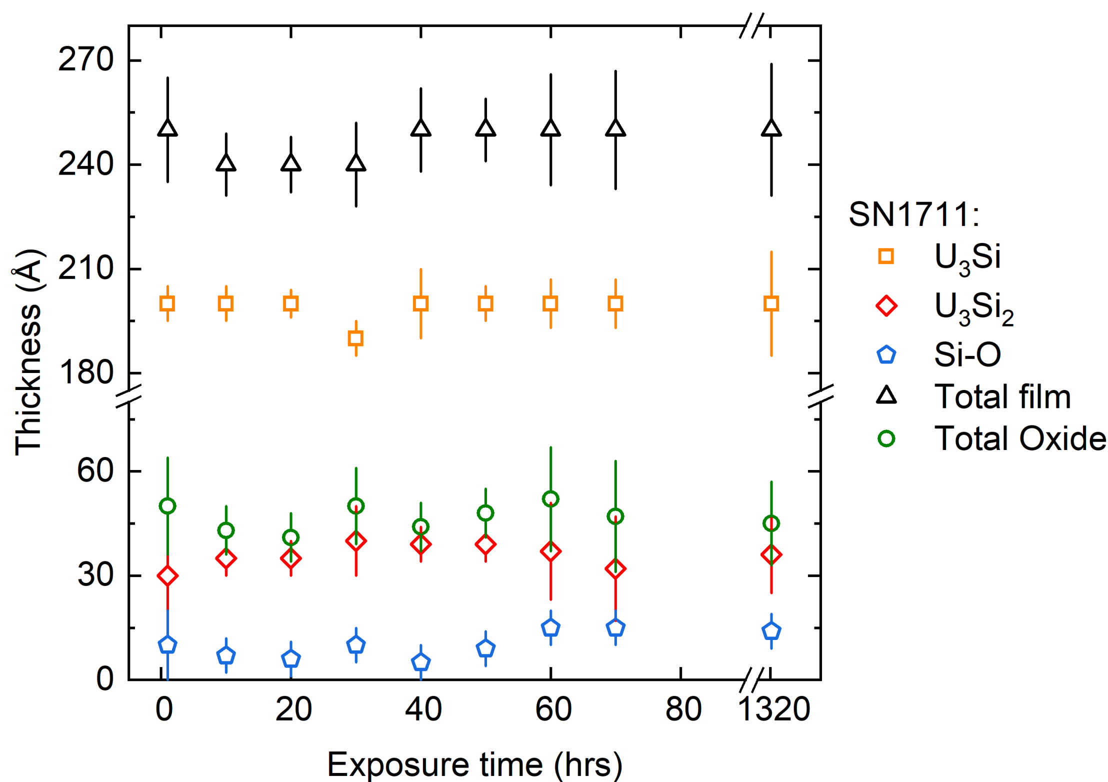

FIGURE 6.36. Modelled layer and total thicknesses extracted from oxidised [001] oriented U_3Si. Total thickness (black open triangles), total oxide thickness (green open circles), epitaxial film thickness (orange open squares), U_3Si_2 (red open diamonds), and silicon oxide (blue open pentagons). Data collected from SN1711.

6.4.2 U_3Si_2

X-ray reflectivity (XRR) was used to understand the thickness of the oxide that grows on the surface of metallic U_3Si_2 under ambient conditions. The sample used to probe this thickness, SN1707, is poly-crystalline in nature. Upon previous high angle XRD experiment, the sample was shown to have inclusions of U_3Si, oriented in the [001] direction. The XRR data collected from the surface of SN1707 was collected dynamically, allowing for the surface oxide formation to be probed in-situ. Initially, spectra was collected over a initial period of 4 days, with the sample being probed for a maximum of 55 days. However, the modelling of the entire data set required parameters that were not physical. Therefore, only the final data set, collected after 55 days is presented to indicate the total oxide layer formed on the surface of SN1707.

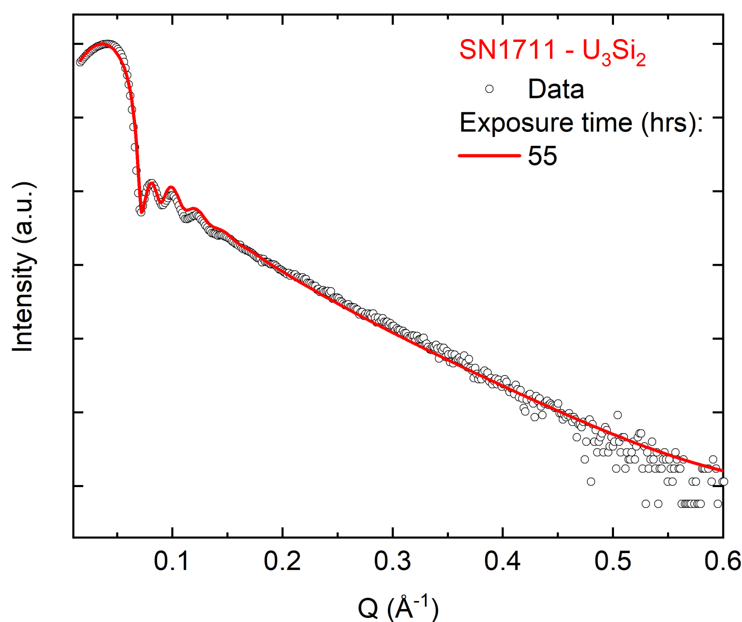

FIGURE 6.37. XRR data collected from oxidised, poly-crystalline U_3Si_2. Data is presented with open circles, and model indicated with a red solid line. Spectra collected after 55 days of exposure. Data collected from SN1711.

Figure 6.37 shows the XRR data collected from the surface of SN1707. The figure presents a close up region of the entire spectra collected from SN1707 after 55 days of atmospheric exposure. This allows for the regions of interest located at lower Q values to be showcased. The raw data is shown with open black circles, and the total fit is indicated with a solid red line. To model the spectra, a layered model was constructed in GenX software. Structural and chemical information about the SN1711 film and the corresponding oxide layer was utilised,

thus the model contained U_3Si_2, U_3Si, and a silicon oxide. The simulated data indicated that the total poly-crystalline film of U_3Si_2 had a thickness of 290 ± 5 Å, with an oxide layer of 30 ± 5 Å.

6.4.3 U_3Si_5

The evolution of the surface oxide native to U_3Si_5 was not tracked as a function of atmospheric exposure time. However, x-ray reflectivity spectra was still collected from the surface of SN1645 in order to understand the total thickness of the oxide that had formed. Utilising the previous high-angle XRD data, and the oxidation information extracted from XPS depth profiling techniques it was possible to create a model using GenX software that would simulate oxidised U_3Si_5. Figure 6.38 shows the XRR spectra collected from SN1645. Here, the data is indicated with open black circles, and the model is indicated with a teal solid line. The spectra has been modified to present the region of interest which is located at lower Q values.

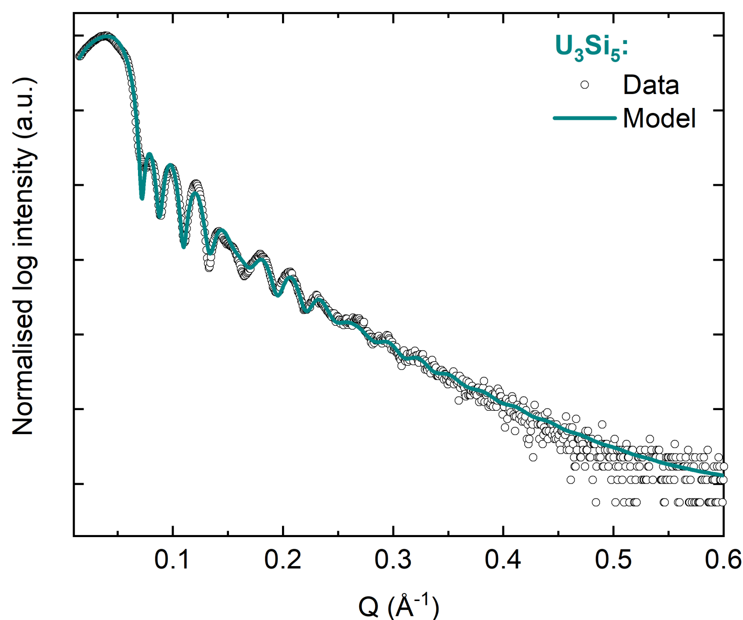

FIGURE 6.38. XRR data collected from oxidised [100] oriented U_3Si_5. Data is presented with open circles, and model indicated with a solid line. Data collected from SN1644.

To model the spectra, a series of uranium silicide phases, observed in the stoichiometry data collected using XPS, were used with a final silicon oxide layer at very surface of the sample. Table 6.12 presents the thicknesses of each layer modelled. The thickness of the surface oxide that

developed on U_3Si_5 was modelled to be 110 ± 12Å, with the total film thickness being around 269 ± 17$\AA$. Here, the oxide thickness refers to the total thickness summation of USi, USi_2, and Si-O.

Table 6.12: Layer thicknesses extracted from the modelled U_3Si_5 XRR spectra, SN1644.

Phase	Thickness ($\AA$)
Si-O	59 ± 8
USi_2	8 ± 4
USi	42 ± 8
U_3Si_5	160 ± 12

6.4.4 α-USi_2

The x-ray reflectivity (XRR) spectra collected from the surface of $\alpha-USi_2$, was observed dynamically. Spectra was collected as the surface oxidation changed over a initial period of 4 days, and was monitored for around 55 days. Figure 6.39 shows the evolution of the spectra collected from SN1702, [001] oriented $\alpha-USi_2$, up to 90 hours of ambient exposure. Each plot has been offset to enable the changes in the spectra to be viewed. The figure presents a close up region of the entire spectra, to showcase specific regions of the data sets located at lower Q values. The data points for each spectra is shown with open grey circles, and the total fits are shown with solid lines.

The plotted XRR data in Figure 6.39, shows that the changes that occur on the surface of $\alpha-USi_2$ as a function of surface oxidation are very subtle. The most notable changes occur between Q = 0.15 − 0.25$\AA^{-1}$. Here, the data gets slightly rougher as the exposure time increases. A small feature around Q = 0.06$\AA^{-1}$, also becomes less defined as this exposure increases. The features at lower Q values are more influenced by rougher surface layers, so this indicates that the surface of $\alpha-USi_2$ is changing as a function of time. The small variation in the data sets does indicate, much like the high-angle XRD data collected from SN1702, that the oxidation forming on the surface does not effect the structure of the sample.

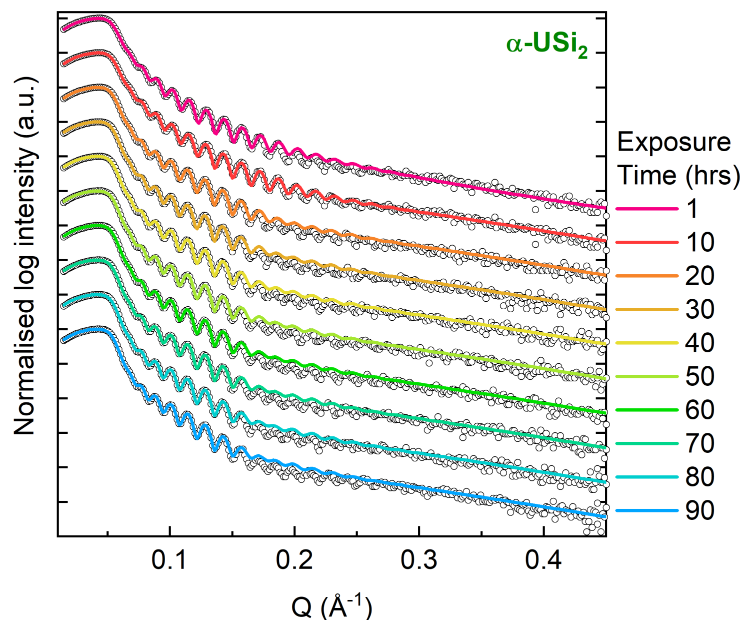

FIGURE 6.39. XRR data collected from oxidised [001] oriented α-USi_2 . Spectra is indicating the thickness and interface roughness change of α-USi_2 as a function of exposure time to air. Data is presented with open circles, and models indicated with solid lines. Data collected from SN1702.

Through modelling the data in Figure 6.39, it was possible to extract film, oxide, and total thicknesses from the sample as a function of exposure time. These values are shown in Figure 6.40. Here, the total thickness is shown with black triangles, $\alpha - USi_2$ with green squares, and the oxide thickness is presented as red circles.

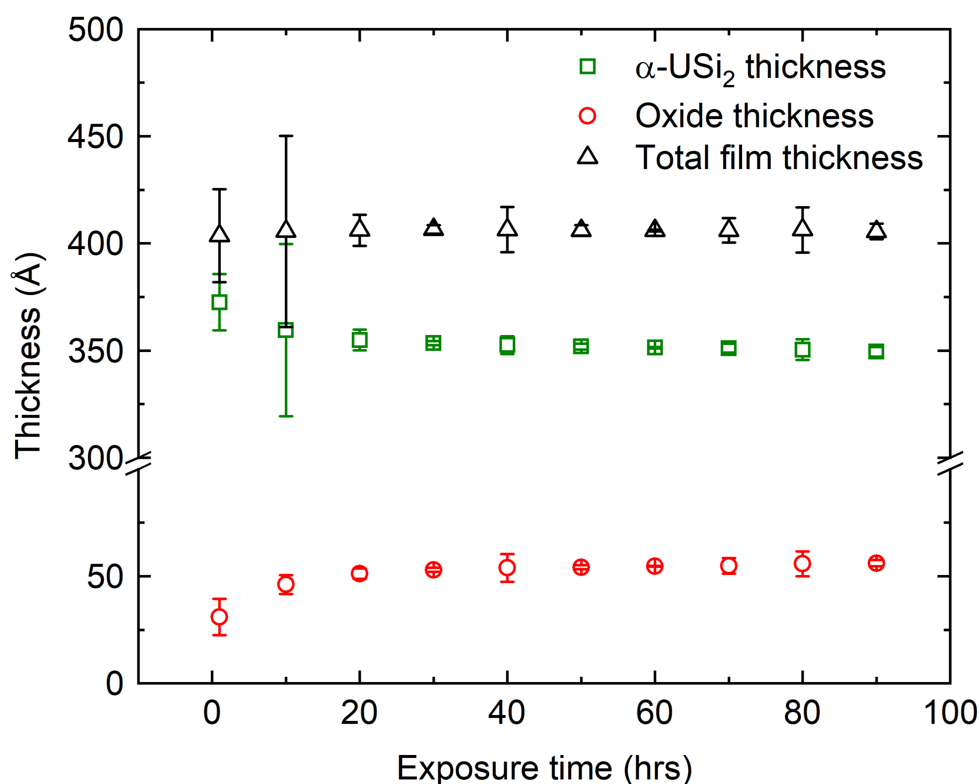

FIGURE 6.40. Graph showing the changes in α-USi_2 (green squares), oxide (red circles), and total thicknesses (black triangles) of SN1702 obtained from XRR fitting. Data collected from SN1702.

The evolution of the native oxide that forms on (001) epitaxial $\alpha - USi_2$ by observing SN1645. Figure 6.41 presents the x-ray reflectivity spectra collected from the surface of SN1645 as a function of ambient atmospheric exposure. Here, the spectra presented was collected after 1 hour of exposure, and then after 10 hour intervals with the final data set being collected after roughly 55 days. Here, the spectra has been modified to showcase the region of interest at lower Q values, between $0.01 - 0.45 \mathring{A}^{-1}$. The spectra indicates minimal changes to the sample as a function of exposure to air. The fringe periodicity does not drastically change, inferring that the surface oxide growth does not progressively develop during this time.

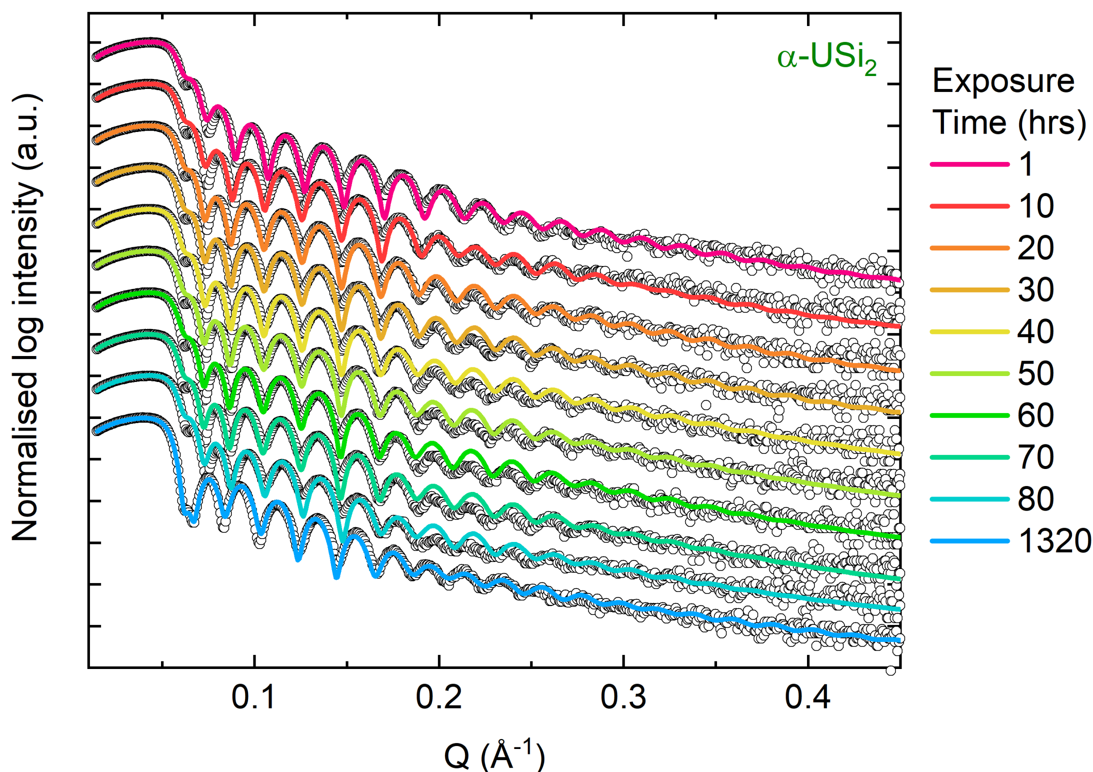

FIGURE 6.41. XRR data collected from oxidised [001] oriented α-USi_2 . Spectra is indicating the thickness and interface roughness change of α-USi_2 as a function of exposure time to air up to 80 hours initially, with the final data set collected after 55 days. Data is presented with open circles, and models indicated with solid lines. Data collected from SN1645.

From modelling the XRR spectra, it was possible to extract the total thicknesses associated with the film and oxide layer. Figure 6.42 presents the change in thickness from each compound used to model the surface oxidation of $\alpha - USi_2$ (SN1645). From observing the total oxide thickness, it can be seen that the majority of the native oxide has formed prior to the first measurement being taken after 1 hour of exposure. Initially, the contribution from the USi_3 layer is not present within the model until 50 hours of exposure. As the thickness of USi_3 increases, the contributing thickness from USi (yellow stars) beings to decrease. This could suggests the oxidation of uranium within the sample, resulting in the formation of high silicon content uranium silicide phases. Cyclic oxidation behaviour is a type of mechanism seen in samples that exhibit a weight change over time, with the reformation of material after cyclic heating and cooling processes [173, 174].

The reduction in the oxide thickness (Figure 6.42) could be attributed to this mechanism, as a sudden decrease in thickness from the USi layer (yellow stars), alongside an increase in the USi_3 phase. Through observing the evolution in the oxide growth, the final film thickness attributed to $\alpha - USi_2$ was found to be $226 \pm 5\AA$. The total oxide thickness was modelled to be $63 \pm 5\AA$.

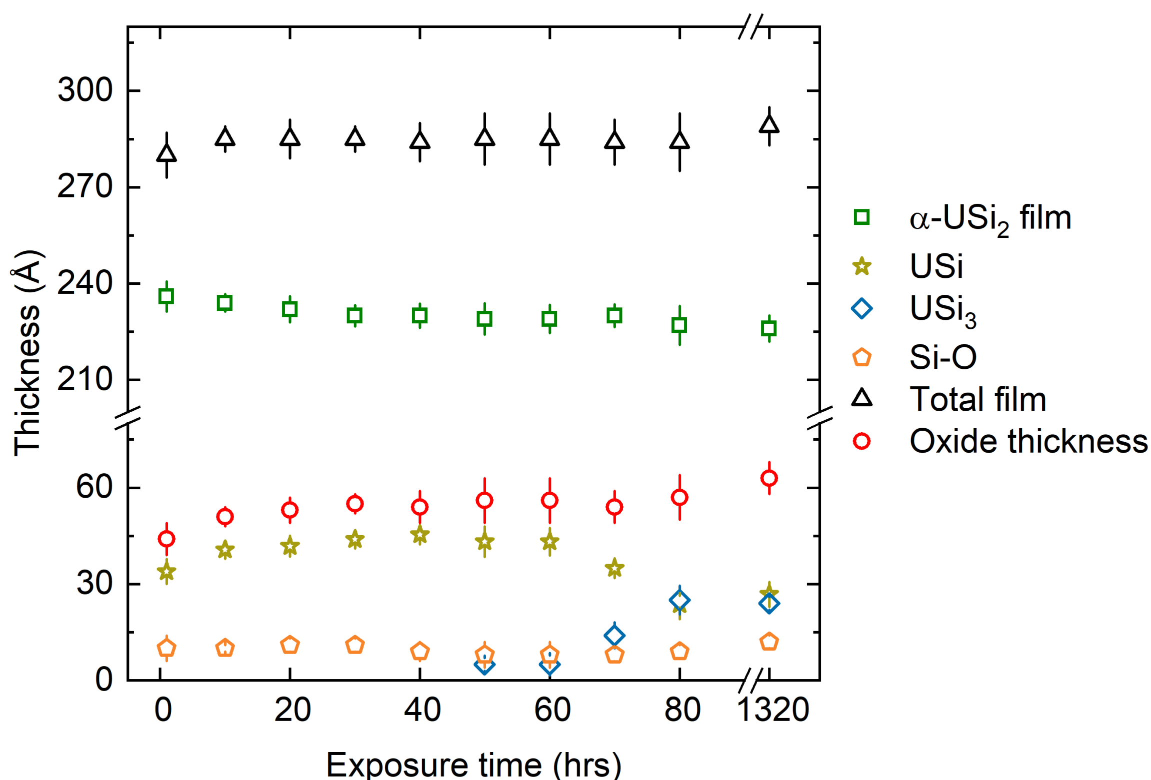

FIGURE 6.42. Graph showing the changes in α-USi_2 (green squares), total oxide (red circles), and total thicknesses (black triangles) of SN1645 obtained from XRR fitting. Individual oxides are presented: USi - yellow stars, USi_3 - dark blue diamonds, and Si-O - orange pentagons. Data collected from SN1645.

6.4.5 USi_3

The ambient surface oxidation of USi_2 was observed using x-ray reflectivity (XRR). The evolution of the native oxide was probed dynamically, with the changes occurring on the surface of USi_3 being observed *in-situ*. Figure 6.43, presented the XRR spectra collected from SN1700 over an initial period of 4 days. Here, the spectra collected after every 10 hour period is shown. A final

spectra was collected from the surface of SN1700 after 55 days of ambient exposure. This data set is also included in Figure 6.43, labelled as 1322 hours, shown in blue. Each plot presented in Figure 6.43 has been off-set to allow for the changes in each data set top be viewed. This figure also presents a close up region of the entire spectra, allowing for specific regions of each data set to be showcased. There are significant features within the spectra that provide an indication of specific changes occurring to SN1700. Comparing the evolution of the spectra, it is clear there is an contraction in the broader periodicity, which initially extends from around $0.2-0.4\AA^{-1}$. The spectra collected after 10 hours of exposure indicates that this periodicity has contracted, extending from $0.2-0.3\AA^{-1}$, indicating the surface oxide has increased in thickness. This particular periodicity continues to contract until the spectra collected after 70 hours of exposure.

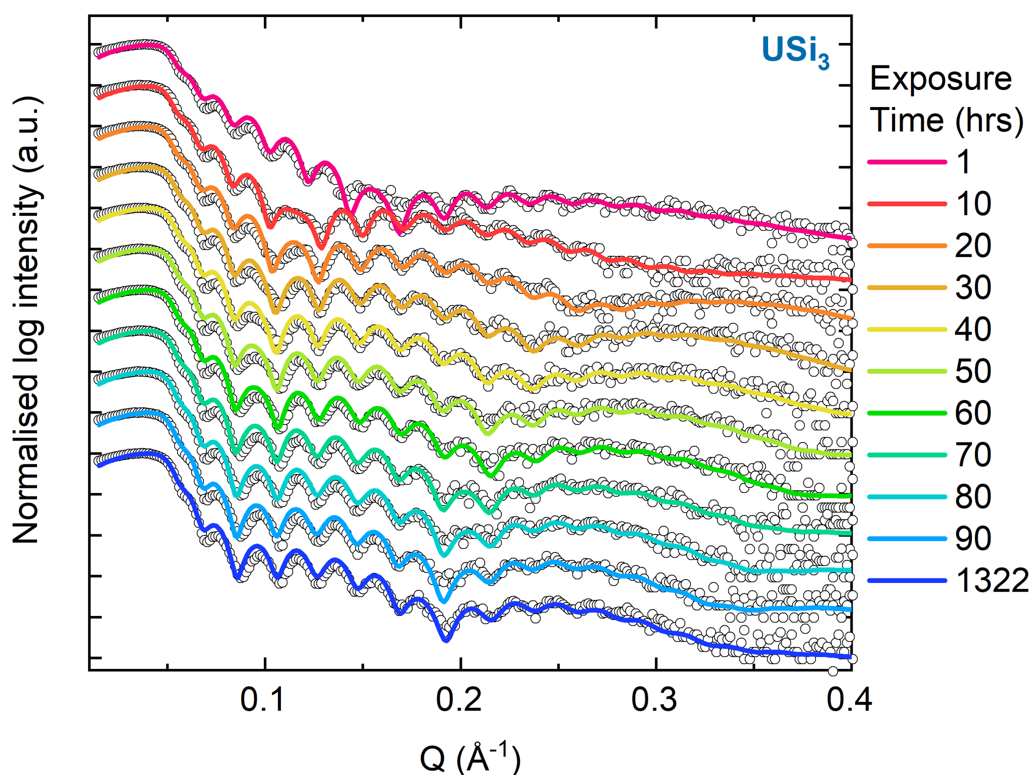

FIGURE 6.43. XRR data collected from oxidised [001] oriented USi_3. Spectra is indicating the thickness and interface roughness change of USi_3 as a function of exposure time to air. Data is presented with open circles, and models indicated with solid lines. Data collected from SN1700.

Through the modelling of this spectra, conducted using GenX, it was possible to extract the thicknesses of each layer as a function of time. Figure 6.44, indicates the changes in thickness from each layer as the surface oxide evolves. Here, the USi_3 film (blue squares), USi_{3+x} hyper-stoichiometric layer (purple diamonds), and the Si-O oxide (orange pentagon) are all presented. The total film thickness (black triangles) and total oxide thickness (red circles) are also presented as a function of time. Observing the change in thickness of the oxide layers, it can be seen that the Si-O oxide has the biggest change as a function of time, when compared to the hyper-stoichiometric USi_3 layer. Therefore, this oxide thickness increase can be attributed to the contraction in the broader periodicity noted in the XRR spectra in Figure 6.43. This also infers that the hyper-stoichiometric USi_3 layer has formed on the surface of SN1700 prior to the first measurement being taken after 1 hour of exposure.

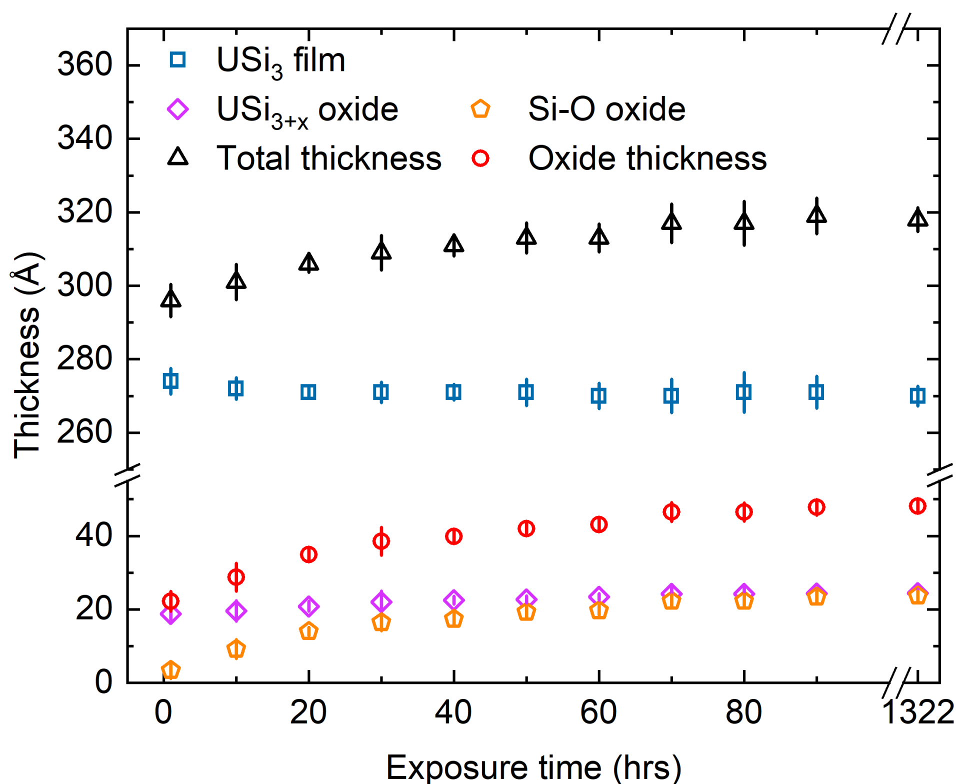

FIGURE 6.44. Graph showing the changes in USi_3 (dark blue squares), total oxide (red circles), and total thicknesses (black triangles) of SN1702 obtained from XRR fitting. Individual oxide thicknesses from USi_{3+x} (purple diamonds) and Si-O oxide (orange pentagon) also presented. Data collected from SN1700.

From the data presented in Figure 6.44, the final oxide thickness, extracted from SN1700 after 1322 hours, was found to be 48.4 ± 1.47$\AA$. The oxide thickness modelled after 90 hours of exposure was 47.8 ± 2.18$\AA$, indicating a less than 0.5$\AA$ difference between the two thicknesses. This could suggest the passivation of the native oxide that forms on the surface of USi_3.

6.5 Discussion of the Oxidation of U-Si phases

The work presented here set out to answer three fundamental questions about the ambient oxidation of uranium silicide phases: (1): How much do the uranium silicide phases change as a function of uranium content once exposed to ambient conditions?, (2) What compounds form within each uranium silicide oxide layer?, and (3) How thick is the oxide layer that grows upon each uranium silicide under ambient conditions? Through the use of x-ray diffraction, x-ray photoelectron spectroscopy, and x-ray reflectivity, these questions have been investigated for uranium silicide phases. It is here that the results obtained from each experiment will be pieced together for individual compounds in order to understand the ambient oxidation of uranium silicides.

6.5.1 U_3Si

Following the characterisation work conducted on pristine U_3Si in Chapter 5, this phase was epitaxially stabilised onto CaF_2 to understand how the compound behaves once exposed to ambient conditions. As the uranium silicide phase with the lowest silicon content, understanding how the increased uranium loading alters the oxidation is vital for U-Si studies. X-ray diffraction was initially deployed to understand the structural changes that may occur as a result of exposing U_3Si to ambient conditions. The specular XRD data collected from oxidised U_3Si indicated the formation of U_3Si_2 inclusions alongside the (002) of U_3Si. A comparison of the pristine and oxidised data collected from U_3Si is presented in Figure 6.45. The pristine data collected from SN1513 is shown with a dotted orange line, with the oxidised data (SN1711) shown with a solid orange line. From the data presented in Figure 6.45, it is clear that there are structural differences between pristine and oxidised data. Off-specular ϕ scans conducted on the (206) reflection of U_3Si confirmed the epitaxy of the phase, confirming the formation of a two domain crystal, much like the pristine counterpart - SN1513. Furthermore, SN1711 was confirmed to have a tetragonal crystal structure with lattice parameters, a = 6.027 ± 0.001° and c = 8.776 ± 0.002°. These values indicate a 0.3% contraction in the in-plane parameter, and a 0.8% expansion in the specular parameter. Omega data collected from the specular (002) Bragg reflection of U_3Si indicated a 31% increase from 0.79 ± 0.01° for SN1513 to 1.08 ± 0.01° for SN1711. This increase in the FWHM could be attributed to multiple factors. Firstly, the presence of U_3Si_2 inclusions

within the sample could have an influence on the overall strain on the sample, however, this behaviour is not suggested with the minor changes in the lattice parameters. Furthermore, a change in sample thickness can also cause changes in the FWHM of specular peaks. Alongside the structural characterisation, changes to the high-angle diffraction collected from SN1711 was observed as a function of time. This was in order to observe changes occurring as a result of ambient surface oxidation. From the data collected, presented in Figure 6.3, there were no notable changes to the spectra as a function of atmospheric exposure.

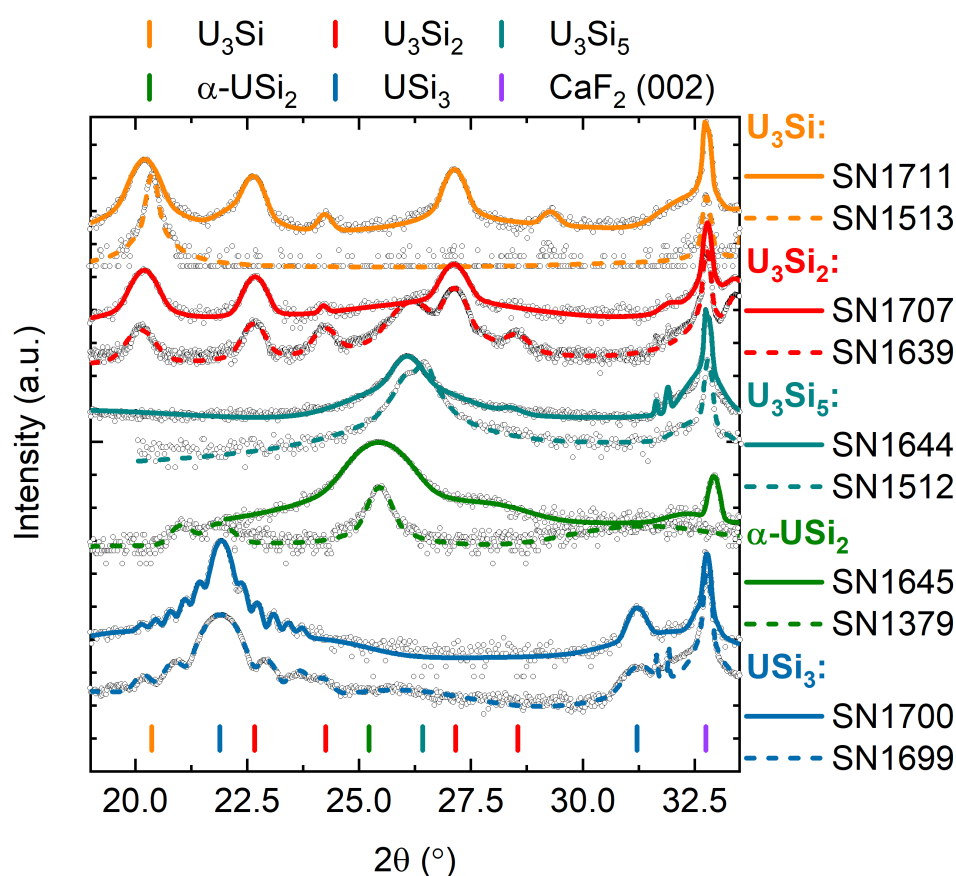

FIGURE 6.45. Spectra showing the structural changes measured using high-angle XRD on pristine and oxidise uranium silicide phases. Pristine samples are shown with dashed lines, with oxidised samples being shown with solid lines. Data points from each spectra are indicated with open circles. U_3Si, U_3Si_2, U_3Si_5, α-USi_2, USi_3, and CaF_2 are indicated with orange, red, teal, green, blue, and purple drop lines respectively.

Using x-ray diffraction as a stand alone technique does not provide enough information about how the surface of U_3Si oxidises under ambient conditions. However, what this does indicate,

is that the compound of interest, U_3Si has epitaxially matched to CaF_2, suggesting this is the first layer deposited on the substrate. Inferring that U_3Si_2, an inclusion in the high-angle XRD spectra, is situated above the U_3Si layers.

To probe the surface oxidation further, x-ray photoelectron spectroscopy (XPS) was used to investigate the bonding mechanisms present within the epitaxial sample. From the x-ray diffraction data, it was known that the stoichiometry calculated between the U-4f and Si-2s sites would align with U_3Si and U_3Si_2 stoichiometries. Through the use of XPS depth profiling techniques, surface layers were removed using Ar^+ sputtering, and data was acquired after each sputter cycle. This provided an indication of the oxide and metallic bonding environments as a function of sputter depth. Data collected from the very surface of SN1711 suggested that a uranium-oxide compound had formed. However, all stoichiometries calculated between uranium and oxygen sites suggested that none of the compounds were stoichiometric U-O phases. As the sputtering cycles commenced, spectra collected from the Si-2s and O-1s Si-O sites indicated the formation of hyper-stoichiometric Si-O compounds with increased oxygen content. The final sputter cycle, which was collected after 28 minutes of surface sputtering, indicated the formation of a hyper-stoichiometric SiO_2 phase forming on the surface of U_3Si. Ratios calculated between the metallic bonding sites in the U-4f and Si-2s were also monitored as a function of depth. Metallic bonding was not modelled in the data until 4 minutes of surface sputtering had commenced. At this point, the Si:U ratio was calculated to be 0.659 ± 0.07, suggesting the formation of a sub-stoichiometric phase that is U_3Si_{2-x} like. As the sputtering time increased, the Si:U ratio collected from SN1711 tended towards a Si:U ratio of 0.3. After 12 minutes of surface sputtering, this Si:U ratio had plateaued, suggesting the formation of stoichiometric U_3Si, with a Si:U ratio of 0.33.

The XPS data collected from the surface of epitaxial U_3Si furthered the ambient oxidation model of this phase. Firstly, the data collected from XPS strongly suggested that stoichiometric uranium oxides and silicon oxides do not form on the very surface of U_3Si. Secondly, after 28 minutes of surface sputtering, the data collected from Si-2s oxides and O-1s Si-O bonding sites suggested the formation of stoichiometric SiO_2. Finally, the metallic Si:U ratios collected from the depth profiling experiment, replicate the data collected from the high-angle XRD data - suggesting the formation of two uranium silicide phases, U_3Si, and U_3Si_2, with the former phase epitaxially stabilised to the CaF_2 substrate.

Utilising the structural information extracted from the high-angle XRD diffraction, and the chemical bonding information gathered from XPS depth profiles, it was possible to model the x-ray reflectivity data collected from U_3Si. The change in layer thickness and roughness was monitored simultaneously with the high-angle diffraction data collected from SN1711. Collecting

this XRR data allows for the changes in thickness to be understood as a function of exposure time, providing an indication of how the oxide that forms on U_3Si behaves, and if this oxide is a passivation layer. The XRR spectra collected from Sn1711 indicated that the total epitaxial layer of U_3Si had a total thickness of 200 ± 15Å. The oxide layer that had formed on the surface of SN1711 consisted of U_3Si_2 and a silicon dominated Si-O layer. The total thickness of this oxide layer was modelled to be 45 ± 12Å. From this a schematic diagram depicting the structure of SN1711 is presented in Figure 6.46, indicating the epitaxial U_3Si film in orange, with the subsequent U_3Si_2 and Si-O layer indicated with red and light blue.

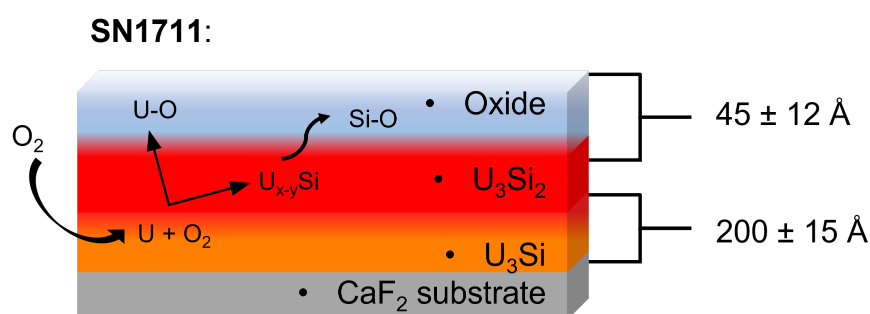

FIGURE 6.46. Schematic diagram depicting the oxidised structure of U_3Si, SN1711. Formation of multiple uranium silicide phases indicated with U_3Si film in orange and U_3Si_2 in red, underneath silicon dominated oxide layer (light blue). Total oxide layer thickness shown to be 45 ± 12Å.

6.5.2 U_3Si_2

As the uranium silicide compound that has been identified as an advanced technology fuel (ATF) candidate, understanding the ambient surface oxidation is vital. Probing this native oxide formation will further the understanding on how the fuel compound behaves in storage prior to *in-operando* use within a LWR reactor.

The surface oxidation of U_3Si_2 was investigated structurally through the used of high-angle XRD. This technique was used to structurally characterise the U_3Si_2 sample (SN1707), and to probe the evolution of surface oxide growth as a function of time. The high-angle XRD data collected from SN1707 is presented in Figure 6.45, alongside it's pristine counterpart, SN1639. There are notable structural changes in the high-angle XRD data collected from oxidised U_3Si_2, SN1707, when compared to SN1639. The spectra collected from SN1707, indicated the crystallisation of the (110), (001), (200), (210), and (111) Bragg reflections from U_3Si_2. The oxidised U_3Si_2 sample includes the (002) Bragg reflection of U_3Si. Where this is very similar to the high angle data collected for epitaxial U_3Si (SN1513, SN1711) the inclusion found in poly-crystalline U_3Si_2

(SN1707), does not exhibit any uniqueness in phi when probing the off-specular (206) reflection of U_3Si. Spectra collected from the oxidised sample of U_3Si_2 does not include the (100) Bragg reflection of U_3Si_5 which was noted in SN1639 high-angle XRD data. The (001) Bragg reflection of U_3Si_2, situated around a 2θ position of 22°, is much smaller when compared to the same reflection detected in SN1639. Furthermore, the (111) Bragg reflection at a 2θ position around 28.5° noted in SN1639, is not present in SN1707. By definition, a perfect poly-crystalline sample has crystallites that exhibit perfect random orientation, whereas a preferred orientation crystal has crystallites that are deposited in the specular direction, perpendicular to the substrate below. This would suggest that both SN1707 and SN1639 have a textured poly-crystalline nature due to the presence of multiple Bragg reflections. From the spectra collected from SN1707, as a function of exposure, there were no notable changes to the structure. Changes to the high-angle diffraction collected from oxidised U_3Si_2 would suggest large structural changes as a result of ambient surface oxidation.

Crystallite sizes were calculated for SN1707 using the Scherrer equation, as described in Chapter 3. A comparison of the crystallite sizes extracted from both pristine and oxidised U_3Si_2 phases are presented in Table 6.13. Here, we can see that the U_3Si crystallite size extracted from SN1707 has decreased by around 23% when compared to the pristine sample. The crystallite sizes extracted from oxidised U_3Si_2 differ by around 5% and 10% when comparing the (001) and (210) reflections found in SN1707 to the (002) reflection in SN1639. The crystallite size of U_3Si_5 could not be compared because this phase did not crystalise within the oxidised U_3Si_2 sample SN1707.

Table 6.13: Table showing crystallite size for each phase within SN1639 and SN1707.

Sample	Phase	2θ position °	FWHM °	Crystallite size (nm)
SN1639	U_3Si_2 (002)	46.283 ± 0.002	0.48 ± 0.01	19 ± 2
	U_3Si (002)	20.146 ± 0.003	0.35 ± 0.01	24 ± 1
	U_3Si_5 (100)	26.203 ± 0.004	0.63 ± 0.01	14 ± 1
SN1707	U_3Si_2 (001)	22.72 ± 0.01	0.39 ± 0.01	22 ± 2
	U_3Si_2 (210)	27.098 ± 0.002	0.469 ± 0.007	18 ± 3
	U_3Si (002)	20.176 ± 0.001	0.443 ± 0.004	19 ± 2

From the high-angle XRD data collected from SN1707, it is clear that the sample consists of U_3Si_2 and U_3Si, however, using the diffraction data alone is not enough to construct an image that represents how the sample is physically structured.

To further investigate the ambient oxidation of SN1707, XPS depth profiling was utilised to probe the oxide and metallic bonding states as a function of oxide thickness. Data was acquired

from the surface of SN1707 after every sputtering cycle to understand how the oxide layer, formed on the surface of U_3Si_2, evolves as a function of thickness. Firstly, from the uranium oxide data extracted from the U-4f and O-1 U-O bonding sites, it was found that as a function of sputter time, the O:U ratio suggests the formation of a uranium oxide compound, similar to UO_2, with an increased oxygen content. The Si:O ratios were investigated by modelling the Si-2s oxide regions, and the O-1s Si-O component. Ratios calculated as a function of sputtering time gave minimal indication that a stoichiometric Si-O compound had formed, with each of the ratios exhibiting a excess of oxygen. Si:U ratios were extracted using the metallic components of the U-4f and Si-2s spectra. Metallic stoichiometries were only extracted from the surface of SN1707 after 4 minutes of sputtering, as it was not possible to model the components for the 0 and 2 minute sputter cycles. The Si:U ratio after 4 minutes of surface sputtering was calculated to be 0.69 ± 0.07. This ratio indicates the formation of a hyper-stoichiometric U_3Si_{2+x} compound, suggesting preferential oxidation of uranium sites when compared to metallic silicon. As the sputtering time increases, the ratio between Si:U tends towards 0.5. This stoichiometry could infer a mixing of the two phases present in the high-angle XRD data collected from SN1707: U_3Si_2 and U_3Si. These two compounds should exhibit Si:U ratios of 0.667 and 0.333, respectively. As the U_3Si compound present in SN1707 is not epitaxially matched to the CaF_2 substrate, this further suggests a sample with a structural mixing of the two phases. Figure 6.47 indicates a schematic of how this system may physically look.

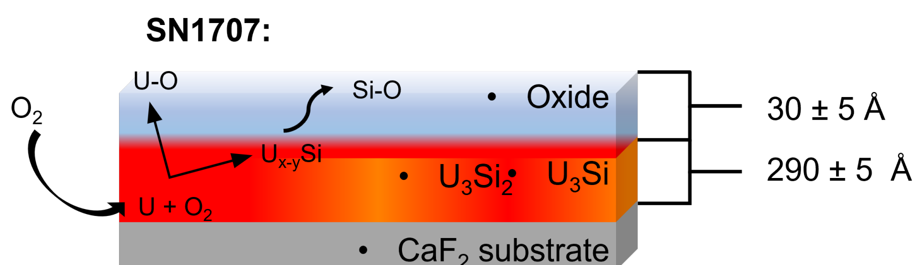

FIGURE 6.47. Schematic diagram depicting the oxidised structure of U_3Si_2, SN1707. Formation of multiple uranium silicide phases indicated with red for U_3Si_2, orange for U_3Si, underneath a silicon dominated oxide layer indicated with light blue. Total oxide layer thickness shown to be $30 \pm 5\mathring{A}$.

The structural and chemical information gathered about SN1707, from specular XRD and XPS depth profiling, allowed for the x-ray reflectivity data to be modelled. Structurally it is understood that the sample has inclusions of both U_3Si_2 and U_3Si. From the chemical characterisation, it was suggested that the oxide layer has inclusions of a hyper-stoichiometric U_3Si_{2+x} phase. Using this information, it was possible to model the thickness of the bulk film, and the oxide thickness. These final thicknesses, shown in Figure 6.47, indicate that the mixed U_3Si_2 and U_3Si

layer was around 290 ± 5Å, with the oxide having a thickness of 30 ± 5Å after around 55 days.

6.5.3 U_3Si_5

The epitaxial stabilisation of [100] U_3Si_5 onto [001] CaF_2 sparked significant interest due to the recipe used to engineer this uranium silicide phase. SN1644 was stabilised using a uranium deposition power of 30 W. This would suggest the stabilisation of poly-crystalline U_3Si_2. However, from the high angle XRD spectra collected from SN1644, presented in Figure 6.45, the two Bragg reflections present in the data match the (100) of U_3Si_5 and the (002) of CaF_2, with no indication of U_3Si_2 forming. This matches the data collected from SN1512, pristine (100) U_3Si_5. Further structural characterisation conducted on SN1644, showed that the sample was epitaxially matched to CaF_2, exhibiting a two-domain crystal system indicated with 4 reflections stemming from the (201) off-specular reflection of U_3Si_5. Lattice parameter calculations of SN1644 showed that the specular 'a' constant was 1.12% lower when compared to the constant obtained from SN1512. Table 6.14 indicates the final lattice constants obtained from SN1644. Here, it is shown that both the 'a' and 'c' lattice constants are smaller than those extracted from SN1512, resulting in a contraction of the unit cell of U_3Si_5 of around 4%. Furthermore, the in-plane 'c' lattice parameter has contracted by around 7%. The contraction in all structural parameters extracted from SN1644, may signify an overall lattice tension which could be due to the increased uranium content used to stabilise this phase.

Table 6.14: Table of structural constants collected from pristine and oxidised epitaxial (100) U_3Si_5 thin films. Parameters extracted from SN1512 and SN1644.

Sample	Phase	a ($\AA$)	c ($\AA$)	c/a	Unit Cell ($\AA^3$)	Parameter Change %
SN1512	(100) U_3Si_5	3.89 ± 0.01	3.97 ± 0.05	1.02	59.7 ± 0.8	a = 1.3% c = 7.1%
SN1644	(100) U_3Si_5	3.939 ± 0.003	3.697 ± 0.005	0.94	57.4 ± 0.1	Vol. = 3.9%

From the high-angle XRD structural characterisation of SN1644, it was shown that there are no additional phases that form under the influence of a native oxide, retaining it's original phase of U_3Si_5. However, from the lattice parameter calculations conducted on SN1644, it was shown that there is a contraction in the specular and in-plane lattice constants, resulting in a 3.9% contraction in the unit cell. This suggests that the native oxide is altering the phase. Through the use of XPS depth profiling, the chemical bonding environments on oxide and metallic sites were investigated. Observing the Si-O and U-O it was found that no stoichiometric compounds were forming as part of the oxidation process, however there was evidence of hyper-stoichiometric compounds forming with increased oxygen loading for both cases. The Si:U ratio was monitored as a function of sputtering time. These investigations indicated the formation of a stoichiometric

USi_2 phase within error. As the depth profiles continues, the Si:U ratio is reduced indicating the presence of a compound between U_3Si_2 and USi. The final ratio collected after 18 minutes of surface sputtering was 1.1 ± 0.1, suggesting the formation of a hyper-stoichiometric USi-like phase.

The analysis conducted on XRD and XPS data sets collected from SN1644, allowed for the oxide thickness to be measured through XRR. A model was constructed using GenX software, which included the U:Si phases found in the XPS data. For the model, all compounds were assumed to be layers. Here, the total film thickness, was measured to be 269 ± 17 $\mathring{A}$, with the total oxide thickness modelled to be 110 ± 12 $\mathring{A}$. The total oxide was comprised of USi, USi_2, and a Si-O compound.

Combining all of the oxide evidence collected from XRD, XPS, and XRR measurements, a schematic of the sample was constructed. This is presented in Figure 6.48, indicating the layers of the sample. Here, the epitaxial U_3Si_5 layer is adjacent to the [001] CaF_2 substrate. A USi layer sits between the epitaxial film and $\alpha - USi_2$ layer. The preferential oxidation model does not align with the oxidation of U_3Si_5 into USi. This is because the binary phase diagram for uranium silicide phases indicates that USi has a reduced silicon content when compared to U_3Si_5. Therefore, if uranium is preferentially oxidising, as predicted by [94**?**], the oxidation of U_3Si_5 should result in the formation of Si-rich phases only. The top layer, labelled 'Oxide', was predicted to be a non-stoichiometric Si-O compound. The total film and oxide thicknesses are labelled on Figure 6.48.

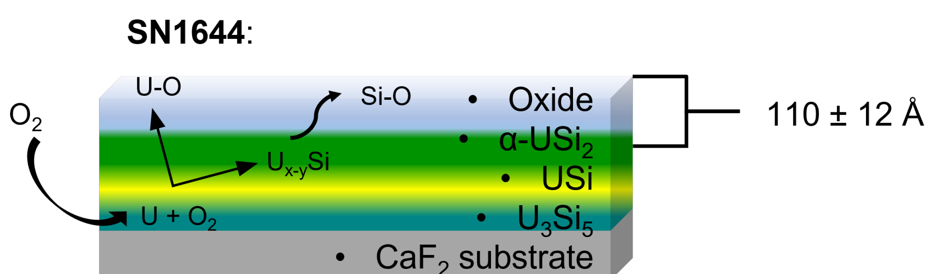

FIGURE 6.48. Schematic diagram depicting the oxidised structure of U_3Si_5, SN1644. Formation of multiple uranium silicide phases indicated with yellow (USi) and USi_2 (green), underneath silicon dominated oxide layer. Total oxide layer thickness shown to be 110 ± 12 $\mathring{A}$.

6.5.4 α-USi$_2$

The characterisation carried out on oxidised uranium disilicide, $\alpha - USi_2$ sparked further interest in the stabilisation of higher uranium silicides. The structural characterisation of the $\alpha - USi_2$ phase was showcased using two epitaxial thin film samples: SN1645 and SN1702. These samples were stabilised using uranium deposition powers of 19 W and 10 W, respectively. This large range indicates that the stabilisation of $\alpha - USi_2$ occurs with a varied uranium content. Observing the modified binary phase diagram of uranium and silicon, presented in Figure 6.49, it can be seen that both U_3Si_5 and $\alpha - USi_2$ exist within a small range with regards to silicon content. Therefore, it could be proposed that the formation of two epitaxial phases, presented as part of this oxidation work, is a result of the formation of non-stoichiometric phases that retain their ordered crystal structures. Furthermore, the epitaxial lattice between each uranium silicide phase and [001] CaF_2, will also have a strong influence in the formation of each compound. This infers that a combination of epitaxial lattice matching and non-stoichiometric phase formation influences the stabilisation of uranium silicide thin film.

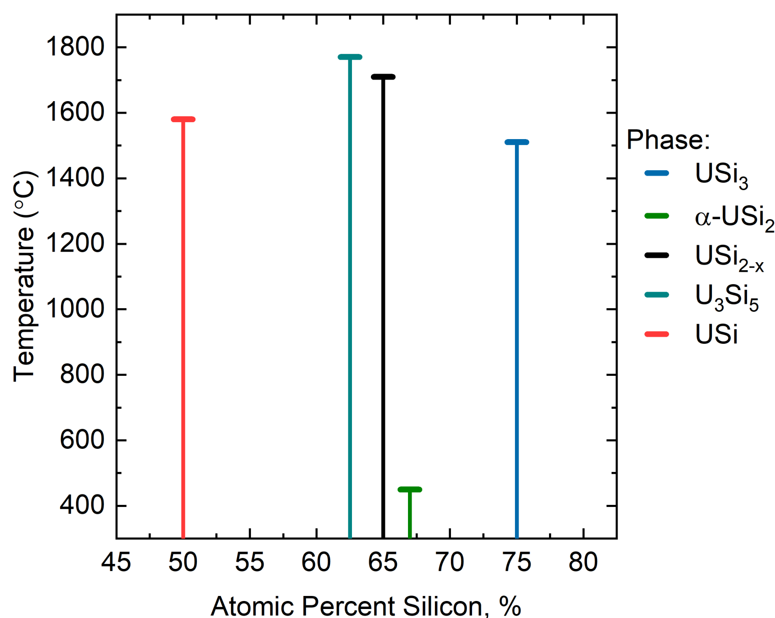

FIGURE 6.49. Modified binary phase diagram showing uranium and silicon phases as a function of atomic silicon content. USi and USi_3 are shown as reference points compared to U_3Si_5 and α-USi_2. Atomic silicon content values extracted from [44] and [175].

The structural characterisation of SN1645 and SN1702 showed the stabilisation of two epi-

taxial $\alpha-USi_2$ thin films. The high-angle data presented from both samples indicated that the crystals are orientated in the [001] direction with the (004) Bragg reflection being the specular reflection. For SN1645, stabilised using a uranium deposition power of 19 W, had a specular 2θ position modelled at 25.375 ± 0.001°. Epitaxial $\alpha-USi_2$ deposited using 10 W of uranium (SN1702), was found to have a specular (004) 2θ position of 25.655 ± 0.001°. Furthermore, the 10 W $\alpha-USi_2$ specular position changed as a function of exposure time. This was noted in the high-angle XRD spectra collected from the sample. Table 6.15 indicates the 2θ positions of both SN1645 and SN1702 as a function of surface oxidation. Here, the corresponding specular lattice parameter for each oxidation cycle is also presented. The largest difference between the bulk lattice parameter, obtained from *Sasa et al.,* [50], is around 2%. This indicates the even once exposed to ambient temperatures and environments, the α phase of uranium disilicide, oriented in the [001] direction, does not exhibit large structural changes.

Table 6.15: Table of structural constants collected from pristine and oxidised epitaxial (004) α-USi_2 thin films. Parameters extracted from SN1645 and SN1702. Bulk values shown for structural comparison.

Sample	Phase	Exposure time (hrs)	2θ (°)	c (Å)	Ref.
SN1645	α-USi_2 (004)	1	25.375 ± 0.001	14.02 ± 0.01	This work
		10	25.435 ± 0.001	13.99 ± 0.01	
		24	25.435 ± 0.001	13.99 ± 0.01	
		48	25.435 ± 0.001	13.99 ± 0.01	
		1322	25.435 ± 0.001	13.99 ± 0.01	
SN1702	α-USi_2 (004)	1	25.655 ± 0.001	13.87 ± 0.03	This work
		10	25.475 ± 0.001	13.97 ± 0.03	
		24	25.445 ± 0.001	13.99 ± 0.03	
		48	25.415 ± 0.001	14.00 ± 0.03	
		1322	25.415 ± 0.001	14.00 ± 0.03	
Bulk	α-USi_2	-	25.147	14.154 ± 0.002	*Sasa et al.,* [50]

The high-angle XRD investigations allowed for both $\alpha-USi_2$ samples to be characterised structurally, however, it was also important to understand this phase chemically. For the chemical characterisation investigation, SN1645 was chosen. Here, XPS depth profiling techniques were used to probe the oxide and metallic bonding environment that appear as a function of oxide growth. Previous chemical characterisation investigations conducted on pristine $\alpha-USi_2$ (SN1379, Chapter 5), suggested that the Si:U stoichiometry was likened to a uranium monosilicide (USi), rather than a uranium disilicide, producing a Si:U ratio of around 1. Therefore, it was important to understand how a native oxide may influence this chemical bonding. From investigating the potential uranium oxide compounds, it was inferred that a hyper-stoichiometric compound, similar to UO_2 may have formed at the very surface of $\alpha-USi_2$. As the depth profile sputtering time increased, the oxide content relating to U-O compounds fluctuated. Through

investigating the silicon-oxides, the data suggested that a hyper-stoichiometric Si-O formed at the very surface of SN1645, with an increased oxygen content. As the sputtering cycles commenced, this oxygen content reduced, to suggest the formation of a hyper-stoichiometric compound, similar to SiO_2. It was possible to also probe the metallic compounds, by investigating the relative ratios between the metallic components in the U-4f and Si-2s. By normalising these components to their respective photoionisation cross section values, as provided by *Yeh et al.,* [145], it was found that a sub-stoichiometric USi_3 phase had formed at the very surface of SN1645. This suggests preferential oxidation of the uranium sites, allowing for uranium silicide phases with increased silicon content to form. As the surface oxide layers of SN1645 were removed, the Si:U content decreased, inferring the formation of a mixed layer of USi/$\alpha - USi_2$. The Si:U ratio fluctuated around a value of 1.5, suggesting a mixed phase.

Combining the information gathered about the ambient surface oxidation of USi_2, it was possible to model the oxide thickness through the use of x-ray reflectivity (XRR). From the high-angle XRD, it was concluded that SN1645 and SN1702 were epitaxial $\alpha - USi_2$ stabilised upon (001) CaF_2. The XPS showed that there is a mixed USi/$\alpha - USi_2$ phase formed above the epitaxial film, with a USi_3 layer above this. The very surface of the sample (SN1645) was concluded to be a Si-O oxide. From this, GenX software was use to model the growth evolution of the surface oxide. From this data, it was found that the total film thickness was around $230 \pm 5\,Å$, with the oxide layer having a thickness of $63 \pm 5\,Å$.

The combination of all three techniques has allowed for a deeper understanding into how the sample looks physically. Figure 6.50 indicates SN1645 with each layer labelled, alongside the film and oxide thicknesses. Here, the total film thickness, attributed to the epitaxial $\alpha - USi_2$ film, with the total oxide thickness being the thickness modelled from the remaining U-Si phases, alongside the Si-O compound measured through XPS depth profiling.

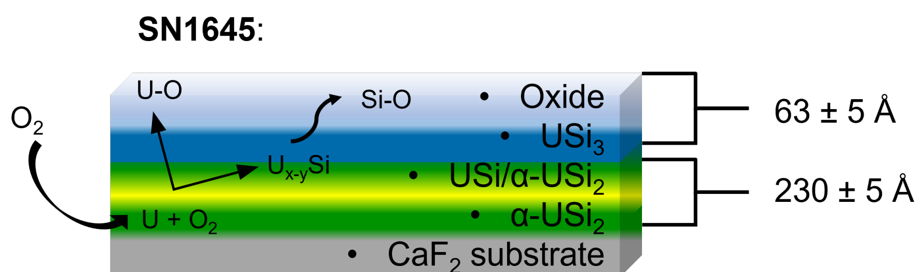

FIGURE 6.50. Schematic diagram depicting the oxidised structure of α-USi_2, SN1645.

Despite not being used as part of the XPS depth profile investigation, SN1702 was also

utilised to understand the oxide formation on the surface of $\alpha - USi_2$. From the data collected, the total film thickness after 90 hours of exposure was found to be 405 ± 3$\AA$, with the oxide layer being around 56 ± 2$\AA$. From the evolution of this native oxide, it was concluded that the native oxide passivates, with the initial oxide growth occurring prior to the measurements starting. This is noted in the increase in oxide thickness after 1 hour of exposure presented in Figure 6.40.

6.5.5 USi_3

The epitaxial stabilisation of USi_3 was conducted at 800$°C$ onto [001] CaF_2 for the purpose of studying the ambient surface oxidation. As the uranium silicide phase with the highest silicon content, understanding how this phase structurally changes as a function of exposure time is invaluable to understanding the surface oxidation of all uranium silicide compounds. Studies within the literature [94], have suggested that at elevated temperatures, uranium silicide compounds exhibit preferential oxidation at the metallic uranium sites, causing the formation of metallic uranium silicon phases with increased silicon content. Uranium trisilicide is thought to be the final phase formed before uranium and silicon sites begin to form uranium oxide and silicon oxide compounds [94].

High-angle XRD spectra collected from (001) USi_3 (SN1700) as a function of time was used to observe the structural changes occurring in the sample as a result of surface oxidation. Table 6.16 presents the specular structural changes as a function of exposure time. Here, comparisons are made between the pristine USi_3 sample, SN1699, and the bulk structure data provided by *Brixner et al.,* [51]. As there were no changes to the 2θ position of 21.935 ± 0.001°, only one measurement is shown as a comparison from SN1700. From the specular lattice parameters presented in Table 6.16, it can be seen that both the pristine (SN1699) and oxidised (SN1700), match within their calculated errors. The specular lattice parameter, extracted from both epitaxial thin films, are contracted by around 0.2%, suggesting that the surface oxidation of USi_3 does not effect the cubic crystal structure. Additional off-specular phi scans conducted on oxidised USi_3 further showed that the oxidation does cause distortions to the structure, with unique reflections being present in the (113) reflection of USi_3. The off-specular reflections collected from the film and substrate of SN1700, confirmed that the two systems epitaixally match with a $\sqrt{2}$ rotation.

The structural characterisation of SN1700 it was shown that the changes that occur as a result of surface oxidation are minimal. XPS depth profiling techniques were deployed to study the evolution of metal and oxide chemical bonding environments within USi_3. Here, the surface layers of SN1700 were removed using Ar sputtering, with data acquired from the new surface after each sputter cycle. The data collected from the U-4f oxide and O-1s U-O components suggested that the USi_3 surface oxide compounds exhibit O:U ratios of uranium oxides with increased

Table 6.16: Table of structural constants collected from pristine and oxidised epitaxial (001) USi_3 thin films. Parameters extracted from SN1700 and SN1699. Bulk values shown for structural comparison.

Sample	Phase	2θ (°)	c ($\AA$)	Ref.
SN1700	USi_3 (001)	21.935 ± 0.001	4.05 ± 0.01	This work
SN1699	USi_3 (001)	21.907 ± 0.001	4.05 ± 0.01	This work
Bulk	USi_3 (001)	21.874	4.060 ± 0.005	*Brixner et al.,* [51]

oxygen content. From this analysis, there was minimal indication that a stoichiometric uranium oxide compound had formed. Investigating the silicon oxide ratios, there was a suggestion that a stoichiometric SiO_2 compound had formed on the very surface of SN1700. By analysing the areas of the U-4f and Si-2s metallic components, the Si:U stoichiometry was probed as a function of oxide depth. This data suggested the formation of a hyper-stoichiometric compound on the very surface of SN1700, with a Si:U ratio of 8.7 ± 0.9. The binary phase diagram for uranium and silicon only has stoichiometric line compounds up to USi_3. Therefore suggesting this compound is not stoichiometric and has an excess of metallic silicon. As the sputter cycles commence, the data is interpreted to have a Si:U ratio that fluctuates around a value of 3.0, suggesting the formation of a hyper-stoichiometric USi_3 compound that has formed on the surface of the epitaxially stabilised film.

The analysis conducted on the surface of USi_3 using XRD and XPS, allowed for the thickness of the native oxide to be probed. The formation of the surface oxide was observed as a function of time using x-ray reflectivity (XRR). This surface sensitive technique allows for the layer thickness, interface roughness, and electron density to be probed. The final parameters extracted from the final x-ray reflectivity spectra, presented in Figure 6.44, indicates that the total film thickness was $300 \pm 3\AA$, with the total oxide thickness being around 50 ± 2Å. From the XPS Si:U metallic stoichiometry, it was concluded that the oxide layer was comprised of a hyper-stoichiometric USi_3 layer alongside a stoichiometric SiO_2 layer. The combination of all results obtained from the oxidation studies conducted on USi_3 has allowed for a schematic to be formed, depicting the physical structure of SN1700 as a result of ambient surface oxidation. Figure 6.51 presents this schematic diagram of the individual compounds present in SN1700 with the film and oxide thicknesses labelled. Here, the stoichiometric USi_3 layer is presented in dark blue, with the USi_{3+x} layer starting above this and extending into the bulk of the oxide layer. This layer mixing is represented with a blue to white gradient, suggesting a change in the amount of the USi_{3+x} present. From the XPS data collected from SN1700, it can be concluded that the bulk of the oxide layer in Figure 6.51, is dominated with silicon and silicon oxides.

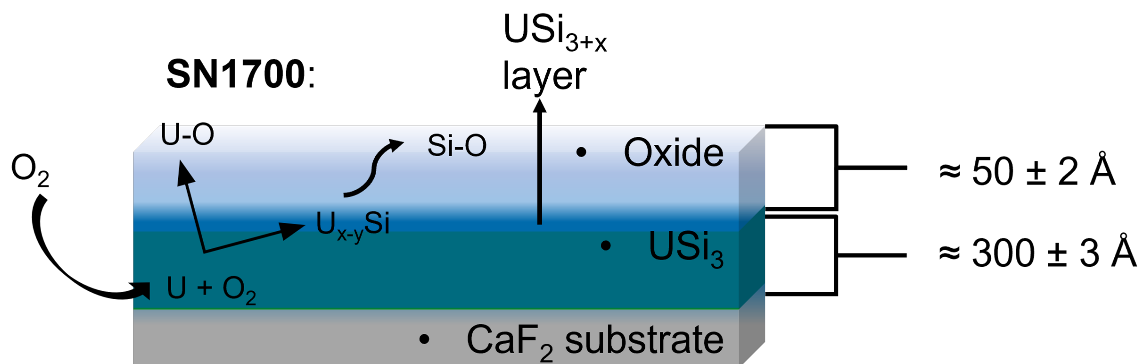

FIGURE 6.51. Schematic diagram depicting the oxidised structure of USi_3, SN1700. Formation of hyper-stoichiometric USi_3 shown as inter-layer between epitaxial USi_3 film and silicon dominated oxide layer.

6.6 Conclusions

The work presented in this chapter set out to answer three questions regarding the surface oxidation of uranium silicide phases: (1) How much to do uranium silicide phases change as a function of uranium content once exposed to ambient conditions? (2) What compounds form within each uranium silicide phase oxide layer? and (3) How thick is the oxide layer that grows on each uranium silicide phase under ambient conditions? Through the use of structural and chemical characterisation techniques, these questions regarding the oxidation behaviour have been answered.

X-ray diffraction was utilised to investigate the structural changes that may occur to uranium silicide phases as a result of ambient surface oxidation. For the purpose of this work, epitaxial uranium silicide thin films were exposed to air under ambient conditions to probe the surface oxidation as a function of uranium content. The structural characterisation presented in this chapter, built upon the characterisation conducted on uranium silicide phases in Chapter 5. The work presented there firstly showed that x-ray diffraction techniques could be used to probe the crystalline nature of uranium silicide phases. By replicating the techniques used to characterise pristine samples, it was possible to probe the structural nature of oxidised uranium silicide phases. This chapter required a new series of samples, that utilised the synthesis recipes detailed in Chapters 4 and 5. The samples used for these oxidation studies were all stabilised upon [001] oriented CaF_2 single crystal substrates. The stark difference between the samples presented in this chapter and those previously showcased in Chapter 5, is that the oxidation samples were not capped with a protective niobium capping layer. Allowing for the surface of each sample to be exposed to an atmospheric environment.

The structural characterisation of uranium silicide phases has shown that through the use of DC magnetron sputtering, samples can be replicated to form a range of uranium silicide phases that extend across the binary phase diagram. Characterisation of uncapped uranium silicide phases has reinforced that this form of synthesis can be reproduced to stabilise each phase as an epitaxial thin film. Figure 6.45 showcases the uncapped uranium silicide phases, shown with solid lines, alongside their pristine counterparts, shown with dashed lines, which were structurally and chemically characterised in Chapter 5. The work presented here provides an indication into how the uncapped samples structurally vary when compared to pristine samples.

Overall, the structural work presented here has shown that DC magnetron sputtering can be used to produce uncapped uranium silicide thin films through the stabilisation of epitaxial thin films. This has been shown with the stabilisation of [001] U_3Si, [100] U_3Si_5, [001] $\alpha-USi_2$, and [001] USi_3 epitaxial samples, alongside polycrystalline U_3Si_2 samples. The work presented in this chapter has also shown that the high-angle XRD characterisation techniques can also be used on oxidised epitaxial uranium silicide thin films. The ability to do so has shown that the ambient surface oxidation of all uranium silicide phases presented still retain and match their pristine crystal structure. The most significant structural change was exhibited by [100] U_3Si_5 (SN1644), where the specular (a) and in-plane (c) lattice parameters contracted by 1.3% and 7.1%, respectively. This contraction results in an overall decrease in the unit cell of U_3Si_5 to $57.4 \pm 0.1\text{Å}^3$. The minimal changes occurring to each structure, as a result of ambient oxidation, may infer the retention of the metallic nature of each phase.

The chemical bonding of each uranium silicide phase, which had been structurally characterised, was investigated using a x-ray photoelectron spectroscopy (XPS) depth profiling technique. The aim of this experiment was to probe oxide layers as a function of oxide thickness in order to understand the compounds that form under ambient conditions. Additionally, the oxide layers were investigated as a function of uranium content. To gather this information about the oxidised surface, layers were removed using a Ar^+ sputtering source with data acquired from the newer surface after each sputter cycle. The largest take away from the XPS depth profile experiments, was the formation of higher silicon content uranium silicide phases as a product of surface oxidation. This showed, that each uranium silicide phase has the tendency to preferentially oxidise at the metallic uranium sites. This work aligns with the high-temperature steam experimental studies conducted on U_3Si_2 by [94], as well as the theoretical oxidation studies conducted by *Jossou et al.,* [87]. In both cases, the work showed the preferential oxidation of U_3Si_2 at the uranium sites. The work conducted by *Yang et al.,* [94] showed U_3Si_2 formed uranium silicide compounds up to USi_3 before oxidising to UO_2 as a function of temperature. The work presented in this thesis, indicates that all uranium silicides do this, even under ambient conditions. This

is the first time a study like this has been conducted on uranium silicide layers, especially for the epitaxial layers. Additionally, it was clear that in this work, the mineral coffinite ($USiO_4$) was not found to be present in any of the ambient oxide layers forming on the U-Si phases. This contradicts the work conducted by Yeh *et al.,* [58], which concluded that U_3Si_2 oxidised to form $USiO_4$ when exposed to ambient oxygen environments. Finally, the XPS spectra collected from the surface of U_3Si_5 has been presented again. The first time pristine U_3Si_5 spectra was presented was in Chapter 5 of this thesis.

Finally, the identification of surface oxide compounds for each uranium silicide phase through the use of x-ray photoelectron spectroscopy (XPS) made it possible for the oxide thickness to be modelled using x-ray reflectivity (XRR). The presence of both U-O and Si-O phases were detected using XPS, and as a result were added into each XRR model. What must be stressed here is that the neither oxide phase was detected in the specular and off-specular diffraction studies. For the Si-O, this may suggest the formation of an amorphous material within the oxide layer of each uranium silicide. In addition to the oxide thickness, the potential passivation of each oxide layer was also probed. The thickness of each uranium silicide native oxide has been measured and modelled at an $\AA$ngstrom level for the first time. Table 6.17 presents the oxide thickness modelled for each uranium silicide phase alongside the compounds deemed to be part of the surface oxide.

Table 6.17: The oxide thicknesses and oxidation products forming on the surface of each uranium silicide phase under ambient conditions.

Phase	Oxide Thickness ($\AA$)	Oxidation Products
U_3Si	45 ± 12	U_3Si_2, U-O, Si-O
U_3Si_2	30 ± 5	U_3Si_2, U-O, Si-O
U_3Si_5	110 ± 12	USi, USi_2, U-O, Si-O
α-USi_2	63 ± 5	USi, USi_3, U-O, Si-O
USi_3	50 ± 2	USi_{3+x}, U-O, Si-O

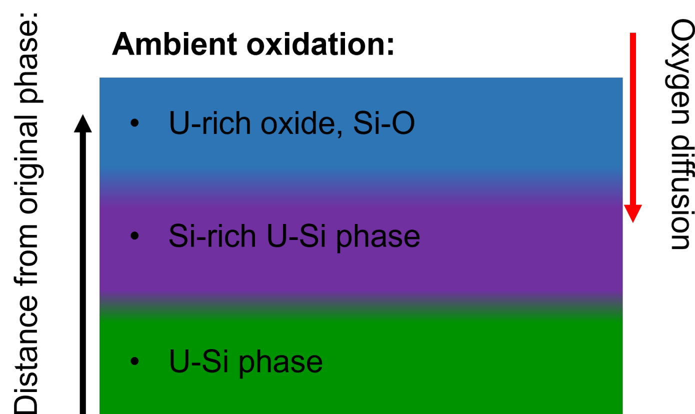

FIGURE 6.52. Schematic diagram depicting the proposed model for the ambient oxidation of U-Si phases. Diagram indicates the formation of compounds as a function of distance from the original U-Si phase.

Finally, the combination of all three techniques has allowed for a deeper understanding into the mechanism that governs the ambient oxidation for all uranium silicide phases. Figure 6.52 presents a schematic diagram of how uranium silicide phases oxidise under ambient conditions. Here, the compounds that form are indicated as a function of distance from the original phase. This mechanism agrees with the oxidation work conducted by *Jossou et al.,* [87] on U_3Si_2 and with the high-temperature work conducted by *Yang et al.,* [94]. The ambient oxidation work presented here on uranium silicide phases has accounted for multiple compounds and how they oxidise as a function of time, thus combining the models proposed by *Jossou et al.,* and by *Yang et al.,*, regarding the preferential oxidation of uranium sites within uranium silicide phases. Presenting the ambient oxidation of uranium silicide thin films has paved the way for additional experimental work to be conducted on these phases.

CHAPTER 7

The Corrosion of Uranium Silicide Compounds

This chapter details an investigation into the aqueous corrosion mechanisms of U-Si compounds. The work presented here aims to piece together trends that occur between the individual phases that extend across the U-Si binary phase diagram as a function of uranium content by utilising engineered single crystal thin films. Here the corrosion behaviour of U-Si phases is investigated when the interfaces are in contact with H_2O and H_2O_2. Comparisons are drawn between the uranium silicide phases and the reported termination oxide species: UO_2 and SiO_2.

7.1 The Corrosion of U-Si Phases in Water

This investigation provides an indication of how the U-Si and oxidation phases formed during room temperature exposures behave within aqueous environments prior to in-reactor operation. In particular, observing the dissolution behaviour of U-Si phases in water allows for a simplistic model to be formed, building a foundation for how to predict the behavior of U-Si phases in extreme aqueous environments.

7.1.1 Experimental Set up

The dissolution of U-Si phases in water was investigated using single crystal U_3Si, $\alpha-USi_2$, USi_3, and poly-crystal U_3Si_2. Epitaxial U_3Si_5 (SN1644) has been omitted from this investigation, due to the growth parameters used to synthesise the crystal. The increased uranium content used to engineer SN1644 may result in unreliable corrosion results. Single crystal UO_2 and

amorphous silicon samples were also used in this experiment to investigate how U-Si oxidation products behave when exposed to water. The use of UO_2 also allowed for a direct comparison between proposed U-Si ATFs and current nuclear fuel.

The samples used for this investigation had previously been used for oxidation studies in Chapter 6. These samples had been cut into 5 x 5 mm samples with the exception of the UO_2 and Si. This allowed for sample consistency across both the oxidation and dissolution studies for the U-Si phases. To investigate the corrosion in water, one piece of each phase was placed in 5 ml of MilliQ water at room temperature for total exposure times of: 60, 900, 8100, and 86400 seconds. 5 ml of MilliQ water was sufficient to completely cover the surface of each sample tested. The effect of each exposure time was then monitored used x-ray reflectivity (XRR), and high-angle x-ray diffraction (XRD). Data collected from these measurements were analysed using the methods detailed in Chapter 3.

7.1.2 Results

7.1.2.1 U_3Si

Initial dissolution studies were performed on triuranium silicide, U_3Si by exposing the oxidised surface of SN1711 to MilliQ water. Here, the exposure was studied under ambient conditions, with the changes to the surface being monitored through the use of high-angle XRD, and x-ray reflectivity (XRR). The structural characterisation of SN1711 was presented in Chapter 6, so will not be presented again. Here, it was confirmed that SN1711 is a two domain epitaxial crystal of U_3Si, with U_3Si_2 inclusions. Figure 7.1 presents the high-angle XRD data extracted from SN1711 as a function of H_2O exposure. Data is indicated with open black circles, and the models used to simulate the data are presented with solid lines. The exposure times are indicated in the figure legend. Phases identified within the spectra are indicated with drop lines, alongside the corresponding Bragg reflection. Spectra collected from SN1711, prior to H_2O exposure is presented in yellow. Bragg reflections from the (001) and (210) of U_3Si_2 are present, alongside the specular (002) reflection from U_3Si.

The most significant change to the spectra occurs after 60 s of H_2O exposure, with the immediate growth of a reflection situated around a 2θ value of $25°$. This peak has been attributed to the (004) Bragg reflection of $\alpha-USi_2$, indicated with a green drop line. The presence of this phase within the sample agrees with the preferential oxidation model discussed in Chapter 6, which suggests the oxidation of uranium over silicon, allowing for the formation of silicon-rich phases.

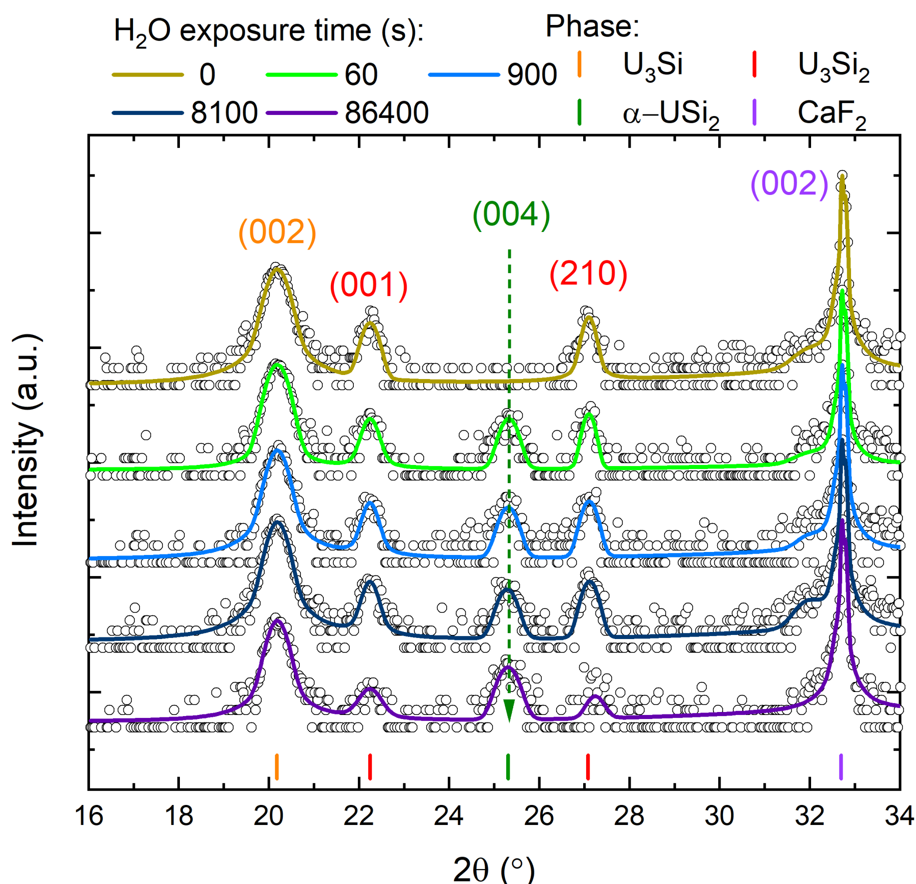

FIGURE 7.1. High angle XRD data (open circles) and model (solid lines) of U_3Si single crystal (SN1711) after exposure to MilliQ H_2O for 0, 60, 900, 8100, 86400 s. Phases within the sample are indicated with drop lines, and corresponding Bragg reflections. Intensity presented on a log scale.

The presence of this phase was confirmed structurally by observing the higher order Bragg reflection of the (004). Figure 7.2 presents a isolated region of the specular diffraction spectra collected from SN1711 after 24 hours of H_2O exposure. Here, additional reflections from U_3Si_2 were found, further confirming its poly-crystalline nature, alongside the second order reflections stemming from the (004) of U_3Si and the (008) of $\alpha-USi_2$. The crystalline nature of $\alpha-USi_2$ was probed, however, there were no unique reflections found for this phase when conducting off-specular ϕ scans. The 2θ position of the (008) reflection was found to be $51.83 \pm 0.01°$. This has a 2θ difference of 0.48° when compared to the standardised Bragg reflection positions, provided by *Guo et al.,* [176], for $USiO_4$ when using an x-ray wavelength of 1.54Å.

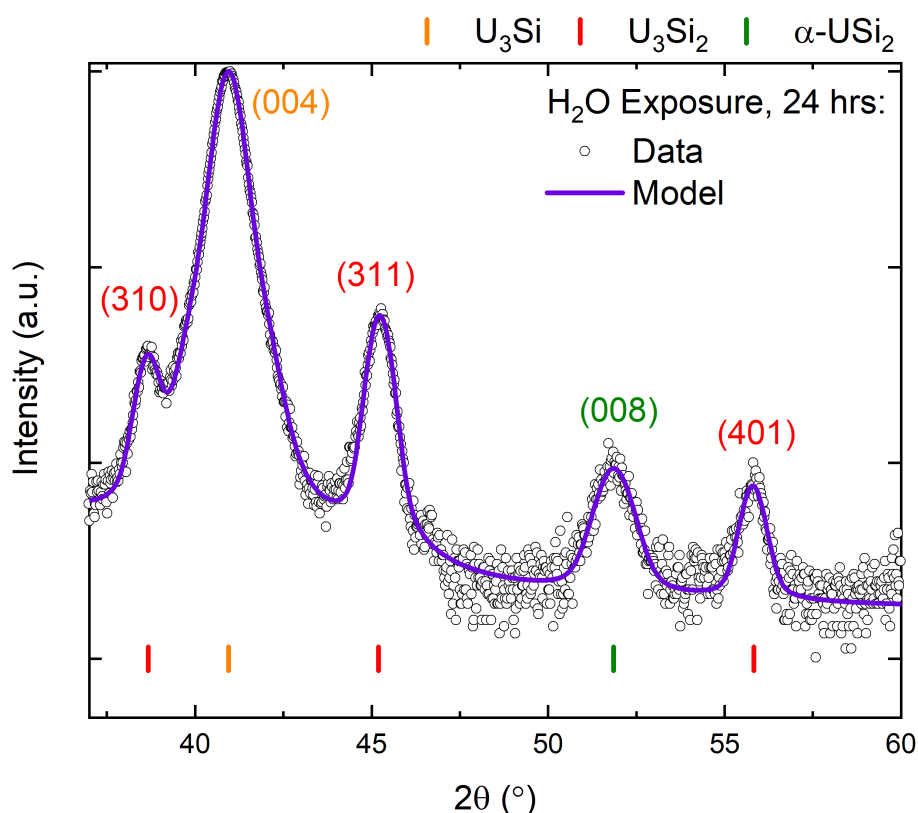

FIGURE 7.2. Isolated high-angle XRD data (open circles) and model (solid lines) of U_3Si single crystal (SN1711) after exposure to MilliQ H_2O for 24 hours. Data highlighting the (008) of α-USi_2. Data taken from SN1711. Intensity presented on a log scale.

The dissolution effect of water on U_3Si was also monitored using x-ray reflectivity. Figure 7.3 presents the XRR data collected from SN1711. Here, the spectra has been offset to allow for an easier visual comparison. The H_2O exposure times are indicated in the figure legend. Furthermore, the region of the XRR spectra presented here has been cut to highlight regions of interest within the data at lower Q values. It can be seen from the spectra that there is significant roughening of the layer interfaces present within SN1711, this is indicated with the lack of Keissig fringes. Small features can be noted around a Q value of 0.1Å^{-1}. As the exposure time increases, there is a significant blurring in the fringes, and a decrease in the ability to resolve any fringes stemming from the spectra. This indicates a change in the overall thickness of the film, thus indicating that once exposed to H_2O, changes occur to (001) U_3Si.

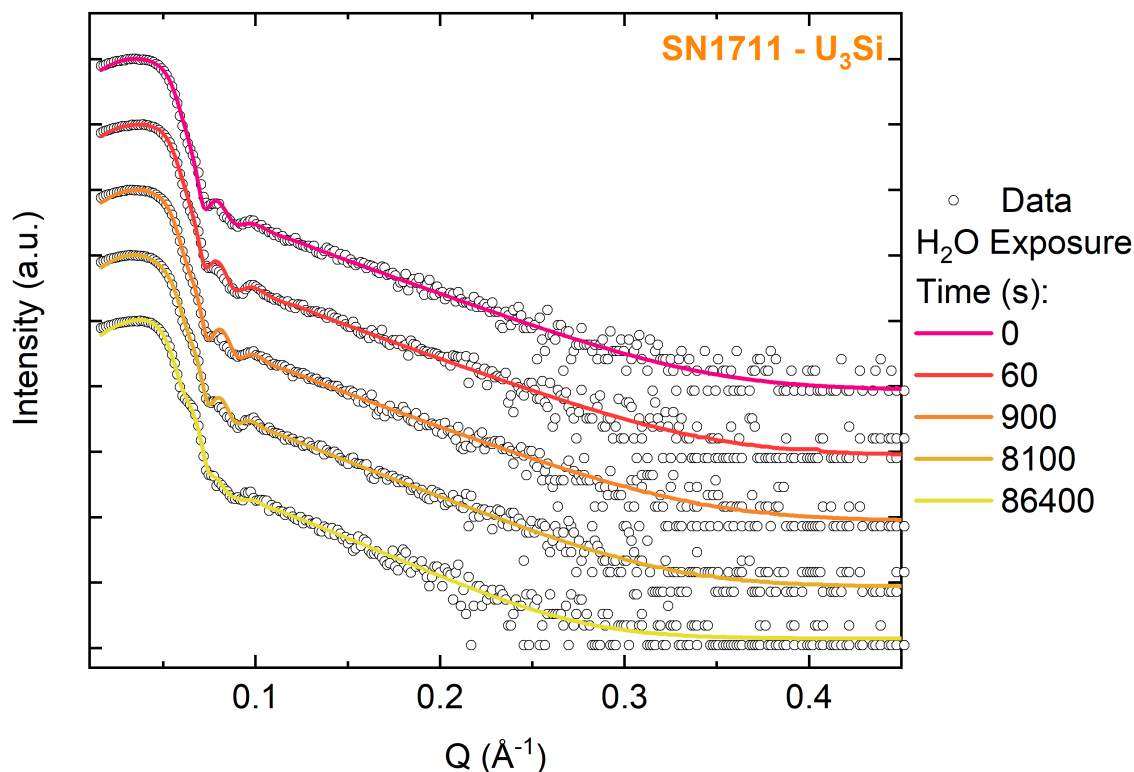

FIGURE 7.3. X-ray reflectivity data (open circles) and model (solid lines) of U_3Si single crystal (SN1711) after exposure to MilliQ H_2O for 0, 60, 900, 8100, 86400 s. Exposure times are indicated in figure legend. Data from SN1711. Intensity presented on a log scale.

Figure 7.4 presents the layer thicknesses modelled in SN1711 as a function of exposure to H_2O. The total film thickness is indicated with open black triangles, the epitaxial U_3Si film with open orange squares, U_3Si_2 with open red diamonds, the silicon-rich oxide layer with open blue pentagons, and the USi_2 phase with open green stars. The inclusion of the uranium disilicide phase was included after 60 s of exposure. Over the duration of the H_2O corrosion experiment, the thickness simulated from the XRR data increased by 93 ± 25Å. This suggests that U_3Si exhibits a structural expansion once exposed to H_2O under ambient conditions. From Figure 7.4, all three layers considered to be part of the oxide increase as a function of time, suggesting they all contribute to this overall growth.

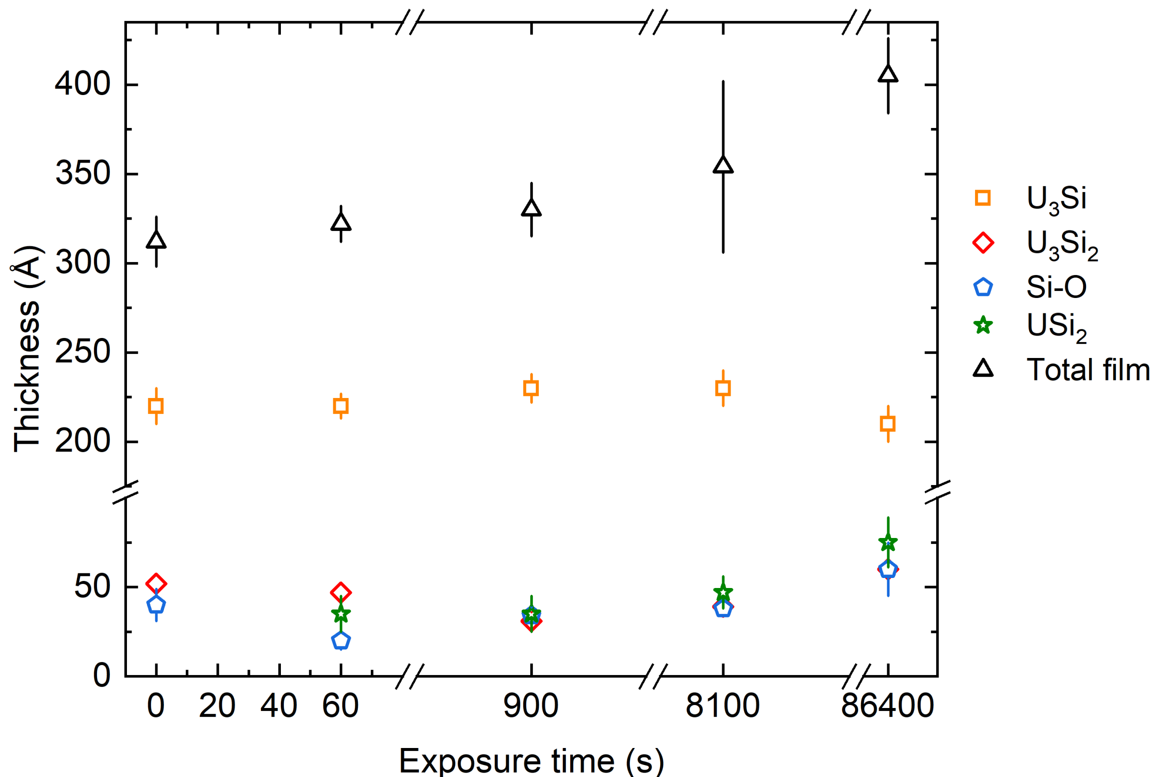

FIGURE 7.4. Layer thickness evolution of SN1711, (001) U_3Si, after exposure to MilliQ H_2O for 0, 60, 900, 8100, 86400s. Compounds are indicated in figure legend with, total thickness in open black triangles, U_3Si with open orange squares, U_3Si_2 with open red diamonds, Si-O rich oxide layer with open blue pentagons, and USi_2 with open green stars. Data from SN1711.

7.1.2.2 U_3Si_2

Previous structural and chemical characterisation of SN1707 indicated that this sample is a mixed poly-crystalline sample consisting of U_3Si_2 and U_3Si. Through previous XRR studies, it was found that the surface oxide, native to SN1707 is around 30 ± 5 Å. Probing the behaviour of this phase when in contact with an aqueous environment is the next logical step in understanding the ambient corrosion of U_3Si_2.

The high-angle XRD spectra collected from SN1707, poly-crystalline U_3Si_2, as a function of exposure time to MilliQ H_2O, is presented in Figure 7.5. The data collected from SN1707 is indicated with open black circles, and the models used to simulate each spectra are indicated with

solid lines. Here, each colour corresponds to a different exposure time to H_2O. Phases present within the sample are indicated with drop lines, with red, orange, and purple corresponding to U_3Si_2, U_3Si, and CaF_2, respectively. Bragg reflections (hkl), are indicated above each peak. Observing the spectra, is it clear there are minimal structural and phase changes occurring to SN1707 as a result of aqueous interaction.

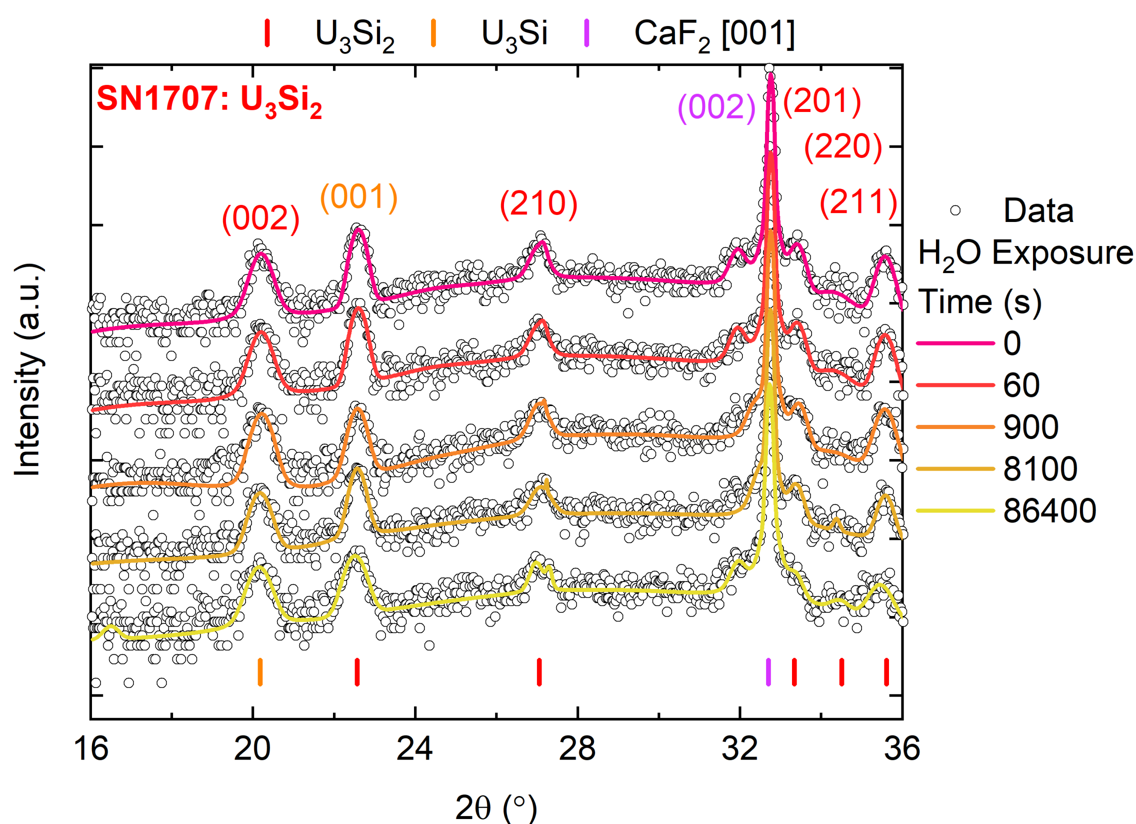

FIGURE 7.5. High angle XRD data (open circles) and model (solid lines) of poly-crystalline U_3Si_2 (SN1707) after exposure to MilliQ H_2O for 0, 60, 900, 8100, 86400 s. Phases within the sample are indicated with drop lines, and corresponding Bragg reflections. Intensity presented on a log scale.

To further probe the ambient water/fuel interface interaction, the changes in thickness of each film and oxide layer were investigated using x-ray reflectivity (XRR). Figure 7.6 presents the XRR spectra collected from poly-crystalline U_3Si_2 during the exposure to MilliQ water. The spectra collected as a function of exposure time has been offset to allow for an easier visual comparison. As the H_2O exposure times increase, the data changes in such a way that suggests a

roughening of layer interfaces. This is noted with the blurring of fringes within the final two data sets, presented in orange and yellow. The removal of fringes, and increase in overall roughness suggests that poly-crystalline U_3Si_2 exhibits structural changes once exposed to H_2O.

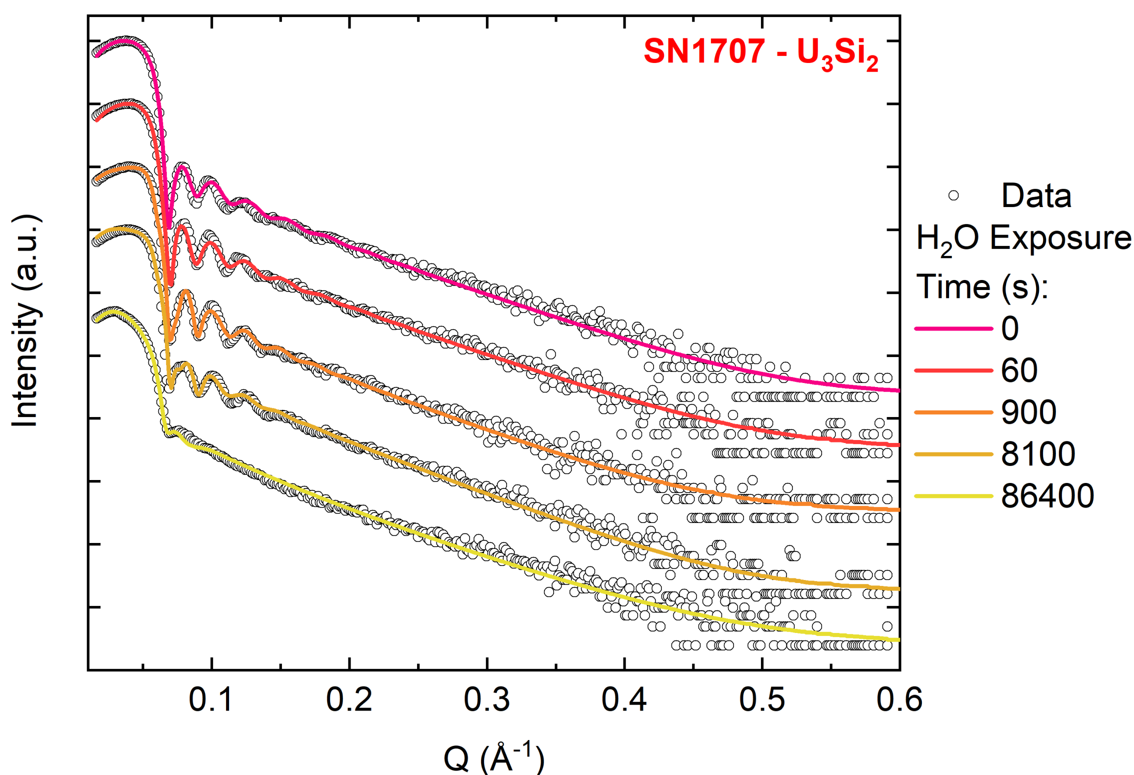

FIGURE 7.6. X-ray reflectivity data (open circles) and model (solid lines) of poly-crystalline U_3Si_2 (SN1707) after exposure to MilliQ H_2O for 0, 60, 900, 8100, 86400 s. Exposure times are indicated in figure legend. Data from SN1707. Intensity presented on a log scale.

The thickness of each layer was monitored through simulating the XRR spectra in Figure 7.6. The evolution of each layer thickness is presented in Figure 7.7. The total film thickness is indicated with open black triangles, the poly-crystalline U_3Si_2 film in open red squares, the U_3Si inclusion with open orange diamonds, and the silicon rich oxide layer with open blue pentagons. Initially, there is an increase in the total film thickness, with the silicon rich oxide contributing to this increase the most. This thickness gain was modelled to be around 68 ± 39 Å. After 900 s of exposure to H_2O, the film thickness begins to decrease as a function of time. This is noted

significantly in the overall thickness of the U_3Si_2 film. The overall decrease was measured to be 58 ± 52Å, with the change in thickness for the U_3Si_2 film being around 90 ± 30Å. The effect of H_2O on SN1707 resulted in a net gain of material, which was measured to be around 10 ± 40Å. However, this large error associated with this value suggests that other factors are preventing the true value to be modelled.

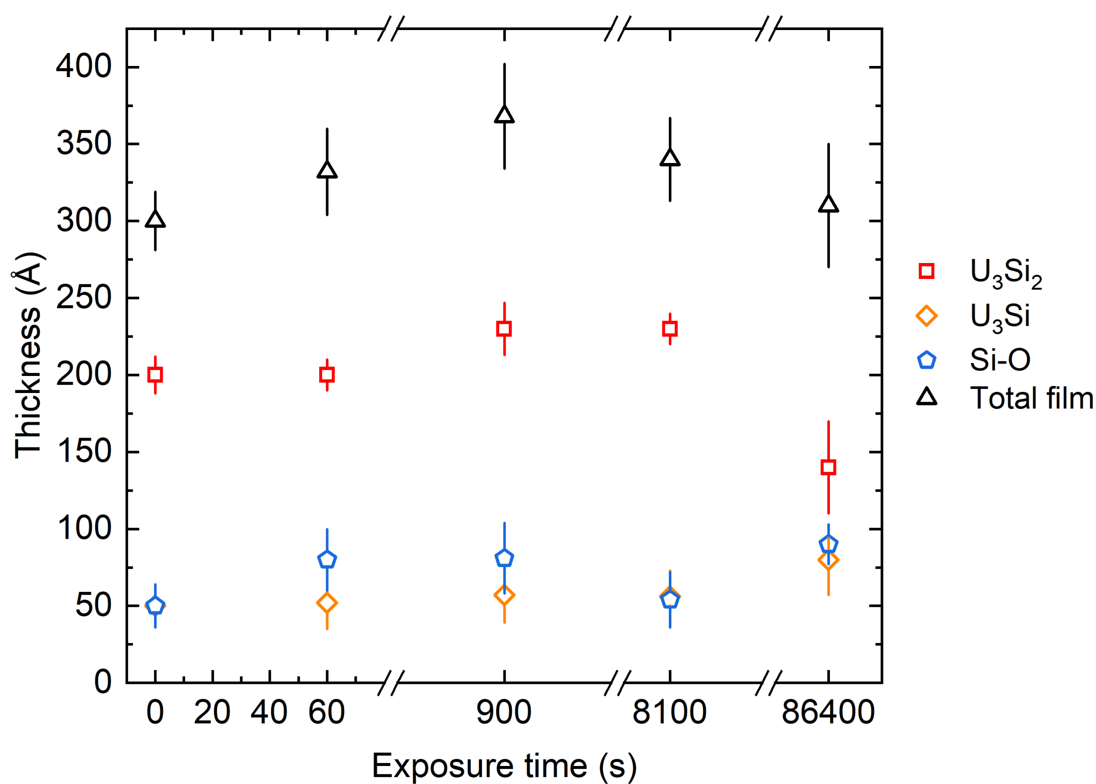

FIGURE 7.7. Layer thickness evolution of SN1707, poly-crystalline U_3Si_2, after exposure to MilliQ H_2O for 0, 60, 900, 8100, 86400s. Compounds are indicated in figure legend with, total thickness in open black triangles, U_3Si_2 with open red squares, U_3Si with open orange diamonds, and Si-O rich oxide layer with open blue pentagons. Data from SN1707.

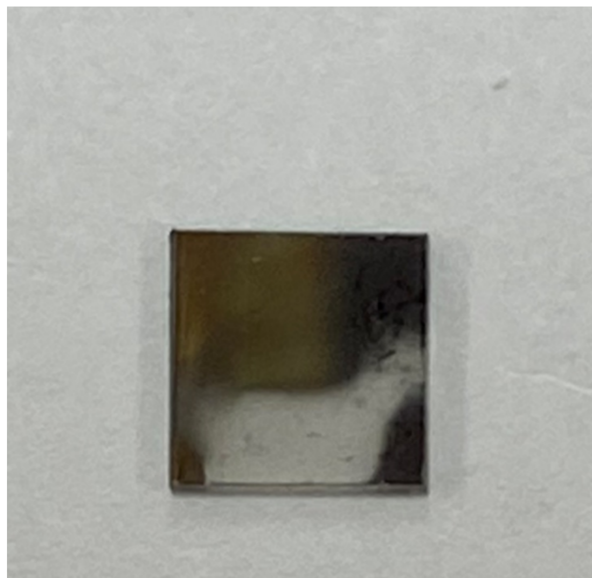

FIGURE 7.8. Photo of SN1707, poly-crystalline U_3Si_2, after exposure to MilliQ H_2O for 86400s. Data from SN1707.

Figure 7.8 presents photographic evidence of the eventual dissolution of U_3Si_2 once exposed to H_2O for 86400 s. Observing the film it is clear that some of the metallic film has been removed, uncovering the CaF_2 substrate below. This suggests why the roughness of the film is so high, as indicated in Figure 7.6, with the poor resolution of the Keissig fringes in the XRR spectra. The image presented here further indicates that H_2O has a significant effect on the aqueous dissolution of U_3Si_2.

7.1.2.3 α-USi$_2$

The corrosion behaviour of uranium disilcide, $\alpha-USi_2$, was initially investigated by exposing the surface of SN1702 to MilliQ H_2O. For this investigation, SN1702 was used. This sample had been previously investigated as part of the ambient oxidation study presented in Chapter 6. Here, SN1702 was shown to be a [001] oriented single crystal of $\alpha-USi_2$. The structural characterisation of SN1702 will not be presented again. Through probing the ambient oxidation of $\alpha-USi_2$ it was found that the native oxide consisted of USi, USi_3, and a silicon oxide rich layer at the very surface. The total oxide thickness was modelled to be 63 ± 5Å. Utilising this information about the oxide of $\alpha-USi_2$, it is possible to track and understand the dissolution of this phase once exposed to various media. Here the dissolution of SN1702 is presented as a function of exposure time to MilliQ H_2O.

Figure 7.9 presents the high-angle XRD data collected from SN1702. Data is indicated with

open black circles, with models being indicated with solid lines. The H_2O exposure time is indicated in the figure legend. The dissolution of $\alpha-USi_2$ in H_2O was monitored for up to 24 hours, this is indicated in yellow. From the data collected from SN1702 there is minimal change to the spectra as a function of exposure time. The Bragg reflections noted on the figure represent the (004), (100), and (002) of $\alpha-USi_2$, U_3Si_5, and CaF_2, respectively.

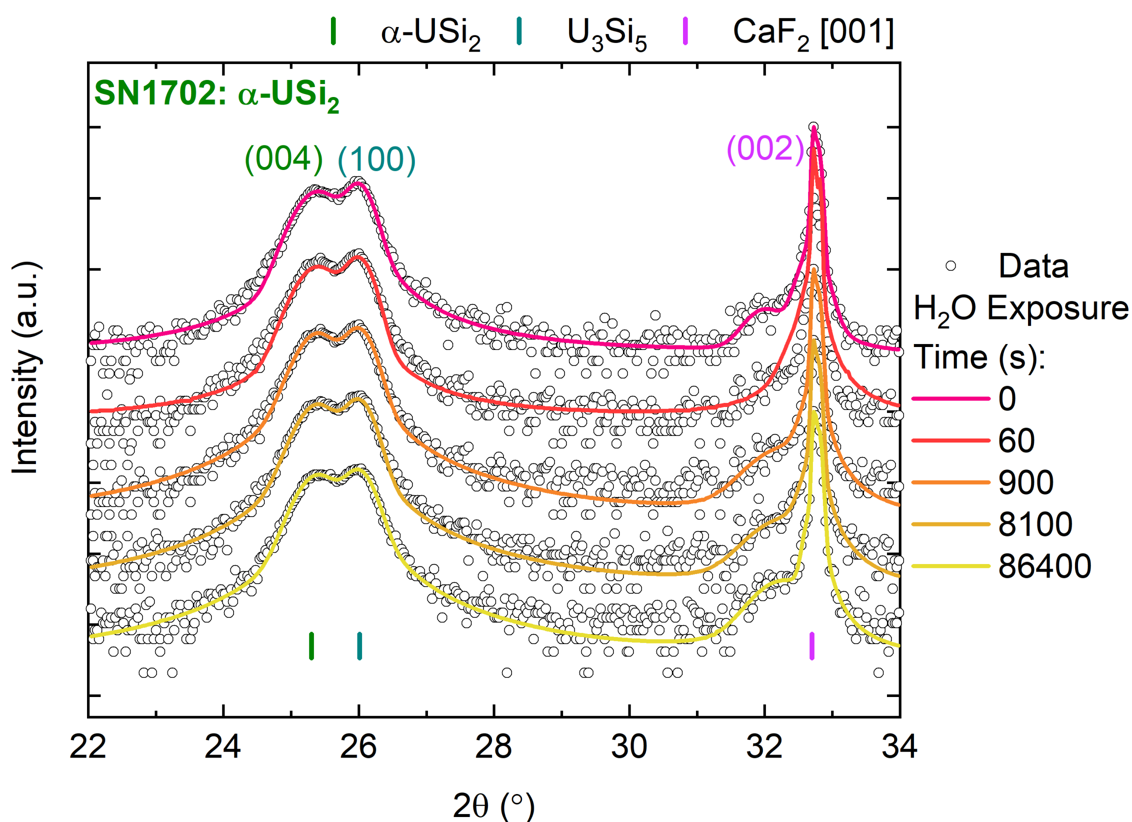

FIGURE 7.9. High angle XRD data (open circles) and model (solid lines) of α-USi_2 single crystal (SN1702) after exposure to MilliQ H_2O for 0, 60, 900, 8100, 86400 s. Phases within the sample are indicated with drop lines, and corresponding Bragg reflections. Intensity presented on a log scale.

The x-ray reflectivity spectra collected from SN1702 is presented in Figure 7.10. Five spectra are presented as a function of increasing exposure to MilliQ H_2O up to 24 hours. The data sets have been offset to allow for an easier visual comparison, with the spectra being presented between Q = 0.01 – 0.45 Å^{-1}, showcasing the spectral features present at lower Q values. Observing the spectra, there is a clear broader periodicity situated between 0.08 – 0.15 Å^{-1} indicating the

presence of a thinner additional layer presented within the sample, when compared to the bulk of the epitaxial film.

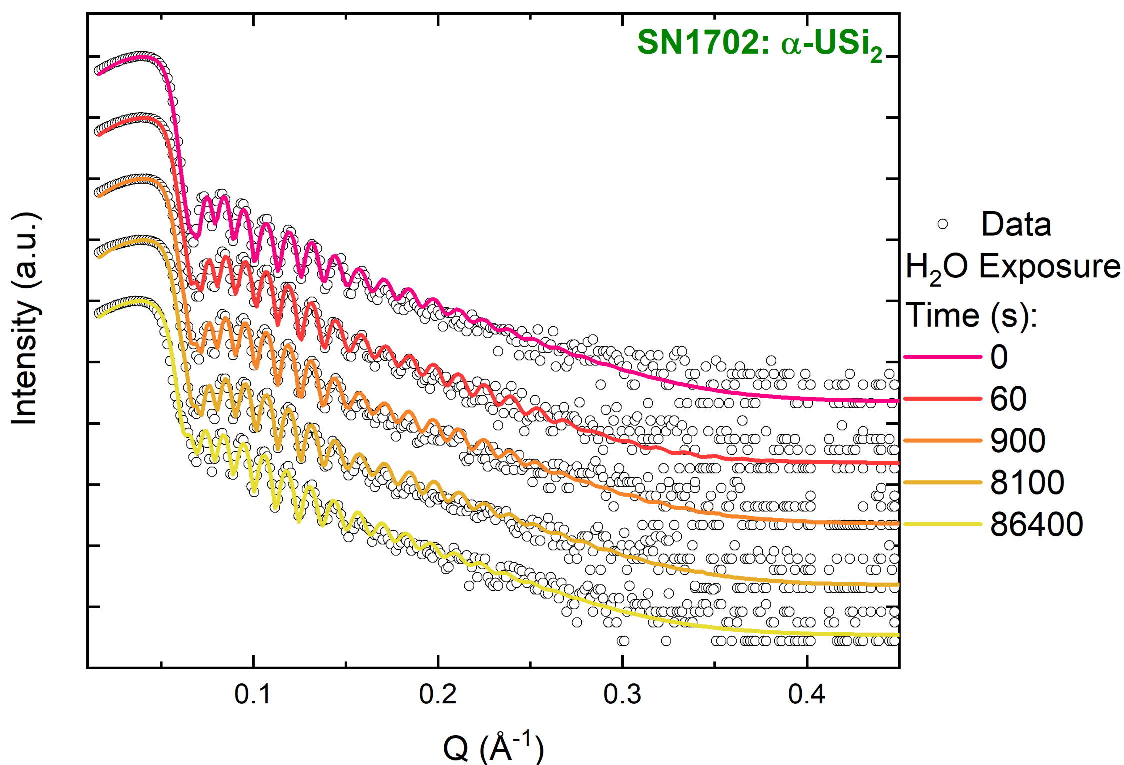

FIGURE 7.10. X-ray reflectivity data (open circles) and model (solid lines) of α-USi_2 single crystal (SN1702) after exposure to MilliQ H_2O for 0, 60, 900, 8100, 86400 s. Intensity presented on a log scale.

The thicknesses of each compound modelled for SN1702 is presented in Figure 7.11. The total thickness modelled using GenX was found to be 545 ± 11Å initially. This is indicated in Figure 7.11 with open black squares. The evolution of the total thickness of SN1702 is tracked as a function of H_2O exposure. The final thickness, measured after 24 hours of H_2O was found to be 553 ± 15Å, which indicates a total gain of around 8 ± 19Å. Through tracking the compounds considered to be the native oxides of $\alpha - USi_2$, it is clear that the Si-O compound contributes the most to the final increase in the oxide layer. There appears to be minimal thickness change inflicted upon the Si-rich uranium silicide oxide phases as a result of exposure to H_2O.

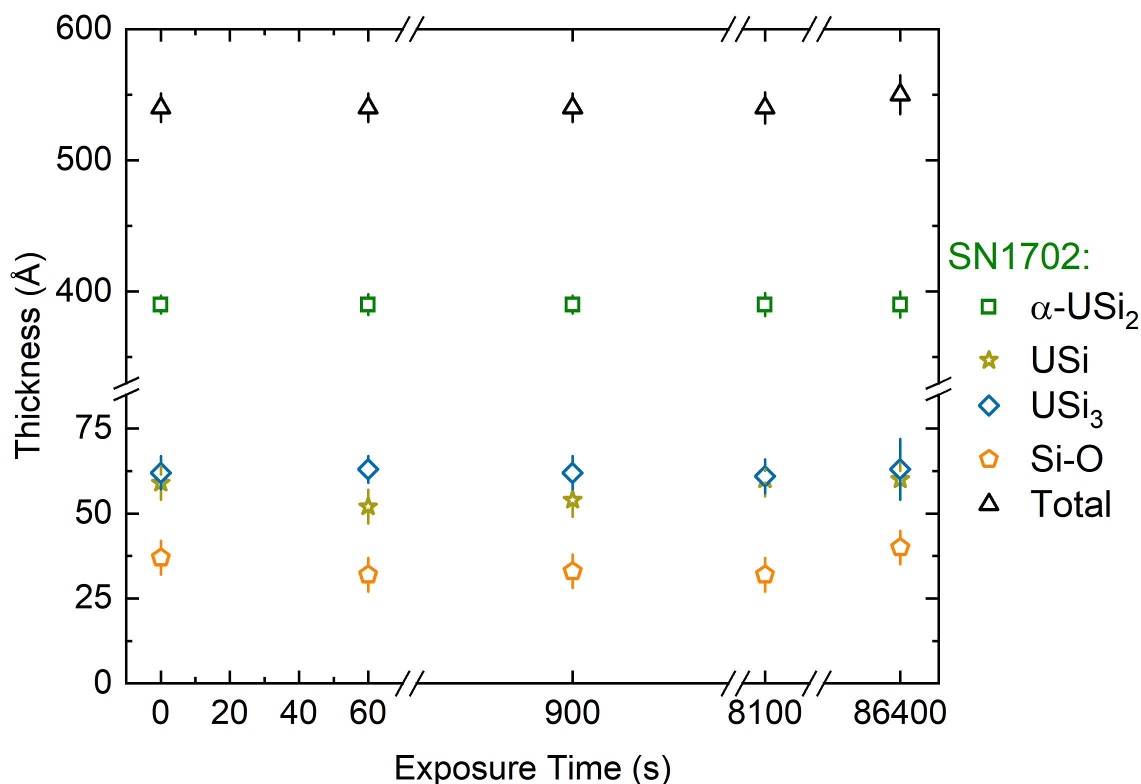

FIGURE 7.11. Thicknesses of each layer modelled in SN1702 as a function of H_2O exposure time. Total thickness of SN1702 indicated with open black triangles, α-USi_2 with open green squares, USi with open yellow stars, USi_3 with open blue diamonds, and Si-O with open orange pentagons. Data extracted from SN1702.

7.1.2.4 USi_3

Uranium trisilicide was exposed to MilliQ H_2O in order to investigate the effect water has on USi_3 under ambient conditions. For this investigation, SN1700 was used. This sample was previously characterised in Chapter 6, where the epitaxial nature of USi_3 was confirmed through off-specular ϕ scans. The structural characterisation of SN1700 will not be presented in this chapter. The compounds forming the native oxide of USi_3 were found to be a hyper-stoichiometric USi_{3+x} phase, with a Si-rich oxide layer at the very surface. The thickness of this oxide was modelled to be 50 ± 2Å. By utilising this oxidation information, it is possible to track and understand the dissolution of this uranium silicide phase one exposed to various aqueous solutions. Here, the dissolution of SN1700 within H_2O is presented.

Figure 7.12 presents the high-angle XRD spectra collected from SN1700 after various exposure times to MilliQ H_2O. Data is indicated with open black circles, with the models used to simulate the data indicated with solid lines. The H_2O exposure times are shown in the figure legend. The dissolution of (001) USi_3 was monitored for up to 24 hours, this data set is indicated with a yellow line. Two Bragg reflections that originate from USi_3 are noted on the figure, (001) and (011). These two reflections were previously noted during ambient air oxidation experiments (Chapter 6) and during the characterisation of pristine USi_3 (Chapter 5). The high-angle spectra presented here indicates minimal structural or phase change to SN1700 as a result of exposure to H_2O.

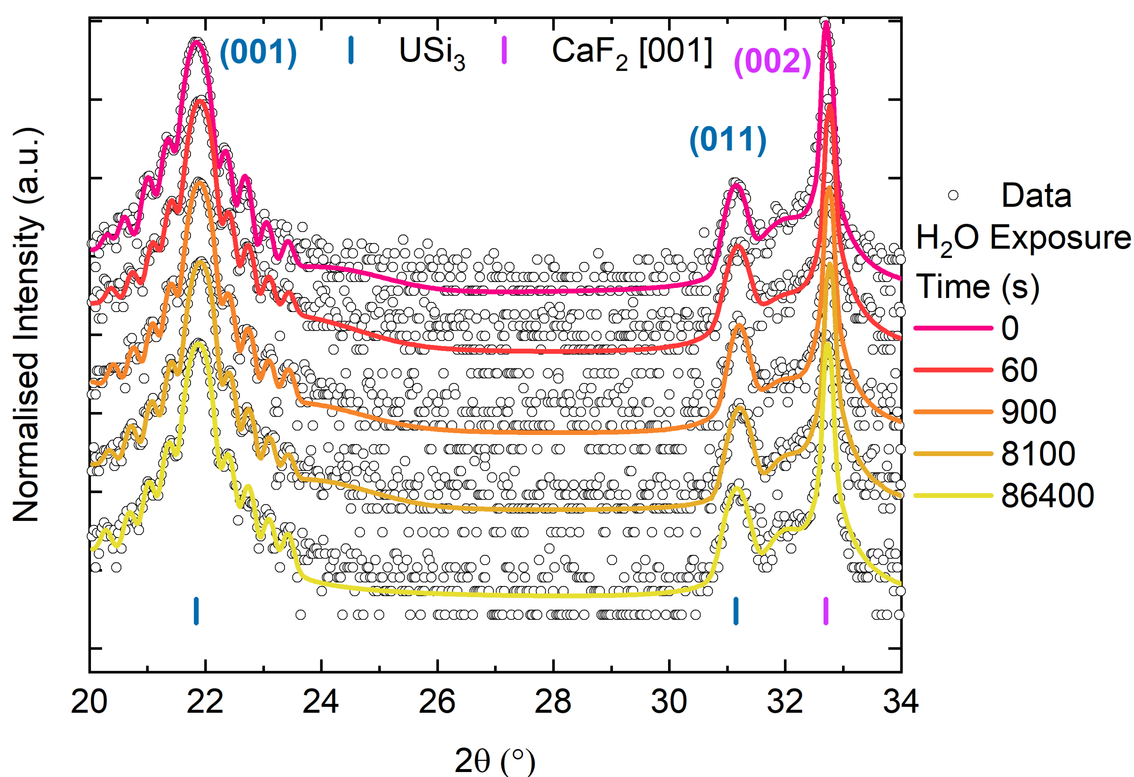

FIGURE 7.12. Change in high-angle XRD spectra, collected from of USi_3 as a function of H_2O exposure. Exposure times of 0, 60, 900, 8100, and 86400 seconds presented. USi_3 and CaF_2 are indicated with dark blue and purple drop lines, respectively. Data extracted from SN1700. Intensity presented on a log scale.

Figure 7.13 presents the XRR spectra collected from the surface of USi_3 after being exposed

to MilliQ H_2O. The data collected is indicated with open black circles, and the models for each spectra being presented with solid lines. Data was collected from the surface of SN1700 prior to the experiment, this spectra is indicated in pink. Spectra was then collected after each H_2O exposure. These data sets were modelled using GenX software. The model was constructed using the oxidation data from Chapter 6, thus, the model was comprised of USi_3, USi_{3+x}, and a silicon oxide. The thickness and roughness of each layer was allowed to vary and the electron density was kept constant. Figure 7.13 (b) indicates the total thicknesses from each layer as a function of exposure time. The total thickness of the film at 0 s of exposure was modelled to be 322 ± 3Å, with the oxide contributing 56 ± 3Å. After 60 seconds of H_2O exposure, 8 ± 5Å was lost from the surface of SN1700. Observing the evolution of the silicon-oxide layer in Figure 7.13 (b), it can be seen that there is a slight increase in the thickness. This could be due to a conversion from U-Si phases into silicon oxides. However, there is a net loss in the overall thickness of SN1700. After 24 hours of exposure to H_2O around 7 ± 4Å was lost from SN1700, indicating a dissolution rate of $(7.7 \pm 0.3) \mathrm{x} 10^{-5}$ Ås^{-1}.

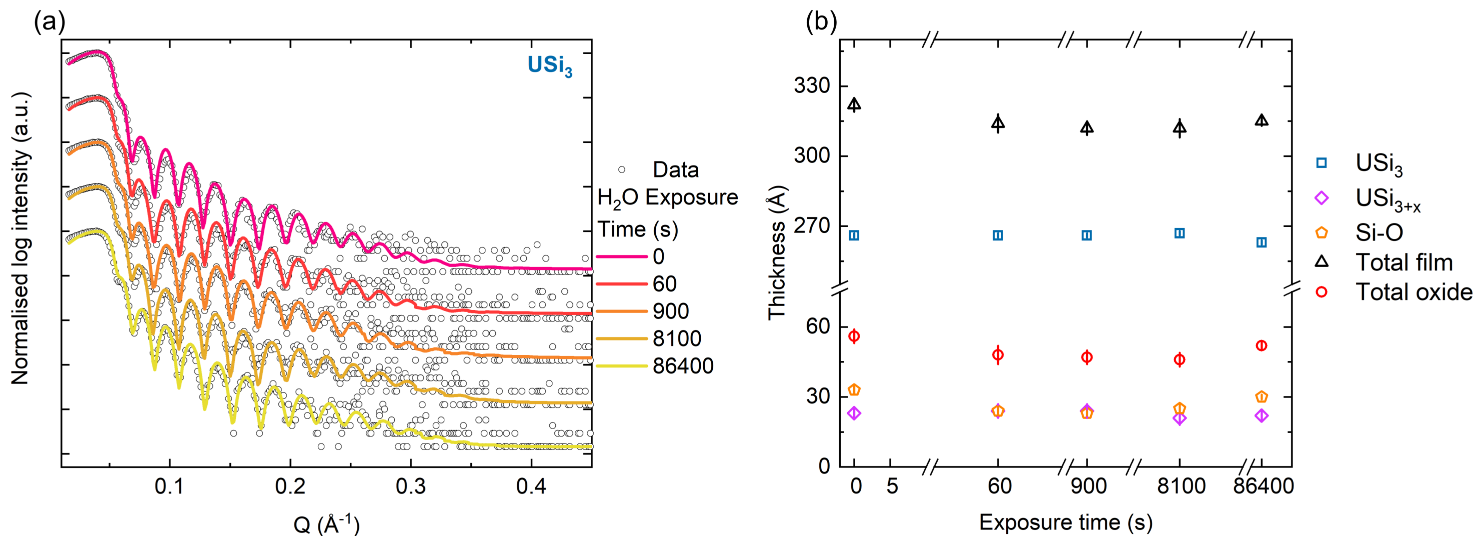

FIGURE 7.13. (a) XRR data extracted from [001] oriented USi_3 once exposed to MilliQ water. Data indicated with open circles, models indicated with solid lines. Intensity presented on a log scale. (b) Shows the thickness changes to each layer modelled in SN1700 as a function of H_2O exposure time. Total film thickness is shown with open black triangles, and total oxide thickness is shown with open red circles. Data extracted from SN1700.

7.1.2.5 UO_2 and SiO_2

The effect of water on the surface of UO_2 and SiO_2 samples were investigated as part of a control experiment. From the oxidation experiments conducted on each uranium silicide phase in Chapter 6, it was found that all phases exhibit a form of preferential oxidation at the uranium sites, permitting the formation of compounds with increased silicon loading. Alongside this preferential oxidation of uranium, uranium oxide and silicon oxide compounds were found to have formed as part of the native oxide layer. However, through conducting area analysis between the U-4f, Si-2s, and O-1s core levels, it was concluded that these U-O and Si-O bonds did not form stoichiometric phases. By conducting water dissolution experiments on UO_2 and SiO_2 thin films, similarities and disparities between the water dissolution of uranium silicides can be drawn.

The XRR results collected from UO_2 is presented in Figure 7.14. Here, three spectra are presented, indicating the state of epitaxial (001) oriented UO_2 stabilised upon [001] yttria-stabilised zirconia (YSZ), after exposure to Milli-Q water after 0, 24, and 48 hours. Data points are presented as open black circles, with the fits after 0, 24, and 48 hours indicated with straight, dashed, and dashed-dot purple lines, respectively. There was change initially between the 0 and 24 hour exposure data sets, indicating the formation of a hyper-stoichiometric UO_{2+x} phase at the surface of the sample. There is minimal change between the remaining two data sets. The total film thickness was initially measured to be 549 ± 11Å, and subsequently 531 ± 8Å after 24 hours of exposure. The final thickness measured after 48 reduced this thickness further by 5 ± 11Å. A total 23 ± 13Å was lost from SN1829. This indicates that the dissolution rate of (001) UO_2 in H_2O is around $(1.3 \pm 0.8) \mathrm{x} 10^{-4}$ Ås^{-1}.

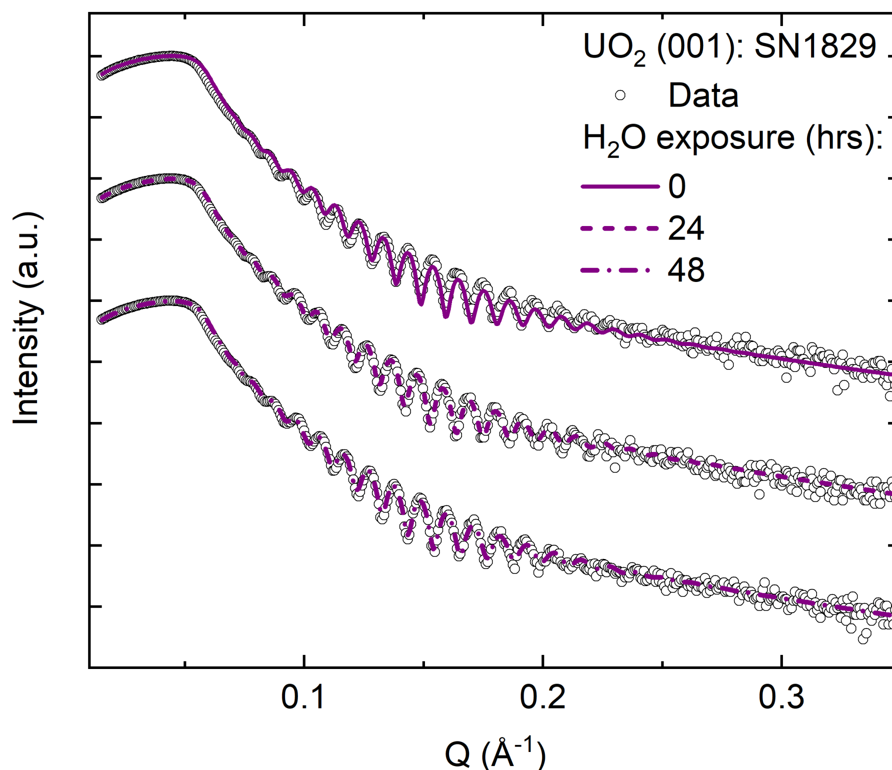

FIGURE 7.14. XRR data extracted from [001] oriented UO_2 once exposed to MilliQ water. XRR spectra collected after 0, 24, and 48 hours of H_2O exposure. Data indicated with open circles, models indicated with solid, dotted, and dashed lines. Data extracted from SN1829. Intensity presented on a log scale.

Similar to UO_2, the corrosion of silicon and silicon oxide was investigated when exposed to H_2O. Figure 7.15 presents the x-ray reflectivity (XRR) spectra collected from a silicon thin film, SN1519, deposited onto Corning glass. The growth parameters of this sample are presented in Chapter 4. Spectra is presented prior to exposure to MilliQ H_2O and after 24 hours of submersion. The two data sets collected from SN1519 have been offset to allow for an easier comparison. Here, the data has been modified to only present the region of interest within the spectra between 0.01 – 0.6$Å^{-1}$. Observing the spectra, there is a clear increase in interface roughness after 24 hours of H_2O exposure. The initial total thickness of SN1519 was modelled using GenX software, and was found to be 177 ± 5Å. After 24 hours of exposure to H_2O, this film thickness had increased to 202 ± 5Å, indicating a total increase of 25 ± 6Å. This change is noted in the XRR spectra, with a change in the Keissig fringes. From this, the dissolution rate for the Si/Si-O

surface (SN1519) when exposed to H_2O was calculated to be: $-(2.9 \pm 0.8)x10^{-4}$.

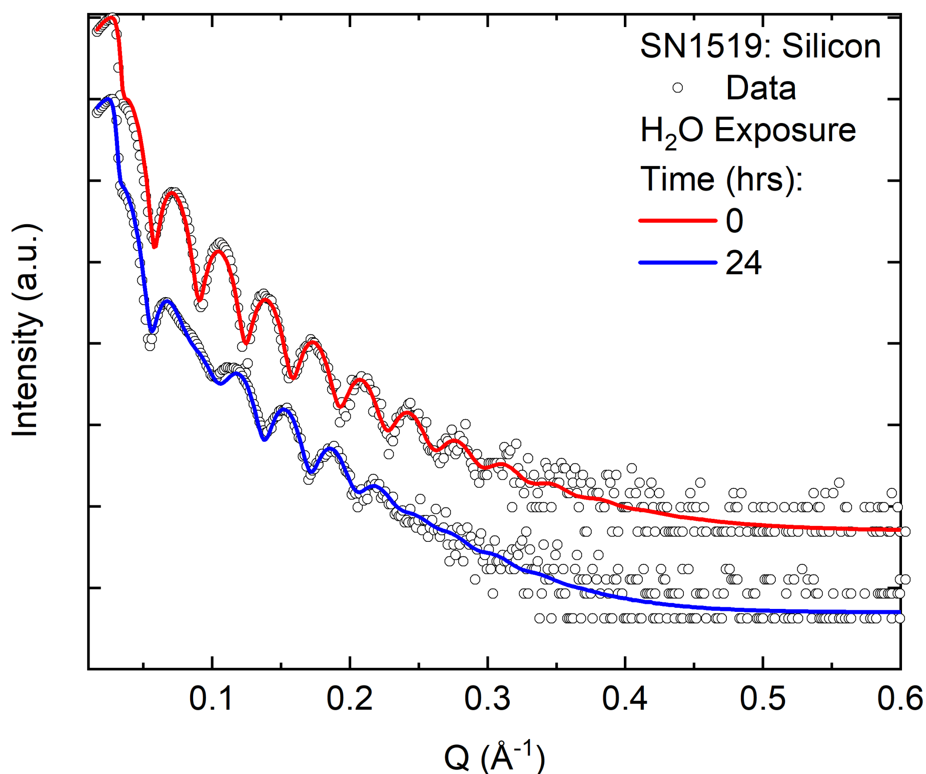

FIGURE 7.15. XRR data extracted from amorphous silicon deposited onto Corning glass once exposed to MilliQ water. XRR spectra collected after 0 (red), and 24 (blue) hours of H_2O exposure. Data indicated with open circles, models indicated with a solid lines. Data extracted from SN1519. Intensity presented on a log scale.

The dissolution data collected from UO_2 indicate that the changes occurring to uranium silicide surfaces could be a combination of the corrosion behaviour of both these materials when exposed to H_2O.

7.2 Corrosion of U-Si phases in Hydrogen Peroxide

7.2.1 Experimental Set up

To investigate the effects of radiation on the corrosion of U_3Si, U_3Si_2, $\alpha-USi_2$, and USi_3, samples of each phase were exposed to a H_2O_2 solution for varying times. Samples of UO_2 and Si were also used as control phases. The change in thickness of each sample was probed using XRR and high-angle XRD. A concentration of 0.1 mol. H_2O_2 was chosen to simulate the corrosive conditions that may arise as a result of the radiolysis of water as a result of spent nuclear fuel. Despite the concentration of H_2O_2 being much higher than would be expected at the surface of a submerged fuel pellet, the concentration was picked to simulate the dissolution rates of actinide thin film samples [112], particularly when radiolysis is simulated with a synchrotron source [40, 111]. Where these literature values may not be representative of spent nuclear fuel/ground-water conditions, the higher concentration of H_2O_2 and therefore an accelerated dissolution rate is more representative of an accident scenario. Furthermore, a higher concentration of H_2O_2 allows for the experiments to be conducted over a much shorter time scale, which limits the errors that could arise from the decomposition of H_2O_2.

The single crystals presented in this study were previously investigated to understand their oxidation behaviour in Chapter 6. The dissolution was investigated for all phases with the exception of U_3Si_5 (SN1644), which has been omitted due to the higher uranium content used to engineer the phase. The remaining phases had 0.1 mol. H_2O_2 placed on the surface using a 5 ml pipette, for time periods of 5, 15, 30, 60, 300, 900, 2700, and 8100 seconds, with samples dried following exposure to the solution.

XRR was used to monitor the overall change in surface morphology, tracking the film and oxide thickness, alongside the interface roughness as a function of time exposure. The XRR data was modelled using GenX software, as described in Chapter 3. For the modelling, all instrumental parameters were kept constant, with only the roughness and thickness of each layer allowed to vary. The structural of each sample was monitored using high-angle XRD, allowing for any large structural changes occurring as a result of H_2O_2 exposure to be monitored as a function of time.

7.2.2 Results

7.2.2.1 U_3Si

Understanding the radiolytic dissolution of triuranium silicide, U_3Si is vital for predicting fuel/water interface scenarios. This uranium silicide phase has been tested within the RERTR Program to understand its performance as a nuclear fuel. Despite the low resistance to radiation

damage, causing the tetragonal crystal structure of U_3Si becoming amorphous, it is still important to predict and understand how this fuel type may degrade as a result of aqueous corrosion. Furthermore, legacy exotic fuels like U_3Si will require eventual storage within a geological disposal facility (GDF) as spent nuclear fuel (SNF); a key scenario where nuclear fuel may come into contact with aqueous solutions. Therefore, the surface of SN1711 was exposed to 0.1 mol. H_2O_2 in order to simulate the radiolytic dissolution of epitaxial U_3Si.

The dissolution of U_3Si was investigated through probing the structure of SN1711 via high-angle XRD and x-ray reflectivity (XRR). This has allowed for phase changes occurring within the sample to be probed alongside the change in thickness as a function of exposure time. Figure 7.16 presents the high-angle spectra collected from SN1711 as a function of increasing exposure times when in contact with H_2O_2. The data is presented with open black circles, with the models indicated with solid lines. The figure legend shows the H_2O_2 exposure times. Observing the spectra as a function of exposure time, there is minimal phase change occurring to the sample. However, the (200) Bragg reflection of U_3Si_2 decreases as a function of time, with the complete removal of this reflection after 300 s. The specular Bragg reflection stemming from the epitaxial U_3Si phase has exhibits no change once exposed to H_2O_2.

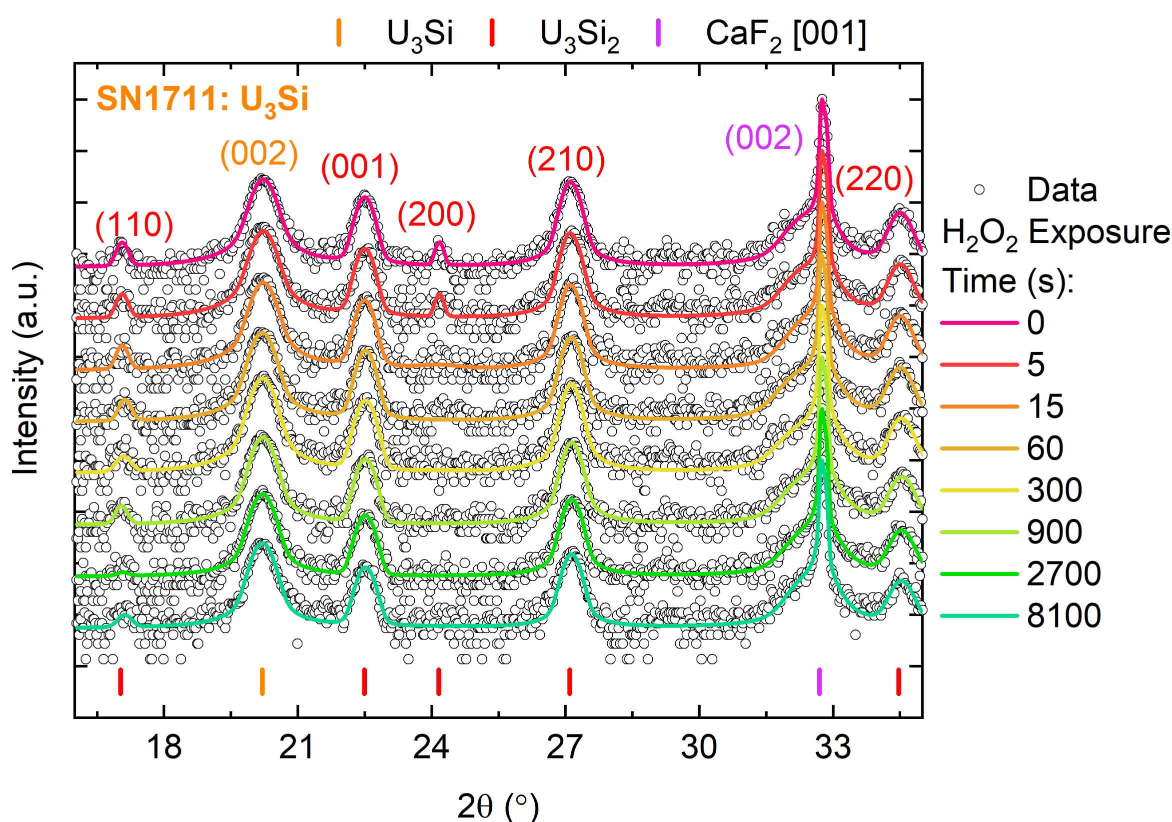

FIGURE 7.16. High-angle XRD data extracted from U_3Si once exposed to H_2O_2. Data indicated with open circles, models indicated with a solid lines. Data extracted from SN1711. Intensity presented on a log scale.

Figure 7.17 presents the XRR spectra collected from SN1711 after exposure to H_2O_2. Each spectra has been offset to allow for an easier visual comparison between data sets, and the spectra has been presented in shortened region to highlight the regions of interest at lower Q values. The H_2O_2 exposure times are indicated in the figure legend. Data is indicated with open black circles, with models used to simulate the spectra indicated with solid lines. GenX software was used to simulate the data sets. The chemical and structural information obtained from the ambient oxidation of U_3Si in Chapter 6 was used here to construct a layered model in GenX, allowing for the simulation of the aqueous corrosion of this uranium silicide phase.

Through observing the spectra, is can be seen that the sample has significant roughening of layer interfaces, thus preventing the appearance of Kessig fringes. As the exposure to H_2O_2 increases, there is an alteration in the electron density region around the critical edge of the

spectra at 0.05 Å^{-1}. This could be an indication that regions of the film are becoming so thin, as to expose some of the CaF_2 substrate below, or that one particular layer within the structured system is becoming increasingly rougher when compared to the other compounds.

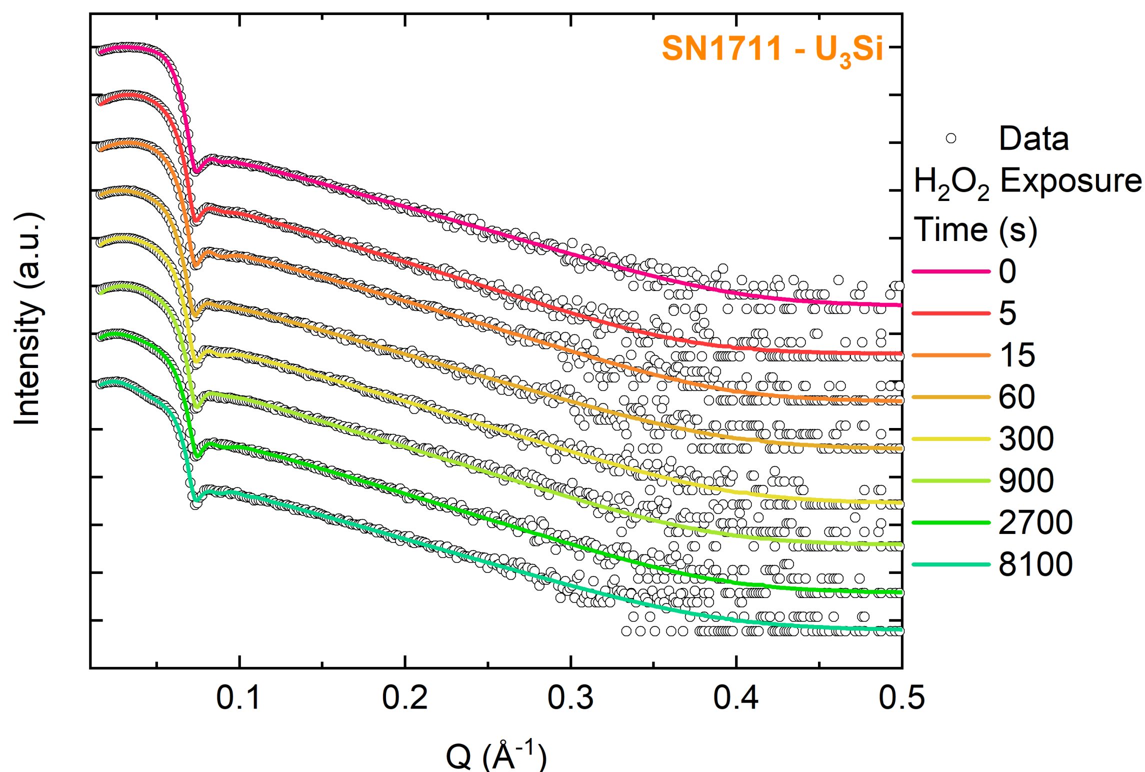

FIGURE 7.17. XRR data extracted from U_3Si once exposed to H_2O_2. Data indicated with open circles, models indicated with a solid lines. Data extracted from SN1711. Intensity presented on a log scale.

The thickness evolution of each layer is presented in Figure 7.18. Here the thickness of each layer is indicated as a function of increasing exposure time to H_2O_2. The total thickness of the film is indicated with open black triangles, with the epitaxial (001) U_3Si film indicated with open orange squares. The U_3Si_2 inclusion is indicated with open red diamonds, and the silicon rich oxide layer is indicated as open blue pentagons. Initially, there are fluctuations occurring to the total thickness of the film. This behaviour is replicated in the thickness of the silicon rich oxide layer. Overall the total film thickness exhibited a total net loss of around 80 ± 40 Å as a result of exposure to H_2O_2, thus indicating a dissolution rate of (9.8 ± 5.4)x10^{-3} Ås^{-1}.

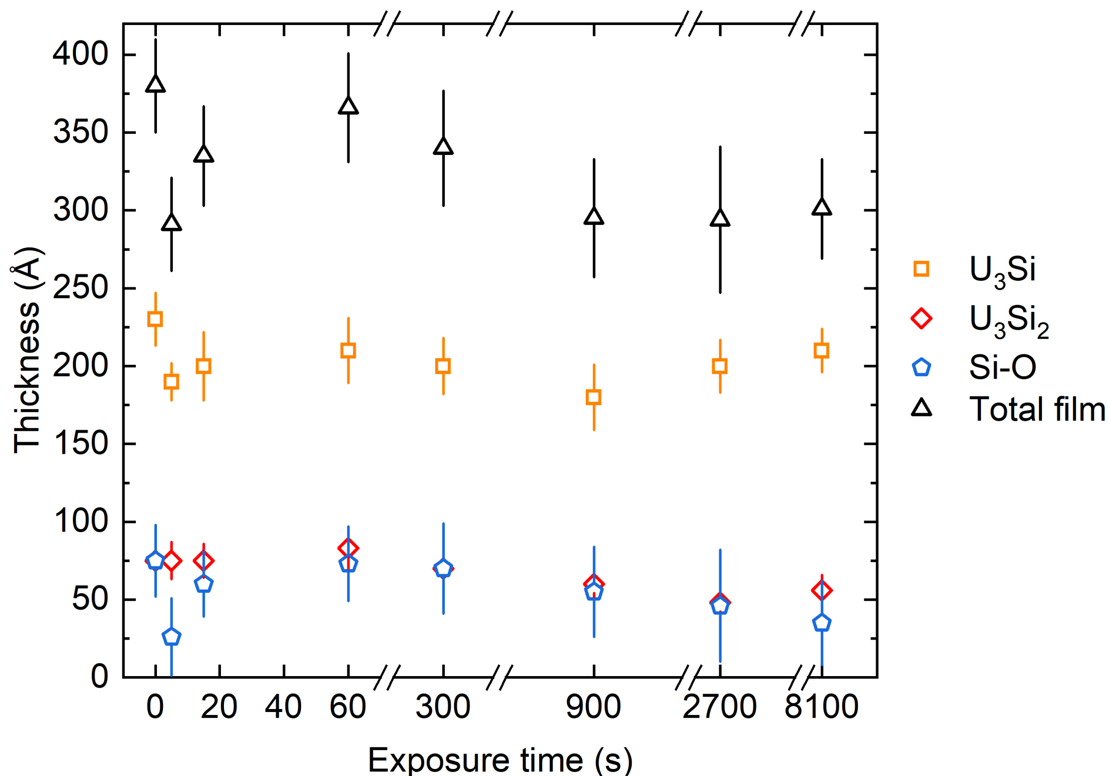

FIGURE 7.18. Layer thicknesses extracted from (001) U_3Si once exposed to H_2O_2. Total thickness indicated with open black triangles, epitaxial U_3Si film with open orange squares, U_3Si_2 inclusions with open red diamonds, and the silicon rich oxide layer with open blue pentagons. Data extracted from SN1711.

7.2.2.2 U_3Si_2

The radiolytic dissolution of U_3Si_2 was simulated by exposing a poly-crystalline film to H_2O_2 for increasing time increments. Understanding the corrosion behaviour of this proposed ATF is vital if U_3Si_2 is to be implemented into current and next-generation LWRs. The behaviour of U_3Si_2 was probed using high-angle XRD and x-ray reflectivity (XRR) to understand the evolution of the crystallinity and surface morphology of the phase. The sample used was previously characterised in Chapter 6, where the surface oxidation was monitored. This allowed to a model of the sample to be created, depicting the surface oxide compounds and total oxide thickness. Here, it was found that SN1707 was comprised of two phases, U_3Si_2 and U_3Si, with a hyper-stoichiometric U_3Si_2

oxide layer which was accompanied by a silicon oxide.

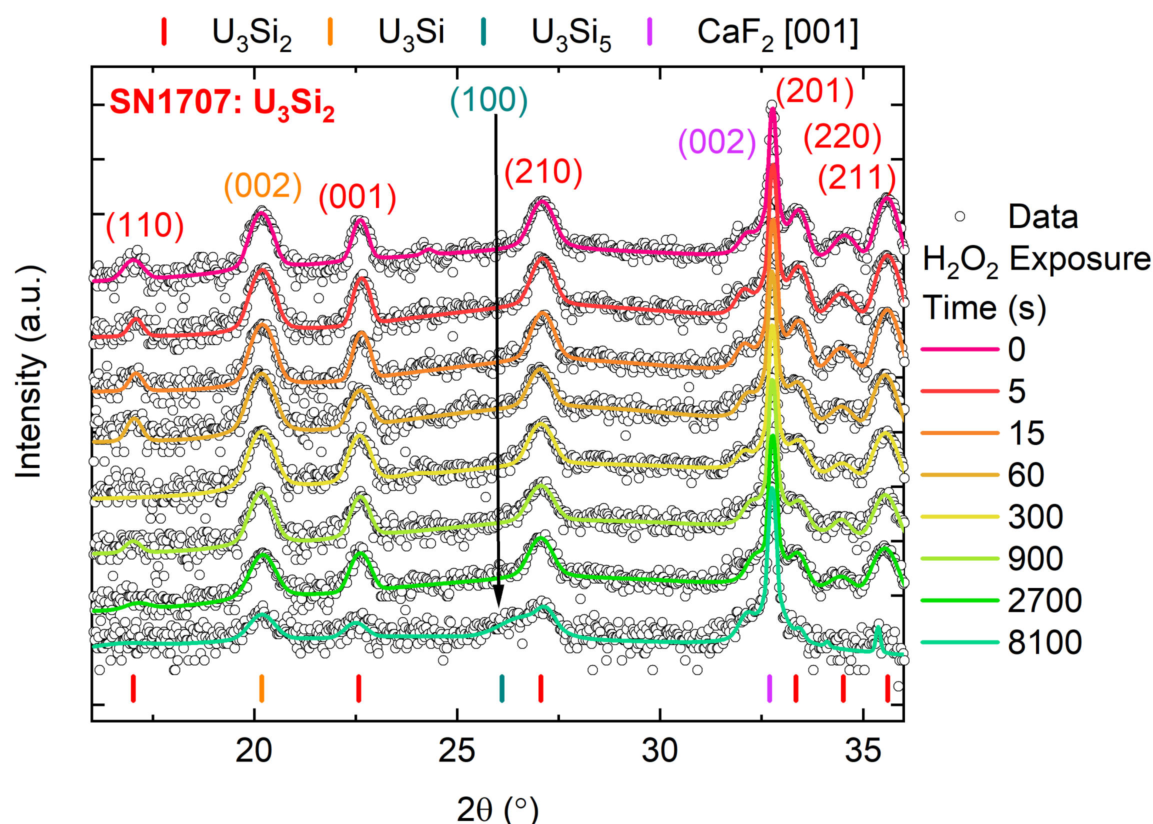

FIGURE 7.19. High-angle XRD data extracted from U_3Si_2 once exposed to H_2O_2. Data indicated with open circles, models indicated with a solid lines. Data extracted from SN1707. Intensity presented on a log scale.

The understanding of this sample allows for the dissolution behaviour in H_2O_2 to be tracked as a function of exposure time. Figure 7.19 presents the high-angle XRD spectra collected from SN1707 after each H_2O_2 exposure cycle. Reflections from U_3Si_2 and U_3Si are indicated with red and orange drop lines, respectively. The substrate material, [001] CaF_2 is indicated with purple drop lines. As the exposure time increases, there are some significant changes in the spectra collected from SN1707. Tracking the (110) Bragg reflection of U_3Si_2, with a 2θ value of $17.049 \pm 0.001°$, it can be seen that the overall intensity of this reflection decreases with the increasing exposure time.

A similar decrease in intensity is noticed with the (001), (201), (220), and (211) reflections

of U_3Si_2. As the intensity of the (210) Bragg reflection of U_3Si_2 decreases, there is an increase in a shouldering peak situated around 2θ = 26.13°, a position similar to the (100) of U_3Si_5 as quoted by [49]. The presence of this peak could be linked to the preferential oxidation of uranium silicides, noticed in the work conducted in Chapter 6, and the high-temperature corrosion work conducted by *Yang et al.,* and *Sooby Wood et al.,* [94, 101].

Figure 7.20 presents the x-ray reflectivity spectra collected from SN1707 during the H_2O_2 exposure experiment. The spectra collected from poly-crystalline U_3Si_2 has been offset to allow for the spectral details at lower Q values to be showcased individually. Exposure times are indicated in the figure legend, with the pristine sample being indicated in pink. Data is presented with open black circles, with models indicated with solid lines. The data was simulated using GenX software, with the model initially constructed using the oxidation information gathered about the sample in chapter 6. Here, it was found that the sample had both U_3Si_2 and U_3Si phases present, alongside a silicon-rich oxide surface layer. These compounds were used a construct a layered model, with thicknesses and roughnesses allowed to vary.

Observing the initial spectra, presented in pink, there are prominent fringes within the data set. The total film thickness was modelled to be around 320 ± 29Å. As the exposure to H_2O_2 commences, the prominent fringes within the spectra begin to disappear, suggesting an increased roughening in the layer interfaces. At 300 seconds of exposure, the induced radiolytic dissolution begins to alter the critical angle situated at 0.05Å^{-1}. This feature at the critical edge becomes more prominent with exposure time, and suggests a significant roughening of interfaces, alongside the potential exposure of the [001] CaF_2 substrate across regions of the sample.

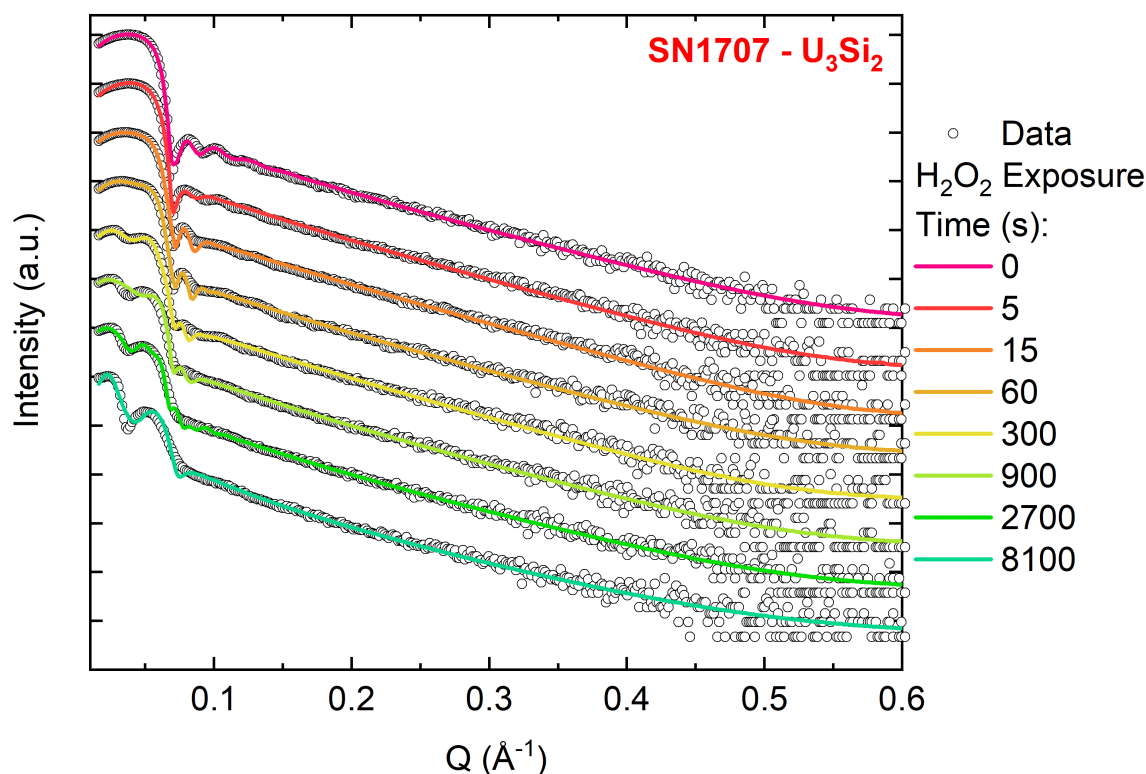

FIGURE 7.20. XRR data extracted from U_3Si_2 once exposed to H_2O_2. Data indicated with open circles, models indicated with a solid lines. Data from SN1707. Intensity presented on a log scale.

Through simulating the XRR data, it was possible to extract thicknesses associated to each layer and the total thickness of the thin film sample. Figure 7.21 presents the thickness change as a function of exposure to 0.1 mol. H_2O_2. The evolution of the total thickness is indicated with open black triangles, the poly-crystalline U_3Si_2 film with open red squares, U_3Si with open orange diamonds, and the silicon rich oxide with open blue pentagons. As previously stated, the total film thickness modelled prior to the exposure to H_2O_2 was found to be 320 ± 29Å. As the dissolution cycles commence, there is a gradual increase in the total thickness up to 900 s of exposure. This large increase aligns with the increase with the silicon-rich oxide, and was measured to be around 440 ± 34A. Following this, the overall thickness drops, resulting in a decrease in the silicon-rich oxide. After 8100 s of exposure, the U_3Si_2 layer exhibits a significant decrease of 100 ± 30Å. Overall the sample experience an overall net gain of 69 ± 46Å, with a peak gain of 120 ± 45Å.

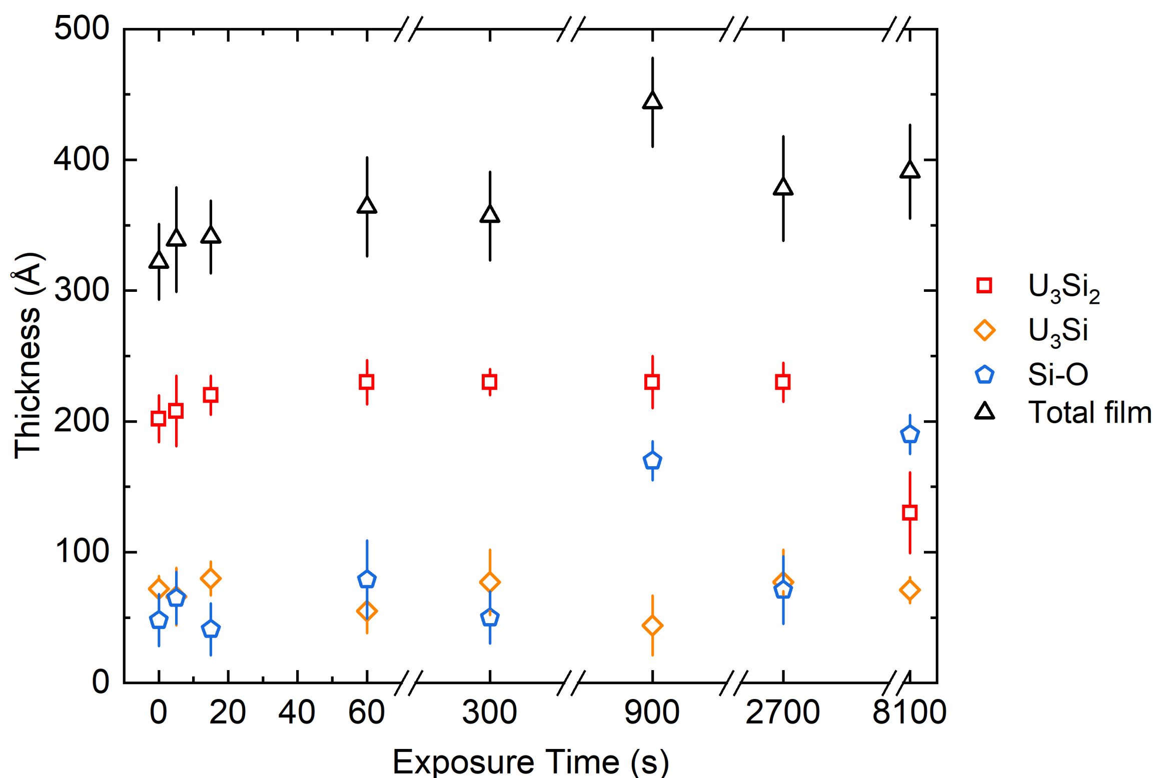

FIGURE 7.21. Layer thicknesses extracted from U_3Si_2 once exposed to H_2O_2. Total thickness indicated with open black triangles, U_3Si_2 indicated with open red squares, U_3Si with open orange diamonds, and the silicon-rich oxide with open blue pentagons. Data from SN1707.

Figure 7.22 presents photographic evidence of the state of SN1707 after 8100 s of exposure to 0.1 mol. H_2O_2. This image indicates that the sample has been subjected to significant corrosion of the surface, with some regions of the sample completely removed. The gradient pattern created could indicate that particular crystallographic directions corrode at a faster rate than others. This behaviour is reflected in the high-angle XRD spectra presented in Figure 7.19, with the (110), (001), and (210) Bragg reflections of U_3Si_2 exhibiting a reduction in overall intensity after 8100 s of exposure to H_2O_2.

FIGURE 7.22. Photo of SN1707, poly-crystalline U_3Si_2, after exposure to 0.1 mol. H_2O_2 for 8100s. Data from SN1707.

7.2.2.3 α-USi_2

The dissolution of $\alpha - USi_2$ was investigated by exposing the oxidised surface of SN1702, an epitaxial thin film, to 0.1 mol. H_2O_2. The oxide layer of SN1702 was previously measured using XRR in Chapter 6, and was found to be 63 ± 5$\mathring{A}$. Through the use of XPS depth profiling, the compounds that form as part of the oxide layer, separate to the epitaxial $\alpha - USi_2$ film, were found to be: USi, USi_3, and a silicon oxide. Combining these results, it is possible to follow the dissolution of these layers via x-ray reflectivity.

Figure 7.23 (a) presents the x-ray reflectivity spectra collected from SN1702 as a function of H_2O_2 exposure. The data points are presented with open black circles, and the models are indicated with solid lines. The total exposure times, measured in seconds, are indicated in the figure legend. Each XRR spectra has been offset to allow for an easier visual comparison between data sets and exposure times. The x-axis has also been limited to 0.35$\mathring{A}^{-1}$, allowing for the spectral features at lower Q-values to be showcased.Through observing the XRR spectra collected from SN1702, it can be seen that there is a significant roughening of the layer interfaces as a function of H_2O_2 exposure. This is reflected in the inability to resolve Keissig fringes as the exposure time increases. The spectra collected prior to H_2O_2 exposure, shown in pink, exhibits well-defined fringes up to around 0.2$\mathring{A}^{-1}$, whereas the final spectra collected after 8100 s, shown in blue, only has fringes up to 0.12$\mathring{A}^{-1}$. This therefore indicates that the H_2O_2 solution does have an effect on oxidised $\alpha - USi_2$. After 300 s of H_2O_2 exposure, there is a significant roughening feature noticed near the critical edge of the spectra, around 0.03$\mathring{A}^{-1}$.

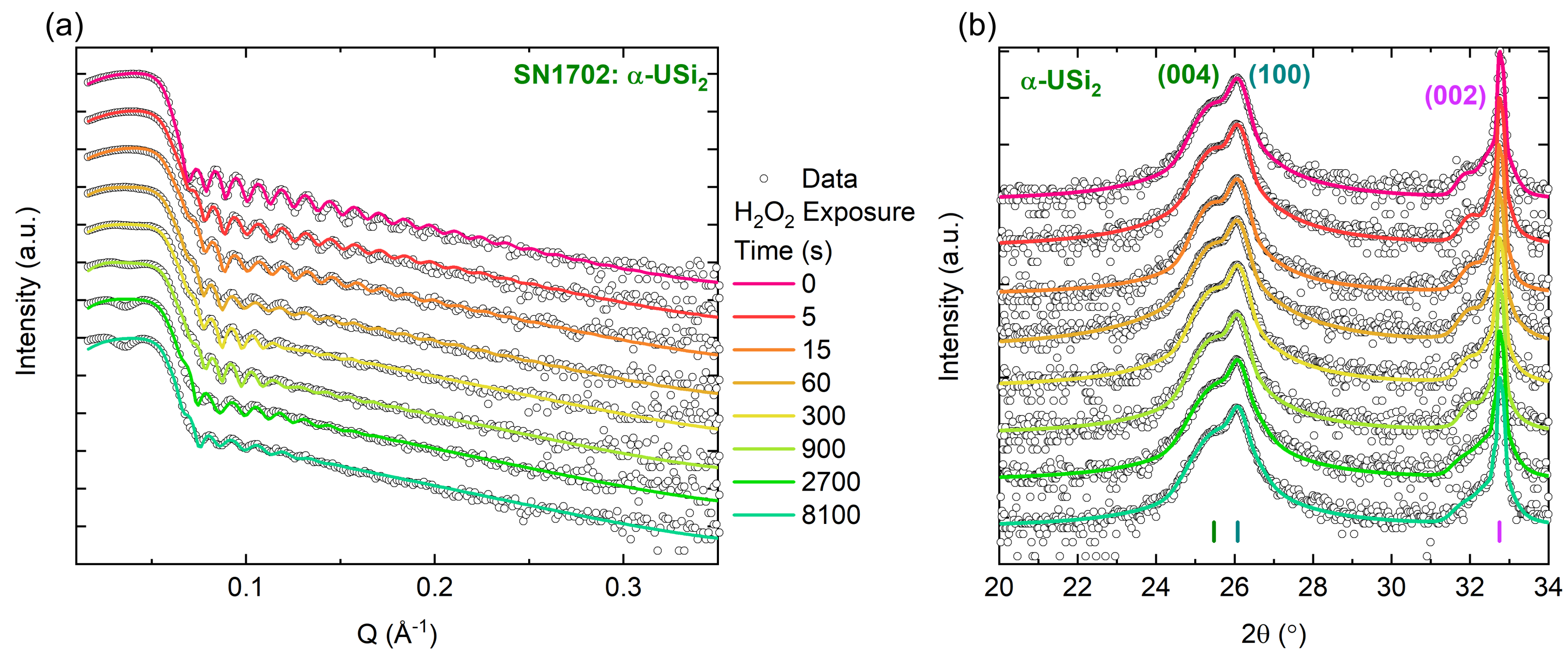

FIGURE 7.23. Graphs showing the surface and structural changes as a result of H_2O_2 exposure on the surface of [001] α-USi_2. (a): Shows the XRR spectra collected from α-USi_2 as a function of H_2O_2 exposure. Exposure times indicated in legend. Data points shown with open circles, with models indicates with solid lines. (b) Shows the high-angle XRD data collected from SN1702, indicated structural changes to SN1702 as a function of exposure time. Data taken from SN1702. Intensity presented on a log scale.

As the exposure time continues to increase, this feature becomes more prominent. This secondary critical angle, at a Q value of $0.03\mathring{A}^{\circ}$ is attributed to the CaF_2 substrate indicating that regions of the substrate interface is exposed. Furthermore, this is also attributed to the roughening of the sample, which is indicated by the shortening of fringe height. In order to model this feature, the roughness of each layer must be increased, reducing the ability to simulate the thickness of the film. As the thickness of the film is the parameter of interest for this study, the double critical angle feature has been ignored.

Figure 7.23 (b) presents the high-angle XRD data as a function of exposure time. Observing the spectra, it can be seen that minimal change occurs to the structure, with no additional peaks forming as a result of H_2O_2 exposure. Within the spectra, there are two peaks present alongside the (002) of CaF_2. Here, the (004) and (100) Bragg reflections of $\alpha-USi_2$ and U_3Si_5 are both present. These two phases are indicated on the figure with green and teal drop lines, respectively. The presence of these two phases was not indicated in the oxidation study conducted on SN1702 in Chapter 6. The cutting of the sample to form a 5x5mm sample could have resulted in a more challenging alignment process. This therefore infers that by cutting the sample in preparation for aqueous corrosion studies, an additional change has occurred to the sample, revealing an additional U_3Si_5 layer alongside the epitaxial $\alpha-USi_2$ phase. The presence of this additional phase does not effect the results relating to the previous XRR studies, as both $\alpha-USi_2$ and U_3Si_5 have extremely similar scattering length densities, making then indistinguishable when simulating x-ray reflectivity spectra.

The changes occurring to the XRR spectra as a function of H_2O_2 exposure indicates that the thickness of each layer must be investigated. Figure 7.24 presents the change in thickness for each layer, alongside the total thickness of the sample, as a function of exposure. Figure 7.24 (a) presents all the layers simulated as part of the model, including the epitaxial $\alpha-USi_2$ indicated with open green squares, USi with open yellow stars, USi_3 with open dark blue diamonds, silicon oxide with open orange pentagons, and the total thickness indicated with open black triangles. Here, both the thicknesses of the total film and epitaxial layer can be seen to decrease as a function of H_2O_2 exposure time. The initial film thickness was measured to be 553 ± 9Å, with the USi_2 layer contributing 374 ± 5Å. After 8100 s of H_2O_2, the total film thickness was modelled to be: 432 ± 46Å, with $\alpha-USi_2$ contributing 309 ± 42Å. This indicates that over the 8100 s total exposure period, around $121 \pm 46\mathring{A}$ was removed, inferring a dissolution rate of $(1.5 \pm 0.6)x\,10^{-2}\,\mathring{A}s^{-1}$.

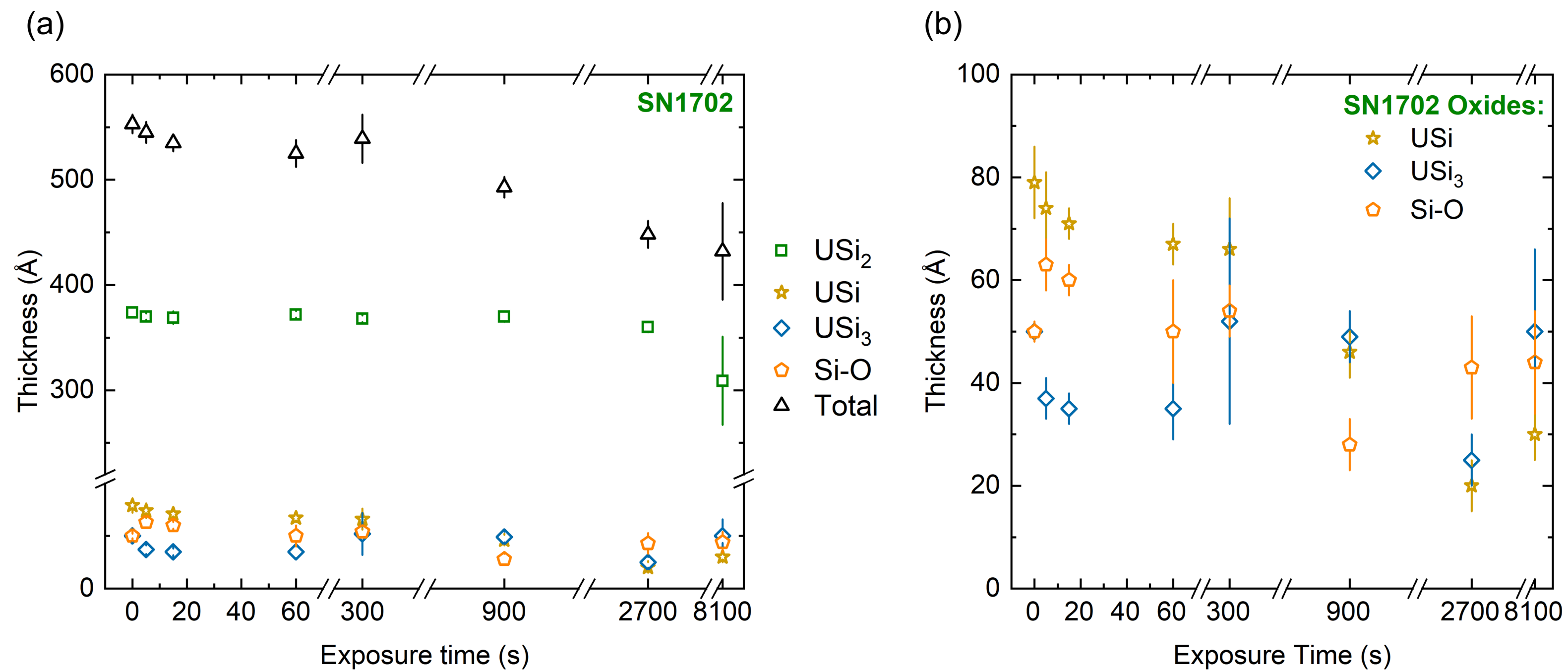

FIGURE 7.24. Graphs indicating the change in total and individual layer thicknesses as a function of exposure time. (a) Presents the change in thickness of all layers as a result of H_2O_2 exposure. (b) Presents the change in layers considered to be oxides present in α-USi_2. Total film thickness indicated with black triangles, epitaxial film (α-USi_2) indicated with green squares, USi with yellow stars, USi_3 with dark blue diamonds, and Si-O with orange pentagons. Data taken from SN1702.

Figure 7.24 (b) showcases the change in the individual oxide compounds as a function of H_2O_2 exposure. The thickness of the modelled USi layer, shown with open yellow stars, consistently decreases as a function of exposure time with the exception of the final thickness, extracted after 8100 s, which increases by $10 \pm 7 Å$. Overall a total of $49 \pm 9 Å$ was lost from the USi layer, suggesting a dissolution rate of $0.006(6) Å s^{-1}$. Both the USi_3 and Si-O layers fluctuate as a function of H_2O_2 exposure. However, the total loss from both layers were modelled to be $0 \pm 16 Å$ and $6 \pm 10 Å$.

7.2.2.4 USi_3

The surface of uranium trisilicide, USi_3 was exposed to 0.1 M H_2O_2 to investigate the dissolution of the phase. As the uranium silicide with the highest silicon content, it is vital to understand how the surface of this phase may alter as a result of exposure to corrosive environments.

The XRR data collected from SN1700, (001) USi_3, as a function of H_2O_2 exposure time is presented in Figure 7.25 (a), with the change in thickness occurring to each layer presented in Figure 7.25 (b). For the reflectivity spectra, the data points are shown with open black circles, and the spectra models indicated with solid lines. The spectra has been modified to only show the spectra up to $0.4 Å^{-1}$. This is to highlight the region of interest in the spectra, which is located at lower Q values, between 0.05 – $0.3 Å^{-1}$.

Observing the XRR data initially, it can be seen that there are minimal changes occurring to the sample as a result of H_2O_2 exposure. The most significant change noticed in the spectra occurs after 5 seconds of H_2O_2 exposure. Here, the shape of the Keissig fringes changes around $0.15 Å^{-1}$, suggesting a change at the surface of the sample. As the H_2O_2 exposure time increases, there is a slight increase in the overall roughness of the data, with Keissig fringes becoming less defined at higher Q values. Comparing this to the thicknesses presented in Figure 7.25 (b), it is shown that the most significant change occurring in the layers of SN1700, is inflicted on the Si-O layer. This is noted in the initial change between the data points at 0 and 15 s of H_2O_2 exposure. This thickness change inflicted on the Si-O layer was measured to be $15 \pm 8 Å$. The total thickness lost initially was measured to be $16 \pm 8 Å$. This suggests there are additional contributions, alongside the loss in the Si-O layer, to the dissolution of USi_3. From the data presented in Figure 7.25 (b), it is also shown that the total thickness does not continue to decrease. This suggests that the USi_3 and Si-O layers are impenetrable to the corrosive H_2O_2 conditions.

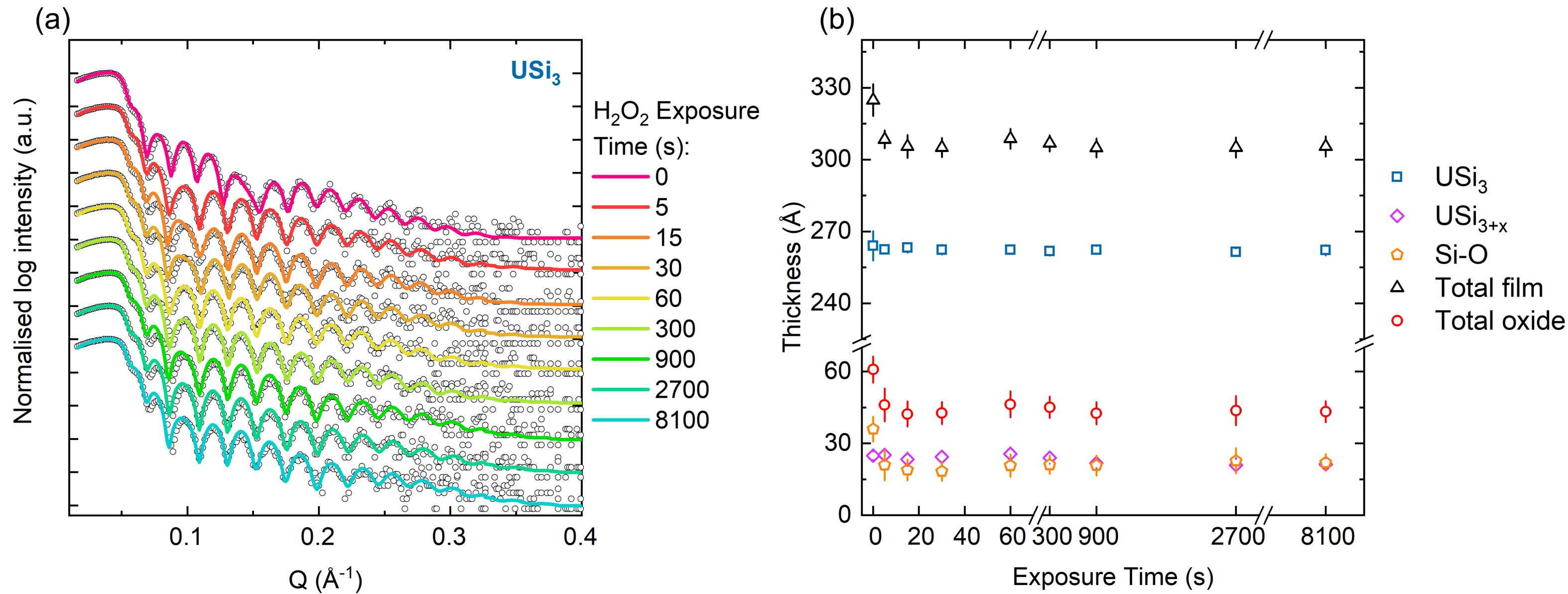

FIGURE 7.25. Graphs showing the thickness change as a result of H_2O_2 exposure on the surface of [001] USi_3. (a): Shows the XRR spectra collected from USi_3 as a function of H_2O_2 exposure. Exposure times indicated in legend. Data points shown with open circles, with models indicates with solid lines. (b) Shows the thickness changes to each layer modelled in SN1700 as a function of exposure time. Total film thickness is shown with open black triangles, and total oxide thickness is shown with open red circles. Data taken from SN1700.

The high-angle XRD spectra collected from the surface of SN1700 being exposed to H_2O_2 is presented in Figure 7.26. Here, five exposure times are presented. The spectra presented here has been offset to allow for an easier comparison between data sets. Data points from each spectra are indicated with open black circles, and models are shown with solid lines. USi_3 and CaF_2 are indicated with blue and purple drop lines, respectively. The (001) and (011) reflections from USi_3 are also labeled on the figure. There is minimal change between each data set, which was previously noted in the XRR spectra collected from SN1700. This further suggests that USi_3 has does not succumb to the corrosive behaviour of H_2O_2.

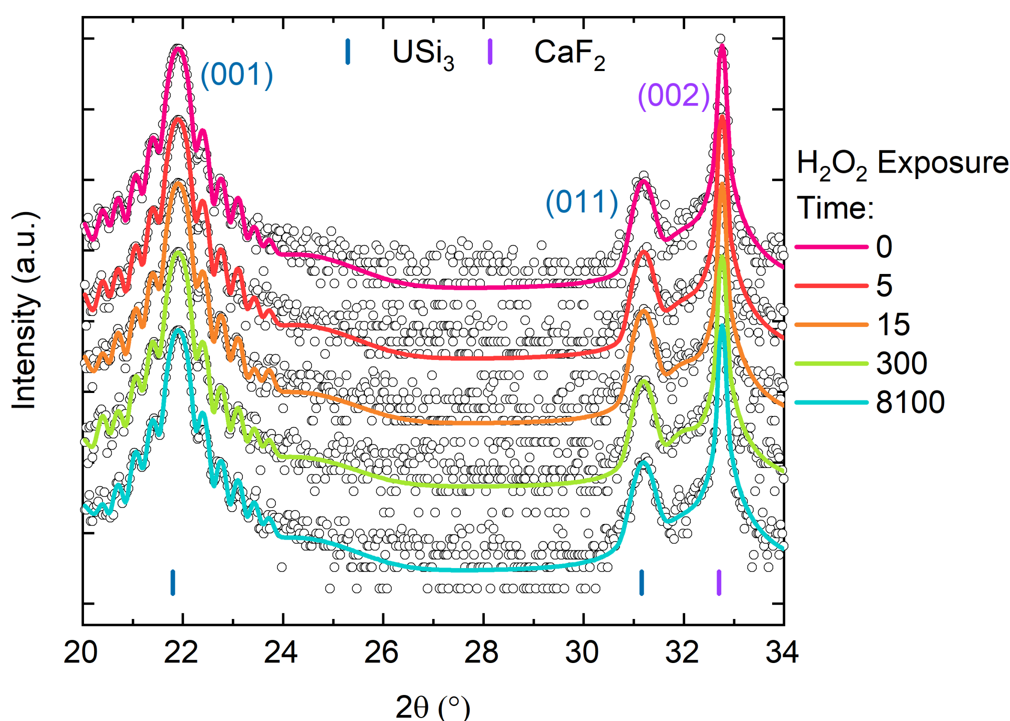

FIGURE 7.26. Change in high-angle XRD spectra, collected from of USi_3 as a function of H_2O_2 exposure. Exposure times of 0, 5, 15, 300, and 8100 seconds presented. Data extracted from SN1700. Intensity presented on a log scale.

7.2.2.5 UO_2 and SiO_2

Much like the water dissolution experiments, both UO_2 and SiO_2 were used as control compounds in the hydrogen peroxide investigations. As the two compounds expected to form as a result of the oxidation termination for U-Si phases, data collected from the H_2O_2 dissolution of both

materials will prove useful in understanding the corrosion of U-Si phases. This will also allow for the dissolution behaviour of ATF candidates to be compared against the current ceramic fuel, UO_2.

Figure 7.27 presents the high-angle XRD data collected from epitaxial UO_2 deposited on [001] oriented yttria-stabilised zirconia (YSZ) at 550 °C. Growth parameters and details for SN1507 can be found in Chapter 4. Two spectra are presented in this figure indicating the state of the sample prior to H_2O_2 corrosion, indicated in red, and after 8100 s of exposure, indicated in blue. Here, the data is indicated with open black circles, with the models indicated with solid lines. The initial and final spectra are presented to compare the structural effect of the corrosion process. For the XRD measurement, the specular (002) reflection of YSZ was aligned to, allowing for changes in the UO_2 specular peak to be monitored. There is no indication of an additional phase being formed, nor a significant reduction in the (002) Bragg reflection of UO_2. A significant loss of material could be indicated by a reduction in the overall intensity of the specular Bragg reflection for [001] oriented UO_2, as noted by the dissolution work conducted by Rennie *et al.,* [40].

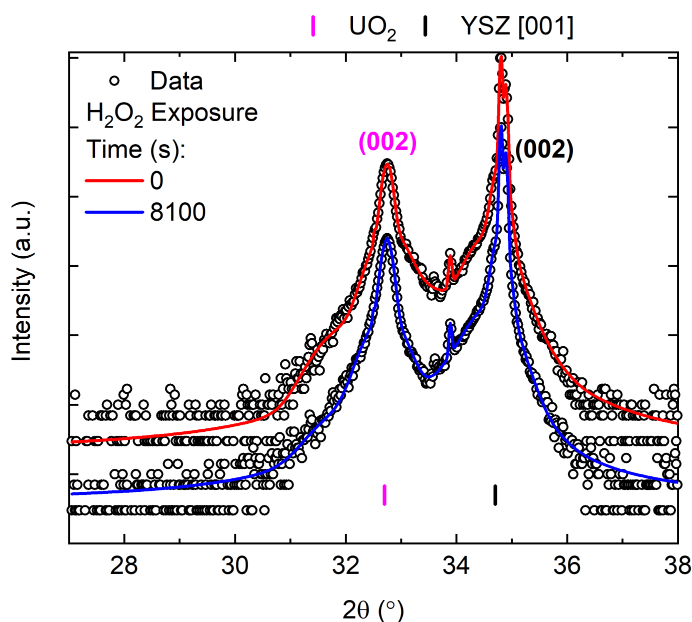

FIGURE 7.27. High-angle XRD data collected form the initial and final H_2O_2 dissolution experiments conducted on epitaxial (001) UO_2. Two spectra are presented, collected after 0 (red) and 8100 (blue) seconds of H_2O_2 exposure. Data is indicated with open black circles, with models indicated with solid lines. The specular (002) Bragg reflections are indicated with pink and black drop lines for UO_2 and YSZ, respectively. Data extracted from SN1507. Intensity presented on a log scale.

The crystallinity of the UO_2 crystal was investigated by conducting omega scans on the (002) specular peak. Figure 7.28 shows the omega data collected from the (002) Bragg reflection of UO_2 after 0 and 8100 seconds of H_2O_2 exposure. Minimal change was noted in the crystallinity of the sample after the final H_2O_2 exposure of 8100 seconds. This is reflected in the Gaussian and Lorentzian^2 components of the FWHM modelled for each rocking curve. There is a slight decrease in the Lorentzian^2 component, with minimal broadening in the Gaussian component.

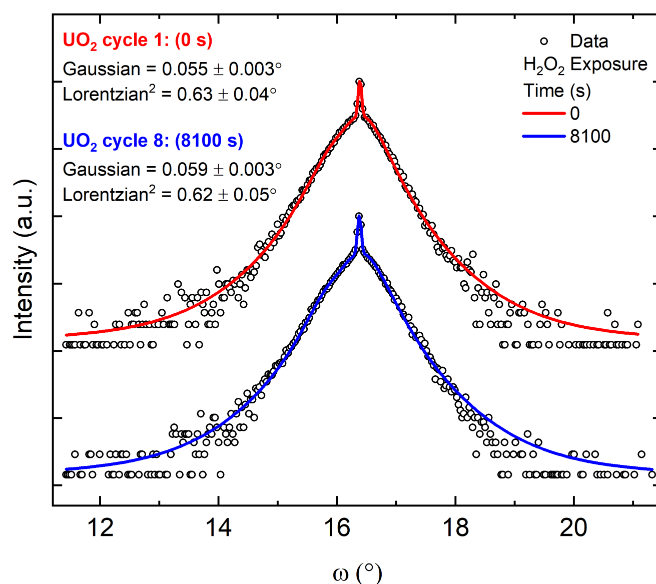

FIGURE 7.28. Omega data collected form the initial and final H_2O_2 dissolution experiments conducted on (001) UO_2. Two rocking curves are presented, collected after 0 (red) and 8100 (blue) seconds of H_2O_2 exposure. Data is indicated with open black circles, with models indicated with solid lines. Gaussian and Lorz^2 FWHM components are presented for each model in Figure legend. Data extracted from SN1507. Intensity presented on a log scale.

The most significant information was extracted using x-ray reflectivity. Figure 7.29 presents the XRR spectra collected from SN1507, alongside the plotted total thickness of the epitaxial film as a function of time. The XRR data have been offset to allow for an easier visual inspection between each spectra. Observing the XRR spectra in Figure 7.29 (a) initially, changes in the periodicity, fringe spacing, fringe resolution, and electron density can be noted in the spectra as a function of H_2O_2 exposure. The first seven data sets were possible to model using GenX software, however, the final data set collected after 8100 s of H_2O_2 exposure (presented with open blue circles), was not simulated.

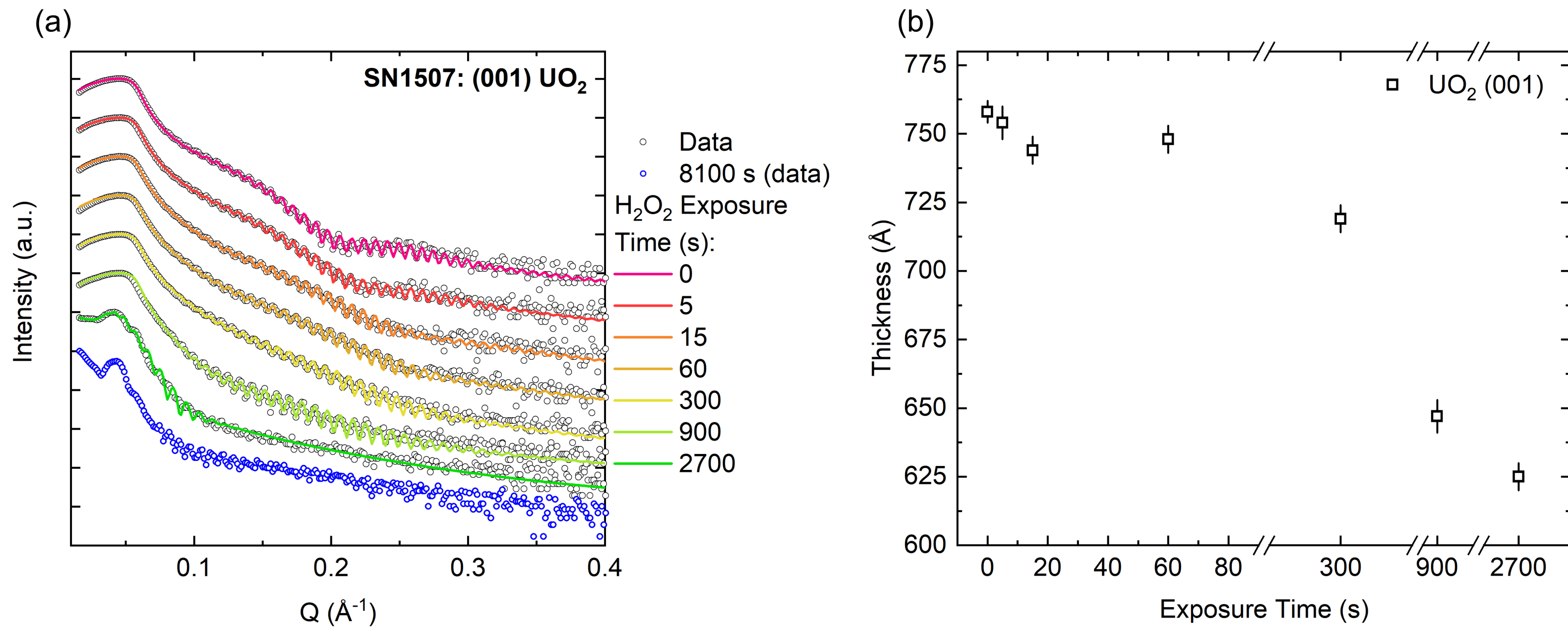

FIGURE 7.29. Graphs showing the thickness change as a result of H_2O_2 exposure on the surface of [001] oriented UO_2. (a): Shows the XRR spectra collected from UO_2 as a function of H_2O_2 exposure. Exposure times indicated in legend. Data points shown with open circles, with models indicates with solid lines. Final data set collected after 8100 s of exposure presented but not modelled. Intensity presented on a log scale. (b) Shows the thickness changes to each layer modelled in SN1507 as a function of exposure time. Total film thickness is shown with open black squares. Data collected from SN1507.

Figure 7.29 (b) presents the total thickness of SN1507 as a function of exposure time, up to 2700 s of exposure. There are some slight fluctuations in the total thickness, however, the general trend is that the thickness of the film reduces with time. The initial thickness of the sample was modelled to be 758 ± 4Å, with the final thickness after 2700 s being modelled as 625 ± 5Å. This equates to a total material loss of around 133 ± 6Å, and therefore a dissolution rate of $(4.9 \pm 0.2) \times 10^{-2}$ Ås^{-1}. This dissolution rate is of the same order as the values presented by *Bright et al.,* [112].

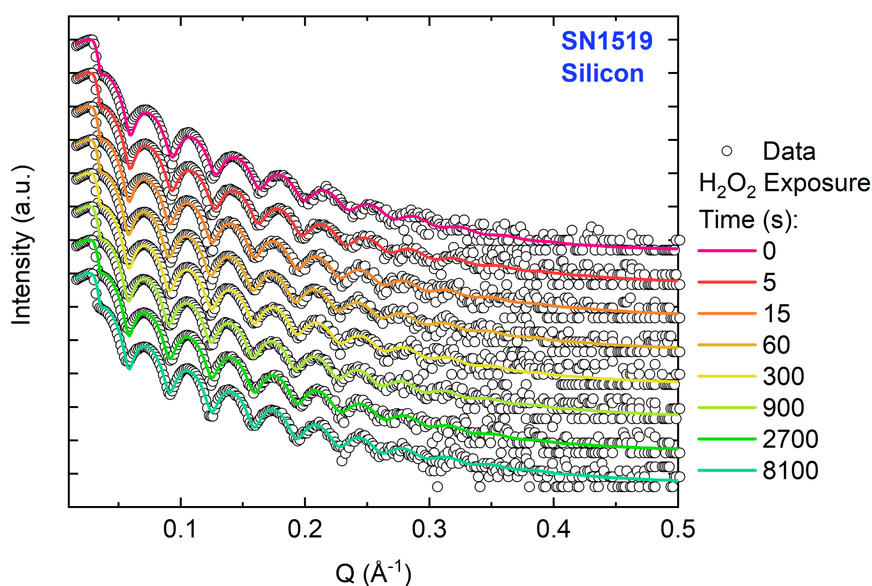

FIGURE 7.30. Change in the surface of silicon after exposure to 0.1 mol. H_2O_2. Total exposure times are indicated in figure legend. Data presented with open black circles, and models with solid lines. Data extracted from SN1519. Intensity presented on a log scale.

Silicon was deposited onto Corning glass at room temperature to investigate the corrosion of elemental silicon and silicon-oxides when exposed to 0.1 mol. H_2O_2. Similar to the work conducted on UO_2, silicon was used as a control substance. when conducting high-angle XRD measurements on SN1519, no Bragg reflections were present indicating the formation of amorphous silicon and silicon oxide. Figure 7.30 indicates the XRR spectra collected after each H_2O_2 exposure cycle. Each spectra has been offset to allow for an easier visual comparison between data sets. The spectra is presented between a range of 0.01 – 0.5Å^{-1} in order to showcase the region of interest. The model used to simulate the XRR data was comprised of two layers: elemental silicon, and a silicon oxide that had an electron density similar to SiO_2. The modelling of the electron density

at Q = 0.02 suggests the simulation fits the data well. The most significant change in the spectra is the roughening of Keissig fringes at Q = 0.3 Å^{-1}.

Figure 7.31 presents the modelled thicknesses extracted from the XRR spectra of SN1519 as a function of H_2O_2 exposure. The total film thickness is indicated with purple triangles, with the total thickness stemming from the silicon and silicon oxide being indicated with yellow circles and green diamonds, respectively. The initial thicknesses measured indicate a slight increase in the overall thickness of the film which is dominated by the Si layer. However, this increase was modelled to be 5 ± 7A, indicating the error on the thickness increase is greater than the overall change in thickness. After this initial increase, the overall thickness of the sample remains relatively constant within error. The final thickness modelled from the XRR spectra was 174 ± 4Å.

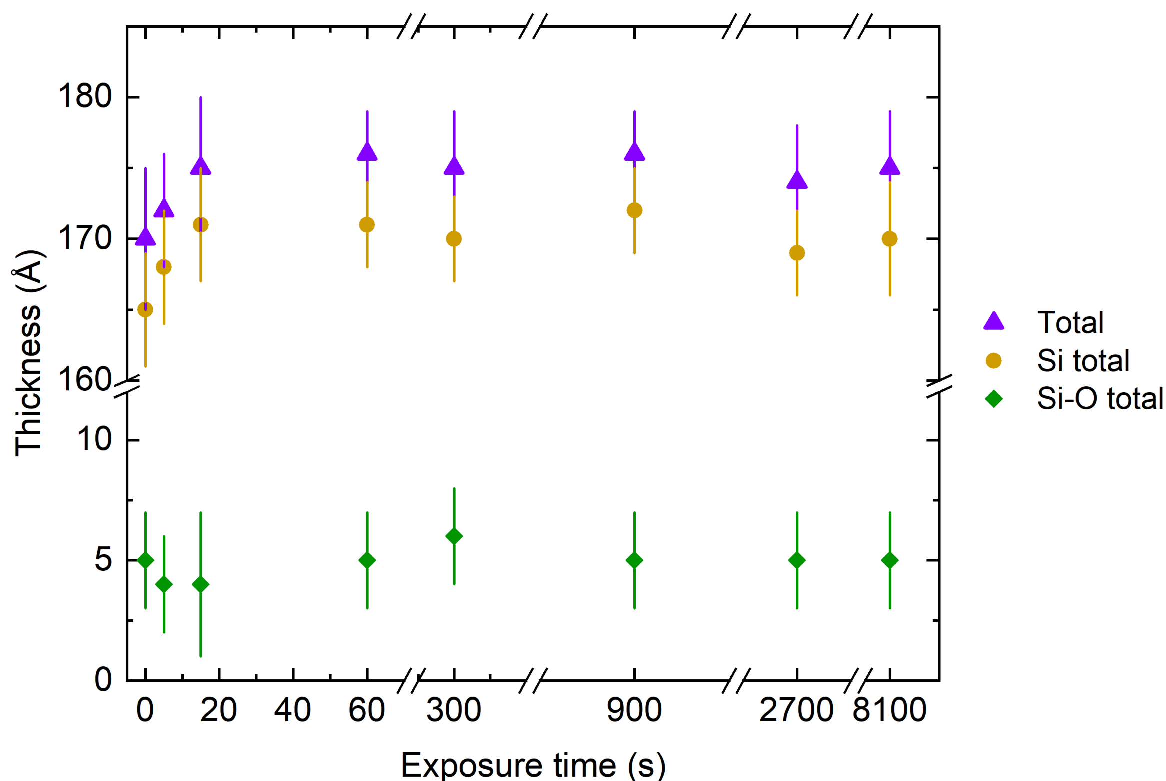

FIGURE 7.31. Thickness of total film, Si, and Si-O after each H_2O_2 exposure cycle. Total thickness presented with solid purple triangles, Si total with yellow solid circles, and Si-O with solid green diamonds. Data extracted from SN1519.

The data collected from both UO_2 (SN1507) and Silicon/Si-O (SN1519) samples suggest that UO_2 has the most significant structural change when exposed to H_2O_2. The silicon sample exhibited little to no change when compared to UO_2, with the total thickness remaining constant within error. This data infers that thickness changes occurring as a result of corrosion with uranium silicide compounds must indicate the presence of a uranium oxide phase, as the silicon oxide are unaffected when exposed to oxidising conditions. This differing behaviour could also be affected by the crystalline nature of each sample. The UO_2 is a well oriented single crystal, whereas, the silicon/si-o sample is deposited onto a Corning glass substrate and exhibits no indication of a crystalline structure.

7.3 Discussion of Corrosion Studies of U-Si Phases

The corrosion behaviour of uranium silicide phases within aqueous environments has been presented. Here, U_3Si, U_3Si_2, $\alpha-USi_2$, and USi_3 have all been exposed to MilliQ H_2O and 0.1 mol. H_2O_2 solutions in order to understand the dissolution behaviour of each phase as a function of uranium content. The ability to probe such behaviour is vital for furthering the understanding of ATF candidates, and how they may behave in the presence of aqueous environments. Conducting these experiments under ambient conditions will allow for comparisons to be drawn between the high-temperature aqueous corrosion studies discussed in Chapter 2, against the ambient oxidation investigations conducted in Chapter 6. The uranium silicide phases presented here were also tested alongside two control materials: UO_2 and silicon.

Evaluating the corrosion behaviour of uranium silicide phases within a H_2O solution was been presented. Structural, phase, and thickness changes were monitored as a function of exposure time. The most significant changes were noted in the highest uranium content uranium silicide phase: U_3Si. This compound exhibited the formation of Si-rich uranium silicide phases when exposed to H_2O. SN1711, epitaxial U_3Si formed $\alpha-USi_2$ after 60 s of exposure. The formation of a peak at this 2θ position was compared to the specular (200) Bragg reflection of coffinite, $USiO_4$. This phase has been noted in two studies [170, 177], which both claim that the oxidation of U_3Si_2 results in the formation of this material. However, in this work, it was confirmed to be uranium disilicide via the observation and measurement of the (004) and (008) Bragg reflections of $\alpha-USi_2$. The remaining uranium silicide thin films did not appear to have any significant phase transformations. The formation of $\alpha-USi_2$ within U_3Si could be an indication of the preferential oxidation model of uranium silicide phases proposed by [87, 94, 101]. Despite the work conducted by *Yang et al.,* [94] and *Sooby Wood et al.,* [101] being at elevated temperatures and within steam environments, the work presented here does align with the mechanism of the uranium sites preferentially oxidising allowing for the formation of Si-rich uranium silicide

phases. As the lower uranium content uranium silicide phases ($\alpha-USi_2$, USi_3) do not exhibit the same type of behaviour when exposed to H_2O, it is difficult to conclude that the aqueous environment is the sole reason for the phase change within U_3Si.

The radiolytic dissolution of uranium silicide phases was simulated by exposing the surface of each thin film to 0.1 mol. H_2O_2. The purpose of this experiment was to induce the dissolution of each phase in order to understand how fast the sample disintegrates within a high-concentration of H_2O_2. Again, UO_2 and silicon were used as control substances. Through observing the high-angle XRD data collected from each uranium silicide, it was found that the high uranium content compounds (U_3Si, U_3Si_2) exhibited the largest structural phase change. The epitaxial U_3Si sample, SN1711, had a drop in intensity for the (200) Bragg reflection of U_3Si_2. As discussed in Chapter 6, this phase was believed to be part of the oxide forming on the surface of U_3Si. When exposed to H_2O_2, U_3Si_2 (SN1707) exhibited a phase change, with the formation of U_3Si_5. This was noted with the presence of the (100) Bragg reflection of U_3Si_5 at $2\theta = 26.136°$. The remaining Si-rich U-Si phases, $\alpha-USi_2$ and USi_3 exhibited minimal changes in the specular direction, with no indication of additional compounds presented in the high-angle XRD data.

Alongside phase changes, the total thickness of each phase was also investigated as a function of exposure time to H_2O and H_2O_2. Table 7.1 presents the net thickness changes exhibited by all uranium silicide phases when exposed to both MilliQ H_2O and 0.1 mol. H_2O_2, with comparison to the thickness changes exhibited by (001) UO_2 and silicon/silicon-oxide. The values presented with a negative sign indicate an overall net loss from the sample after being exposed to the relevant aqueous environment. Observing the thickness changes as a result of exposure to H_2O, there is a clear indication that the higher the uranium content within the phase, the larger the net thickness gain. Comparing the thickness change observed in the control materials: UO_2 and Si/Si-O, indicates that the expansion inflicted on the uranium silicide phase must be attributed to the formation of silicon oxide or dissociation of elemental silicon from the original stabilised phase.

Table 7.1: The modelled net thickness changes for each uranium silicide phase when exposed to H_2O for 24 hours, and H_2O_2 for 8100 s, with comparison to UO_2 and silicon.

Phase	H_2O Thickness Change (Å)	H_2O_2 Thickness Change (Å)
U_3Si	+(93 ± 23)	-(79 ± 44)
U_3Si_2	+(10 ± 44)	+(69 ± 46)
α-USi_2	+(8 ± 18)	-(120 ± 46)
USi_3	-(6 ± 3)	-(19 ± 8)
UO_2	-(23 ± 13)	-(133 ± 6)
Si/Si-O	+(25 ± 6)	+(4 ± 6)

Uranium silicide phases in the presence of H_2O_2 exhibit different behaviours when compared to H_2O. Observing the net thicknesses presented in Table 7.1, each uranium silicide phase has

a decrease in the overall thickness with the exception of U_3Si_2, within error. The corrosion experiments conducted on the poly-crystalline U_3Si_2 sample, SN1707, in both aqueous environments, experience an almost pulverisation of the sample. This resulted in the removal of regions of the thin film during the aqueous exposures. For the hydrogen peroxide experiments, the sample exhibited an initial gain of 120 ± 45Å gain over a total H_2O_2 exposure time of 900 s. This sample then proceeded to lose around 100 ± 34Å from the U_3Si_2 layer. The most drastic difference between this U_3Si_2 sample, when compared to the remaining uranium silicide phases presented, is its crystallographic nature. SN1707 is a poly-crystalline sample, this will exhibit grain boundaries between different crystallographic directions, therefore each crystallite orientation may have varying behaviours when exposed to aqueous environments. Similar behaviour is noted when the three principal crystallographic directions of UO_2 are exposed to radiolytic conditions, as shown with the work conducted by Rennie *et al.,* [40]. This could explain the significant thickness, and thus volume change of U_3Si_2 when exposed to aqueous environments. The thickness gain of U_3Si_2 seen with the thin films samples in this work, resonates with the work conducted by Sooby Wood *et al.,* [101, 102]. Here, the drastic volume expansion occurring within the tetragonal structure of U_3Si_2 resulted in the complete pulverisation of bulk fuel pellets when exposed to high-temperature aqueous environments. Furthermore, studies investigating the formation of a uranium silicide hydride phase, $U_3Si_2H_x$ [99, 100], noted a 10% volume expansion in tetragonal U_3Si_2. This volume expansion due to a hydride formation could be linked to the thickness gain found for U_3Si_2 when exposed to aqueous media, however, a deeper investigation would be required to fully realise this. With SN1707 being poly-crystalline, it may also suggest that comparing the aqueous corrosion of this sample to the remaining epitaxial crystals may not permit for conclusive arguments to be made. Despite this, the photographic evidence gathered from the aqueous corrosion of U_3Si_2 in both H_2O and H_2O_2 suggests that this phase may not be suitable for operation in LWRs. Furthermore, the gain in thickness aligns with the pulverisation mechanism of U_3Si_2 under high-temperature aqueous environments reported by [91, 94, 101, 102].

From monitoring the total change in thickness for each phase it was possible to extract dissolution rates. Table 7.2 presents the dissolution rates extracted from both experiments, providing a corrosion rate for H_2O and H_2O_2. Negative rates indicate a net gain in thickness for the phase. Observing the dissolution rates calculated for each phase, it is clear that any thickness loss is a result of the conversion of U_xSi_y to uranium oxide phases, as predicted by the high-temperature work conducted by Sooby Wood *et al.,* [101] and Yang *et al.,* [94]. This aligns well the with data extracted from the thickness changes, which showed that the growth of silicon/silicon-oxide was responsible for the net gain in material for the uranium silicide phases. From the rates calculated here, it is shown that the uranium silicide with the faster dissolution rate when exposed to a H_2O_2 aqueous environment, and this indicating a loss of material, is $\alpha - USi_2$. The

only phase to exhibit a loss due to the presence of H_2O is USi_3. This is reflected in the dissolution rate calculated. The dissolution rate for (001) UO_2 within H_2O_2 exceeds the rates calculated for each uranium silicide phase, suggesting that U-Si materials are more corrosion resistive to highly oxidising environments. This contradicts the aqueous corrosion work conducted on U_3Si_2 by Maier *et al.,* [118], which suggested U_3Si_2 is more reactive to H_2O_2 when compared to the behaviour of UO_2. Additionally, the preservation of the metallic U-Si film for each phase studied could be explained with the presence of silicon-oxide within the native oxide. The Si/Si-O sample is resistive to the oxidising behaviour of both aqueous environments, and exhibits a thickness growth when exposed to both H_2O and H_2O_2. This may suggest that the sub-stoichiometric Si-O phases found from the XPS depth profiling in Chapter 6, are oxidising further, tending towards SiO_2. This silicon oxide phase has the largest unit cell volume when compared to the silicon oxide phases with lower valence states. The presence of the Si-O phases was only noted by the XPS depth profiling work conducted in Chapter 6, and these were subsequently included into the x-ray reflectivity models presented in both oxidation and dissolution studies. The Si-O sites were not found within either specular or off-specular diffraction investigations, suggesting that these phases as not crystalline. However, the XRR models presented indicate their presence, and evolution as a function of exposure time to both aqueous media.

Table 7.2: The calculated dissolution rates for each uranium silicide phase when exposed to H_2O and H_2O_2 with comparison to UO_2 and silicon. Negative rates indicate a thickness gain.

Phase	H_2O Rate (Ås^{-1})	H_2O Rate (gm^{-2} day^{-1})	H_2O_2 Rate (Ås^{-1})	H_2O_2 Rate (gm^{-2} day^{-1})
U_3Si	$-(1.1 \pm 0.3)x10^{-3}$	$-(1.7 \pm 0.4)x10^{-1}$	$(9.8 \pm 5.4)x10^{-3}$	(1.3 ± 0.7)
U_3Si_2	$-(1.2 \pm 5.1)x10^{-4}$	$-(1.3 \pm 5.4)x10^{-2}$	$-(8.5 \pm 5.7)x10^{-3}$	$-(8.9 \pm 6)x10^{-1}$
α-USi_2	$-(9.4 \pm 2.2)x10^{-5}$	$-(7.3 \pm 1.7)x10^{-3}$	$(1.5 \pm 0.6)x10^{-2}$	(1.2 ± 0.5)
USi_3	$(7.7 \pm 0.3)x10^{-5}$	$(5.3 \pm 0.2)x10^{-3}$	$(2.4 \pm 0.2)x10^{-3}$	$(1.7 \pm 0.1)x10^{-1}$
UO_2	$(1.3 \pm 0.4)x10^{-4}$	$(1.2 \pm 0.4)x10^{-2}$	$(4.9 \pm 0.2)x10^{-2}$	(4.6 ± 0.2)
Si/Si-O	$-(2.9 \pm 0.8)x10^{-4}$	-$(5.8 \pm 1.6)x10^{-3}$	$-(5.7 \pm 2.9)x10^{-4}$	$-(1.1 \pm 0.6)x10^{-2}$

The presence of both uranium and silicon oxides within the native oxide of each phase could result in opposing results when dealing with the aqueous dissolution of uranium silicide compounds. Each phase, with the exception of USi_3, exhibited some deformation to the critical edge region of the x-ray reflectivity spectra. This particular feature could be the result of two possible scenarios: (1) an increased roughness between layers, and (2) the removal of sample material, causing the substrate below to appear. From the evidence collected from U_3Si_2, both scenarios were noted, however, for the remaining phases this behaviour associated with scenario (2) was not noticed. Therefore, one mechanism that could be proposed for not only for the aqueous corrosion, but for the ambient oxidation of uranium silicide phases is that the oxide layers that form as a result of ambient exposure could form compounds that do not exist as uniform layers. Figure 7.32 presents the difference between an idealised uniform oxide layer, and an oxide that has island formation. The implication of this could be that more susceptible sites could be targeted first by

an oxidising specie, thus removing or dissolving that region prior to the more corrosion resistant material. This in turn, exposes a vulnerable metallic site situated below and induces further oxidation to that material.

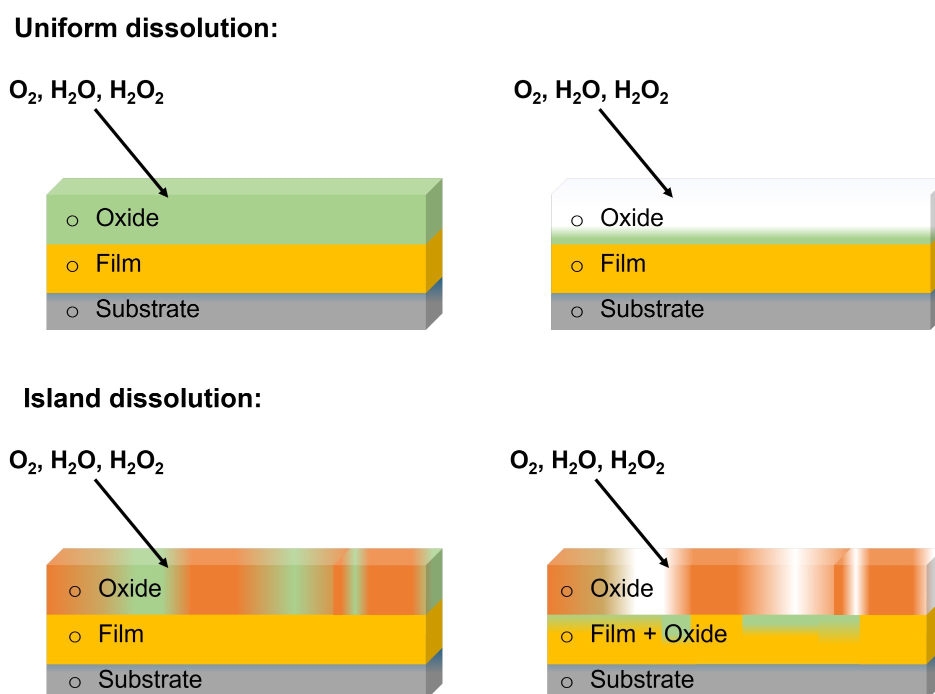

FIGURE 7.32. Schematic diagram presented two potential dissolution mechanisms: Uniform dissolution, and island dissolution.

7.4 Conclusions

The experiments presented here have investigated the aqueous corrosion of uranium silicide phases via two media: MilliQ H_2O and 0.1 mol. H_2O_2. The investigation into how each uranium silicide behaves within ambient H_2O allowed for a deeper understanding into how these silicide phases may react in aqueous environments prior to reactor operation and subsequent radiation fields. For the first time, epitaxial thin films of uranium silicide compounds have been exposed to such scenarios. It was shown that the under the influence of H_2O, the uranium silicide phases, with the exception of USi_3, exhibit a thickness (or volume) gain. This was attributed to the formation of silicon oxides, or dissociated silicon. The thickness change was further influenced by the amount of uranium present within the phase, i.e. U_3Si exhibited the most significant net gain, with USi_3 exhibiting a net loss of 6 ± 3 Å. In addition to this, it was shown that the water corrosion of U_3Si produces an additional U-Si phase after 60 seconds of exposure. This phase was

identified as $\alpha-USi_2$.

Radiolytic dissolution of uranium silicide compounds was investigated by exposing each phase to 0.1 mol. H_2O_2, and drawing comparisons to both (001) UO_2 and a Si/Si-O thin film. This experiment allowed for the potential effect of water radiolysis to be investigated, thus simulating the potential phase change and dissolution rate of each uranium silicide phase. Both high-angle XRD and XRR were used to investigate the corrosion of each phase within H_2O_2. The corrosion rates were found to be much smaller when compared to (001) UO_2, which was modelled to be $(4.9 \pm 0.2) x 10^{-2} As^{-1}$. Uranium disilicide, $\alpha-USi_2$ was of the same order as UO_2, with a modelled dissolution rate of $(1.5 \pm 0.6) x 10^{-2} Å s^{-1}$.

Observations made from the dissolution of uranium silicide phases within both H_2O and H_2O_2 allowed for the formation of the native oxide forming on the surface of each phase to be investigated. Here it was shown that the silicon-oxide is responsible for the growth of the oxide, with uranium-oxide responsible for the dissolution. Therefore, an island dissolution mechanism was attributed to the overall aqueous corrosion of uranium silicide phases. Furthermore, the observations made from the ambient aqueous corrosion of U_3Si_2 align with the high-temperature steam corrosion work conducted on bulk material by [101] and [102].

The overall comparison of uranium silicide phases with both uranium and silicon oxides is intriguing, and suggests that a deeper investigation into the radiolytic corrosion, or elevated temperature aqueous corrosion of these materials. By altering parameters such as microstructure, for example by synthesising a fleet of poly-crystalline samples, or a single crystal of U_3Si_2. These experiments would also provide a good basis for understanding the high-temperature steam corrosion of epitaxial uranium silicide thin films, allowing for these samples to be subjected to more realistic scenarios.

Chapter 8

Conclusions and Future Work

Probing the fundamental behaviour of nuclear fuel is imperative to the overall economics and safety of the nuclear industry. Mechanisms, such as thermal conductivity and oxidation, are key in this understanding, and are ultimately the deciding factors on whether a material is introduced into the nuclear fuel cycle. Uranium silicide has been primed as a advanced nuclear fuel (ATF) candidate since the 2011 Fukushima Daiichi nuclear accident. The advanced thermal behaviours and increased uranium density of the uranium silicide phase, U_3Si_2, made this fuel appealing for use in current and future nuclear reactors. However, multiple set-backs, including swelling, high-temperature oxidation, and structural pulverisation have committed this material unusable for commercial use. This thesis aimed to understand the many compounds that form the uranium-silicon binary system, and investigate their corrosion mechanisms on a fundamental level.

When exploring the mechanics of oxidation and dissolution it is preferable to take a fundamental approach, particularly when investigating a series of line-compounds. The uranium-silicon binary phase diagram is comprised of around six line-compounds with fixed stoichiometries. Rather than using realistic bulk fuel samples for fundamental investigations, this encouraged the use of idealistic samples, allowing for the complexity of the experiments to be reduced, and providing an easier comparison with theoretical studies. This was achieved through the fabrication of epitaxial thin films. Utilising the physical vapour deposition method of DC magnetron sputtering, a series of samples were synthesised which extended across the U-Si phase diagram, delicately mapping the phase diagram as a function of silicon content. From this, epitaxial [001] U_3Si, [100] U_3Si_5, [001] $\alpha-USi_2$, and [001] USi_3 were engineered, alongside poly-crystalline U_3Si_2. These samples were the first of their kind, making their nature extremely novel. If these

samples were not epitaxially matched to [001] CaF_2, or [001] MgO in the case of $\alpha - USi_2$, the characterisation of single phase uranium silicide phases would have not been possible. The requirement for pristine epitaxial single phase samples was highlighted by the multiple phases present within the poly-crystalline samples of U_3Si_2, as shown throughout this thesis. The ability to produce such samples led to a better control over the characterisation, and thus over the subsequent corrosion experiments that followed. The capability to epitaxially stabilise four of the main six uranium silicide compounds is promising. It suggests that this synthesis method could be used to engineer the remaining uranium silicide phases, U_3Si_2 and USi as epitaxial surfaces. Additionally, it provides the basis for a deeper exploration of the potential phases that could be formed between uranium and silicon. Fine tuning the deposition rates even further during the sputtering process could unlock these remaining compounds.

The synthesis of these samples led to their unique structural and chemical properties being probed through the use of x-ray diffraction and x-ray spectroscopy. The epitaxial matching of each U-Si phase to [001] CaF_2 was probed and understood. This revealed the way in which each phase is matched to the lattice of the substrate, with most U-Si phases exhibiting multi-domain systems. X-ray photoelectron spectroscopy (XPS), was deployed to understand the chemical bonding environments present within each phase. For the first time, the spectra collected from [100] oriented U_3Si_5 was presented. Providing this spectra furthers the knowledge about uranium silicide phases. Here, it was shown that, much like the remaining phases, U_3Si_5 exhibits a metallic bonding behaviour, with the U-4f state existing within a U(0) valency around 377 eV. This behaviour was replicated when observing the valence band spectra of U_3Si_5, which exhibited a strong metallic structure at the Fermi Edge. Each phase did exhibit uranium-oxide bonding, however, the nature of the oxide was not determined due to the shake-up satellite positioning being inconsistent. However, it was confirmed in this work, that the uranium-oxide present within each U-4f spectra was not a result of the formation of coffinite, $USiO_4$. Observing the metallic component areas of the Si-2p and U-4f, the U:Si ratio was calculated for each phase. This allowed for the stoichiometry of each thin film to be measured. These calculations confirmed that each phase was stoichiometric within error. The stoichiometry calculated for $\alpha - USi_2$ was found to exhibit a U:Si stoichiometry closer to that of a uranium monosilicide (USi). Probing this stoichiometric-structure mismatch further would prove useful in understanding the formation of the uranium disilicide phases, both $\alpha - USi_2$ and $\beta - USi_2$, thus expanding the knowledge on the phase diagram.

The ability to structurally and chemically characterise pristine uranium silicide thin films permitted for an investigation into the native oxide that forms on the surface of each compound as a function of uranium content. This experiment set out to answer three questions regarding the oxidation of uranium silicide phases: (1) How much do the uranium silicide phases change as

a function of uranium content once exposed to ambient conditions? (2) What compounds form within each uranium silicide oxide layer? and (3) How thick is the oxide layer that grows on each uranium silicide under ambient conditions? These three questions were probed using a multi-technique approach. Through the use of high-angle XRD, it was possible to structurally characterise the uranium silicide phases. For this, epitaxial uranium silicide compounds were produced again via DC magnetron sputtering, alongside poly-crystalline U_3Si_2. The stabilisation of these samples without protective niobium capping layers confirmed that these materials can be engineered and are stable under the influence of ambient atmospheric environments. Structural characterisation of these uncapped samples matched the pristine structural data presented in Chapter 5. Additional stabilisation of $\alpha - USi_2$ onto [001] CaF_2 improved the overall crystallinity of the epitaxial crystal by roughly 84%. Through the use of high-angle XRD, it was shown that structurally the uranium silicide compounds do not change as a result of ambient atmospheric exposure, and ultimately, retain their prototypical crystal structures. The most significant structural change was exhibited by [100] U_3Si_5, where the unit cell contracted by around 4%. Here the specular and in-plane lattice constants expanded and contracted as to alter the hexagonal c/a ratio to 0.94. This structural tension was attributed to the increased uranium content required to stabilise U_3Si_5. Further investigations on the crystallisation of uranium silicide phases within this high-silicon content region of the phase diagram would prove invaluable to the understanding of these compounds.

The chemical bonding environments were probed using x-ray photoelectron spectroscopy (XPS). A depth profiling technique was deployed in order to investigate the valency of uranium and silicon oxides, alongside the metallic stoichiometry as a function of oxide depth. These experiments allowed for a deeper understanding into the compounds that form as part of the native oxides on the surface of metallic uranium silicide compounds, thus addressing question (2). From the depth profiling it was found that the uranium and silicon oxides forming on the surface, or part of the native oxide of each phase are not initially stoichiometric *dioxide* phases. The difficulty experienced with identifying the true nature of the uranium and silicon oxide phases within each U-Si phase probes, could be investigated using *extended x-ray absorption fine structure* (EXAFS) techniques to determine the valency of the oxides present. This technique enables a high elemental sensitivity, which is particularly useful for low concentrations of elements and materials present in the sample. Using EXAFS on the uranium silicide phases probed in this work would be particularly beneficial in the understanding of the amorphous-like silicon oxide materials present within the surface oxide layers. The major breakthrough was the identification of silicon-rich uranium silicide phases forming as a result of ambient surface oxidation. This mechanism was identified for each phase studied in this thesis. Previous work had predicted this mechanism for U_3Si_2 via theoretical studies, with experimental studies showing this mechanism under high-temperature aqueous environments. The preferential oxidation of uranium sites

within each uranium silicide phase provides a predictive model that can be utilised for high-temperature oxidation and aqueous corrosion experiments. The understanding of this mechanism could be furthered through probing this preferential oxidation until the termination phases, UO_2 and SiO_2, are formed for each uranium silicide phase. This would provide a deeper insight into the effect of temperature on these materials, as well as the rate of oxidation at elevated temperatures. This could be conducted through a combination of *in-situ* x-ray photoelectron spectroscopy, alongside the use of high-angle x-ray diffraction techniques. The high-temperature oxidation of these epitaxial thin films would prove useful in understanding the structural changes that occur as a result of the surface oxidation. Such experiment could be conducted via *in-situ* high-angle x-ray diffraction. The ability to form such epitaxial surfaces could permit for an investigation in how the crystallographic orientation of the sample effects the overall oxidation and oxidation rate. If this were achieved, a true comparison against the oxidation of UO_2 could be conducted.

The thickness of each native oxide was probed using x-ray reflectivity in order to answer question (3). The formation of the surface oxide of each compound was probed *in-situ* initially for around four days. Changes to the surface were monitored for up to 55 days. The data presented in Chapter 6 indicated that the majority of the oxide growth had occurred as soon as the samples were exposed to ambient conditions. However, using x-ray reflectivity, the thickness of each native oxide was probed. The thickest oxide layer formed on the surface of [100] U_3Si_5 and was measured to be 110 ± 12 Å, with the thinnest oxide layer forming on the surface of poly-crystalline U_3Si_2. With the exception of U_3Si_5, the thickness of the native oxide forming on the surface of each uranium silicide phase was between 30 ± 5 Å and 63 ± 5 Å. The data presented here quantified the thickness of these ambient oxide phases for the first time. In-situ probing of the initial nucleation of the oxide layer would benefit this aspect of the work. Tracking of the oxidation thickness could also be explored if these epitaxial compounds are subjected to elevated temperatures.

The degradation of uranium silicides via aqueous dissolution was investigated by exposing these idealised surfaces to both H_2O and H_2O_2. Probing this corrosion behaviour is vital for the eventual implementation of any nuclear fuel candidate. Uranium silicides, namely U_3Si_2, have been known to behave poorly within high-temperature steam environments, exhibiting the same preferential oxidation mechanism as noticed in high-temperature gaseous testing. Thus, testing these uranium silicide thin films in both aqueous media allows for an insight into the ambient water corrosion and into the effect of simulated radiolytic dissolution. Monitoring the aqueous dissolution of each phase within ambient MilliQ H_2O indicated that each phase, with the exception of uranium trisilicide, exhibits thickness increase which suggests an overall volume expansion. This mechanism was attributed to the formation of additional silicon oxides within the native oxide. This thickness increase corresponded with the uranium content within the phase, therefore the higher the uranium content, the larger the net gain. The material loss inflicted

on each uranium silicide phase was attributed to the presence of uranium oxides, i.e. UO_{2+x} in water dissolution, and the formation of U(VI) ions in the uranium oxides during H_2O_2 exposure.

Through probing both the ambient air oxidation and ambient aqueous corrosion, a model was constructed to understand the overall oxidation mechanism of uranium silicide phases. Through the use of XPS and XRR, it was shown that the preferential oxidation of uranium sites occurs within each uranium silicide compound. This results in the formation of silicon-rich uranium silicide phases, and an oxide layer that consists of both uranium and silicon oxides. However, this oxide layer is notoriously silicon rich. The aqueous corrosion furthered this model by showing that the oxidation products forming on the surface of each U_xSi_y phase do not exist as uniform layers. It was therefore proposed that the formation of the native oxide for each uranium silicide phase manifests as islands. This therefore explains the inconsistent net gain and loss of material during this dissolution experiments.

For the aqueous corrosion of uranium silicide phases there are additional mechanisms that could be investigated using the same techniques. For example, in-plane crystallographic directions of each epitaxial uranium silicide phase could be probed *in-situ* to explore how the aqueous dissolution changes as a function of crystallographic orientation. This would also be achieved via the synthesis and subsequent aqueous dissolution of epitaxial uranium silicide surface in various crystallographic orientations. i.e engineering (111) and (110) epitaxial thin film of U_3Si. This would allow for a true comparison between the dissolution work on UO_2 conducted by [40]. Additional atomic force microscopy (AFM) studies could be conducted to probe the potential formation of island-like surface layers. The use of this technique would allow for the surface morphology and texture to be explored further, and for the change in surface morphology to be probed *in situ* as the U-Si phases are exposed to both aqueous media. Furthermore, high-temperature corrosion studies that involve subjecting the epitaxial uranium silicide compounds to steam environments would further the current body of literature. This would allow for all of the uranium silicide phases, including the chosen ATF materials, to be investigated under the same conditions. An experiment like this would be the first of its kind. The chemistry of the water that the uranium silicide phases are subjected to could be tailored to be more representative of LWR coolant water, or of the groundwater surrounding a GDF facility.

Overall, this work has produced a plethora of novel epitaxial and poly-crystalline uranium silicide samples that have allowed measurements to be conducted that are the first of their kind. The results collected have given a new insight into the structure, chemical bonding, ambient oxidation, and aqueous corrosion of uranium silicide phases. This work has helped to further the understanding of the uranium-silicon phase diagram, alongside the fundamental physical behaviour and structural degradation of these materials. The information collected from each

compound has furthered the understanding of these materials, and these studies have been vital in assessing the viability of using uranium silicides as nuclear fuels.

Appendix A

FIGURE A.1. Artistic depiction of the changes within the nuclear industry regarding researching nuclear fuel circa October 2018.

Bibliography

[1] Mathers. M.
Without Me.
The Eminem Show, May 2002.

[2] Eugene S. Ilton and Paul S. Bagus.
XPS determination of uranium oxidation states.
Surface and Interface Analysis, 43(13):1549–1560, dec 2011.

[3] World Nuclear.
Nuclear Power in the United Kingdom | UK Nuclear Energy - World Nuclear Association.
2017.

[4] Nuclear Innovation and Research Advisory Board.
Achieving Net Zero: The role of Nuclear Energy in Decarbonisation.
pages 1–27, 2020.

[5] NN Greenwood and A Earnshaw.
Chemistry of the Elements.
2012.

[6] Lise Meitner and O. R. Frisch.
Disintegration of uranium by neutrons: A new type of nuclear reaction [1].
143(3615):239–240, feb 1939.

[7] By E Fermi, E Amaldi, F R Asetti, and E Segre.
Artificial radioactivity produced by neutron bombardment.
134(3391):668, sep 1934.

[8] H. L. Anderson, E. Fermi, and Leo Szilard.
Neutron production and absorption in uranium.
Physical Review, 56(3):284–286, aug 1939.

[9] Michael F. L'Annunziata.
Radioactivity: Introduction and History, From the Quantum to Quarks: Second Edition.
Elsevier Science,, Atlanta :, 2016.

[10] Enrico Fermi.
Experimental Production of a Divergent Chain Reaction.
American Journal of Physics, 20(9):536, jul 2005.

[11] S E Jensen and E Nonboel.
Description of the magnox type of gas cooled reactor (MAGNOX).
1999.

[12] Stephen C. Whitfield, Eugene A. Rosa, Amy Dan, and Thomas Dietz.
The Future of Nuclear Power: Value Orientations and Risk Perception.
Risk Analysis, 29(3):425–437, mar 2009.

[13] GIF Portal - Technology Roadmap.
A Technology Roadmap for Generation IV Nuclear Energy Systems, 2002.

[14] Elmer E. Lewis.
Fundamentals of Nuclear Reactor Physics.
Fundamentals of Nuclear Reactor Physics, 2008.

[15] Yoshiaki Oka.
Nuclear Reactor Design, volume 2 of *An Advanced Course in Nuclear Engineering*.
Springer Japan, Tokyo, 2014.

[16] Britannica.
liquid-metal fast-breeder reactor | Britannica.
https://www.britannica.com/technology/liquid-metal-fast-breeder-reactor.

[17] P. D. (Peter D.) Wilson.
The nuclear fuel cycle from ore to wastes.
Oxford University Press, 1996.

[18] *Nuclear Power Reactors in the World*.
Number 2 in Reference Data Series. INTERNATIONAL ATOMIC ENERGY AGENCY, Vienna, 2021.

[19] Britannica.
pressurized-water reactor | nuclear energy | Britannica.
https://www.britannica.com/technology/pressurized-water-reactor.

[20] S. J. Zinkle, K. A. Terrani, J. C. Gehin, L. J. Ott, and L. L. Snead.
Accident tolerant fuels for LWRs: A perspective.
Journal of Nuclear Materials, 448(1-3):374–379, may 2014.

[21] V. Saenko, V. Ivanov, A. Tsyb, T. Bogdanova, M. Tronko, Y. U. Demidchik, and S. Yamashita.
The Chernobyl Accident and its Consequences.
Clinical Oncology, 23(4):234–243, may 2011.

[22] Evelyn O. Talbott, Ada O. Youk, Kathleen P. McHugh-Pemu, and Jeanne V. Zborowski.
Long-term follow-up of the residents of the Three Mile Island accident area: 1979-1998.
Environmental Health Perspectives, 111(3):341–348, mar 2003.

[23] RS Denning.
The three mile island unit 2 core: a post-mortem examination.
Annual review of energy, 10(1):35–52, 1985.

[24] PG Martin.
The 2011 Fukushima Daiichi Nuclear Power Plant Accident: An Analysis From The Metre to The Nano-Metre Scale.
Springer, 2019.

[25] Akira Hasegawa, Dapeng Zhao, Shuichiro Hori, Akira Yamamoto, and Shigeki Horiuchi.
Deep structure of the northeastern Japan arc and its relationship to seismic and volcanic activity.
Nature 1991 352:6337, 352(6337):683–689, 1991.

[26] International Atomic Energy Agency (IAEA).
The Fukushima Daiichi Accident. Technical Volume 1/5. Description and Context of the Accident.
Director General, pages 1–222, 2015.

[27] S. Rennie, E. Lawrence Bright, J. E. Darnbrough, L. Paolasini, A. Bosak, A. D. Smith, N. Mason, G. H. Lander, and R. Springell.
Study of phonons in irradiated epitaxial thin films of <math xmlns.
Physical Review B, 97(22):224303, jun 2018.

[28] Judy W.L. Pang, William J.L. Buyers, Aleksandr Chernatynskiy, Mark D. Lumsden, Bennett C. Larson, and Simon R. Phillpot.
Phonon lifetime investigation of anharmonicity and thermal conductivity of UO2 by neutron scattering and theory.
Physical Review Letters, 110(15):157401, apr 2013.

[29] CT Walker, T Kameyama, S Kitajima, and M Kinoshita.
Concerning the microstructure changes that occur at the surface of uo2 pellets on irradiation to high burnup.
Journal of nuclear materials, 188:73–79, 1992.

[30] Byung-Ho Lee, Yang-Hyun Koo, and Dong-Seong Sohn.
Rim characteristics and their effects on the thermal conductivity in high burnup uo2 fuel.
Journal of Nuclear Science and technology, 38(1):45–52, 2001.

[31] T. R. Allen, R. J.M. Konings, and A. T. Motta.
Corrosion of Zirconium Alloys.
Comprehensive Nuclear Materials, 5:49–68, 2012.

[32] Donghwi Lee, Barret Elward, Paul Brooks, Rajnikant Umretiya, Jessika Rojas, Matteo Bucci, Raul B. Rebak, and Mark Anderson.
Enhanced flow boiling heat transfer on chromium coated zircaloy-4 using cold spray technique for accident tolerant fuel (ATF) materials.
Applied Thermal Engineering, 185:116347, feb 2021.

[33] Kyle A. Gamble.
ATF material model development and validation for priority cladding concepts.
Technical report, Idaho National Laboratory, Idaho Falls, ID (United States), aug 2019.

[34] NNL.
Accident Tolerant Fuel: A UK Perspective Position Paper 3.
National Nuclear Laboratory Position Paper, 2018.

[35] Benjamin Maier, Hwasung Yeom, Greg Johnson, Tyler Dabney, Jorie Walters, Peng Xu, Javier Romero, Hemant Shah, and Kumar Sridharan.
Development of cold spray chromium coatings for improved accident tolerant zirconium-alloy cladding.
Journal of Nuclear Materials, 519:247–254, jun 2019.

[36] Bowen Qiu, Jun Wang, Yangbin Deng, Mingjun Wang, Yingwei Wu, and S. Z. Qiu.
A review on thermohydraulic and mechanical-physical properties of SiC, FeCrAl and Ti3SiC2 for ATF cladding.
Nuclear Engineering and Technology, 52(1):1–13, jan 2020.

[37] Kurt A. Terrani, Bruce A. Pint, Chad M. Parish, Chinthaka M. Silva, Lance L. Snead, and Yutai Katoh.
Silicon Carbide Oxidation in Steam up to 2 MPa.
Journal of the American Ceramic Society, 97(8):2331–2352, aug 2014.

[38] Yutai Katoh, Lance L. Snead, Izabela Szlufarska, and William J. Weber.
Radiation effects in SiC for nuclear structural applications.
Current Opinion in Solid State and Materials Science, 16(3):143–152, jun 2012.

[39] M. Snead, L Snead, K Terrani, K Field, A Worrall, K Robb, Y Yamamoto, J Powers, S Dryepondt, B. A. Pint, and X Hu.
Technology Implementation Plan: ATF FeCrAl Cladding for LWR Application.
Technical Report May, 2015.

[40] K. Gofryk, S. Du, C. R. Stanek, J. C. Lashley, X. Y. Liu, R. K. Schulze, J. L. Smith, D. J. Safarik, D. D. Byler, K. J. McClellan, B. P. Uberuaga, B. L. Scott, and D. A. Andersson.
Anisotropic thermal conductivity in uranium dioxide.
Nature Communications, 5, 2014.

[41] S. Rennie, E. Lawrence Bright, J. E. Sutcliffe, J. E. Darnbrough, R. Burrows, J. Rawle, C. Nicklin, G. H. Lander, and R. Springell.
The role of crystal orientation in the dissolution of UO2 thin films.
Corrosion Science, 145:162–169, dec 2018.

[42] A. Travelli.
The RERTR Program, 1992.

[43] S. C. Middleburgh, R. W. Grimes, E. J. Lahoda, C. R. Stanek, and D. A. Andersson.
Non-stoichiometry in U3Si2.
Journal of Nuclear Materials, 482:300–305, dec 2016.

[44] Afiqa Mohamad, Wanthana Silpawilawan, Hiroaki Muta, Ken Kurosaki, and Yuji Ohishi.
Thermal and mechanical properties of U3Si and USi3.
Annals of Nuclear Energy, 133:186–193, nov 2019.

[45] S. C. Middleburgh, P. A. Burr, D. J.M. King, L. Edwards, G. R. Lumpkin, and R. W. Grimes.
Structural stability and fission product behaviour in U3Si.
Journal of Nuclear Materials, 466:739–744, nov 2015.

[46] Jin Wen Yang and Li An.
Elasticity, lattice dynamics and ideal strengths of USi3 and U3Si via first principles calculations.
Journal of Nuclear Materials, 512:407–416, dec 2018.

[47] G. Kimmel, S. Nadiv, and IUCr.
Atomic positions in U3Si.
urn:issn:0567-7408, 31(5):1351–1353, may 1975.

[48] K. Remschnig, T. Le Bihan, H. Noël, and P. Rogl.
Structural chemistry and magnetic behavior of binary uranium silicides.
Journal of Solid State Chemistry, 97(2):391–399, apr 1992.

[49] W.H. Zachariasen and IUCr.
Crystal chemical studies of the 5f-series of elements. VIII. Crystal structure studies of uranium silicides and of CeSi2, NpSi2, and PuSi2.
urn:issn:0365-110X, 2(2):94–99, apr 1949.

[50] A. Brown and J. J. Norreys.
Beta-polymorphs of uranium and thorium disilicides.
Nature, 183(4662):673, 1959.

[51] Yoshihiko Sasa and Masayuki Uda.
Structure of stoichiometric USi2.
Journal of Solid State Chemistry, 18(1):63–68, may 1976.

[52] L. H. Brixner.
Journal of Inorganic and Nuclear Chemistry, 25(7):783–787, jul 1963.

[53] Tong Wang, Nianxiang Qiu, Xiaodong Wen, Yonghui Tian, Jian He, Kan Luo, Xianhu Zha, Yuhong Zhou, Qing Huang, Jiajian Lang, and Shiyu Du.
First-principles investigations on the electronic structures of U3Si2.
Journal of Nuclear Materials, 469:194–199, feb 2016.

[54] Xiaohong Zhang, Jiajian Lang, Qing Huang, Timothy C. Germann, Yingjie Qiao, Jun Ding, Haigen Gao, and Shiyu Du.
Electronic structures, mechanical properties and defect formation energies of U3Si5 from density functional theory calculations.
Progress in Nuclear Energy, 116:87–94, sep 2019.

[55] V. Kocevski, D. A. Lopes, and T. M. Besmann.
Investigation of the on-site Coulomb correction and temperature dependence of the stability of U–Si phases using DFT+U.
Journal of Nuclear Materials, 524:157–163, oct 2019.

[56] Jin Wen Yang and Li An.
Lattice vibrational behavior and thermodynamic properties of uranium disilicide USi2.
Solid State Communications, 248:47–52, dec 2016.

[57] Yoshihumi Tokiwa, Hisatomo Harima, Dai Aoki, Sayaka Nojiri, Masao Murakawa, Kousaku Miyake, Narumi Watanabe, Rikio Settai, Yoshihiko Inada, Hitoshi Sugawara, Hideyuki Sato, Yoshinori Haga, Etuji Yamamoto, and Yoshichika Onuki.
Fermi Surface Properties of USi 3.
http://dx.doi.org/10.1143/JPSJ.69.1105, 69(4):1105–1112, nov 2013.

[58] S. Krummacher and D. D. Sarma.
XPS studies of the oxidation of USi compounds.
Surface Science, 178(1-3):842–849, dec 1986.

[59] Tingwen Yan, Donghua Xie, Zhilei Chen, Ruilong Yang, Kangwei Zhu, Chunli Jiang, Ce Ma, Jing Liu, Xiaofang Wang, Kezhao Liu, Lizhu Luo, Qifa Pan, and Yin Hu.
Initial oxidation of U3Si2 studied by in-situ XPS analysis.
Journal of Nuclear Materials, 520:1–5, jul 2019.

[60] J.L. Snelgrove, G.L. Hofman, C.L. Trybus, and T.C. Wiencek.
Development of very-high-density fuels by the RERTR program, 1996.

[61] Juan J. Carbajo, Gradyon L. Yoder, Sergey G. Popov, and Victor K. Ivanov.
A review of the thermophysical properties of MOX and UO2 fuels.
Journal of Nuclear Materials, 299(3):181–198, dec 2001.

[62] C. Ronchi, M. Sheindlin, M. Musella, and G. J. Hyland.
Thermal conductivity of uranium dioxide up to 2900 K from simultaneous measurement of the heat capacity and thermal diffusivity.
Journal of Applied Physics, 85(2):776, dec 1998.

[63] J. T. White, A. T. Nelson, D. D. Byler, J. A. Valdez, and K. J. McClellan.
Thermophysical properties of U3Si to 1150 K.
Journal of Nuclear Materials, 452(1-3):304–310, sep 2014.

[64] U. Carvajal Nunez, D. Prieur, R. Bohler, and D. Manara.
Melting point determination of uranium nitride and uranium plutonium nitride: A laser heating study.
Journal of Nuclear Materials, 449(1-3):1–8, jun 2014.

[65] Steven B. Ross, Mohamed S. El-Genk, and R. Bruce Matthews.
Thermal conductivity correlation for uranium nitride fuel between 10 and 1923 K.
Journal of Nuclear Materials, 151(3):318–326, feb 1988.

[66] J. T. White, A. T. Nelson, J. T. Dunwoody, D. D. Byler, D. J. Safarik, and K. J. Mcclellan.
Thermophysical properties of U3Si2 to 1773 K.
Journal of Nuclear Materials, 464:275–280, sep 2015.

[67] J. T. White, A. T. Nelson, D. D. Byler, D. J. Safarik, J. T. Dunwoody, and K. J. McClellan.
Thermophysical properties of U3Si5 to 1773 K.
Journal of Nuclear Materials, 456:442–448, jan 2015.

[68] Sean T. Barlow, Daniel J. Bailey, Adam J. Fisher, Martin C. Stennett, Clémence Gausse, Hao Ding, Viktor A. Krasnov, Sergey Yu Sayenko, Neil C. Hyatt, and Claire L. Corkhill.
Synthesis, characterisation and corrosion behaviour of simulant Chernobyl nuclear meltdown materials.
npj Materials Degradation 2020 4:1, 4(1):1–8, jan 2020.

[69] Tetsuji Imanaka, Gohei Hayashi, and Satoru Endo.
Comparison of the accident process, radioactivity release and ground contamination between Chernobyl and Fukushima.
Journal of Radiation Research, 56, dec 2015.

[70] J. T. White and A. T. Nelson.
Thermal conductivity of UO2+x and U4O9-y.
Journal of Nuclear Materials, 443(1-3):342–350, nov 2013.

[71] M. D. Hou and S. Klaumünzer.
Heavy ion-induced deformation of radiation-amorphized U3Si.
Nuclear Instruments and Methods in Physics Research Section B: Beam Interactions with Materials and Atoms, 209:149–153, aug 2003.

[72] C. Ronchi, M. Sheindlin, D. Staicu, and M. Kinoshita.
Effect of burn-up on the thermal conductivity of uranium dioxide up to 100.000 MWdt-1.
Journal of Nuclear Materials, 327(1):58–76, apr 2004.

[73] Yeon Soo Kim and Gerard L. Hofman.
Interdiffusion in U3Si–Al, U3Si2–Al, and USi–Al dispersion fuels during irradiation.
Journal of Nuclear Materials, 410(1-3):1–9, mar 2011.

[74] R. C. Birtcher, J. W. Richardson, and M. H. Mueller.
Amorphization of U3Si by ion or neutron irradiation.
Journal of Nuclear Materials, 244(3):251–257, apr 1997.

[75] J. Gan, D. D. Keiser, B. D. Miller, J. F. Jue, A. B. Robinson, J. W. Madden, P. G. Medvedev, and D. M. Wachs.
Microstructure of the irradiated U3Si2/Al silicide dispersion fuel.
Journal of Nuclear Materials, 419(1-3):97–104, dec 2011.

[76] Yeon Soo Kim, G. L. Hofman, J. Rest, and A. B. Robinson.
Temperature and dose dependence of fission-gas-bubble swelling in U3Si2.
Journal of Nuclear Materials, 389(3):443–449, jun 2009.

[77] Yinbin Miao, Jason Harp, Kun Mo, Yeon Soo Kim, Shaofei Zhu, and Abdellatif M. Yacout.
Microstructure investigations of U3Si2 implanted by high-energy Xe ions.

Journal of Nuclear Materials, 503:314–322, may 2018.

[78] Yinbin Miao, Jason Harp, Kun Mo, Shaofei Zhu, Tiankai Yao, Jie Lian, and Abdellatif M. Yacout.
Journal of Nuclear Materials, 495:146–153, nov 2017.

[79] Tiankai Yao, Bowen Gong, Lingfeng He, Jason Harp, Michael Tonks, and Jie Lian.
Radiation-induced grain subdivision and bubble formation in U3Si2 at LWR temperature.
Journal of Nuclear Materials, 498:169–175, jan 2018.

[80] D. A. Andersson, X. Y. Liu, B. Beeler, S. C. Middleburgh, A. Claisse, and C. R. Stanek.
Density functional theory calculations of self- and Xe diffusion in U3Si2.
Journal of Nuclear Materials, 515:312–325, mar 2019.

[81] Tiankai Yao, Bowen Gong, Lingfeng He, Yinbin Miao, Jason M. Harp, Michael Tonks, and Jie Lian.
In-situ TEM study of the ion irradiation behavior of U3Si2 and U3Si5.
Journal of Nuclear Materials, 511:56–63, dec 2018.

[82] Hj Matzke.
Rare-gas mobility in some anisotropic ceramic oxides: Al2O3, Cr2O3, Fe2O3, TiO2, U3O8.
Journal of Materials Science 1967 2:5, 2(5):444–456, sep 1967.

[83] Hj Matzke and A. Turos.
Ion implantation studies of UO2 and UN.
Journal of Nuclear Materials, 1992.

[84] Adel Mesbah, Stephanie Szenknect, Nicolas Clavier, Janeth Lozano-Rodriguez, Christophe Poinssot, Christophe Den Auwer, Rodney C. Ewing, and Nicolas Dacheux.
Coffinite, USiO4, Is Abundant in Nature: So Why Is It so Difficult to Synthesize?
Inorganic Chemistry, 54(14):6687–6696, jul 2015.

[85] LR Stieff, TW Stern, AM Sherwood Science, and undefined 1955.
Preliminary description of coffinite—a new uranium mineral.
science.org, 74(3147):17, apr 1952.

[86] V. Pointeau, A. P. Deditius, F. Miserque, D. Renock, U. Becker, J. Zhang, N. Clavier, N. Dacheux, C. Poinssot, and R. C. Ewing.
Synthesis and characterization of coffinite.
Journal of Nuclear Materials, 393(3):449–458, sep 2009.

[87] Ericmoore Jossou, Ubong Eduok, Nelson Y. Dzade, Barbara Szpunar, and Jerzy A. Szpunar.
Oxidation behaviour of U 3 Si 2 : an experimental and first principles investigation.
Physical Chemistry Chemical Physics, 20(7):4708–4720, feb 2018.

[88] issn = 0022-3115 journal = Journal of Nuclear Materials month = feb pages = 245–257 publisher = North-Holland title = Oxidation behaviour of U-Si compounds in air from 25 to 1000 C volume = 484 year = 2017 Sooby Wood, E. and White, J. T. and Nelson, A. T., doi = 10.1016/J.JNUCMAT.2016.12.016.

[89] Tashiema L. Ulrich, Sven C. Vogel, Joshua T. White, David A. Andersson, Elizabeth Sooby Wood, and Theodore M. Besmann.
High temperature neutron diffraction investigation of U3Si2.
Materialia, 9:100580, mar 2020.

[90] R. W. Harrison, C. Gasparrini, R. N. Worth, J. Buckley, M. R. Wenman, and T. Abram.
Corrosion Science, 174:108822, sep 2020.

[91] Kyle Johnson, Valter Strom, Janne Wallenius, and Denise Adorno Lopes.
Oxidation of accident tolerant fuel candidates.
https://doi.org/10.1080/00223131.2016.1262297, 54(3):280–286, mar 2016.

[92] MJ Snyder and WH Duckworth.
Properties of some refractory uranium compounds.
1957.

[93] MA Feraday.
OXIDATION, HYDRIDING, AND AQUEOUS CORROSION OF U Si ALLOYS.
1971.

[94] Jae Ho Yang, Dong Seok Kim, Dong Joo Kim, Sunghwan Kim, Ji Hae Yoon, Heung Soo Lee, Yang Hyun Koo, and Kun Woo Song.
Oxidation and phase separation of U3Si2 nuclear fuel in high-temperature steam environments.
Journal of Nuclear Materials, 542:152517, dec 2020.

[95] D.T. Goddard, D.P. Mathers, D.G. Eaves, P. Xu, E.J. Lahoda, and J.M. Harp.
Manufacturability of U3Si2 and its high temperature oxidation behaviour.
TOPFUEL, 2016.

[96] Adrian Gonzales, Jennifer K. Watkins, Adrian R. Wagner, Brian J. Jaques, and Elizabeth S. Sooby.
Challenges and opportunities to alloyed and composite fuel architectures to mitigate high uranium density fuel oxidation: uranium silicide.
Journal of Nuclear Materials, 553:153026, sep 2021.

[97] R. W. Harrison, R. N. Worth, J. Buckley, and T. Abram.
Atomistic level study of Ce3Si2 oxidation as an accident tolerant nuclear fuel surrogate.

Corrosion Science, 164:108332, mar 2020.

[98] S. C. Middleburgh, A. Claisse, D. A. Andersson, R. W. Grimes, P. Olsson, and S. Mašková. Solution of hydrogen in accident tolerant fuel candidate material: U3Si2. *Journal of Nuclear Materials*, 501:234–237, apr 2018.

[99] Silvie Mašková, Khrystyna Miliyanchuk, and Ladislav Havela. Hydrogen absorption in U3Si2 and its impact on electronic properties. *Journal of Nuclear Materials*, 487:418–423, apr 2017.

[100] A. P. Shivprasad, V. Kocevski, T. L. Ulrich, J. R. Wermer, D. A. Andersson, and J. T. White. The u3si2-H system. *Journal of Nuclear Materials*, 558:153278, jan 2022.

[101] E. Sooby Wood, J. T. White, C. J. Grote, and A. T. Nelson. U3Si2 behavior in H2O: Part I, flowing steam and the effect of hydrogen. *Journal of Nuclear Materials*, 501:404–412, apr 2018.

[102] A. T. Nelson, A. Migdisov, E. Sooby Wood, and C. J. Grote. U3Si2 behavior in H2O environments: Part II, pressurized water with controlled redox chemistry. *Journal of Nuclear Materials*, 500:81–91, mar 2018.

[103] E. Sooby Wood, J. T. White, and A. T. Nelson. The effect of aluminum additions on the oxidation resistance of U3Si2. *Journal of Nuclear Materials*, 489:84–90, jun 2017.

[104] Afiqa Mohamad, Tiankai Yao, Bowen Gong, Jason Harp, Adrian R. Wagner, Andrew T. Nelson, and Jie Lian. Aluminum-doped U3Si2 composite fuels with enhanced oxidation resistance. *Journal of Alloys and Compounds*, 853:157319, feb 2021.

[105] Afiqa Mohamad, Bowen Gong, Tiankai Yao, Adrian R. Wagner, Michael T. Benson, and Jie Lian. 3Y-TZP Toughened and Oxidation-resistant U3Si2 Composites for Accident Tolerant Fuels. *Journal of Nuclear Materials*, 544:152691, feb 2021.

[106] Bowen Gong, Lu Cai, Penghui Lei, Kathryn E. Metzger, Edward J. Lahoda, Frank A. Boylan, Kun Yang, Jake Fay, Jason Harp, and Jie Lian. Cr-doped U3Si2 composite fuels under steam corrosion. *Corrosion Science*, 177:109001, dec 2020.

[107] Kweon Ho Kang, Keon Sik Kim, Kil Jeong Kim, Yong Chil Seo, and Young Moo Park.

Oxidation behavior of U3Si (3.9 wt% Si) in air at 250-400°C.
Journal of Nuclear Materials, 228(2):220–226, mar 1996.

[108] S. Sunder, N. H. Miller, and D. W. Shoesmith.
Corrosion of uranium dioxide in hydrogen peroxide solutions.
Corrosion Science, 46(5):1095–1111, may 2004.

[109] D W Shoesmith.
Used Fuel and Uranium Dioxide Dissolution Studies-A Review.
Technical report, 2007.

[110] G Choppin, JO Liljenzin, and J Rydberg.
Radiochemistry and nuclear chemistry.
4th edition, 2002.

[111] Ross Springell, Sophie Rennie, Leila Costelle, James Darnbrough, Camilla Stitt, Elizabeth Cocklin, Chris Lucas, Robert Burrows, Howard Sims, Didier Wermeille, Jonathan Rawle, Chris Nicklin, William Nuttall, Thomas Scott, and Gerard Lander.
Water corrosion of spent nuclear fuel: Radiolysis driven dissolution at the UO2/water interface.
Faraday Discussions, 180(0):301–311, jul 2015.

[112] E. Lawrence Bright, S Rennie, A Siberry, K. Samani, K. Clarke, D. T. Goddard, and R. Springell.
Comparing the corrosion of uranium nitride and uranium dioxide surfaces with H 2 O 2.
Journal of Nuclear Materials, 518:202–207, 2019.

[113] D. W. Shoesmith and S. Sunder.
The prediction of nuclear fuel (UO2) dissolution rates under waste disposal conditions.
Journal of Nuclear Materials, 190(C):20–35, aug 1992.

[114] S. Sunder, D. W. Shoesmith, and N. H. Miller.
Oxidation and dissolution of nuclear fuel (UO2) by the products of the alpha radiolysis of water.
Journal of Nuclear Materials, 244(1):66–74, mar 1997.

[115] R. T. Sweet, Y. Yang, K. A. Terrani, B. D. Wirth, and A. T. Nelson.
Performance of U3Si2 in an LWR following a cladding breach during normal operation.
Journal of Nuclear Materials, 539:152263, oct 2020.

[116] Sophie Le Caër.
Water Radiolysis: Influence of Oxide Surfaces on H2 Production under Ionizing Radiation.
Water 2011, Vol. 3, Pages 235-253, 3(1):235–253, feb 2011.

[117] Arthur T. Motta and Long Qing Chen.
Hydride formation in zirconium alloys.
JOM, 64(12):1403–1408, dec 2012.

[118] Annika Carolin Maier, Anna Benarosch, Ghada El Jamal, and Mats Jonsson.
Radiation induced dissolution of U 3 Si 2 - A potential accident tolerant fuel.
Journal of Nuclear Materials, 517:263–267, apr 2019.

[119] O Glasser.
Wilhelm Conrad Röntgen and the early history of the Roentgen rays.
1993.

[120] Mark Ladd and Rex Palmer.
Structure determination by X-ray crystallography: Analysis by X-rays and neutrons.
Springer US, jan 2013.

[121] Johanna M. Wagner.
X-ray photoelectron spectroscopy.
Number December. Nova Science Publishers,, New York :, 2011.

[122] Kenneth S. Krane.
Introductory nuclear physics.
John Wiley and Sons, 2014.

[123] David. Schmool.
Solid State Physics.
Mercury Learning and Information,, 2016.

[124] D Als-Nielsen, J; McMorrow.
Elements pf Modern X-ray Physics.
2nd edition, 2011.

[125] C. Suryanarayana, M. Grant Norton, C. Suryanarayana, and M. Grant Norton.
Crystal Structure Determination. II: Hexagonal Structures.
In *X-Ray Diffraction*, pages 125–152. Springer US, 1998.

[126] PhysicsOpenLab.
Bremsstrahlung Radiation | PhysicsOpenLab, 2017.

[127] C Kittel.
Introduction to solid state physics. Fifth edition.
Wiley, 1976.

[128] HM Rosenberg.
The Solid State: An Introduction to the Physics of Crystals for Students of Physics.
Materials Science, and Engineering, 3rd ed.(Oxford University Press, Oxford, New York, 1988), 1988.

[129] N. Anderson.
Motion of Charged Particles in Electromagnetic Fields.
Springer, Boston, MA, 1968.

[130] F. (Franz) Mandl.
Quantum mechanics.
Wiley,, Chichester [England] ;, 1992.

[131] P Hofmann.
Solid state physics.
Wiley, 2 edition, 2015.

[132] M. Björck, G. Andersson, and IUCr.
GenX: an extensible X-ray reflectivity refinement program utilizing differential evolution.
urn:issn:0021-8898, 40(6):1174–1178, nov 2007.

[133] M Yasaka The Rigaku Journal and undefined 2010.
X-ray thin-film measurement techniques.
eng.uc.edu.

[134] L. G. Parratt.
Surface Studies of Solids by Total Reflection of X-Rays.
Physical Review, 95(2):359, jul 1954.

[135] L. Névot and P. Croce.
Caractérisation des surfaces par réflexion rasante de rayons X. Application à l'étude du polissage de quelques verres silicates.
Revue de Physique Appliquée, 15(3):761–779, 1980.

[136] S. K. Sinha, E. B. Sirota, S. Garoff, and H. B. Stanley.
X-ray and neutron scattering from rough surfaces.
Physical Review B, 38(4):2297–2311, 1988.

[137] Krassimir Stoev and Kenji Sakurai.
Recent theoretical models in grazing incidence X-ray reflectometry.
The Rigaku J, 14(2):22–37, 1997.

[138] C. J. Foot.

Atomic physics.
Oxford master series on atomic, optical and laser physics. Oxford University Press,, Oxford ;, 2005.

[139] Thomas Gouder and Ladislav Havela.
Examples of Quantification in XPS on 5f Materials.
Microchimica Acta 2002 138:3, 138(3):207–215, 2002.

[140] John Wolstenholme.
Auger electron spectroscopy : practical application to materials analysis and characterization of surfaces, interfaces, and thin films.
Momentum Press,, 2015.

[141] N Fairley, A Carrick, and N Fairly.
The casa cookbook.
2005.

[142] Woodruff, D.P. Delchar, T.A.
Modern Techniques of Surface Science — Second Edition.
Cambridge University Press, first edition, 1986.

[143] Paul S. Bagus and Eugene S. Ilton.
Theory for the XPS of Actinides.
Topics in Catalysis, 12(56):1121–1128, aug 2013.

[144] T. Gouder.
Electronic structure of uranium overlayers on magnesium and aluminium.
Surface Science, 382(1-3):26–34, jun 1997.

[145] J. J. Yeh and I. Lindau.
Atomic Data and Nuclear Data Tables, 32(1):1–155, jan 1985.

[146] M. Sayer and K. Sreenivas.
Ceramic Thin Films: Fabrication and Applications.
Science, 247(4946):1056–1060, mar 1990.

[147] Kiyotaka. Wasa, Makoto. Kitabatake, and Hideaki. Adachi.
Thin film materials technology : sputtering of compound materials.
William Andrew Pub., 2004.

[148] R. Springell, R. C. C. Ward, J. Bouchet, J. Chivall, D. Wermeille, P. S. Normile, S. Langridge, S. W. Zochowski, and G. H. Lander.
Malleability of uranium: Manipulating the charge-density wave in epitaxial films.
Physical Review B, 89(24):245101, jun 2014.

[149] D. Chaney, A. Castellano, A. Bosak, J. Bouchet, F. Bottin, B. Dorado, L. Paolasini, S. Rennie, C. Bell, R. Springell, and G. H. Lander.
Tuneable correlated disorder in alloys.
Physical Review Materials, 5(3):035004, mar 2021.

[150] E. Lawrence Bright, S. Rennie, M. Cattelan, N. A. Fox, D. T. Goddard, and R. Springell.
Epitaxial UN and α-U2N3 thin films.
Thin Solid Films, 661:71–77, sep 2018.

[151] IAEA.
IAEA Safety Standards for protecting people and the environment Regulations for the Safe Transport of Radioactive Material No. SSR-6 (Rev.1).
2018.

[152] PF Fewster.
X-Ray scattering from semiconductors and other materials.
2015.

[153] A Garg.
Growth and characterization of epitaxial oxide thin films.
2001.

[154] LW Martin, YH Chu, R Ramesh Materials Science R, Engineering:, and undefined 2010.
Advances in the growth and characterization of magnetic, ferroelectric, and multiferroic oxide thin films.
Elsevier.

[155] C.E. MOROSANU.
Evolution of CVD Films.
Thin Films by Chemical Vapour Deposition, pages 19–27, jan 1990.

[156] Donald M. Mattox.
Handbook of Physical Vapor Deposition (PVD) Processing.
Elsevier Inc., 2010.

[157] Milton Ohring.
Materials science of thin films : deposition and structure.
Academic Press, San Diego, CA :, 2002.

[158] R. Springell.
Growth and characterisation of uranium multilayers.
PhD thesis, 2008.

[159] Peter Taylor.
Thermodynamic and kinetic aspects of UO2 fuel oxidation in air at 400–2000 K.
Journal of Nuclear Materials, 344(1-3):206–212, sep 2005.

[160] J. M. Purswani, T. Spila, and D. Gall.
Growth of epitaxial Cu on MgO(001) by magnetron sputter deposition.
Thin Solid Films, 515(3):1166–1170, nov 2006.

[161] Qiancheng Liu, Xianming Zhou, Xiaolong Zeng, and SN Luo.
Sound velocity, equation of state, temperature and melting of lif single crystals under shock compression.
Journal of Applied Physics, 117(4):045901, 2015.

[162] K. Momma, F. Izumi, and IUCr.
Vesta.
urn:issn:0021-8898, 44(6):1272–1276, oct 2011.

[163] K. J.S. Sokhey, S. K. Rai, and G. S. Lodha.
Oxidation studies of niobium thin films at room temperature by X-ray reflectivity.
Applied Surface Science, 257(1):222–226, oct 2010.

[164] Chiara Gattinoni and Angelos Michaelides.
Atomistic details of oxide surfaces and surface oxidation: the example of copper and its oxides.
Surface Science Reports, 70(3):424–447, nov 2015.

[165] JT White, AT Nelson, JT Dunwoody, DD Byler, and KJ McClellan.
Thermophysical properties of usi to 1673 k.
Journal of Nuclear Materials, 471:129–135, 2016.

[166] T Le Bihan, H Noël, and P Rogl.
Crystal structure of the uranium monosilicide usi.
Journal of alloys and compounds, 240(1-2):128–133, 1996.

[167] John Walton, Paul Wincott, Neal Fairley, and Alan Carrick.
Peak Fitting with CasaXPS: A Casa Pocket Book.
Accolyte Science, 2010.

[168] S. Van Den Berghe, F. Miserque, T. Gouder, B. Gaudreau, and M. Verwerft.
X-ray photoelectron spectroscopy on uranium oxides: A comparison between bulk and thin layers.
In *Journal of Nuclear Materials*, volume 294, pages 168–174. North-Holland, apr 2001.

[169] F. J. Himpsel, F. R. McFeely, A. Taleb-Ibrahimi, J. A. Yarmoff, and G. Hollinger. Microscopic structure of the SiO2/Si interface. *Physical Review B*, 38(9):6084–6096, sep 1988.

[170] Artaches Migdisov, Haylea Nisbet, Nan Li, Joshua White, Hongwu Xu, Andrew Nelson, and Robert Roback. Instability of U3Si2 in pressurized water media at elevated temperatures. *Communications Chemistry 2021 4:1*, 4(1):1–6, may 2021.

[171] G. Hollinger and F. J. Himpsel. Multiple-bonding configurations for oxygen on silicon surfaces. *Physical Review B*, 28(6):3651, sep 1983.

[172] Shin Ichi Fujimori, Yasuharu Saito, Ken Ichirou Yamaki, Tetsuo Okane, Noriaki Sato, Takemi Komatsubara, Shoji Suzuki, and Shigeru Sato. Photoemission study of the U/Si(111) interface. *Surface Science*, 444(1-3):180–186, jan 2000.

[173] Carl E Lowell, Charles A Barrett, Raymond W Palmer, Judith V Auping, and Hubert B Probst. Cosp: a computer model of cyclic oxidation. *Oxidation of Metals*, 36(1):81–112, 1991.

[174] JL Smialek, DT Jayne, JC Schaeffer, and WH Murphy. Effects of hydrogen annealing, sulfur segregation and diffusion on the cyclic oxidation resistance of superalloys: a review. *Thin solid films*, 253(1-2):285–292, 1994.

[175] A. Berche, C. Rado, O. Rapaud, C. Guéneau, and J. Rogez. Thermodynamic study of the U–Si system. *Journal of Nuclear Materials*, 389(1):101–107, may 2009.

[176] Xiaofeng Guo, Stéphanie Szenknect, Adel Mesbah, Sabrina Labs, Nicolas Clavier, Christophe Poinssot, Sergey V. Ushakov, Hildegard Curtius, Dirk Bosbach, Rodney C. Ewing, Peter C. Burns, Nicolas Dacheux, and Alexandra Navrotsky. Thermodynamics of formation of coffinite, USiO4. *Proceedings of the National Academy of Sciences of the United States of America*, 112(21):6551–6555, may 2015.

[177] Tingwen Yan, Donghua Xie, Zhilei Chen, Ruilong Yang, Kangwei Zhu, Chunli Jiang, Ce Ma, Jing Liu, Xiaofang Wang, Kezhao Liu, Lizhu Luo, Qifa Pan, and Yin Hu. Initial oxidation of U3Si2 studied by in-situ XPS analysis. *Journal of Nuclear Materials*, 520:1–5, jul 2019.